Testing and application of luminescence techniques using sediment from the southeast African coast

Simon James Armitage

Thesis submitted in fulfilment of the requirements for the degree of PhD

University of Wales Aberystwyth
March 2003

DECLARATION

This work has not previously been accepted in substance for any degree and is not being concurrently submitted in candidature for any degree

Signed.....(candidate)

Date.....

STATEMENT 1

This thesis is the result of my own investigations, except where otherwise stated.

Other sources are acknowledged by explicit references. A bibliography is appended.

Signed.....(candidate)

Date.....

STATEMENT 2

I hereby give consent for my thesis, if accepted, to be available for photocopying and for inter-library loan, and for the title and summary to be made available to outside organisations.

Signed.....(candidate)

Date.....

Contents

Declaration i

Contents ii

Chapter 1: Introduction 1

1.1 Overview and aims 1

1.2 Sediment dating using luminescence 1

1.3 The mechanism by which luminescence is produced 2

1.4 TL traps in quartz 4
1.4.1 Thermal stability of electrons in TL traps 5

1.5 The OSL signal from quartz 6
1.5.1 The relationship between OSL and the 325°C TL signal 7
1.5.2 OSL derived from geologically unstable traps 9
1.5.2.1 OSL from traps filled by photo-transfer of charge 10
1.5.2.2 Thermal transfer to the OSL trap (recuperation) 12
1.5.3 OSL from geologically stable traps 13

1.6 Sensitivity change in quartz 17
1.6.1 The Zimmerman model for sensitivity change in quartz 18
1.6.1.1 L-centres 19
1.6.1.2 R-centres associated with the OSL signal 19
1.6.1.3 R-centres associated with the 110°C TL signal 20
1.6.1.4 Electron transfer pathways used by the OSL and 110°C TL traps 21

1.7 Summary 22

Chapter 2: Measurement procedures, sample preparation and equipment 24

2.1 Introduction 24

2.2 The single-aliquot regenerative-dose measurement procedure 24
2.2.1 Preheat 25
2.2.2 OSL measurement 26
2.2.3 Test dose 26
2.2.4 Cut heat 27
2.2.5 Regeneration doses 27

2.3 Sample collection and preparation 27
2.3.1 Sample collection 27

2.3.2 Quartz separation 28
2.3.3 Aliquot preparation 29
2.3.4 Assessment of sample purity using infra-red stimulation 30

2.4 Luminescence measurement and irradiation equipment 31
2.4.1 Computer control of the TL/OSL reader 31
2.4.2 β irradiators 31
2.4.2.1 Risø β source calibrations 33
2.4.2.2 Daybreak β source calibrations 34
2.4.2.3 Risø β source performance 34
2.4.3 Optical stimulation sources 35
2.4.3.1 Risø blue LED sources used in this study 36
2.4.3.2 Blue LED stimulation power 38
2.4.3.3 Cross-bleaching 39

2.5 Samples used in this study 39
2.5.1 Inhaca and Bazaruto Islands, Mozambique 40
2.5.2 Maputaland dosimetry samples 41
2.5.3 Miscellaneous samples 41

2.6 Summary 42

Chapter 3: Validation of the SAR technique 43

3.1 Introduction 43
3.1.1 Standard measurement conditions 44

3.2 D_e values for modern samples 44
3.2.1 Measured data 46
3.2.2 Modelled data 47

3.3 Repeated regeneration points 47

3.4 Zero dose point luminescence measurements 51

3.5 Dose recovery experiments 53

3.6 Elevated temperature stimulation 55

3.7 D_e variation with PH1 temperature 56

3.8 Conclusions 57

Chapter 4: Equivalent dose variation with stimulation time 59

4.1 Introduction 59
4.1.1 Previous work 59

4.2 Samples and measurement equipment 59

4.3 $D_e(t)$ plots using integrated luminescence intensities 60

4.4 Possible causes for $D_e(t)$ plot dependence on PH1 temperature 61

4.5 Evidence for the presence of a geologically unstable OSL signal 62

4.6 Evidence for charge accumulation during SAR measurement sequences 63

4.7 Investigating the relative importance of charge accumulation and the loss of geologically unstable charge using a modified SAR method 64
4.7.1 $D_e(t)$ and replacement plots produced using a modified SAR method 66
4.7.2 Summary and discussion 67

4.8 Inappropriate sensitivity correction using long signal integration periods 67

4.9 Thermal stability of the geologically unstable trap 68

4.10 Which signal integration period yields the correct value of D_e? 70

4.11 Discussion 71

4.12 Conclusions 72

Chapter 5: Sensitivity changes in quartz **73**

5.1 Introduction 73

5.2 Characterising the pattern of sensitivity change during an SAR measurement sequence 73
5.2.1 Sensitivity changes observed using a repeated single regeneration dose 74
5.2.2 Possible causes for the sensitivity changes observed 75
5.2.3 Sensitivity changes in individual aliquots 78

5.3 SAR sensitivity correction 79
5.3.1 Preheat dependence of sensitivity correction 80
5.3.2 R_x reproducibility derived from repeated regeneration dose data 81

5.4 Sensitivity changes observed during D_e measurement sequences 82

5.5 Monitoring sensitivity changes using the 110°C TL peak 84

5.6 Thermal stability of the 110°C TL signal 85
5.6.1 Calculations 86
5.6.2 Discussion 88
5.6.3 110°C TL peak order 88
5.6.4 Erosion of the 110°C TL signal at laboratory temperatures 89

5.7 110°C TL peak saturation 91
5.7.1 Sensitivity correction for repeated regeneration points 92
5.7.2 Sensitivity corrected growth curves for the 110°C TL signal 92

5.8 Use of the 110°C TL peak to monitor OSL sensitivity change 94
5.8.1 Implications for electron transfer pathways used by charge from the OSL and 110°C TL traps 95
5.9 Conclusions 96

Chapter 6: Equivalent dose determination 98

6.1 Introduction 98

6.2 Growth curves 98
6.2.1 Measured growth curves 98
6.2.2 The standardised growth curve 99

6.3 Measured D_e distributions 100
6.3.1 Patterns in the D_e distributions 101

6.4 Likely causes of scatter for aeolian sediments 101
6.4.1 Modelling the minimum achievable scatter 102
6.4.2 Sources of scatter in the datasets presented in this study 104
6.4.3 Large dose distributions obtained from older samples 107
6.4.4 The natural luminescence intensity "misses" the growth curve 108
6.4.4.1 Restricted regeneration dose range 109
6.4.4.2 Measurement reproducibility 110
6.4.4.3 Inappropriate sensitivity correction of the natural luminescence intensity 110
6.4.4.4 Inappropriate sensitivity correction of the regenerated luminescence intensities 113
6.4.4.5 Discussion 114

6.5 Calculation of the sample D_e from an SAR dataset 114
6.5.1 Best estimate of the sample equivalent dose 115
6.5.2 Calculated equivalent doses 116

6.6 Conclusions 118

Chapter 7: Environmental dose rate evaluation 119

7.1 Introduction 119
7.1.1 Radiation derived from the bulk sediment matrix 119
7.1.2 Cosmic radiation 120

7.2 Methods for assessing radioisotope concentrations and cosmic ray dose rate 120
7.2.1 Thick-source alpha counting 121
7.2.2 GM-beta counting 122
7.2.3 Atomic absorption spectrophotometry 122

7.2.4 Calculation of dose rates 123
7.2.5 Cosmic ray dose rates 123

7.3 Comparison of AAS and TSAC/GM-beta derived potassium concentrations 123

7.4 Assessment of water content during burial 124

7.5 Post depositional alteration of the environmental dose rate 125
7.5.1 Changes in overburden thickness 126
7.5.2 Carbonate cementation/leaching 126

7.6 Environmental dose rates for dated samples 128

7.7 Conclusions 128

Chapter 8: Geological setting and evolution of Inhaca and Bazaruto Islands, Mozambique **129**

8.1 Introduction 129

8.2 Geological setting and evolution of the southeast coast of Africa 129
8.2.1 The Maputaland coastal plain 129
8.2.2 The Maputaland lithostratigraphic group 130
8.2.3 Present climate 133
8.2.4 Marine geology 134
8.2.5 Past and present sediment status of the Maputaland coast 135
8.2.5.1 Sediment supply 136
8.2.5.2 Sediment transport 136
8.2.5.3 Sediment sinks 136
8.2.6 Late Quaternary sea-level history of the southeast African coast 137
8.2.6.1 Which Holocene sea-level curve is most appropriate for this study? 137
8.2.6.2 Calibration of the radiocarbon ages presented by Ramsay (1995) 138

8.3 Inhaca Island 139
8.3.1 Description of the main dune ridges and sample sites 139
8.3.1.1 Luminescence ages and discussion 140
8.3.1.2 Do the main dune ridges represent one or more depositional event? 141
8.3.2 Description of the interior of Inhaca Island and sample sites 142
8.3.2.1 Luminescence ages and discussion 142
8.3.2.2 Sediment supply to the centre of Inhaca 144
8.3.3 A model for the evolution of Inhaca Island 145

8.4 Bazaruto Island 146
8.4.1 Description of the sample sites on Bazaruto 147
8.4.1.1 Zingalema Point 147
8.4.1.2 Interior Dune 147
8.4.1.3 Parabolic dune limb 147
8.4.1.4 Northern tip of Bazaruto 148
8.4.1.5 Sailfish Bay 148

8.4.2 Luminescence ages and discussion 148
8.4.3 A model for the evolution of Bazaruto Island 150

8.5 Conclusions 151

Chapter 9: general conclusions and recommendations for further study 152

9.1 Introduction 152

9.2 General conclusions 152

9.3 Suggested topics for further research 154

References 156

Acknowledgements 166

Appendix 2.1 Glossary of shorthand terms used to describe actions and measurements performed during standard SAR sequences

Appendix 6.1 Equivalent dose error analysis using Analyst and LD Base

Appendix 7.1 Dose rate calculations: A worked example

Appendix 7.2 Alpha counting data

Appendix 7.3 Beta counting data

Appendix 8.1 Radiocarbon calibration

Figures

Chapter 1: Introduction **Preceding Page**

1.1 Energy level diagram for TL production 3
1.2 A configuration coordinate diagram illustrating the process of thermal assistance in quartz 6
1.3 Typical quartz OSL curve 6
1.4 The bleach response spectra of the 514.5μm stimulated OSL signal 7
1.5 The light sums of the OSL decay curves and separated 325°C TL peaks 8
1.6 Pulse anneal curves for sample WIDG8 8
1.7 TL curves for dosed and bleached quartz 9
1.8 OSL decay curves measured at various temperatures 12
1.9 3 exponential components separated from an OSL decay curve 13
1.10 A pulse annealing curve for an aliquot of bleached natural quartz 15
1.11 An energy level diagram for quartz 16
1.12 A contour map of the 3D TL spectrum from quartz 19

Chapter 2: Measurement procedures, sample preparation and equipment

2.1 A typical growth curve 25
2.2 Block diagrams showing computer control of the Risø reader 31
2.3 Switch off times for various Risø stimulation sources 37
2.4 Emission spectrum for the blue LEDs and filters used in this study 37
2.5 Initial and complete decay curves for an aliquot of natural quartz 38
2.6 A map showing the location of the three main study areas 39

Chapter 3: Validation of the SAR technique

3.1 A plot of D_e versus PH1 temperature for a sample of Aber/40-SA10 46
3.2 Recycling ratio versus sensitivity change and PH1 temperature 48
3.3 Normalised sensitivity versus cycle number for aliquots of Aber/28-IN19 48
3.4 OSL intensity versus PH1 temperature for two aliquots of Aber/40-SA10 49
3.5 Recuperation versus PH1 temperature for three samples 51
3.6 Growth curves for aliquots of Aber/28-IN22 55
3.7 Elevated and room temperature OSL from bleached quartz 56
3.8 D_e versus PH1 temperature for selected samples 57

Chapter 4: Equivalent dose variation with stimulation time

4.1 Typical decay curves measured using Risø 1 60
4.2 Typical decay curves measured using Risø 2 60
4.3 A $D_e(t)$ plot for Aber/28-IN16 for a range of PH1 temperatures 61
4.4 $D_e(t)$ plots for individual aliquots of Aber/28-IN16 61
4.5 Normalised OSL decay curves for aliquots of Aber/28-IN16 62
4.6 Replacement plots for Aber/28-IN21 64

4.7 Replacement plots for Aber/28-IN12 64
4.8 A $D_e(t)$ plot for Aber/28-IN16, using standard and modified SAR methods 66
4.9 Replacement plots for Aber/28-IN21, using the modified SAR method 66
4.10 $D_e(t)$ and R_1 replacement plots for CalQtz 68
4.11 D_e versus PH1 temperature plots using various signal integrationintervals 70

Chapter 5: Sensitivity changes in quartz

5.1 Relative sensitivity versus measurement cycle, using a 10 Gy regeneration dose 74
5.2 Relative sensitivity versus measurement cycle, using 0 and 50 Gy regeneration doses 74
5.3 Inter aliquot variability in the size of sensitivity changes during a constant regeneration dose SAR sequence 78
5.4 Sensitivity corrected luminescence intensities versus measurement cycle for three aliquots of Aber/12-MAP3 78
5.5 Sensitivity corrected luminescence intensities versus measurement cycle for aliquots of Aber/12-MAP3 and Aber/29-BA14, using various regeneration doses 80
5.6 Sensitivity corrected luminescence intensities versus measurement cycle for two aliquots of Aber/29-BA14 81
5.7 R_x variability versus PH1 temperature 81
5.8 Relative sensitivity versus measurement cycle for routing SAR measurement sequences 82
5.9 ln (I/I_o) versus time for an aliquot of Aber/29-BA14 held at 60°C 87
5.10 ln (m) versus $1/T$ for an aliquot of Aber/29-BA14 87
5.11 ln (T_m^2/β) versus $1/T_m$ for an aliquot of Aber/29-BA14 87
5.12 An isothermal decay curve plotted on It versus ln$t$ coordinates 88
5.13 Uncorrected and corrected 110°C TL intensities using a constnt regeneration dose of 15 Gy 92
5.14 TL curves measured in response to a 1 Gy test dose 92
5.15 Sensitivity-corrected 110°C TL growth curves 93
5.16 Sensitivity corrected OSL intensity versus measurement cycle using the 110°C TL signal as a proxy for OSL sensitivity 94

Chapter 6: Equivalent dose determination

6.1 A selection of growth curves 98
6.2 SGC D_e versus SAR D_e for 14 samples from Inhaca and Bazaruto Islands 100
6.3 D_e distributions for the majority of samples dated during this study 101
6.4 Modelled scatter versus equivalent dose 103
6.5 Scatter versus D_e for samples measured in this study 103
6.6 Growth curves for individual aliquots of Aber/28-IN1 107
6.7 Growth curves for two aliquots of Aber/29-BA14 108
6.8 A plot showing the percentage of aliquots where modelled L_n/T_n does not intercept the growth curve, versus equivalent dose 110
6.9 D_e/known dose versus test dose for aliquots of Aber/28-IN21 111
6.10 Aliquots where L_n/T_n dose not intercept the growth curve versus PH1 113
6.11 Calculated D_e/population mean D_e versus population mean D_e 115

Chapter 7: Environmental dose rate evaluation

7.1	^{40}K decay	119
7.2	^{232}Th decay series	119
7.3	^{235}U decay series	119
7.4	^{238}U decay series	119
7.5	Maximum spheres of influence for various radiation types	120
7.6	Sealed/unsealed TSAC ratios	122
7.7	The effect of water content on environmental dose rate	124

Chapter 8: Geological setting and evolution of Inhaca and Bazaruto Islands, Mozambique

8.1	An annotated satellite photograph of the Maputaland coastal plain	129
8.2	The Maputaland Stratigraphic group	131
8.3	All year wind rose for Maputaland	133
8.4	The main ocean currents around southern Africa	136
8.5	Annual swell observations for Maputaland	136
8.6	Eddy of the Mozambique Current in Maputo Bay	136
8.7	A map showing the location of sites used by Ramsay and Cooper (2002) to produce their Southern African Late Quaternary sea-level curve.	137
8.8	The Late Quaternary sea-level curve for southern Africa	137
8.9	Alternative Holocene sea-level curves for southern Africa	137
8.10	A modified version of Ramsay's (1995) sea-level curve	138
8.11	Geology and sample sites on Inhaca Island	139
8.12	OSL ages shown on the modified version of Ramsay's sea-level curve	142
8.13	Holocene shorelines of Bazaruto Island	146
8.14	Geology and sample sites on Bazaruto Island	147

Photographs

		Preceding page
8.1	Cabo Inhaca	139
8.2	The palaeo-tidal flat at the northern end of Inhaca	142
8.3	The sea-cliff at Zingalema Point	147

Tables

Chapter 1: Introduction **Preceding Page**

1.1 Estimates of the thermal stability of the traps responsible for the OSL and 325°C TL signals 9
1.2 Half lives and fractional contributions to the total signal of the fast, medium and slow components of the natural OSL decay curve 14

Chapter 2: Measurement procedures, sample preparation and equipment

2.1 The standard SAR measurement sequence 24
2.2 Standard Aberystwyth mask sizes and capacities 29
2.3 Risø reader specifications 32
2.4 Risø β source calibrations 33
2.5 Daybreak irradiator dose rates 34
2.6 Risø β source performance 35
2.7 Stimulation wavelengths of a selection of OSL stimulation sources 35
2.8 Optical half-lives and stimulation powers for the blue LED stimulation sources used in this study 38
2.9 Cross bleaching energies for the readers used in this study 39
2.10 Brief descriptions of the samples taken from Inhaca Island. 40
2.11 Brief descriptions of the samples taken from Bazaruto Island 41
2.12 Brief descriptions of the samples taken from Maputaland 41
2.13 Brief descriptions of the samples used in the study, which were not collected by the author 41

Chapter 3: Validation of the SAR technique

3.1 Standard measurement conditions used during this study 44
3.2 Mean equivalent dose estimates for four modern samples 47
3.3 Commands received by a Risø TL/OSL reader to perform a 300°C preheat 50
3.4 Results of dose recovery experiments performed on a variety of samples 54

Chapter 4: Equivalent dose variation with stimulation time

4.1 Sample details and equivalent doses measured using standard and modified SAR measurement procedures 60

Chapter 5: Sensitivity changes in quartz

5.1 Measurement sequences for the two trap depth determination methods used in this study 86
5.2 Kinetic parameters for the 110°C TL peak trap 87
5.3 Electron lifetimes in the 110°C TL peak trap at various temperatures 89

5.4 Percentage decay of the 110°C TL signal for various storage times 90
5.5 Measurement sequence for the 110°C TL growth curve 91
5.6 Measurement sequence designed to compare OSL sensitivity correction procedures using the 110°C ($T_{x(TL)}$) and OSL ($T_{x(OSL)}$) responses to a constant test dose 94

Chapter 6: Equivalent dose determination

6.1 Principal causes of scatter and their remedies 104
6.2 Aliquots where the natural signal does not intercept the growth curve 109
6.3 Final D_e estimates for samples from Inhaca Island 117
6.4 Final D_e estimates for samples from Bazaruto Island 117

Chapter 7: Environmental dose rate determinations

7.5 Potassium contents determined using TSAC/GM-beta counting and AAS 124
7.6 Modern percentage water content 125
7.7 Dose rates to a sample before and after carbonate cementation 127
7.8 Depth, radioisotope and water content values for sample from Inhaca Island 128
7.9 Equivalent dose, dose rates and ages for samples from Inhaca Island 128
7.10 Depth, radioisotope and water content values for sample from Bazaruto Island 128
7.11 Equivalent dose, dose rates and ages for samples from Bazaruto Island 128

Chapter 8: Geological setting and evolution of Inhaca and Bazaruto Islands, Mozambique

8.1 A geologic timescale 130
8.2 Descriptions and ages for samples taken from the main dune ridges on Inhaca Island 140
8.3 Descriptions and ages for samples taken from the parabolic dunes and palaeo-tidal flat 143
8.4 Descriptions and ages for samples taken from Bazaruto Island 148

Chapter 1: Introduction

1.1 Overview and aims

This thesis contains two main parts. The first part aims to determine the most appropriate method for producing an age for sedimentary quartzes using optically stimulated luminescence (OSL). This work concentrates on testing and applying the single-aliquot regenerative-dose (SAR) technique (Murray and Wintle, 2000), using samples from the southeast coast of Africa. Measurement conditions and data manipulation techniques have been studied, and a range of parameters which yield acceptable results for the samples measured have been identified. In addition, methods for determining the environmental dose rate have been compared.

The second section of this thesis uses the SAR technique to date samples from the Mozambican islands of Inhaca and Bazaruto. These islands are composed of large dunes, and these were dated, in an attempt to understand the evolution of each island in relationship to previously published records of sea-level change.

The remainder of this chapter is intended to provide the reader with a summary of the theoretical framework within which this luminescence research has been conducted. Significantly more detailed summaries are provided by Aitken (1985, 1998), Taylor and Aitken (1997), Stokes (1999) and Wintle (1996).

1.2 Sediment dating using luminescence

The luminescence methods constitute a family of techniques[a] which assess the total ionizing radiation dose (palaeodose) absorbed by mineral grains during burial. This radiation exposure occurs due to the decay of radioisotopes within the sediment. Ionizing cosmic rays may also be significant. In an ideal sedimentary environment the radiation flux (environmental dose rate) is constant, and consequently

---

[a] In geochronological studies using quartz, TL and OSL are the most commonly measured luminescence signals. A variety of luminescence wavelengths and measurement sequences have been used for both signals, and hence "luminescence dating" cannot be regarded as a single technique.

the age of the mineral grain may be calculated thus:

Age = Palaeodose / Environmental dose rate (1.1)

Mineral grains (usually quartz or feldspar owing to their ubiquity) retain a record of the radiation dose which they have absorbed. This record consists of electrons that have been evicted from the stable ground state and trapped at metastable defect sites within the crystal lattice. The trapped charge population is proportional to the total radiation dose absorbed by the mineral. When energy is added to the crystal (stimulation), electrons may be detrapped and returned to the ground state. This electron movement is accompanied by the emission of light (luminescence) proportional to the number of electrons detrapped. Stimulation may be by either heat or light, with the resulting luminescence being termed thermoluminescence (TL) or optically stimulated luminescence (OSL) respectively. In the laboratory, this "natural" luminescence signal is measured using a photomultiplier tube. By comparing this signal with signals induced by known laboratory radiation doses, an estimate of the palaeodose (termed the equivalent dose, D_e) is produced.

Subaerial movement of sedimentary mineral grains leads to these grains being exposed to sunlight. This detraps electrons trapped by prior exposure to ionizing radiation. Provided that the sunlight exposure is long enough, it reduces the luminescence signal to a negligible level (termed bleaching or zeroing). On burial, the mineral grain is no longer exposed to sunlight, and the luminescence signal grows. Consequently, the age produced by a luminescence dating method, is the time elapsed since the mineral grain was last exposed to sunlight, i.e. formation of the geomorphological unit from which the sample was extracted.

1.3 The mechanism by which luminescence is produced

Although the specific detail of the luminescence mechanism is not fully understood, there is some consensus on the nature of the fundamental processes involved. These are best discussed with reference to an energy level diagram (Figure 1.1), which represents the electronic environment of the mineral grain. During exposure to ionizing radiation

(irradiation, Figure 1.1(i)), either during burial or in the laboratory, electrons acquire sufficient energy to become detached from their parent atoms (where they were said to have been in the valence band). These electrons diffuse around the crystal lattice, and are described as being in the conduction band. Subsequently, a proportion of the electrons transferred to the conduction band, are captured by electron traps[b] (T in Figure 1.1). These are defects in the crystal lattice, capable of storing charge. The parent atom, from which the electron has been detached is said to be charged with a hole. This hole (electron vacancy) diffuses freely in the valence band, and can be trapped at a hole trap. When this occurs the hole trap is said to have been activated and is termed a recombination centre, since recombination of electrons can only occur at such a site when there is an electron vacancy.

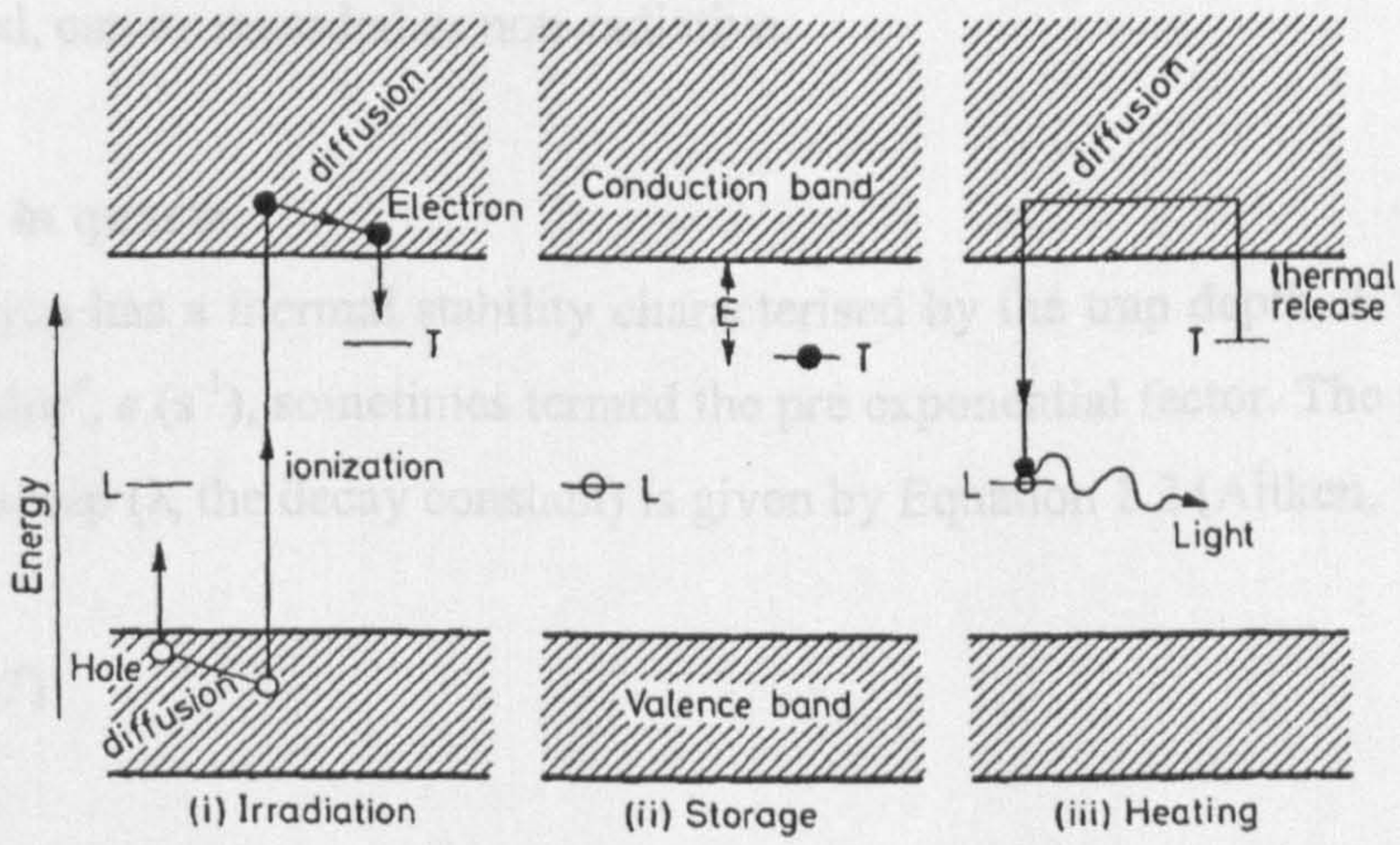

Figure 1.1. A simple energy-level representation of TL production for a single trap/luminescence centre pair (from Aitken, 1985). Filled circles represent electrons while open circles represent an electron deficiency. T is the TL trap, E its thermal depth and L the luminescence centre which it uses.

Figure 1.1 (ii) shows the storage of electrons in traps during burial of the crystal. As will be discussed in Section 1.4.1, the lifetime of the electron in a trap is dictated by its depth below the conduction band (E) and storage temperature.

---

[b] A significant proportion of these electrons recombine at luminescence centres instead of finding traps, resulting in radioluminescence.

Figure 1.1 (iii) illustrates the process by which thermoluminescence occurs. Increased lattice vibrations, caused by heating the crystal, allow the electron to be released from the trap into the conduction band. The electron then diffuses through the conduction band and subsequently recombines at an activated recombination centre (L in Figure 1.1). During recombination, energy is dissipated as a photon, whose energy is characteristic of the recombination centre itself.

In practice two groups of recombination centre exist. The first group, termed radiative recombination centres or luminescence centres (L-centres), emit a photon on recombination. The second group are non-radiative recombination centres, also termed reservoir centres (R-centres) and do not emit a photon during recombination. For practical purposes, L-centres which emit photons outside the waveband measured by the apparatus used, can be regarded as non-radiative.

1.4 TL traps in quartz

An electron trap has a thermal stability characterised by the trap depth, E (eV[c]) and the frequency factor[d], s (s^{-1}), sometimes termed the pre exponential factor. The probability of escape from a trap (λ, the decay constant) is given by Equation 1.2 (Aitken, 1985, p48),

$$\lambda = s \exp(E/kT) \qquad (1.2)$$

where k is Boltzmann's constant[e] and T is temperature (K). Other factors being equal, the TL intensity is proportional to the probability of electron escape, multiplied by the number of electrons remaining trapped. Using a linear heating rate (ramp rate) the TL intensity, due to eviction of electrons from a single trap, rises to a maximum and then decreases to zero. This process results in a TL signal reaching its maximum intensity at a temperature (T_m), characteristic of the trap stability and ramp rate.

---

[c] 1 eV = 1.60×10^{-19} J (Aitken, 1985).
[d] This is usually thought to be close to the lattice vibration frequency, c.10^{12} – 10^{14} s^{-1} (Chen and McKeever, 1997, p20).
[e] $k = 1.38 \times 10^{-23}$ J/K (Aitken, 1985).

In practice quartz contains several electron traps, and hence a plot of TL intensity versus temperature (glow curve) contains several TL peaks. Traps (and TL peaks) are generally identified by their characteristic T_m using a ramp rate of 5°C/s. Peaks at 110, 160, 210, 280, 325, 375 and 480°C are commonly observed in quartz under these conditions, although other peaks exist (see for example Petrov and Bailiff (1995)).

1.4.1 Thermal stability of electrons in TL traps

For the purposes of dating sedimentary deposits, it is important that negligible loss of charge from the trap used has occurred during burial of the sample. The mean residence time of electrons in a single trap (lifetime, τ) is a useful measure of the thermal stability of the trap, and can be calculated using Equation 1.3 (Aitken, 1985, p50),

$$\tau = \lambda^{-1} \qquad (1.3)$$

When the radiation dose is absorbed in a single event prior to storage, as in laboratory irradiation and accident dosimetry, the number of electrons trapped after storage (n_t) for time t, is related to the number of electrons trapped at $t = 0$ (n_o) by Equation 1.4 (Aitken, 1985, p50)

$$n_t = n_o \exp(-t/\tau) \qquad (1.4)$$

However, in dating, the number of trapped electrons on burial is zero, and increases at a uniform rate thereafter. In this case, the proportion of electrons trapped during burial, which remain trapped after burial period t, is given by Equation 1.5 (Aitken, 1985, p59).

$$n_t = (\tau/t)(1-\exp(-t/\tau)) \qquad (1.5)$$

In practice, Aitken (1985) suggests a figure of 5 % as the maximum loss of electrons acceptable over the burial period. For burial periods of c.100 ka, this precludes the use of TL traps giving rise to peaks below 265°C (Godfrey-Smith, 1994).

1.5 The OSL signal from quartz

OSL is produced when electrons are detrapped as a result of photon absorption, and recombine at L-centres. The thermal depth of the trap (E) does not describe its optical stability (Aitken, 1998). The detrapping process is strongly wavelength dependent, with shorter wavelengths causing higher eviction rates (Spooner *et al.*, 1988, and Spooner, 1994).

At a given stimulation power and wavelength, the rate of optical eviction of electrons increases rapidly as the stimulation temperature increases. This phenomenon is termed thermal assistance, and is believed to occur since charge in the OSL trap has access to a number of excited levels, to which it can be thermally raised (Bailey *et al.*, 1997, and Figure 1.2). This effectively reduces the optical trap depth as stimulation temperature increases, allowing more rapid photoeviction of electrons. Similarly, electrons can be raised to the conduction band from excited states by lower energy photons than those required for eviction from the ground state.

The above discussion assumes that electrons are evicted via a single photon-absorption mechanism. This has been demonstrated to be the case for quartz by Spooner (1994), who showed that luminescence intensity increased linearly when stimulation power was varied over three orders of magnitude.

During stimulation, the signal intensity decreases with illumination time and is consequently termed a decay curve (Figure 1.3). At a constant stimulation power, the OSL signal from a single trap should decay exponentially with time (Bailey *et al.*, 1997). However, non-exponential OSL decay curves appear to be the norm, and have been reported by several authors, notably Huntley *et al.* (1985), Smith *et al.* (1986), Bailey *et al.* (1997) and Murray and Wintle (1998). This indicates that several traps, with different optical stabilities, contribute to the OSL signal. Since optical stability is not determined by thermal stability, any or all of these traps could be unstable over geological time, and hence not suitable for dating applications. Consequently, the signal induced by laboratory irradiation may not be comparable with that from natural irradiation. To circumvent this

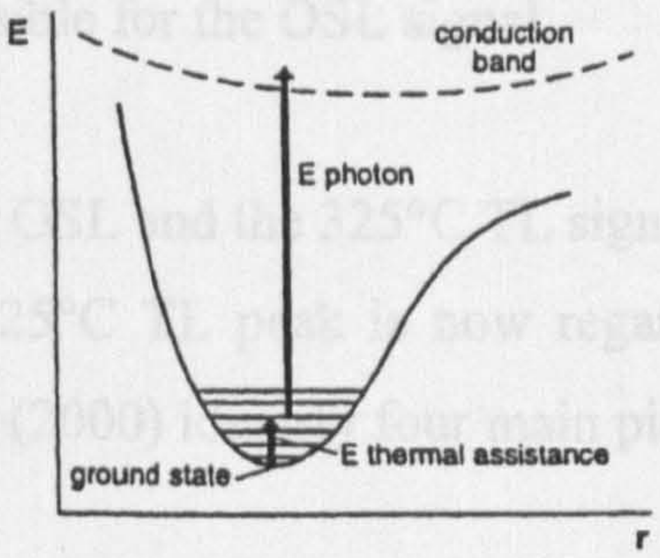

Figure 1.2. A configuration coordinate diagram illustrating the process of thermal assistance in optical eviction of charge from an electron trap (from Spooner, 1994).

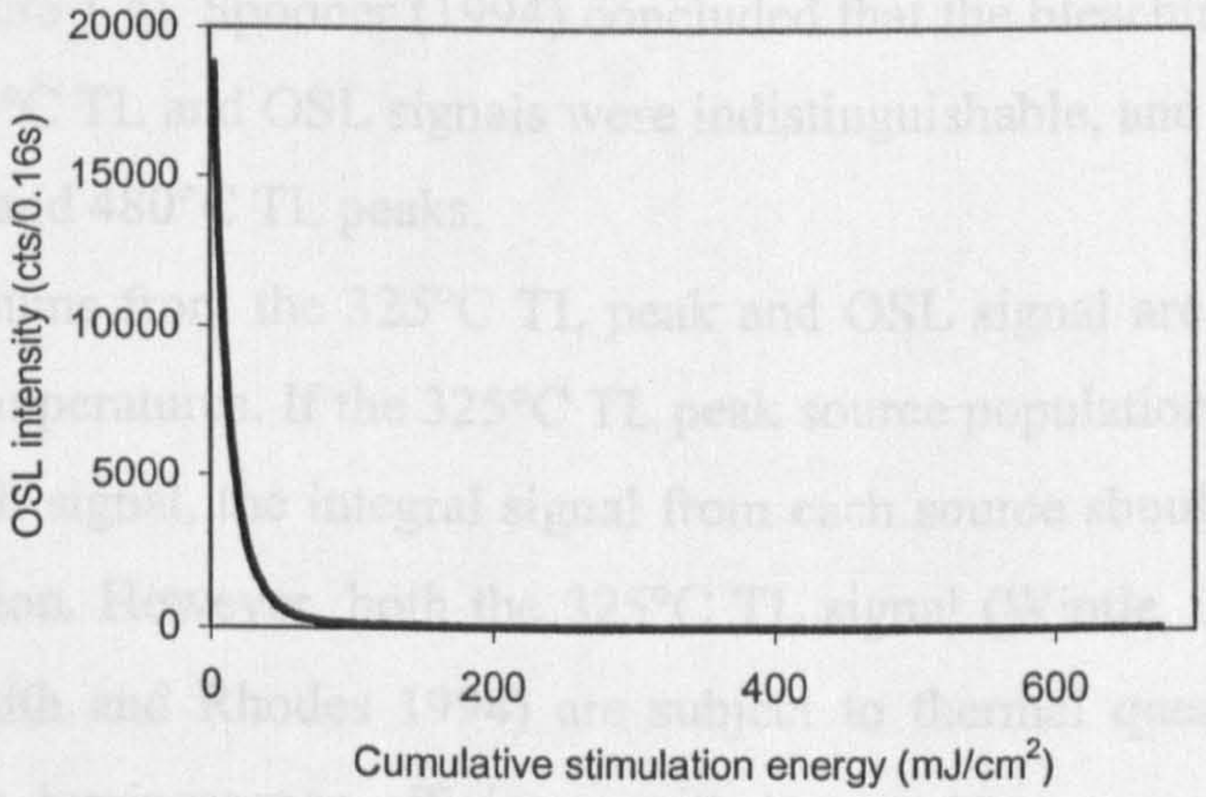

Figure 1.3. A typical quartz OSL decay curve. This curve was measured from a natural aliquot of sample Aber/28-IN16, at a stimulation temperature of 125°C, using a Risø blue-LED stimulation source (see Chapter 2).

potential problem, samples have traditionally been heated (preheating) prior to measurement of the OSL, to thermally deplete all geologically unstable traps. However, the exact thermal treatment required has been extremely contentious (Roberts *et al.*, 1994, and Stokes, 1996). Consequently, considerable research effort has been expended identifying the TL traps responsible for the OSL signal.

1.5.1. The relationship between OSL and the 325°C TL signal

The trap responsible for the 325°C TL peak is now regarded as being the main OSL source trap. Wintle and Murray (2000) identify four main pieces of evidence for this.

1) The two signals have similar bleaching response spectra. Spooner (1994) illuminated aliquots of sedimentary quartz using a range of narrow wavebands ranging from c.400-900 nm, to characterize the bleaching response spectrum of the OSL signal[f]. These data were compared with the results of similar experiments performed by Spooner *et al.* (1988) on the 325, 370 and 480°C TL peaks (Figure 1.4). Spooner (1994) concluded that the bleaching response spectra for the 325°C TL and OSL signals were indistinguishable, and distinct from those of the 370 and 480°C TL peaks.
2) The light sums from the 325°C TL peak and OSL signal are equal over a wide range of temperatures. If the 325°C TL peak source population is the same as that for the OSL signal, the integral signal from each source should be identical after normalization. However, both the 325°C TL signal (Wintle, 1975) and the OSL signal (Smith and Rhodes 1994) are subject to thermal quenching. This is the decrease in luminescence efficiency with temperature, caused by the increased probability of non-radiative recombination at L-centres (Wintle, 1975). Consequently, during conventional TL and OSL measurements, the two signal intensities cannot be compared since they are measured at different temperatures. Spooner (1994) used a range of ramp rates to shift the 325°C TL[g] peak to

---

[f] Measured at room temperature using 514.5 nm stimulation.

[g] The rapidly bleachable 325°C TL peak was "separated" from the slow bleaching TL signals, using a separate, bleached aliquot to characterize the slow bleaching signal (Franklin and Hornyak, 1990 and Spooner, 1994).

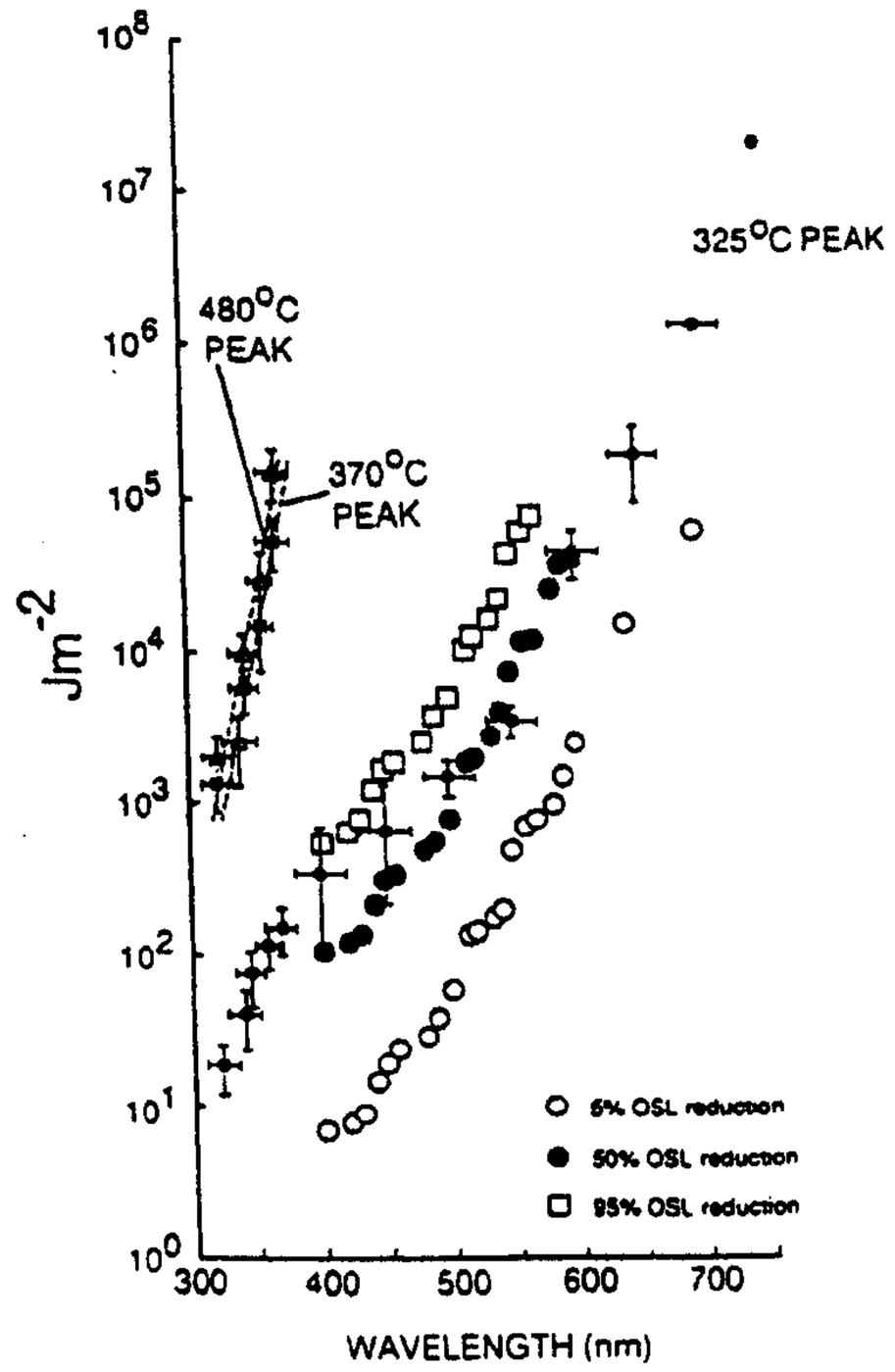

Figure 1.4. The bleach response spectra of the 514.5 nm stimulated OSL signal. The TL data are energies required to completely remove the 325°C TL peak, or reduce the 370 or 480°C peaks to 80% of their initial intensity. From Spooner (1994).

temperatures between 200 and 350°C. These data were compared with OSL (measured using 514.5 nm stimulation) integrals obtained at stimulation temperatures ranging from c.20-250°C. Over the range of comparable temperatures, the two signal intensities were indistinguishable (Figure 1.5).

3) The OSL and 325°C TL signals have similar thermal stabilities. Wintle and Murray (1998) made a series of measurements to characterize the sensitivity change and thermal erosion of the quartz OSL trap. Single aliquots were preheated to 160°C for 10 s and then illuminated for 0.1s, during which the OSL intensity was observed. Using the same aliquot, this procedure was repeated using sequentially higher temperature preheats in 10°C steps. Each illumination was estimated to reduce the OSL signal by <0.2%, and thus signal intensity changes were caused primarily by changes in sensitivity (see Section 1.6), or the thermal erosion of charge from the OSL trap(s). Their results are shown in Figure 1.6 (their Figure 7c). Below c. 250°C, sensitivity changes dominate the observed signal; however above this temperature, both natural and irradiated aliquots showed a rapid decrease in signal intensity until at c. 330°C the signal intensity was reduced to <1% of its initial value. These data suggested (qualitatively) that the OSL signal has a similar thermal stability to the 325°C TL signal. Quantitative estimates of the stability of the OSL signal were attempted, but these were subsequently rejected. Murray and Wintle (1999a) produced isothermal decay curves for aliquots which had been stored at elevated temperatures for up to 22 hours. Datasets were produced for natural (N), bleached and irradiated (N+β) and heated and irradiated (500°C+β) aliquots. Each dataset was corrected for sensitivity changes which occurred during storage (Wintle and Murray, 1999). Corrected datasets were fitted using three exponential terms[h], from which trap depths and frequency factors were calculated. Values of E and s for the main trap (trap A of Murray and Wintle, 1999a) are given in Table 1.1. They are in good

[h] The minimum number of exponential terms required to fit these data was three, suggesting that three separate traps contributed to the OSL signal observed. The decay observed in all three datasets is dominated by a single trap, (trap A of Murray and Wintle, 1999a, discussed here). The OSL signal due to the other two traps (B and C) is discussed in Sections 1.5.2 and 1.5.3.

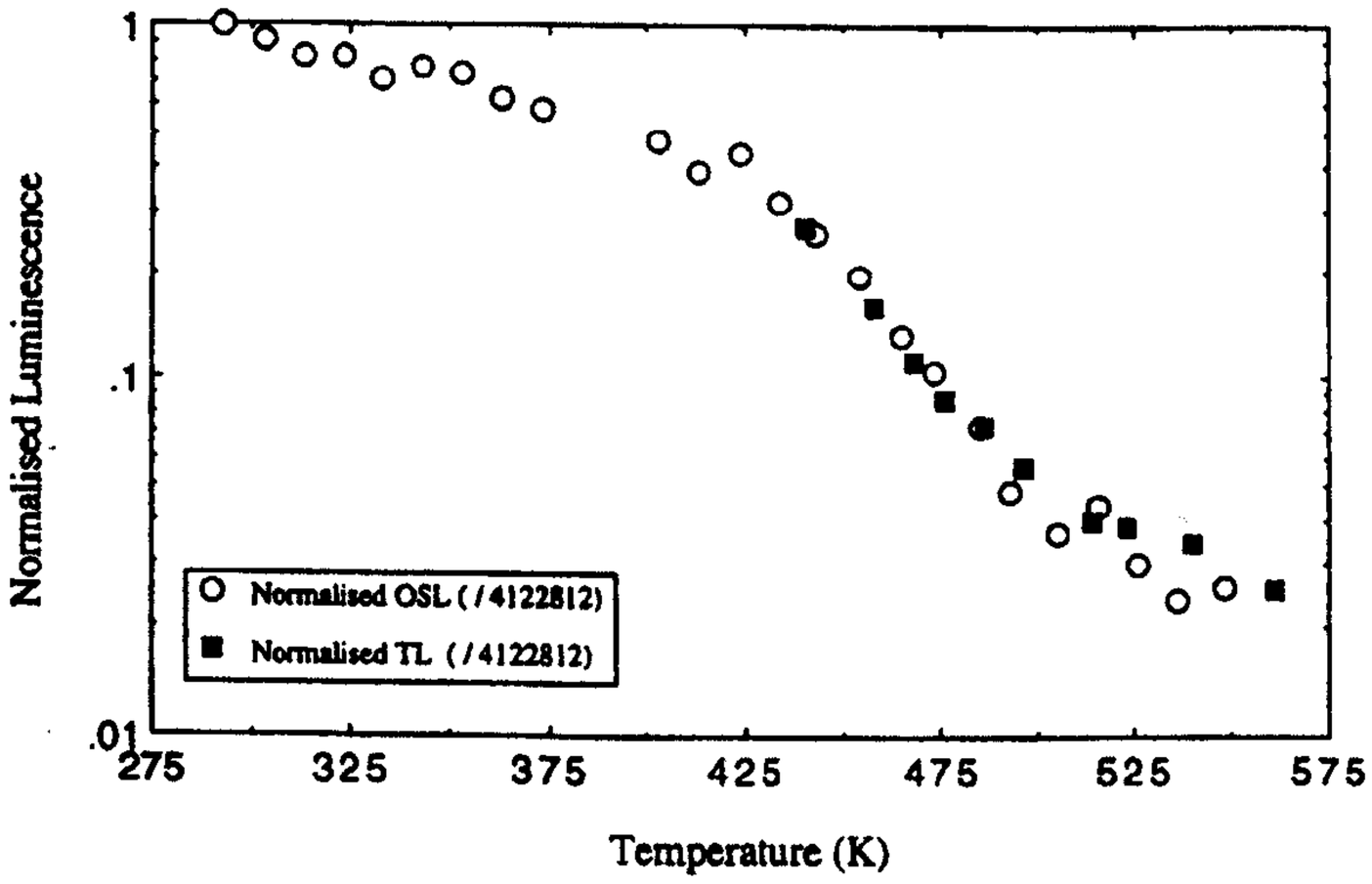

Figure 1.5. The light sums of OSL decay curves and separated "325°C" TL peaks. All data are normalised to the OSL light sum obtained stimulating at 20°C. From Spooner (1994).

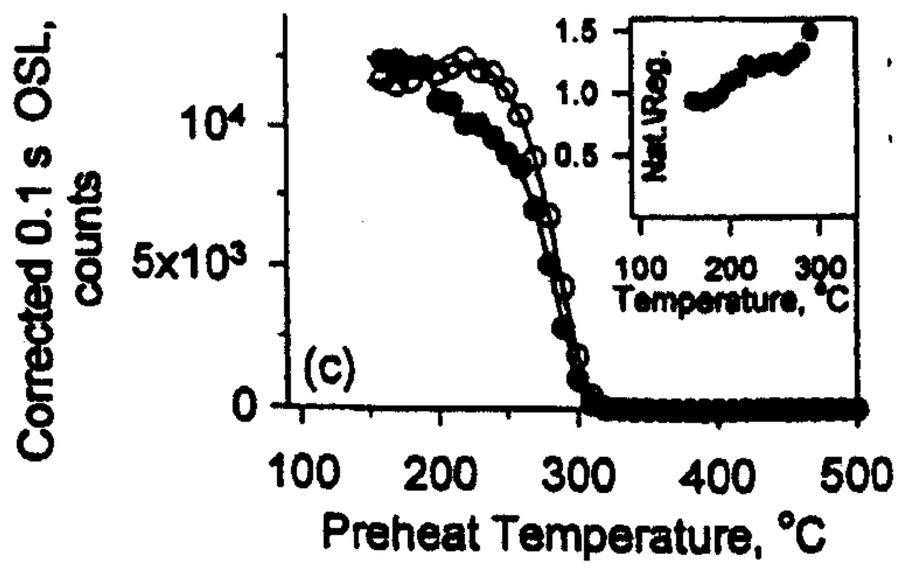

Figure 1.6. Pulse anneal curves for sample WIDG8, a sedimentary quartz (from Wintle and Murray, 1998).Open circles, natural luminescence. Solid circles, the aliquot was optically bleached at 125°C for 200s and then given a 56 Gy dose prior to measurement. Sensitivity changes were monitored using the 110°C TL peak response to a small test dose, prior to each short shine measurement.

agreement with E and s values for the 325°C peak trap, and other estimates for the OSL trap.

4) Illumination of quartz results in "loss" of signal from the 325°C region of the glow curve. Smith *et al.* (1986) measured the glow curve from an aliquot of irradiated natural (N + 40Gy β) quartz. This was compared with the glow curve from a similar aliquot, which had been exposed to the 514 nm line (1.5 J/cm^2) from an argon-ion laser. The only high temperature peak which was reduced in intensity by this treatment, was that at 325°C, leading them to conclude that the corresponding trap was the main OSL source trap. A similar experiment carried out by Wintle and Murray (1997), using a mixed blue-green stimulation source (420-575 nm), yielded comparable results. However, a significant "loss" of TL was also observed at c.150 and 400°C (Figure 1.7).

Signal	Method	E (eV)	s (s^{-1})	τ_{20} (a)	Reference
OSL	Isothermal decay	1.65 ± 0.01	2.7E + 13	2.8E + 7	Huntley *et al.* (1996)
OSL	Isothermal decay	1.66 ± 0.03	1E +13	1.1E + 8	Murray and Wintle (1999a)
OSL	Isothermal decay	1.59	2.8E + 12	2.1E + 7	Spooner and Questiaux (2000)
325°C TL	Isothermal decay	1.7 ± 0.1	-	c. 3E +7	Wintle (1975), Wintle (1977)
325°C TL	Hoogenstraaten's	1.69 ± 0.02	-	c. 3E +7	Wintle (1975), Wintle (1977)
325°C TL	Isothermal decay	1.60	5.7E + 12	1.7E + 7	Spooner and Questiaux (2000)
325°C TL	Hoogenstraaten's	1.65	3.9E + 13	2.0E + 7	Spooner and Questiaux (2000)

Table 1.1. Estimates of the thermal stability of the traps responsible for the OSL and 325°C TL signals in quartz. The values given by Huntley *et al.* (1996) and Murray and Wintle (1999a) relate to the trap contributing the largest signal. Thermal stabilities calculated by Rhodes (1990, quoted in Smith *et al.* (1990a)) and Wintle and Murray (1998) are both significantly higher than those presented in Table 1.1. Neither of these studies used a sensitivity correction, leading Murray and Wintle (1999a) to suggest that the discrepancy is caused by sensitivity change.

1.5.2. OSL derived from geologically unstable traps

Although the main OSL trap appears to be that responsible for the 325°C TL peak, other traps may be significant under certain circumstances. Charge in the traps responsible for relatively low temperature TL peaks (<c.250°C) is geologically unstable. Consequently, these peaks are not observed in samples irradiated in nature. However, laboratory irradiation occurs very rapidly in comparison with that in nature, and hence TL peaks at

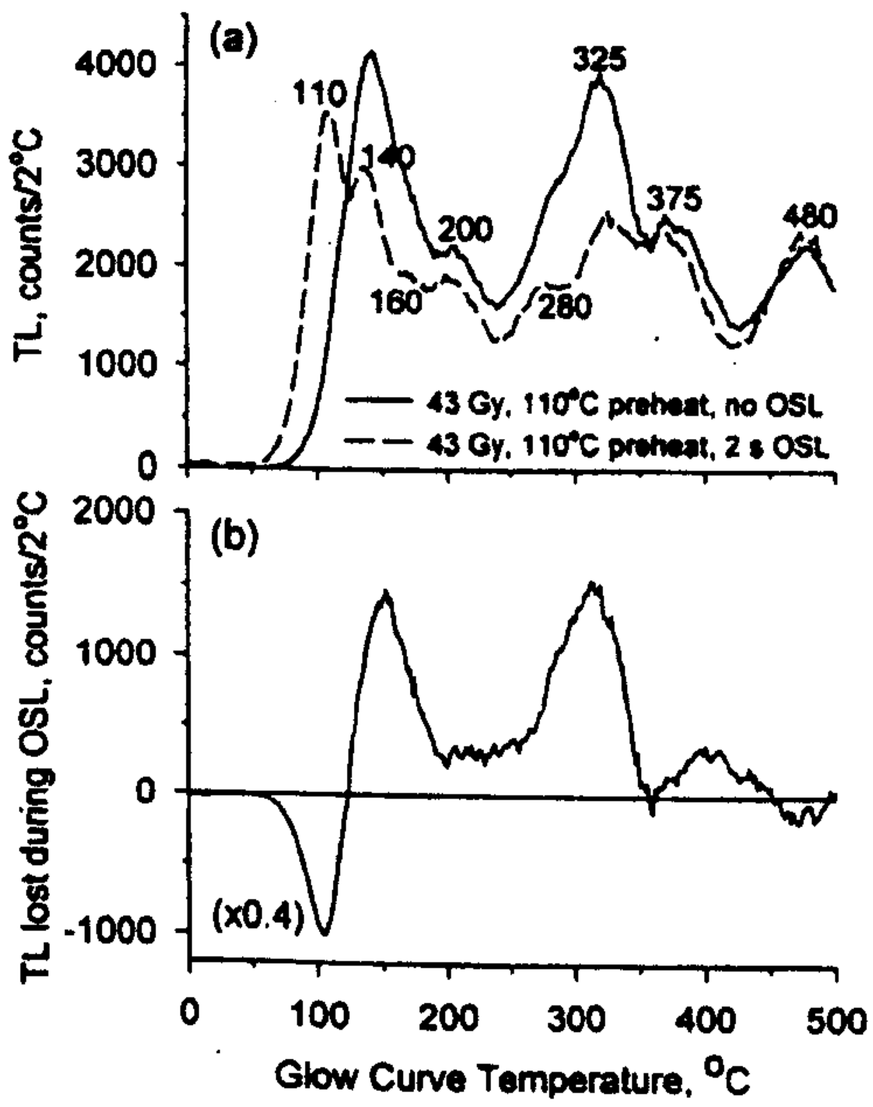

Figure 1.7. a) TL curves from quartz which had been bleached, given a dose of 43 Gy, and preheated to 110°C for 10s. Solid line, TL measured immediately after preheating. Dashed line, the aliquot was bleached for another two seconds prior to measurement of the TL. b) The difference between the two curves shown in (a), showing the TL "lost" and "gained" during the 2 s bleaching. From Wintle and Murray (1997).

110, 160 and 220°C are commonly observed in glow curves measured immediately after irradiation. Consequently, these traps may contribute to the OSL signal from irradiated, but not natural aliquots.

Isothermal OSL decay studies performed on irradiated aliquots have demonstrated that thermally unstable traps filled by laboratory irradiation may contribute a significant proportion of the total OSL signal under certain circumstances. Godfrey-Smith (1994) monitored the luminescence intensity of three sedimentary quartzes for 68 days after irradiation. Two of the samples showed a significant decrease in intensity (approximately one third) over the first few days of storage at 15°C. She fitted this data to the isothermal decay equation (Equation 1.4), and predicted a TL peak temperature of 110°C[i]. Murray and Wintle (1999a) measured isothermal decay curves at a range of temperatures between 160 and 280°C, for both irradiated and natural samples. They found that three traps were required to describe the isothermal decay data obtained from irradiated aliquots, while only two were required for natural aliquots. The additional trap required for the irradiated data had a lifetime at 20°C of c.380 years, and accounted for approximately one third of the total OSL signal from these aliquots. They predicted that, at a ramp rate of 5°C/s, this peak would give a TL peak at around 290°C[j]. Both studies demonstrate that, for these samples at least, some form of preheating is required if luminescence intensities from natural and artificially irradiated aliquots are to be compared.

1.5.2.1. OSL from traps filled by photo-transfer of charge

During optical stimulation, electrons are released from their traps into the conduction band. Electrons in the conduction band may either recombine, be re-trapped in their original optically stimulable trap, or become trapped in a different trap[k]. The latter process gives rise to thermoluminescence signals from traps which were not populated prior to illumination, and is consequently referred to as photo-transferred thermoluminescence (PTTL). Smith and Rhodes (1994) demonstrated that phototransfer

---

[i] τ for this sample was 1.48×10^{-2} years, an order of magnitude larger than the values cited by Aitken (1985) for the 110°C peak.

[j] Spooner and Questiaux (2000) calculated a lifetime (at 20°C) of 160,000 years for the 280°C TL peak in quartz.

[k] Assuming a delocalised conduction band, see Section 1.6.1.3.

into the 110, 160 and 210°C TL peak traps occurred during stimulation with 514 nm light, while Figure 1.7 indicates some PTTL at c.480°C using mixed blue-green illumination. If the PTTL peak traps are optically stimulable, photo-transfer will reduce the initial OSL intensity, since these traps compete with the recombination centres for charge. Subsequent optical stimulation of photo-transferred charge will lead to an increase in the OSL intensity in the latter part of the decay curve. Smith and Rhodes (1994) observed that, for their sample, the intensity of the photo-transferred TL at 160 and 210°C was less than 2% of that at 110°C. Consequently, the majority of research has concentrated on the lowest temperature peak.

Smith and Rhodes (1994) noted that the size of the 110°C PTTL peak first increased and then decreased with increasing laser exposure times. They also calculated the relative probability of charge being transferred to the 110°C TL region by comparing the OSL emitted during photo-transfer with the resultant 110°C TL. With increasing laser exposure, the ratio of TL counts to integrated OSL counts fell from an initial value of 0.087 to 0.042 at 2 ks. After observing the PTTL induced by a 2 ks laser exposure, they repeated a short measurement and obtained a TL:OSL ratio of 0.087. Since the 110°C TL peak intensity did not exceed 10% of its saturation value, they concluded that the decrease in TL:OSL ratio with laser exposure was caused by thermal and/or optical eviction of charge. These data may also be explained by a decrease in radiative recombination probability, caused by deactivation of L-centres caused by recombination of optically detrapped charge (optical desensitization, see also Section 1.6.1). Bailey (1997) measured the relative sensitivity of the 110°C TL peak after a range of OSL measurement times (0-1075s), and concluded that for his sample a 9% loss of luminescence centres occurred following depletion of the OSL signal to 1% of the initial intensity. This occurred in the first 75s of illumination, and no further loss of luminescence centres was noted. Bailey (1997) demonstrated that the 110°C TL trap was optically bleachable by comparing the loss of PTTL with time for two sets of aliquots. Both had been bleached for 75s to complete photo-transfer and loss of luminescence centres. One was then stored under OSL excitation light, while the other was stored in the dark. Those aliquots stored in the dark displayed only thermal depletion of charge, while

the illuminated aliquots were subject to both optical and thermal depletion. By subtracting the former from the latter, Bailey (1997) produced an optical decay curve for the 110°C TL peak. These data were fitted to an exponential decay and yielded an optical half-life of ~600s under his experimental conditions (~12mW/cm^2, 420-560nm @ 25°C).

Wintle and Murray (1997) demonstrated that, for their experimental conditions, the dose-induced 110°C TL peak had an optical lifetime of 132s at 24°C. They estimated that in this time, thermal decay reduced the peak area by less than 3%. Therefore, it seems likely that the optical stimulation of charge from this trap has a more significant effect on OSL production at room temperature than thermal decay. Since Wintle and Murray (1997) demonstrated that the optical bleaching characteristics of the 110°C PTTL and dose-induced 110°C TL peaks were indistinguishable, this observation is likely to apply to both sources of charge.

Wintle and Murray (1997) also studied the bleaching of the 160°C PTTL peak, and concluded that it was relatively insensitive to optical stimulation compared with the 110°C peak. This, combined with its higher thermal stability and smaller trapping cross-section relative to the 110°C trap, suggests that the 160°C TL peak should not have a significant effect on the production of OSL from quartz.

Murray and Wintle (1998) investigated the variation in decay curve shape with stimulation temperature (Figure 1.8). They found that the decay curve shape changed dramatically between 50 and 100°C. Wintle and Murray (1998) suggested that at 100°C and above, the 110°C TL trap remained almost empty. Consequently, the decay rate was greater, since retrapping and subsequent stimulation from the 110°C TL trap did not occur.

1.5.2.2 Thermal transfer to the OSL trap (recuperation)

When thermal depopulation of an electron trap occurs, a proportion of the charge promoted to the conduction band becomes retrapped. This leads to an increase in the electron population of traps more stable than the initial donor trap, and is termed thermal

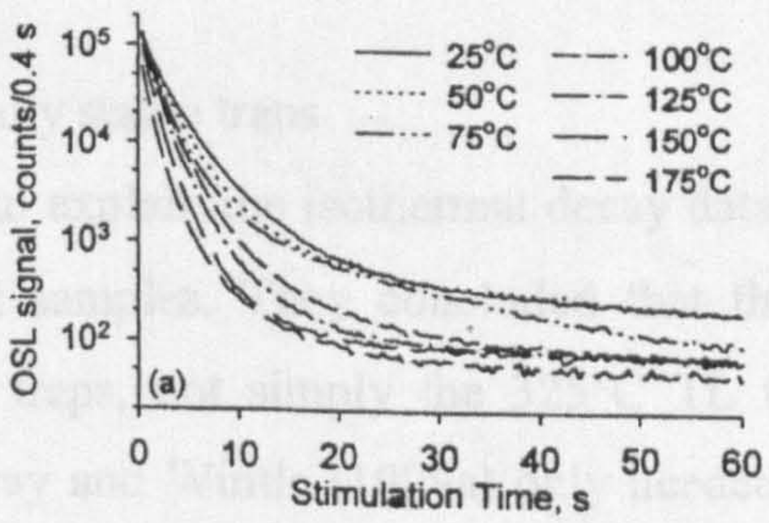

Figure 1.8. OSL decay curves measured at various stimulation temperatures. Aliquots were held at measurement temperature for 100 seconds prior to illumination to reduce thermally stimulated contributions. Phosphorescence measured after illumination was subtracted from the data. From Murray and Wintle (1998).

transfer. Under certain circumstances, charge evicted from the 110°C and 280°C TL traps can be transferred to the 325°C trap, leading to an increase in the OSL signal. This process is termed recuperation, and was first observed by Aitken and Smith (1988). They demonstrated that a proportion of the charge photo-transferred to the 110°C trap during optical stimulation (and presumably during natural bleaching) was subsequently transferred back to the OSL trap as the PTTL peak decayed at room temperature. If this occurred in nature, it would lead to an overestimate of the palaeodose. Banerjee (2000) suggested that charge from the 280°C TL trap could be transferred to the OSL trap during preheating. Since the 280°C TL trap is relatively optically stable, it may not be fully bleached on deposition of the quartz grain. Consequently, thermal transfer from this trap to the OSL trap will lead to an overestimation of the palaeodose.

1.5.3. OSL from geologically stable traps

Four traps were required to explain the isothermal decay data obtained by Huntley *et al.* (1996) for natural quartz samples. They concluded that the natural OSL signal was derived from a range of traps, not simply the 325°C TL trap as suggested by other authors. In contrast, Murray and Wintle (1999a) only needed two traps to fit their data, for a sample irradiated in nature. They concluded that the main trap, which contributed over 99% of the OSL signal, was the 325°C TL trap (Section 1.5.1). The remaining 1% of the signal was provided by a much more thermally stable trap.

The number of traps contributing to the OSL signal may also be assessed by analysis of the OSL decay curve, provided that these traps have different optical decay rates. To prevent re-trapping and subsequent optical stimulation of charge from the 110°C TL trap, several authors have advocated measuring OSL at elevated temperatures (e.g. Murray and Wintle, 1998 and Smith and Rhodes, 1994). Under these conditions, each optically stimulable trap should yield an exponentially decaying signal. Smith and Rhodes (1994) demonstrated that, for their sample, the OSL signal observed at 220°C was best fitted by three exponential terms. Bailey *et al.* (1997) termed these three signals the "fast", "medium" and "slow" components of OSL signal, due to their different optical decay rates (Figure 1.9 and Table 1.2). The OSL signal from a single trap, with a single optical

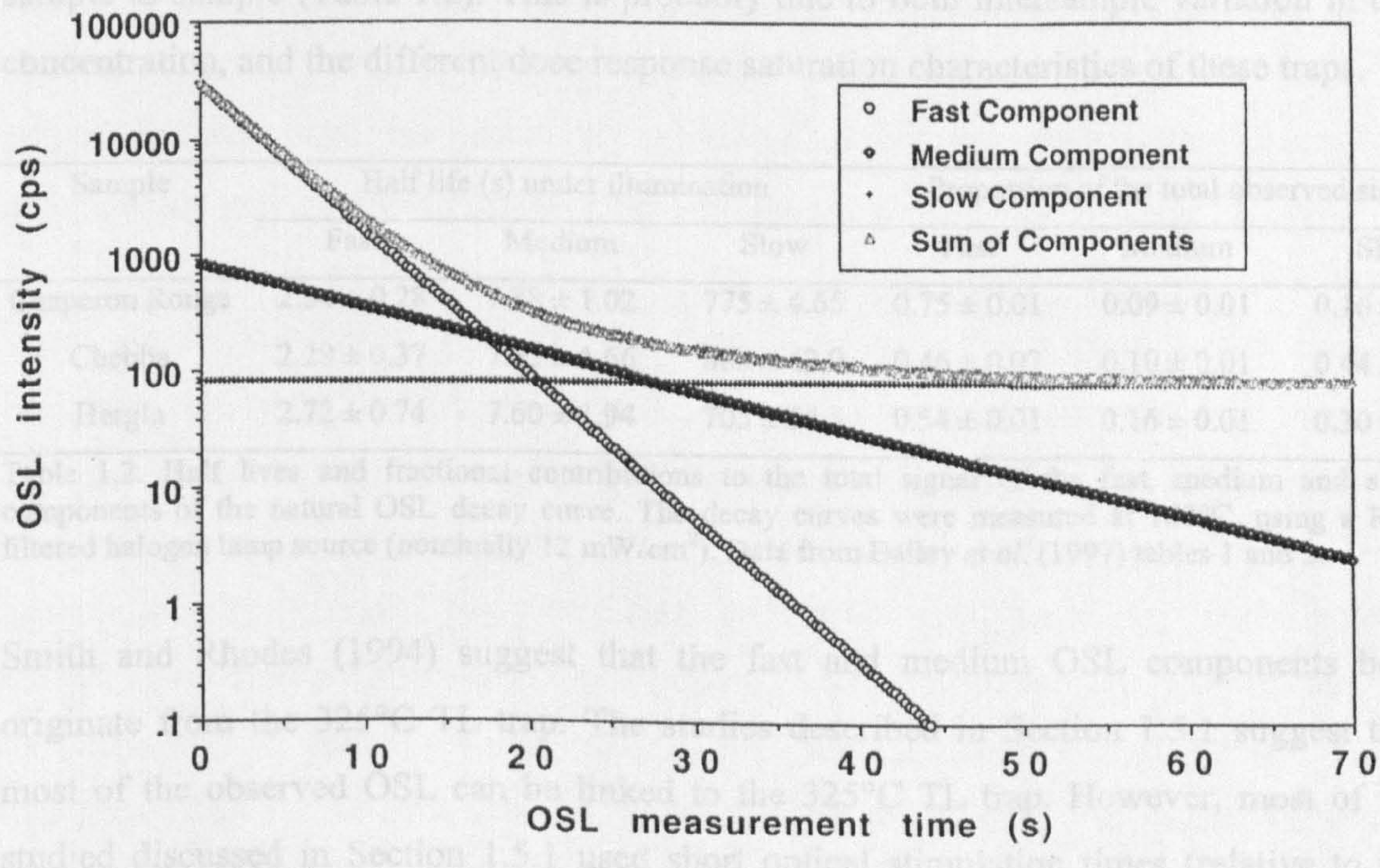

Figure 1.9. The OSL decay curve measured from a natural quartz sample held at 160°C, separated into three exponential components, with different decay rates. From Bailey *et al.* (1997)

decay rate, may be composed of two or more exponential decays where significant non-first order effects occur. Possible mechanisms include charge retrapping with subsequent optical/thermal eviction, sensitivity changes and changes in the paths available to detrapped charge during measurement of the decay curve. Bailey *et al.* (1997) argue that these mechanisms are unlikely to account for the decay shape they observed, concluding that the OSL decay form is due to the presence of several traps, with different optical stabilities. The proportion of the total OSL signal derived from each trap varies from sample to sample (Table 1.2). This is probably due to both intersample variation in trap concentration, and the different dose response saturation characteristics of these traps.

Sample	Half life (s) under illumination			Proportion of the total observed signal		
	Fast	Medium	Slow	Fast	Medium	Slow
Chaperon Rouge	2.34 ± 0.28	7.88 ± 1.02	775 ± 4.65	0.75 ± 0.01	0.09 ± 0.01	0.16 ± 0.05
Chebba	2.29 ± 0.37	7.65 ± 1.66	883 ± 42.9	0.46 ± 0.07	0.10 ± 0.01	0.44 ± 0.08
Hergla	2.72 ± 0.74	7.60 ± 1.94	705 ± 54.5	0.54 ± 0.01	0.16 ± 0.01	0.30 ± 0.02

Table 1.2. Half lives and fractional contributions to the total signal of the fast, medium and slow components of the natural OSL decay curve. The decay curves were measured at 160°C, using a Risø filtered halogen lamp source (nominally 12 mW/cm^2). Data from Bailey *et al.* (1997) tables 1 and 2.

Smith and Rhodes (1994) suggest that the fast and medium OSL components both originate from the 325°C TL trap. The studies described in Section 1.5.1 suggest that most of the observed OSL can be linked to the 325°C TL trap. However, most of the studied discussed in Section 1.5.1 used short optical stimulation times (relative to the 700-900s optical half life of the slow component measured by Bailey *et al.*, 1997), and consequently the OSL signal observed is dominated by the fast and medium components. In addition, the slow component OSL is emitted at a longer wavelength than the other two components (Smith and Rhodes, 1994 and Bailey *et al.*, 1997). Consequently, the slow component is not observed in studies using efficient red-rejecting filters. This can be seen from the results of Spooner (1994), who was able to reduce OSL observed through a 2mm Schott BG39 and 5.1mm Corning 7-51 to near zero in 100s, using 514.5nm stimulation. Using the same sample and stimulation source, but replacing the 7-51 filters with less efficient red rejecting 7-59 filters, Smith and Rhodes (1994) observed a third, slowly bleaching component.

Smith and Rhodes (1994) were able to demonstrate that the bleaching of the 325°C TL peak also contains faster and slower components, the fast component bleaching at approximately the same rate as its OSL counterpart. Similarly, Spooner (1994) found that the 325°C TL peak bleaching response was different under ultraviolet and visible regions, suggesting that charge was being evicted from traps with different optical stabilities. By elaborating on the model for thermal assistance in the production of OSL (Figure 1.2), Bailey *et al.* (1997) were able to explain the existence of two OSL signals from the same region of the TL glow curve. They suggest that the number and/or spacing of the available excited levels may vary depending on the exact location of the trap within the lattice. This will affect the probability of optical excitation to the conduction band and consequently give a range of optical half-lives, in this case two, for a single TL peak.

There are several characteristics of the slow component that suggest that it does not originate from the 325°C TL trap. Firstly, the slow component appears to be thermally stable to above 650°C. Bailey *et al.* (1997) heated a bleached[1] sample to progressively higher temperatures, measuring the OSL at 140°C between preheats, to produce a pulse annealing curve (Figure 1.10). Their data are dominated by sensitivity increase up to 650°C, at which the signal drops dramatically, though not to zero. They concluded that the luminescence centres are unstable at 650°C, though charge was still present in the trap responsible for the slow component, and hence a small signal was observed after this temperature. Bailey (2000a) has also suggested that the decrease in OSL above 650°C may be caused by thermal depletion of the trapped charge population responsible for the signal. In either case, the slow component is stable at far higher temperatures than the fast and medium components.

The very high thermal stability of the slow component led Bailey *et al.* (1997) to suggest that charge evicted from this trap did not proceed to its luminescence centre via the conduction band, since a trap that is thermally stable above 650°C will have an optical depth greater than the energy of the stimulating photons they used (2.95-2.21 eV). Instead, they postulate localized transitions from the trap to the luminescence centre via a

[1] To remove the fast and medium components, but not the slow component.

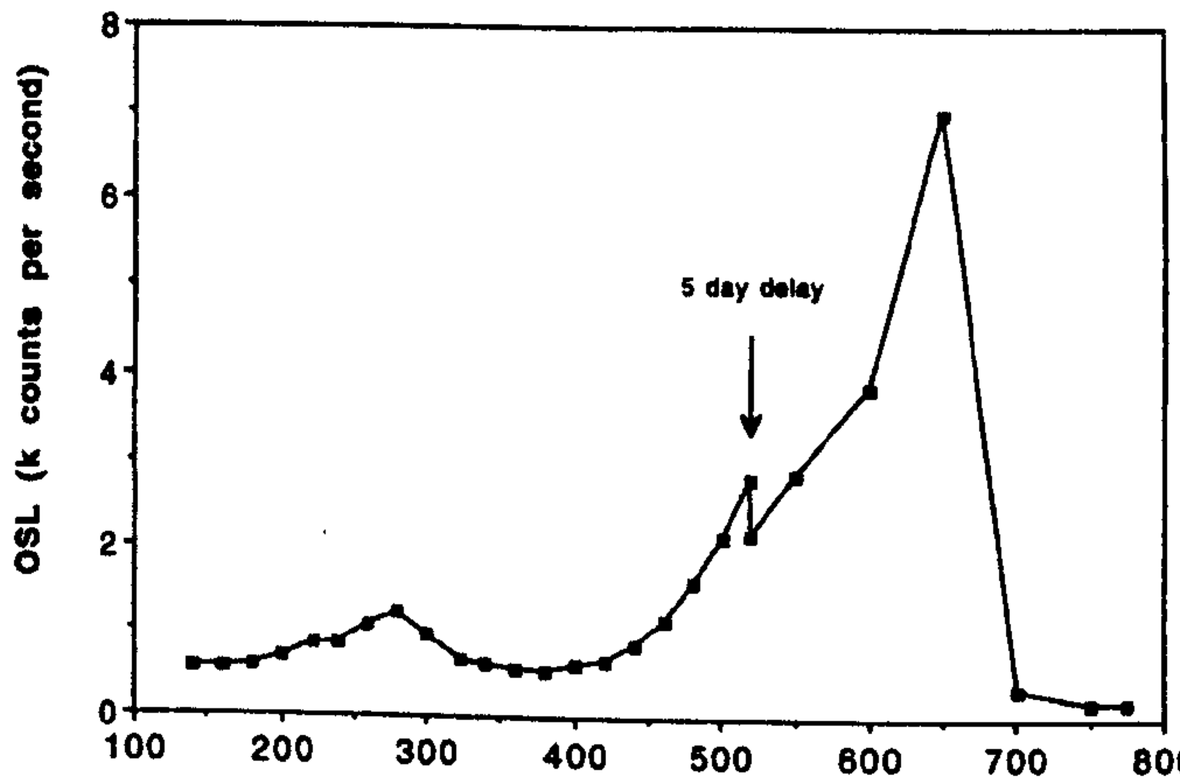

Figure 1.10. A pulse annealing curve for an aliquot of bleached (11 minute exposure to 514.5 nm light at 7mW/cm^2) natural quartz. Each OSL measurement was 2 minutes long, and was carried out at 140°C. From Bailey *et al.* (1997).

shared excited level. This is shown schematically in Figure 1.11. This hypothesis is supported by several other lines of evidence. As noted above, Smith and Rhodes (1994) and Bailey *et al.* (1997) suggest that the slow component results from OSL emitted at a longer wavelength than the other components, consequently it must use different luminescence centres (see also Section 1.6.1.1). Bailey (2000a) also noted that depletion of the slow component did not cause optical desensitization of the 110°C TL signal, as would be expected if the two signals were derived from the same recombination centres. In addition, unlike the fast and medium components, both the decay rate and form of the slow component are dose dependent (Bailey, 2000a). This is consistent with localized charge transition rather than recombination via the conduction band, as is postulated for the fast and medium components. Finally, the recombination centre responsible for the slow component exhibits thermal quenching. However, the activation energy and pre-exponential factor for quenching of the slow component are different from those of the rapidly bleaching components (Bailey, 2000a and Wintle and Murray, 2000)[m].

It is worth noting at this point that although the slow component can contribute significantly to the OSL signal, it may not be observed in many routine dating procedures. Although the slow component can contribute a significant proportion of the total signal observed (Table 1.2), the high optical stability of the trap means that, for relatively short stimulation times, the fast and medium components will dominate (Huntley *et al.*, 1996). Under these circumstances, the slow component constitutes a small, constant background signal (Smith and Rhodes, 1994). In addition, the use of efficient red-rejection filters for the measurement of OSL reduces the slow component signal to near zero, even at elevated stimulation temperatures. Despite this, two recent studies by Singarayer *et al.* (2000) and Bailey (2000a) have observed the slow component using Hoya U-340 filters.

---

[m] The activation energy and pre exponential factor for quenching of the slow component were 0.79 ± 0.023 eV and (5.75 ± 0.15) x 10^8 s^{-1} (Bailey, 2000a). Corresponding values for the rapidly bleaching OSL signal are 0.636 ± 0.013 eV and (3.4 ± 0.9) x 10^7 s^{-1} (Wintle and Murray, 2000).

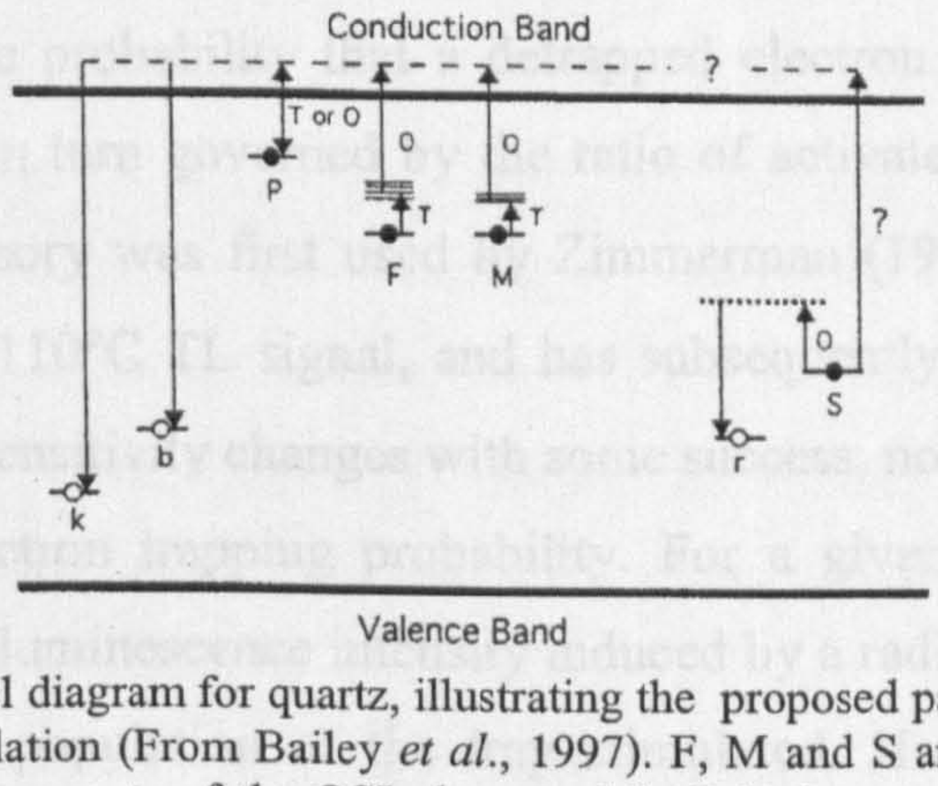

Figure 1.11. An energy level diagram for quartz, illustrating the proposed paths for movement of charge in quartz during optical stimulation (From Bailey *et al.*, 1997). F, M and S are the traps responsible for the fast, medium and slow components of the OSL decay, while P is the trap responsible for the 110°C TL signal. O represents an optical transition while T is a thermal transition. b and k are the radiative and non-radiative recombination centres used by electrons from traps F and M. r is the radiative recombination centre used by trap S.

1.6 Sensitivity change in quartz

The luminescence intensity per unit radiation dose (sensitivity) is not constant, and varies according to prior treatment of the sample in both nature and the laboratory. Standard laboratory procedures such as irradiation, optical stimulation and preheating are all known to alter the sensitivity of a sample. Consequently, meaningful comparisons between the luminescence signals induced by natural and laboratory irradiations can only be made either if the sensitivity is constant, or if sensitivity changes have been measured and "corrected for". There are two possible mechanisms for sensitivity change.

1) Changes in radiative recombination probability. The sensitivity of the sample is governed by the probability that a detrapped electron will recombine at an L-centre. This is in turn governed by the ratio of activated R and L centres in the crystal. This theory was first used by Zimmerman (1971) to explain sensitivity changes in the 110°C TL signal, and has subsequently been used to model and explain quartz sensitivity changes with some success, notably by Bailey (2001).
2) Changes in electron trapping probability. For a given radiative recombination probability, the luminescence intensity induced by a radiation dose is proportional to the electron population of the trap stimulated. However, the proportion of electrons promoted to the conduction band during irradiation, which become trapped in a specific trap, may vary. Consequently, identical radiation doses may lead to different trapped charge concentrations in a trap, leading to variation in the luminescence signal observed. This phenomenon has been observed in sedimentary feldspar (Wallinga *et al.*, 2000).

The remainder of this section concentrates on sensitivity changes due to changes in radiative recombination probability, since electron trapping probability changes during the first preheat do not appear to occur in the samples studied (see Section 3.5). Similarly, other authors (e.g. Wintle and Murray, 2000 and Chen *et al.*, 2000) have concluded that sensitivity changes in their quartz samples relate primarily to recombination processes rather than electron trapping.

1.6.1 The Zimmerman model for sensitivity change in quartz

The original Zimmerman (1971) model, which was designed to explain sensitivity change in the quartz 110°C TL signal, can be summarized as follows.

1) A hole at the R-centre is less thermally stable than one at the L-centre. When the sample is heated sufficiently, electrons in the valence band gain enough energy to recombine at the R-centre, thereby deactivating it. The resultant hole diffuses through the crystal lattice, and is subsequently captured at a recombination centre. Since holes at L-centres are more thermally stable than those at R-centres, this process leads to a net increase in activated L-centres relative to R-centres. Consequently, the sensitivity of the sample increases. This process is termed thermal activation.
2) At lower temperatures (where holes at R-centres are stable), the R-centre has a larger hole trapping cross-section, since it is energetically closer to the valence band in which holes diffuse. Consequently, during irradiation R-centres are preferentially activated, and the sensitivity of the sample is reduced. This process is termed dose quenching.
3) Illumination at ultra-violet (UV) wavelengths excites electrons in the valence band and enables them to reach recombination centres. However, they acquire too much energy to recombine at R-centres (which are energetically closer to the valence band) and preferentially recombine at L-centres. The resultant hole diffuses through the valence band and is preferentially trapped at R-centres, which have a greater hole-trapping cross-section than L-centres. Consequently, UV illumination causes a net movement of holes from L to R-centres, leading to a decrease in sample sensitivity. This process is termed optical desensitization.

For the purposes of the discussion which follows, it is also assumed that activated recombination centres are more numerous than optically/thermally stimulable charge. This assumption is important since, if an equal number of stimulable electrons and activated recombination centres existed, luminescence measurements would cause greater sensitivity changes than are actually observed. To maintain charge neutrality, there must

be an equal number of trapped electrons and holes (trapped at recombination centres). However, quartz is known to contain very optically/thermally stable electron traps. Hence, electrons in these very stable traps are (effectively) not stimulable. During the geological history of the quartz crystal, a proportion of the charge promoted to the conduction band (during natural irradiation and sunlight exposure etc) becomes trapped in these very stable traps. Consequently, holes are more numerous than stimulable electrons, yet the crystal maintains charge neutrality (Bailey, 2001).

1.6.1.1 L-centres

By using 3D TL emission spectra, Scholefield *et al.* (1994) demonstrated that the 325°C and 375°C TL peaks emitted luminescence at different characteristic wavelengths (c.440 and 482 ± 3.6 nm respectively). Consequently, they concluded that the TL peaks used different luminescence centres. In an extension of this work, Franklin *et al.* (1995) suggested that quartz TL peaks could be divided into two groups, each using a different luminescence centre. The first group, containing the TL peaks centred around 110, 160, 210 and 325°C, uses a luminescence centre which displays marked thermal quenching. The energy of the photons emitted by this luminescence centre decrease in a predictable manner as stimulation temperature is increased (Figure 1.12). The room temperature OSL emission wavelength, measured by Huntley *et al.* (1991), is also shown on Figure 1.12 and follows the pattern of emission wavelength change with temperature. This indicates that the different emission wavelengths observed for this family of traps, is not due to a range of luminescence centres, since the OSL signal originates (primarily) from the 325°C peak. The second group includes TL peaks at 260, 375 and 450°C; these use a luminescence centre which emits at approximately 470 nm and does not display thermal quenching.

1.6.1.2 R-centres associated with the OSL signal

Since it is not possible to observe a luminescence signal from R-centres, their existence and properties are inferred from changes in a sample's sensitivity. Li and Chen (2001) performed both pulse annealing and isothermal decay experiments on a 17 ka old sedimentary quartz. Assuming that the sensitivity increases observed during these

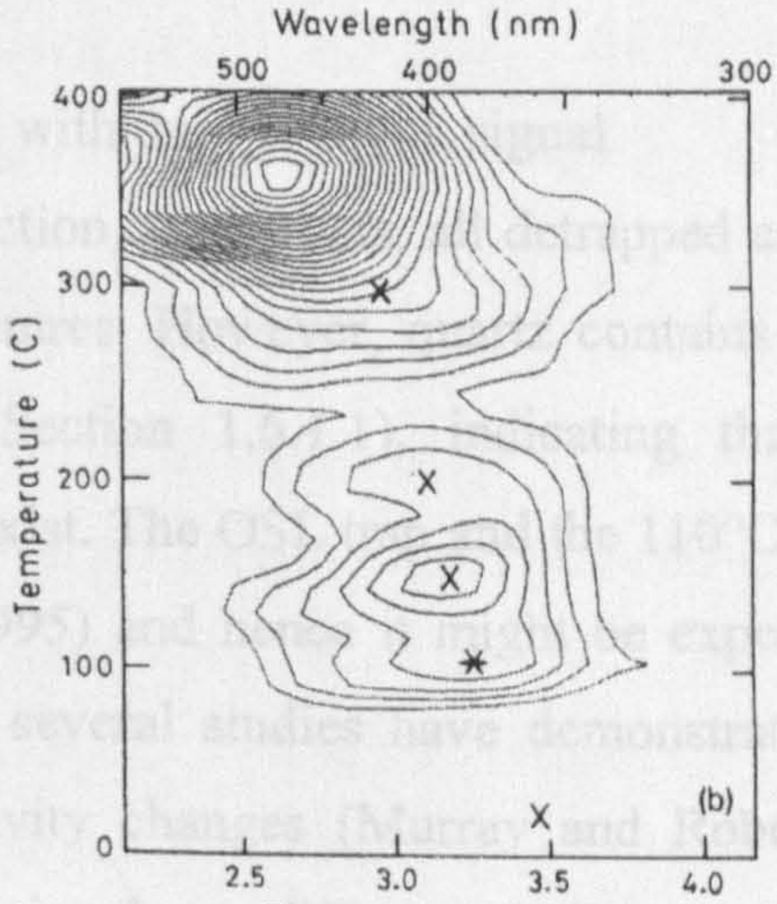

Figure 1.12. A contour map of the 3D spectrum, obtained from a natural quartz sample which has been given a 60 Gy dose, stored in the dark for 48 hours, and then given a 0.6 Gy dose prior to measuring the spectrum (From Franklin *et al.*, 1995). The crosses above 100°C represent the approximate peak positions of the 110, 160, 210 and 325°C peaks (using the nomenclature described in Section 1.4). The cross at 22°C represents the OSL emission from a similar quartz sample measured by Huntley *et al.* (1991).

experiments were caused by the thermal transfer of holes from R to L-centres, they calculated kinetic parameters for the R-centre used by the OSL traps[n]. They concluded that only one R-centre was required to explain the sensitivity change in this sample, and that it had a lifetime of 10^4 years at 20°C. This value is similar to that for the main component (A component) of TL sensitivity increase measured by Wintle and Murray (1999) for their sample. This component had a lifetime of 40 ka at 20°C, and was also interpreted as resulting from the deactivation of thermally unstable R-centres (Wintle and Murray, 1999). Consequently, OSL sensitivity change appears to be controlled by the concentrations of one R- and one L-centre only.

1.6.1.3 R-centres associated with the 110°C TL signal

Where a delocalised conduction band exists, all detrapped charge should have access to the same recombination centres. However, quartz contains two groups of traps which feed separate L-centres (Section 1.6.1.1), indicating that a genuinely delocalised conduction band does not exist. The OSL trap and the 110°C TL peak trap feed the same L-centre Franklin *et al.* (1995) and hence it might be expected that they use the same single R-centre. However, several studies have demonstrated that the timing (Stokes, 1994a) and size of sensitivity changes (Murray and Roberts, 1998 and Murray and Mejdahl, 1999) for the two signals are different. This has led several authors to conclude that charge from one of the traps can recombine at an R-centre which is not accessible to charge in the conduction band (e.g. Chen *et al.*, 2000).

Chen and Li (2000) carried out a series of experiment to characterize sensitivity change in the 110°C TL peak. They found that a minimum of three R-centres were required to explain the phenomena observed, though no kinetic parameters were calculated. These R-centres were termed R_1 to R_3 in order of increasing thermal stability. The effects of R_1 were only observed in artificially irradiated aliquots, suggesting that holes trapped there were thermally unstable over the burial period (17 ka) of the sample. In a pulse annealing

[n] It is possible to explain the results of their pulse annealing experiment in terms of charge transfer from the 280°C TL trap to the optically sensitive trap (Banerjee, 2000). However, the lifetime of charge associated with the 280°C TL trap (Spooner and Questiaux, 2000) is an order of magnitude longer than that of the R-centre calculated by Li and Chen (2001), suggesting that this is not the case.

experiment, thermal deactivation of this R-centre was observed from the starting temperature (160°C) to c.220°C. During an isothermal annealing experiment, R_2 was not deactivated by 2000s at temperatures below 180°C, while rapid (complete after <200s) deactivation occurred at 260°C. Similarly, no significant deactivation of R_3 centres occurred after 2000s at 260°C. It is unclear what temperature is required to rapidly deactivate R_3 centres, though the process appears to be complete by about 470°C in the pulse annealing experiment.

1.6.1.4 Electron transfer pathways used by the OSL and 110°C TL traps

From the temperature ranges in which the three 110°C TL R-centres deactivate, it is possible to draw tentative conclusions about the pathways followed by electrons from the OSL and 110°C TL traps.

1) No sensitivity change was observed by Li and Chen (2001) over the temperature range which deactivates R_1 centres. Consequently, charge from the OSL trap cannot recombine at this centre. Since several TL traps feed the L-centre used by the 110°C TL and OSL traps, it is likely that charge recombining at this centre does so via the conduction band, since multiple localized transitions are considered unlikely. Consequently, charge recombining at the R_1 centres must be due to localized charge transition.
2) The range of temperatures over which the R_2 centre deactivates is broadly similar to that over which the OSL signal increases in sensitivity (Li and Chen, 2001 and Armitage *et al.*, 2000). Consequently, it is possible that R_2 and the OSL R-centre are the same. It is highly likely that the two traps share at least one R-centre, since although the OSL and 110°C TL signal sensitivities are not identical, they are very similar (Aitken and Smith, 1988, Stoneham and Stokes, 1991 and Murray and Roberts, 1998).
3) Holes trapped at the R_3 centre appear to be at least as stable as electrons in the main OSL trap. Consequently, sensitivity increases due to the deactivation of this centre would not be observed in pulse annealing experiments such as that performed by Li and Chen (2001). It is therefore possible that charge from the

OSL trap also recombines at the R_3 centre. It is likely that charge from the OSL trap has access to a thermally stable non-radiative recombination, centre since Bailey (2001) required such a centre (which he termed a K-centre) when modelling quartz luminescence.

1.7 Summary

1) Luminescence methods, when applied to unheated sediments, measure the radiation dose which a mineral grain has absorbed since burial. In an ideal sediment, the environmental dose rate is constant, and hence the age of the deposit can be calculated.
2) During irradiation, electrons may be detached from their parent atoms, and become trapped at electron traps. Electrons are subsequently detrapped by heating or illuminating the crystal. When an electron is detrapped it recombines at a recombination center, dissipating energy as heat or light. The latter is referred to as luminescence. Quartz contains several trap types, each with a different thermal stability, giving rise to several peaks in the TL glow curve.
3) The initial OSL signal is dominated by the recombination of charge from the 325°C TL trap. However, some geologically unstable traps may also contribute to this initial signal when they are populated either by laboratory irradiation or photo-transfer.
4) The OSL decay curve shape is not a single exponential decay, and can be resolved into at least three components. The fast and medium components are derived from the 325°C TL trap while the slow component is derived from a deeper trap. Unlike the fast and medium components, charge evicted from the trap responsible for the slow component probably proceeds to the recombination center by a localized transition. During relatively short stimulations the slow component may be regarded as a constant background signal.
5) Luminescence sensitivity of quartz is dictated by the concentrations of activated L- and R-centres (i.e. radiative recombination probability). The different thermal stability and electron/hole trapping cross-sections of these two groups of recombination centers, lead to sensitivity changes in nature and the laboratory.

The OSL and 110°C TL traps appear to feed a common L- and R-centre. A second, thermally stable, R-centre used by charge from the 110°C TL trap, may also be available to charge from the OSL traps. In addition, a thermally unstable R-centre is available to charge from the 110°C TL trap, via a localized charge transition.

Chapter 2: Measurement procedures, sample preparation and equipment

2.1 Introduction

The purpose of this chapter is to provide details of the standard procedures and equipment used in this thesis. In many instances these details will be familiar to the reader, but bear repetition for the purposes of clarity. Where non-standard equipment or procedures have been used, they are described elsewhere in the thesis.

2.2 The single-aliquot regenerative-dose measurement procedure

The majority of OSL measurements reported in this thesis were made using the single-aliquot regenerative-dose (SAR) procedure described by Murray and Wintle (2000), and outlined in Table 2.1. The SAR technique allows monitoring of, and correction for, luminescence sensitivity changes that occur during the measurement sequence.

Step	Treatment	Observed
1	Give β regeneration dose (β_x)[a]	-
2	Preheat for 10s, routinely between 160-300°C (PH1)	-
3	Stimulate with blue LEDs for 100s @ 125°C	L_x
4	Give β test dose	-
5	Preheat to 160°C and cool immediately (cut heat, PH2)	-
6	Stimulate with blue LEDs for 100s @ 125°C	T_x
7	Repeat steps 1 to 6 using a range of regeneration doses	-

Table 2.1. The standard SAR measurement sequence. An explanation of shorthand terms used in this thesis is given in Appendix 2.1.

Correction for sensitivity change is achieved by measuring the OSL signal (T_x) in response to a test dose immediately after the natural/regenerated luminescence intensity (L_x) has been measured. Assuming no sensitivity change occurs between the measurement of L_x and T_x, or that the size of sensitivity change that does occur does not vary with measurement cycle, the sensitivity-corrected luminescence intensity may be calculated by dividing the former by the latter. The natural sensitivity corrected

[a] For the natural sample no dose is administered.

luminescence intensity (L_n/T_n) is defined as N, while sensitivity corrected regenerated luminescence intensity (L_x/T_x) is defined as R.

The sensitivity-corrected regenerated luminescence intensities (R_x) were used to form a growth curve, from which the equivalent dose can be calculated (Figure 2.1). All equivalent doses were calculated using the Analyst software (version 2.24) written by Dr. Geoff Duller. In all cases, a saturating exponential plus linear fit was used, with a small constant y-axis offset[b]. This consists of two components, the saturating exponential (Equation 2.1)

$$I = A\,(1\text{-}\exp^{-D/B}) \qquad (2.1)$$

where I is the signal intensity, A is the intensity at saturation, D is the dose and B is a parameter defining the onset of signal saturation. The linear component was added to account for continued signal growth at high regeneration doses (Equation 2.2)

$$I = mD + c \qquad (2.2)$$

where m is a fitting parameter and c is the y-axis intercept.

2.2.1. Preheat

Prior to measurement of the natural/regenerated luminescence intensity, each aliquot is preheated for 10 seconds (PH1). The reasons for preheating were summarized by Murray and Wintle (2002) as follows.

1) To remove charge from optically sensitive but thermally unstable traps that are filled during laboratory irradiation.

---

[b] This offset is defined by the sensitivity-corrected luminescence intensity measured for the zero dose regeneration point (Section 2.2.5). It is unclear whether this offset is appropriate (Section 3.5), however, owing to its small size, this offset is unlikely to have a significant deleterious effect on the D_e values produced.

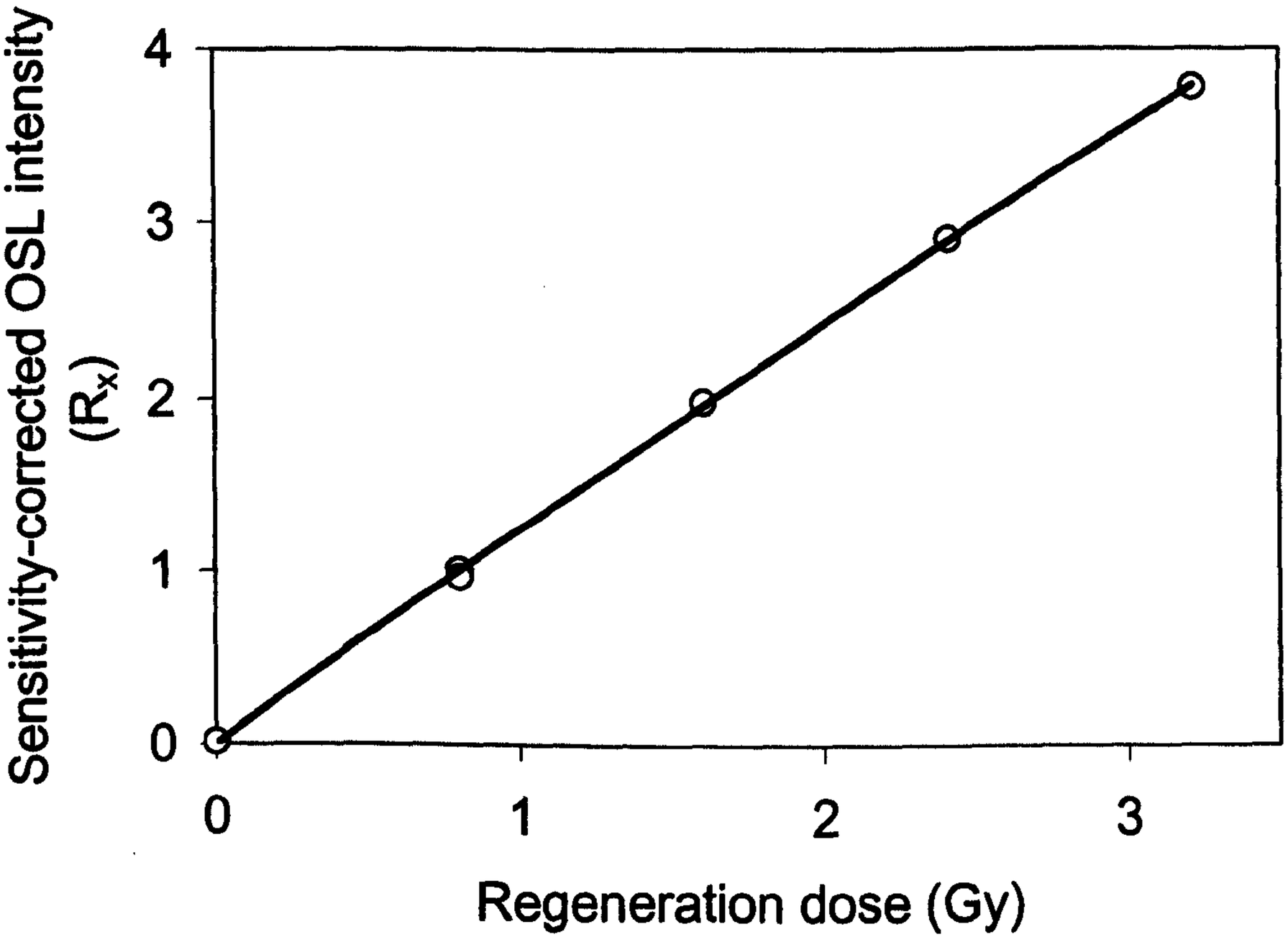

Figure 2.1. A typical growth curve for Aber/28-IN16, using a test dose of 1 Gy.

2) To thermally transfer charge from optically insensitive traps to the OSL trap, to at least an extent equivalent to that which occurred in nature.
3) To equalize the luminescence efficiency for all the OSL measurements (more important for single-aliquot additive-dose sequences than the SAR measurements reported in the present study).

During dating sequences, eight PH1 temperatures were routinely used, ranging from 160-300°C at 20°C intervals.

2.2.2. OSL measurement

OSL was routinely measured while holding the sample at 125°C, to keep the 110°C TL trap empty during stimulation, without significantly quenching the OSL luminescence centres. Stimulation time was varied depending on the intensity of the stimulating light (see Table 2.3, p31). The signal accumulation time was split into 250 channels. Both L_x and T_x were derived from the first channel of the optically stimulated luminescence signal, minus a background estimated from the last 25 channels of L_x. This procedure is intended to sample the most bleachable OSL signal, while subtracting instrument noise and slower bleaching signals, which may not be fully removed during stimulation. The aliquot was held at 125°C for 10 seconds prior to optical stimulation, to allow the sample to attain the same temperature as the heater plate (Jain *et al.*, 2001). This is particularly important since, other factors being equal, the quartz OSL intensity is dependent on stimulation temperature due to thermal quenching, thermal assistance and peak emission wavelength shift. The latter may significantly affect the OSL intensity measured since the detection filters used in this study (Figure 2.4) only transmit the higher energy photons emitted by quartz at 125°C (Figure 1.12). Consequently, small temperature changes will alter the proportion of the emitted OSL measurable by the photomultiplier tube.

2.2.3. Test dose

The test dose remains constant throughout the measurement sequence for any given aliquot. The majority of experiments reported in this thesis used a c.5 Gy test dose, since this resulted in a bright T_x signal (>5000 counts per mJ/cm^2 stimulation energy). Where

the likely D_e was smaller than 5 Gy, the test dose was reduced to c.1-2 Gy. In this study, the test dose was always less than half the equivalent dose, although Murray and Wintle (2000) demonstrate that test doses up to three times the size of the equivalent dose may be acceptable.

2.2.4 Cut heat

Irrespective of PH1 temperature (Section 2.2.1), a cut heat (PH2) of 160°C followed by immediate cooling was used after each test dose had been administered. This treatment is intended to empty the 110°C TL trap while causing little or no sensitivity change. Higher temperature or longer duration "cut heats" risk altering the sensitivity of the aliquot, thereby rendering the SAR sensitivity correction procedure inappropriate. This is especially true when PH2 approaches thermodynamic equivalence with PH1.

2.2.5 Regeneration doses

The regeneration dose regime for any given sample was designed to "bracket" the expected equivalent dose, thereby allowing the calculated equivalent dose to be derived by interpolation. Six regeneration dose points were usually measured, related to the equivalent dose as follows - $\beta_1 < \beta_2 = D_e < \beta_3 < \beta_4$. The fifth and sixth regeneration points were 0 Gy and identical to β_1 respectively.

2.3 Sample collection and preparation

2.3.1 Sample collection

A range of sampling methods were used, depending on sediment type and consistency. A terminological distinction is made between modern samples, those collected from active depositional environments, and geological samples collected from relict deposits.

Geological samples were collected by hammering opaque PVC cylinders (dia. c.10 cm x 20 cm) into vertical exposures within sampling pits or "cleaned" eroding faces. The cylinders were immediately sealed at both ends using several layers of opaque duct tape.

The entire cylinder was then sealed into an opaque plastic bag to allow subsequent assessment of field moisture content. Where compaction or post-depositional carbonate cementation prevented the insertion of PVC cylinders, blocks of sediment were collected (typically a cube with sides c.10 cm) and sealed in opaque plastic bags. Where possible, samples were taken at least 30 cm from any lithostratigraphic boundary to guarantee an effectively homogenous matrix for dosimetric purposes (see also Section 7.1.1).

Modern samples were obtained from active depositional environments, with the aim of assessing the equivalent dose of geological samples on deposition. Loose sands were collected from the upper 1-2 cm of the deposit and placed in an opaque plastic bag. One modern tidal-flat deposit was collected in a PVC cylinder as described above. Ollerhead (2001) has demonstrated that very thin (<1 cm) layers of sand reduce light transmittance to negligible levels, allowing the underlying sand to accumulate a luminescence signal. However, the modern samples were collected from active depositional environments, and should be fully bleached to a greater depth. Modern samples were processed under identical conditions to those used for geological samples.

2.3.2 Quartz separation

Samples were processed under subdued red light[c], with the aim of extracting pure, 211-180 μm quartz. The first stage of preparation involved removing sediment which had been exposed to sunlight during collection. Where samples had been collected in PVC cylinders, the 5 cm of sediment at each end of the sample were removed, and used for dosimetry measurements (Section 7.2). The remaining sediment was then sealed in an opaque plastic bag and stored in a light-tight cupboard prior to further processing.

Samples collected as blocks required more laborious processing. Firstly, a dosimetry sample was removed from the outside of the block. Subsequently, the block was measured and submerged in 10% HCl to dissolve the carbonate cement. Periodically the block was remeasured, and the HCl replaced when effervescence ceased. When all axes of the block had been reduced by a minimum of 4 cm, equating to the removal of a 2 cm

[c] Fluorescent tubes filtered using EncapSulite OA30 film.

thick outer layer, the block was thoroughly rinsed in deionised water. This step removed loose grains from the dissolved outer layer of the sample.

The two sample types were then prepared in an identical manner.

1) Carbonates were removed using 10% HCl. The sample was periodically agitated, and acid was added until no further effervescence was observed. The sample was then rinsed in deionised water.
2) Organic matter was removed using 20 vols H_2O_2. The sample was periodically agitated, and remained in the H_2O_2 for not less than 12 hours. The sample was then rinsed in deionised water.
3) The sample was dried at 50°C and sieved through a stack containing 90, 125, 150, 180, 212, 250, 300 and 335 μm meshes.
4) The 211-180 μm fraction was then density separated in sodium polytungstate solution, at a density of 2.62 g/cm^3. The "heavy" (quartz, plagioclase feldspar and heavy minerals) fraction was retained and then separated at 2.70 g/cm^3. The "light" fraction, containing quartz and plagioclase feldspar, was retained.
5) This fraction was then etched in 40% HF for 40/45 minutes to remove the remaining feldspars. Fluoride precipitates were removed by submersion in conc. HCl for 40 minutes, following which the samples were thoroughly rinsed in deionised water[d].
6) The etched material was then dried and resieved using a 180 μm sieve mesh to remove any partially etched grains. The response to infra-red (IR) stimulation was used to check sample purity (Section 2.3.4)

2.3.3 Aliquot preparation

Etched quartz was mounted, as a monolayer, on 10 mm diameter aluminium discs using Silkospray silicone oil. Silkospray was applied to the disc through a mask, thereby dictating the approximate mass of grains adhering to each disc. The sprayed face of the disc was briefly placed on a loose pile of the sample, and then tapped repeatedly to

[d] The HF etch is believed to remove a c. 10 μm skin from the outside of the quartz grain (Hong, 1998).

remove loose grains. Three mask sizes were used, with hole diameters of 2, 5 and 8 mm. The maximum mass of sample for each mask size has been calculated (Table 2.2). Aliquot mass was routinely monitored, and overweight aliquots were discarded, since the sample cannot be mounted as a monolayer. In practice, measured aliquot masses were generally two thirds of the maximum.

Mask diameter (mm)	Maximum number of grains	Maximum mass (mg)
2	80	0.8
5	500	5.2
8	1300	13.6

Table 2.2. Standard Aberystwyth mask sizes and capacities (assuming a monolayer of spherical quartz grains, 196 μm in diameter, with a density of 2.65 g/cm^3).

2.3.4 Assessment of sample purity using infra-red stimulation

Quartz aliquots were routinely tested for feldspar contamination by measuring their response to IR stimulation (diodes or one single laser diode depending on reader, see Table 2.3). At high measurement temperatures (>175°C), infra-red stimulated luminescence (IRSL) can be observed from pure quartz (Bailey, 1998a, and Wallinga *et al.*, submitted). However, at lower temperatures, IRSL is observed from feldspar but not quartz. Consequently, IR stimulation was carried out at 50°C when testing sample purity. Two types of IR stimulation test were used during this study, both of which were performed at the end of the SAR measurement sequence.

1) A c.10 Gy β dose was administered, followed by a cut heat to 160°C. IRSL was then measured for 100 seconds at 50°C. Aliquots yielding a recognizable decay curve under IR stimulation were rejected.
2) Two sensitivity-corrected (L_x/T_x), blue LED stimulated, OSL intensities were measured in response to a c. 10 Gy β dose. Prior to the first L_x measurement, the aliquot received 100 seconds IR stimulation at 50°C. Where the first L_x/T_x value was considerably lower than the second, the aliquot was rejected. It should be noted that small variations in L_x/T_x values (c. 1.5 %), for identical radiation doses,

should be expected due to imperfect measurement reproducibility (Section 5.3.2 and Armitage *et al.*, 2000).

In practice, very few aliquots were rejected due to feldspar contamination (< 1 %).

2.4 Luminescence measurement and irradiation equipment

All luminescence measurements reported in this thesis were made on one of three Risø TL/OSL readers. As the author carried out no equipment development work, detailed description of instrumentation is beyond the scope of this section. However, this section aims to provide enough detail to allow comparison with other studies. Details of the three Risø readers used in this thesis are provided in Table 2.3. Where these details are not self-explanatory, a brief discussion is provided below.

2.4.1 Computer control of the TL/OSL reader

Currently, all three Risø readers used in this study are controlled by a "Mini-Sys" unit, described in Markey *et al.* (1997). Prior to 21/10/99, Risø 1 was controlled using a TL-DA-12 interface board mounted in the host computer. These two control configurations are shown in Figure 2.2. Various versions of the Risø control software have been used. All the software used postdates version 4.64, prior to which optical stimulation times were 0.4s longer than that specified by the user (Murray *et al.*, 1997). No similar flaws have been found in the software used in the production of this thesis. However, between 20/4/99 and 21/10/99 all preheat and measurement temperatures using Risø 1 were 5/7 of the stated value. This error occurred because an incorrect parameter had been entered during the installation of new control software. Data subject to this error are identified in the text.

2.4.2 β irradiators

Most laboratory radiation doses were administered using a Risø mounted β irradiator, containing a 40 mCi $^{90}Sr/^{90}Y$ β source. During some experiments, samples were irradiated outside the Risø reader using a Daybreak Model 801 irradiator. This contained

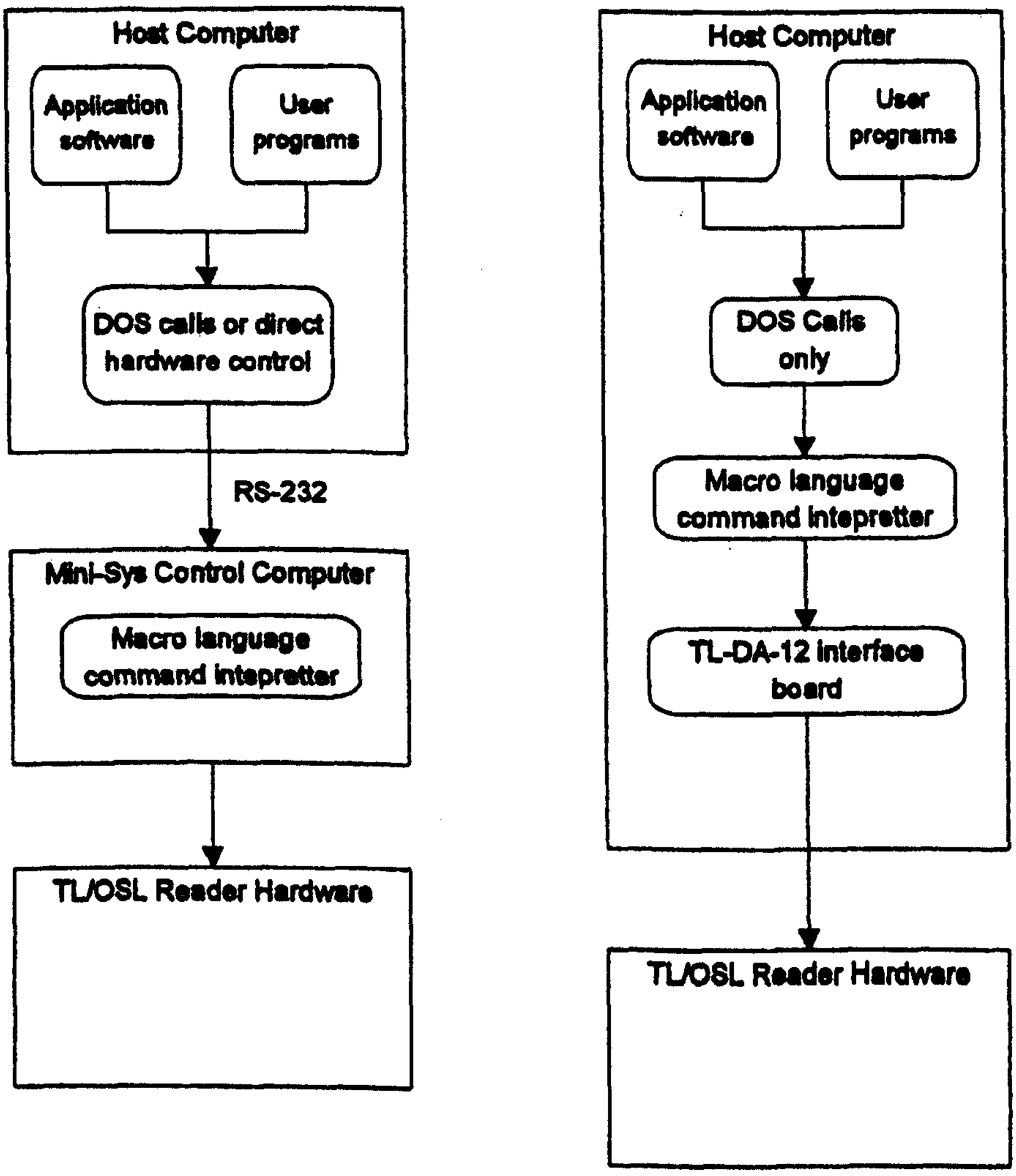

Figure 2.2. Block diagrams for a) (left) the Risø reader equipped with a Mini-Sys control unit and b) (right) the pre Mini-Sys system using a TL-DA-12 interface board mounted in the host computer (from Markey *et al.*, 1997).

	Risø1	Risø 2	Risø 3
System type	TL-DA-10	TL-DA-12	TL-DA-15
PMT type	9635Q	9635Q	9235Q
PMT dark count (cts/s)[e]	29	25	84
Sample positions	24	24	48
β source type	40 mCi $^{90}Sr/^{90}Y$	40 mCi $^{90}Sr/^{90}Y$	40 mCi $^{90}Sr/^{90}Y$
Irradiation mechanism	Shutter	Shutter	Rotating source
Source to sample distance (mm)	13	13	7
Dose rate at 1/10/01 (Gy/min)[f]	0.965	1.177	5.894
Visible wavelength stimulation			
Blue LED type	NISHIA (type NSBP-500S)	NISHIA (type NSBP-500S)	NISHIA (type NSBP-500S)
Emission wavelength (nm)	470 Δ 20	470 Δ 20	470 Δ 20
Number of diodes	13	35	21
Stimulation power (mW/cm^2)	2.2	16.9	6.5
Typical stimulation time (s)	100	40	100
Cumulative stimulation energy (mJ/cm^2)	220	676	650
Typical signal depletion by end of stimulation (% of initial natural signal)	> 99.5	> 99.5	> 99.5
Stimulation light breakthrough (cts/s)[e]	29	14	66
Breakthrough/dark noise ratio	0.99	0.57	0.78
Infra red wavelength stimulation			
IR diode type	TEMT 484	Laser diode	Laser diode
Emission wavelength (nm)	875 Δ 75	830 Δ 10	830 Δ 10
Number of diodes	11	1	1
Stimulation power (mW/cm^2)[g]	40-50	400	400
Quartz vacuum window	No	Yes	Yes[h]
OSL Filters	2 * 2.5mm U340	3 * 2.5mm U340	3 * 2.5mm U340

Table 2.3. Risø reader specifications.

[e] Measured on or around 1/10/01.
[f] Dose rate applies to 211-180μm quartz grains mounted in a monolayer on an aluminium disc.
[g] Approximate values from Bøtter-Jensen *et al.* (2000).
[h] Removed for single grain work.

a 125 mCi $^{90}Sr/^{90}Y$ β source and is referred to as "Daybreak 1" hereafter. Risø 1 and 2 are fitted with the older style irradiator described by Markey *et al.* (1997). Irradiation occurs when a shutter interposed between the source and sample is withdrawn under computer control. A similar irradiation mechanism is employed in Daybreak 1. Risø 3 is fitted with a more modern irradiator, described in Markey *et al.* (1997, Figure 2). The source is mounted on a rotating stainless steel wheel, and "points" upwards when not irradiating. Irradiation occurs when the wheel is rotated through 180° so that the source is positioned immediately above the sample.

2.4.2.1 Risø β source calibrations

The Risø mounted β sources were calibrated by Dr. Geoff Duller using a γ irradiated (4.65 Gy) calibration quartz provided by Dr. Andrew Murray. In each case, aliquots of the calibration sample were measured using a standard SAR measurement sequence. The resulting equivalent dose was then used to calculate the β dose rate. Results are shown in Table 2.4.

Source	Date	D_e (s irradiation)	Dose rate (Gy/min)
Risø 1 (calibration #1)	30/10/99	276 (n=24)	1.01
Risø 1 (calibration #2)	20/08/00	286 (n=12)	0.98
Risø 2 (calibration #1)	15/11/99	226 (n=24)	1.23
Risø 2 (calibration #2)	19/08/00	227 (n=12)	1.23
Risø 3	13/01/00	45.4 (n=24)	6.15

Table 2.4. Risø β source calibrations (performed by Dr. Geoff Duller).

Risø 1 and 2 were both calibrated twice during this study. Since the half-life of $^{90}Sr/^{90}Y$ is 28.79 years (Chu *et al.*, 1999), an appreciable decrease in dose rate occurred between calibrations, consequently the values are not directly comparable. The expected dose rate at the time of the second calibration, based upon the first calibration, was calculated using Equation 2.3.

$$N(t) = N_0 e^{-\lambda t} \qquad (2.3)$$

where N_0 is the dose rate at time (t) = 0 and λ is the decay constant (Krane, 1987). For both sources, the predicted and measured dose rates are in good agreement, lying within 2 % of each other. The 1999 calibrations have been used for both sources.

2.4.2.2. Daybreak β source calibrations

Both Daybreak β sources were calibrated relative to Risø 1 by the author. 24 aliquots of Aber/12-MAP3, which had previously been dated using a standard SAR measurement sequence, were bleached for one hour using a dr.Honle SOL2 solar simulator. They were subsequently given a c.5 Gy dose in the Daybreak source, and measured on Risø 1 using a standard SAR measurement sequence. Results are presented in Table 2.5. The ratio of dose rates, Daybreak : Risø 1, is also presented since this ratio remains constant as the sources decay.

Source	Date	Dose rate (Gy/min)	Ratio (Daybreak : Risø 1)
Daybreak 1	19/3/99 (n=24)	2.66 ± 0.03	2.58
Daybreak 2[i]	15/2/99 (n=24)	0.91 ± 0.02	0.88

Table 2.5. Daybreak irradiator dose rates.

2.4.2.3. Risø β source performance

Three sources of error occur during irradiation using the Risø β sources. These are 1) Dose under-delivery due to shutter/source movement time. 2) Irradiation of samples positioned under a source in the "off" position (leakage). 3) Unintentional irradiation of aliquots next to the intended aliquot (cross-talk). These values were measured for both Risø β source types by Markey *et al.* (1997). Using their data, equivalent values were calculated for the sources used in this study, and are given in Table 2.6.

[i] Daybreak 2 is a Model 801 irradiator housing a 40 mCi $^{90}Sr/^{90}Y$ source. It was calibrated by the author, but not used in subsequent experimental work.

Reader	Leakage (μGy)	Dose under-delivery (μGy)	Cross-talk (μGy/Gy)	
			nn	2nn
Risø 1	2,379	640	42	12
Risø 2	2,901	780	42	12
Risø 3	197	10,810	60	6

Table 2.6. Risø β source performance, based on source dose rates at 1/10/01. Leakage values are for 30 minutes under a source in the "off" position. Crosstalk values are given for the nearest neighbour (nn) and second nearest neighbour (2nn) samples and are given in units of μGy per Gy received by the irradiated sample. Cross-talk measurements were also made by Bray *et al.* (2002) using a modern rotating wheel type β-irradiator. Their values are in good agreement with those of Markey *et al.* (1997).

The leakage and cross-talk values are both negligible. The dose under-delivery is constant irrespective of irradiation time and can be subtracted from the intended radiation dose to give the "true" radiation dose. In practice, dose under-delivery is several orders of magnitude smaller than the smallest dose administered in this study, and hence has been ignored.

2.4.3 Optical stimulation sources

Huntley *et al.* (1985) first demonstrated the feasibility of optically stimulating luminescence from quartz, using 514 nm light from an argon ion laser. Subsequently, a range of optical stimulation sources have been used (Table 2.7). The wide range of stimulating wavelengths used leads to the possibility that each may access charge from different trap(s) and/or in different proportions[j], leading to the possibility that data produced using different stimulation sources cannot be compared.

Stimulation source	Emission wavelength (nm)	Reference
Argon ion laser	514	Huntley *et al.* (1985)
Filtered halogen lamp	420-550	Bøtter-Jensen and Duller (1992)
Green LEDs	565 (peak)	Galloway (1993)
Blue LEDs	470 (half-width 20 nm)	Bøtter-Jensen *et al.* (1999a,b)

Table 2.7. Stimulation wavelengths of a selection of OSL stimulation sources.

[j] For example, Singarayer and Bailey (in press) found that the photoionisation cross-sections of the fast and medium components converged at lower stimulation wavelengths.

Murray and Wintle (1998) concluded that the effective stimulation wavelength of the Risø filtered halogen lamp was 468 nm. This value, determined on the basis of their measurement of the thermal assistance energy for quartz OSL, is almost identical to the emission peak for the Risø blue diode unit. Subsequently, Bøtter-Jensen *et al.* (1999a) compared data obtained using a filtered halogen lamp and a blue LED stimulation source. They found that normalised OSL decay curve shapes, and OSL intensity as a function of preheat temperature, were very similar for the two stimulation sources. In addition, for a suite of 34 samples, they could not distinguish between dating results obtained using the two stimulation sources. These data led them to conclude that both stimulation sources accessed the same traps in quartz. All the single-aliquot luminescence measurements reported in this thesis were made using Risø blue LED stimulation sources[k]. Consequently, data obtained using either blue LEDs or a filtered halogen lamp stimulation source should be comparable. Comparability with argon ion laser or green LED stimulation sources has not been demonstrated, though the argon ion laser emission does fall within the emission band of the filtered halogen lamp source. Also, Duller and Bøtter-Jensen (1996) suggest that wavelengths in the range 420-575 nm stimulate the same range of traps and use the same charge transport mechanisms to produce OSL.

2.4.3.1 Risø blue LED sources used in this study

The Risø blue LED stimulation sources all use NISHIA (type NSB-500S) diodes. These have a peak emission at around 470 nm, half-width 20 nm (Bøtter-Jensen *et al.*, 1999a). The stimulation source attached to Risø 1 is a prototype Risø combined IR/blue LED OSL unit, described by Bøtter-Jensen *et al.* (1999a, Figure 2). This consists of a ring of 13 blue LEDs and 11 IR LEDs focused on the sample. Risø 2 and 3 contain standard Risø OSL units (Bøtter-Jensen *et al.*, 1999a, Figure 1) in which LEDs are grouped in clusters of seven, with a maximum of six clusters. The Risø 2 unit contains 5 blue diode clusters and 1 IR laser diode. Risø 3 houses 3 blue diode clusters and 1 IR laser diode, the remaining two cluster positions are used by the single-grain attachment.

---

[k] All three units also contain IR diodes (Table 2.3), which were only used for measuring sample purity (Section 2.3.4).

Because only the first channel of stimulated signal was used to determine luminescence intensities (Section 2.2.2), the resulting values are strongly dependent on illumination response time. This is the time between switching the stimulation source on, and illumination reaching the correct intensity. Bøtter-Jensen *et al.* (1999b) have demonstrated that for blue LED stimulation sources, the illumination reaches maximum intensity almost instantaneously (Figure 2.3), and hence should not introduce significant errors into the data. They measured significantly longer illumination response times for the filtered halogen lamp source fitted with an electromechanical shutter. Consequently, similar experiments using a halogen lamp stimulation source, may not be directly comparable with data presented in this study.

OSL stimulation using blue LEDs requires carefully selected filter combinations to prevent stimulation light being measured along with the luminescence emission. The blue diode emission is filtered using Schott GG-420 green long pass filters, while the OSL emission is detected via several Hoya U-340 filters. The emission spectrum of the blue LEDs overlain by the transmission curves for GG-420 and U-340 filters is shown in Figure 2.4. The red transmission window present in U-340 filters (Bøtter-Jensen *et al.*, 1999a) is suppressed by including one metal oxide coated U-340 filter in each detection filter pack (not shown in Figure 2.4). Using this filter combination, Bøtter-Jensen *et al.* (1999a) measured the scattered stimulation light breakthrough into the detection transmission window and compared it with the dark noise of the system. They obtained a breakthrough/dark noise ratio of < 8 %. Similar results for the readers used in this study are presented in Table 2.3. These values are higher than those observed by Bøtter-Jensen *et al.* (1999a), however they should be highly reproducible. If this is the case, the breakthrough count rate will be subtracted from the signal (Section 2.2.2) and introduce negligible errors into the data.

It is interesting to note that the breakthrough count rate is not proportional to stimulation power or detection filter thickness, leading to two possible explanations.

1) The breakthrough/dark noise ratio is no controlled by scattered stimulation light breakthrough, but by some other cause of PMT noise.

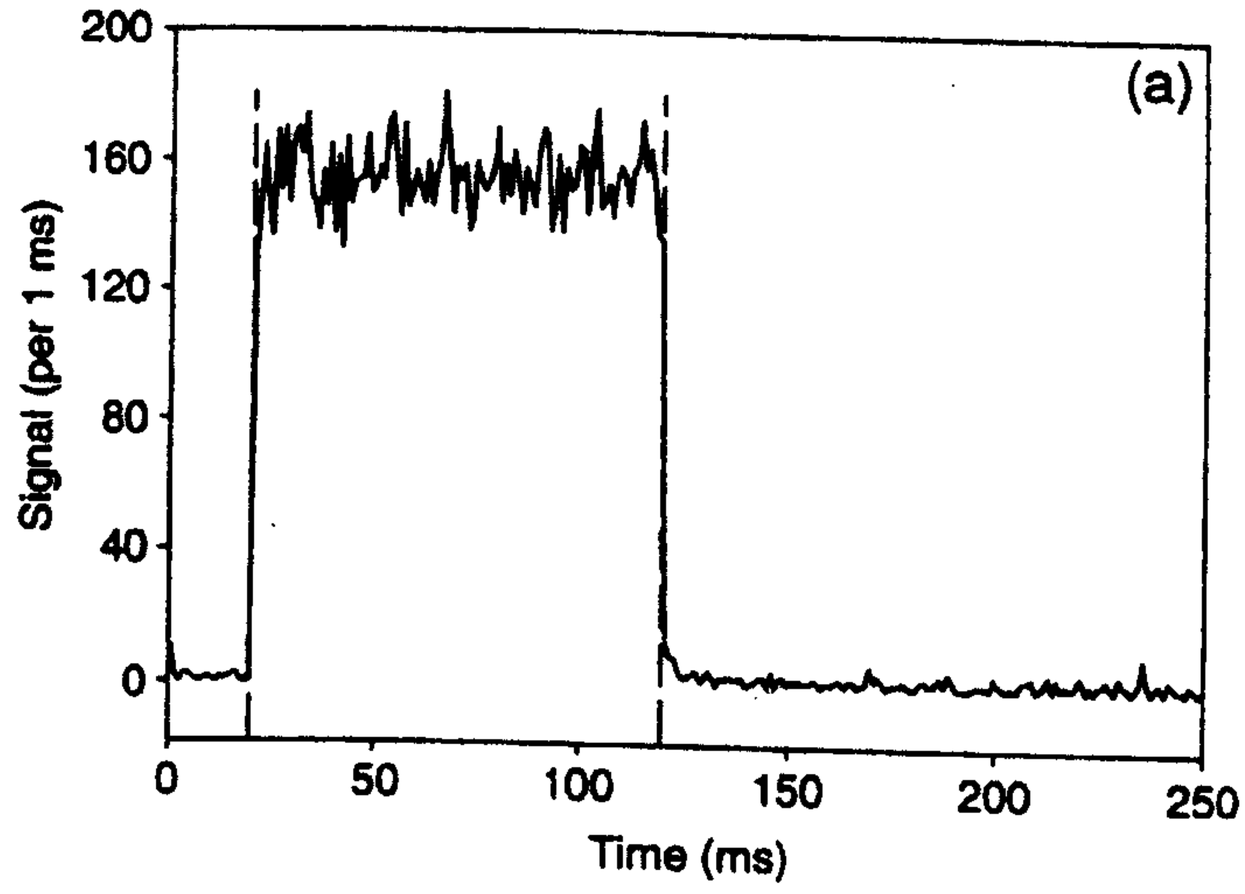

Figure 2.3. Scattered stimulating light from a 100 ms duration pulse. The dashed vertical lines indicate the time at which the on and off commands were issued, for: a) a blue LED array, and b) the filtered halogen lamp system (from Bøtter-Jensen *et al.*, 1999b).

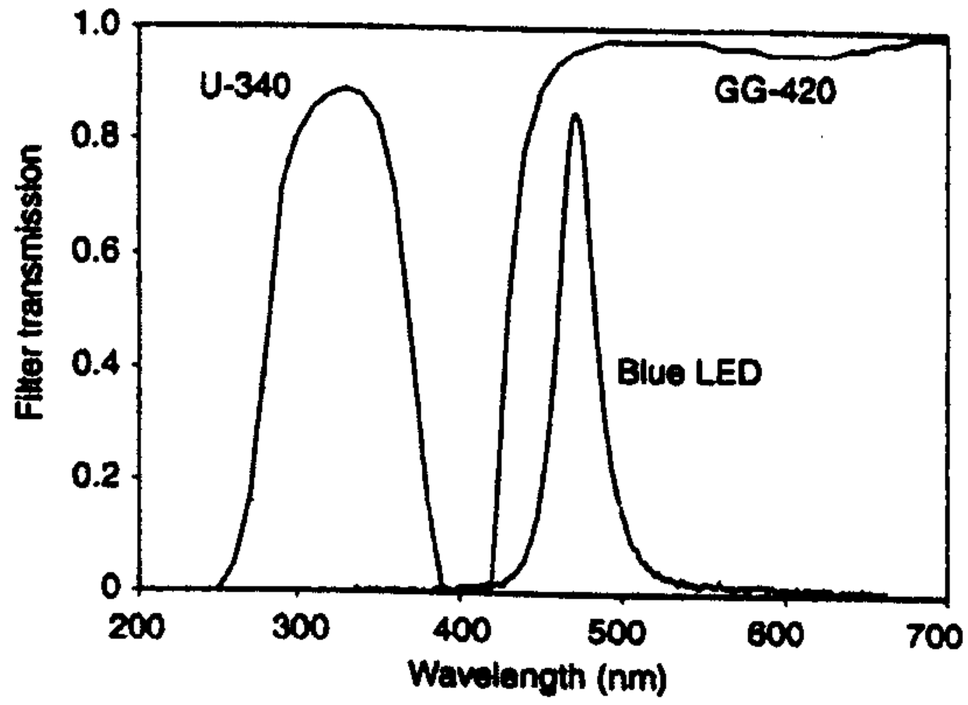

Figure 2.4. Emission spectrum of the blue LEDs overlain with transmission curves for Schott GG-420 and Hoya U-340 filters (from Bøtter-Jensen *et al.*, 1999b). TL observed in the 95-110°C region has a peak emission wavelength of 376 nm (Franklin *et al.*, 1995). The OSL is believed to be emitted by the same L-centre. Consequently, at a stimulation temperature of 125°C, the OSL emission is likely to peak at a similar wavelength, meaning that the lower energy tail of this emission will not be measured using this filter combination.

2) The U-340 filters used in each Risø reader have different efficiencies at rejecting scattered stimulation light.

2.4.3.2 Blue LED stimulation power

Risø 2 has a known stimulation power of 16.9 mW/cm^2 (Roberts and Wintle, 2001). Since the stimulation wavelength of all three blue stimulation sources is identical (Section 2.4.3.1), the stimulation power of Risø 1 and Risø 3 can be calculated from the signal decay rates obtained with these readers relative to that from Risø 2 (Spooner, 1994). This calculation was performed using decay curves measured during SAR equivalent dose measurement sequences.

The optical half-life of the initial (first 4 signal channels) signal was obtained by plotting $\ln(I/I_o)$ versus time for each aliquot, where I is the OSL intensity and I_o is the OSL intensity of the first signal channel (Figure 2.5.a). Interpolation/extrapolation was used since the temporal resolution of the measured decay curves was insufficient to calculate precise half-lives[1]. In addition, since the initial part of the decay curve primarily consists of signal from a single (fast decaying) OSL component, this approach reduced potential errors due to inter-aliquot variation in the proportion of the signal derived from each OSL component. For all samples, the optical half-life of the initial signal was found to be independent of both measurement cycle and PH1 temperature. Optical half-lives and resulting stimulation powers for the three stimulation sources are shown in Table 2.8.

Reader	Optical half-life (s)	Stimulation power (mW/cm^2)
Risø 1	3.54 ± 0.28	2.22 ± 0.17
Risø 2	0.466 ± 0.03	16.9 (± 0.94)
Risø 3	1.21 ± 0.09	6.51 ± 0.49

Table 2.8. Optical half-lives and stimulation powers for the blue LED stimulation sources used in this study. The stimulation power error for Risø 2 relates to the error on the optical half-life determination, not the stimulation source calibration value quoted by Roberts and Wintle (2001), and hence is given in parentheses.

[1] 250 signal channels were measured per decay curve. This gives a relatively coarse temporal resolution of 0.4, 0.16 and 0.4 seconds for decay curves measured using Risø 1, 2 and 3, when compared with the optical half lives measured for these readers.

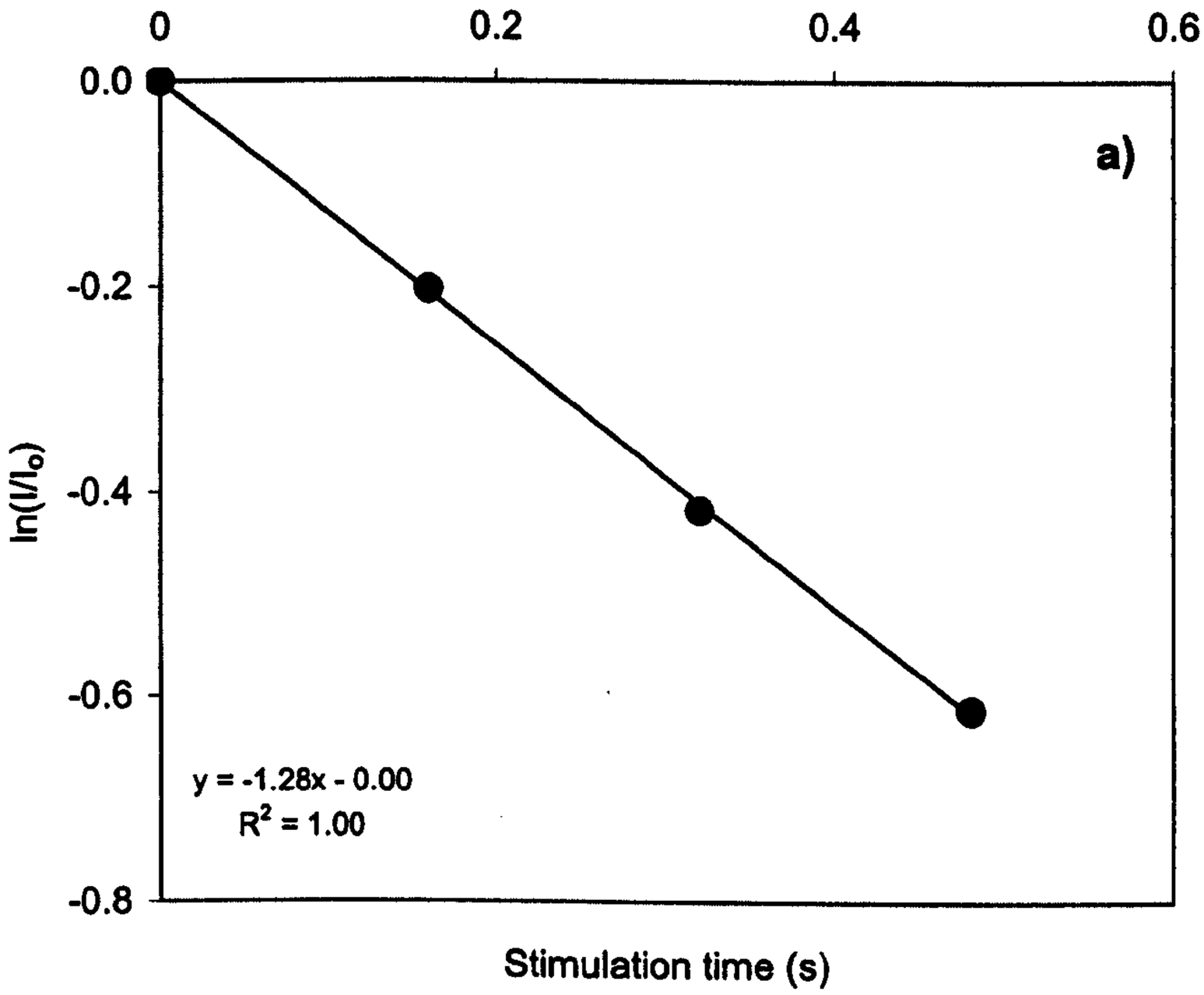

Figure 2.5. a) Initial portions of the OSL decay curve displayed on a semi-logarithmic scale. This decay curve was measured in Risø 2, from a natural aliquot of Aber/28-IN16, which had been given a 160°C PH1. The half-life of this decay is 0.54 s. b) The same decay curve displayed on a linear scale.

2.4.3.3 Cross-bleaching

Bray *et al.* (2002) have demonstrated that, using a 48 position sample carousel in a Risø TL/OSL DA-15 reader, optical stimulation of one aliquot inadvertently illuminates adjacent aliquots. They calculated that the adjacent aliquot receives 0.014% of the stimulation energy received by the aliquot being measured. Consequently, the adjacent aliquots may be bleached prior to measurement. Using the 0.014% cross-bleaching value calculated by Bray *et al.* (2002), cross-bleaching energy exposure experienced by an adjacent aliquot during a typical stimulation has been calculated for each reader (Table 2.9).

Reader	Typical stimulation energy (mJ/cm^2)	Cross-bleaching energy (mJ/cm^2)
Risø 1	220	0.03
Risø 2	676	0.09
Risø 3	650	0.09

Table 2.9. Cross-bleaching energies for the readers used in this study.

For a single measurement the cross-bleaching energy is negligible, and will not cause a significant depletion of the luminescence signal from the adjacent aliquot. However, repeated measurement of an aliquot prior to measurement of the adjacent aliquot may cause significant signal depletion in the latter. Consequently, each component of the measurement sequence was performed on all aliquots prior to proceeding to the next component (i.e. L_n was measured on all aliquots prior to measurement of T_n etc). Using this method, for any given luminescence measurement, the aliquot will have been exposed to a maximum of one episode of cross-bleaching. In practice, the cross-bleaching energies presented in Table 2.9 represent "worst-case" values, since Risø 1 and 2 use 24 position sample carousels, thereby increasing the distance between adjacent aliquots.

2.5 Samples used in this study

Brief descriptions of the samples used in this study are given below. More detailed descriptions and geological interpretations are provided in Sections 8.3 (Inhaca) and 8.4 (Bazaruto). The location of the three main study areas are shown in Figure 2.6.

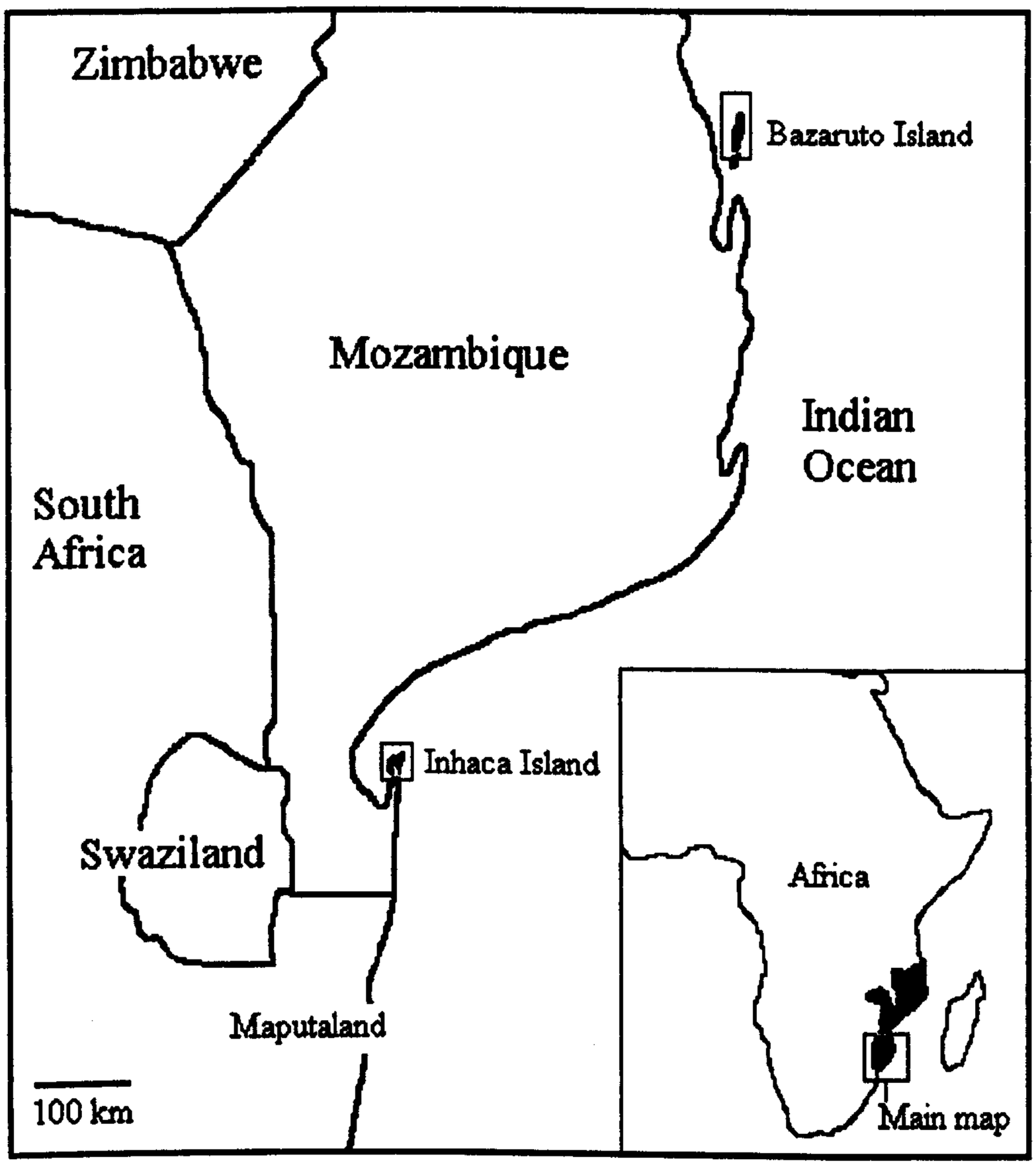

Figure 2.6 A map showing the location of the three main study areas referred to in Section 2.5.

2.5.1 Inhaca and Bazaruto Islands, Mozambique

The majority of samples dated during this study were collected from Inhaca and Bazaruto Islands, Mozambique. Brief descriptions are provided in Tables 2.10 (Inhaca) and 2.11 (Bazaruto).

Sample (Aber/28-...)	Deposit type	Exposure type	D_e (Gy)	Age (ka)
IN1	aeolianite	cliff	101 ± 10	149 ± 23
IN3	aeolianite	cliff	96.2 ± 6.5	99.6 ± 15.6
IN4	aeolianite	cliff	242 ± 18	>250
IN9	modern tidal-flat	surface	0.060 ± 0.005	0.071 ± 0.006
IN11	dune	cliff	133 ± 6	102 ± 5
IN12	dune	cliff	22.4 ± 0.5	22.5 ± 0.8
IN14	dune	pit	14.5 ± 0.3	11.7 ± 0.4
IN15	dune	pit	5.16 ± 0.06	6.09 ± 0.20
IN16	dune	pit	2.41 ± 0.02	2.16 ± 0.06
IN18	dune	pit	12.2 ± 0.3	14.5 ± 0.6
IN19	dune	pit	2.04 ± 0.30	2.48 ± 0.37
IN20	palaeo tidal-flat	pit	4.28 ± 0.07	3.68 ± 0.15
IN21	dune	pit	3.12 ± 0.30	2.69 ± 0.27
IN22	modern beach sand	surface	0.006 ± 0.004	-

Table 2.10. Brief descriptions for samples taken from Inhaca Island, Mozambique. A minimum age is quoted for Aber/28-IN4 since a significant number of aliquots yield natural luminescence intensities greater than the saturation luminescence intensity of the growth curve. This phenomenon is explored in Section 6.4.4. Aeolianites are cemented dunes, while the term dune was applied to any uncemented aeolian deposit sampled. Tidal flats are broad flat caused by tides. Samples were taken from three exposure types, pits dug into the surface of dunes, sea-cliffs which gave natural sections through the deposit, and surface exposures.

Sample (Aber/29-…)	Deposit type	Exposure type	D_e (Gy)	Age (ka)
BA1	aeolianite	cliff	124 ± 7	90.0 ± 5.8
BA2	beachrock	*in situ* block	7.83 ± 0.83	7.30 ± 0.79
BA4	dune	pit	0.114 ± 0.004	0.088 ± 0.004
BA5	modern dune	surface	0.003 ± 0.010	-
BA8	beachrock	*in situ* block	1.70 ± 0.15	0.94 ± 0.09
BA10	dune	pit	17.1 ± 1.1	8.37 ± 0.54
BA11	dune	cliff	3.37 ± 0.43	2.41 ± 0.32
BA12	palaeosol	cliff	7.02 ± 0.77	4.02 ± 0.46
BA13	dune	cliff	29.7 ± 2.4	24.1 ± 2.1
BA14	dune	cliff	176 ± 13	128 ± 10

Table 2.11. Brief descriptions for samples taken from Bazaruto Island, Mozambique. Beachrocks are cemented sand, which form in the intertidal zone of a beach.

2.5.2 Maputaland

A modern beach sand (Aber/40-SA10) was collected from Maputaland, South Africa.

Sample (Aber/40-…)	Deposit type	Exposure type
SA10	modern beach sand	surface

Table 2.12. A brief description the sample taken from Maputaland, South Africa.

2.5.3 Miscellaneous samples

The samples described in Tables 2.10-12 were collected by the author. However, four samples not collected by the author have also been used in this study. Aber/12-MAP3, Aber/12-RBM2 and Aber/12-RBM2a are sedimentary quartzes from Maputaland, South Africa, and were collected by Professor Ann Wintle. CalQtz is a calibration sample, which was annealed (500°C) and then given a 4.6 Gy γ dose. CalQtz was provided to the Aberystwyth laboratory by Dr. Andrew Murray. Brief descriptions of these samples are given in Table 2.13.

Sample	Deposit type	D_e (Gy)	Age (ka)
Aber/12-MAP3	dune	29.0 ± 0.6	41.0 ± 1.3
Aber/12-RBM2	cemented dune	93.5 ± 9.5	67.2 ± 7.2
Aber/12-RBM2a	uncemented dune	-	-
CalQtz	annealed, γ irradiated calibration sample	4.6	-

Table 2.13. Brief descriptions for the samples used in this study, which were not collected by the author.

2.6 Summary

1) The SAR method has been used to produce equivalent doses throughout this study. This procedure compensates for sensitivity changes by measuring the OSL signal in response to a test dose administered immediately after the natural/regenerated luminescence intensity has been measured. Growth curves were fitted using a saturating exponential plus linear fit, with a small y-axis offset.
2) Geological samples were collected in opaque tubes or as blocks. Modern material was collected from the surfaces of presently accumulating deposits.
3) Samples were prepared under subdued red light. Standard techniques were used to remove organic and carbonate material, after which the material was sieved. Quartz was then isolated from the 211-180 μm fraction and further purified using an HF etch. Etched quartz was mounted, as a monolayer, on aluminium discs. Sample purity was routinely checked using infra-red stimulation.
4) Measurements were performed using Risø automated TL/OSL readers.
5) Risø or Daybreak β irradiators were used to administer radiation doses. Leakage, dose under-delivery and cross-talk are all believed to be negligible using these irradiators.
6) Risø blue diode units were used for optical stimulation. The emission filters used efficiently reject stimulating light, leading to limited breakthrough. Inadvertent bleaching of samples adjacent to the aliquot being measured is small.
7) The samples dated in this study were collected from sedimentary deposits on Inhaca and Bazaruto Islands, Mozambique. A single modern sample was collected from Maputaland, South Africa. Work was also carried out on four miscellaneous samples not collected by the author.

Chapter 3: Validation of the SAR technique

3.1 Introduction

The SAR technique has been successfully applied to both fired and sedimentary quartzes by a number of authors (e.g. Murray and Wintle, 2000). However, it does not always yield ages which are in agreement with stratigraphic inference, or other radiometric techniques. For example, Stokes *et al.* (2000) found that 16 % (n=112) of their samples yielded implausible ages when measured using the standard SAR method.

Using samples from Inhaca, Bazaruto and Maputaland (see Section 2.5), this chapter presents a series of experiments designed to test a) the suitability of these samples for OSL dating and b) the applicability of the SAR technique to these samples. Most of these tests use the standard measurement conditions described by Murray and Wintle (2000) and outlined in Section 3.1.1, and hence only test the assumptions of the original version of the SAR technique. Some of the assumptions and measurement conditions used during the development of the original SAR technique are tested in Chapters 4 and 5.

The suitability of these samples for OSL dating has been tested in Section 3.2 by measuring D_e values for four samples from active sedimentary environments. This tests the fundamental assumption of OSL dating techniques – that the OSL signal of the sample, was reduced to zero prior to deposition.

A variety of experiments have been performed to test the applicability of the SAR technique to these samples. The reproducibility of the SAR sensitivity correction is tested in Section 3.3, by measuring the same regeneration dose at the beginning and end of each measurement sequence, and comparing the sensitivity-corrected OSL intensities (R_x). Zero dose luminescence measurements are discussed in Section 3.4, in order to investigate the potential impact of recuperation on the D_e measured. Together, the tests presented in Sections 3.3 and 3.4 indicate that the laboratory use of quartz as a dosimeter is appropriate. The ability of the SAR technique to accurately measure a known laboratory radiation dose is assessed in Section 3.5, thereby testing whether quartz

changes its luminescence characteristics during measurement of the first (natural) OSL signal. Experiments to test for the presence of a time dependant increase in OSL at elevated (125°C) measurement temperatures (as observed by Stokes *et al.*, 2000) are presented in Section 3.6. Finally, in Section 3.7, the effect of PH1 temperature on measured D_e is assessed.

3.1.1 Standard measurement conditions

The SAR method allows several measurement conditions and parameters to be varied. Unless otherwise stated, all measurements reported in this thesis were taken using the conditions described in Chapter 2 and Table 3.1.

Variable	Standard conditions	Variable investigated
PH1	10s, between 160 – 300°C, heating at 5°C/s	Chapters 3-5
OSL stimulation temperature	125°C, after a 10s pause at temperature	Section 3.6
OSL signal integration period	1st signal channel, minus a background estimated from the last 25 channels of L_x	Chapter 4
Test dose	5 Gy, unless D_e is less than 5 Gy, in which case 1-2 Gy	-
PH2	160°C, cooled immediately, heating at 5°C/s	-

Table 3.1. Standard measurement conditions used during this study. The effects of varying some of these standard conditions has been investigated in this and subsequent chapters.

3.2 D_e values from modern samples

The successful application of OSL methods to sediments can only occur where the signal measured has been reduced to zero prior to deposition. This event is termed zeroing, resetting or bleaching, and occurs when mineral grains are exposed to sunlight. If insufficient exposure to sunlight occurs, the signal is not fully reset to zero. Consequently, the OSL signal is "partially bleached", and the age based on the measured equivalent dose is erroneously large.

Even when mineral grains are fully bleached prior to deposition, the quartz OSL signal is known to "recuperate" (see Section 1.5.2.2). This involves the transfer of charge from

relatively optically insensitive, thermally unstable traps, to the main trap responsible for the OSL signal, either during burial or preheating[a] (Aitken and Smith, 1988 and Banerjee, 2000). Consequently, L_n contains a contribution from the previous burial period[b], and the age based on the measured equivalent dose is erroneously large.

Banerjee (2000) suggests that the main sources of recuperated OSL are the 110 and 280°C TL traps. The 110°C TL trap is empty during burial, due to the low thermal stability of charge contained in this trap (lifetime at 20°C of 70 minutes, Table 5.3). When the sediment is exposed to sunlight prior to deposition, charge is evicted from optically sensitive traps via the conduction band. Some of this charge is phototransferred to the 110°C TL trap, which is significantly less optically sensitive than the main trap responsible for the OSL signal (Bailey, 1997). If the sediment is deposited at this point, charge is untrapped from the 110°C TL trap at burial temperature, via the conduction band. A proportion of this charge is retrapped in optically sensitive traps, leading to the occurrence of a non-zero OSL signal shortly after deposition. If a sediment is subjected to several bleaching events, or one prolonged bleach, the recuperated signal caused by this mechanism will be reduced to a negligible level. In contrast with the 110°C TL trap, the 280°C trap is relatively thermally stable (lifetime c.160,000 years at 20°C, Spooner and Questiaux, 2000), and consequently accumulates charge during burial. Charge in this trap is far more optically stable than that in the main trap responsible for the OSL signal. Consequently, the 280°C trap in a sediment that has had its OSL signal fully zeroed prior to deposition, may still contain a significant proportion of the trapped charge accumulated during the previous burial period. During measurement of such a sample, preheats that erode charge from the 280°C TL trap, may cause a proportion of this charge to be transferred to the more thermally stable OSL traps, and thereby contribute to L_n[c].

---

[a] This is also known as thermal transfer.

[b] If the preheat does not remove all the charge from the optically insensitive, thermally unstable trap, subsequent luminescence signals may also contain a contribution from the previous burial dose. However, the effect will be largest for L_n.

[c] It is also possible that during a subsequent burial period, the charge in this trap will decay at ambient temperature, and be retrapped at the more thermally stable traps responsible for the OSL signal. However, since charge in the 280°C TL trap is relatively stable, this effect will only be observable in relatively old samples. Unless the concentration of 280°C traps is large relative to the that of the OSL traps, this signal will be negligible in comparison with the OSL relating to the burial dose.

It is interesting to note that, since the 280°C and 325°C traps appear to use different L-centres (Section 1.6.1.1), they cannot have access to a truly delocalised conduction band, and hence thermal transfer of charge between the two traps should not be possible. It is possible that only a small amount of charge from the 280°C trap has access to the same L-centres as the 325°C trap. This which would account for Franklin *et al*'s (1995) conclusion that the two traps use different L-centres, while allowing a small amount of thermal transfer from the 280° to the 325°C TL traps during heating.

3.2.1 Measured data

To determine the likelihood that partial bleaching and/or recuperation has adversely affected the equivalent doses measured for geological samples, samples from active depositional environments within the study area have been measured. In this study, four modern samples that are analogues for the geological samples being dated, were used. These consisted of two samples from beaches (the likely sediment source), and one each from an active sand dune and tidal flat (the geomorphological features dated). A typical D_e versus PH1 temperature plot is shown in Figure 3.1 (closed circles), where PH1 is the 10s preheat given prior to measurement of L_n or L_x (see Appendix 2.1). Using PH1 temperatures between 160 and 240°C the equivalent dose is consistent with zero. This indicates that the sample was completely bleached prior to deposition, and that ambient temperature recuperation from the 110°C TL trap is negligible. The equivalent dose rises at higher PH1 temperatures, reaching a mean value of 0.25 Gy at 300°C. This is the largest mean equivalent dose obtained for the modern samples, and equates to an age overestimate of c.100-300 years, depending on the environmental dose rate (Chapter 7). Bailey *et al.* (2001) and Rhodes (2000) observed similar trends in D_e with PH1 temperature for aeolian sands from Anglesey, Wales and glacigenic sediments from the Himalayas respectively. However, in both cases, the D_e rise at higher PH1 temperatures was larger than that observed here[d].

[d] Using a PH1 temperature of 300°C, Bailey *et al.* (2001, Figure 3) measured a D_e 1.5 Gy higher than that obtained using PH1 temperatures in the range 160-260°C. Using laboratory bleached glacigenic sediment, Rhodes (2000, Figure 1) measured D_e values up to 10 Gy using a PH1 temperature of 300°C.

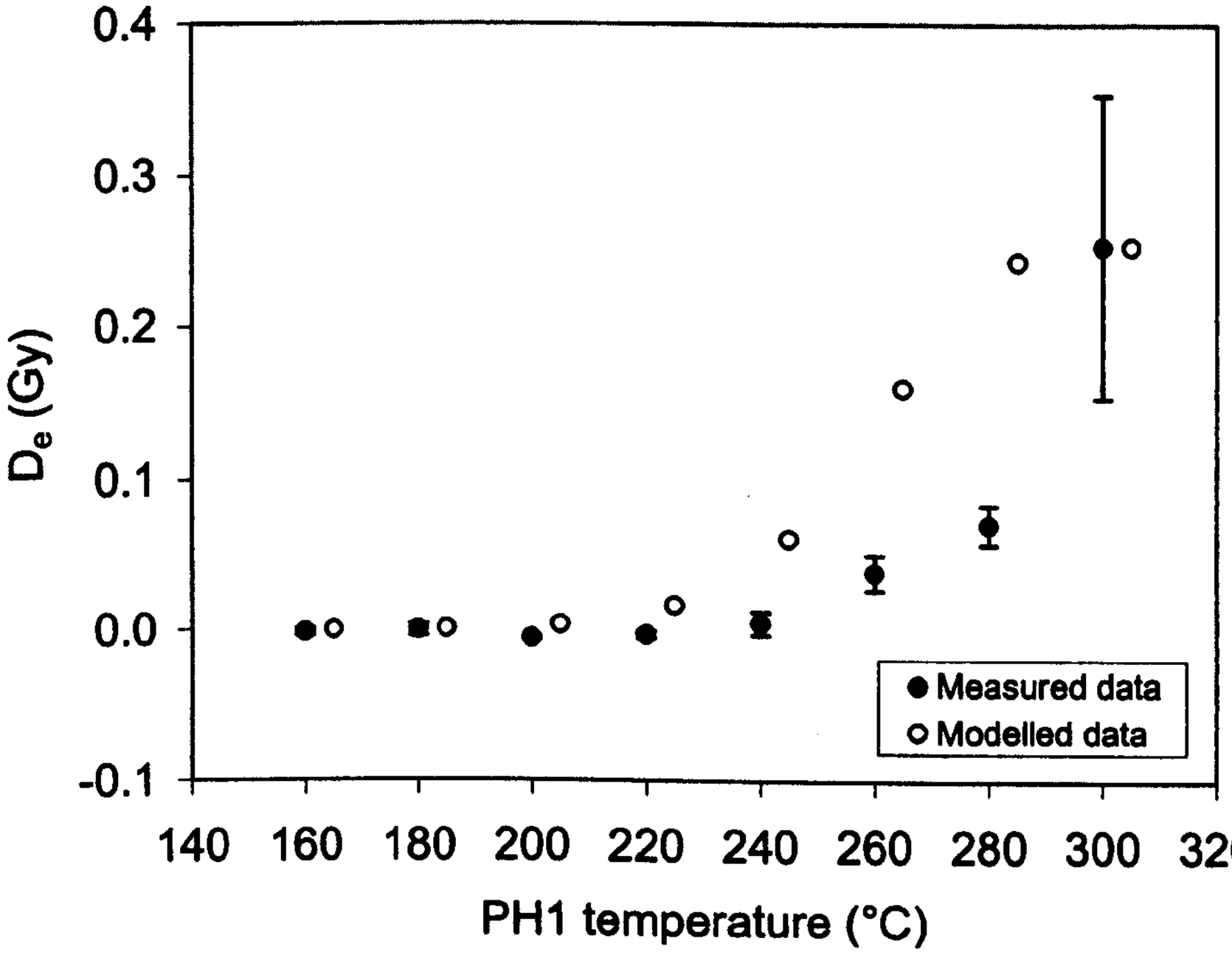

Figure 3.1. A plot of D_e versus PH1 temperature for a sample of Aber/40-SA10, taken from a modern beach. The closed circles represent the mean value of three aliquots, with one standard deviation errors. The open circles represent modelled recuperation data. The recuperation data were modelled by calculating the proportion of charge evicted from the 280°C TL trap, by 10s at the PH1 temperature. This figure was multiplied by 0.25 Gy (the mean recuperation using a 300°C PH1) to yield modelled recuperation appropriate for this sample. For clarity the modelled data have been displaced by 5°C on the x-axis.

3.2.2 Modelled data

The rise in D_e at higher PH1 temperatures seen in Figure 3.1, is consistent with thermal transfer of charge from the 280°C TL trap to the OSL traps during preheating. This effect has been modelled (Figure 3.1, open circles) using the kinetic parameters for the 280°C TL trap calculated by Spooner and Questiaux (2000). The recuperation seen in the modelled data appears to start at slightly lower PH1 temperatures than for the measured data. This observation may be explained by a reduction in the effective preheat temperature, caused by the thermal lag between heater plate temperature and aliquot temperature (Jain *et al.*, 2001), although a lag of 30-40°C would be required.

For the modern samples used in this study, the effect of recuperation from the 280°C TL trap is small. Consequently, in most geological samples, the effect will be obscured by other sources of D_e variability. Mean D_e values for the four modern samples are shown in Table 3.2, and effective ages are calculated using typical radioactivity data from Chapter 7.

Sample (Aber/…)	Context	D_e plateau region (°C)	D_e (Gy)	Effective age (yrs)
28-IN9	Tidal bar	160-260	0.060 ± 0.005	71 ± 6
28-IN22	Beach	160-260	0.006 ± 0.004	6 ± 4
29-BA5	Dune face	160-260	0.003 ± 0.010	2 ± 7
40-SA10	Beach	160-240	-0.001 ± 0.005	-1 ± 5

Table 3.2. Mean equivalent dose estimates, obtained using SAR, for four modern samples from the study area. Dosimetry measurements were only made on Aber/28-IN9. For the other samples, effective ages have been calculated using typical environmental dose rates of 1 and 1.5 Gy/ka for Inhaca (Aber/28-IN22) and Bazaruto (Aber/29-BA5) respectively. An arbitrary environmental dose rate of 1 Gy/ka has been used for Aber/40-SA10. These effective ages represent the age overestimate that would be measured for these samples after a period of burial.

3.3 Repeated regeneration points

Murray and Wintle (2000) suggest that the SAR sensitivity correction should be tested for each aliquot measured. This is achieved by measuring the same regeneration dose twice during the SAR dating sequence. When the sensitivity correction is appropriate, the sensitivity corrected OSL intensities (R_x) measured on the two occasions should be identical. To maximize the sensitivity change, and therefore the robustness of the test, the identical regeneration doses should be the first and last ones measured (Armitage *et al.*,

2000). The "recycling ratio" (R_x/R_1) is used to express the similarity between these two regeneration points. Values close to unity indicate similar regenerated luminescence intensities, and by inference, accurate sensitivity correction. Murray and Wintle (2000) advocate rejecting aliquots with recycling ratios deviating from unity by >10 % (i.e. <0.9 and >1.1). This limit has been adopted in the present study. Figure 3.2a shows sensitivity change (T_x/T_1 i.e. the test dose intensities measured after L_x and L_1) plotted against recycling ratio for all the aliquots dated (n=652). Positive sensitivity change ratios indicate that sensitivity increased during the measurement sequence, while the opposite is true of negative values. The mean recycling ratio is 0.989 ± 0.099, indicating that the SAR sensitivity correction procedure is accurately correcting for sensitivity change in these samples. Despite the wide range of sensitivity changes measured (T_x/T_1 ranges from 0.6 to 1.9), no trend in the recycling ratio with sensitivity change is observed in Figure 3.2a.

Although the mean recycling ratio indicates adequate sensitivity correction, individual values are occasionally very poor, especially at high PH1 temperatures (Figure 3.2b). Less than 5 % of the aliquots preheated at temperatures from 160 to 260°C were rejected on the basis of poor recycling ratios, whereas >50% of the aliquots preheated at 300°C were rejected[e]. There were no obvious errors in either the L_x or T_x decay curves for the repeated dose points, and they did not contain "spikes" indicative of electrical interference. Therefore, other explanations for the poor recycling using higher PH1 temperatures were investgated.

The pattern of sensitivity change was investigated by plotting test dose OSL (T_x) against measurement cycle. Figure 3.3 shows such a plot for two aliquots of Aber/28-IN19. For one aliquot (#19) the recycling ratio was good (0.99), whereas for the other (#22) it was poor (0.82). In both cases, the sensitivity changed smoothly with cycle, suggesting that errors in test dose OSL measurements did not cause the poor recycling ratio[f].

---

[e] The mean recycling ratio for PH1 temperatures in the range 160-260°C is 0.992 ± 0.046. This is not significantly different from the mean recycling ratio obtained using all PH1 temperatures, though the uncertainty on the latter is larger.

[f] Patterns of sensitivity change during SAR measurement sequences are investigated in Chapter 5.

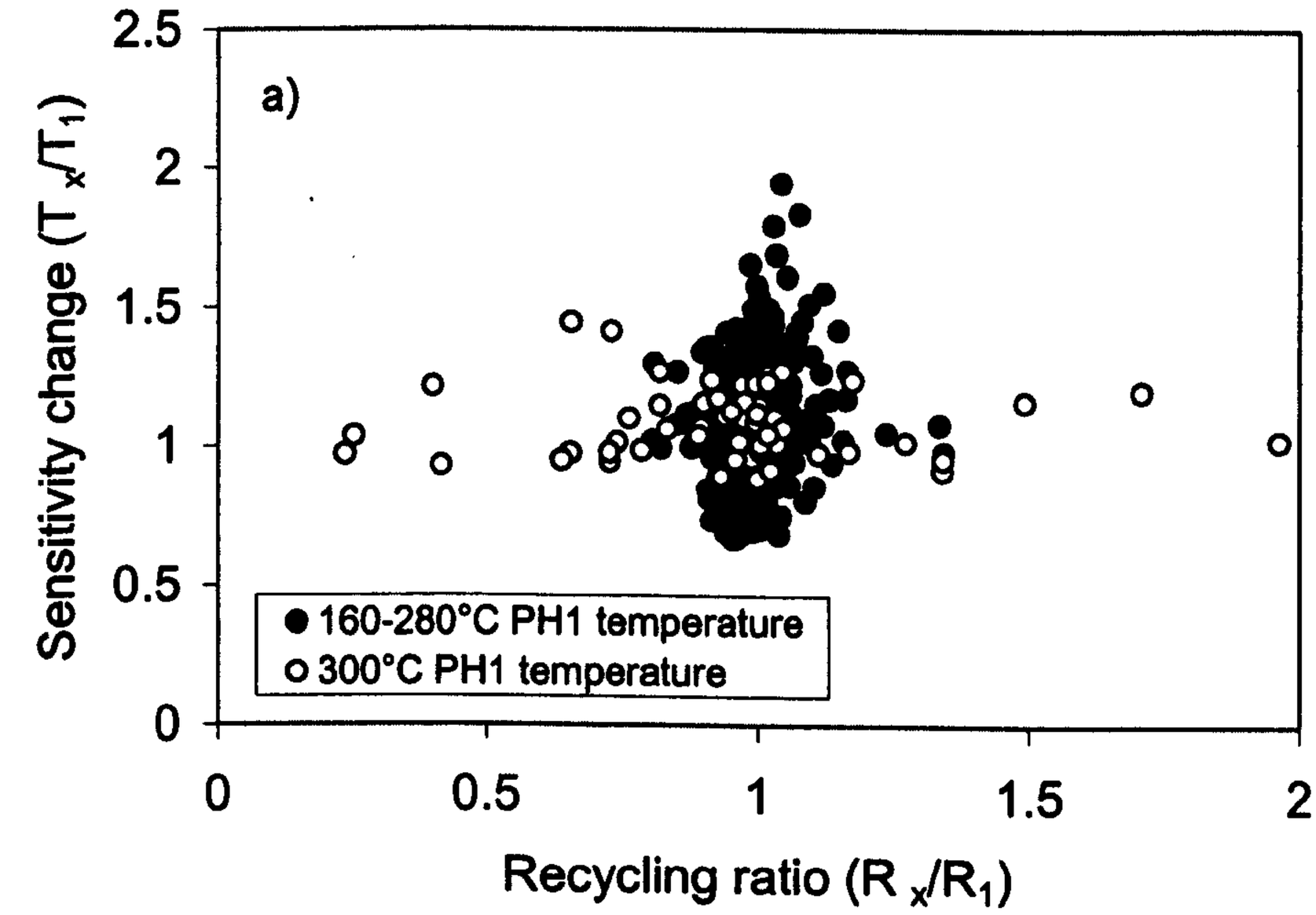

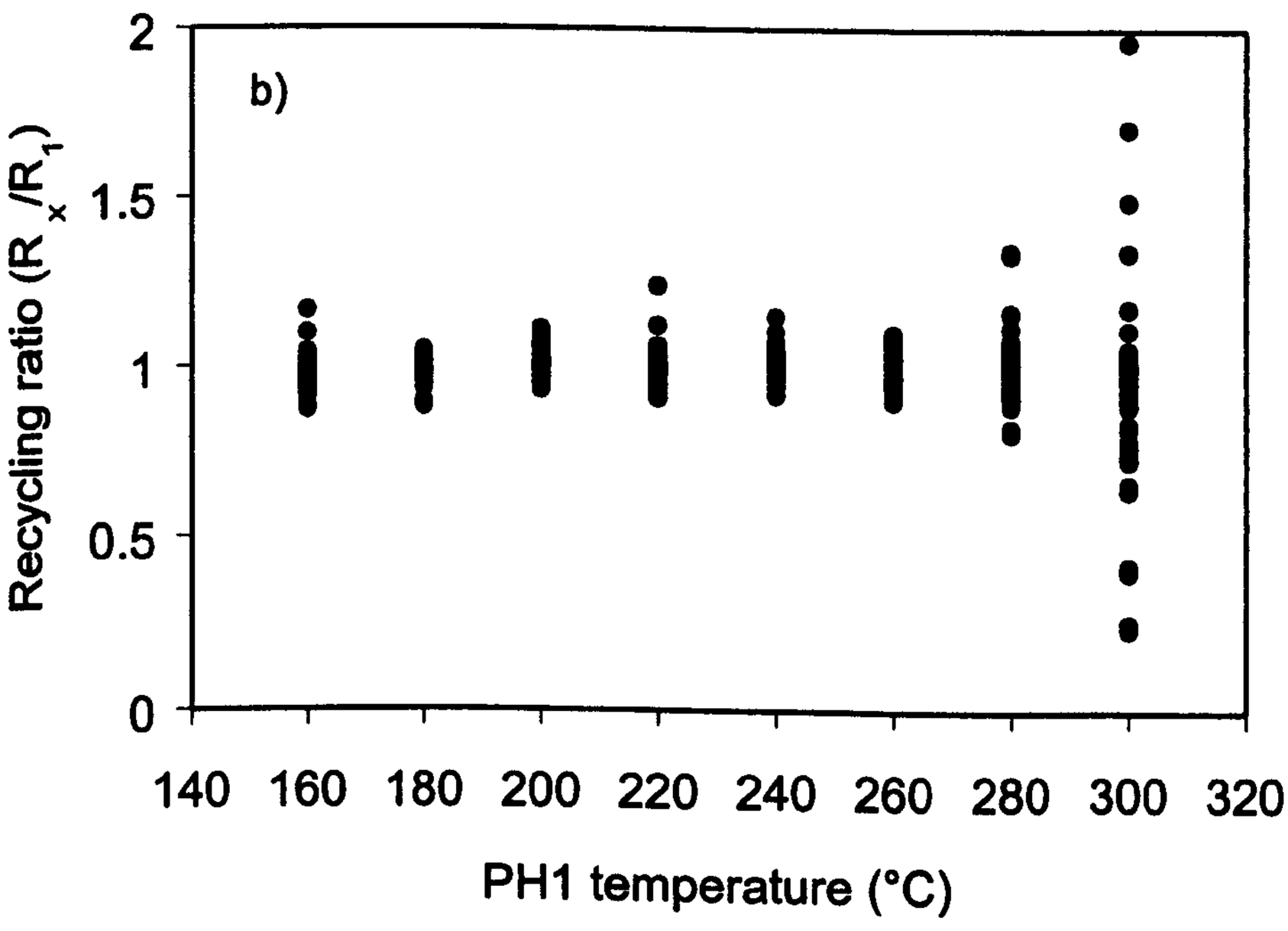

Figure 3.2. a) Sensitivity change (T_x/T_1) versus recycling ratio (R_x/R_1) for 652 aliquots used in this dating programme. The open circles represent aliquots measured using a PH1 temperature of 300°C, while aliquots measured at lower PH1 temperatures are represented by closed circles. Sensitivity change was calculated as T_x/T_1, when x is the number of the repeated regeneration dose. This value is usually smaller than T_x/T_n, and is used in this diagram because it expresses the sensitivity change that occurred between measurement of L_1 and L_x, the identical regeneration doses. b) Recycling ratio versus PH1 temperature. Data collected between 20/4/99 and 21/10/99 have been excluded due to erroneously low measurement and preheat temperatures (Section 2.4.1).

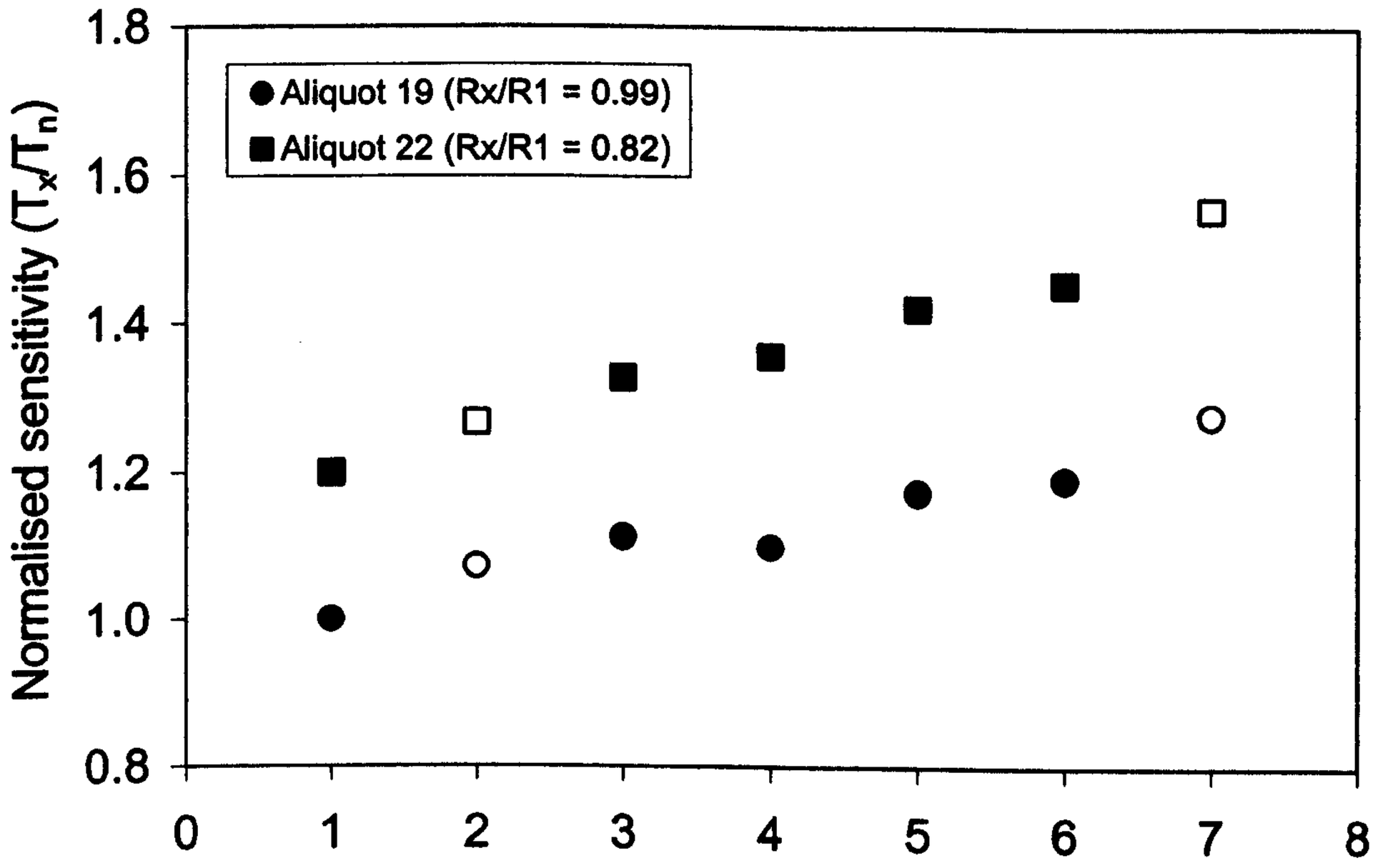

Figure 3.3. Normalised sensitivity versus cycle number for two aliquots of Aber/28-IN19. All data are normalised to T_n. The data for aliquot 22 have been offset by 0.2 units for clarity. The open symbols represent the test dose responses for the repeated dose points.

Consequently, it is likely that the poor recycling ratio is caused by fluctuations in L_x not related to luminescence sensitivity changes.

One possible cause for this is signal depletion at higher PH1 temperatures. The exact temperature and time for which an aliquot is preheated, will have a significant impact on L_x. Both factors may vary slightly with measurement cycle. The temperature reached by an aliquot, for a given heater plate temperature, is dependant on the thermal contact between the heater plate and the aluminum disc. Slight blemishes on the underside of the disc will alter the efficiency of conduction, and consequently the temperature reached by the aliquot. Since the disc is known to rotate during measurement sequences, and the heater plate is not in contact with the entire disc, the temperature reached by the aliquot during preheating may vary slightly during a measurement sequence. High PH1 temperatures significantly deplete the OSL signal (Figure 3.4), while lower preheat temperatures do not. Therefore, the effect on L_x will be more significant at high PH1 temperatures, because the rate of thermal erosion of the OSL signal is higher. Aliquot temperature variations were assessed by measuring the TL during PH1, and comparing the 110°C TL peak position for the two repeated regeneration dose points. Small (<5°C) changes in 110°C peak position were observed, but the effect is not more marked for aliquots which yield poor recycling ratios. Although the 110°C TL peak position is not a very sensitive measure of thermal lag at 300°C, variable thermal contact between the heater plate and aliquot can be tentatively discounted as a cause of poor recycling ratios at high PH1 temperatures.

It is also possible that PH1 times vary slightly during a measurement sequence. During a 300°C, 10s PH1, the Risø reader performs four separate operations (Table 3.3). The heating rates and pause times are very precisely controlled using a timing mechanism in the Mini-Sys (Figure 2.2), and are likely to be reproducible. However, on completion of each command, the Mini-Sys waits for the next command from the host computer. The speed with which this command is supplied is governed by the processor activity of the host computer, and this varies. Consequently, the delay time between completion of one command and commencement of the next will vary. Because the sample is at the preheat

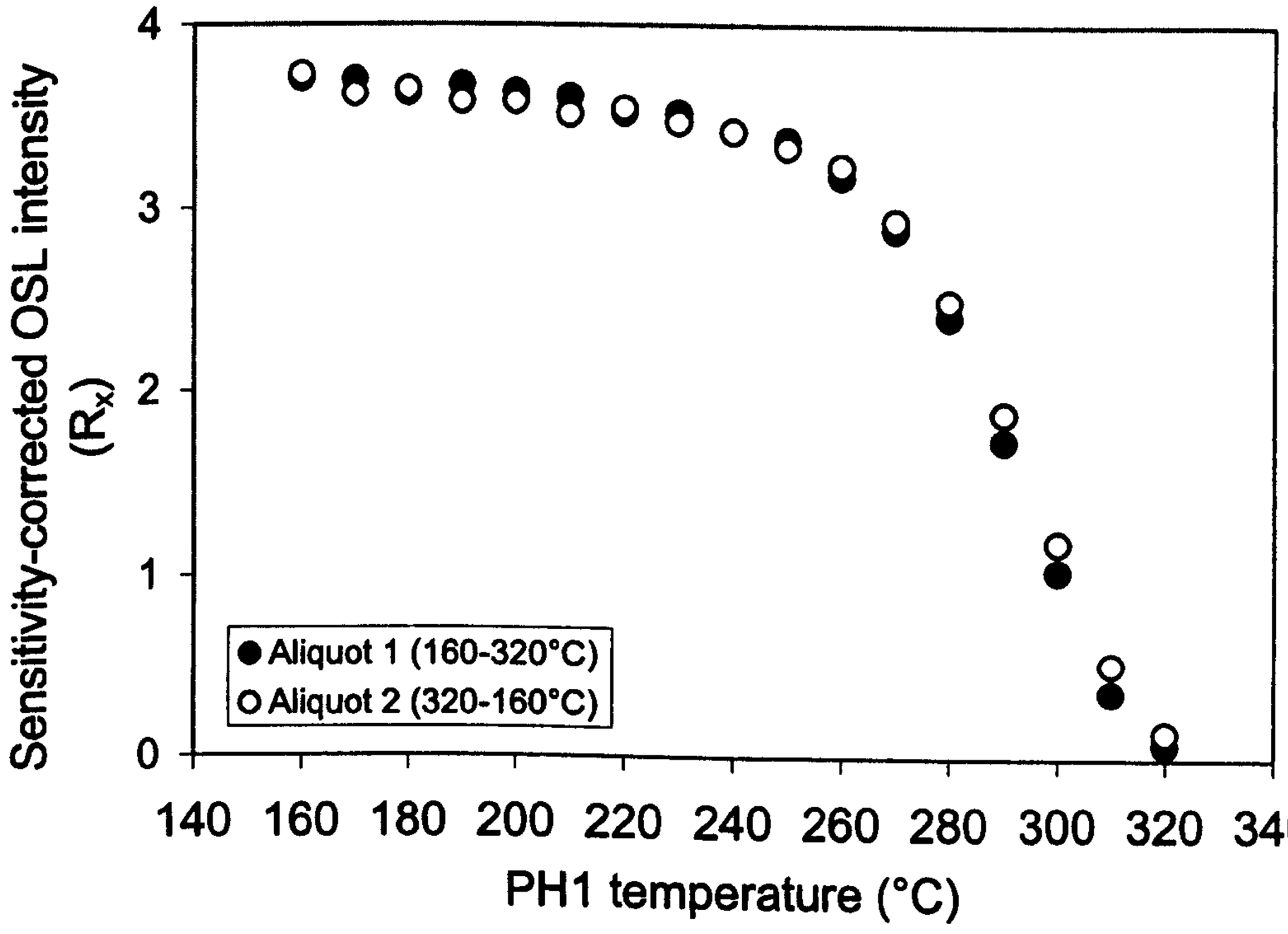

Figure 3.4. Sensitivity-corrected OSL intensity versus PH1 temperature for two aliquots of Aber/40-SA10. Each aliquot was heated to 500°C, immediately cooled, and then given a c.10 Gy regeneration dose. A standard SAR measurement cycle was then performed, using a test dose of c.5 Gy. Following the test dose measurement the aliquot was heated to 500°C to remove charge from the low temperature TL traps, thereby preventing charge accumulation in these traps from obscuring the pattern of OSL depletion. The cycle was then repeated using a PH1 temperature 10°C higher/lower than in the previous cycle. The aliquot represented as solid circles used an initial PH1 temperature of 160°C, rising to 320°C in 10°C steps. The aliquot represented as open circles used an initial PH1 temperature of 320°C, falling to 160°C in 10°C steps. The two datasets are almost identical indicating that the sensitivity correction is appropriate and charge accumulation in traps not emptied by the 500°C thermal treatment did not contribute significantly to the measured OSL signal.

temperature from the completion of command 2 to the completion of 4, the aliquot may not spend an identical time at temperature during each preheat. During low temperature PH1 and all PH2, the rate of OSL signal depletion is low, and hence small fluctuations in the preheat time do not affect the OSL intensity significantly. At high PH1 temperatures however, the effect can be significant. Using the OSL trap kinetic parameters obtained by Murray and Wintle (1999a and b), a discrepancy between the two PH1 times of c.4s is required to generate a recycling ratio error of 10%[g]. In practice however, the discrepancy required may be considerably smaller due to the c.10s lag between heater plate and sample temperature reported by Jain *et al.* (2001).

Command number	Operation
1	Lift up
2	Ramp temperature to 300°C @ 5°C/s
3	Pause @ 300°C for 10s
4	Lift down

Table 3.3. Commands received by a Risø TL/OSL reader to perform a 300°C, 10s preheat.

The reduced L_x intensity observed after a high temperature preheat is believed to be due to thermal erosion of charge from the main, rapidly bleaching, OSL trap. Consequently, OSL derived from traps which normally make only a minor contribution to L_x, may become significant. The main OSL trap does not suffer significant thermal depopulation during PH2 (a 160°C cut heat) and hence T_x is dominated by charge from this trap. Consequently, L_x and T_x may not be derived from the same traps in the same proportion. In this situation, the assumed 1:1 relationship between L_x and T_x sensitivity may not exist, resulting in poor recycling ratios. It is also possible that the signal depletion caused by higher PH1 temperatures leads to a decreased signal:noise ratio, and consequently increased susceptibility to random fluctuations in the background signal. This effect is unlikely to be significant in the present study since L_x, after a 300°C preheat, is generally two to three orders of magnitude larger than the instrument dark noise (see Table 2.3).

[g] Assuming a heating rate of 5°C/s and instantaneous cooling. The discrepancy quoted is time at preheat temperature, in this case 300°C.

In conclusion, no single cause for the high occurrence of poor recycling ratios, using a PH1 temperature of 300°C, can be confidently identified.

3.4 Zero dose point luminescence measurements

An assumption of the SAR technique is that L_x results solely from regeneration dose (β_x). In other words, if β_x is 0 Gy, L_x (and consequently R_x) should also be zero. However, Murray and Wintle (2000) observed a detectable recuperated OSL signal from two samples where this assumption was tested. They suggested two potential mechanisms for this recuperation.

1) Thermal transfer of charge from optically-insensitive traps during PH1. These traps were filled in nature and/or during subsequent artificial irradiation. In such a case, some PH1 temperatures will incompletely drain the optically insensitive trap (with associated charge transfer to the OSL traps). Consequently, the charge available for thermal transfer will be dependant on prior irradiation history, and the contribution made by thermally transferred charge to L_x will vary with cycle, leading to a distortion of the growth curve.
2) The recuperation is derived from the test dose. Traps are filled by the test dose irradiation, but not emptied by the low temperature cut-heat (PH2). Subsequently, the more rigorous PH1 transfers this charge to the OSL trap. In this instance, the recuperation signal will be constant with cycle, and contribute to all R_x values (but not to L_n/T_n). Consequently, true R_x values can be calculated by subtracting the zero-dose R_x value.

All routine dating sequences performed during this study included a zero dose regeneration point immediately after the largest regeneration dose. Recuperation versus PH1 temperature plots are shown in Figure 3.5. A range of patterns are seen in these diagrams, suggesting that more than one mechanism contributes to the recuperation observed. Figure 3.5a. (Aber/28-IN12) strongly resembles the D_e versus PH1 plot for modern samples (Figure 3.1). The shape of the latter was attributed to charge transfer from the 280°C TL trap at high PH1 temperatures (Section 3.2.2), and a similar explanation appears to be valid for Figure 3.5a. The origin of the charge being transferred

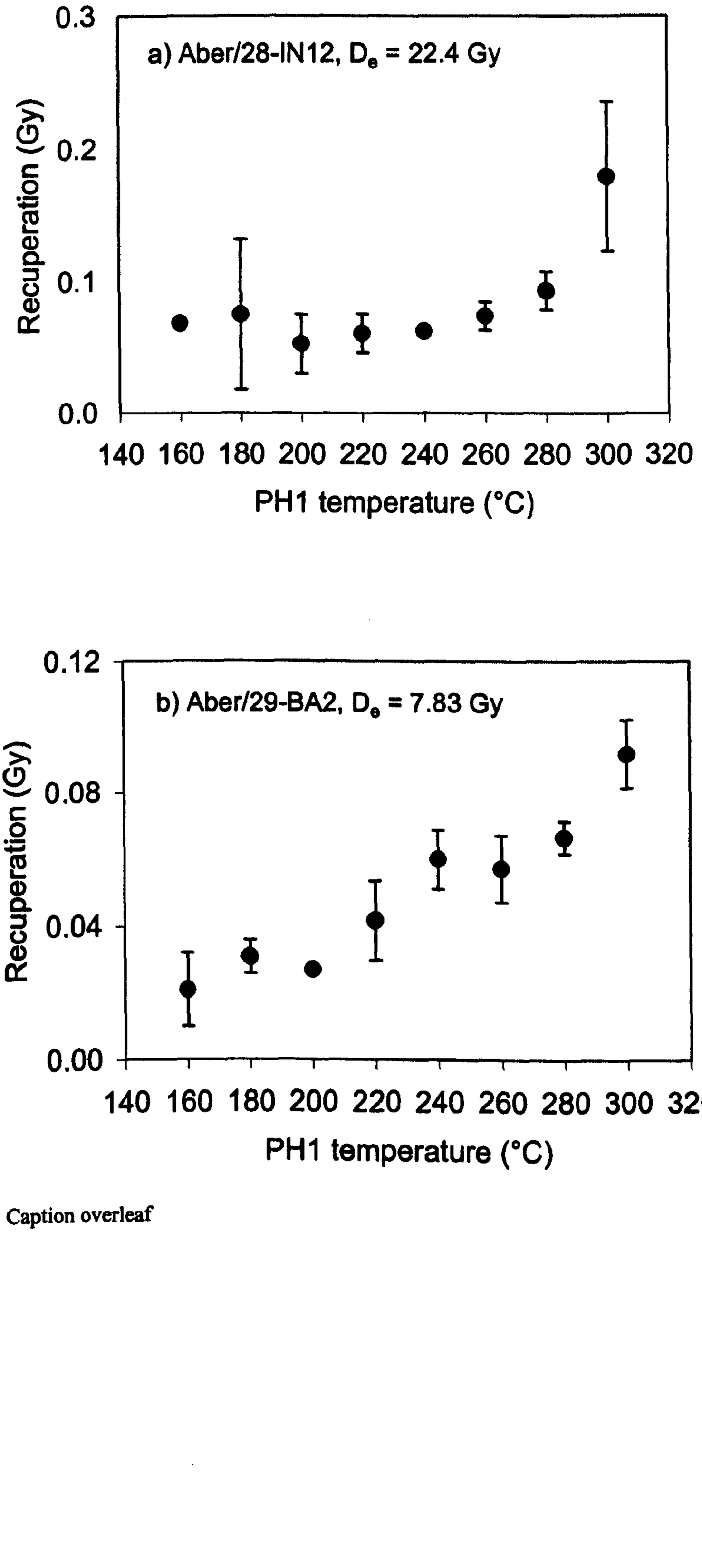

Figure 3.5. Caption overleaf

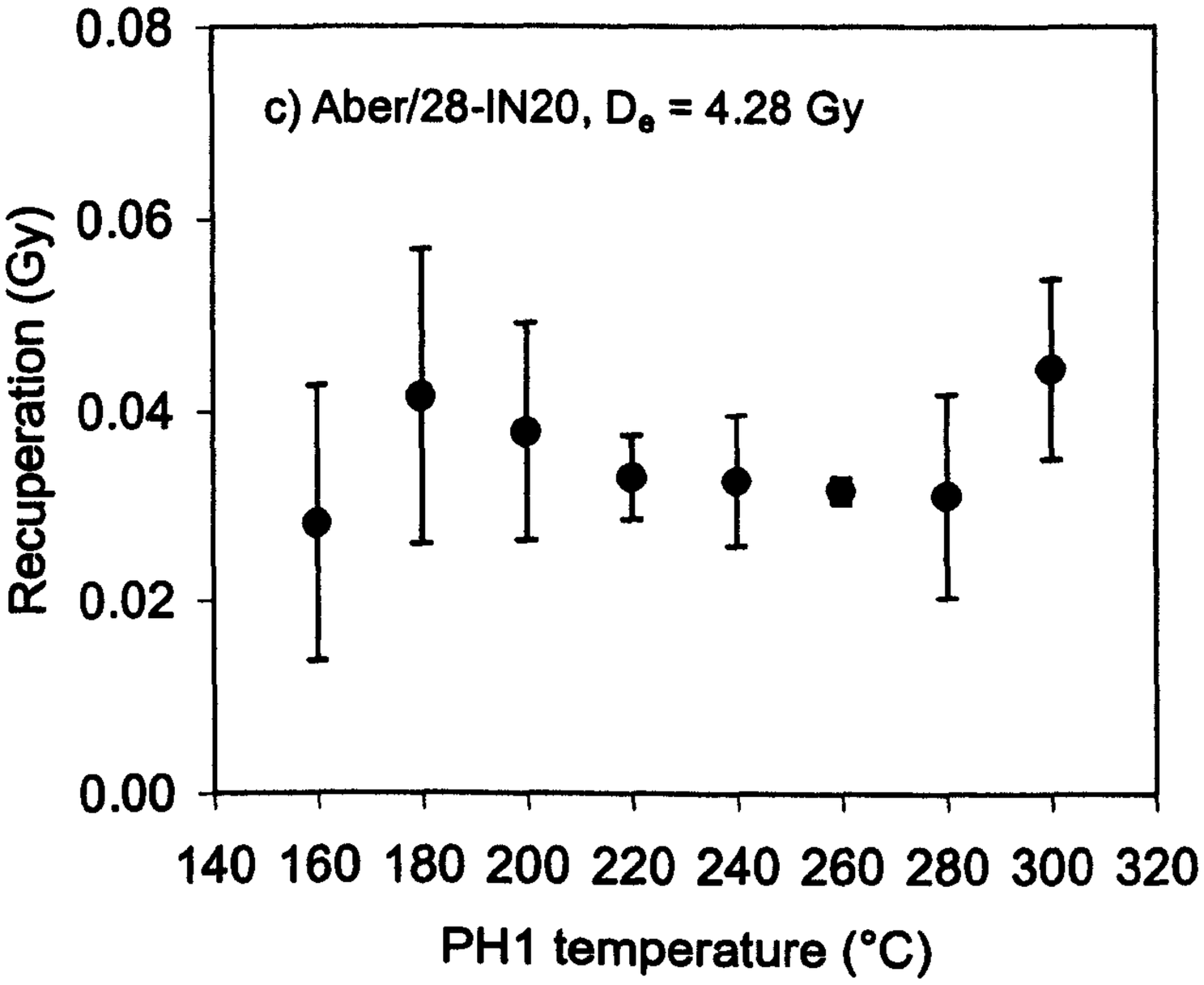

Figure 3.5. Recuperation versus PH1 temperature for a) Aber/28-IN12, b) Aber/29-BA2 and c) Aber/28-IN20. All points represent the mean of three aliquots, with one standard deviation errors. Recuperation was calculated using simple linear interpolation between zero and R_1.

is potentially complex. A 300°C PH1 is sufficient to completely empty the 280°C trap, and consequently the charge responsible for recuperation at this temperature must only originate from the preceding test dose irradiation (mechanism 2 above). However, at lower PH1 temperatures, incomplete emptying of the 280°C trap occurs (Figure 3.1, open circles), and so mechanism 1 is also applicable. In contrast, Aber/29-BA2 (Figure 3.5b) shows a constant increase in recuperation, suggesting thermal transfer from more than one optically insensitive trap. Consequently, both mechanisms 1 and 2 may apply to the recuperated signal at any given PH1 temperature, because more than one source trap is available. Aber/28-IN20 (Figure 3.5c) shows no systematic trend in recuperation with PH1 temperature, though a recuperated signal is observed. This suggests thermal transfer from a trap that is not completely emptied by the 160°C cut-heat, but completely emptied by the whole range of PH1 temperatures used (mechanism 2 above). In this scenario, charge trapped in an optically stable trap as a result of the test dose irradiation, is not removed during the subsequent PH2 or OSL measurement. However, during the following PH1, this charge is thermally transferred to the OSL trap(s). This is possible even when using 160°C for both PH1 and PH2, since PH2 is a cut-heat, and hence the aliquot probably never reaches 160°C (Jain *et al.* 2001), whereas the aliquot is held at temperature for 10 seconds during PH1.

Alternatively, photo-transfer of charge during measurement of L_x, to a trap stable at 125°C (measurement temperature), followed by thermal transfer during PH1, may explain this result.

No single mechanism satisfactorily explains the patterns observed in Figure 3.5. Consequently, the SAR datasets presented in this study have not been corrected for recuperation effects, since the appropriate correction is dependent on the source of the recuperated signal. The recuperated OSL signal for these samples is small, rarely exceeding 2% of the natural signal for geological samples. Consequently, recuperation is unlikely to have a significant deleterious effect on the dates produced.

3.5 Dose recovery experiments

Dose recovery experiments involve giving bleached aliquots a known laboratory radiation dose, and subsequently performing a measurement sequence upon those aliquots to determine the equivalent dose. Assuming the sample had a negligible OSL signal prior to irradiation, the equivalent dose should be identical to the known dose if the technique is appropriate. This procedure only tests the equivalent dose measurement protocol, and consequently is not as robust as the measurement of known age samples, which also test the dosimetric measurements and calculations. However, no sample of known age could be collected from the study area.

Dose recovery experiments were performed on a selection of geological and modern samples analysed during this dating program. Prior to irradiation, the geological samples were bleached using a blue diode stimulation source. The cumulative bleaching energy was c. 440 mJ/cm^2 (Risø 1) or c.1350 mJ/cm^2 (Risø 2), causing the OSL signal to decay to < 0.5 % of the initial intensity. This stimulation was carried out at 125°C to avoid charge transfer to the 110°C trap, and subsequent recuperation[h] (Murray and Wintle, 1998 and Aitken and Smith, 1988). The known dose administered to geological samples after bleaching, was approximately equal to the natural equivalent dose. Aliquots of the modern samples were not bleached prior to laboratory irradiation, since their natural equivalent dose is negligible (Section 3.2.1). Known doses ranging from 2.5 to 200 Gy were administered to aliquots of the modern samples (Table 3.4). This range of doses is similar to the range of equivalent doses measured for the geological samples dated during this study. The majority of aliquots of both geological and modern samples, yield apparent doses within 5 % of the administered dose[i] (Table 3.4), strongly suggesting that the SAR technique is applicable to these samples across a wide range of PH1 temperatures.

---

[h] Since elevated temperature illumination did not occur to the samples prior to burial, bleaching at 125°C may have undesirable effects. However, no bleaching step was required for the laboratory dosed modern samples measured (Table 3.4 and next paragraph).

[i] Though the standard error of the recovered dose estimate frequently fails to encompass the administered dose.

Sample (Aber/...)	PH1 range (°C)	No. of aliquots	Administered dose (Gy)	Recovered dose (Gy)	Recovered / Administered
Geological samples (bleached with blue light prior to being given the known dose).					
28-IN15	160-200	6	5.62	5.28 ± 0.05	0.94
28-IN18	160-260	12	11.2	11.6 ± 0.3	1.04
28-IN19	160-300	16	1.37	1.39 ± 0.05	1.01
29-BA2	160-300[j]	8	1.70	1.74 ± 0.05	1.02
29-BA8	160-300	8	7.81	7.99 ± 0.22	1.02
29-BA11	160-300	8	0.98	0.97 ± 0.07	0.99
29-BA13	160-300	8	14.8	15.4 ± 0.4	1.04
Modern samples (no pretreatment prior to being given the known dose).					
28-IN22	200	3	25.6	24.6 ± 0.9	0.96
28-IN22	200	3	40.9	42.8 ± 1.4	1.05
28-IN22	200	3	102.3	102.3 ± 5.8	1.00
28-IN22	200	3	204.5	178.4 ± 8.4	0.87
40-SA10	160-300	8	2.54	2.64 ± 0.06	1.04
40-SA10	160-300	8	5.08	5.33 ± 0.19	1.05
40-SA10	160-300	8	10.16	10.21 ± 0.19	1.00

Table 3.4. Results of dose recovery experiments performed on a variety of samples from the study area.

Wallinga *et al.* (2000) performed similar experiments on artificially bleached coarse-grain feldspars, and observed significant (27 ± 11 %) underestimation of the equivalent dose. They deduced that this phenomenon was caused by an increase in the electron trapping probability during PH1. Consequently, T_n (the luminescence signal measured in response to the test dose administered after measurement of the natural luminescence intensity, see Appendix 2.1) did not reflect the sensitivity of the natural aliquot, leading to an erroneously low L_n/T_n value. The data presented above demonstrate that this effect does not occur in the quartz samples measured in this study. As part of the bleaching procedure, the geological samples were heated to 125°C prior to being irradiated, hence changes in the trapping probability occurring below that temperature would not be detected during this dose recovery experiment. However, the modern samples were not bleached prior to irradiation, and consequently were only exposed to ambient laboratory

[j] Thermal transfer was observed at the 280 and 300°C preheats. Data for these aliquots have not been included in the mean equivalent dose.

temperature. The ability of the SAR method to recover known doses from unbleached modern samples, indicates that no change in the electron trapping probability occurs between natural/laboratory temperature and 125°C. Because no artificial bleaching step is required, dose recovery experiments performed on modern samples are a more robust test of the SAR method than those on geological samples. Bleaching geological samples in daylight is arguably still more robust, since it avoids the assumption that modern samples are good luminescence analogues of older samples. However, this approach was not used in the present study.

Despite the general success of the dose recovery experiments, a 13 % underestimation occurred when attempting to recover a dose of c.200 Gy from three aliquots of Aber/28-IN22 (Table 3.4). The growth curves for these aliquots are not in saturation (Figure 3.6), though L_n/T_n is greater than the curve fitting parameter B, which defines the onset of saturation (Equation 2.1, page 25). Aliquots of the same sample yielded acceptable recovered doses when attempting to recover smaller known doses (25, 40 and 100 Gy). It is possible that the SAR technique does not function well at high equivalent doses. However, Murray *et al.* (in prep) have measured considerably larger (geologically plausible) equivalent doses for a suite of Eemian samples. They also performed dose recovery experiments on these samples, with recovered doses ranging from 200-420 Gy, and observed a c.5 % systematic underestimate in the apparent dose. Thus, it is possible that the equivalent dose underestimate noted for the three aliquots of Aber/28-IN22 is anomalous, and would be removed by measuring more aliquots. This possibility has not been explored further since most of the samples measured in this study appear to reach dose response saturation before 200 Gy.

3.6 Elevated temperature stimulation

OSL decay curves were routinely measured at 125°C during this study. This stimulation temperature has several advantages over room temperature stimulation (Section 2.2.2). However, Stokes *et al.* (2000) demonstrated that this approach was not appropriate for a suite of aeolian samples from the United Arab Emirates (Goudie *et al.*, 2000). They

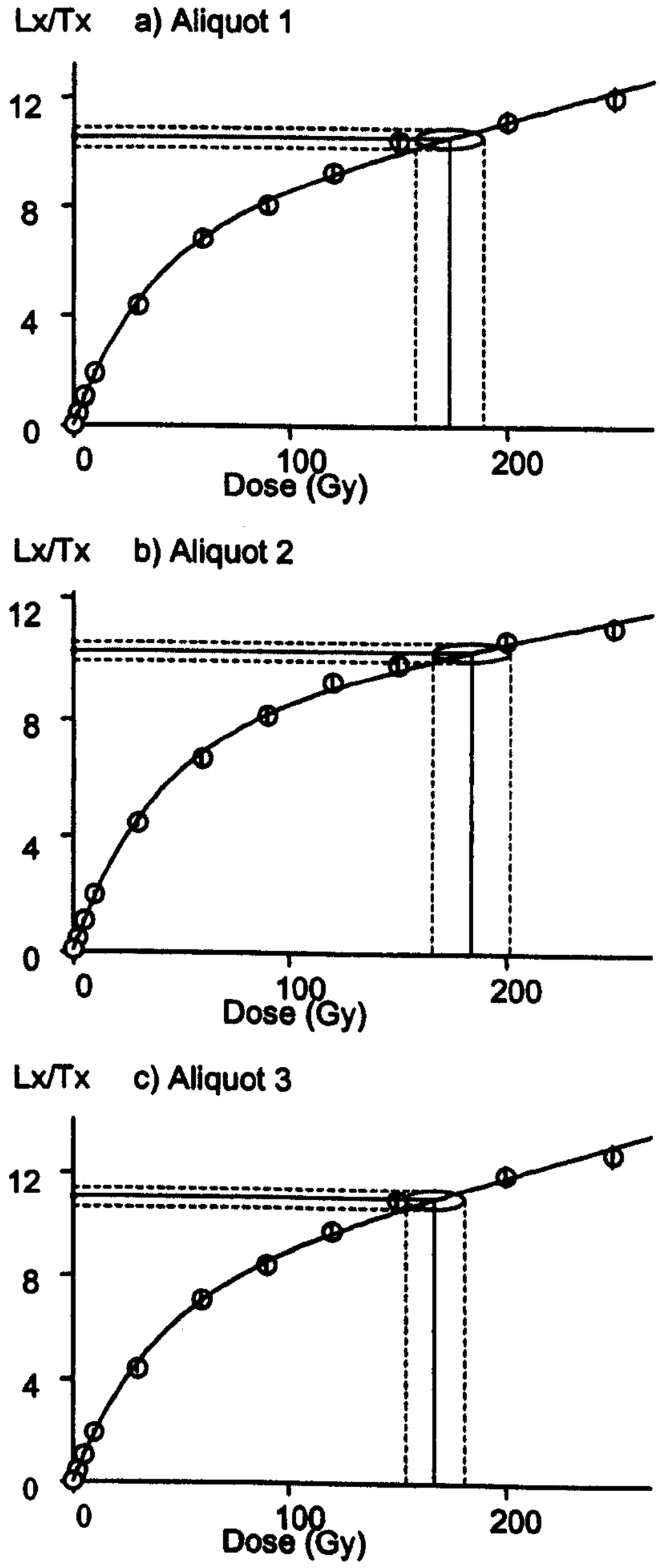

Figure 3.6. Growth curves for three aliquots of Aber/28-IN22, a modern sample, which had been given a laboratory β-dose of 204.5 Gy. An SAR measurement sequence was then performed on each aliquot, treating the initial laboratory β-dose as an unknown "natural" radiation dose. The mean calculated D_e was 178.4 ± 8.4 Gy. The solid line represents the "natural" luminescence intensity, with errors represented by the dashed lines.

artificially bleached aliquots of these samples, using a Risø blue diode unit[k]. They then performed three elevated temperature (125°C), and one lower temperature (50°C), OSL measurements on each aliquot. The 125°C optical stimulation resulted in a highly reproducible, time-dependant increase in the OSL, while stimulation at 50°C yielded a constant, lower signal (Figure 3.7a). Consequently, the use of elevated temperature stimulation resulted in implausible SAR growth curves, because the later parts of the OSL signal are subtracted from the initial signal to produce background subtracted luminescence intensities (Section 2.2.2). Conversely, aliquots measured at 50°C yielded meaningful D_e values.

The experiment performed by Stokes *et al.* (2000) was repeated on two natural aliquots from a large number of the samples dated in this study[l]. No time-dependence or excessive enhancement of the OSL signal was observed when stimulating aliquots at 125°C (Figure 3.7b). However, the OSL at 50°C was lower than that at 125°C for the older (>Holocene) samples (Figure 3.7c). This suggests that stimulation at 125°C thermally assists eviction of charge from a slow-bleaching, geologically stable trap.

3.7 D_e variation with PH1 temperature

When a range of PH1 temperatures are used on aliquots of the same sample, D_e estimates can be plotted as function of preheat temperature. If a single equivalent dose is obtained over a range of PH1 temperatures, this is termed a D_e preheat plateau. The existence of such a plateau indicates that the SAR sensitivity corrections are appropriate and hence the equivalent dose obtained from this plateau is likely to be accurate. However, Bailey (2000b) has argued that a plateau may only indicate that over a given temperature range, there is no change in a critical variable (e.g. sensitivity, thermal transfer or the thermal stability of the OSL traps accessed). Consequently, the equivalent dose at which a D_e preheat plateau is obtained, need not be an accurate estimate of the palaeodose. In this study, at least six, and up to eight PH1 temperatures have been used when dating each sample (160-300 or 160-260°C in 20°C steps). A number of TL traps are emptied over

---

[k] 200 seconds illumination (c.4800 mJ/cm^2) using a Risø blue diode unit.
[l] Aber/28-IN1, 4, 11, 12, 14, 15, 16, 18, 19, 20, 21, Aber/29-BA1, 8, 12, 13, 14, Aber/12-MAP3 and Aber/12-RBM2.

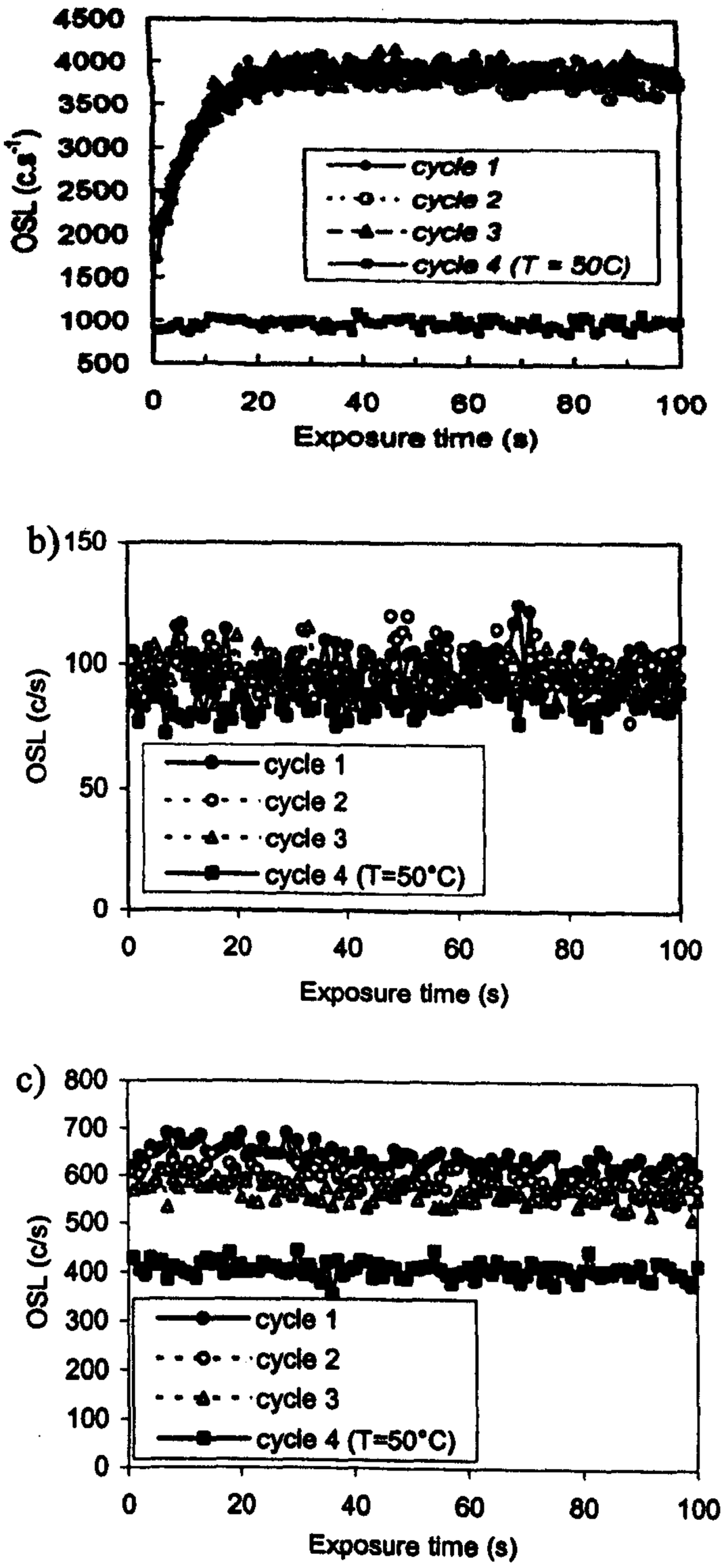

Figure 3.7. Results of repeated optical stimulation performed on single aliquots of quartz after 200 seconds optical stimulation at 125°C. Cycles one to three were performed at 125°C while the fourth cycle was performed at 50°C. a) Quartz from Ras Al Khaima, United Arab Emirates (from Stokes *et al.*, 2000), b) Aber/28-IN16 (D_e 2.41 Gy) and c) Aber/28-IN11 (D_e 133 Gy).

this range of PH1 temperatures, affecting the potential for thermal transfer of charge into the OSL trap(s). Also, the thermal stability of the traps which remain populated after the preheat, and therefore potentially able to contribute to the OSL signal, will vary considerably over this range of PH1 temperatures. Finally, significant sensitivity changes occur over this temperature range (Chapter 5), making D_e versus PH1 temperature plot an excellent test of the accuracy of SAR sensitivity correction. For these reasons, the presence of a D_e preheat plateau across the full range of PH1 temperatures used is regarded as a strong indication that the equivalent dose is accurate.

D_e versus PH1 plots, for a range of samples dated during this study, are shown in Figure 3.8. Some Holocene samples, such as Aber/28-IN20 (Figure 3.8b) show evidence of thermal transfer after a 300°C preheat, while others do not (e.g. Aber/28-IN16, Figure 3.8a). In all cases, with the possible exception of Aber/28-IN3 (Figure 3.8f), it is not possible to detect systematic variation of D_e with PH1 temperature. Consequently the null hypothesis, that no systematic variation of D_e with PH1 temperature occurs, can be accepted, indicating that the SAR technique is appropriate for these samples. However, as the D_e gets larger, the uncertainties on each point generally get bigger, and the ability to detect fluctuations gets poorer. This being the case, and in view of Figures 3.8a-e, it was concluded that the null hypothesis could also be accepted for Aber/28-IN3 (Figure 3.8f).

3.8 Conclusions

1) Samples from active sedimentary environments in the study area yield negligible equivalent doses, suggesting that partial bleaching is unlikely to adversely affect the ages calculated for geological samples. Recuperation consistent with thermal transfer from the 280°C TL trap is observed, though is not large enough to significantly affect the equivalent dose measured from geological samples.

2) The mean recycling ratio for the 652 aliquots dated during this study is 0.989 0.099, indicating that the SAR sensitivity correction procedure accurately corrects for sensitivity change in these samples. However, >50% of the aliquots preheated at 300°C were rejected because they yielded poor recycling ratios. These poor recycling ratios may be due to variable signal depletion during PH1.

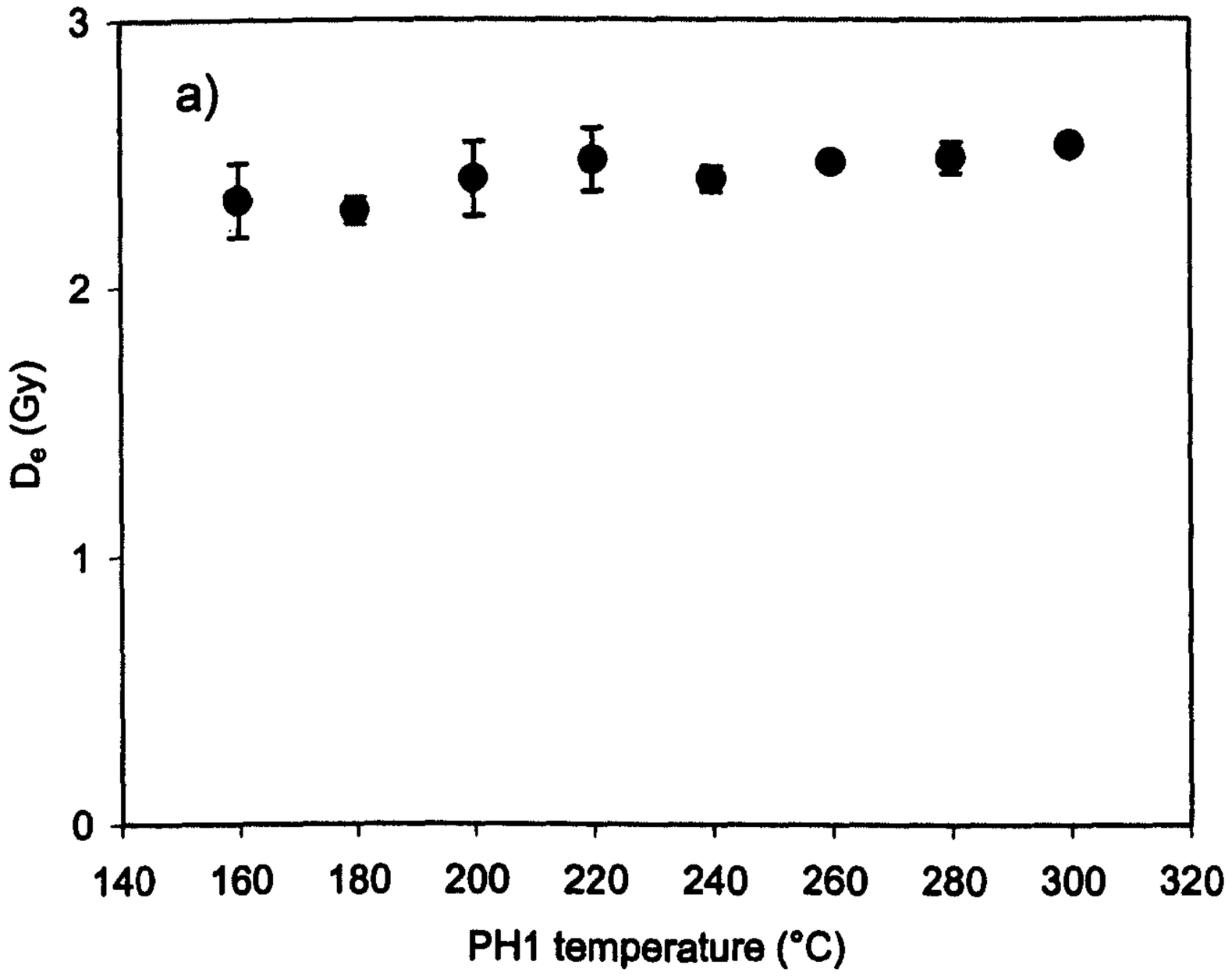

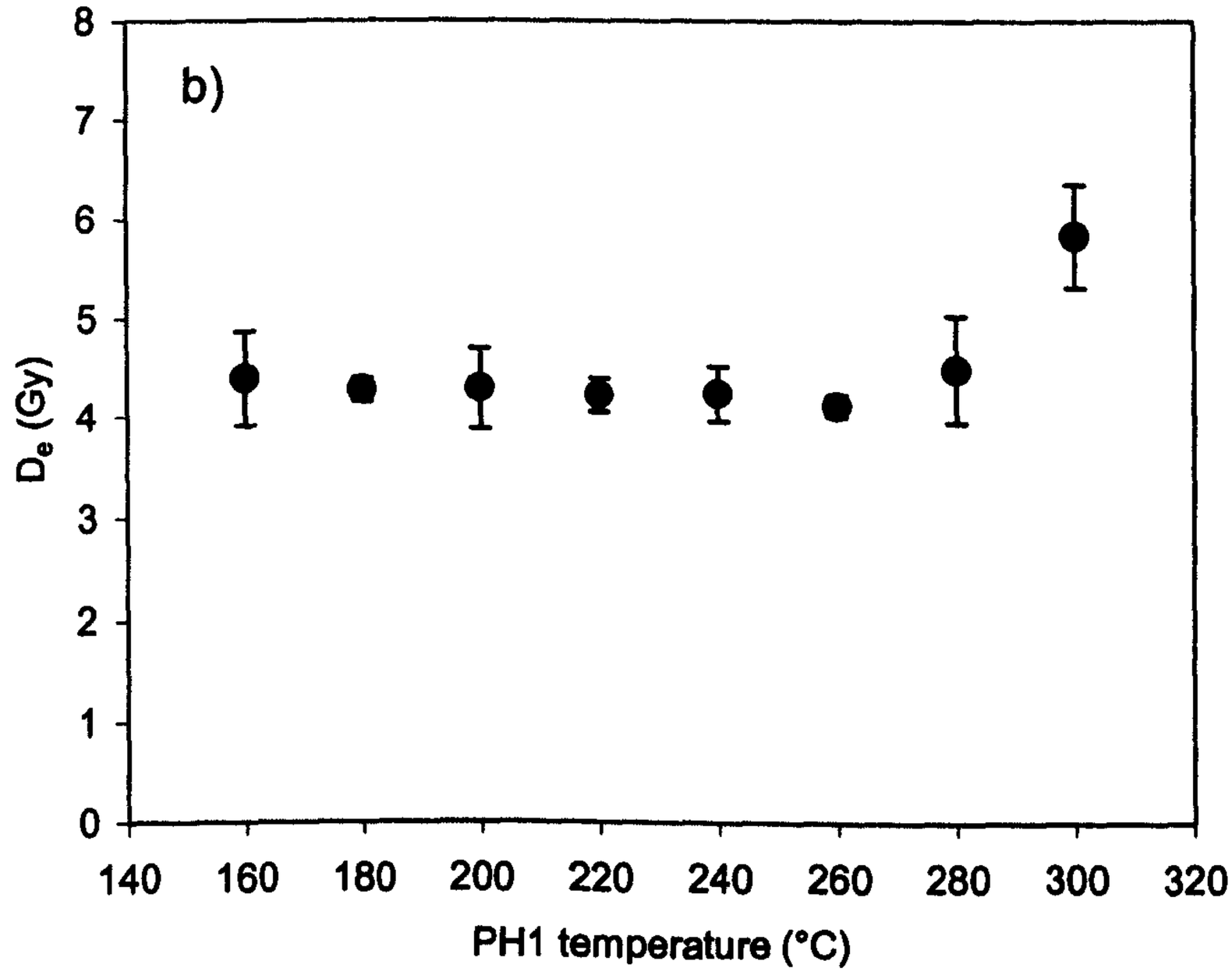

Figure 3.8. Caption overleaf.

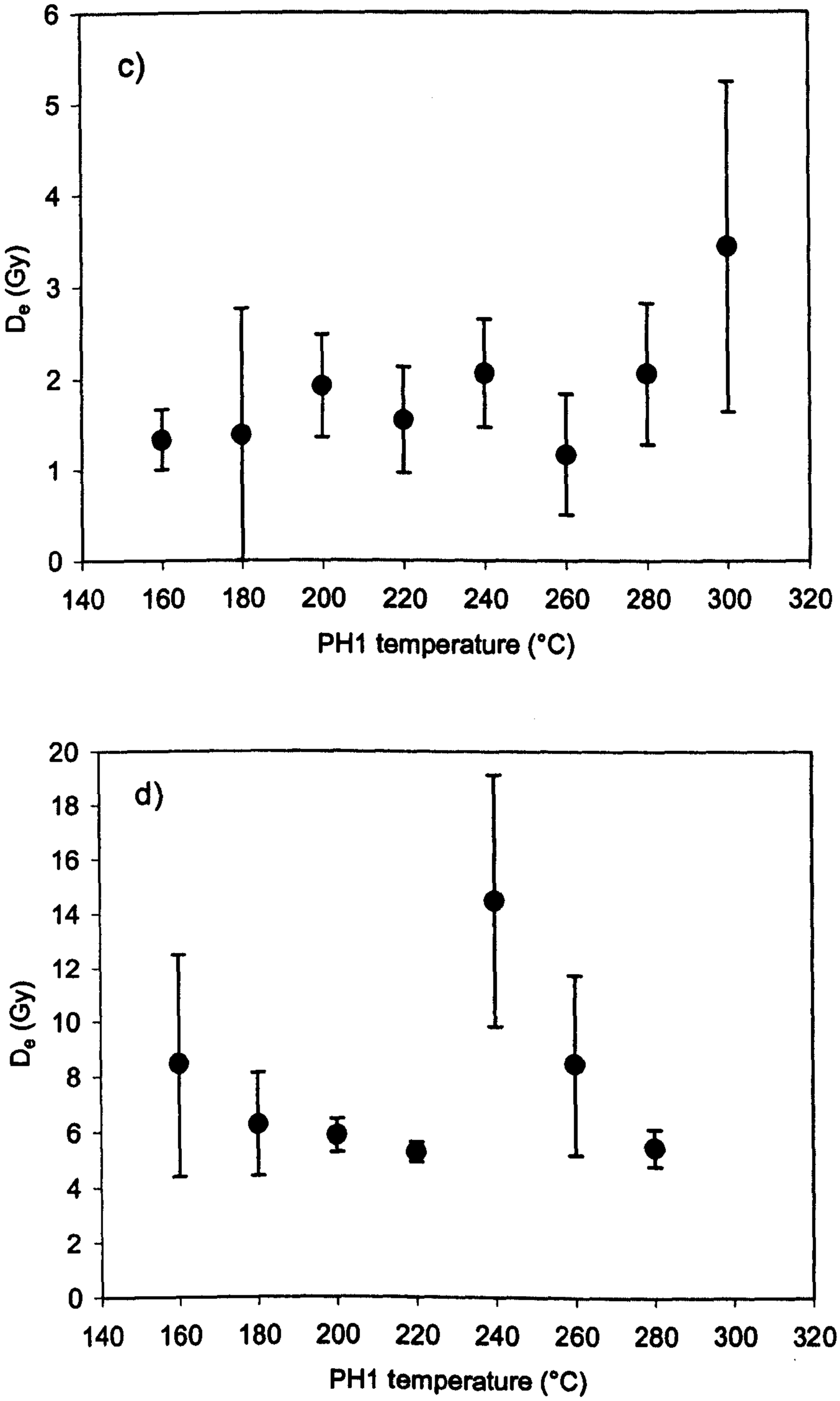

Figure 3.8. Caption overleaf.

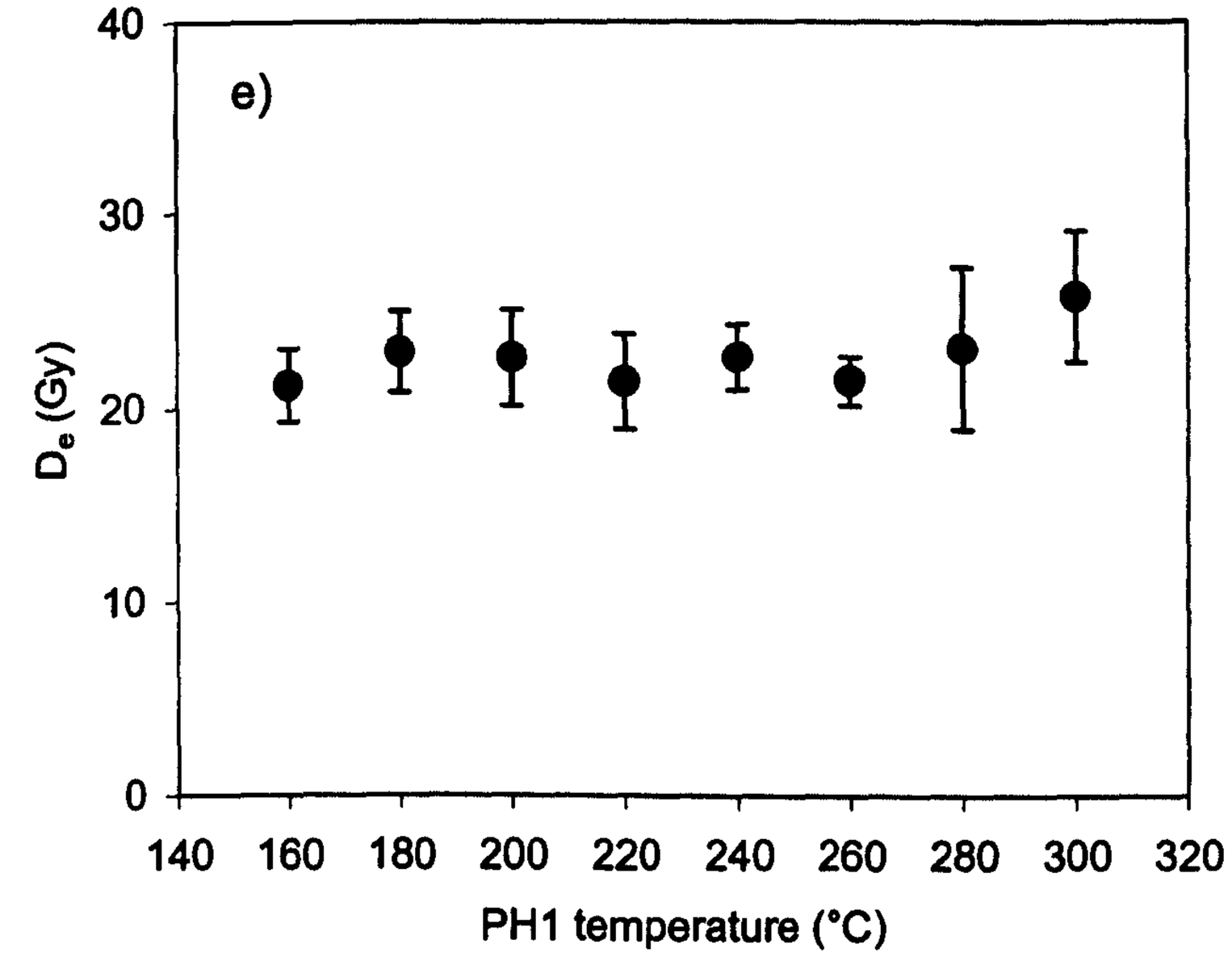

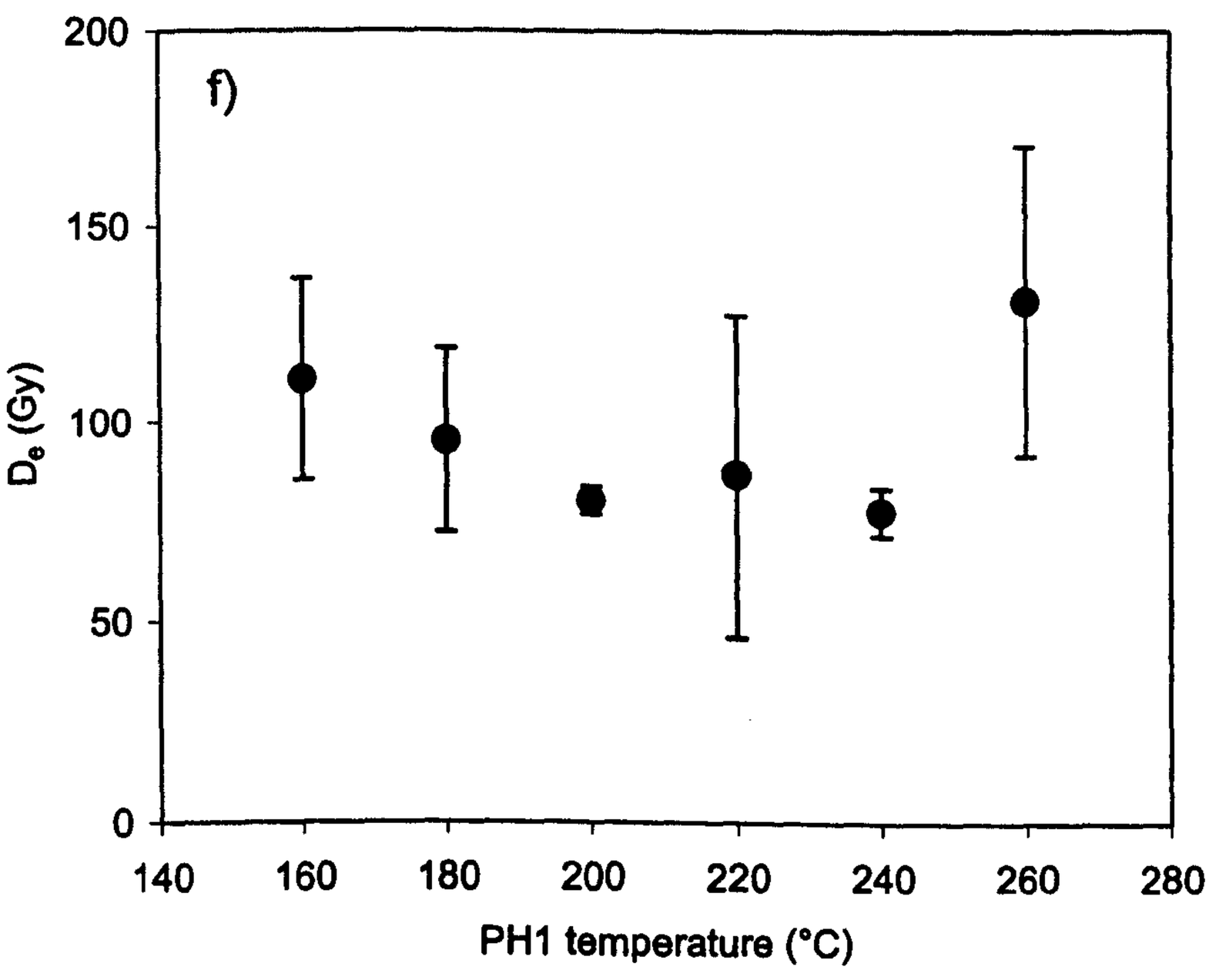

Figure 3.8. D_e versus PH1 temperature plots for a selection of samples analysed. Each point is the mean of three aliquots with one standard deviation errors. a) Aber/28-IN16 (D_e 2.41 Gy), b) Aber/28-IN20 (D_e 4.28 Gy), c) Aber/29-BA8 (D_e 1.70 Gy), d) Aber/29-BA2 (D_e 7.83 Gy), e) Aber/28-IN12 (D_e 22.4 Gy) and f) Aber/28-IN3 (D_e 96.2 Gy).

3) A recuperated OSL signal is observed when a zero dose point is measured during the SAR measurement sequence. No single mechanism satisfactorily explains the patterns observed in plots of recuperation versus PH1 temperature, so no correction has been applied. However, the recuperated OSL signal rarely exceeds 2% of the natural signal, and is unlikely to deleteriously effect the dates produced.
4) Dose recovery experiments, performed on a range of modern and geological samples, generally yielded equivalent doses within 5% of the administered dose. This indicates that the SAR method and measurement conditions used in this study are likely to be appropriate for the samples dated.
5) No time dependant increase of the OSL signal is observed when stimulating these samples at 125°C (cf. Stokes *et al.*, 2000). Consequently, elevated temperature stimulation has been used routinely throughout this study.
6) There is no evidence for the absence of D_e preheat plateau in any of the samples measured, strongly suggesting that the measured equivalent dose is correct. However, as the uncertainties on the D_e at each PH1 temperature increase, the test rapidly becomes less sensitive. The only systematic trend observed in the D_e versus PH1 temperature, relates to thermal transfer at high (280-300°C) preheat temperatures. This behaviour is only observed in samples with small equivalent doses.

Chapter 4: Equivalent dose variation with stimulation time

4.1 Introduction

Initial analysis of single-aliquot regenerative-dose (SAR) datasets produced during this study revealed that for some aliquots, the experimentally determined equivalent dose (D_e) was strongly dependent on signal integration period. Consequently, for any given aliquot, a range of ages could be calculated, depending on the signal integration period used. This section aims to determine the optimum signal integration period for these SAR datasets.

4.1.1 Previous work

The dependence of equivalent dose upon signal integration time is best illustrated by plotting D_e versus stimulation time (or cumulative stimulation energy), yielding a $D_e(t)$ plot. The majority of published $D_e(t)$ plots are for multiple aliquot datasets, and indicate that the experimentally determined equivalent dose can rise (Huntley *et al.*, 1985, Rhodes, 1988, Stokes, 1992), fall (Perkins and Rhodes, 1994) or be insensitive to (Huntley *et al.*, 1985, Rhodes, 1988, Smith *et al.*, 1990) increases in signal integration time. Rising $D_e(t)$ plots have been explained by inappropriate growth curve fitting (Rhodes, 1988), and partial bleaching (Huntley *et al.*, 1985). Consequently, $D_e(t)$ plots have been advocated as a test for insufficient bleaching of sediments prior burial (Huntley *et al.*, 1985, Bailey, 2000c, submitted). In the absence of partial bleaching, SAR $D_e(t)$ plots can be used as a basis for selecting the most appropriate signal integration period for routine D_e determination.

4.2 Samples and measurement equipment

To simplify the interpretation of the $D_e(t)$ plots, only samples believed to be fully bleached prior to deposition have been used in this section. Most of the samples are sedimentary quartzes from Inhaca Island, though a modern sample from Maputaland (Aber/40-SA10) has also been studied (Table 4.1). These samples are likely to have been fully reset prior to deposition (Section 3.2). CalQtz, a calibration quartz provided by Dr. A.S. Murray, has also been studied (Section 4.9).

Sample code (Aber/...)	Reader (Risø)	Sample type	SAR D_e (Gy)	Modified SAR D_e (Gy)	SAR : Modified SAR
28-IN9	2	tidal-flat (modern)	0.060 ± 0.005	-	-
28-IN12	1	aeolian	22.4 ± 0.5	23.3 ± 1.8	0.96±0.08
28-IN14	1	aeolian	14.5 ± 0.3	14.3 ± 0.4	1.01±0.04
28-IN15	1	aeolian	5.16 ± 0.06	5.19 ± 0.13	0.99±0.03
28-IN16	2	aeolian	2.41 ± 0.02	2.49 ± 0.05	0.97±0.02
28-IN18	1	aeolian	12.2 ± 0.3	11.8 ± 0.5	1.03±0.05
28-IN19	2	aeolian	2.04 ± 0.30	-	-
28-IN20	1	tidal-flat	4.28 ± 0.07	-	-
28-IN21	2	aeolian	3.12 ± 0.30	3.22 ± 0.34	0.97±0.14
28-IN22	2	aeolian (modern)	0.006 ± 0.004	-	-
40-SA10	2	aeolian (modern)	0.006 ± 0.004	-	-
40-SA10	2	N + 4.87 Gy β dose	4.87 (β dose)	5.12 ± 0.06	0.95±0.03
CalQtz	2	calibration sample	4.6 (γ dose)	-	-

Table 4.1. Sample details and equivalent doses measured using standard (Section 2.2) and modified (Section 4.7) SAR measurement procedures. No standard SAR equivalent dose determinations were performed on the aliquots of Aber/40-SA10 which had been given a known β dose. The SAR to modified SAR ratio for this sample compares the known β dose with the modified SAR equivalent dose.

Measurements were made using Risø 1 and Risø 2 (see Table 2.3). Stimulation time was 100 s for samples measured using Risø 1, and 40 s for those measured using Risø 2. The total energy delivered per stimulation was 220 mJ/cm^2 (Risø 1) and 676 mJ/cm^2 (Risø 2). All measurements performed on an individual sample were made using the same reader (Table 4.1). Equivalent doses reported in Table 4.1 were calculated using the first channel of the OSL decay curve (0.88 mJ/cm^2 using Risø 1 or 2.7 mJ/cm^2 using Risø 2), with a background signal subtracted (see Section 2.2.2). Typical decay curves measured using Risø 1 and Risø 2 are shown in Figures 4.1 and 4.2 respectively.

4.3 $D_e(t)$ plots using integrated luminescence intensities

$D_e(t)$ plots have been produced using the cumulative OSL signal from channels 1 to x, where x is increased up to the highest signal channel used, equivalent to 198 and 608.4 mJ/cm^2 of stimulation energy for Risø 1 and Risø 2 respectively[a]. This approach is

[a] In both cases, each decay curve was measured in 250 channels, the last 25 of which were used to estimate the background OSL signal. Consequently, the $D_e(t)$ plots shown here are constructed from the first 225 signal channels.

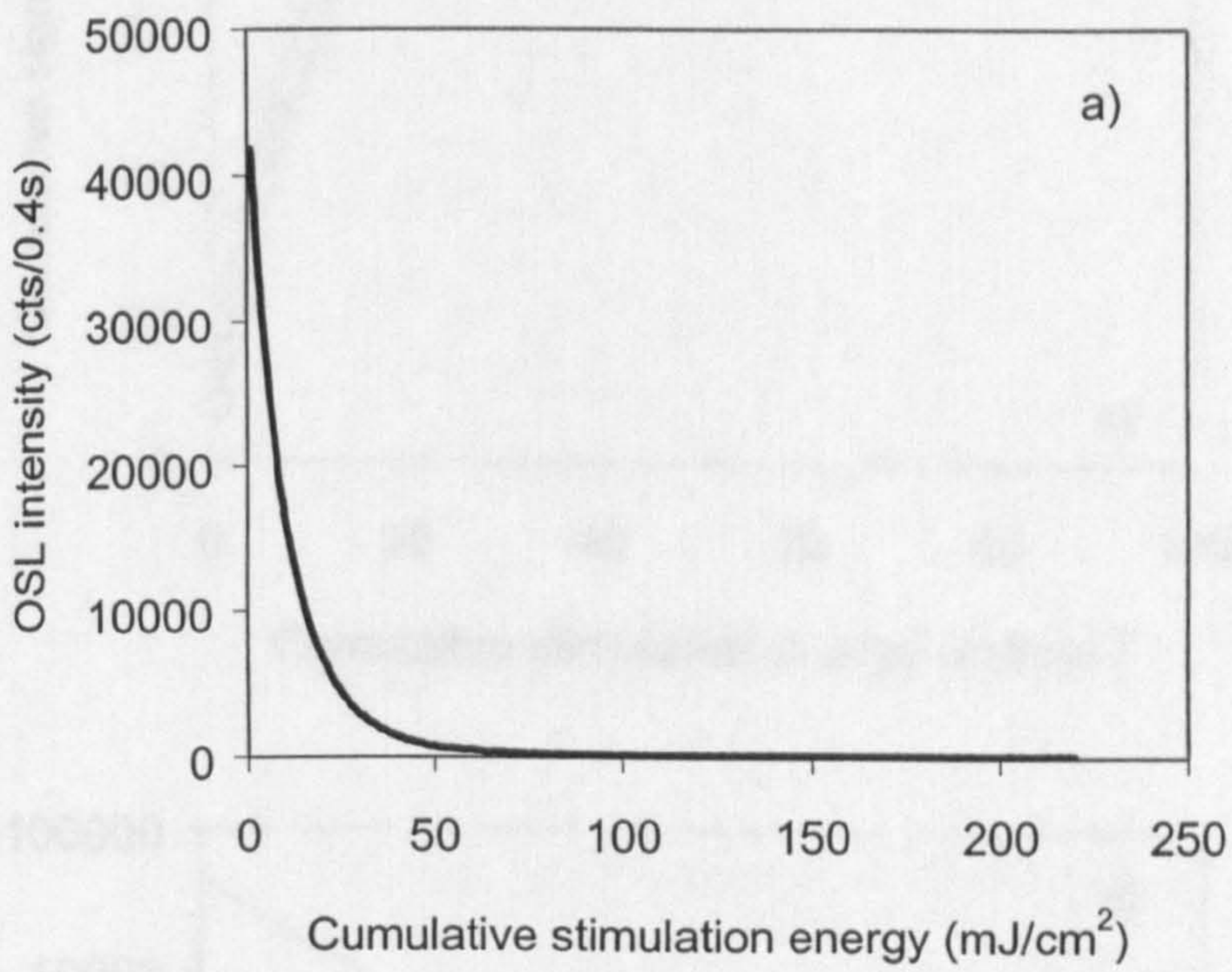

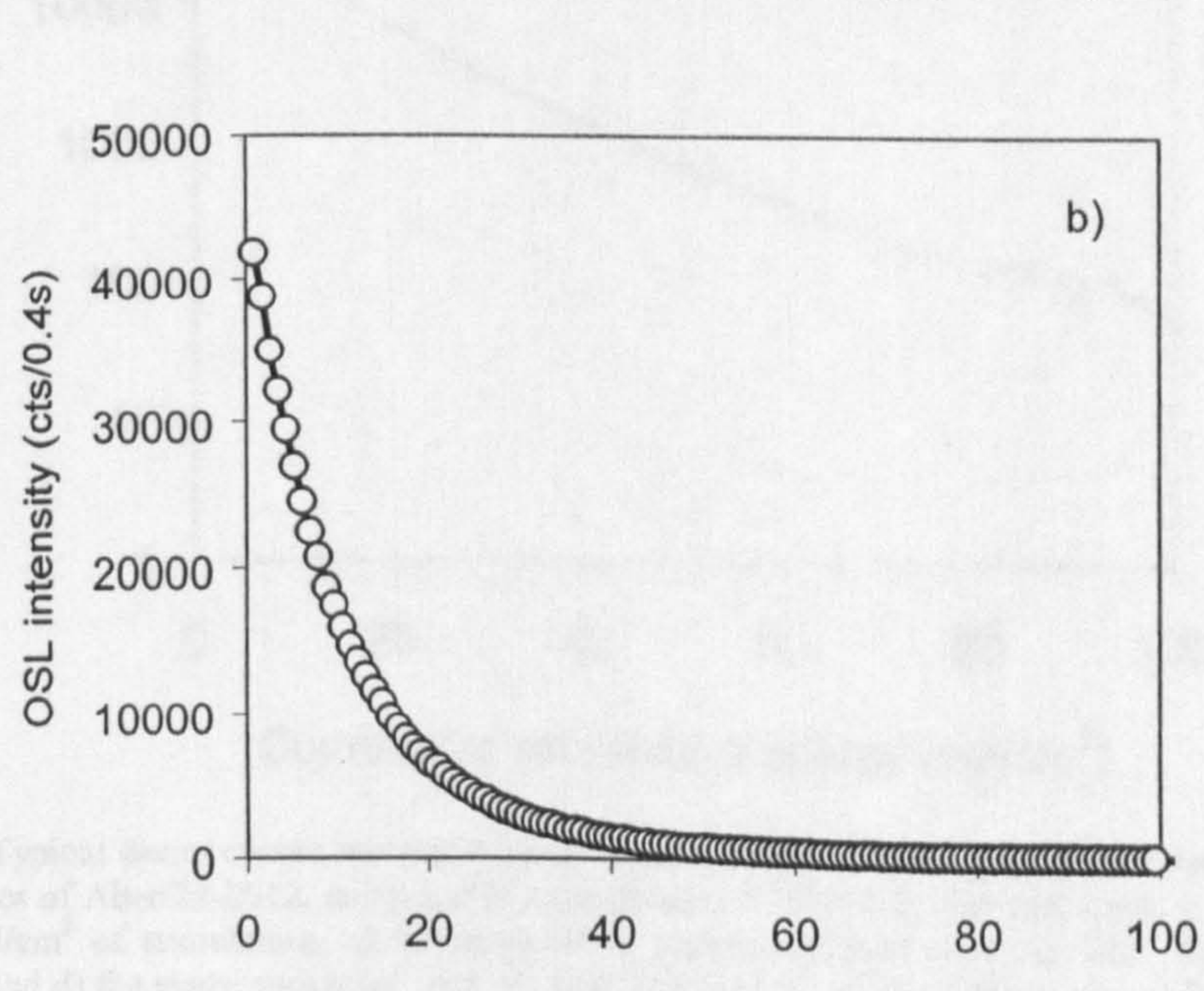

Figure 4.1. Caption overleaf.

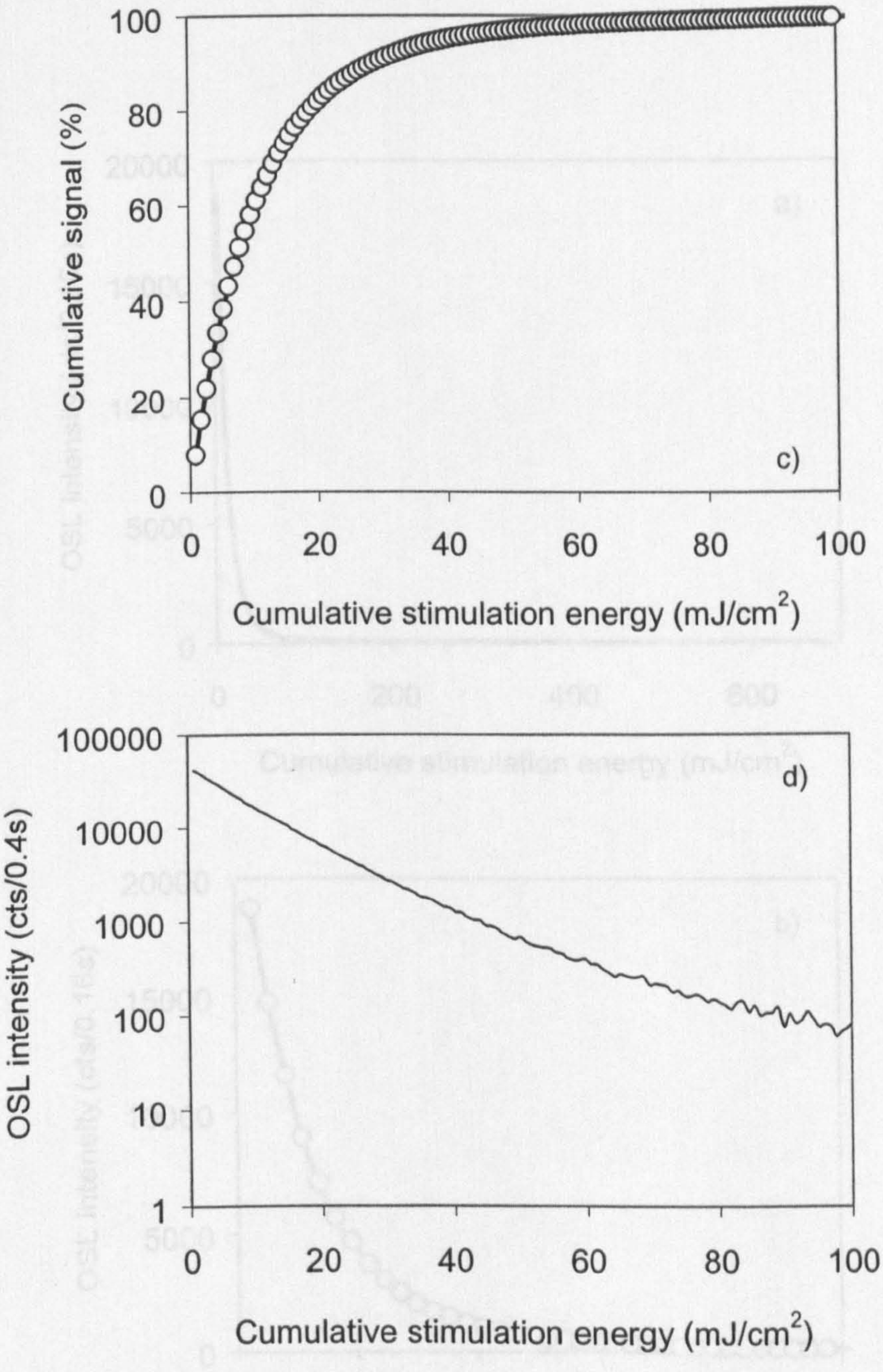

Figure 4.1. Typical decay curves measured using Risø 1. These decay curves were measured from a natural aliquot of Aber/28-IN12, using a PH1 temperature of 160°C. a) The entire decay curve, b) the first 100 mJ/cm^2 of stimulation, c) the cumulative signal measured over the first 100 mJ/cm^2 of stimulation and d) the signal measured over the first 100 mJ/cm^2 of stimulation, using a logarithmic y-axis. Points in Figures 4.1 b and c represent data from individual signal channels. At the end of stimulation, the background count rate is c.100 counts per channel above instrument background.

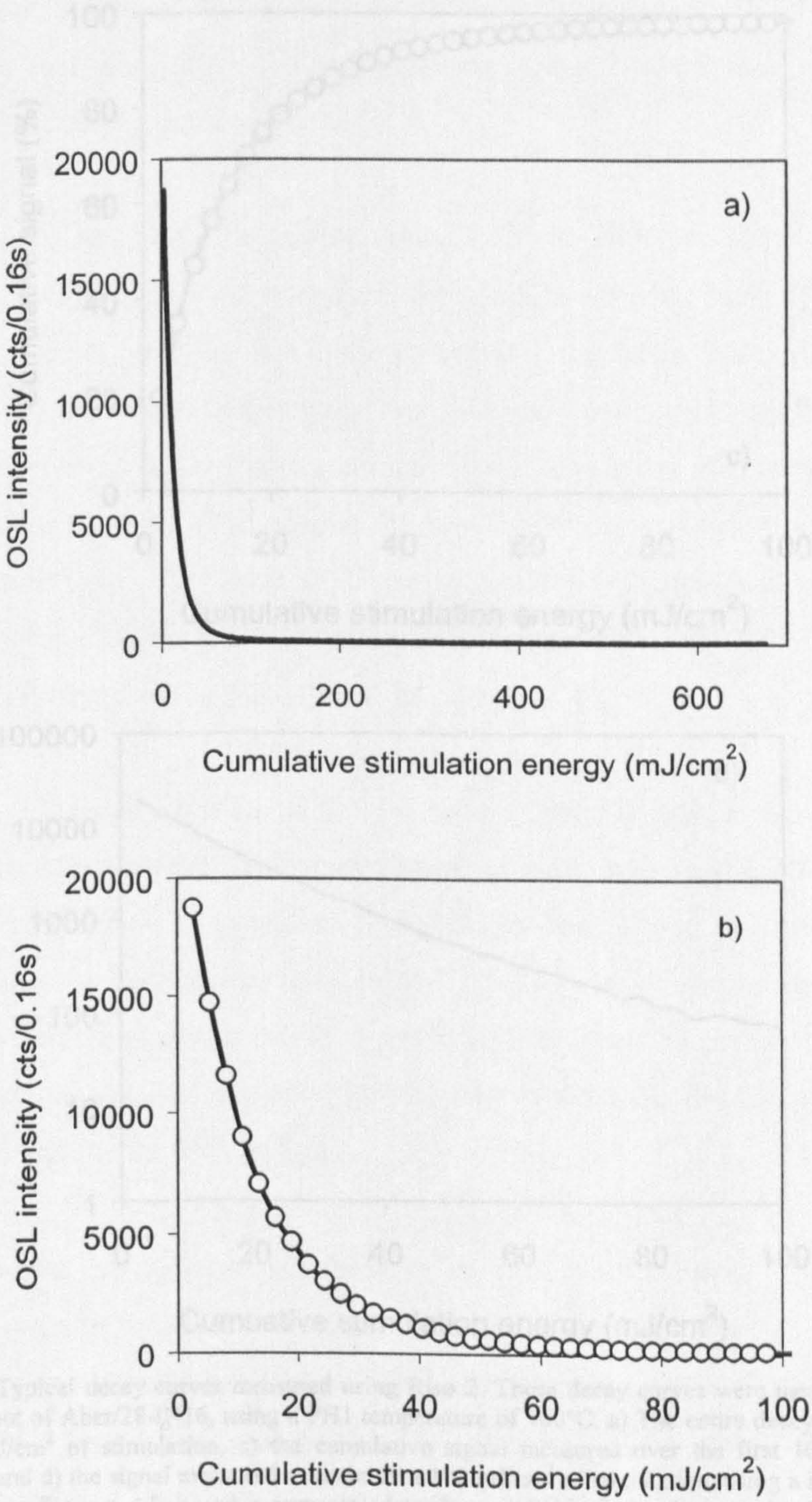

Figure 4.2. Caption overleaf.

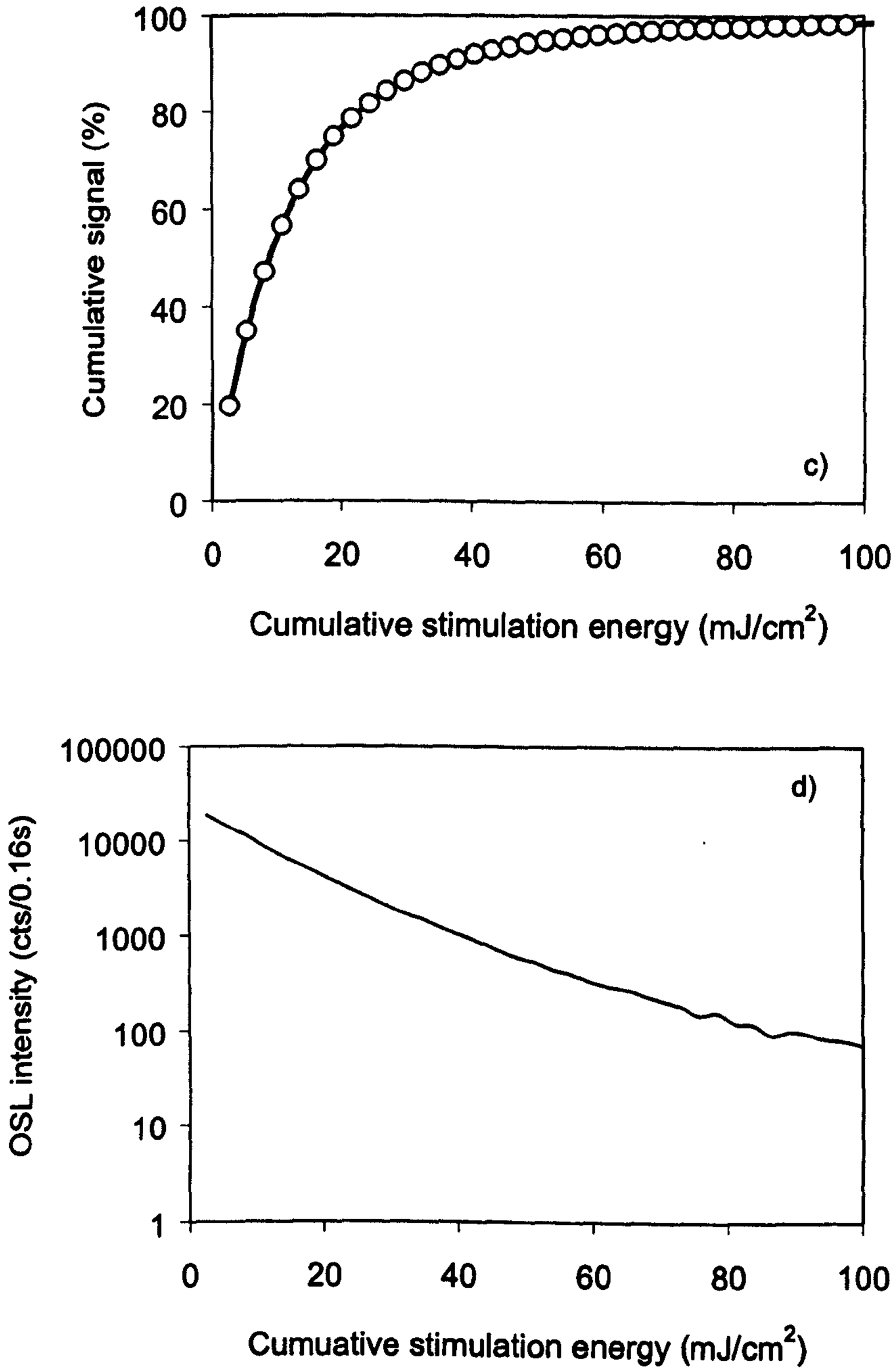

Figure 4.2. Typical decay curves measured using Risø 2. These decay curves were measured from a natural aliquot of Aber/28-IN16, using a PH1 temperature of 160°C. a) The entire decay curve, b) the first 100 mJ/cm^2 of stimulation, c) the cumulative signal measured over the first 100 mJ/cm^2 of stimulation and d) the signal measured over the first 100 mJ/cm^2 of stimulation, using a logarithmic y-axis. Points in Figures 4.2 b and c represent data from individual signal channels. At the end of stimulation, the background count rate is c.20 counts per channel above instrument background.

appropriate for investigation of the effect of progressively larger signal integration periods on the resulting D_e, but would be relatively insensitive to the effects of partial bleaching. The test dose signal (T_x) integration period is identical to that for the corresponding natural/regenerated signal (L_x)[b].

Figure 4.3 shows $D_e(t)$ plot for sample Aber/28-IN16. The data show a small initial increase in D_e at higher PH1 temperatures, though this never exceeds 2% of the initial value. This increase is probably due to the presence of the "ultra fast component" found by Jain *et al.* (2001), which is thermally unstable and hence will only be found in the regenerated and not the natural decay curves. Use of the lower PH1 temperatures (160 and 180°C) causes the equivalent dose to fall rapidly with cumulative stimulation energy (signal integration time). At higher PH1 temperatures this reduction in equivalent dose becomes progressively less marked. Once PH1 temperatures of 260°C or above are reached, the $D_e(t)$ plot shows a reduction in D_e of only 2-4%.

The $D_e(t)$ plots for seven other samples from Inhaca Island display a similar dependence on PH1 temperature. However, the exact pattern of individual $D_e(t)$ plots varies slightly from sample to sample, with considerable variability both within and between samples. When using the entire decay curve to calculate D_e (channels 1-225), the mean value using low PH1 temperatures ranges from 92 to 66 % of that from the first channel. Different amounts of decrease can be seen between aliquots of the same sample, measured using the same PH1 temperature (Figure 4.4).

4.4 Possible causes for $D_e(t)$ plot dependence on PH1 temperature.

There are two possible causes for the shape of the $D_e(t)$ plots described above. Firstly, the SAR sensitivity correction procedure may not be appropriate for the later portions of the OSL decay curve. Secondly, some of the OSL observed in the later parts of the decay curve may be derived from one or more slow-bleaching, geologically-unstable traps.

---

[b] It should be noted that, at larger signal integration periods, an aliquot may fail one or more of the internal SAR performance checks (e.g. recycling ratio or zero dose point luminescence intensity). Where this is the case, researchers using long signal integration intervals would discard data from that aliquot. However, the $D_e(t)$ plot approach used in this chapter is still a valid tool for investigating the potential impact on D_e accuracy of using large signal integration periods. See also Section 4.8.

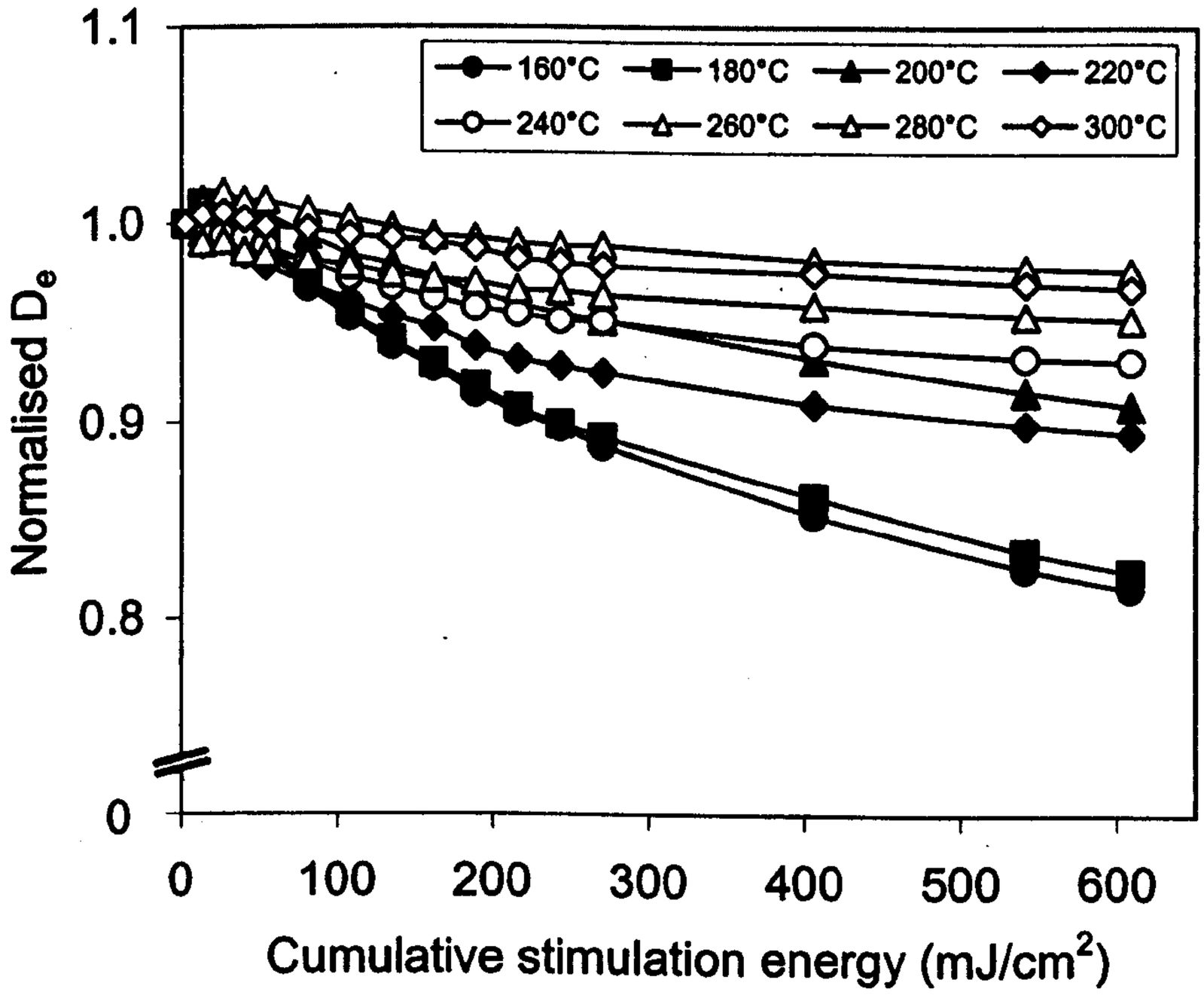

Figure 4.3 A $D_e(t)$ plot for Aber/28-IN16 obtained for a range of PH1 temperatures. Each data point is the mean of three aliquots, which were preheated at the same temperature. The legend gives PH1 temperatures. All data are normalised to the D_e obtained using the first channel of stimulated signal (equivalent to 2.7 mJ/cm^2).

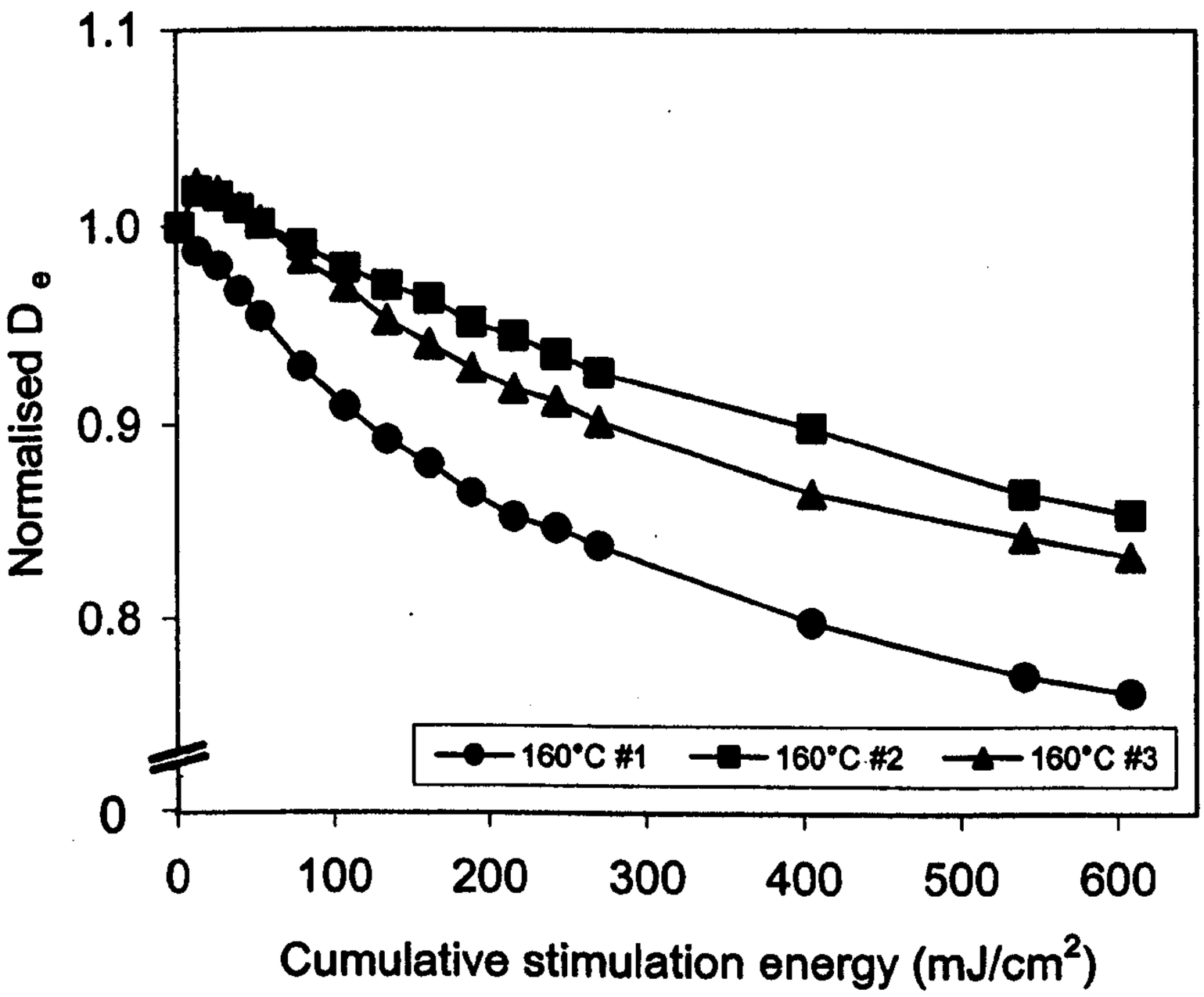

Figure 4.4. $D_e(t)$ plots for individual aliquots of Aber/28-IN16, which had been measured using a PH1 temperature of 160°C. Normalisation as in Figure 4.3.

Evidence for the existence of at least one such trap has been provided by Banerjee *et al.* (2000, Section 3.3) and Singarayer and Bøtter-Jensen (in prep). A slow-bleaching, geologically-unstable trap could have two effects during an SAR measurement sequence.

1) In nature the trap remains empty due to its low thermal stability. Since laboratory irradiation occurs c.10^8 times faster than that in nature, the trap contains charge after laboratory irradiation. Because the trap is slow-bleaching, its contribution to the OSL signal only becomes significant in the later parts of the decay curve. The later parts of the regenerated decay curve are derived, at least in part, from charge stimulated from trap(s) unoccupied in the natural sample. Consequently, D_e decreases with increasing signal integration period. Smaller D_e changes for higher PH1 temperatures suggest that the trap(s) responsible are thermally unstable.
2) Charge accumulates in the trap from one measurement cycle to the next. As larger signal integration periods are used, the regenerated luminescence intensities derived from this trap increase relative to that from the natural sample, "raising" the growth curve, but not the natural signal. Again, smaller D_e changes for PH1 temperatures suggest that the trap(s) responsible are thermally unstable.

4.5 Evidence for the presence of a geologically unstable OSL signal

Figure 4.5a shows the natural, and two regenerated OSL decay curves, on a semi-logarithmic scale, for an aliquot of Aber/28-IN16. This aliquot had been measured using a standard SAR measurement sequence, and a PH1 temperature of 160°C. The regenerated decay curves, for doses close to D_e, are approximately the same shape. The differences between them, at large cumulative stimulation energies, may be ascribed to the effects of charge accumulation resulting from repeated cycling. The natural signal decays to a far lower relative signal level. Figure 4.5b shows similar data for an aliquot of the same sample that has been preheated at 280°C. In this case, all three decay curves have approximately the same shape. Similar patterns were observed for the other samples used in this study, with the discrepancy between natural and regenerated decay curve shapes decreasing with increasing PH1 temperature. Figure 4.5c shows test dose decay

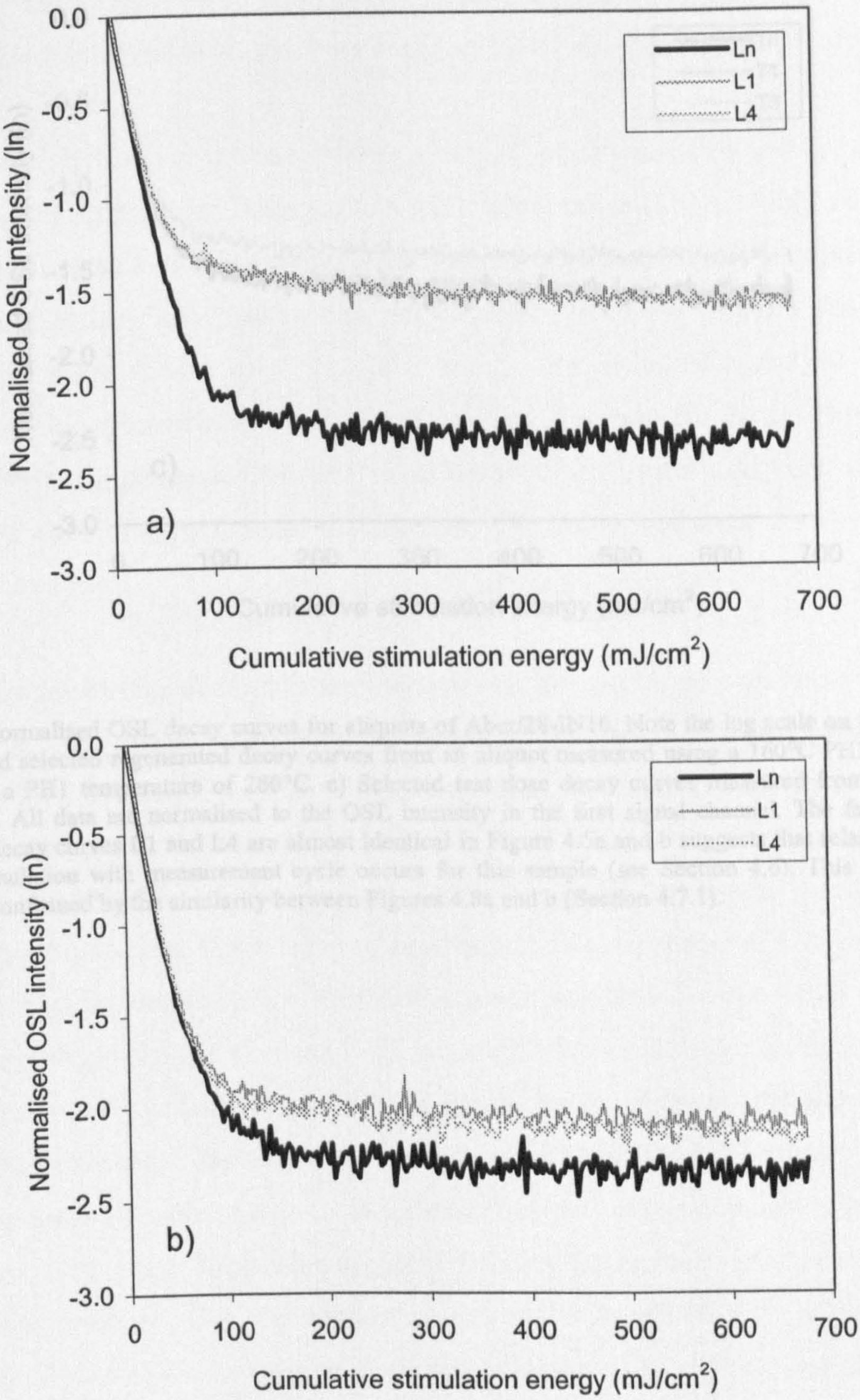

Figure 4.5. Caption overleaf.

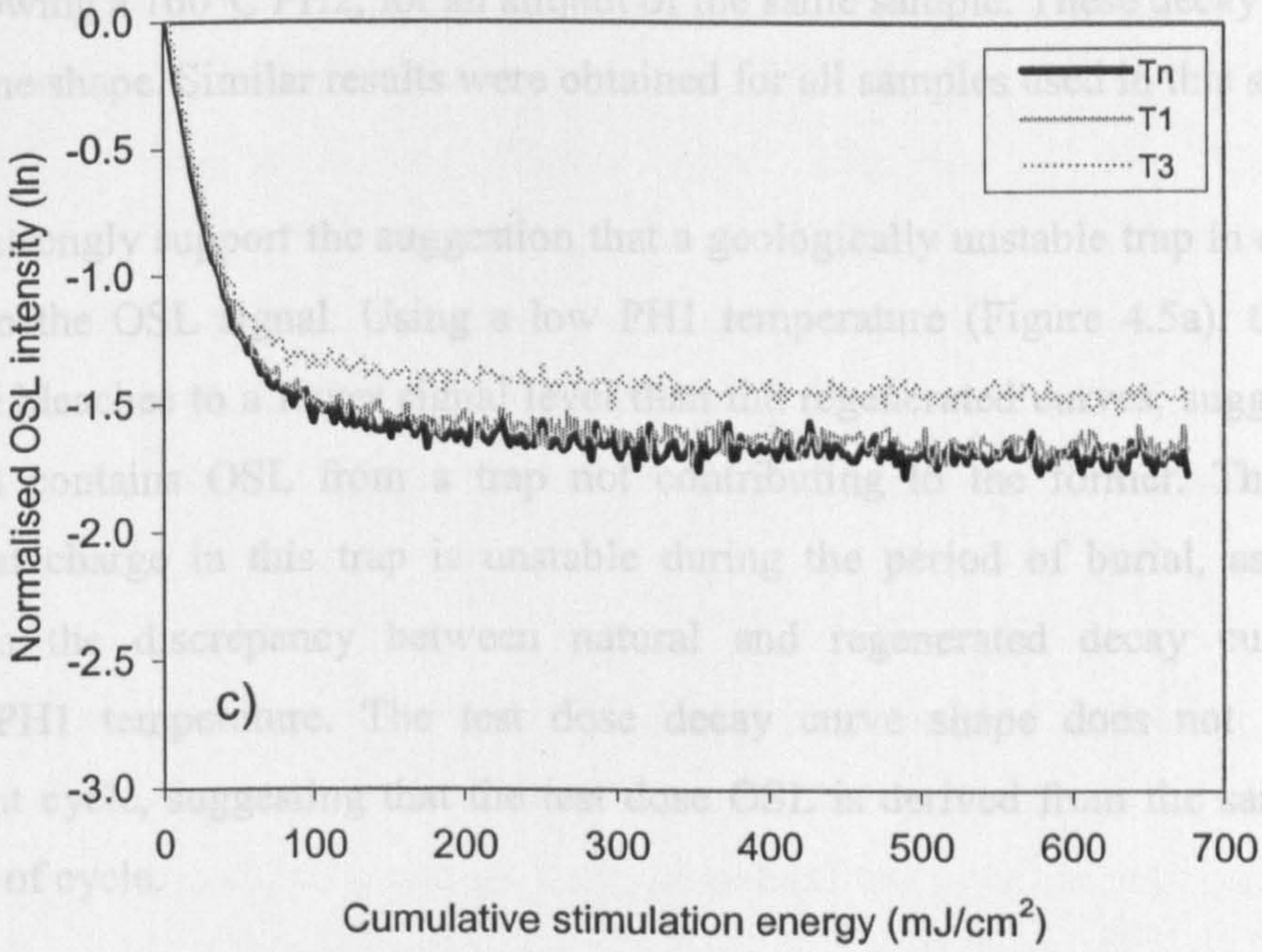

Figure 4.5. Normalised OSL decay curves for aliquots of Aber/28-IN16. Note the log scale on the y-axes. a) Natural and selected regenerated decay curves from an aliquot measured using a 160°C PH1. b) As a) except using a PH1 temperature of 280°C. c) Selected test dose decay curves measured from the same aliquot as b). All data are normalised to the OSL intensity in the first signal channel. The fact that the regenerated decay curves L1 and L4 are almost identical in Figure 4.5a and b suggests that relatively little charge accumulation with measurement cycle occurs for this sample (see Section 4.6). This suggestion seems to be confirmed by the similarity between Figures 4.8a and b (Section 4.7.1).

curves, following a 160°C PH2, for an aliquot of the same sample. These decay curves all have the same shape. Similar results were obtained for all samples used in this study.

These data strongly support the suggestion that a geologically unstable trap in quartz can contribute to the OSL signal. Using a low PH1 temperature (Figure 4.5a), the natural decay curve bleaches to a lower signal level than the regenerated curves, suggesting the latter signal contains OSL from a trap not contributing to the former. This in turn suggests that charge in this trap is unstable during the period of burial, as does the reduction in the discrepancy between natural and regenerated decay curves with increasing PH1 temperature. The test dose decay curve shape does not vary with measurement cycle, suggesting that the test dose OSL is derived from the same trap(s) irrespective of cycle.

4.6 Evidence for charge accumulation during SAR measurement sequences

The effect of charge accumulation on the shape of $D_e(t)$ plots can be investigated by giving fully bleached aliquots a known laboratory dose, and immediately subjecting them to a SAR measurement sequence. If the shape of the $D_e(t)$ plots described in Section 4.3 is caused solely by loss of charge from a slow-bleaching, geologically-unstable trap during burial, the D_e from this laboratory dose should be independent of both stimulation time and PH1 temperature. Since all SAR datasets produced for this thesis contain a repeated regeneration point (Section 3.3), no additional measurements are required to perform this test. By treating one of these repeated points as the natural signal, a $D_e(t)$ plot can be constructed for a known laboratory radiation dose. The dose point that replaces the natural is omitted from the growth curve to prevent autocorrelation. This type of plot is termed a "replacement plot" by Bailey (submitted), and his terminology has been adopted here. Two replacement plots were produced for each of the samples studied. The first used the first regeneration point (termed an R_1 replacement plot), whilst the second used the repeated (usually the sixth and last) regeneration point (termed an R_6 replacement plot).

R_1 replacement plots show a general decrease in D_e with increasing signal integration time (Figure 4.6a). Conversely, R_6 replacement plots show an increase in D_e with increasing signal integration time (Figure 4.6b). The size of this effect varies significantly, with some samples yielding replacement plots that are almost flat (Figure 4.7). Where the shape of the replacement plot is not approximately flat, D_e change with stimulation time is larger for lower PH1 temperatures. However, the D_e decrease seen in R_1 replacement plots for lower PH1 temperatures is always less than half that observed in natural $D_e(t)$ plots for the same sample.

The shape of these replacement plots may be explained in terms of charge accumulation from cycle to cycle. On measurement of the first regeneration dose decay curve, the slow-bleaching trap will contain only charge from the natural test dose and regeneration dose itself. Consequently, this trap will make a relatively small contribution to the later portions of the decay curve measured for this dose point. With each irradiation/measurement cycle, the slow-bleaching trap accumulates charge. Consequently, it makes a larger contribution to the later portions of these decay curves. In effect, the signal from later parts of the decay curve is in response to cumulative laboratory doses. This leads to a decrease in D_e with increasing signal integration for the R_1 replacement plot, and an increase in D_e with increasing signal integration for the R_6 replacement plot. The effect is more marked for the lower PH1 temperatures, indicating that the trap responsible is relatively thermally unstable. As the PH1 temperature is increased, a larger proportion of the charge in this trap is thermally eroded per cycle, and consequently the size of the effect decreases. For samples which do not yield flat replacement plots using the standard SAR procedure, the effect of charge accumulation on the natural $D_e(t)$ plots should be most similar to that for R_1 replacement plots, as the cumulative laboratory radiation dose to the natural aliquot is zero.

4.7 Investigating the relative importance of charge accumulation and the loss of geologically unstable charge using a modified SAR method.

The data presented in Sections 4.5 and 4.6 strongly suggest that both charge accumulation, and loss of charge from a geologically unstable trap, contribute to the

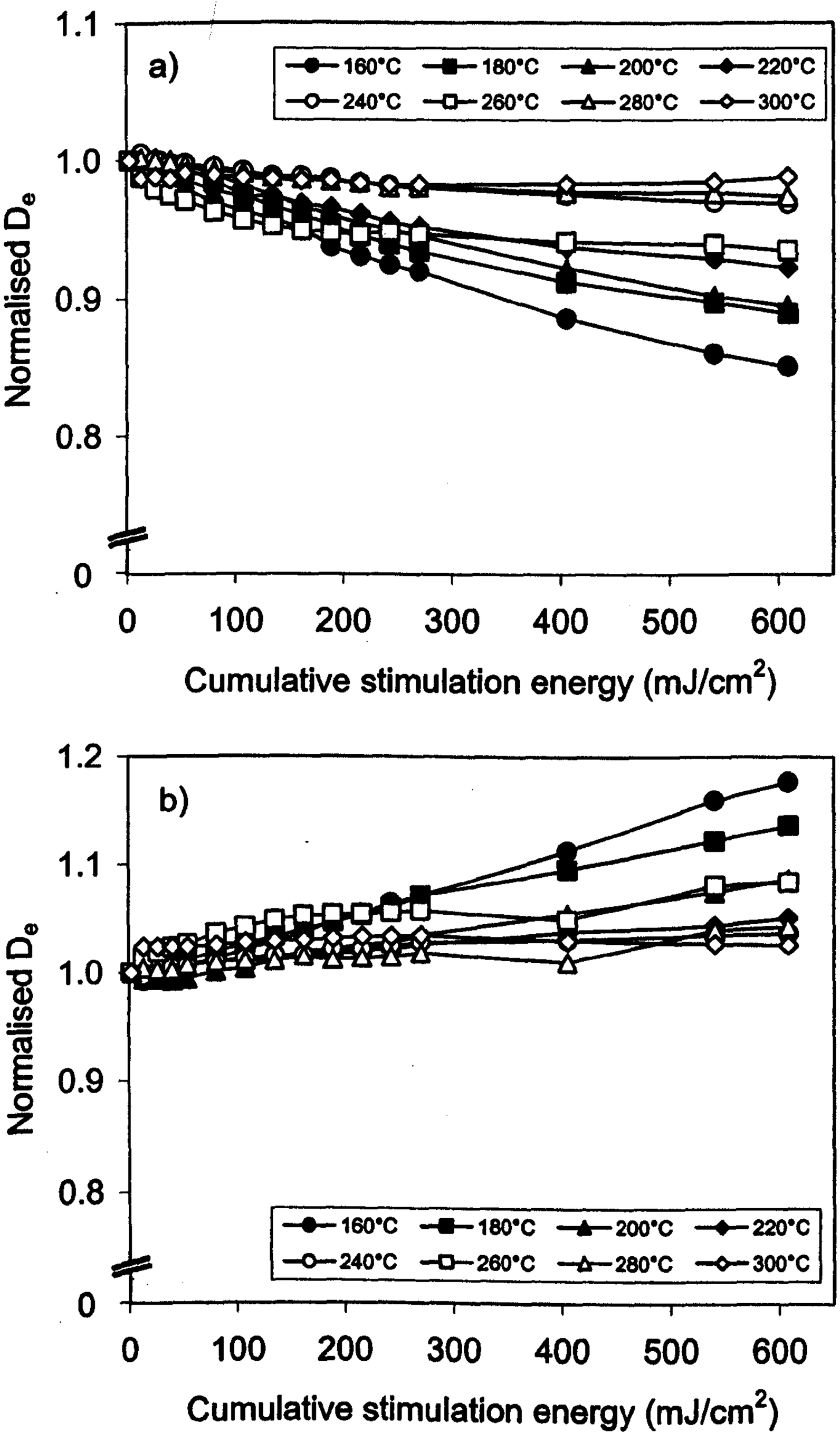

Figure 4.6. Replacement plots for Aber/28-IN21, the sample displaying the most extreme dependence of D_e upon signal integration period. The regeneration dose was 1.2 Gy in both cases. a) R_1 replacement plot. b) R_2 replacement plot. Each data point is the mean of three aliquots. The legend gives PH1 temperatures. Normalisation as for Figure 4.3.

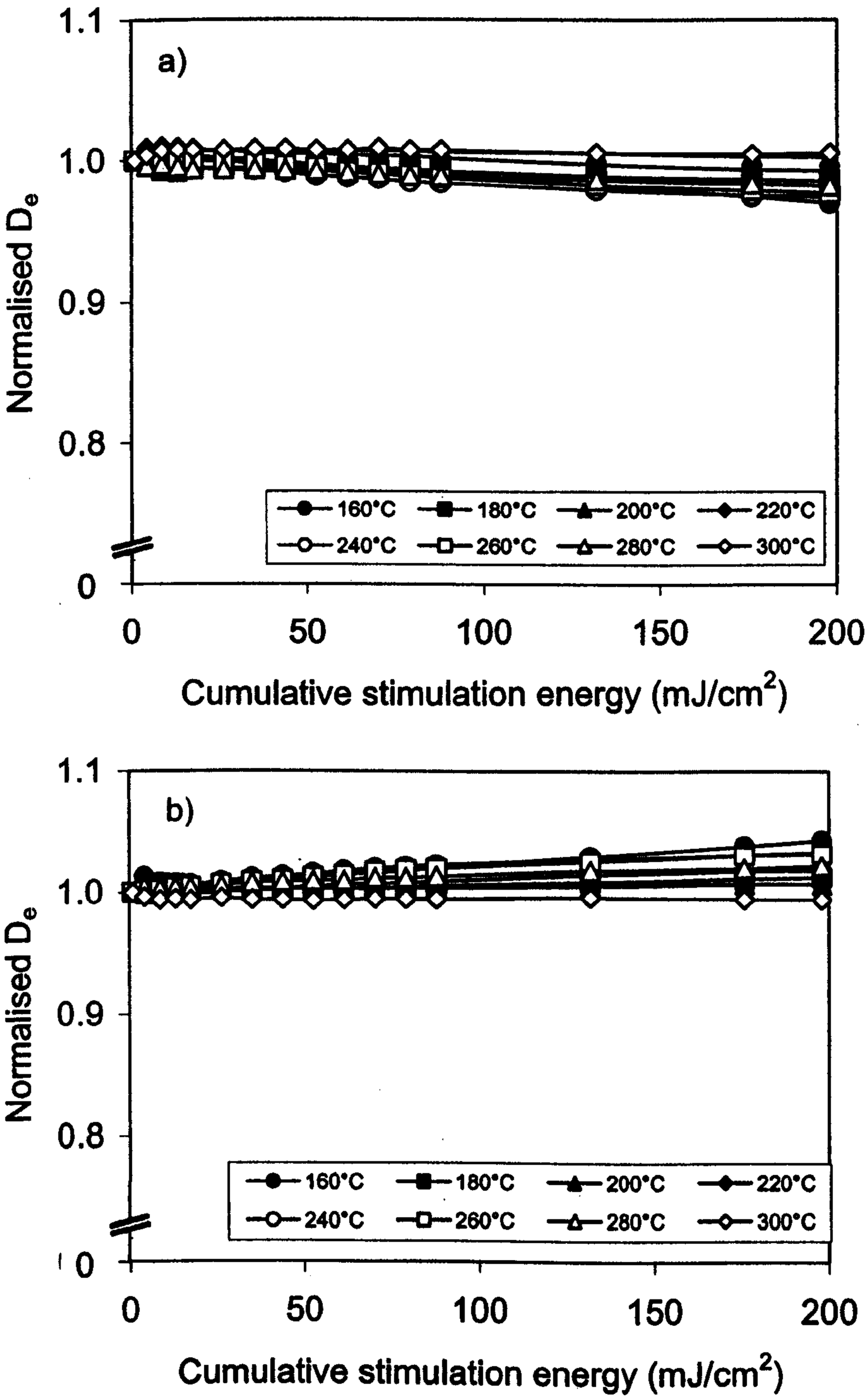

Figure 4.7. Replacement plots for Aber/28-IN12, showing limited D_e variation with signal integration period. The regeneration dose was 13 Gy in both cases. a) R_1 replacement plot. b) R_2 replacement plot. Each data point is the mean of three aliquots. The legend gives PH1 temperature. Normalisation as for Figure 4.3.

shape of natural $D_e(t)$ plots. The effects of charge accumulation can be minimised by removing all the charge from optically stimulable traps in the quartz crystal. This could be achieved by prolonged optical stimulation after completion of each test dose measurement. In practice however, extremely long stimulation times are required to reduce the OSL signal to instrument background levels (Bailey, 2000a). Complete removal of optically stimulable charge could also be hampered by recuperation. A more practical approach is to heat the aliquot to 500°C after each test dose measurement (between steps 6 and 7, Table 2.1), to empty all the lower temperature traps[c]. Theoretically, the SAR method can compensate for any sensitivity change that occurs between the end of the test dose measurement, and the beginning of the subsequent regeneration dose measurement. If this is the case, equivalent dose estimates produced using the standard and modified (incorporating a 500°C cut-heat between steps 6 and 7 in Table 2.1) SAR methods should be consistent for any given sample.

The modified SAR technique was tested on six samples, which had previously been dated using a standard SAR sequence (Table 4.1). In addition, a modern sample (Aber/40-SA10) which had been given a known laboratory dose of 4.87 Gy, was measured using the modified SAR procedure. Sixteen aliquots were measured in each experiment, two at each PH1 temperature. D_e values were calculated using the first signal channel. Aber/40-SA10 yielded a D_e value within 5% of the known laboratory dose. This result is comparable with the dose recovery experiments performed using the standard SAR method (Table 3.4). The naturally-irradiated aliquots gave D_e values consistent with those produced using standard SAR dating sequences (Table 4.1, mean ratio SAR:modified SAR is 0.99 ± 0.03). These data strongly suggest that the modified SAR protocol produces acceptable D_e estimates when calculated using the initial part of the decay curve. Consequently, $D_e(t)$ and replacement plots produced using the two methods should be comparable, and these are examined in Section 4.7.1. In addition, the similarity of the two data sets indicates that charge competition effects caused by the filling of optically

---

[c] This treatment will not remove the most thermally stable slow component of the OSL decay curve (Bailey, 2000a). Over the stimulation times used in this study, this component should provide an approximately constant background signal.

insensitive traps, have a negligible effect on the D_e produced using a standard SAR sequence.

4.7.1 $D_e(t)$ and replacement plots produced using the modified SAR method

A $D_e(t)$ plot for Aber/28-IN16, constructed from data using the modified SAR procedure outlined in Section 4.7, is shown in Figure 4.8a. The overall pattern of the plot is similar to that of Figure 4.8b (a $D_e(t)$ plot for the same sample produced from a standard SAR dataset). However, detailed differences between Figures 4.8a and 4.8b are apparent. These differences may be explained in terms of the aliquot-to-aliquot variation shown in Figure 4.4, and this will be exacerbated by the use of only two aliquots at each PH1 temperature in Figure 4.8a. When all 225 channels of the decay curve are used (608.4 mJ/cm^2 cumulative stimulation energy), the equivalent dose for a 160°C preheat falls to 87% of that calculated from the first channel only. This compared with a decrease to 82% for the same sample using a standard SAR sequence. Similar results were obtained for the other natural samples. The general pattern of the $D_e(t)$ plots (larger D_e decreases when using lower PH1 temperatures) is similar for datasets produced using either the modified or standard SAR technique. However, datasets produced using the modified SAR technique generally show smaller D_e variations (decreases in D_e with increasing signal integration time) than those produced using the standard technique.

Replacement plots for Aber/28-IN21, produced using the modified SAR method with heating to 500°C between measurement cycles, are shown in Figure 4.9. Similar plots for this sample, produced using the standard SAR measurement procedure, showed the largest D_e change with increasing signal integration period of all the samples measured (Figure 4.6). Using the modified SAR procedure, the equivalent dose appears to be independent of both stimulation time and PH1 temperature. Decay curve shapes follow the same pattern as for the standard SAR technique (Section 4.5). Similar results were obtained for all the geological samples measured using the modified SAR.

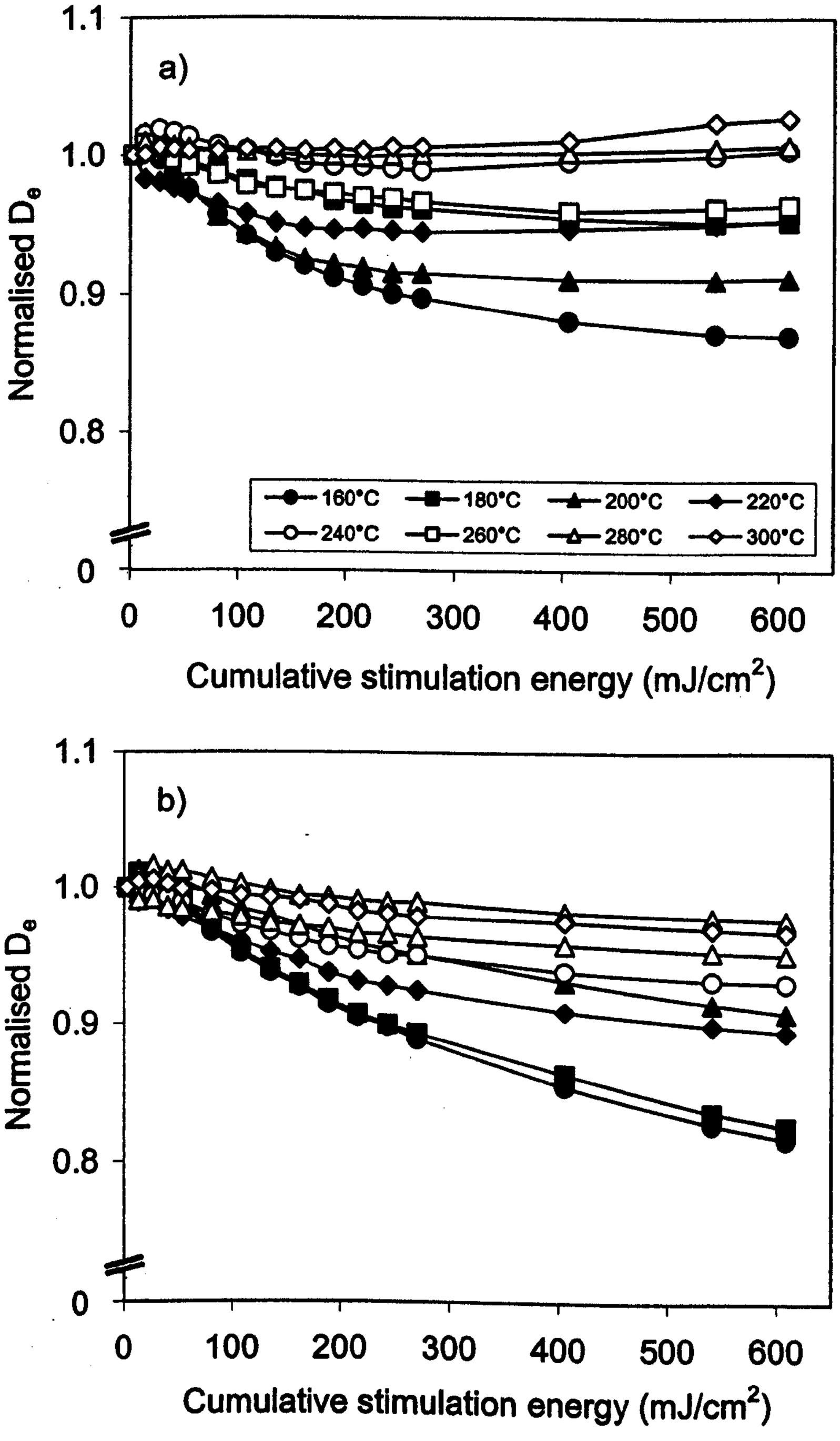

Figure 4.8. $D_e(t)$ plots for Aber/28-IN16, produced using a) data from a modified SAR measurement sequence, in which the aliquot is heated to 500°C after each T_x measurement, and b) data from a standard measurement sequence. Each data point is the mean of three aliquots. The legend gives PH1 temperatures. Normalisation as for Figure 4.3. Figure 4.8b is identical to Figure 4.3, and is reproduced here to aid comparison with Figure 4.8a.

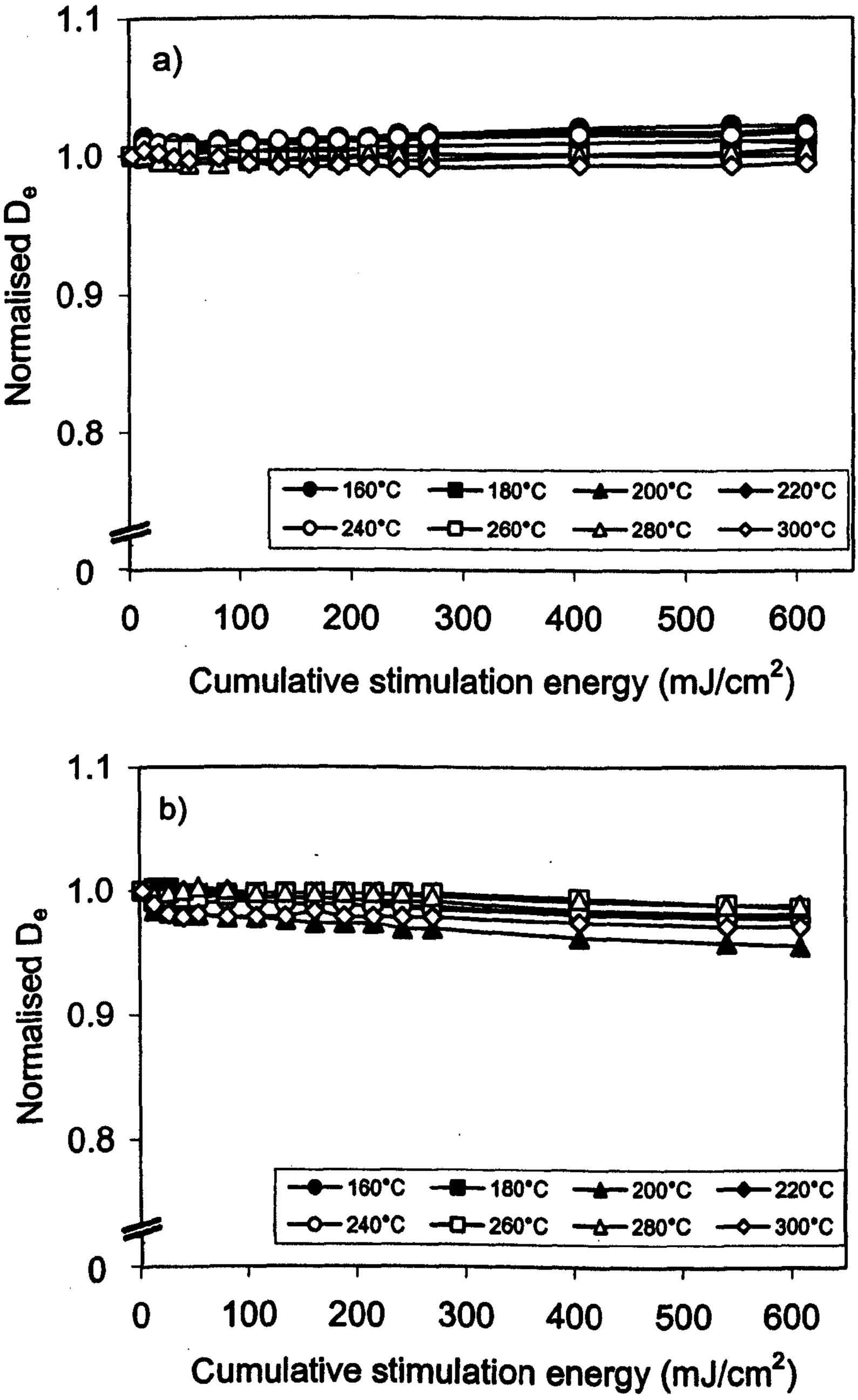

Figure 4.9. Replacement plots for Aber/28-IN21, using the modified SAR procedure. a) R_1 replacement plot. b) R_6 replacement plot. Each data point is the mean of three aliquots. The legend gives PH1 temperatures. Normalisation as for Figure 4.3. These plots should be compared with the replacement plots obtained using the standard SAR method, using the same sample (Figure 4.6).

For sample Aber/40-SA10, which had been given a laboratory radiation dose immediately prior to measurement using the modified SAR method, both $D_e(t)$ and replacement plots were independent of stimulation time and PH1 temperature.

4.7.2 Summary and discussion

All replacement plots, from samples measured using the modified SAR method, are flat. This indicates that charge accumulation causes the non-flat replacement plots observed when using the standard SAR technique. However, $D_e(t)$ plots for modified SAR datasets from geological samples, are similar in pattern to those produced using the standard SAR method. Since the modified SAR method prevents charge accumulation, this suggests that loss of charge from a geologically unstable trap is the main mechanism influencing the shape of $D_e(t)$ plots. But, $D_e(t)$ plots for modified SAR datasets show smaller D_e decreases with increasing signal integration time, than those for the same sample measured using the standard SAR method. This indicates that charge accumulation during the SAR measurement sequence does cause some of the D_e decrease with increasing signal integration time observed in $D_e(t)$ plots produced using the standard SAR technique. Finally, by irradiating the Aber/40-SA10 immediately prior to measurement, and using the modified SAR technique, both loss of charge from geologically unstable traps and charge accumulation were minimized. The $D_e(t)$ plot for this sample was flat. This indicates that loss of charge from a geologically unstable trap, was the cause of non-flat $D_e(t)$ plots for the geological samples measured using the modified SAR technique.

4.8 Inappropriate sensitivity correction using long signal integration periods

The SAR method was designed to correct for sensitivity changes when making measurements using the initial part of the OSL decay curve (primarily the fast component), and several studies have demonstrated this approach to be valid for a wide range of samples (e.g. Armitage *et al.*, 2000, Stokes *et al.*, 2000 and Chapter 5). However, the SAR technique may not accurately correct for sensitivity changes in signals other than the fast component, leading to the possibility that the shape of the R_1 and R_6 replacement plots over longer signal integration periods may also be due to inappropriate

sensitivity correction. This would occur if later parts of the test dose decay curve were not proportional to similar portions of the regenerated decay curve.

It is difficult to devise an experiment to distinguish between the effects of charge accumulation and inappropriate sensitivity correction in the later parts of the decay curve. The approaches of both Armitage *et al.* (2000) and Stokes *et al.* (2000) are inappropriate, since both would indicate sensitivity correction failure where charge accumulation occurred. It is also possible to monitor the OSL sensitivity using the 110°C TL peak response to a small test dose. This approach, based on the observed relationship between the two signals (Aitken and Smith, 1988), allows the OSL sensitivity to be measured when the OSL trap(s) contain charge. However, for samples from the south-east coast of Africa, the 110°C TL peak intensity is not always a reliable proxy for OSL sensitivity (Section 5.8). In addition, the relationship between the 110°C TL peak and OSL sensitivity has only been demonstrated for the fast OSL component. If, as seems likely, the slow-bleaching geologically-unstable signal observed in this chapter is not derived the 325°C trap, most previous research into sensitivity change is not relevant to this signal.

When the possibility of charge accumulation in a low thermal stability trap was removed by heating to 500°C between measurement cycles, flat replacement plots were obtained (Section 4.7.1). This provides circumstantial evidence supporting the role of charge accumulation in producing non-flat replacement plots. However, it does not constitute proof that sensitivity change is not responsible for the form of replacement plots derived from standard SAR measurement sequences.

4.9 Thermal stability of the geologically unstable trap

A $D_e(t)$ plot for CalQtz (Figure 4.10a) yields an insight into the thermal stability of the geologically unstable trap postulated in Section 4.4[d]. This sample was annealed at 500°C, and given a 4.6 Gy gamma dose on cooling. Approximately two years elapsed between

[d] Based on the, currently unproven, assumption that the slow-bleaching geologically-unstable signal observed in this chapter is not an artifact of sensitivity change during the later parts of the decay curve.

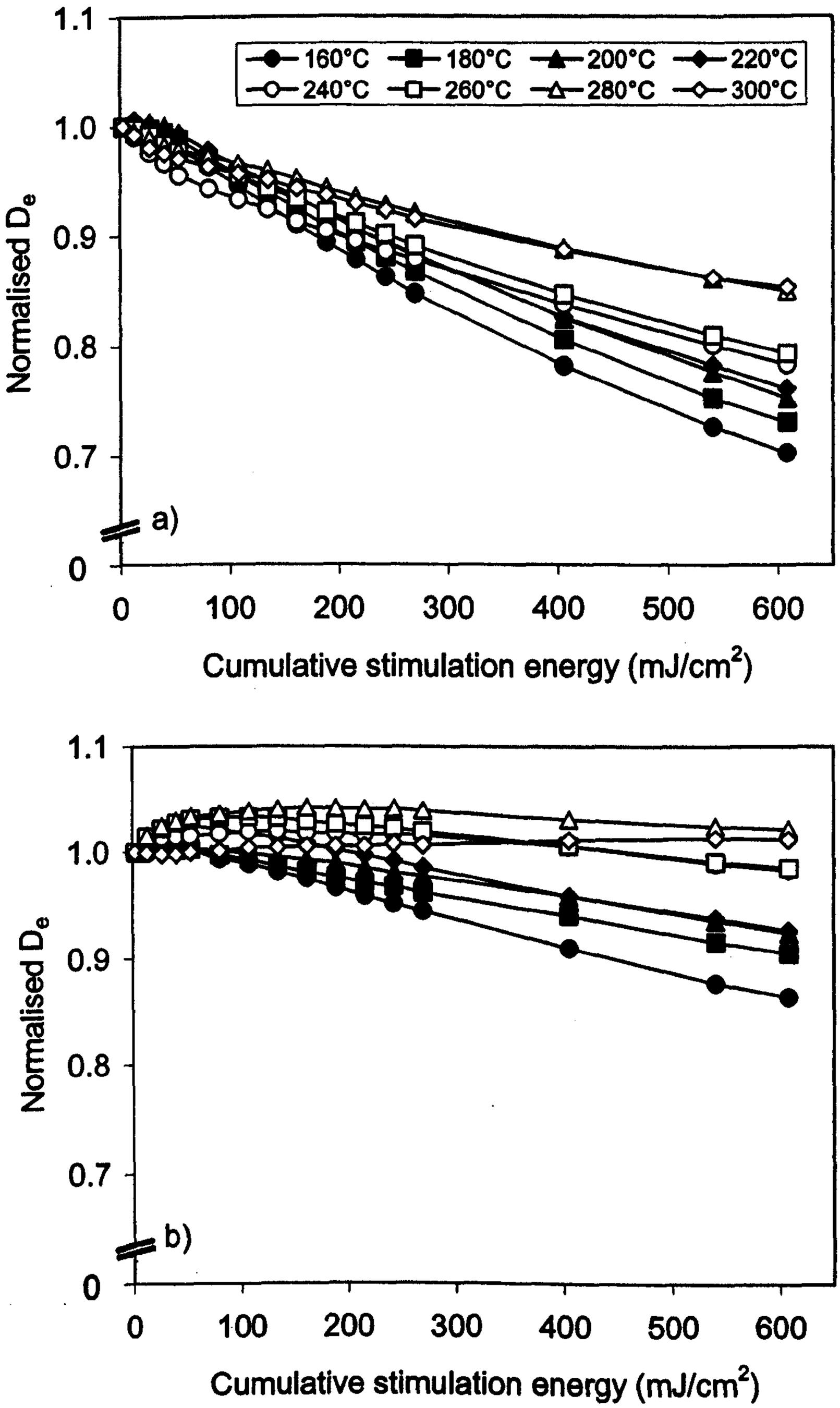

Figure 4.10. a) A $D_e(t)$ plot for CalQtz and b) an R_1 replacement plot for CalQtz. These data were measured using the standard SAR technique, using Risø 2. Each data point is the mean of three aliquots. The legend gives PH1 temperatures. Normalisation as for Figure 4.3.

irradiation and measurement of this sample. The decrease seen in the $D_e(t)$ plots using low PH1 temperatures, is more than twice that observed for the R_1 replacement plot (Figure 4.10b). Both datasets use an artificial radiation dose for their "natural" decay curve. This suggests that at least some of the charge in the geologically unstable trap has decayed during room temperature storage of CalQtz, between gamma irradiation and measurement. Consequently, OSL from this trap is reduced/absent from the "natural" decay curve. In contrast, the regeneration dose decay curves were measured immediately (< 1 hour) after irradiation, and hence contain (more) OSL from the unstable trap than does the "natural" decay curve. These data suggest that the geologically unstable trap must have a lifetime of days to months at room temperature. This is much shorter than the lifetime of the slowly decaying OSL component[c], identified by Singarayer and Bøtter-Jensen (in prep), which is thermally eroded over the range of PH1 temperatures used in this study. The lifetimes of the traps associated with the 160°C (28 days), 180°C (1.9 yrs) and 220°C (8.9 ka) TL peaks make them possible sources of the slow-bleaching, geologically-unstable OSL signal (Spooner and Questiaux, 2000). Since all aliquots are heated to 160°C or higher prior to measurement of the OSL at 125°C, the trap responsible for the 160°C peak should be empty. The trap responsible for the 220°C TL peak appears to be too stable to allow significant decay between irradiation and measurement of CalQtz. However, the 180°C TL peak is an unlikely source for the geologically unstable OSL signal, since it should be completely emptied by PH1 temperatures at which falling $D_e(t)$ curves are observed. In addition, the $D_e(t)$ plot for CalQtz falls even using high PH1 temperatures, whereas that for Aber/28-IN16 does not. This suggests that the effects of more than one geologically unstable trap may contribute to the $D_e(t)$ plot shapes observed. It is not currently possible to identify TL peaks associated with the trap(s) which contribute the geologically unstable OSL signal. Consequently, it is not possible to recommend a PH1 temperature which avoids the deleterious effects of these traps.

[c] Termed the "S2" component by Singarayer and Bøtter-Jensen (in prep).

4.10 Which signal integration period yields the correct value of D_e?

When D_e varies with stimulation time, the palaeodose[f] is difficult to assess. Since D_e variation with stimulation time appears to be caused by differences in the decay curve shape between natural and laboratory irradiated aliquots (see Section 4.5), this question cannot be answered by attempting to recover a known artificial radiation dose immediately after it has been administered. However, when the SAR technique is functioning correctly, the equivalent dose should be independent of PH1 temperature (Section 3.7). Where this situation occurs, it can be assumed that the resulting equivalent dose represents an accurate assessment of the palaeodose.

In Figure 4.11a, D_e is plotted against PH1 temperature for CalQtz. This sample was chosen because it has a uniform "natural" dose, since the geological dose was removed by annealing to 500°C prior to administration of a gamma dose. Consequently, an appropriate signal integration time should yield identical equivalent doses at all PH1 temperatures. Unfortunately, meaningful equivalent doses cannot be calculated for this sample, since the same data were used to calibrate the β-source on this reader. Consequently, independence of D_e on PH1 temperature alone has been taken to indicate accurate assessment of the equivalent dose. D_e values produced using two signal integration periods have been shown in Figure 4.11a. These are the first channel of optical stimulation, and the complete decay curve (channels 1 to 225). Equivalent doses produced using only the first signal channel are independent of PH1 temperature, and yield a mean normalised D_e value of 1.00. When the entire OSL decay curve is used to estimate the equivalent dose, it is strongly dependent on PH1 temperature. Normalised D_e values rise from 0.70 at 160°C to 0.87 at 300°C. Similar results are obtained for the geological samples, though natural variability renders the trend less striking (Figure 4.11b, Aber/28-IN12). The first channel of the decay curve appears to be the most appropriate for D_e estimation. This conclusion is supported by the fact that, by definition, the first signal channels contain signal from the most rapidly bleached trap(s), and hence ought to provide the most accurate D_e estimate for a sedimentary sample.

---

[f] The palaeodose is the radiation dose which the sample has absorbed during burial. The equivalent dose is an estimate of the palaeodose based on laboratory measurements.

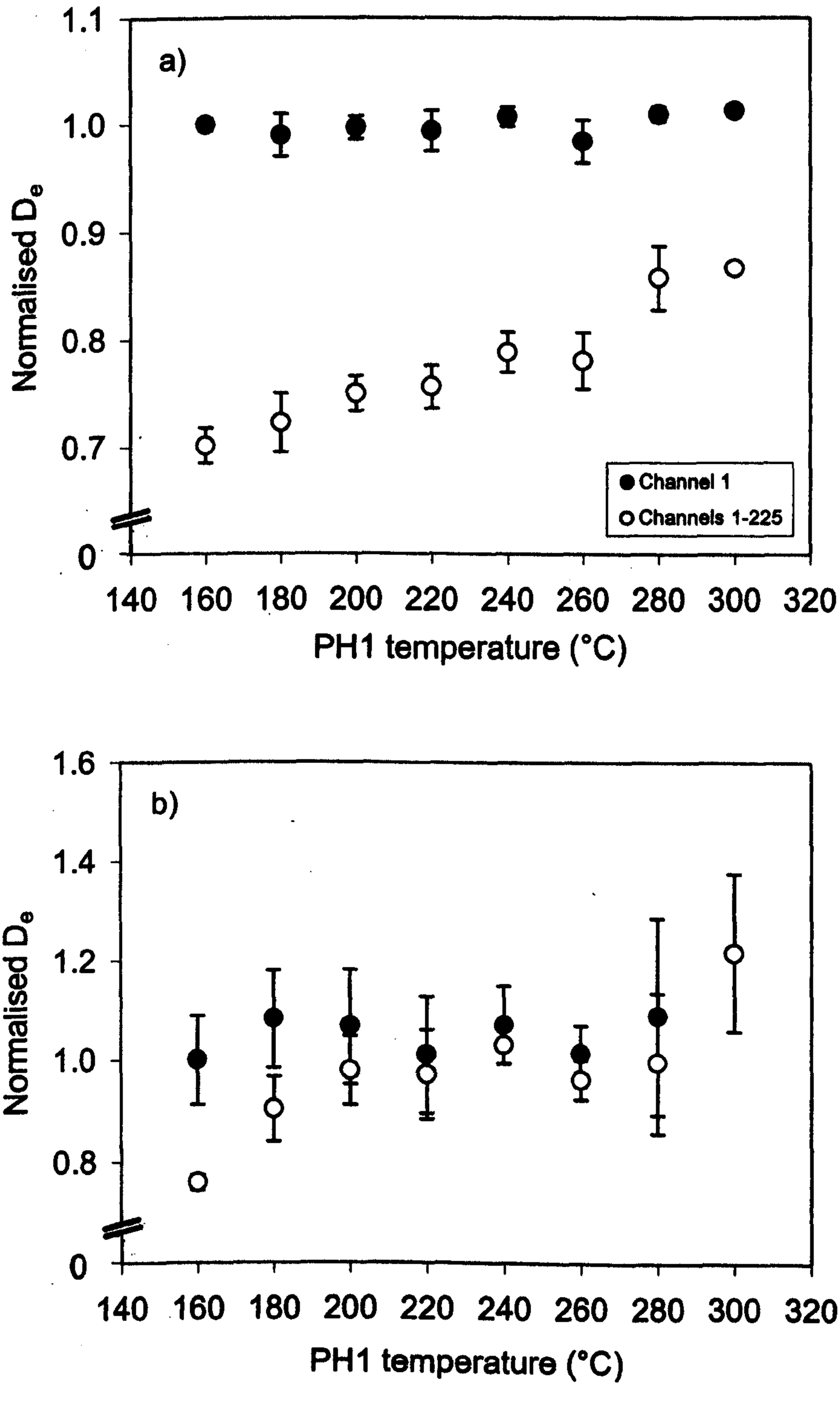

Figure 4.11. D_e versus PH1 plots using the initial (solid circles) and whole (empty circles) OSL signal. All data are normalized to the value for D_e obtained for the initial signal using 160°C PH1. a) CalQtz. b) Aber/28-IN12.

4.11 Discussion

The application of this conclusion has two practical problems. Firstly, when the OSL signal is small, it may be advantageous to use longer signal integration times, to maximize the measured signal. For example, when measuring single quartz grains, Duller *et al.* (1999) integrated the OSL signal over 20 seconds, thereby measuring the entire signal. Secondly, a thermally unstable, ultra optically sensitive OSL signal has been identified for a range of samples (Jain *et al.*, 2001). Using only the first channel of the decay curve will increase the contribution to the OSL signal made by this component, potentially resulting in D_e underestimates relative to the palaeodose. This signal does not appear to be large in the samples used in the present study (Section 4.3 and Figure 4.3). Where longer signal integration times are required, higher PH1 temperatures are advocated, since the ultra-fast component is removed by heating to 200°C (Jain *et al.*, 2001). In addition, the $D_e(t)$ plots described above show less dependence on signal integration time using higher PH1 temperatures.

The modified SAR technique, in which the sample is heated to 500°C at the end of each measurement cycle, may also be used, to reduce the D_e decrease when using longer stimulation times. However, this method does not yield correct equivalent doses for some samples (Murray, pers. comm.), and only eliminates one cause (charge accumulation) of falling $D_e(t)$ plots. Consequently, routine use of this method is not advocated.

It has been suggested that $D_e(t)$ plots may be used to detect partial bleaching of sediments prior to burial (Bailey, submitted) [g]. As stimulation progresses, more optically stable traps dominate the OSL signal. If a sediment is partially bleached, these traps will have a higher unbleached charge population on burial than the less optically stable traps which dominate the initial portion of the decay curve. Consequently, partially bleached samples will yield higher equivalent doses after longer stimulation times, while fully bleached ones yield flat $D_e(t)$ plots. The $D_e(t)$ plots presented here show the opposite dependence of D_e upon stimulation time, leading to the possibility that the two effects may cancel

---

[g] These plots were produced using signal intervals (e.g. channels 1-5, 5-10...) whereas the $D_e(t)$ plots used in this study use integrated signals (channels 1-x). The method used by Bailey (submitted) will enhance the effects of both partial bleaching and the slow-bleaching, thermally unstable signal described above.

each other out. Consequently, the use of $D_e(t)$ plots for identifying partially bleached sediments may not be applicable to these samples. Researchers should be cautious when using $D_e(t)$ plots to infer the absence of partial bleaching in any given sample.

4.12 Conclusions

1) At least one slow-bleaching, geologically-unstable trap contributes to the OSL signal from these samples, becoming more significant in the later parts of the decay curve. Using longer signal integration periods, this trap distorts the growth curve, causing the observed D_e to fall. This effect can be minimised using higher PH1 temperatures. However, the simplest solution is to calculate the D_e using only the first signal channel. In the present study, this equates to the signal measured in response to the first 0.88 or 2.7 mJ/cm^2 of stimulation (Risø 1 and Risø 2 respectively).
2) A modified SAR technique, in which the aliquot is heated to 500°C at the end of each measurement cycle, has been tested for a small number of samples from Inhaca Island. D_e values produced using the standard and modified SAR techniques are similar. However, the observed D_e still falls with increasing signal integration time when using the modified SAR technique, and hence it is not advocated for routine use.
3) $D_e(t)$ plots may not be an appropriate method for detecting partial bleaching in samples containing the slow-bleaching, geologically-unstable trap.

Chapter 5: Sensitivity changes in quartz

5.1 Introduction

The SAR method requires that the natural luminescence intensity is compared with a growth curve, measured using the same aliquot, to calculate the equivalent dose. Changes in the luminescence sensitivity of an aliquot are known to occur in laboratory procedures such as preheating (Jungner and Bøtter-Jensen, 1994, Armitage *et al.*, 2000), irradiation (Zimmerman, 1971) and illumination (Bailey, 1997), and have recently been shown to have occurred in nature (Wintle and Murray, 1998, 1999). Consequently, direct comparison between natural and laboratory luminescence signals may not be possible. Similarly, luminescence sensitivity changes between regeneration doses could distort the shape of a growth curve. Sensitivity changes therefore need to be accurately monitored, and corrected for, if meaningful D_e evaluations are to be made. This chapter presents experiments made to assess the ability of two luminescence signals, to accurately monitor sensitivity change during SAR style (see Section 2.2) dating sequences. These signals are the OSL and 110°C TL response to a test dose administered after the natural/regenerated luminescence measurement. In addition, an attempt is made to reconcile the sensitivity changes observed in these measurements, with previous explanations of the mechanism by which sensitivity change occurs (see Section 1.6).

5.2 Characterising the pattern of sensitivity change during an SAR measurement sequence

The SAR protocol described by Murray and Wintle (2000, outlined in Section 2.2) uses the OSL response to a test dose administered after each dose point, to monitor sensitivity change. By dividing the natural or regenerated luminescence intensities (L_x) by their respective test dose intensity (T_x), a sensitivity-corrected luminescence response is determined (R_x). This technique was developed during a study of the OSL sensitivity change characteristics of a single sample of Australian sedimentary quartz (WIDG8) and tested using six heated and six sedimentary quartzes (Murray and Wintle, 2000).

The pattern of sensitivity change during a measurement sequence was investigated using a standard SAR procedure, but with a constant regeneration dose. Two aeolian quartzes from southern Africa were measured (Aber/12-MAP3 and Aber/29-BA14). Aber/12-MAP3 and Aber/29-BA14 have equivalent doses of 29 and 176 Gy respectively. In each case, sixteen natural aliquots of the sample were used, two at each of eight PH1 temperatures (160-300°C in 20°C steps). Having measured L_n and T_n, up to ten regeneration cycles using a constant regeneration dose of 10 Gy were performed[a]. To observe any dose dependency in sensitivity change, this experiment was repeated on Aber/12-MAP3 using regeneration doses of 0 Gy and 50 Gy (using fresh natural aliquots for each experiment). In all cases the test dose was 5 Gy, this being the standard test dose used in the project.

5.2.1 Sensitivity changes observed using a repeated single regeneration dose

Relative sensitivity (T_x/T_n) changes during the experiments described above are shown in Figures 5.1 and 5.2. For both samples, the size and direction of sensitivity change is dependent on PH1 temperature. In all cases, the lower temperature preheats (160-220°C) result in an initial decrease in sensitivity. This decrease is larger for the lower temperature preheats. Using a 10 Gy regeneration dose (Figure 5.1), the maximum sensitivity decrease for the 160°C preheat data is c.40%. The sensitivity decrease at 160°C appears to be complete after about seven measurement cycles using a 10 Gy regeneration dose. However, using a 0 Gy regeneration dose, the sensitivity is still decreasing after 10 cycles (Figure 5.2.a), while the sensitivity decrease appears to be complete after 3 cycles using a 50 Gy regeneration dose (Figure 5.2.b). The sensitivity of many of the low PH1 temperature aliquots begins to increase after the initial decrease. This effect is seen for all the lower temperature preheats (160-220°C) in the data for 50 Gy regeneration doses. However, it is also apparent in the 220°C data for both samples using a 10 Gy regeneration dose, and that for Aber/12-MAP3 using a 0 Gy regeneration dose.

---

[a] The results of a similar experiment were published as Armitage *et al.* (2000), where these two samples were referred to as MAP3 and BA14. The sensitivity change data from that paper have not been presented here since, unbeknown to the authors at the time of publication, the preheat temperatures stated were 7/5 of the correct value (see Section 2.4.1). Fortunately, the conclusions drawn in that study are still found to be valid, and are elaborated in this section.

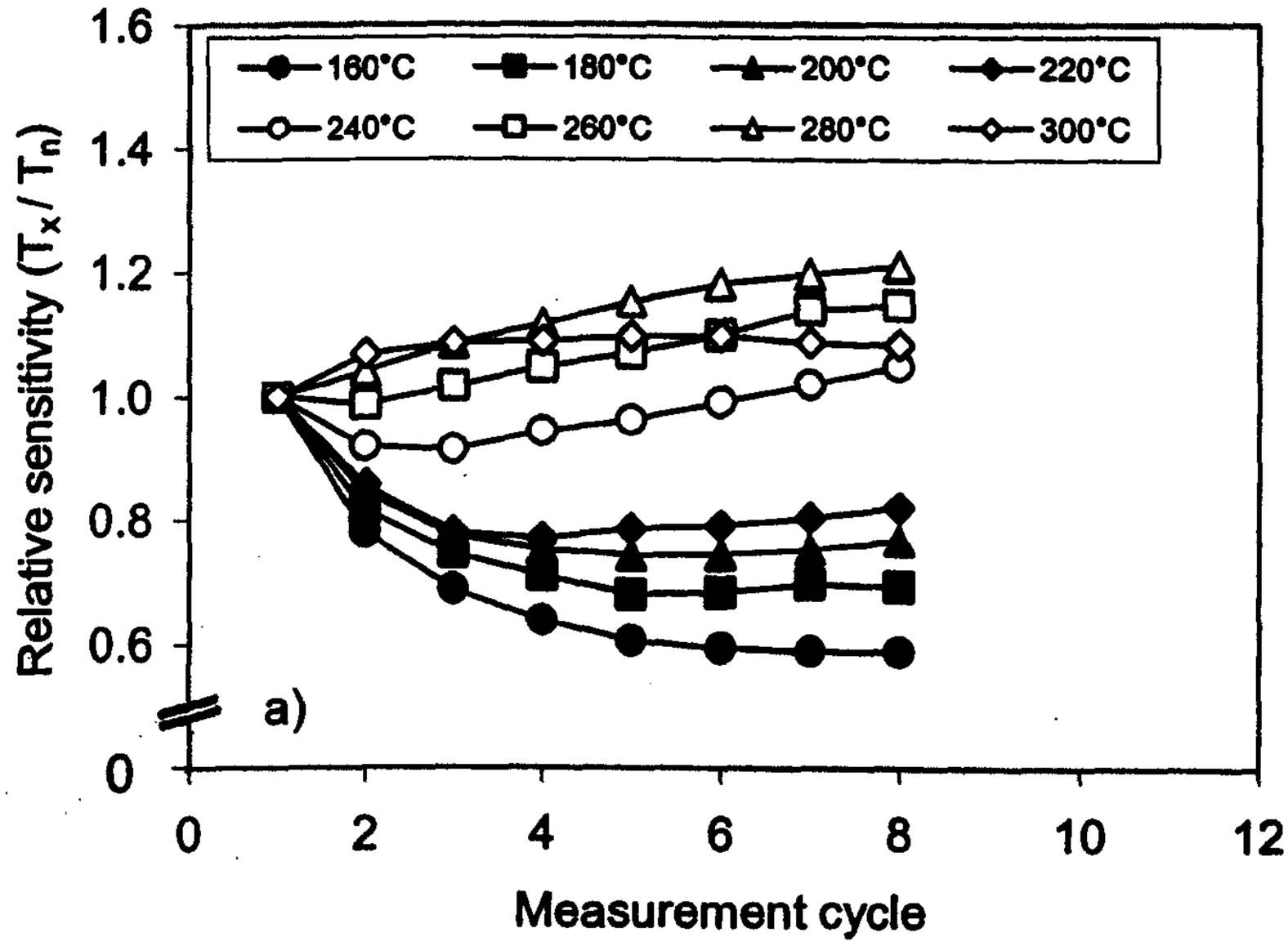

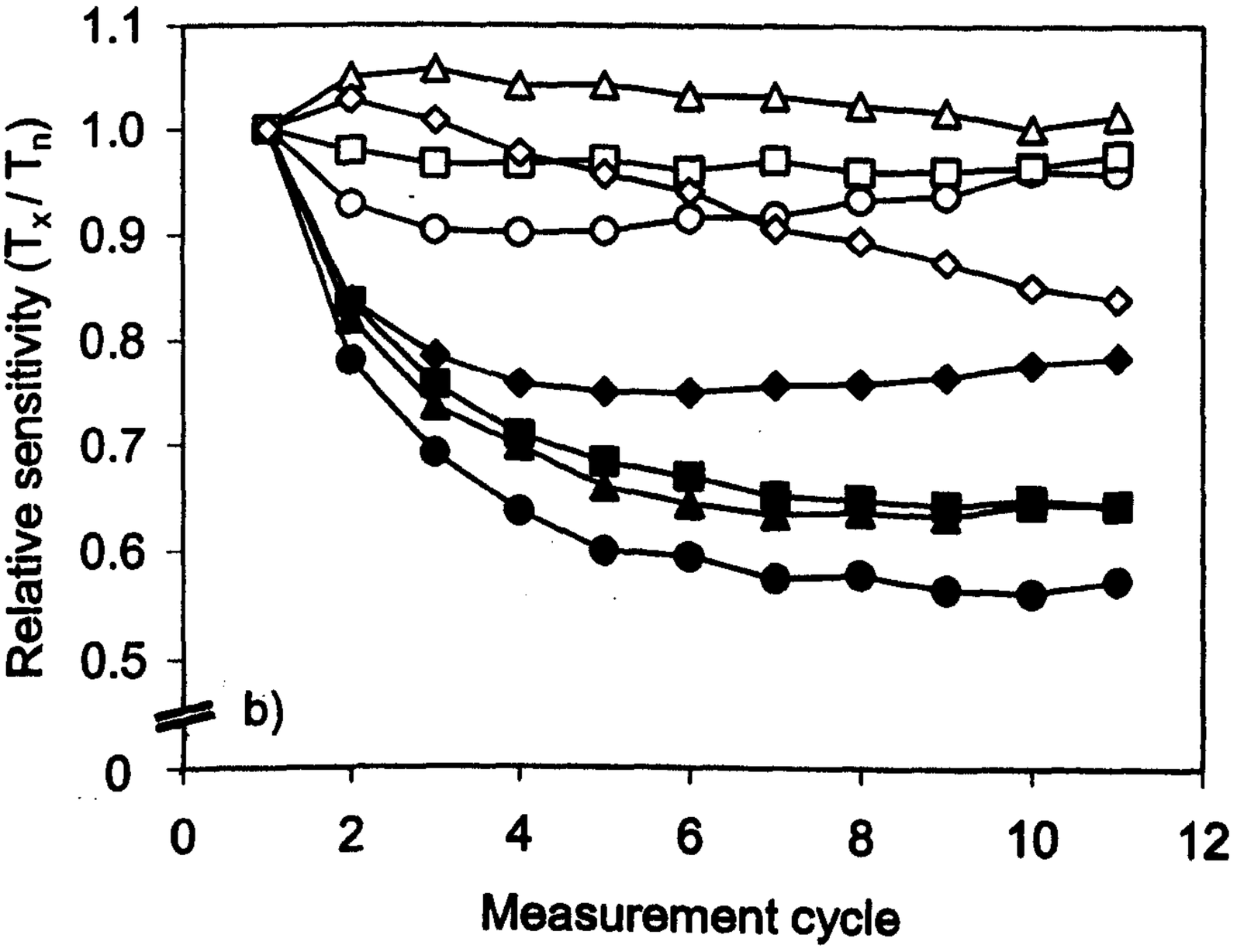

Figure 5.1. Relative sensitivity (T_x/T_n) versus measurement cycle plots for a) Aber/12-MAP3 and b) Aber/29-BA14, using a constant 10 Gy regeneration dose, and a test dose of 5 Gy.

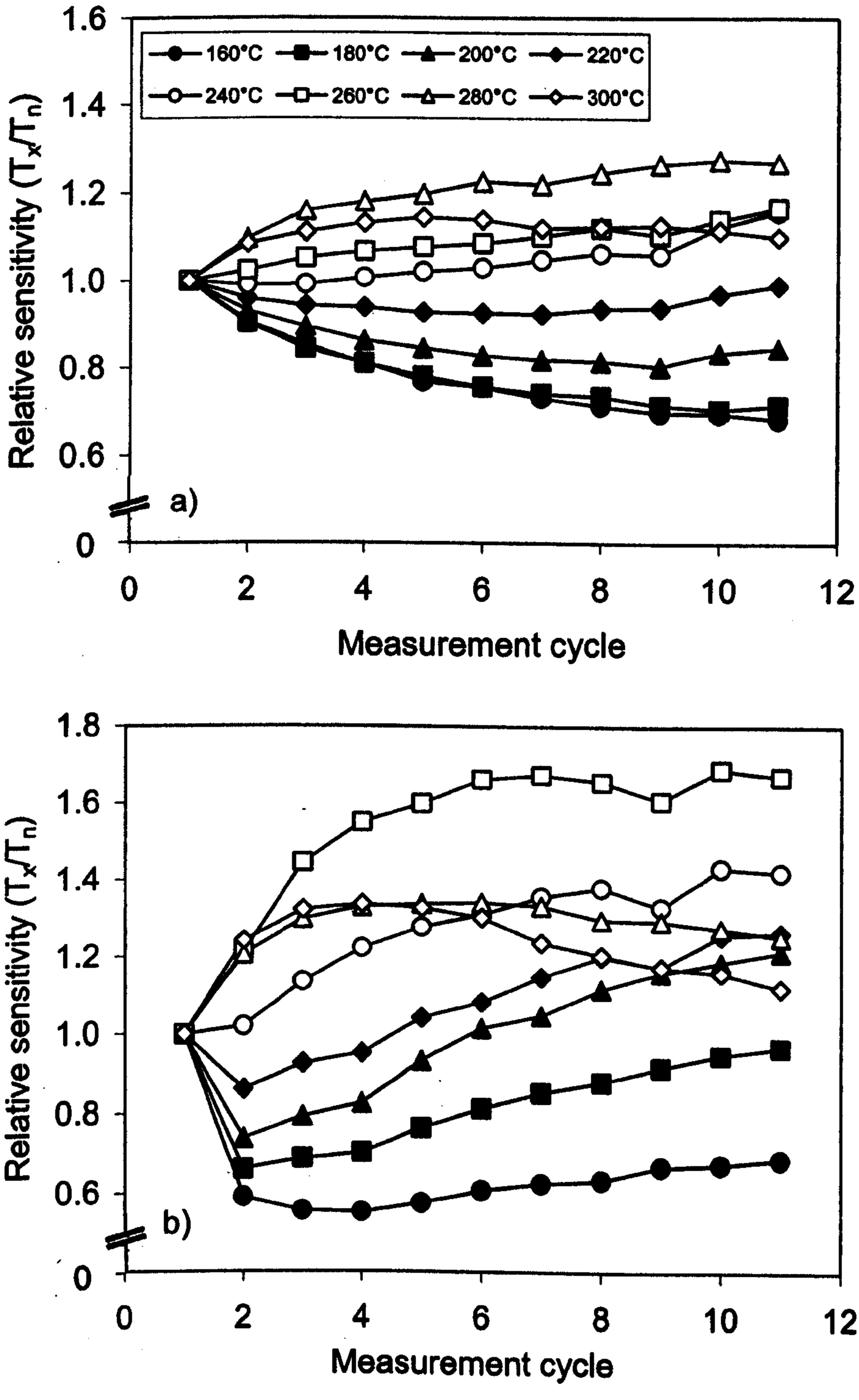

Figure 5.2. Relative sensitivity (T_x/T_n) versus measurement cycle plots for Aber/12-MAP3 using a constant regeneration dose of a) 0 Gy and b) 50 Gy. Note the larger y-axis scale in b).

For any of the regeneration doses used, the higher temperature preheats (260-300°C) result in a general increase in sensitivity in aliquots of Aber/12-MAP3. The data for a 240°C PH1 are intermediate between the behaviour above and below this temperature. The general increase in sensitivity (240-300°C PH1 temperatures) does not appear to be complete after 11 measurement cycles for the 0 Gy regeneration dose, or 8 cycles using 10 Gy. However, using a 50 Gy regeneration dose, this sensitivity increase is completed after c.4-6 cycles, depending on the PH1 temperature used. For preheats between 240 and 280°C, no further sensitivity change is observed. The maximum percentage increase in sensitivity is variable (see Section 5.2.3), ranging from c.30% using PH1 temperatures of 280 and 300°C, to 70% using a 260°C preheat. The data for Aber/29-BA14 using higher PH1 temperatures are different from those using Aber/12-MAP3. For preheats between 240 and 280°C, very little sensitivity change is observed (±c.10%).

For both samples, the data for 300°C preheats are different from those for the other higher PH1 temperatures. In Figures 5.1 and 5.2.b, the sensitivity initially increases, and then decreases, so that no constant value is observed. This effect is small when using a 0 Gy regeneration dose (Figure 5.2.a), and occurs more rapidly with passing cycle using a 50 Gy regeneration dose than when using 10 Gy. The effect is also more marked for Aber/29-BA14 using a 10 Gy regeneration dose, than for Aber/12-MAP3 using the same dose.

5.2.2 Possible causes for the sensitivity changes observed

The initial sensitivity decrease observed for all lower temperature preheats may be explained by dose quenching. During irradiation, holes in the valence band are preferentially captured at R-centres, causing the ratio of activated L:R-centres to drop, leading to a decrease in sensitivity. Some of the holes captured at R-centres are subsequently moved to L-centres by thermal activation during the preheat. Consequently, the sensitivity decrease observed using PH1 temperatures between 160-220°C is less for higher preheat temperatures, as thermal activation partially reverses the dose quenching.

Above a preheat temperature of around 220-240°C, the dominant process changes from dose quenching to thermal activation. Consequently, aliquots of Aber/12-MAP3 show a general increase in sensitivity with measurement cycle above these temperatures. However, aliquots of Aber/29-BA14 show relatively small sensitivity changes using preheat temperatures above 240°C. Since the lifetime of holes at the OSL R-centre[b] is an order of magnitude smaller than the probable age of this sample, significant loss of activated R-centres during burial is likely. Similarly, Wintle and Murray (1998, 1999) suggest that sensitization of their c.30 ka sample occurred during burial, though this process was not complete. It is probable therefore, that the older sample (Aber/29-BA14) contains fewer R-centres which had been activated during natural irradiation, than Aber/12-MAP3. Consequently negligible thermal activation of the natural sample was possible. This is discussed further in Section 5.4.

After an initial decrease, the sensitivity of aliquots given a low temperature preheat begins to increase. This effect is most noticeable using a 50 Gy regeneration dose (Figure 5.2.b). Bailey (2001, Figure 7) observed a similar effect in simulated data when the R-centres[c] became saturated with holes, leading to preferential hole trapping at L-centres. This mechanism appears to be a likely explanation of the above effect.

After an initial increase in sensitivity, most aliquots preheated to 300°C exhibit decreasing sensitivity, the possible exception being that using a 0 Gy regeneration dose on Aber/12-MAP3 (Figure 5.2a). This effect occurs after fewer cycles using a 50 Gy rather than a 10 Gy regeneration dose, using Aber/12-MAP3. Three possible explanations for this phenomenon have been considered.

1) The L-centre saturates and excess holes formed during irradiation, become trapped at R-centres, lowering the sensitivity[d]. However, this seems unlikely since

---

[b] c.14 ka at 20°C (Li and Chen, 2001)

[c] This model uses three non-radiative recombination centres, two thermally unstable R-centres and a stable K-centre. The R-centre referred to here is that with the lower thermal stability, termed the R_1-centre by Bailey (2001).

[d] This mechanism requires a second, more thermally stable R-centre, or the complete absence of hole trapping sites during the preheat, allowing holes to be trapped at the thermally unstable R-centre as the aliquot cools.

in Figure 5.2.b, the aliquots preheated at 280°C do not decrease in sensitivity as much as those preheated at 300°C, despite receiving the same cumulative dose.

2) Holes at the L-centre are not stable at 300°C, leading to preferential capture of holes at a second, more thermally stable R-centre. However, the existence of a TL peak at 325°C, which is thought to use the same L-centre as the OSL signal (Section 1.6.1.1), strongly suggests that this is not the case.
3) The 300°C preheat significantly depletes the trapped charge population in the 325°C trap. A proportion of these thermally evicted electrons would not have been detrapped by the subsequent optical stimulation, since a large residual TL signal is observed in this temperature region even after prolonged bleaching (Franklin and Hornyak, 1990, Spooner, 1994 and Scholefield *et al.*, 1994). Consequently a far larger number of recombination centres[e] are deactivated per measurement cycle than is due to optical stimulation alone. This additional loss of activated L-centres cannot explain the decrease in sensitivity observed without the presence of a thermally stable non-radiative recombination centre. However, the R_3 centre proposed by Chen and Li (2000) for the 110°C TL signal may be available to charge from the OSL trap (Section 1.6.1.4), and is thermally stable at 300°C. Similarly, Bailey's (2001) model required an additional recombination center (termed the K-centre[f]), to account for the 110°C TL/OSL emissions at 420 and 480 nm. These emissions are not visible through the transmission filters used in his (or the present) study, and hence are regarded as non-radiative for the purposes of this discussion. It therefore seems likely that a thermally stable, non-radiative recombination centre (K-centre hereafter) is available to charge from the OSL trap. The ratio of activated L- to K-centres drops each measurement cycle, due to recombination of electrons detrapped during PH1. If the natural sample contains a large number of activated R-centres, this effect may be masked for the first few measurement cycles by thermal activation, leading to sensitivity increase. Once this residual activated R-centre population (from natural rather than laboratory irradiation) is removed, the L- to K-centre ratio dominates

---

[e] Mainly or all L- rather than R-centres due to thermal activation.
[f] So termed by Bailey (2001) to distinguish it from the thermally unstable reservoir (R)-centres of Zimmerman (1971).

sensitivity change. For this mechanism to produce a sensitivity decrease, the L-centre electron trapping cross section must be greater than that of the K-centre, or the activated L-centre population must be significantly greater than that of the K-centre[g]. This theory is regarded, tentatively, as being the most likely explanation of the data for 300°C preheats.

It should be noted that, while studying the changes in the sensitivity of the 110°C TL peak during storage at various temperatures, Wintle and Murray (1999) found a long-term sensitivity decrease for both natural and irradiated samples (their Figures 5a-c). This sensitivity change (termed component D by Wintle and Murray, 1999) may be the same as the effect described above, since it occurred most rapidly at their highest storage temperature (280°C), and followed an initial sensitivity increase. Wintle and Murray (1999) calculated activation characteristics for this sensitivity change, and found that it had a lifetime of 60 years at 20°C. However, it was observed in the data from natural aliquots, and at temperatures between 220 and 280°C its lifetime was three orders of magnitude greater than that of holes trapped at the R-centre[h].

The sensitivity change data for aliquots of Aber/12-MAP3 given various regeneration doses, suggests that all of the processes described above occur more quickly at higher regeneration doses. This is not unexpected, since both dose quenching and thermal activation are dependent on the trapped charge population of the quartz.

5.2.3 Sensitivity changes in individual aliquots

Figures 5.1 and 5.2 show mean sensitivity change values for two aliquots at each PH1 temperature. This approach is valid since, in all cases, the pattern of sensitivity change is similar for both aliquots. However, variation in the size of sensitivity change is observed (Figure 5.3). These differences are probably explained by variations in the concentrations of R, L and K-centres between crystals. Such variations may be expected to exist since

---

[g] The latter condition could be fulfilled in Bailey's (2001) model, since the concentration of L-centres is two orders of magnitude greater than that of the K-centres.

[h] Component A, which was interpreted as the transfer of holes from thermally unstable R-centres to stable L-centres (Wintle and Murray, 1999).

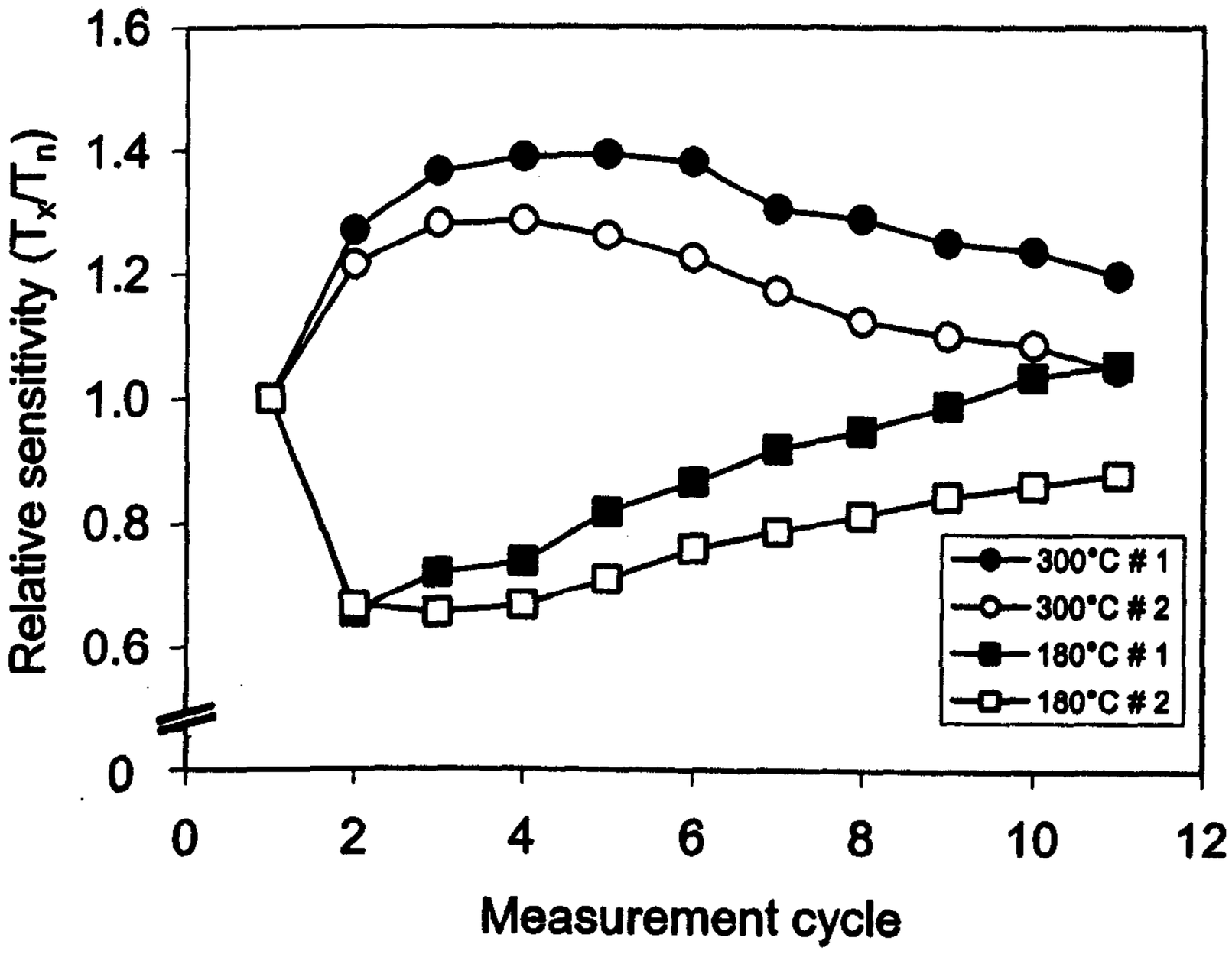

Figure 5.3. Inter aliquot variability in the size of sensitivity changes during a constant regeneration dose SAR sequence. These data are for aliquots of Aber/12-MAP3 using a 50 Gy regeneration dose.

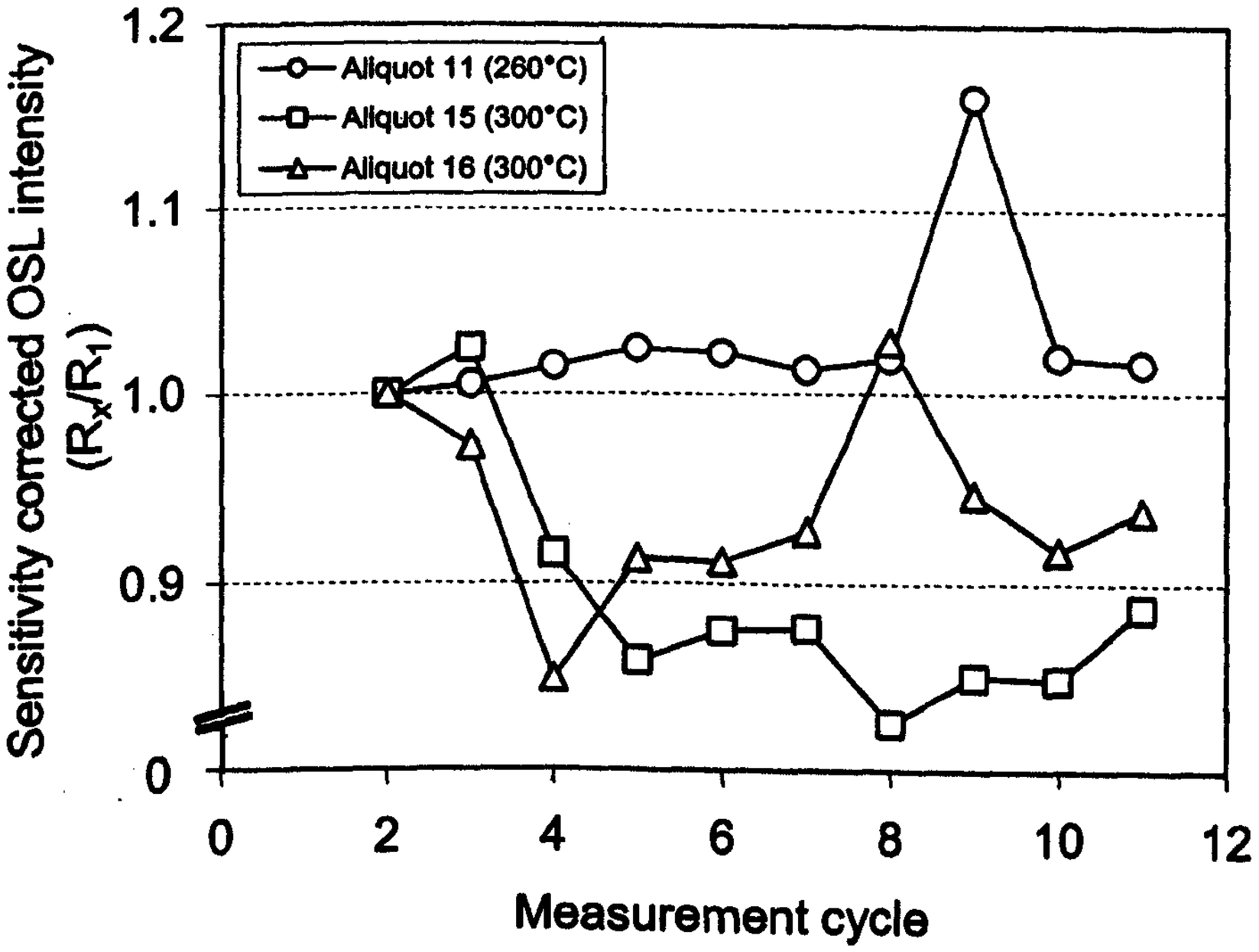

Figure 5.4. Sensitivity corrected luminescence intensities versus measurement cycle for the three aliquots of Aber/12-MAP3, which yielded > 10% recycling ratio errors. R_x values are normalised to unity at R_1, and were obtained using a repeated regeneration dose of 50 Gy.

both intrinsic OSL intensity (Duller *et al.*, 2000, Figure 1) and TL glow curve shape (Adamiec, 2000, Figure 1) are known to vary between grains of the same sample. Both of these indicate that electron trap and/or recombination centre concentration varies between quartz grains. It should be noted that in a study of single grains from a number of samples (Duller *et al.*, 2000) the largest range of intrinsic OSL intensities, and therefore charge trapping site concentrations, was observed for Aber/29-BA14[i].

5.3 SAR sensitivity correction

The fundamental assumption of the SAR protocol is that the OSL response to the test dose (T_x), after measurement of the proceeding regenerated OSL (L_x), gives a true representation of the luminescence sensitivity of the proceeding signal, or that the discrepancy between the sensitivity appropriate to each signal is constant with measurement cycle. This allows the sensitivity corrected luminescence intensity (R_x) to be calculated by dividing L_x by T_x. When the regeneration dose is constant over a number of measurement cycles, R_x should also be constant, irrespective of the sensitivity changes that occur.

R_x values have been calculated for each measurement cycle of the 10 and 50 Gy repeated regeneration dose datasets reported in Section 5.2. Data were normalized to unity at R_1 by dividing R_x by R_1, thereby producing a recycling ratio (Section 3.3) for each regeneration cycle. Of the 48 aliquots measured, 45 yielded acceptable recycling ratios for all measurement cycles (within 10% of unity, see Section 3.3), indicating that the SAR sensitivity correction procedure is appropriate for these aliquots. The majority of these aliquots show no systematic trend in recycling ratio with measurement cycle (but see Section 5.3.1).

Only three aliquots, yielded recycling ratios differing from unity by more than 10%. Recycling ratio versus regeneration cycle for these aliquots are shown in Figure 5.4. Murray and Wintle (2000) suggest 10% as the criterion for rejecting aliquots on the basis of recycling ratio (see Section 3.3). All three aliquots were from Aber/12-MAP3, using a

[i] Referred to in Duller *et al.* (2000) as BA14.

regeneration dose of 50 Gy. The data for aliquot 11 (circles) indicate generally good sensitivity correction, with a single aberrant point in cycle nine. This is caused by an abnormally high L_x value, but a similar increase in L_x intensity is not observed for other aliquots during this regeneration cycle. The decay curve appears normal, and is proportional to that for both the previous and next regeneration doses. Similar aberrant points have been observed using the Risø single-grain reader (Jacobs, pers. comm.). No explanation is given for this data point, however it does not appear to result from systematic failure of the SAR sensitivity correction procedure for this aliquot. Similarly aliquot 16 (triangles) only fails by one point, however this point occurs within a general trend of poor sensitivity correction. The data for aliquot 15 (squares) clearly represent a failure of the sensitivity correction procedure.

5.3.1 Preheat dependence of sensitivity correction

Mean recycling ratio data for each preheat temperature were plotted against measurement cycle to assess the impact of PH1 temperature on the ability of the SAR technique to correct for sensitivity changes (Figure 5.5). For the datasets derived using a 10 Gy regeneration dose (Figure 5.5 a and b), the correction appears to be good for most PH1 temperatures, yielding recycling ratios between 0.95 and 1.05. However, most PH1 temperatures yield recycling ratios differing from unity by more than 5% using a 50 Gy regeneration dose. This is still true of the data for the first 8 measurement cycles, after which the 10 Gy regeneration dose experiment finished, suggesting that it becomes more difficult to correct for sensitivity change using higher regeneration doses. In all three datasets, the sensitivity corrected data obtained using a 160°C PH1 shows a general downward drift. This would depress the growth curve relative to the natural, leading to an overestimate of the equivalent dose. However, using a standard SAR D_e estimation sequence on Aber/12-MAP3, the mean D_e for the 160°C PH1 aliquots is within 1 standard deviation of the sample mean (PH1 = 160-300°C). Similarly, D_e versus preheat diagrams for dated samples do not indicate that a 160°C PH1 leads to a significantly elevated D_e (Section 3.7) and the mean recycling ratio for all samples is consistent with 1 within error. Consequently, the poor sensitivity correction observed in Figure 5.5 using a

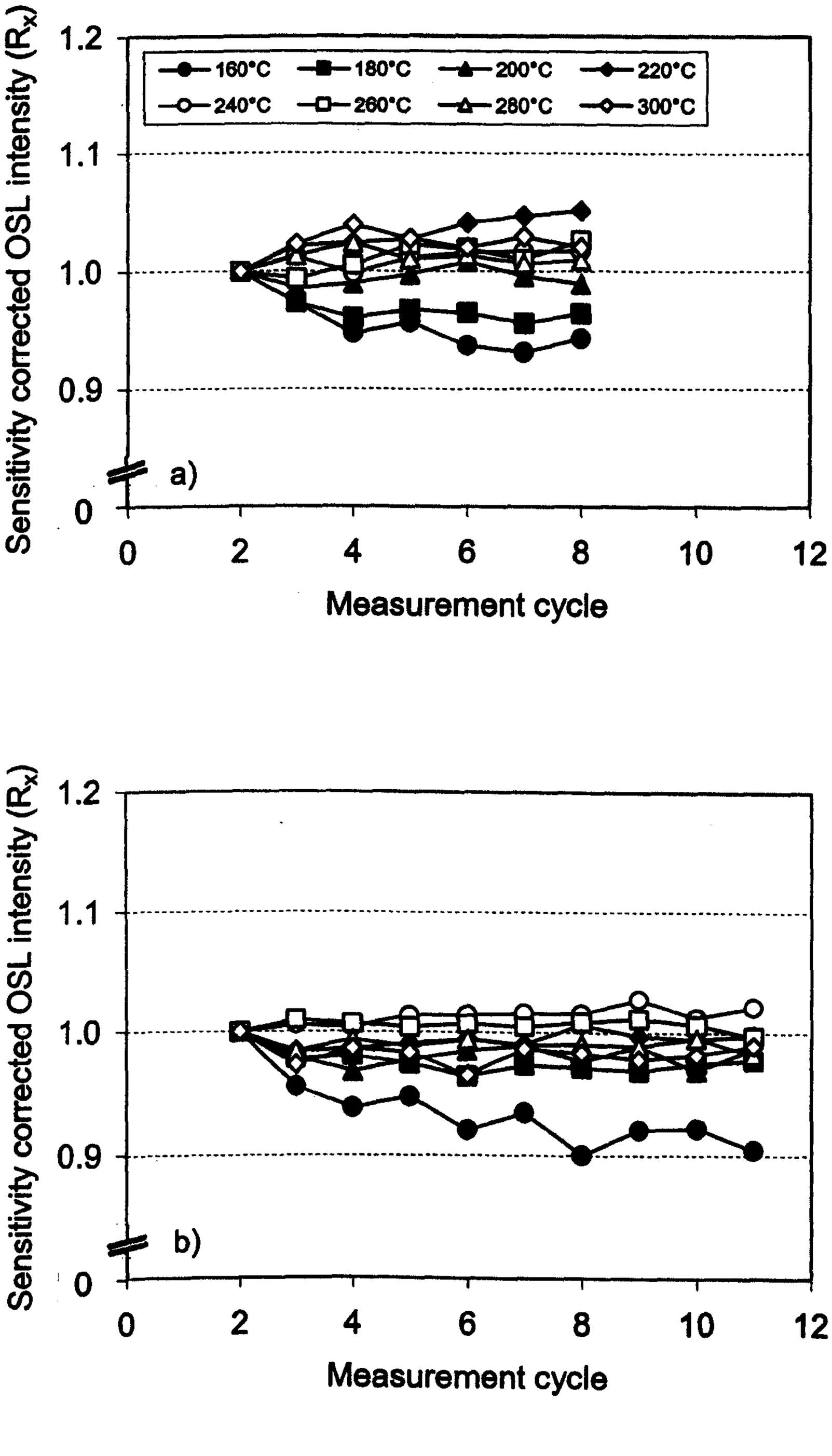

Figure 5.5. Caption overleaf.

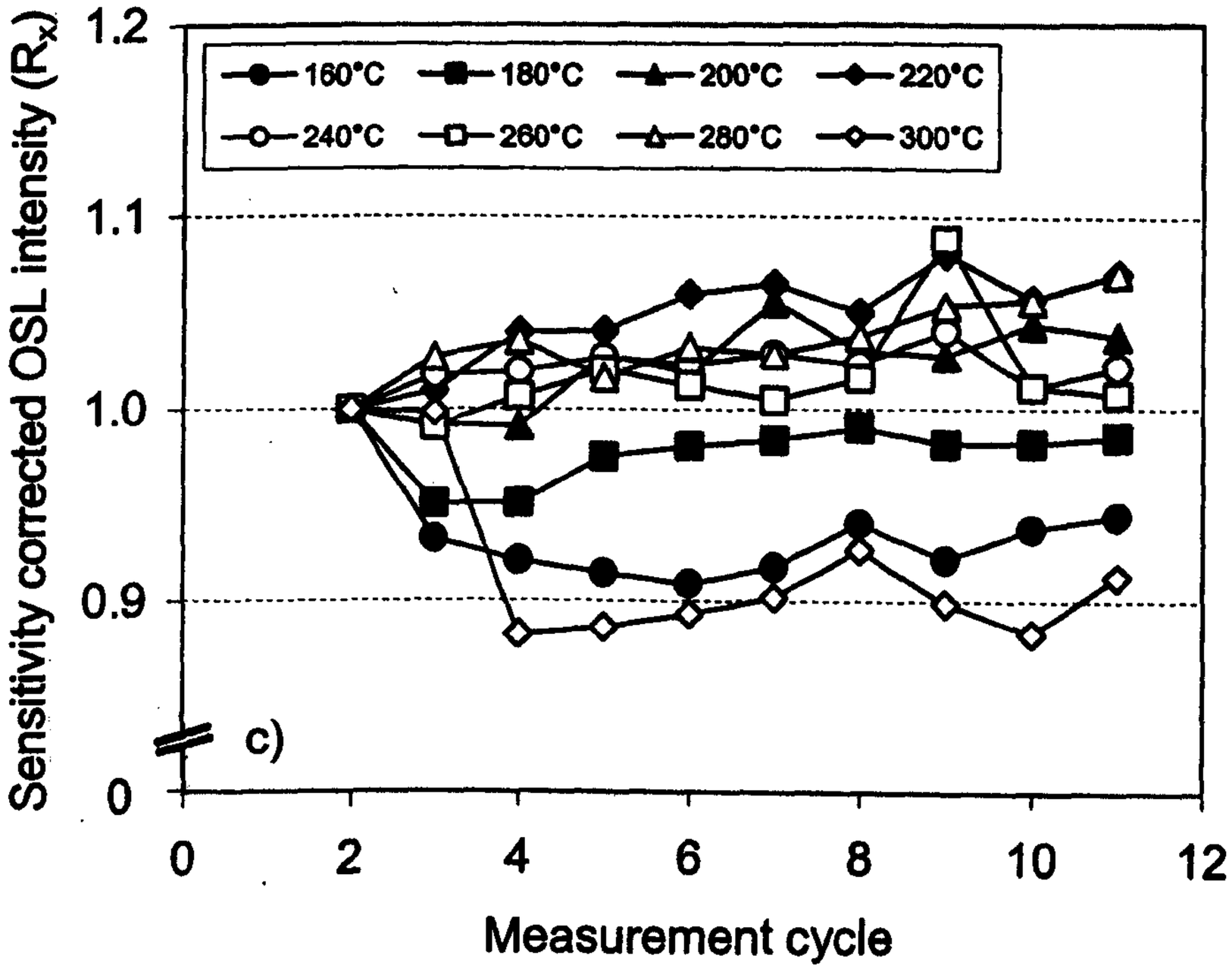

Figure 5.5. Sensitivity corrected OSL intensity versus measurement cycle for, a) Aber/12-MAP3 using a constant 10 Gy regeneration dose, b) Aber/29-BA14 using a constant 10 Gy regeneration dose and c) Aber/12-MAP3 using a constant 50 Gy regeneration dose. All point show the mean of two aliquots, normalised to R_1, which was measured during the second measurement cycle. The rapid decrease in sensitivity corrected OSL intensity between cycles 3 and 4, observed using a 300°C preheat, is present in both aliquots (Figure 5.4). This decline is due to decreases in L_x intensity, and is not observed in T_x measurements (Figure 5.2.b).

160°C PH1 may not be a general phenomenon. Alternatively, the effect may be constant, but the impact on D_e and recycling ratio is within errors.

Poor sensitivity correction using a 300°C PH1 (also shown in Figure 5.4) is only observed for the 50 Gy regeneration dose data. Like that for 160°C, this does not appear to affect the D_e measured during the dating run performed on this sample. However, this PH1 temperature yields by far the largest proportion of recycling ratio failures during routine dating sequences (Section 3.3).

5.3.2 R_x reproducibility derived from repeated regeneration dose data

When using a constant regeneration dose, the observed variation in R_x values is caused by poor sensitivity correction and instrument error. Monotonic changes in sensitivity have been modelled by Bailey (2000b) using Equation 5.1,

$$F_x = a + b * \exp(-x/d) \qquad (5.1)$$

where a, b and d are fitting constants and x is the regeneration cycle number. This function allows both linear and non-linear relationships to be fitted. The R_x data for each aliquot, measured using a 10 Gy regeneration dose, was fitted using Equation 5.1. R_x reproducibility was then assessed by measuring the scatter of these data around the best fit line (Truscott *et al.*, 2000). Curve fitting for two aliquots is shown in Figure 5.6. The scatter was expressed as a percentage of R_1, and yielded a mean value of 0.98 ± 0.31%[j]. The reproducibility for each sample is identical within errors. Both of these datasets were produced using Risø 3. Similar analysis of the dataset presented by Armitage *et al*, (2000), which was produced using Risø 1, yields reproducibility of 1.18 ± 0.47%. This value is indistinguishable from that for Risø 3, despite the significant differences in age and specification of the readers (see Table 2.3).

R_x variability against PH1 temperature is shown in Figure 5.7. The values for each individual PH1 temperature are indistinguishable from the mean value quoted above, and

[j] Mean standard deviation ± standard deviation of individual aliquot standard deviation estimates.

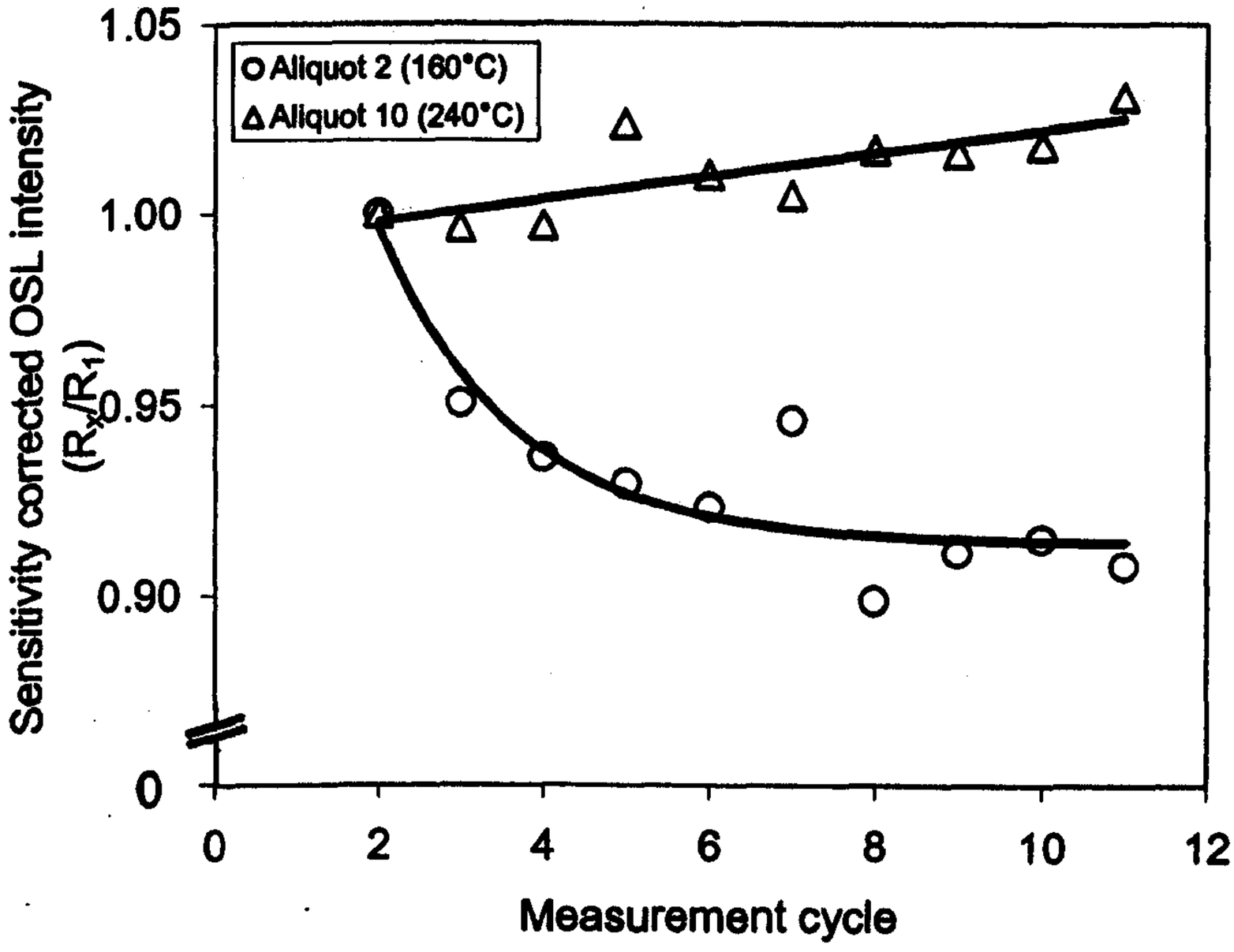

Figure 5.6. Sensitivity corrected OSL intensity versus measurement cycle for two aliquots of Aber/29-BA14. All R_x values are normalised to unity at R_1, and were obtained using a regeneration dose of 10 Gy. Each dataset has been fitted to Equation 5.1.

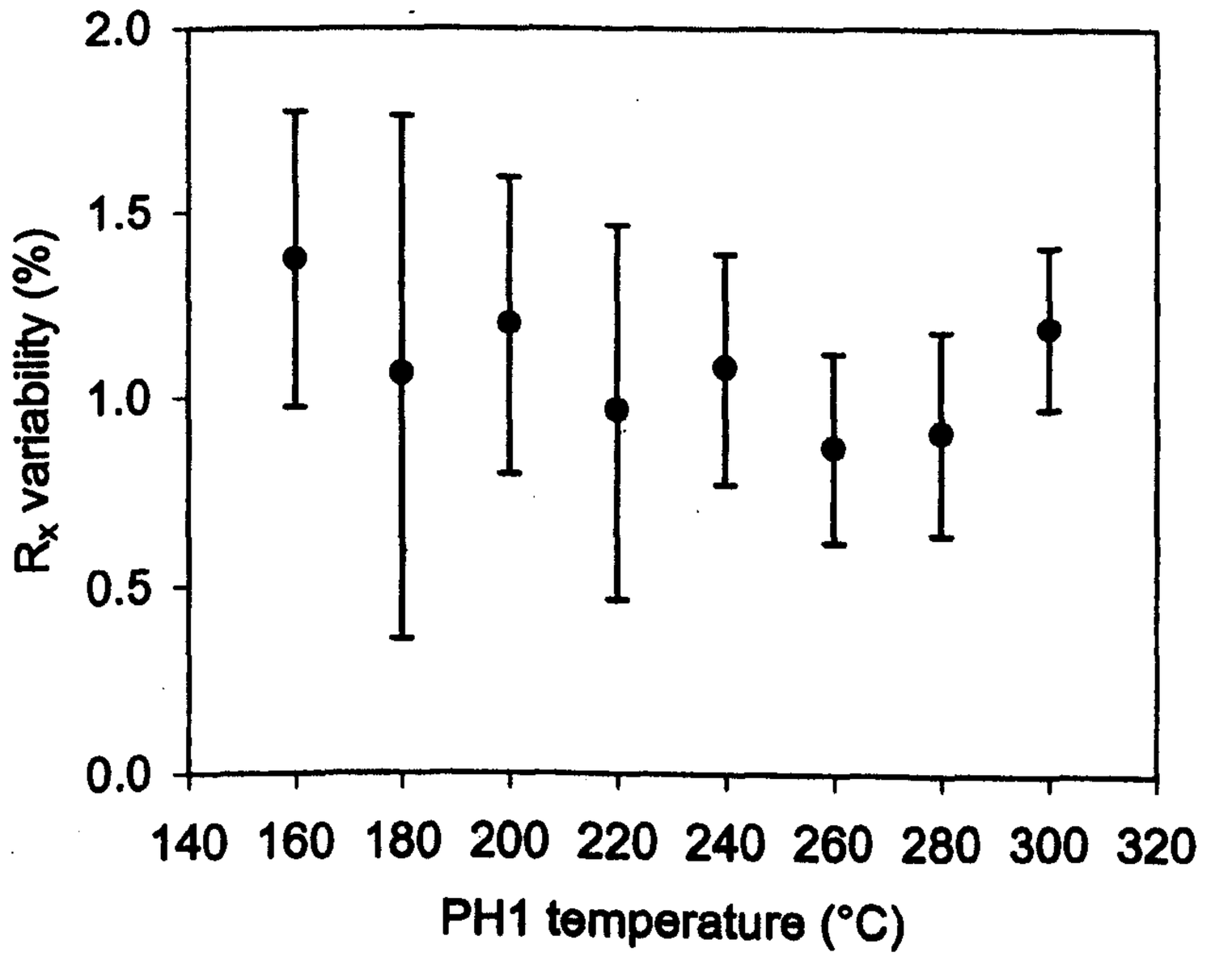

Figure 5.7. R_x variability versus PH1 temperature. R_x variability is the standard deviation of R_x values for an individual aliquot expressed as a percentage of R_1. Each point is the mean of 8 aliquots, with one standard deviation errors.

from the mean using PH1 temperatures from 160-260°C. This indicates that the poor recycling ratios observed using 280 and 300°C PH1 temperatures cannot be explained by fluctuations in preheat time (and therefore signal depletion) caused by variable processor usage (see Section 3.3). The mean reproducibility for the two readers is 1.08 ± 0.41 (n=64) and so a relatively conservative systematic error of 1.5% has been used for all single-aliquot D_e calculations (performed using Analyst v.2.24).

5.4 Sensitivity changes observed during D_e measurement sequences

Although a repeated regeneration dose can be used to measure an equivalent dose (e.g. Murray and Roberts, 1998), most sequences are designed such that the regeneration points bracket the natural, allowing the equivalent dose to be calculated by interpolation. Consequently, dose dependency would complicate the patterns of sensitivity change observed during the constant regeneration dose experiments above. Relative sensitivity (T_x/T_1) versus measurement cycle plots for the samples from Inhaca Island have been studied. Six of these plots have been selected, on the basis of sample age and sensitivity change characteristics, and are shown in Figure 5.8.

The general patterns observed in Section 5.2.1 are also seen in Figure 5.8. Notable amongst these is the general decrease in sensitivity at low PH1 temperatures, and increase at higher temperatures. Sensitivity change in the younger samples (Figures 5.8 a-c) does not appear to reach completion during the measurement sequence, while in the older samples (Figure 5.8 e and f), the T_x/T_n value becomes stable. Since older samples require larger regeneration doses, this phenomenon is similar to the dose dependent rate of sensitivity change observed in Section 5.2.1. For the oldest sample (Aber/28-IN11, Figure 5.8.f), the initial sensitivity decrease seen when using low PH1 temperatures (160-220°C), is followed by an increase in sensitivity. This behaviour is very similar to that observed for Aber/12-MAP3 using a 50 Gy regeneration dose, suggesting that the subsequent increase in sensitivity is dose dependent. The decrease in sensitivity observed for the 300°C preheat in Section 5.2.1 is only seen in the data for Aber/28-IN12, the

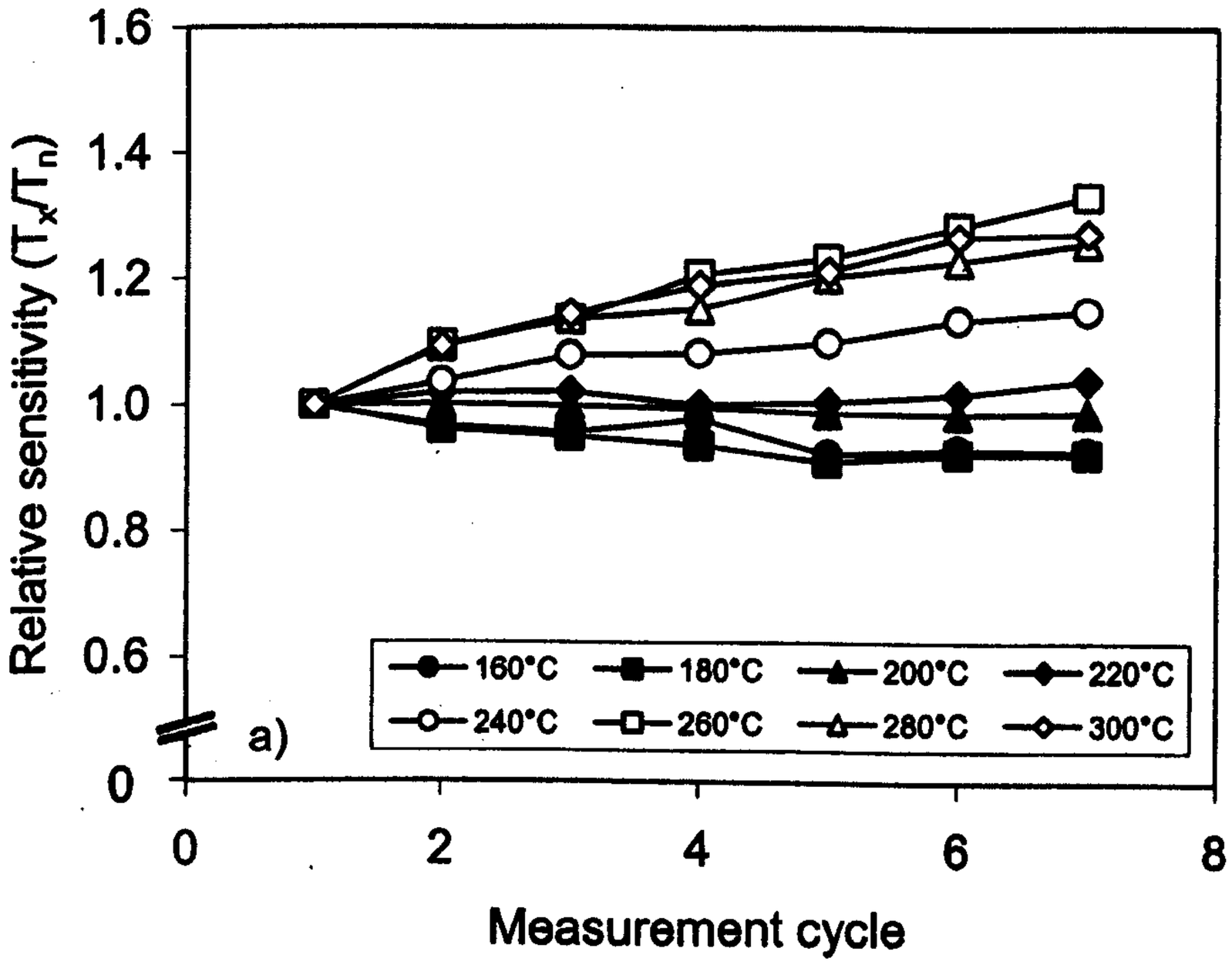

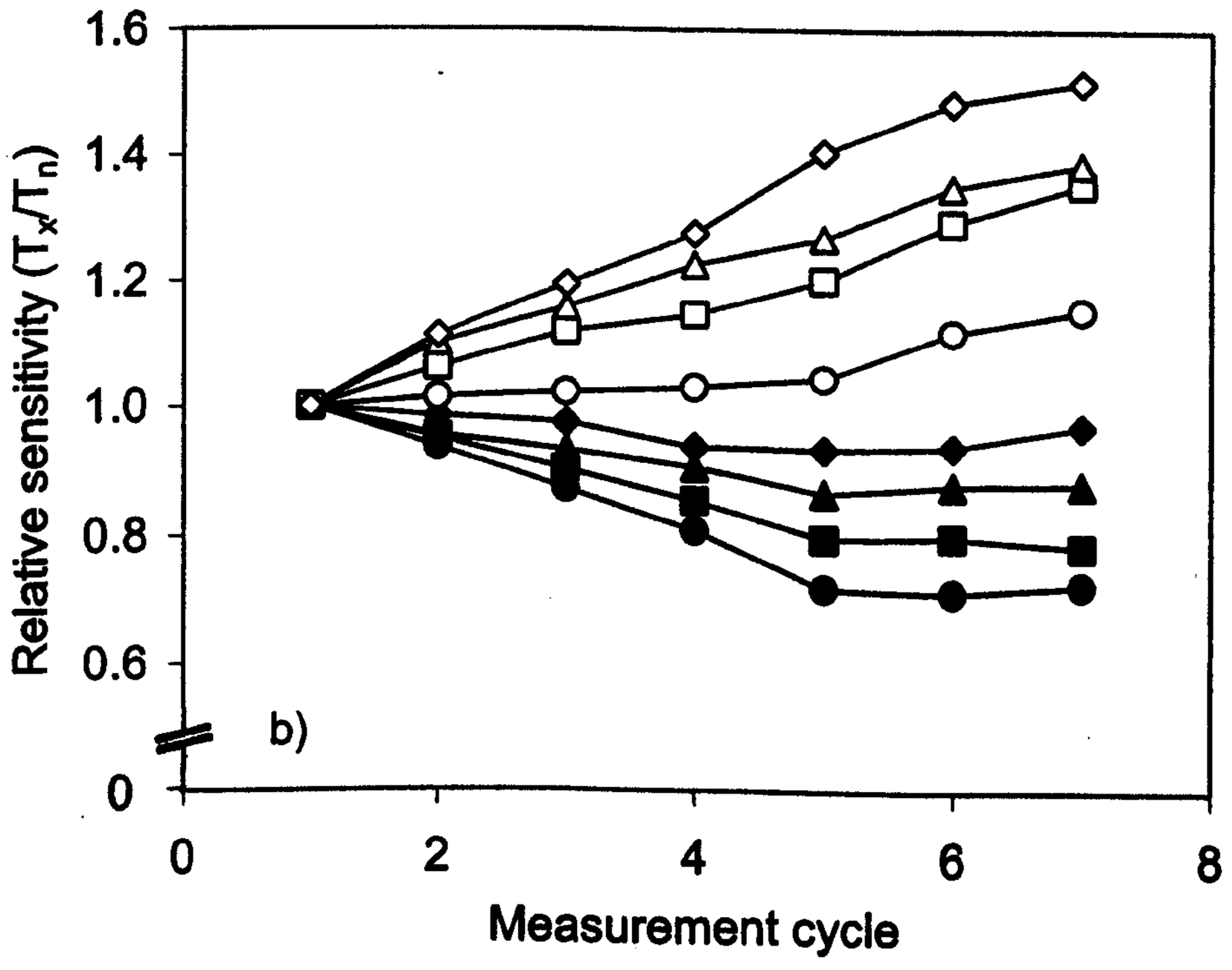

Figure 5.8. Relative sensitivity versus measurement cycle for routine SAR measurement sequences. a) Aber/28-IN22 (modern) and b) Aber/28-IN19 (2.48 ka).

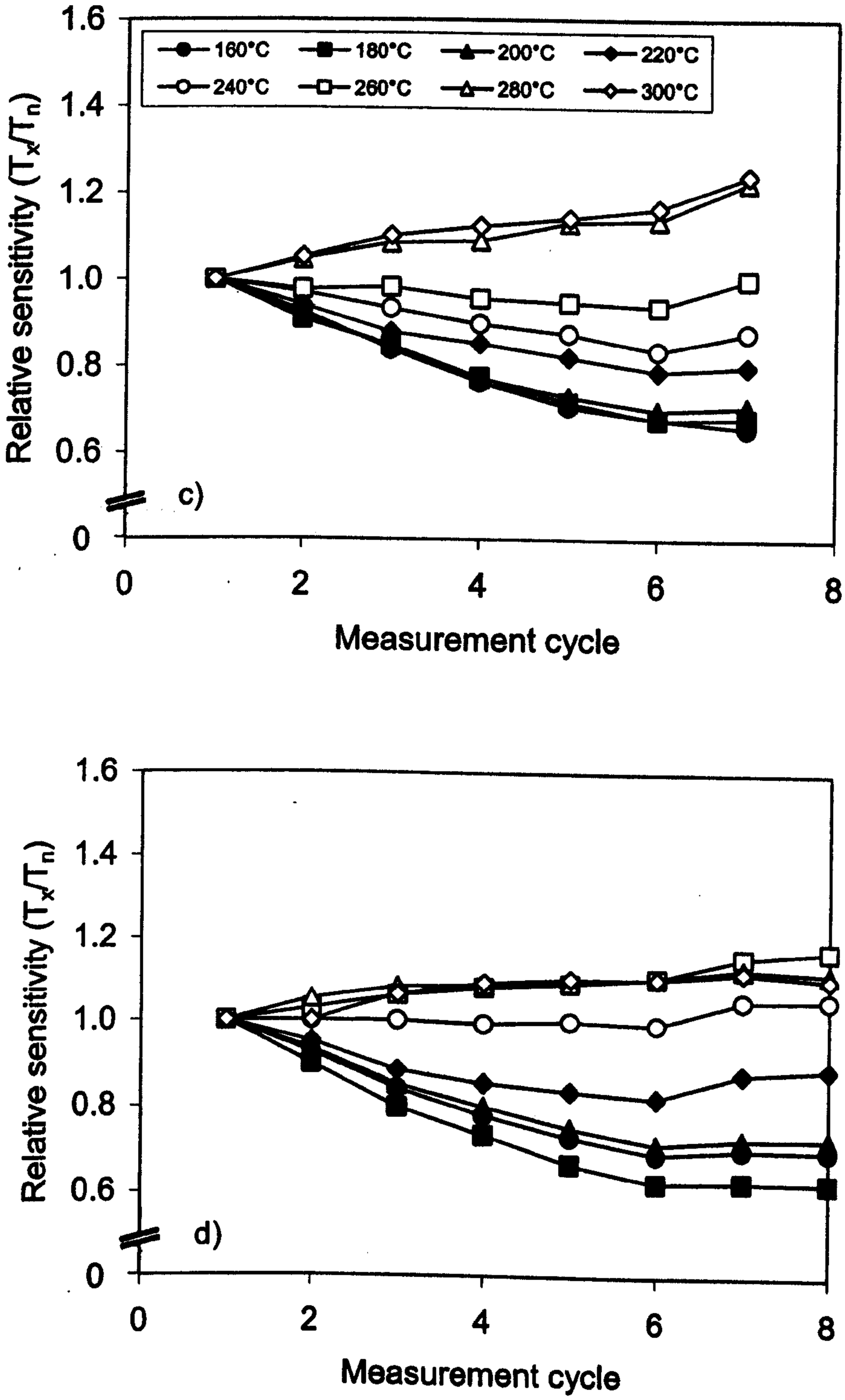

Figure 5.8. Relative sensitivity versus measurement cycle for routine SAR measurement sequences.
c) Aber/28-IN16 (2.16 ka) and Aber/28-IN15 (6.09 ka).

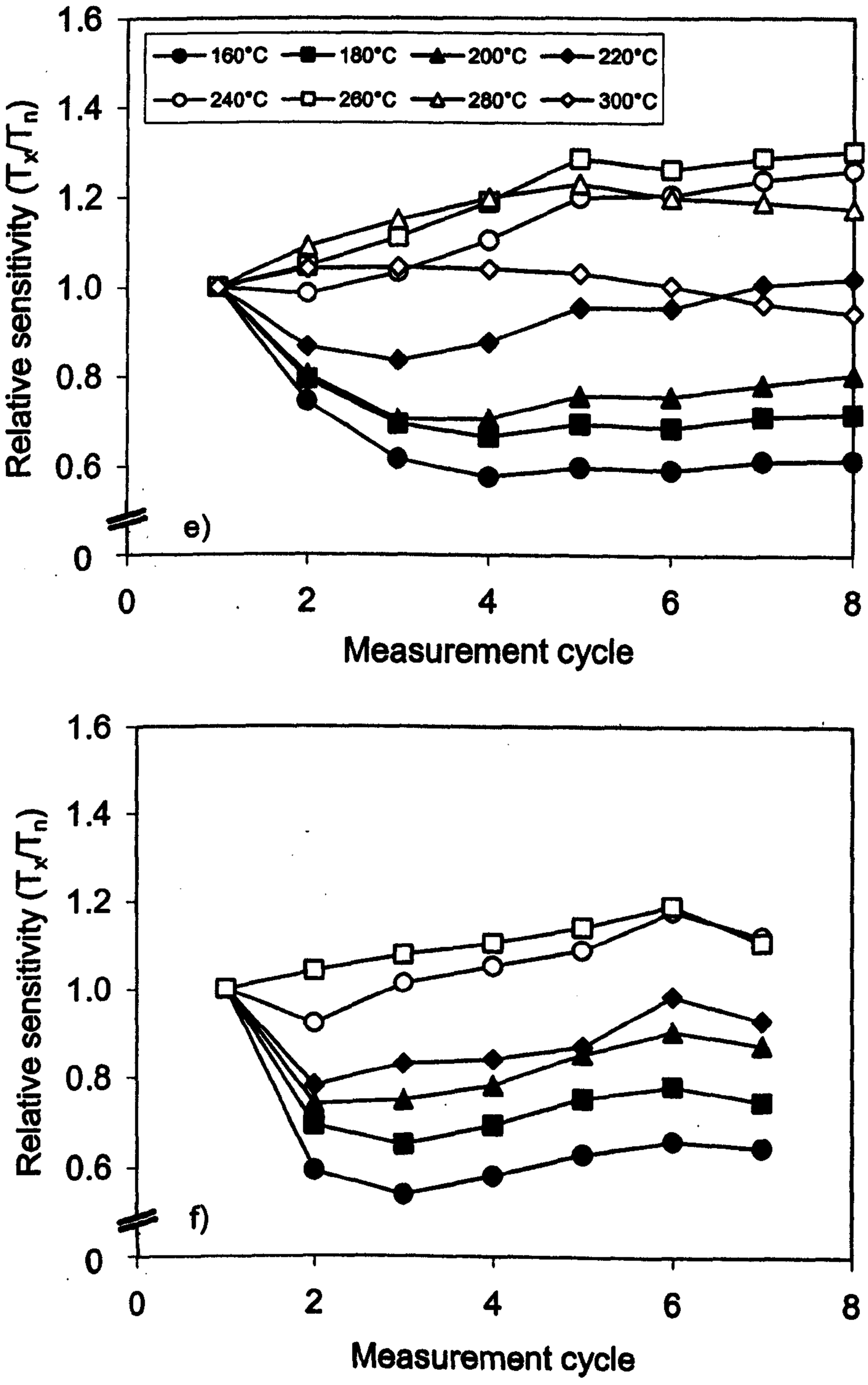

Figure 5.8. Relative sensitivity versus measurement cycle for routine SAR measurement sequences. e) Aber/28-IN12 (22.5 ka) and f) Aber/28-IN11 (102 ka). PH1 temperatures are shown in the legend. Each dataset represents the mean of three aliquots, with the exception of that for Aber/28-IN11, where four aliquots were measured at each preheat temperature.

second oldest sample. Since a restricted range of PH1 temperatures were used for Aber/28-IN11[k], this may indicate that the phenomenon is dose dependent.

Interestingly, the sensitivity changes in these samples appear to be age dependent, as suggested in Section 5.2.2. The youngest sample (Aber/28-IN22, Figure 5.8.a) shows a small <10% decrease in sensitivity at low (160-220°C) PH1 temperatures, and up to 40% increases at higher temperatures. The opposite is true of the oldest sample (Aber/28-IN11, Figure 5.8.f) which shows large (up to 50%) decreases in sensitivity at low PH1 temperatures, and small increases at higher temperatures. Between these ages the sensitivity versus measurement cycle plots are transitional. By 6ka after burial (Aber/28-IN15, Figure 5.8.d), the behaviour of samples more closely resembles Aber/28-IN11 than Aber/28-IN22. This age dependence in the pattern of sensitivity change can be explained as follows. On burial, a sample (e.g. Aber/28-IN22) has relatively few activated recombination centres, since a large number are deactivated as the sample is bleached. Using high PH1 temperatures, thermal activation transfers holes from R-centres to L-centres, causing sensitivity to increase. However, since the regeneration doses required to bracket N are very small for this modern sample, the cumulative dose is also very small (c.11 Gy). Consequently, dose quenching at low PH1 temperatures is small. As D_e increases, so does the cumulative dose required during a measurement sequence, leading to significant dose quenching at low PH1 temperatures (e.g. Aber/28-IN19). Over longer burial periods, holes trapped at R-centres are transferred to L-centres via ambient temperature thermal activation. At a given dose rate and temperature, the number of activated R-centres will reach an equilibrium value. However, the activated L:R-centre ratio continues to rise. Consequently, the size of sensitivity increase which can be caused by thermal activation during PH1, decreases with sample age.

---

[k] 160-260°C in 20°C steps, using four aliquots at each preheat temperature. Since the range of D_e values obtained for samples of this age is large, higher PH1 temperatures were not used to avoid the necessity of rejecting aliquots on the basis of recycling ratio (see Section 3.4).

5.5 Monitoring sensitivity changes using the 110°C TL peak

The SAR technique (Murray and Wintle, 2000) uses the OSL response to a constant test dose to correct for sensitivity changes. For protocols in which the full OSL decay curve is measured, this sensitivity correction is rapid, intuitively sound and generally effective (see Section 5.3). However, it cannot be applied to material containing charge in the trap(s) responsible for the OSL signal, e.g. in the single-aliquot additive-dose (SAAD) procedure (Murray *et al.*, 1997). For the same reason, it is impossible to investigate the exact timing of sensitivity changes within an OSL decay curve, or as a result of preheating, using the OSL signal. A more flexible sensitivity monitoring technique, which can be applied when the OSL traps contain charge, is required to investigate several phenomena reported in the literature. For example, Stokes *et al.* (2000) found the SAAD procedure to be unsuitable for 64% of the 62 samples they investigated, concluding that sensitivity change was partly to blame. In addition, Armitage *et al.* (2000, Figure 5) reported an SAR dataset where the natural luminescence intensity was greater than the saturation level of the growth curve. This may be due to inappropriate sensitivity correction of the natural or regenerated luminescence signals.

Several authors have proposed the use of the 110°C TL peak to monitor OSL sensitivity changes (e.g. Aitken and Smith, 1988), since it can be used when the OSL trap contains charge. This approach, based on the observed relationship between the two signals, formed the basis of an earlier version of the SAR technique (Murray and Roberts, 1998). However, it should be noted that Stokes (1994a) suggested that OSL and 110°C TL sensitivity changes occurred at different stages during multiple aliquot dating procedures. Also, Murray and Mejdahl (1999) found that the 110°C TL signal was not always proportional to the regenerated OSL signal. Despite this, the potential flexibility of the 110°C TL peak as an OSL sensitivity monitor, warrants further investigation.

Three factors may affect the use of the 110°C TL peak as a sensitivity monitor.

1) The thermal stability of the signal. Since the lifetime of electrons in the 110°C TL trap at room temperature (c.20°C) is relatively short, the decay of the 110°C TL signal between irradiation and measurement may be significant. In an automated

reader such as that used in this study, the time between irradiation and measurement ought to be consistent, provided that a fixed sequence is used; hence changes in the TL signal ought to reflect sensitivity changes, even though partial decay of the 110°C TL peak may have occurred. Where laboratory temperature fluctuates during a measurement sequence however, the 110°C TL signal may not accurately monitor sensitivity changes.

2) The non-linear growth of the 110°C TL peak with increasing dose.
3) The proportionality of the TL to the regenerated OSL signal. Several authors have observed that the regenerated OSL and 110°C TL signals are not always proportional (e.g. Stokes, 1994a and Murray and Mejdahl, 1999). However, no attempt has previously been made to study the relationship between this lack of proportionality and PH1 temperature.

Sections 5.6 to 5.8 present experiments designed to investigate each of these aspects of the use of the 110°C TL peak as a sensitivity monitor in SAR measurement sequences.

5.6 Thermal stability of the 110°C TL signal

The thermal trap depth of the 110°C TL peak was determined using an isothermal decay method, and Hoogenstraaten's method. The isothermal decay method was chosen since it produces a meaningful trap depth (E), even when thermal quenching of the associated luminescence centre occurs (Wintle, 1975). In contrast, the initial rise method will be affected by thermal quenching, causing the value of the trap depth to be underestimated by an amount equal to the thermal activation energy of the quenching process, provided that only luminescence from those centres is being detected. By observing the light sums from isothermal OSL decay curves over a range of temperatures, Spooner (1994) has shown that thermal quenching of some luminescence centres can occur at temperatures as low as 30°C (Section 1.5.1, Figure 1.5). Since the 110°C TL signal probably uses the same L-centre as the OSL trap (Section 1.6.1.1), the use of a technique not affected by thermal quenching was therefore imperative. The isothermal decay method is appropriate for measurements on a single trap obeying first order kinetics.

The other method that has been used to study this peak is Hoogenstraaten's method, in which the movement of the TL peak temperature with changing heating rate is investigated. This method was used by Wintle (1975); however it yielded greater uncertainty in the trap depth energy than other methods, since it is difficult to pinpoint the peak position. This method is appropriate for a single trap obeying first order kinetics, and is only slightly affected by thermal quenching. A small error may arise if the peak emission wavelength moves out of the detection window as the temperature is raised (Franklin *et al.*, 1995). The isothermal decay method is not affected by this emission wavelength shift since each measurement is self-contained, and made at a single temperature. Measurement sequences for both trap depth determination methods are shown in Table 5.1.

Step	Isothermal decay	Hoogenstraaten's method
1	TL (400°C @ 5°C/s, Ar flow)	TL (400°C @ 5°C/s, Ar flow)
2	c. 5Gy β irradiation	c. 20 Gy β irradiation
3	100s isothermal TL @ 55°C (10s pause at temperature)	Measure "110°C" peak (100°C @ 0.05°C/s, Ar flow)
4	TL (400°C @ 5°C/s, Ar flow)	Measure incandescence (100°C @ 0.05°C/s, Ar flow)
5	Repeat steps 2-4 using isothermal TL temperatures of 60, 65, 70, 75°C	Repeat steps 1-4 using heating rates of 0.07, 0.1, 0.2, 0.3, 0.4, 0.5, 0.75, 1.0 and 2.0°C/s

Table 5.1. Measurement sequences for the two trap depth determination methods used in this study.

For both methods, the aliquots were heated to 400°C at the beginning of each measurement cycle to remove any charge remaining in the 110°C trap on completion of the TL measurement. A 10 second pause before measurement of the isothermal TL was incorporated into step 3 to ensure that the sample reached measurement temperature. For this range of measurement temperatures, no sensitization of luminescence response is expected (Wintle and Murray, 1999).

5.6.1 Calculations

A trap depth (E) and frequency factor (s) was calculated for each aliquot. For the isothermal decay method, this was achieved by plotting $\ln(I/I_0)$ against t where I is the intensity of the thermoluminescence, t is the time the sample is held at the elevated

temperature and I_o is the TL intensity at t=0 (Figure 5.9). This yields a straight line whose slope m is s exp(-E/kT), where k is Boltzmann's constant and T is the temperature in Kelvin. A plot of ln(m) versus $1/T$ yields a straight line of slope E/k and intercept ln(s) from which E and s can be calculated (Figure 5.10).

Using Hoogenstraaten's method, trap depths were calculated by plotting ln(T_m^2/β) against $1/T_m$, yielding a straight line of slope E/k, where T_m is the peak temperature and β is the heating rate (Figure 5.11). s was then calculated from the intercept ln(ks/E). Kinetic parameters derived using these two methods are given in Table 5.2.

Sample (Aber/)	Method (no. of aliquots)	E *(eV)*	s *(s^{-1})*
12-MAP3	Isothermal decay (3)	0.907 ± 0.004	$8.48 \pm 2.39 \times 10^{11}$
12-MAP3	Hoogenstraaten's (8)	0.871 ± 0.031	$3.42 \pm 4.64 \times 10^{11}$
28-IN22	Isothermal decay (6)	0.915 ± 0.005	$1.13 \pm 0.21 \times 10^{12}$
29-BA14	Isothermal decay (6)	0.913 ± 0.004	$1.34 \pm 0.39 \times 10^{12}$
29-BA14	Hoogenstraaten's (6)	0.877 ± 0.026	$5.49 \pm 4.01 \times 10^{11}$
Mean	Isothermal decay (15)	0.912 ± 0.006	$1.16 \pm 0.34 \times 10^{12}$
Mean	Hoogenstraaten's (14)	0.874 ± 0.028	$4.30 \pm 4.35 \times 10^{11}$

Table 5.2. Kinetic parameters for the 110°C TL peak trap, calculated using the isothermal decay and Hoogenstraaten's methods.

The trap depth values calculated from the isothermal decay data are identical within errors (1 standard deviation), and hence the mean value of 0.912 ± 0.006 eV is assumed to apply to all three samples. This figure is an order of magnitude more precise than previously reported values. The mean frequency factor calculated using this method is $1.16 \pm 0.34 \times 10^{12}$ s^{-1}. It is worth noting that the negligible errors reported above, for a temperature critical process, indicate that the temperature reached by the Risø reader heater plate is highly reproducible. Mean values for E and s produced using Hoogenstraaten's method are 0.874 ± 0.028 eV and $4.30 \pm 4.35 \times 10^{11}$ s^{-1}. Both values are considerably less precise than those produced using the isothermal decay method, possibly due to inaccurate peak position evaluation (Wintle, 1975).

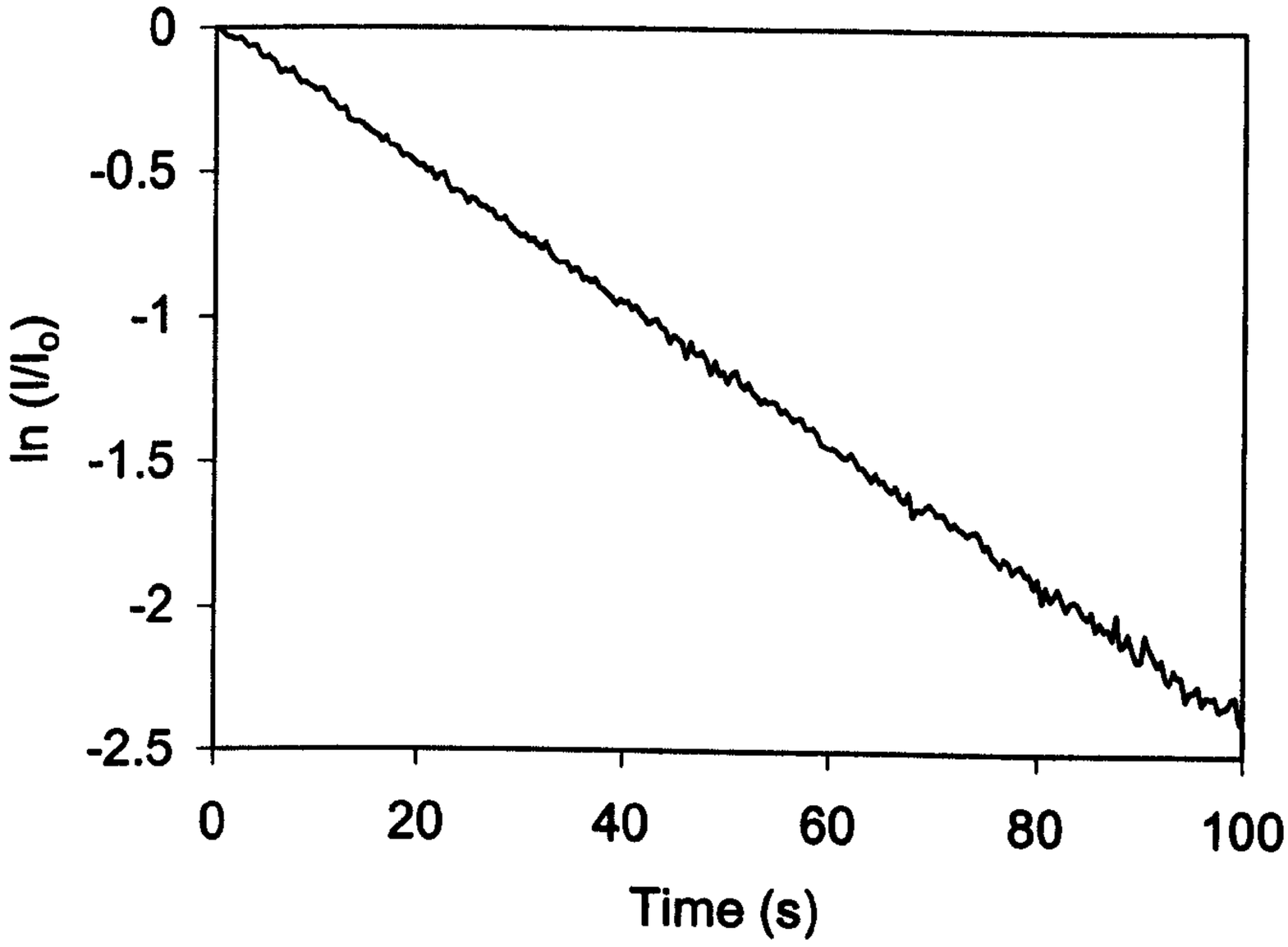

Figure 5.9. ln (I/I_0) versus time for an aliquot of Aber/29-BA14 held at 60°C.

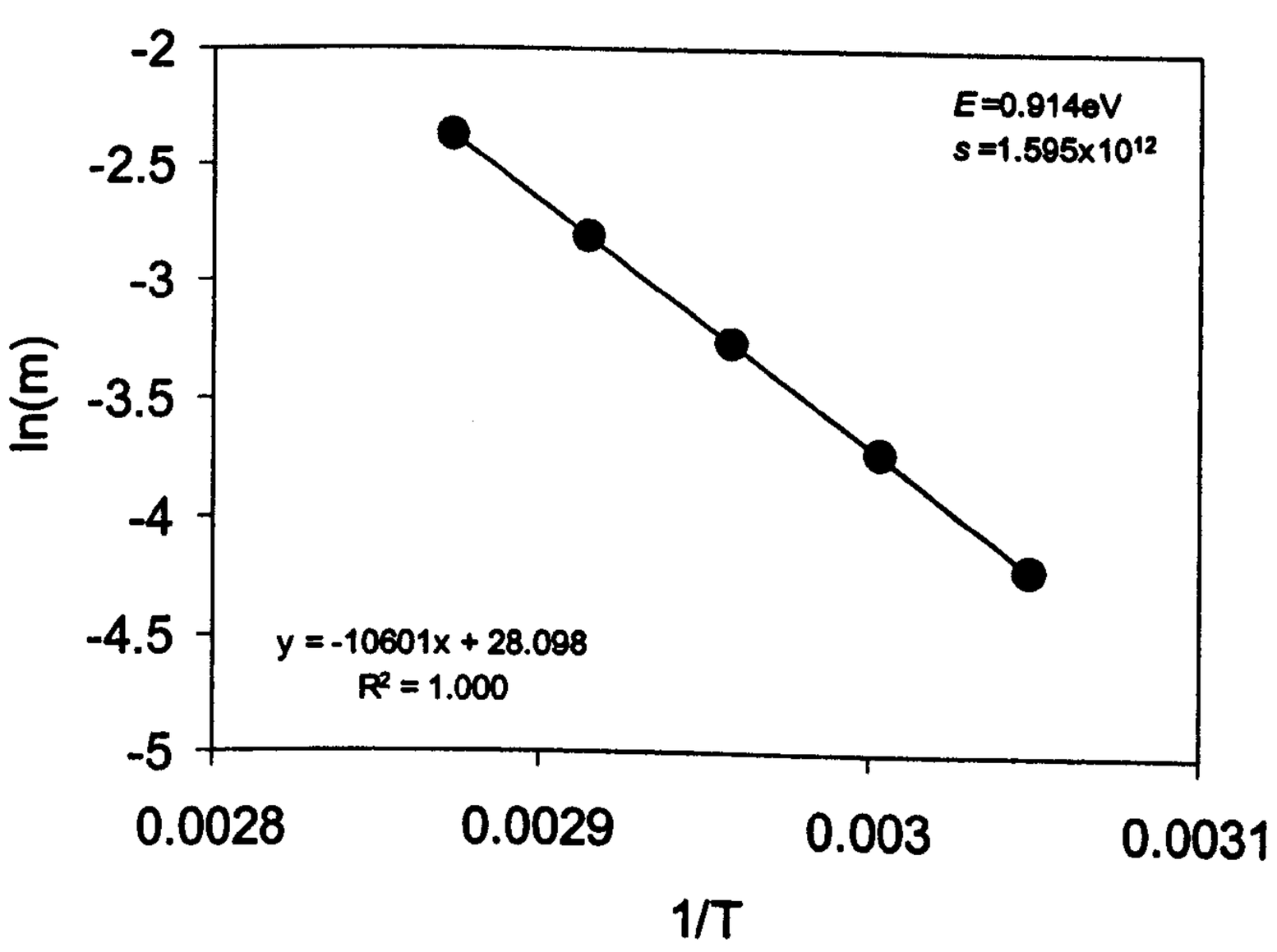

Figure 5.10. ln (m) versus $1/T$ for an aliquot of Aber/29-BA14, for which E and s have been calculated. Data were obtained for 55, 60, 65, 70 and 75°C.

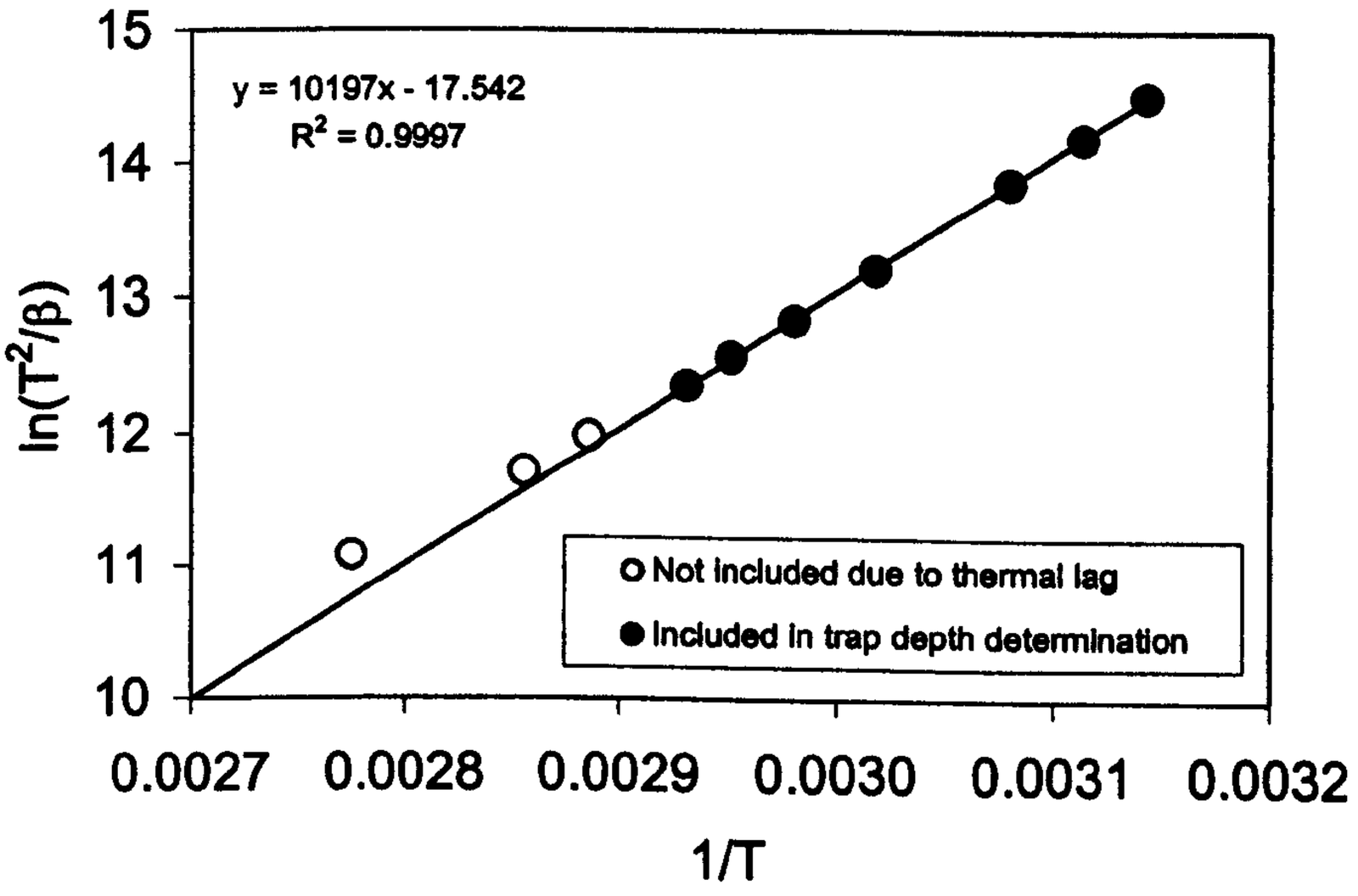

Figure 5.11. ln (T_m^2/β) versus $1/T_m$ for an aliquot of Aber/29-BA14, from which E and s have been calculated. Instrumental and incandescence backgrounds were subtracted prior to calculation of kinetic parameters. Results from heating rates of 2, 1, and 0.75 °C/s are not included in the analysis due to the effects of thermal lag. The measurement sequence used was given in Table 5.1.

5.6.2 Discussion

Although trap depths for the 110°C TL trap reported by Aitken (1985) vary considerably, with values ranging from 0.80 to 0.99 eV, the results presented above fall within this range. More recently, Spooner and Questiaux (2000) have reported trap depths, produced using Hoogenstraaten's method, of 0.90 eV for the red, 0.91 eV for the blue and 0.89 eV for the UV emissions from this peak. These values are in good agreement with those presented here, which was obtained using the UV emission. All subsequent calculations reported in this section use the mean kinetic parameters derived from the isothermal decay data, which is considered to be more accurate, as well as being more precise.

Published frequency factors also vary considerably, and both mean values reported in Table 5.2 are consistent with previous calculations. The wide range of reported values of E and s for the 110°C TL peak noted above may partly be explained by the studies carried out on synthetic quartz by Petrov and Bailiff (1995). For their sample, they suggested that the 110°C peak was composed of several peaks whose relative intensities were strongly dependent on irradiation temperature, with the significance of the lower peaks increasing as irradiation temperature decrease below room temperature. These peaks could affect the kinetic parameters determined for the 110°C TL peak, particularly when using the initial rise method. However, the aliquots used in this study were irradiated at room temperature, and consequently the lower temperature peaks should be absent.

5.6.3 110°C TL peak order

The isothermal decay and Hoogenstraaten's methods are only applicable to single traps obeying first order kinetics. The exponential time dependence of isothermal decay has been advocated by Aitken (1985, p273) as a test for first order kinetics. All the isothermal decay curves measured in this study were exponential, as illustrated in Figure 5.9. A further test, advocated by Chen and Kristianpoller (1986), involves plotting an isothermal decay curve on It versus ln$t$ coordinates. This produces a peak shaped curve, resembling a TL glow peak with the same order of kinetics (Figure 5.12). A symmetry factor for this peak is then calculated, from which the kinetic order can be obtained. In this study, symmetry factors were produced for the 70 and 75°C isothermal decay curves of each

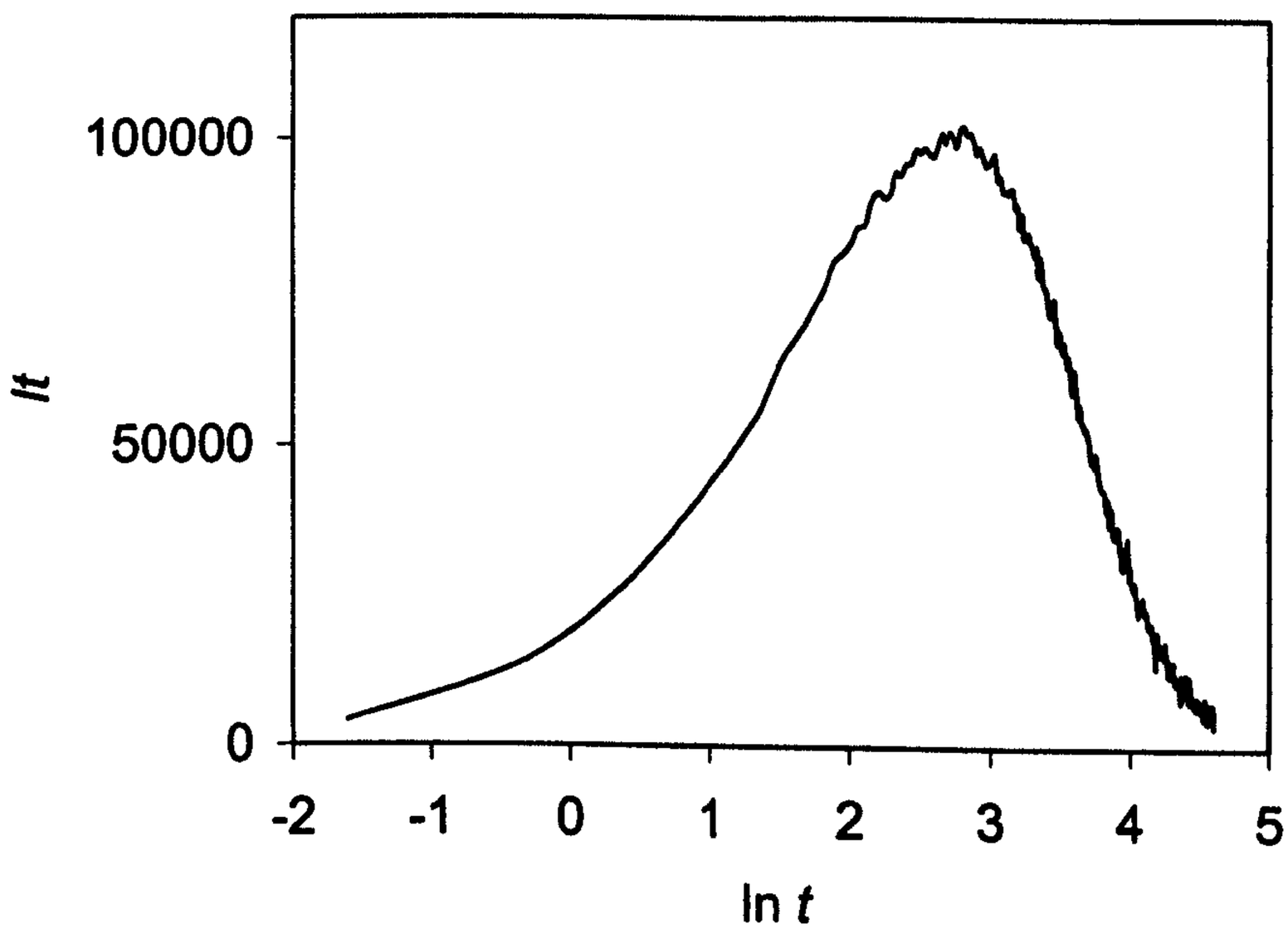

Figure 5.12. An isothermal decay curve plotted on *It* versus ln*t* coordinates. This curve was measured from an aliquot of Aber/28-IN22 held at 75°C for 100 seconds.

aliquot[1]. The mean calculated symmetry factor is 0.41 ± 0.03, identical within errors to the value expected for first order kinetics (0.40, Chen and Kristianpoller, 1986). Peaks obeying second order kinetics yield a symmetry factor of 0.50 using this method. From these data, it is concluded that the trap responsible for the 110°C TL peak in these samples does obey first order kinetics. Consequently, both isothermal decay and Hoogenstraaten's methods should yield meaningful kinetic parameters.

5.6.4 Erosion of the 110°C TL signal at laboratory temperatures

Using the relationship shown in Equation 5.2,

$$\tau = s^{-1} \exp(E/kT) \qquad (5.2)$$

electron lifetimes (τ) at a range of temperatures have been calculated using the mean trap depth and frequency factors obtained from the isothermal decay data (Table 5.2). The calculated lifetimes are given in Table 5.3.

T (°C)	τ (s)	τ (min)
10	14808	251.6
20	4134	70.0
25	2256	38.2
30	1256	21.2
40	412	6.9
50	145	2.4
60	54	0.90
70	21	0.37
80	8.9	0.15
90	3.9	0.07
100	1.8	0.03

Table 5.3. Electron lifetimes in the trap responsible for the 110°C TL peak at various storage temperatures.

[1] Using lower storage temperatures, insufficient signal decay occurred during the measurement period for this analysis to be undertaken.

To check that the values calculated using this method are valid, the isothermal decay signal at 25°C, from an aliquot of Aber/29-BA14, was measured. The electron lifetime obtained from this curve was 2068 seconds, in good agreement with the calculated value given in Table 5.3. The mean trap depths and frequency factors calculated above can also be used to predict loss of signal from the 110°C TL peak. Percentage signal losses for a range of storage times at room temperature (20°C) are presented in Table 5.4.

Storage time (min)	Signal loss (%)
1	1.4
2.5	3.6
5	7.0
10	13.5
20	25.2
50	51.6
100	76.6
200	94.5
500	99.9
1000	100

Table 5.4. Percentage decay of the 110°C TL signal for various storage times at 20°C.

During typical SAR measurement sequences, where an automated reader is used, aliquots are often irradiated and then measured in batches. This leads to aliquots being stored at room temperature for significant periods of time between irradiation and measurement. For example, when giving test doses of 5 Gy using a source with a dose rate of 1 Gy/min to a carousel of 24 aliquots in our Risø reader (Risø 1), the first aliquot is stored at room temperature (20°C for this calculation) for 6900s whilst the other aliquots are being measured; during this time 81% of the 110°C TL signal decays. Similarly, the last sample to be irradiated (irrespective of test dose and source dose rate) is stored at room temperature for nearly 1000s whilst the TL from the previous 23 aliquots is measured[m]; this causes a 22% decay in the TL signal. If the laboratory temperature is raised to 25°C, a fluctuation which is possible in a centrally heated room, these figures become 95 and 36% respectively. If on the other hand, each aliquot is

[m] Heating to 160°C at a heating rate of 5°C/s.

measured immediately after irradiation (c. 40s storage in a Risø TL-DA-12 automated reader), the decay is approximately 1.0% at 20°C and 1.8% at 25°C. Consequently, the effect of temperature fluctuation on the apparent sensitivity of the sample will be small if measurements are made soon after irradiation. Where signal intensity is likely to be low, or where laboratory temperature may fluctuate during the course of a measurement sequence, measurement of the 110°C TL peak intensity should be carried out immediately after irradiation.

5.7 110°C TL peak saturation

In certain circumstances, such as those described in Section 5.5, it may be advantageous to monitor sensitivity changes throughout a sequence, using both OSL and TL measurements. A test dose that induces a high intensity signal from both traps is required. In some samples, though not all, a measurable 110°C TL peak may be produced using very small radiation doses. For example, Murray and Roberts (1998) used 0.02 Gy test doses to monitor sensitivity changes. However, the OSL signal is generally less sensitive to radiation (Murray and Roberts, 1997). Hence, sensitivity monitoring using the OSL signal is likely to require larger test doses than are required using the 110°C TL signal. These higher doses may cause the 110°C TL signal to saturate. A measurement sequence, similar in concept to the SAR protocol (Murray and Wintle, 2000), was first tested, and then used to measure growth curves for the 110°C TL peak. This sequence is outlined in Table 5.5. Sensitivity corrected TL intensities were calculated by dividing the regeneration dose TL (L_x) by the test dose TL (T_x).

Step	Action	Measurement
1	TL (400°C @ 5°C/s, Ar flow)	
2	β regeneration dose	
3	TL (160°C @ 5°C/s, Ar flow)	L_x
4	1 Gy β test dose	
5	TL (160°C @ 5°C/s, Ar flow)	T_x
6	Repeat steps 2-5 to create a growth curve	

Table 5.5. Measurement sequence for the 110°C TL growth curve. The TL signal was integrated from 50-140°C, with instrument background subtracted. Step 1 is included to ensure that the 110°C TL trap is empty at the beginning of each measurement cycle.

5.7.1 Sensitivity correction for repeated regeneration points

This sensitivity correction procedure was tested by measuring seven identical (c.15 Gy) regeneration dose points. Step 1 (Table 5.5) was omitted from this sequence. The corrected TL (R_x) intensity for each regeneration point should be identical irrespective of sensitivity changes that occur. To make the test more robust, sensitivity change was deliberately induced by preheating the aliquots at 300°C for 10s prior to administering the regeneration dose (i.e. between steps 5 and 2 in Table 5.5). Sensitivity corrected (R_x) and uncorrected (L_x) data are shown in Figure 5.13, with all data normalized to those for the first regeneration cycle. The sensitivity changes, shown by the uncorrected TL intensities, are relatively small (c. 10%). The sensitivity corrected TL intensity changes by less than 1% over the seven regeneration cycles, indicating that the sensitivity correction procedure is appropriate.

5.7.2 Sensitivity corrected growth curves for the 110°C TL signal

A fresh aliquot of each sample (Aber/29-BA14, Aber/28-IN22 and Aber/12-MAP3) was used to measure growth curves, using the sequence outlined in Table 5.5. The regeneration doses used were 1, 2.5, 5, 10, 15, 20, 25, 30, 40, 50, 60, and 1 Gy. The recycling ratios for these aliquots never differed from unity by more than 2%, indicating that the sensitivity correction procedure accurately compensated for sensitivity changes (c.30%) through the sequence. For each measurement cycle, the 110°C TL peak area was obtained by integrating the luminescence signal from 50-140°C, and subtracting the equivalent dark count. The upper integration limit of 140°C was used in order to minimise any contribution from an overlapping, higher temperature peak (see Figure 5.14) and differs from that used by other authors (e.g. Wintle and Murray, 1999) who used 160°C. Since the tail of the higher temperature peak is only apparent at high cumulative doses, it must have a significantly lower intrinsic brightness than the 110°C TL peak. In most dating sequences where sensitivity monitoring would be of use, the overlapping peak will be removed by preheating. For example, in SAR sequences, PH1 is likely to be sufficient to remove this overlapping peak. In this case, signal from the overlapping peak will only become important where several sensitivity measurements are performed per regeneration cycle. Incidentally, the regenerated TL curves measured in

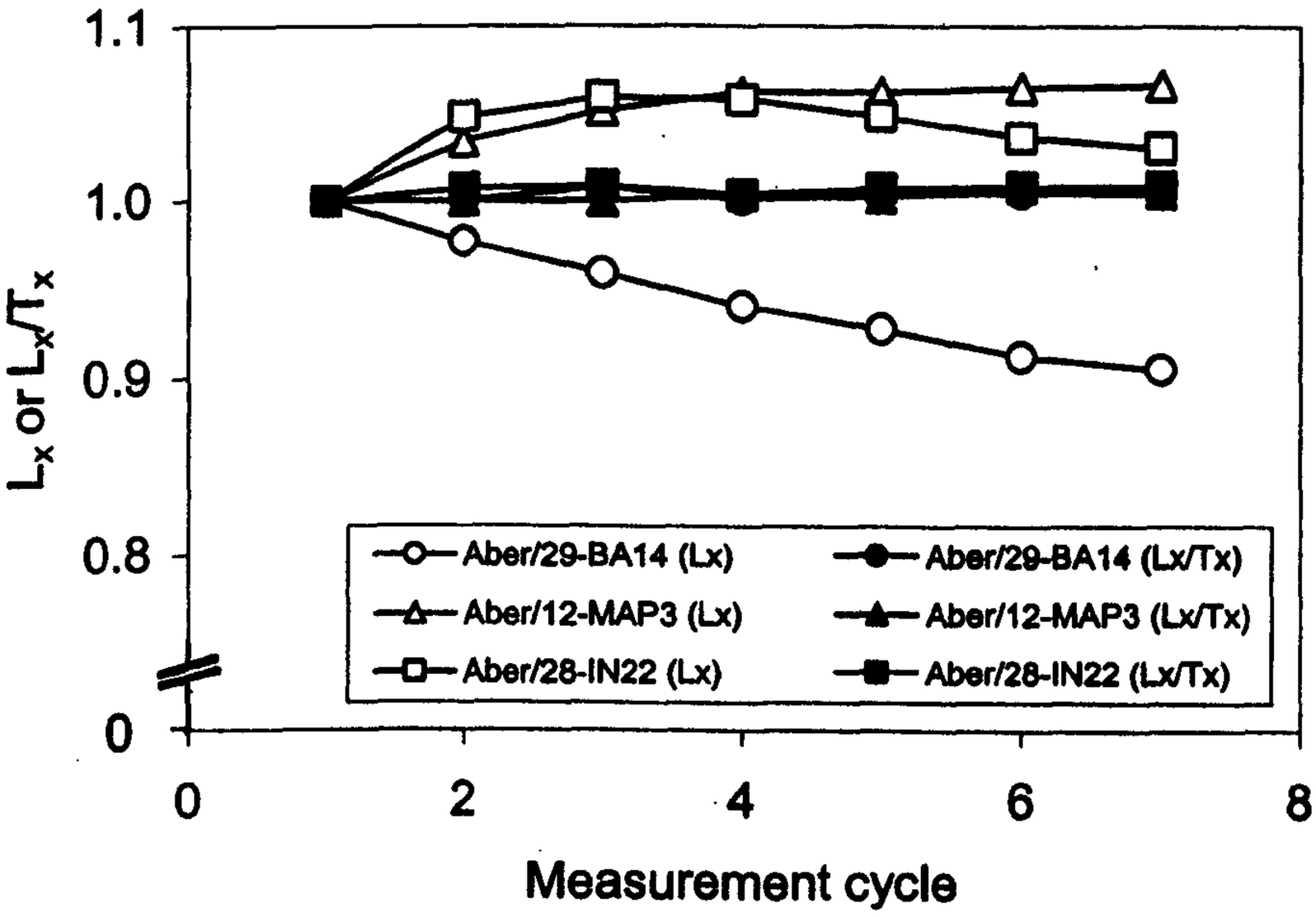

Figure 5.13. Uncorrected (L_x, open symbols) and sensitivity corrected (L_x/T_x, closed symbols) 110°C TL signals versus measurement cycle, using a constant regeneration dose of c.15 Gy regeneration dose. Data are normalised to L_1 or L_1/T_1 as appropriate.

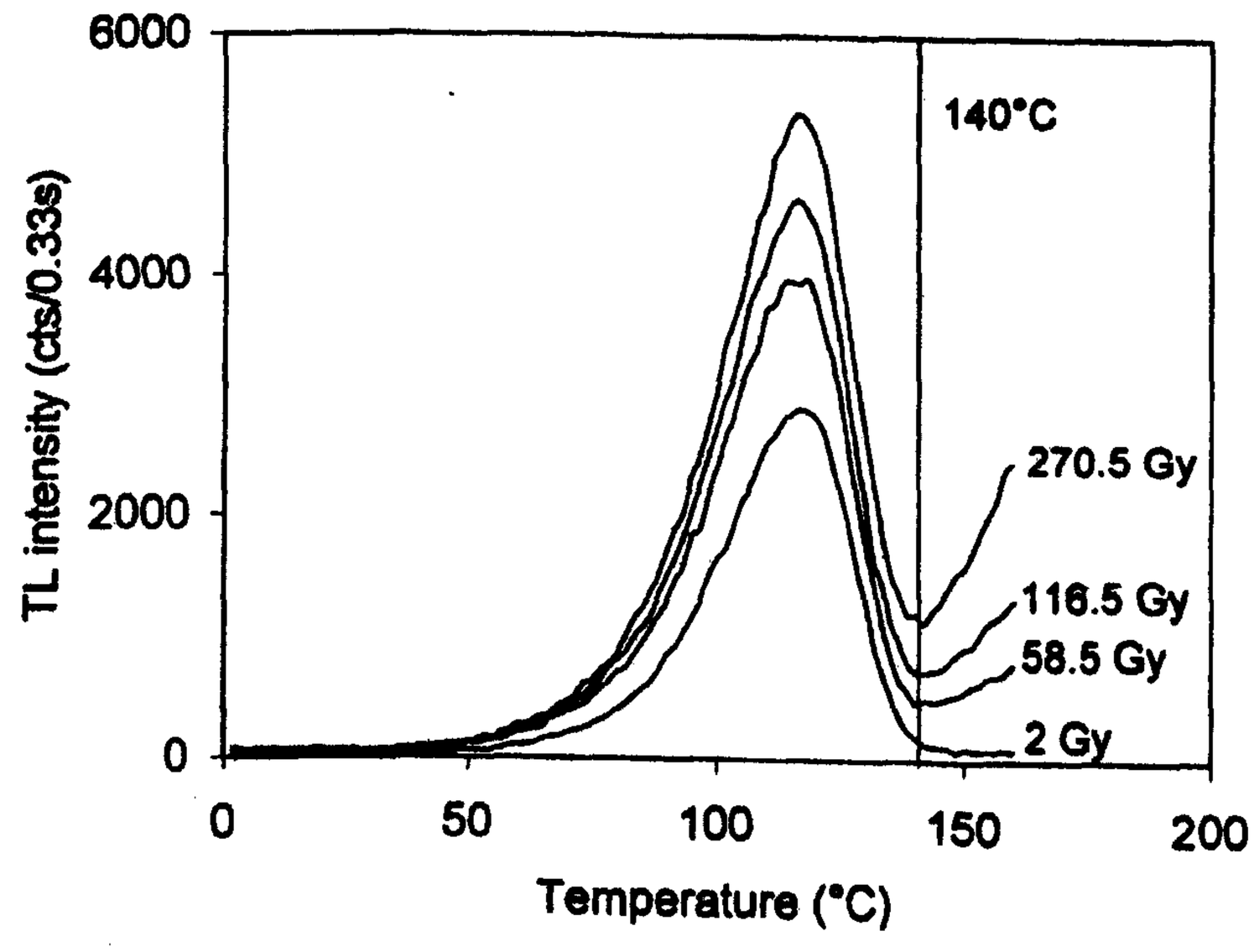

Figure 5.14. TL curves measured in response to a 1 Gy test dose for an aliquot of Aber/28-IN22 as measured in the sequence used to observe the dose response. Only four curves have been shown for clarity. The 110°C TL peak area is obtained by integrating from 50-140°C to avoid interference from the tail of a higher temperature peak that increases with dose during the sequence. The cumulative β-dose that the aliquot had received prior to the measurement of each curve is given on the right side of the figure.

this experiment support the suggestion that the 110°C TL peak obeys first order kinetics. For first order peaks, the peak maximum temperature remains constant with increasing regeneration dose, whereas higher order peaks shift to lower temperatures (Aitken, 1985). In all three samples measured, the 110°C TL peak position remains constant, using regeneration doses ranging from 1 to 60 Gy.

The sensitivity-corrected data were plotted as a function of dose (filled circles in Figure 5.15). A saturating exponential function was fitted to the corrected data (see Section 2.2, Equation 2.1). However, the shape of this growth curve is distorted by decay of the 110°C TL signal during irradiation. This effect is particularly significant for longer irradiation times (larger doses) and causes an apparent saturation of the TL response. The effects of this loss of signal during irradiation can be accounted for using Equation 5.3.

$$c = \tau(1-e^{-t/\tau})/t \qquad (5.3)$$

where t is the irradiation time and c is a correction factor. The sensitivity-corrected TL intensity is then divided by the appropriate value of c to calculate the TL intensity that would have been measured, had no loss of charge occurred during irradiation. This correction was only applied to the regenerated 110°C TL intensities, because the test doses are equal, and consequently subject to the same loss of signal during irradiation. The "true" growth curve, calculated by correcting measured regeneration points using Equation 5.3, is also shown in Figure 5.15 (filled triangles). The values of B (the parameter in Equation 2.1, defining the onset of signal saturation) are 27.0 Gy (Aber/12-MAP3), 26.3 Gy (Aber/28-IN22) and 18.2 Gy (Aber/29-BA14). It is interesting to note that, had the correction factor c not been applied, an apparent value of B would have been 14.8 Gy (about half the corrected value), as obtained from the filled circles in Figure 5.15.

This apparent value depends upon the dose rate used to construct the growth curve; for 5 Gy/min, B would have been calculated to be 23.5 Gy, since little decay of charge would have occurred during the irradiations. When the 110°C TL peak is used for sensitivity

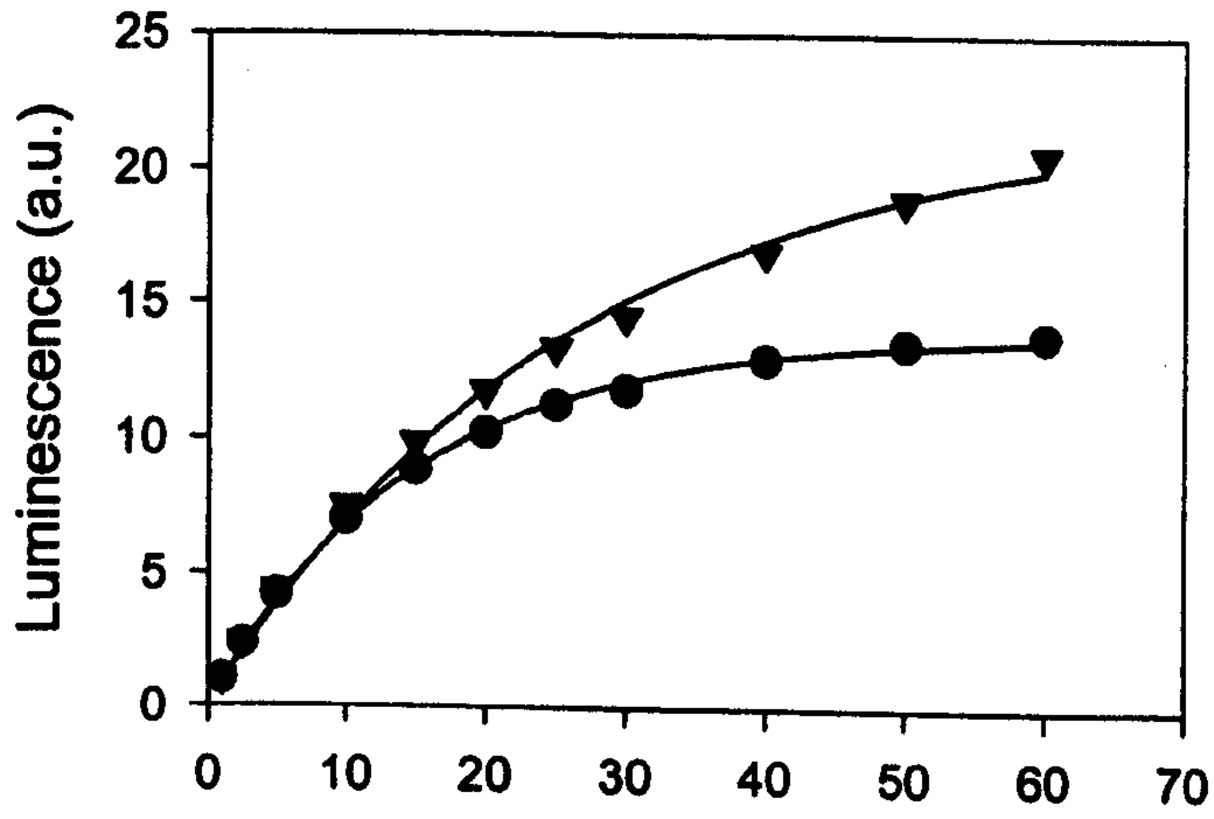

Figure 5.15. Sensitivity-corrected 110°C TL growth curves for an aliquot of Aber/12-MAP3. The lower growth curve (circles) shows apparent saturation of the 110°C TL response, partly caused by the decay of electrons from the associated trap during irradiation. The upper growth curve (triangles) show the data after correction for this effect. The corrected saturating exponential behaviour is characterized by $B = 27.0$ Gy.

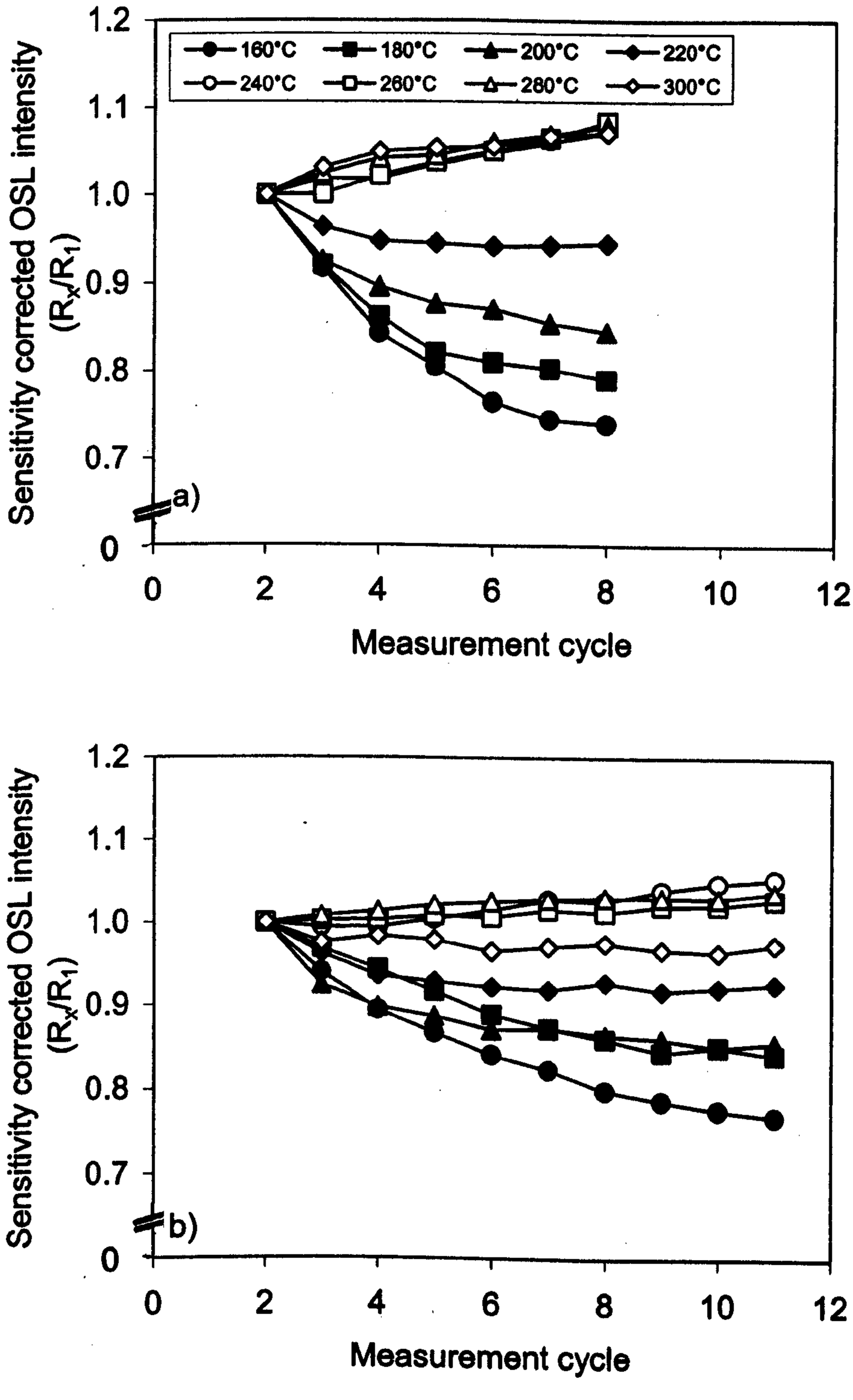

Figure 5.16. Sensitivity corrected OSL intensity versus measurement cycle using the 110°C TL signal as a proxy for OSL sensitivity. Samples used are a) Aber/12-MAP3 and b) Aber/29-BA14. Two aliquots were used at each PH1 temperature, and the data are mean values. A constant regeneration dose of c. 10 Gy was used, and all data are normalised to R_1.

the experiment. These preheats caused negligible sensitivity change in Aber/29-BA14, and up to 30% sensitivity increases in Aber/12-MAP3 (as measured by $T_{x(OSL)}$). The 110°C TL peak response is less appropriate for correcting OSL sensitivity changes in aliquots preheated at lower temperatures. Using a PH1 temperature of 160°C, the corrected data for Aber/12-MAP3 fell by c.25% over the seven measurement cycles°. The sensitivity of both samples fell by 30-40 % when using lower temperature preheats (160-200°C). The data for the 220°C PH1 are intermediate between these two groups.

These results suggest that (at least for these two samples) in SAR measurement sequences, the 110°C TL signal is an accurate proxy for OSL sensitivity only when PH1 temperatures greater than 220-240°C are used. Using a PH1 lower than 220°C, sensitivity correction using the 110°C TL signal is better than using no correction, but still unacceptable for routine use in dating or sensitivity monitoring experiments.

5.8.1 Implications for electron transfer pathways used by charge from the OSL and 110°C TL traps

The lack of proportionality between the OSL and 110°C TL signals has led several authors to suggest that at least some of the charge from these traps does not recombine via the conduction band (Section 1.6.1.4). The results presented in Section 5.8 will be discussed in the light of this suggestion. However, it is interesting to note that Bailey (2001) has demonstrated that this discrepancy can be simulated using his model, without localized charge transitions.

Sensitivity correction using the higher temperature preheats is effective using both correction methods (Figures 5.5 a and b, and 5.16). This suggests that charge from both traps has access to the same recombination centres. Since thermal activation is the dominant process at these temperatures, recombination occurs mainly at L-centres, which have been shown to be accessed by both traps (Franklin *et al.*, 1995). However, the 110°C signal also corrects the 300°C PH1 data accurately. Using this preheat the sensitivity initially rises and then falls, a phenomenon tentatively explained in Section

°A maximum of 7 regeneration points were used in routine D_e estimation sequences.

5.2.2 using a thermally stable, non-radiative recombination centre termed a K-centre. It is likely that both the OSL and 110°C TL traps have access to this centre. The thermal stability of holes trapped at this recombination centre make it likely that it is the R_3 centre required by Chen and Li (2000) to explain the sensitivity changes (in the 110°C TL signal) which occurred during their pulse annealing experiment (Sections 1.6.1.3 and 1.6.1.4). A non-radiative recombination centre with similar thermal stability was required by Bailey (2001) for his model, though its influence on the OSL signal was not demonstrated. The data in Figures 5.5 (a and b) and 5.16, link the OSL signal to the R_3 centre for the first time.

Using PH1 temperatures below c.200°C, sensitivity correction using the 110°C is not appropriate, and the corrected luminescence intensities fall. This indicates that the OSL sensitivity falls faster than that of the 110°C TL sensitivity at these temperatures. This is the opposite of what would be expected from previous work. Li and Chen (2001) have shown that the OSL signal has access to only one thermally unstable R-centre, while the 110°C TL trap has two (Chen and Li, 2000). The more stable R-centre (R_2) is probably shared while the less stable one (R_1) is accessed via a localized transition (Section 1.6.1.4). No explanation of this phenomenon is offered.

5.9 Conclusions

1) The size and direction of sensitivity changes during SAR sequences are dependent on the cumulative radiation dose delivered during the measurement sequence, the age/geological dose of the samples and the PH1 temperature used.
2) These sensitivity changes can be explained in terms of dose quenching and thermal activation. A minimum of three recombination centres are required for this explanation, only one of which is radiative.
3) The SAR sensitivity correction procedure is generally appropriate irrespective of the PH1 temperature applied, and therefore the direction of sensitivity change. The most rapid sensitivity changes occur in the first few measurement cycles. Consequently, the recycling ratio is most robust as a test of the SAR sensitivity correction procedure when the first regeneration dose is repeated.

4) The reproducibility of individual R_x measurements is 1.08 ± 0.41 %.
5) The kinetic parameters of the 110°C TL peak trap were measured using isothermal decay and Hoogenstraaten's methods. The isothermal decay dataset is considered more reliable, and yielded values for E and s of 0.912 ± 0.006 eV and 1.16 ± 0.34 x 10^{12} s^{-1} respectively.
6) The 110°C TL signal is only a reliable proxy for OSL sensitivity using high temperature preheats (>220°C for 10 seconds), i.e. when sensitivity is constant or rising.

Chapter 6: Equivalent dose determination

6.1 Introduction

The most significant advantage of the SAR technique over most other OSL measurement techniques is the ability to rapidly produce many estimates of the equivalent dose (D_e) for any individual sample. Inevitably, the resulting D_e estimates will not be identical, and the inter-aliquot variability is termed "scatter". This chapter explores the causes of scatter in SAR datasets, and their likely effects on the samples measured in the present study. In addition, techniques for producing an equivalent dose from an SAR dataset are discussed.

6.2 Growth curves

Using the SAR method, the growth of the OSL signal with increasing radiation dose is measured for each aliquot, producing a growth curve. The equivalent dose is then estimated by calculating the radiation dose required to give the natural luminescence intensity (L_n/T_n). Consequently, growth curve shape and equivalent dose are intimately linked.

6.2.1 Measured growth curves

In all cases where an equivalent dose was calculated, the regeneration doses "bracketed" the equivalent dose, allowing the D_e to be calculated by interpolation. The curve fitting error is generally very small. A saturating exponential plus linear fit was used (see Section 2.2). A selection of growth curves measured for samples used in this study are shown in Figure 6.1.

Figures 6.1a and b show growth curves for samples with relatively small equivalent doses, and therefore small regeneration doses. The growth curve is almost linear in this dose range, though some curvature can be seen, especially in Figure 6.1b. This curvature becomes more obvious at higher doses (Figures 6.1c and d). At much higher doses, significant curvature of the growth curve is observed (Figures 6.1e and f). The growth curve shape at higher doses is quite variable, ranging from flat (saturated, Figure 6.1f) and steady growth (Figure 6.1e). On occasions, the sensitivity-corrected natural luminescence intensity (L_n/T_n) is greater than the regenerated luminescence intensity at

a)

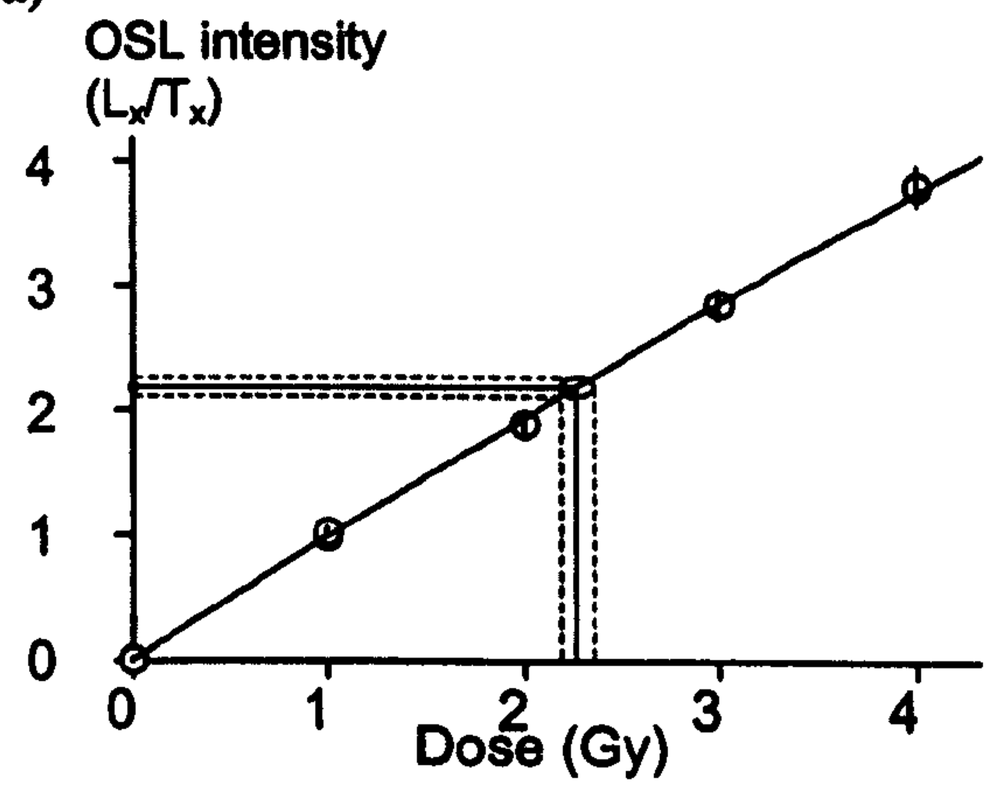
OSL intensity
(L_x/T_x)
4
3
2
1
0
0
1
2
3
4
Dose (Gy)

b)

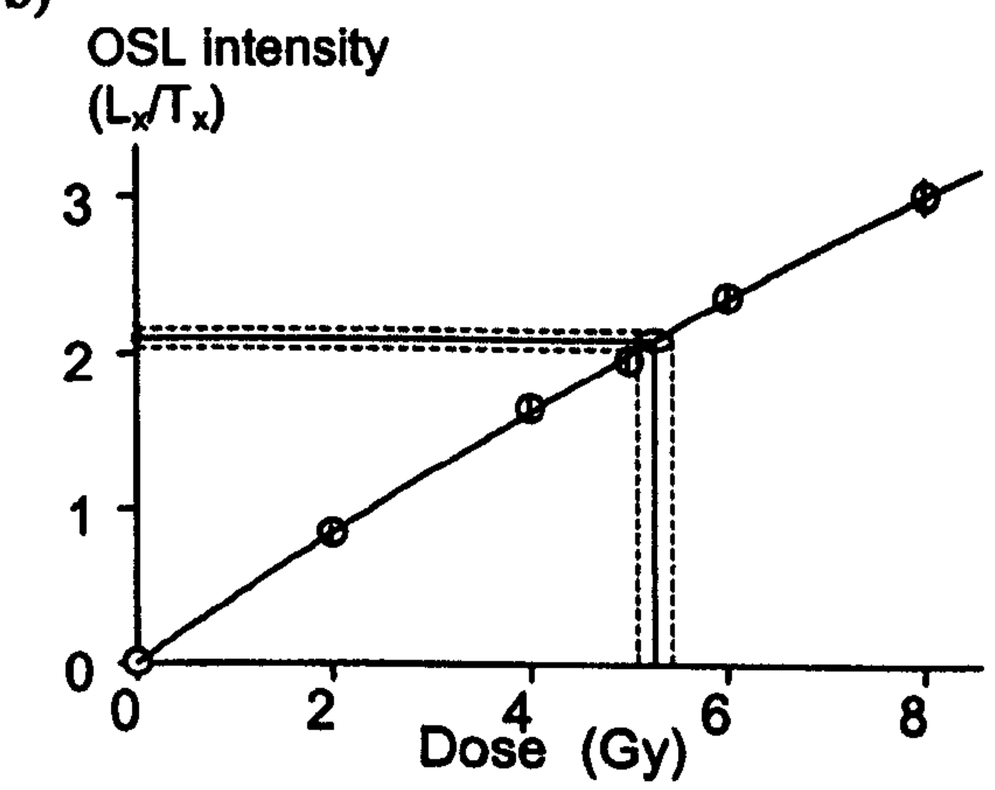
OSL intensity
(L_x/T_x)
3
2
1
0
0
2
4
6
8
Dose (Gy)

c)

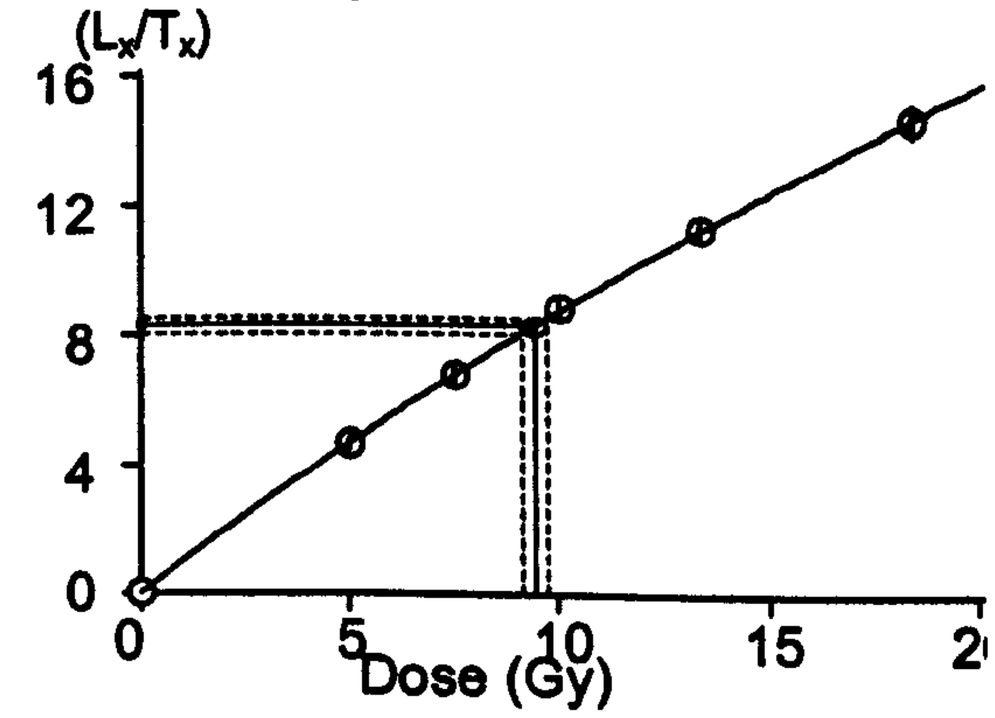
OSL intensity
(L_x/T_x)
16
12
8
4
0
0
5
10
15
Dose (Gy)

d)

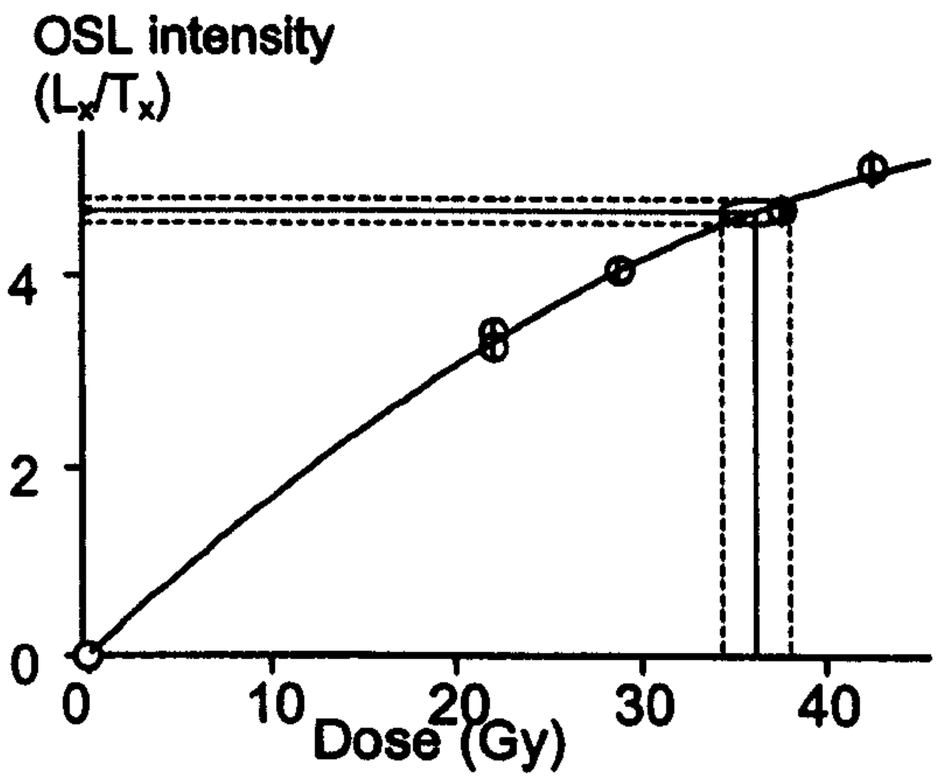
OSL intensity
(L_x/T_x)
0
2
4
0
10
20
30
40
Dose (Gy)

e)

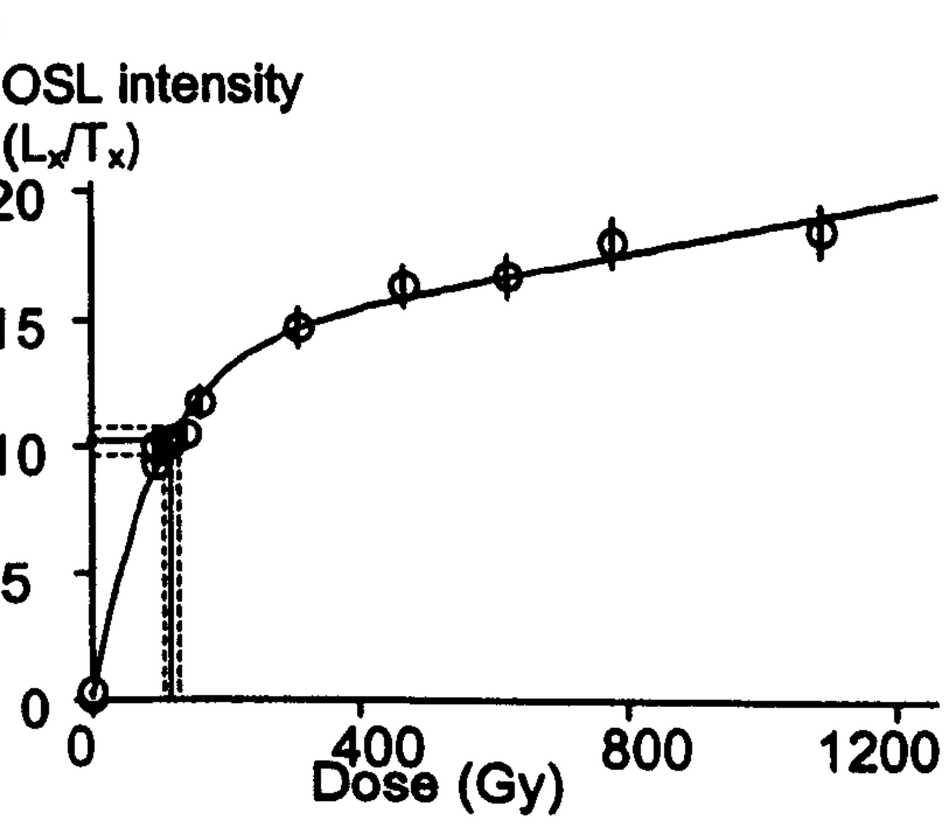
OSL intensity
(L_x/T_x)
0
5
10
15
20
0
400
800
1200
Dose (Gy)

f)

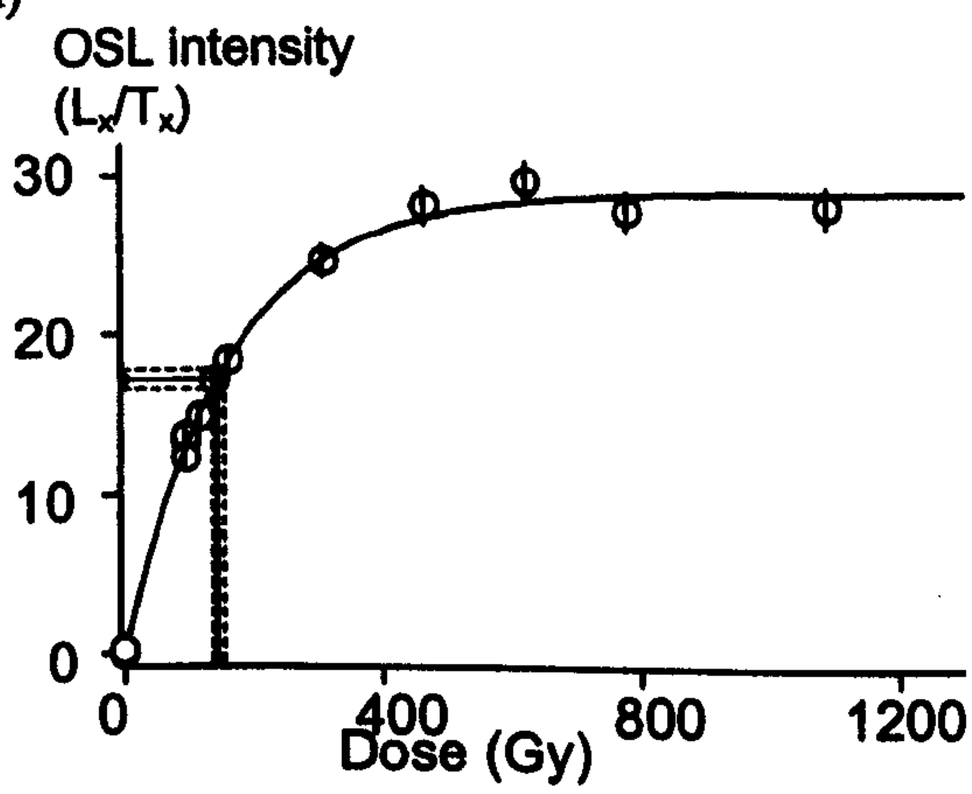
OSL intensity
(L_x/T_x)
0
10
20
30
0
400
800
1200
Dose (Gy)

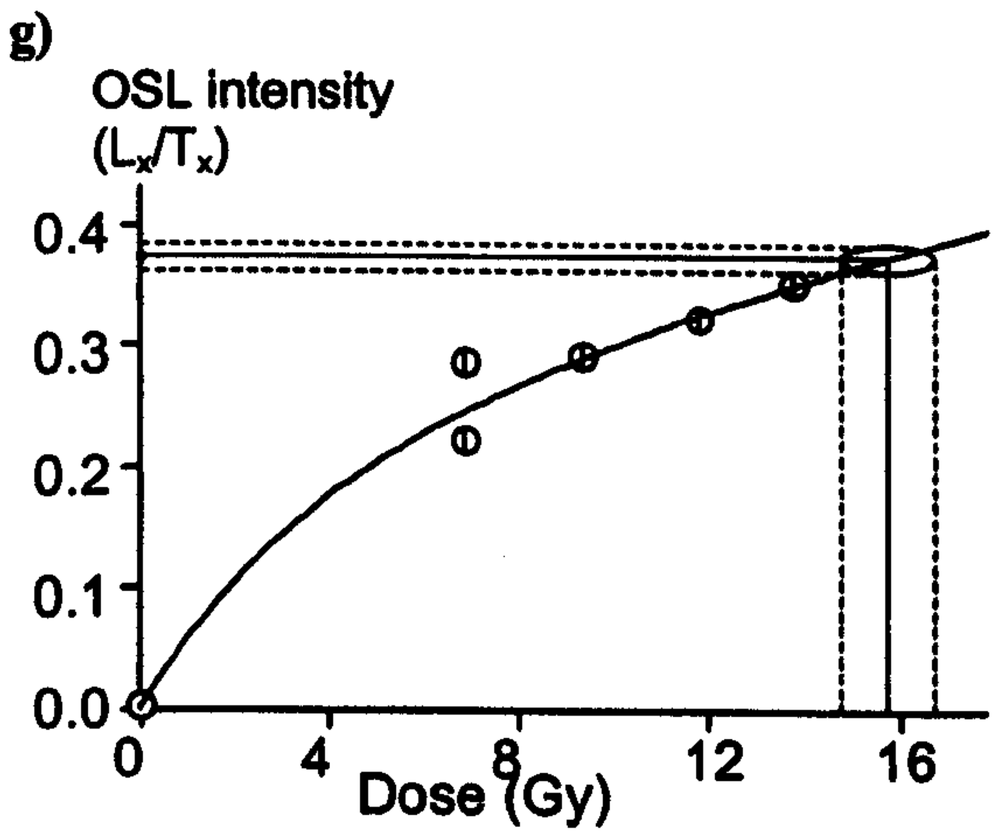

Figure 6.1. Selected growth curves for samples from Inhaca and Bazaruto Islands. All datasets were fitted using a saturating exponential plus linear function, using Analyst v2.24. The open circles are regeneration dose points, and the vertical line represents the error on each point. The solid and dashed lines represent the natural (L_n/T_n) luminescence intensity and one standard deviation errors respectively. The dose axis intercept gives the equivalent dose. In all cases, the lowest non-zero regeneration point has been measured twice, though the second point may overly the first and obscure it. The growth curves were for aliquots of a) Aber/28-IN16 (PH1= 180°C, recycling ratio (RR) = 1.04), b)Aber/28-IN15 (PH1 = 180°C, RR = 0.99), c) Aber/29-BA12 (PH1 = 220°C, RR = 1.01), d) Aber/29-BA13 (PH1 = 160°C, RR = 0.96), e) Aber/29-BA14 (PH1 = 180°C, RR = 1.04), f) Aber/29-BA14 (PH1 = 220°C, RR = 0.92), and g) Aber/28-IN18 (PH1 = 300°C, RR = 1.34).

saturation, and hence no equivalent dose can be calculated. This phenomenon is explored in Section 6.4.4. Figures 6.1a-f all show growth curves with low curve fitting errors, and are typical of the majority of growth curves observed in this study. However, growth curves with larger curve fitting errors are occasionally observed (Figure 6.1g). In this case, the recycling ratio was very poor (1.34), and the aliquot was rejected. Throughout the thesis, aliquots yielding recycling ratios differing from unity by > 10% were rejected (Section 3.3), as were aliquots where a significant infra-red stimulable signal was observed (Section 2.3.4).

6.2.2 The standardised growth curve

Roberts and Duller (submitted) explored the dose response characteristics of several luminescence dosimeters, measured using the SAR technique. Since the SAR procedure normalizes all luminescence intensities to a standard test dose, sensitivity corrected luminescence intensities should be identical for a given regeneration dose. To compare measurements produced using different test doses (D_t), they calculated a "standardised luminescence signal" by multiplying L_x/T_x by D_t, effectively normalizing all growth curves to that for a 1 Gy test dose. For coarse-grained quartz they found that, in the absence of thermal depletion of the OSL signal (i.e. PH1 temperatures from 160-260°C), a general growth curve form ("standardised growth curve") could be defined.

The coarse-grained quartz dataset of Roberts and Duller[a] (submitted) was fitted with a single saturating exponential function, with a small luminescence axis intercept (Equation 6.1)

$$I = I_o + A\,(1 - \exp^{-D/B}) \qquad (6.1)$$

where I_o is the luminescence axis intercept, and other terms are defined in Section 2.2. Equation 6.1 is similar to Equation 2.1, with the exception of the luminescence axis intercept term. Roberts and Duller (submitted) found that Equation 6.1 was applicable to their samples up to regeneration doses of 125 Gy, after which an additional linear term

[a] 27 aliquots from six Tasmanian samples.

was required. However, the scatter increased markedly at higher doses, probably due to variations in the growth curves of individual aliquots at higher doses (see Figures 6.1e and f) and a small amount of feldspar contamination (Roberts and Duller, submitted), limiting the usefulness of this approach for older samples.

The standardised growth curve (SGC) parameters calculated by Roberts and Duller (submitted)[b] were tested by applying them to SAR datasets for 14 samples from Inhaca and Bazaruto Islands, each with equivalent doses less than 125 Gy. The values of D_e obtained using the SGC were plotted against the SAR D_e values calculated using the growth curve measured for each individual aliquot (Figure 6.2). The results are generally encouraging, with the majority of SGC D_e values being consistent with the corresponding SAR D_e, and a mean ratio (SAR:SGC) of 0.98 ± 0.02. However, five SAR:SGC ratios are not consistent with unity. The dose axis intercept (I_o) appears to be too large for this dataset, yielding negative equivalent doses for most aliquots from the four modern samples studied. However, the SGC parameters (for coarse grained quartz) defined by Roberts and Duller (submitted) do appear to be a reasonable approximation of the growth curve followed by these samples.

6.3 Measured D_e distributions

D_e distributions for the majority of samples from Inhaca and Bazaruto are presented in Figure 6.3[c]. Only data from aliquots which were used to calculate the sample D_e have been shown on these plots. Three charts are presented for each sample. The first is a combined probability density function (PDF)/scatter plot. On this plot, the solid line is the PDF, while the open circles represent the equivalent dose for individual aliquots, with the associated error term. The equivalent doses for each sample are ranked, with the lowest D_e being placed at the bottom of the plot. In the PDF, each equivalent dose is represented as a Gaussian of equal area, whose peak height is inversely related to uncertainty. The second plot shows equivalent dose versus PH1 temperature, while the

---

[b] $I_o = 0.11 \pm 0.13$, $A = 51.7 \pm 0.6$ and $B = 55.1 \pm 1.3$ (their Table 4).
[c] The samples for which no D_e distribution has been presented are Aber/28-IN14 and Aber/29-BA1 and 5. The data files for these samples were lost when the hard drive attached to Risø 1 failed.

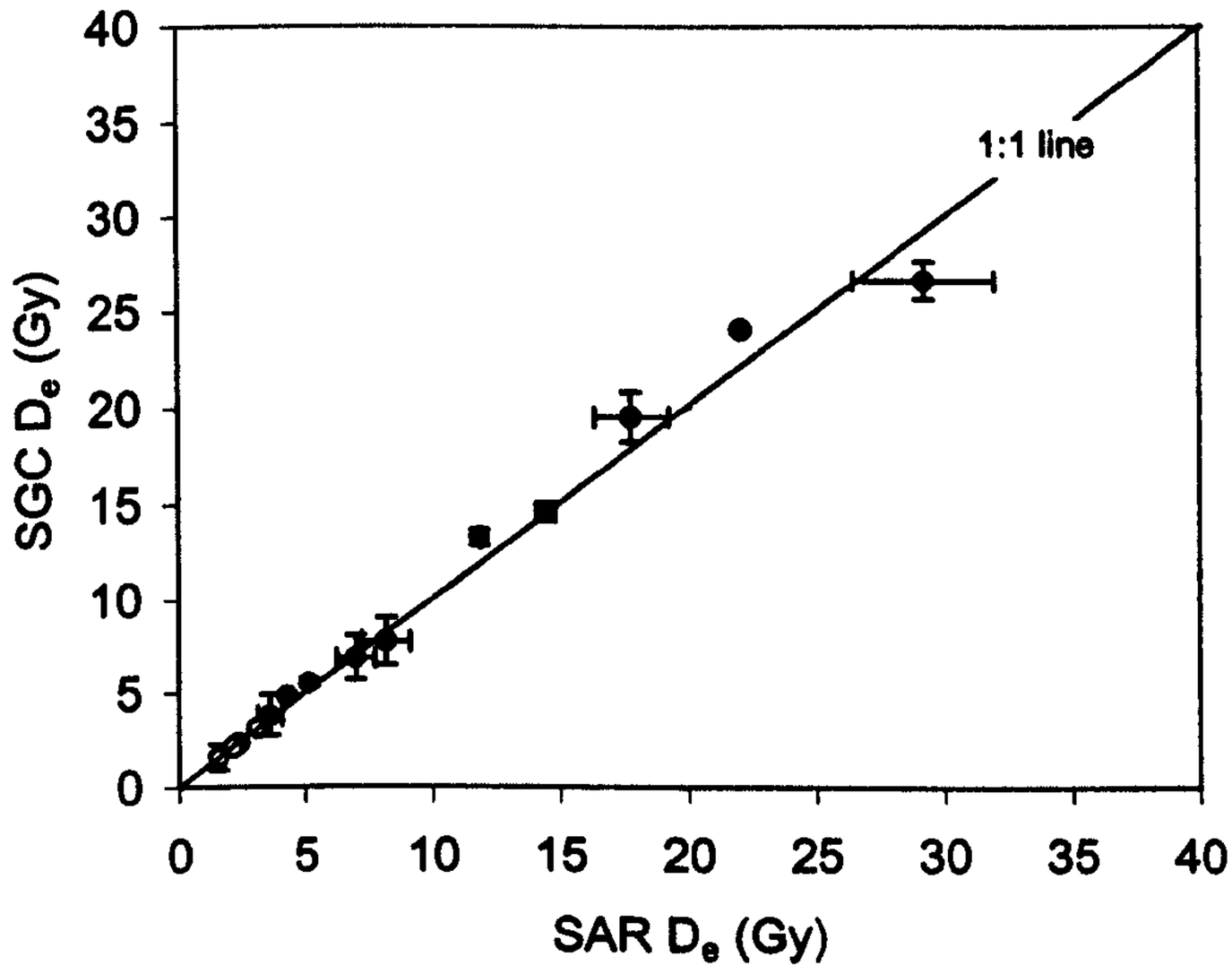

Figure 6.2 SGC D_e versus SAR D_e for 14 samples from Inhàca and Bazaruto Islands. Data collected using Risø 1 is represented by solid circles, while that collected using Risø 2 is represented by open circles. Each D_e is the mean value obtained from aliquots measured using PH1 temperatures from 160-260°C (typically n = 18). Where an aliquot was rejected on the grounds of a poor recycling ratio (SAR D_e dataset), it was also excluded from the SGC dataset. Errors are one standard error.

third plot shows equivalent dose versus natural luminescence intensity (L_x). In both cases, each point represents a single aliquot, with associated errors.

6.3.1 Patterns in the D_e distributions

The D_e distributions shown in Figure 6.3 fall into three main groups. The first group displays relatively little scatter, and each aliquot has a similar error term, leading to a PDF with a single peak (e.g. Aber/28-IN15 and 16, Figures 6.3g and h). These samples are young (sample D_e <50 Gy), and most were taken from Inhaca Island. The second group displays relatively large scatter, and each aliquot yields a precise D_e leading to a PDF with multiple peaks (e.g. Aber/29-BA8 and 10, Figures 6.3p and q). These samples are also relatively young (sample D_e <50 Gy), and most were taken from Bazaruto Island. The third group contains the older samples (D_e >50 Gy), which yield a large spread of equivalent doses (e.g. Aber/28-IN1 and Aber/29-BA14, Figures 6.3a and u). The error on the equivalent dose for each individual aliquot increases with D_e. Consequently, the PDF peaks at a relatively low dose. Potential causes of the scatter observed in Figure 6.3 are discussed in Section 6.4 below.

6.4 Likely causes of scatter for aeolian sediments

Possible causes for the scatter of individual D_e values observed for aliquots of a single sample can be grouped under three headings. These are

1) Irreversible changes in electron trapping probability in the first measurement cycle (i.e. prior to measurement of the first test dose response).
2) Measurement reproducibility (i.e. the 1.5% R_x variability measured in Section 5.3.2)
3) Environmental conditions (β-microdosimetry, partial bleaching, mixing and bioturbation).
4) Measurement procedure errors (e.g. SAR sensitivity correction failure).

It is important to identify the causes of scatter in a dataset since the shape of the sample D_e distribution, and consequently the techniques required to produce a sample equivalent dose depend on its cause. Irreversible changes in electron trapping probability during the first measurement cycle are difficult to demonstrate. The dose recovery experiments

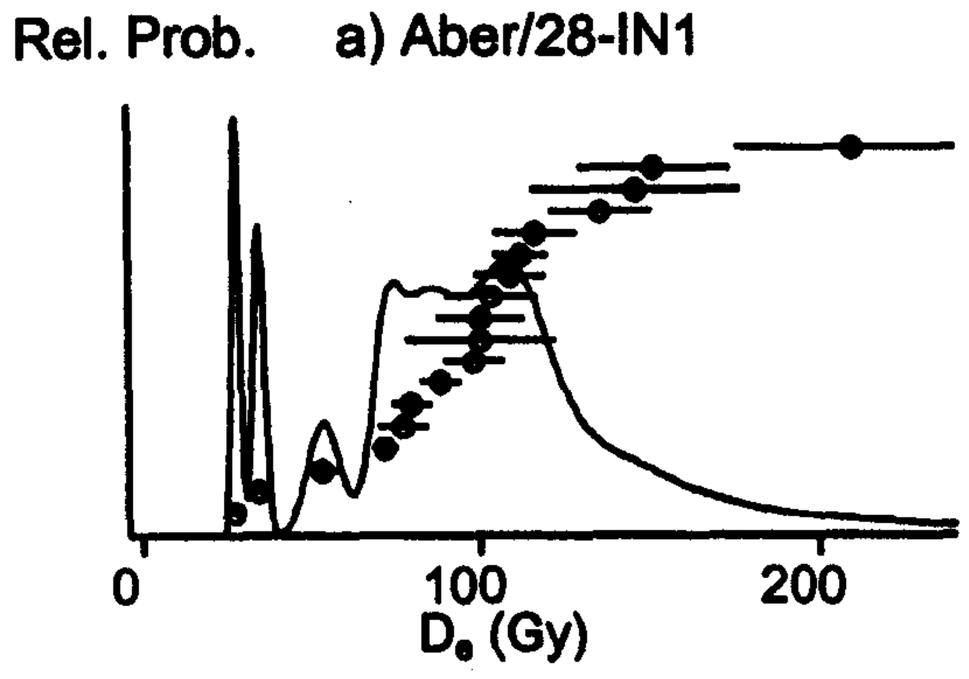

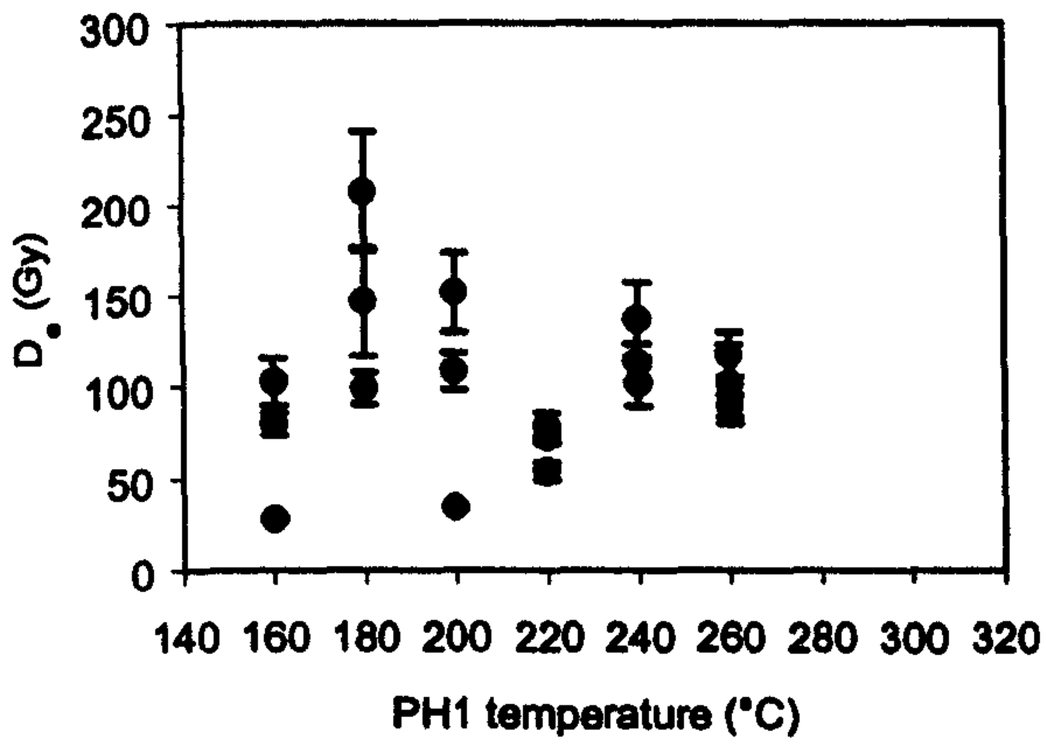

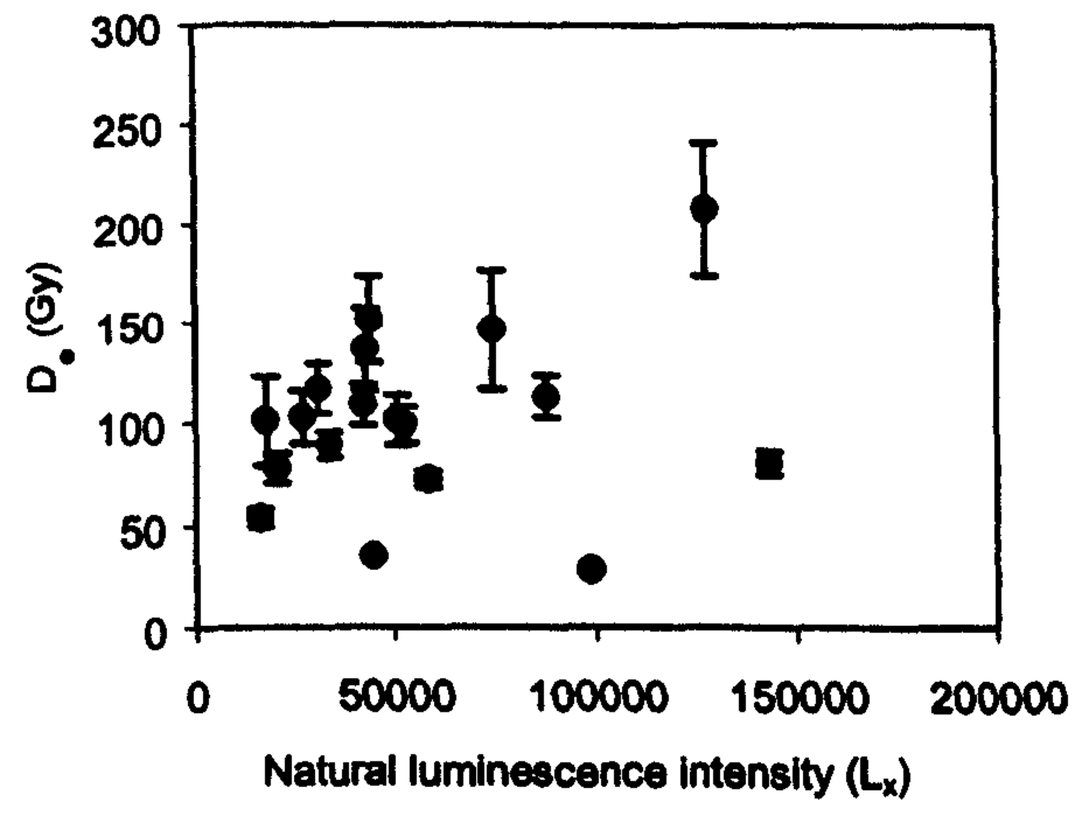

Aber/28-IN1

Exposure: cliff (block)

Average: median

D_e = 101 ± 10 Gy

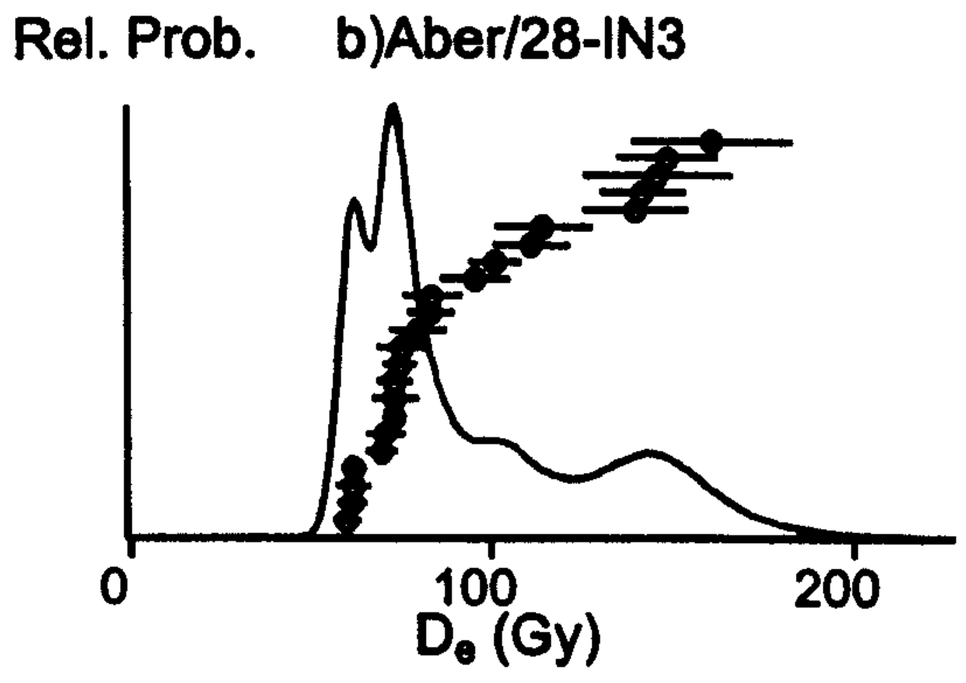

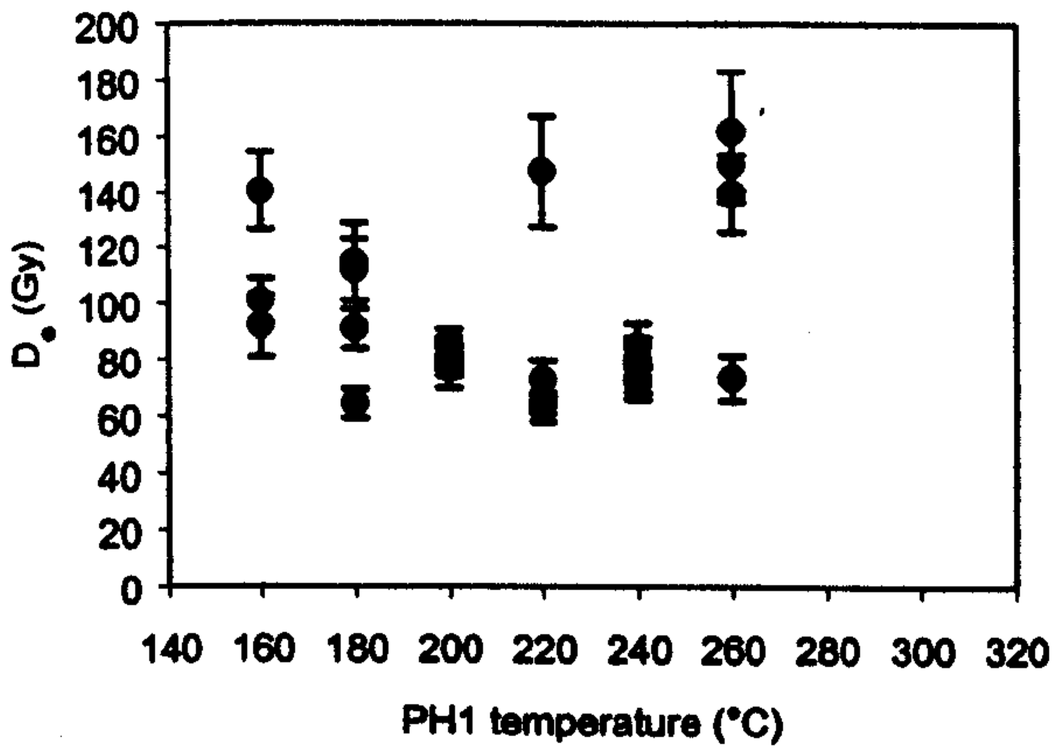

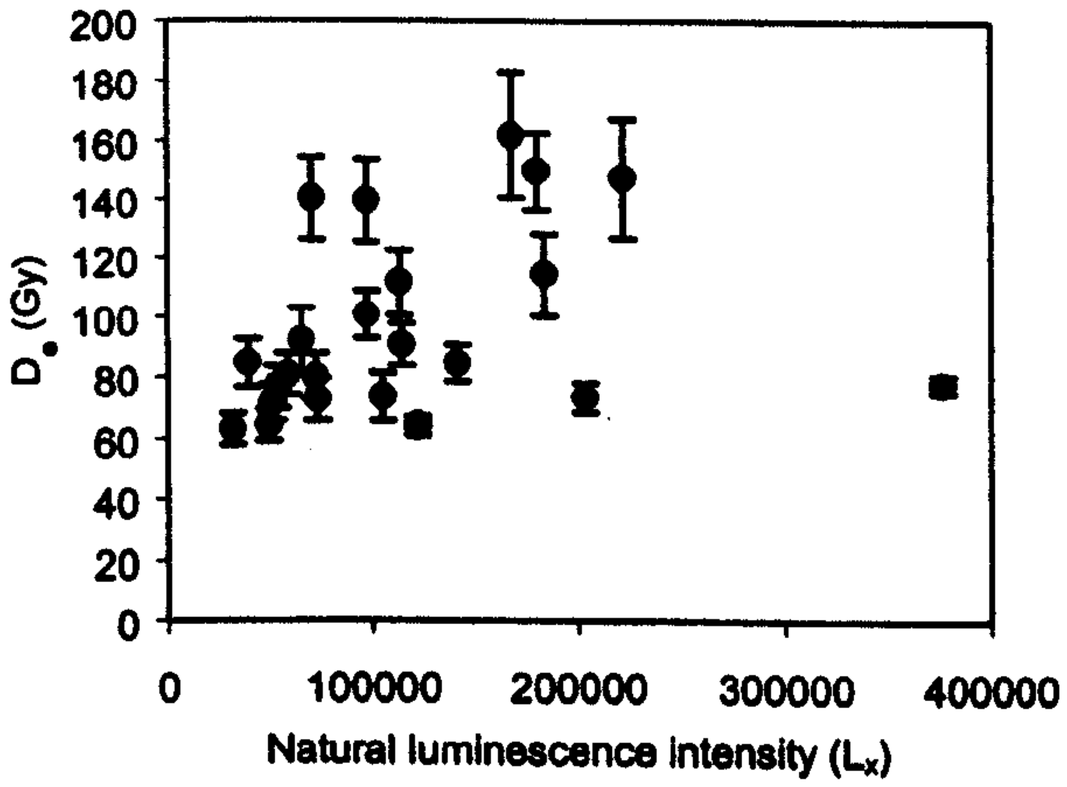

Aber/28-IN3

Exposure: cliff (block)

Average: mean

D_e = 96.2 ± 6.5 Gy

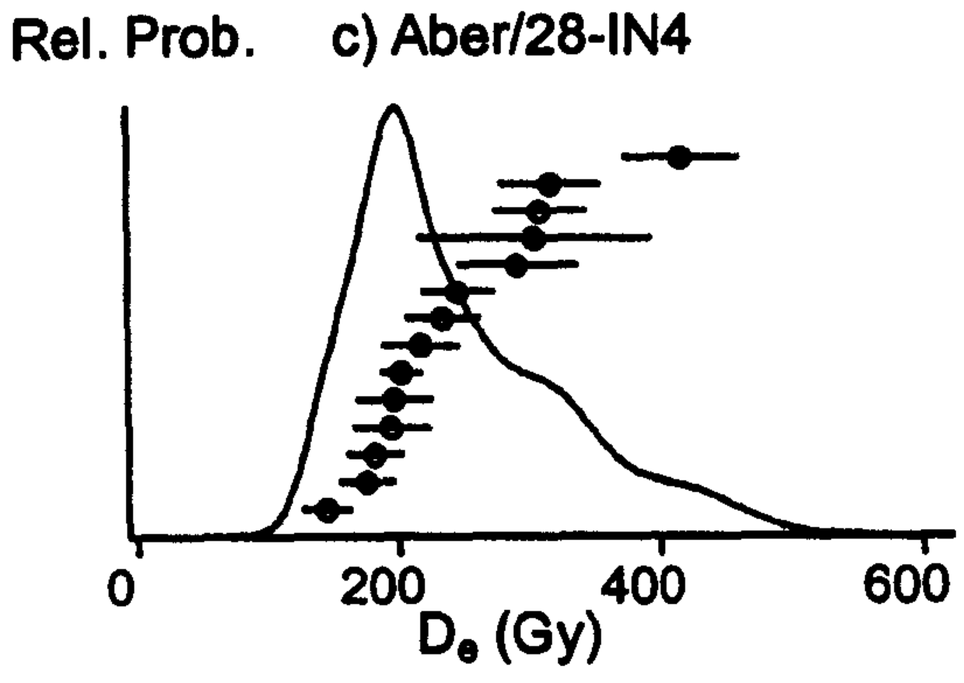

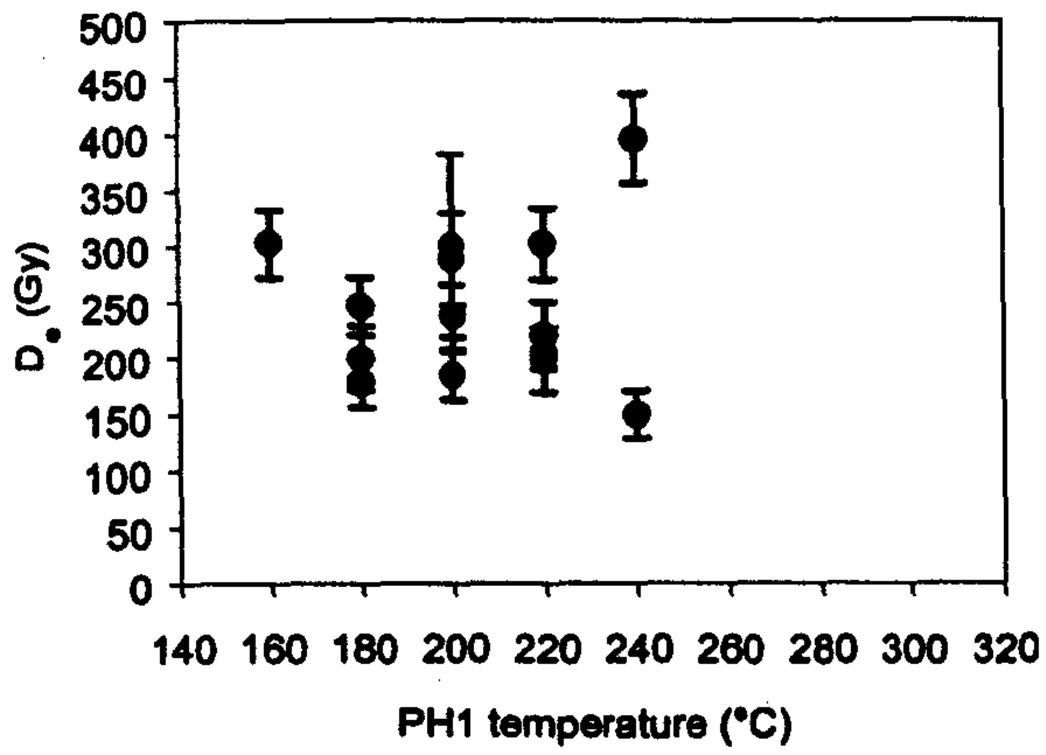

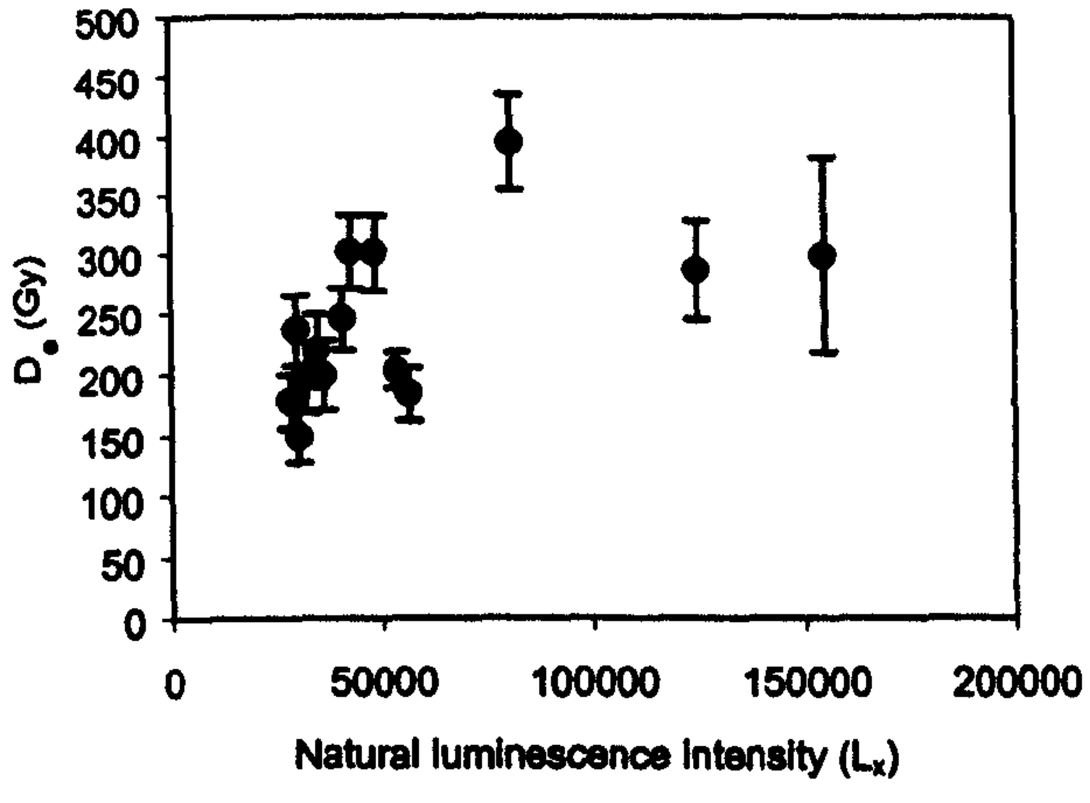

Aber/28-IN4

Exposure: cliff (block)

Average: median

D_e = 242 ± 18

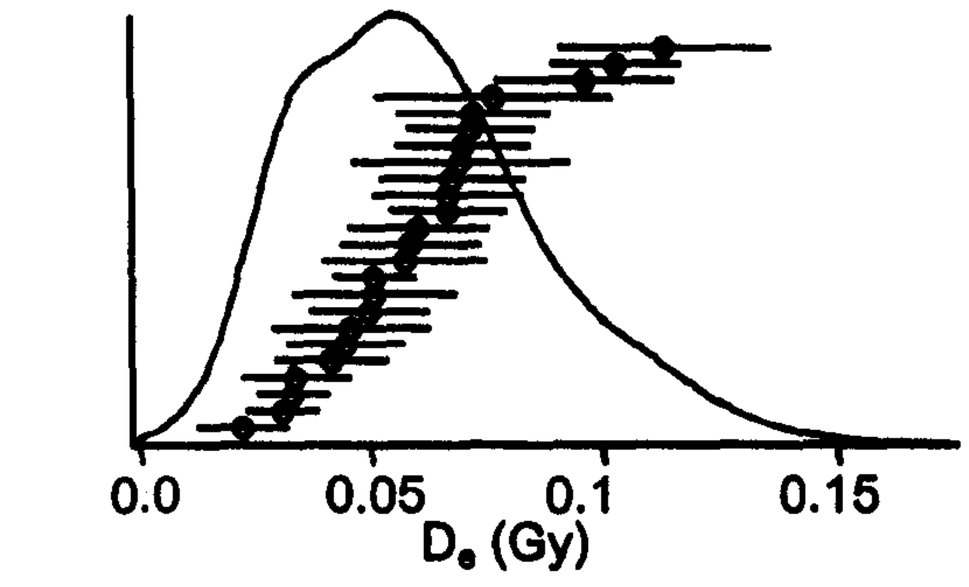

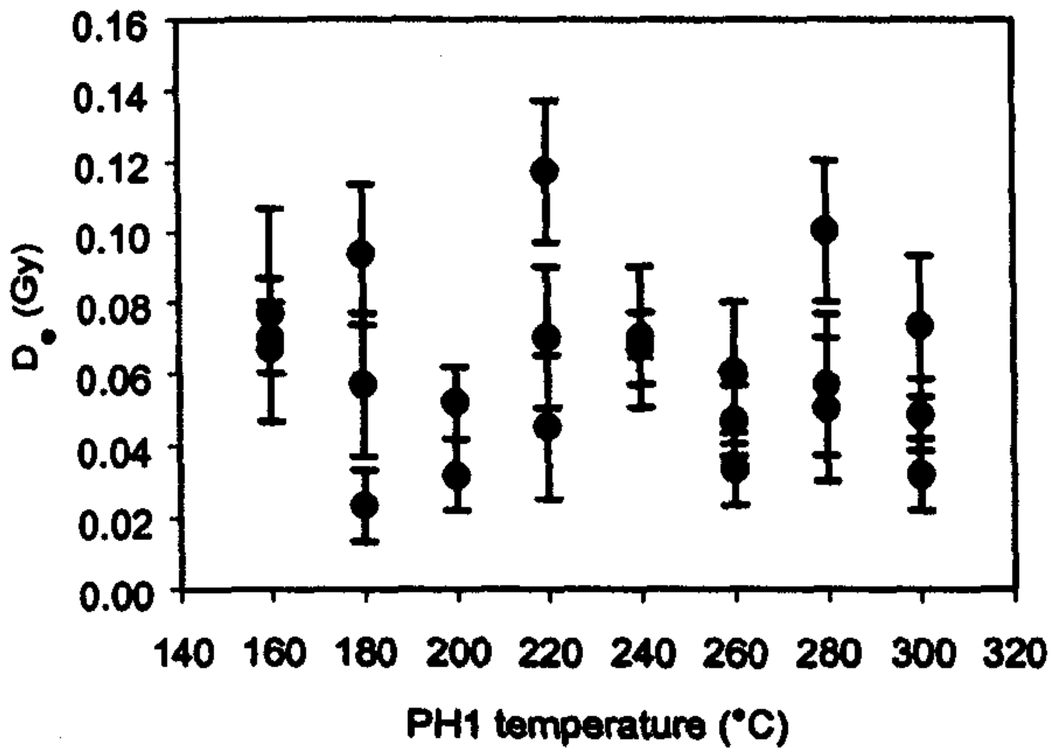

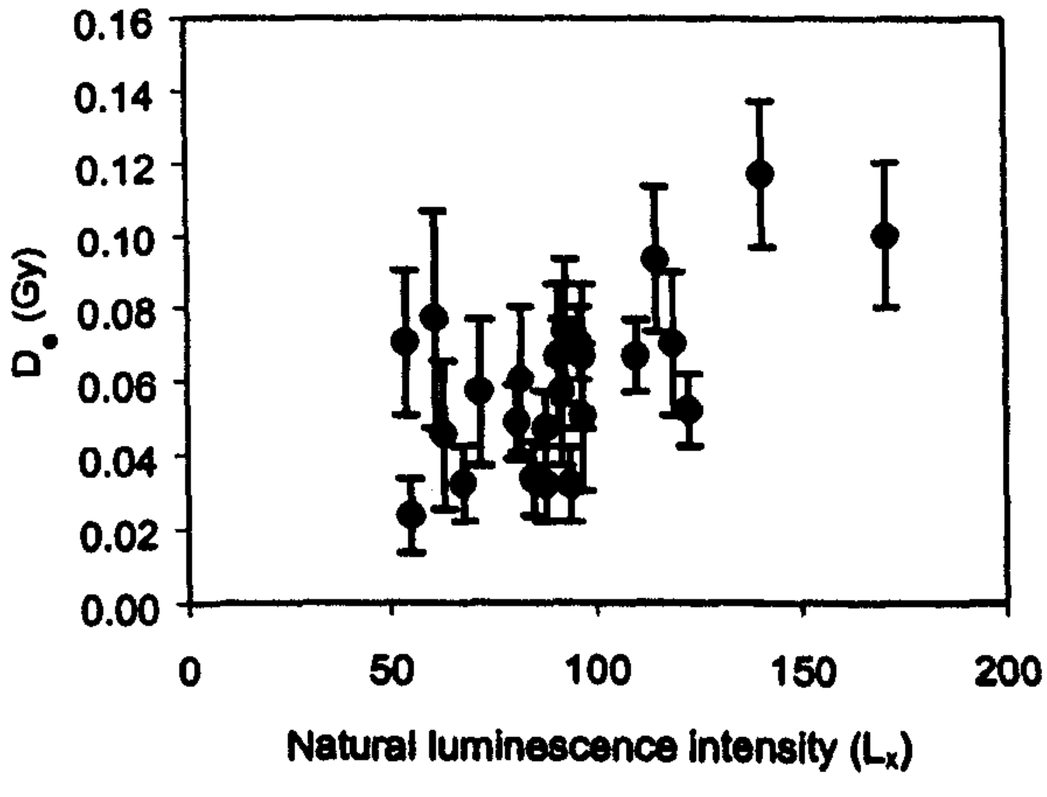

Aber/28-IN9

Exposure: surface (tube)

Average: mean

$D_e = 0.060 \pm 0.005$ Gy

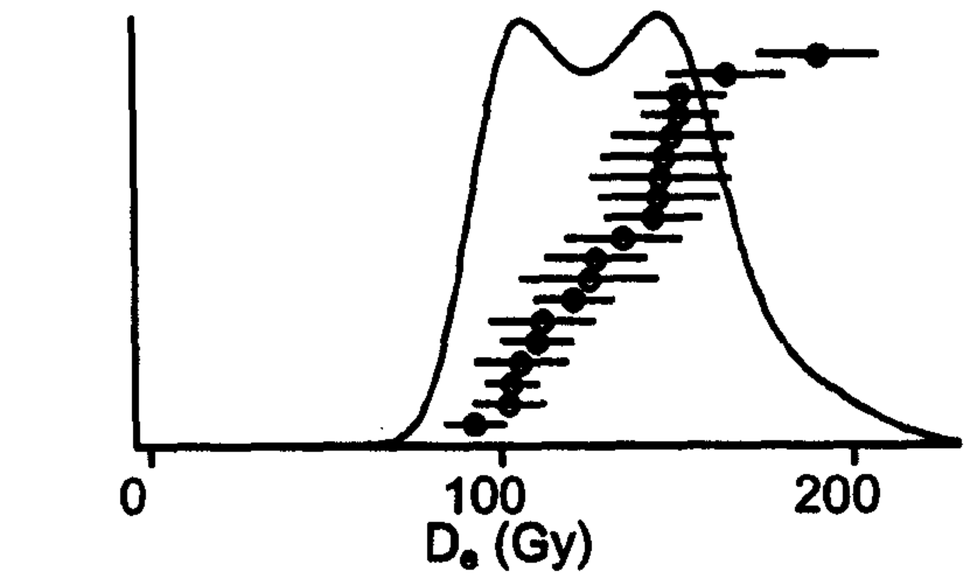

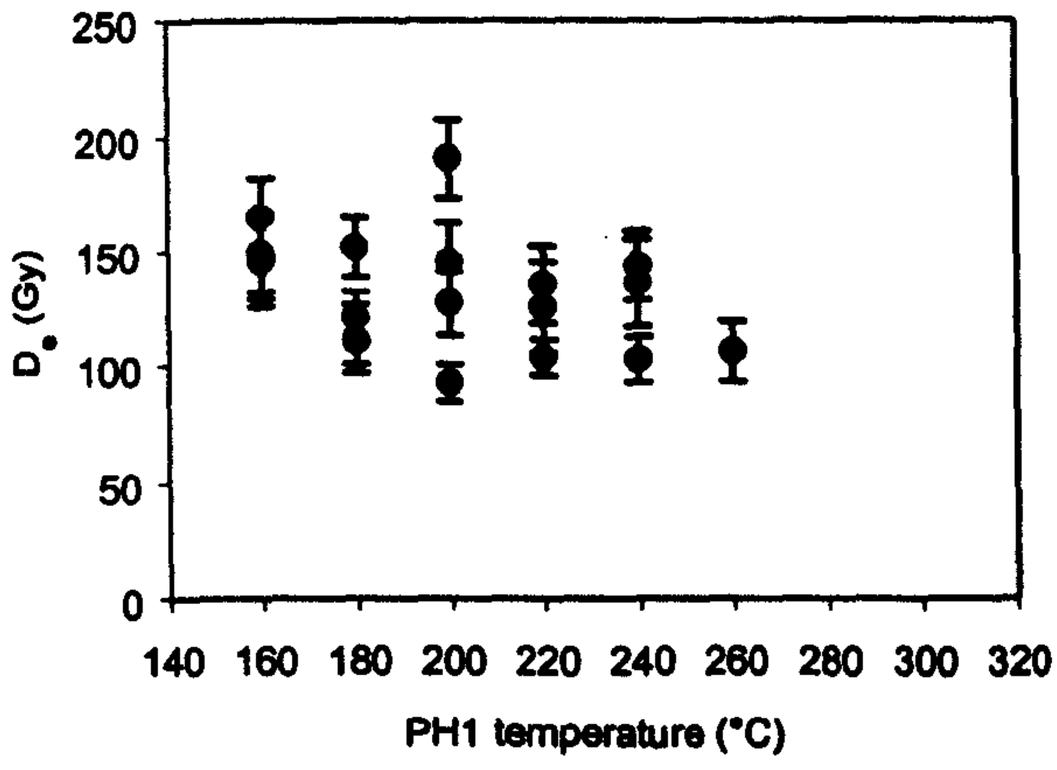

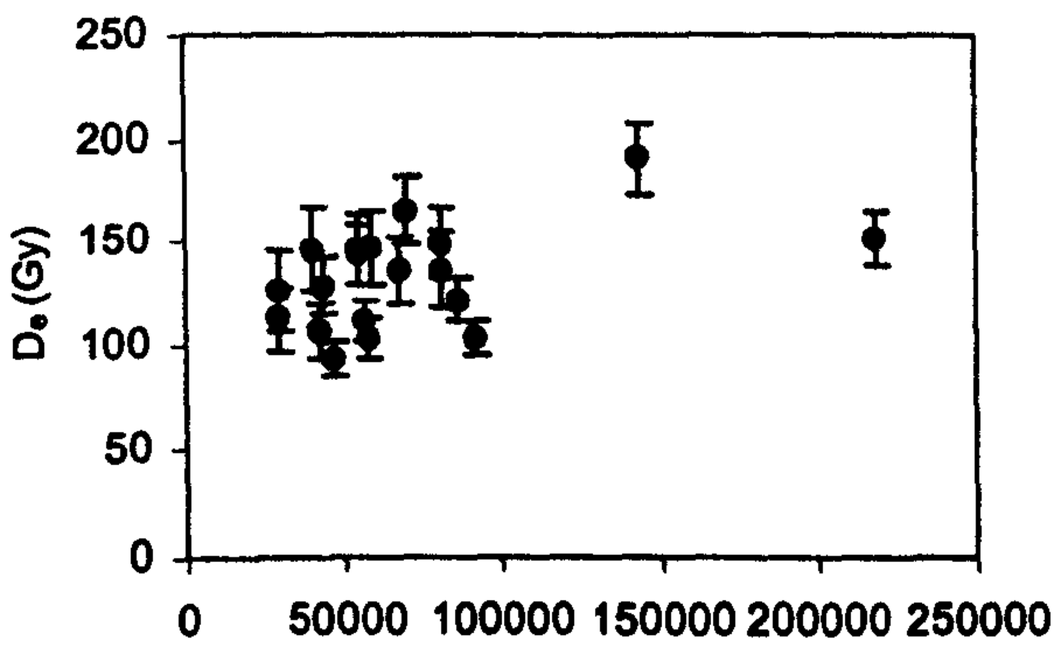

Aber/28-IN11

Exposure: cliff (block)

Average: median

D_e = 133 ± 6 Gy

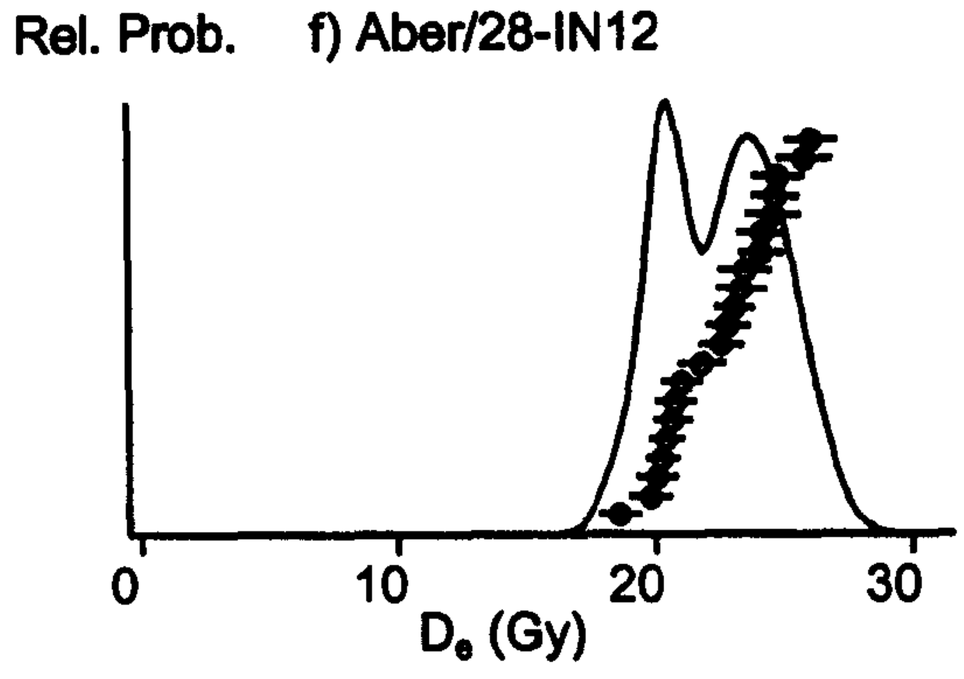

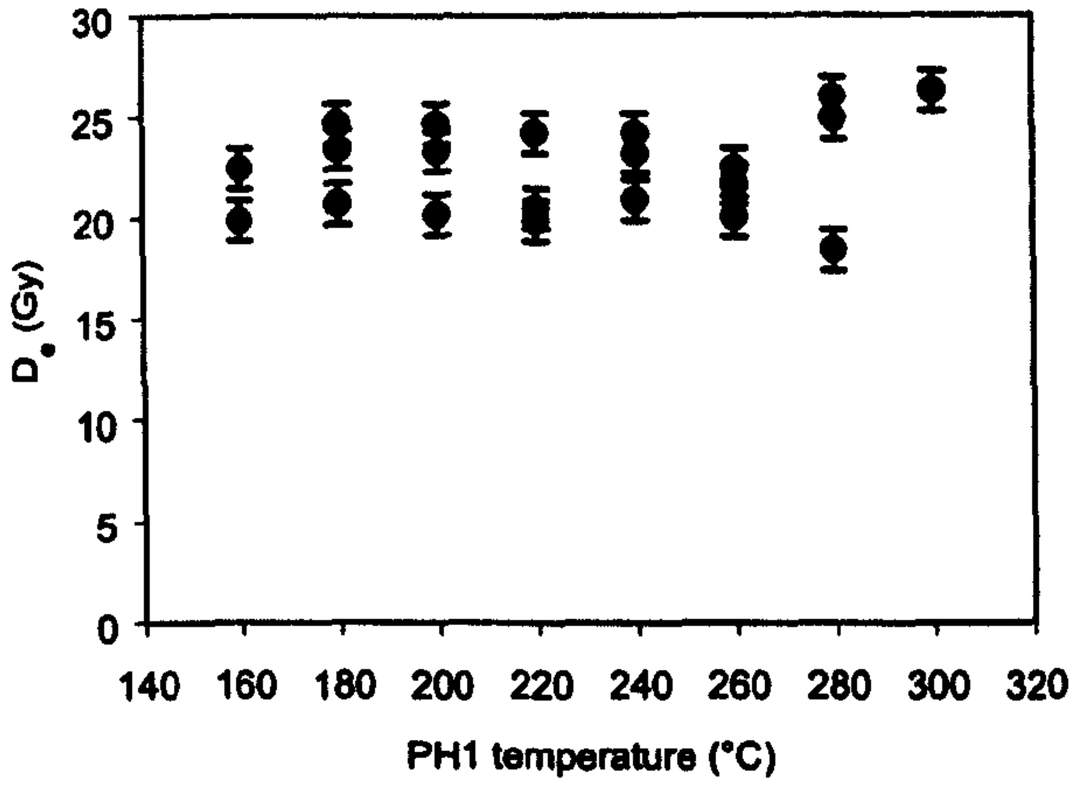

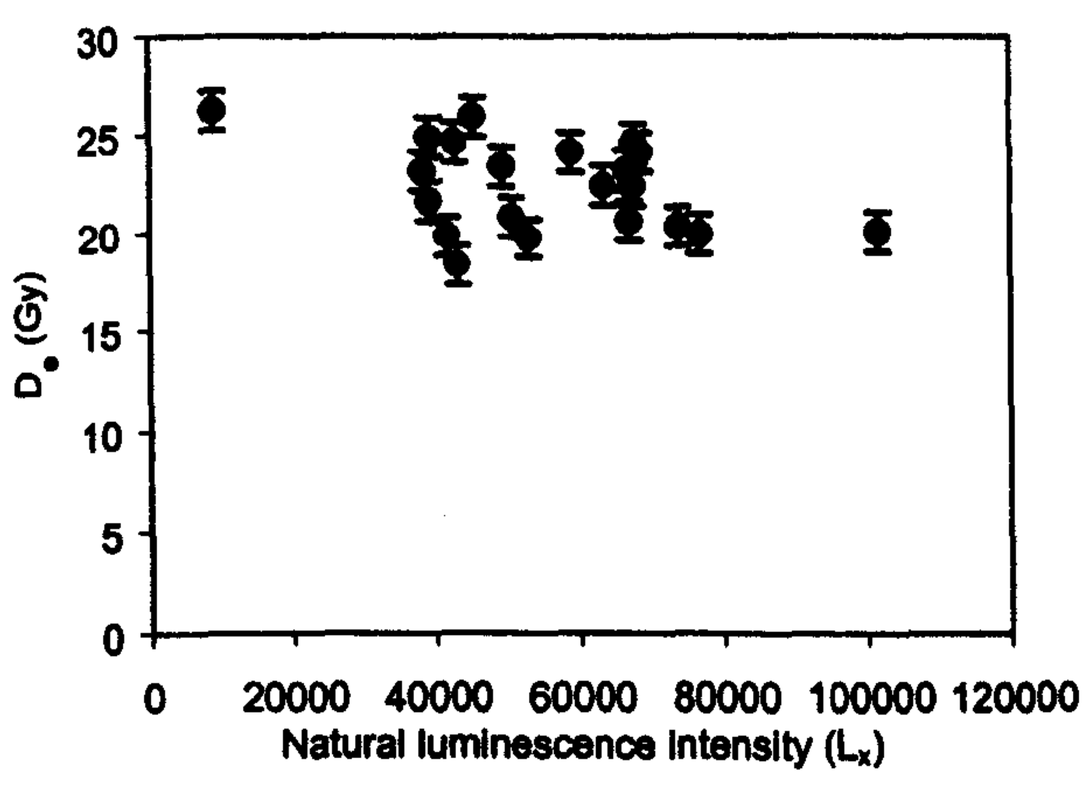

Aber/28-IN12

Exposure: cliff (block)

Average: mean

D_e = 22.4 ± 0.5 Gy

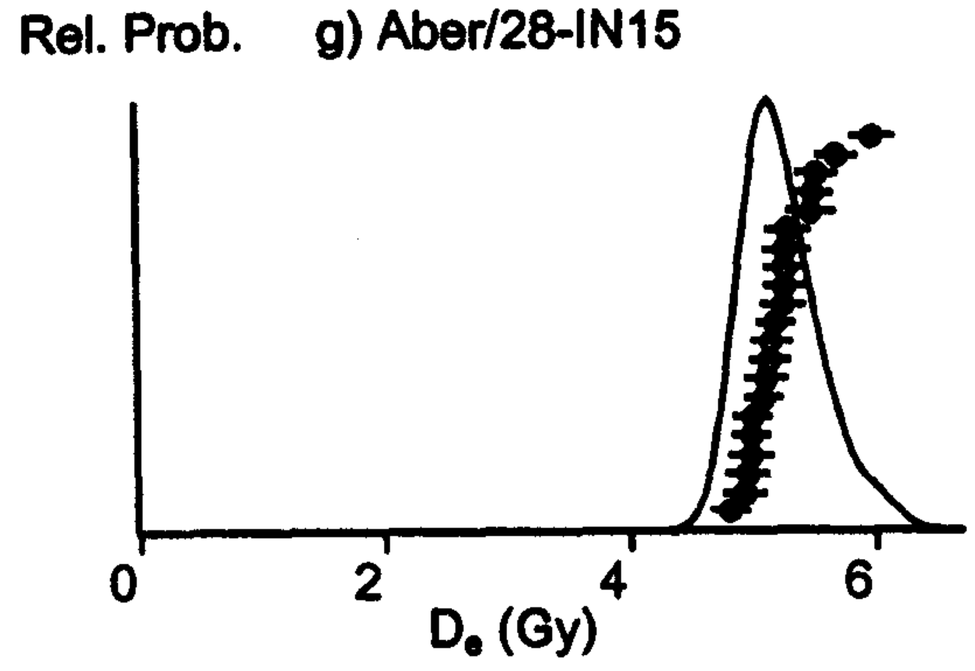

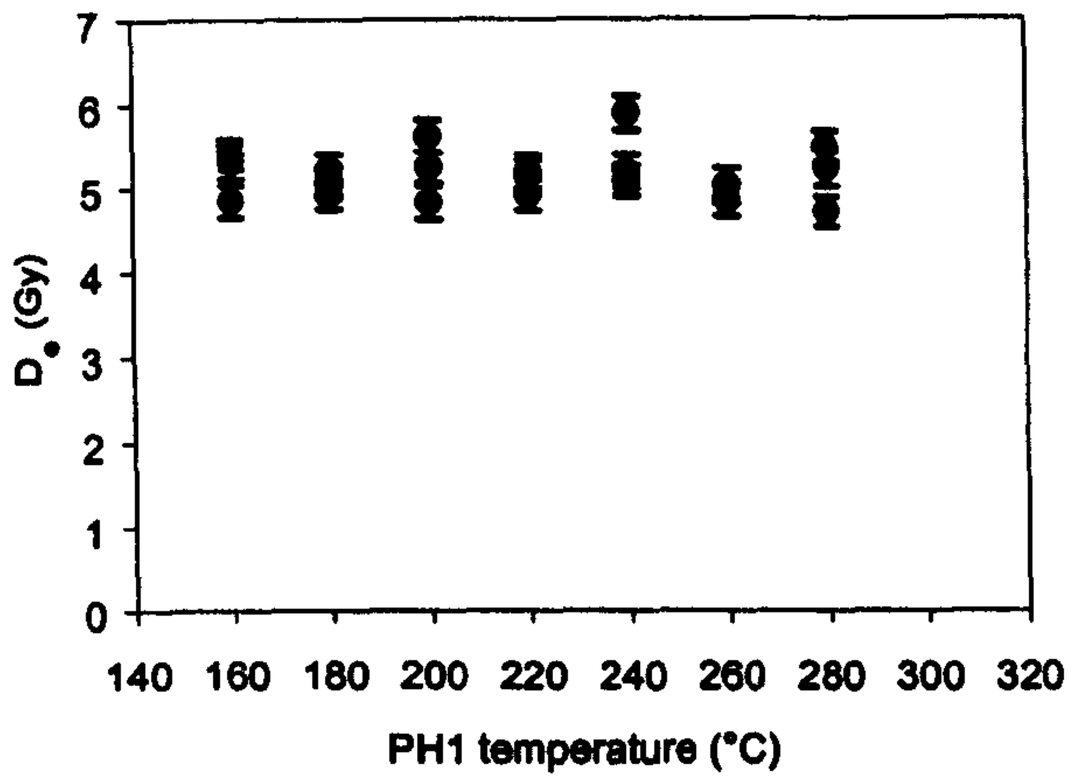

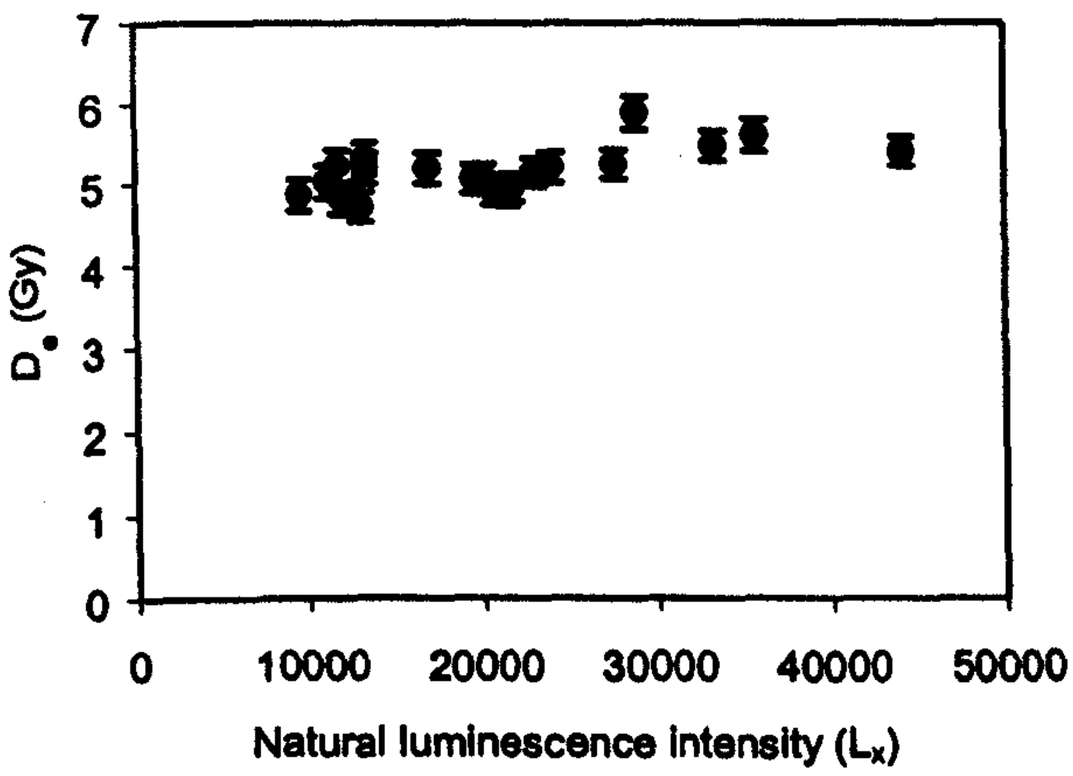

Aber/28-IN15

Exposure: pit (tube)

Average: mean

$D_e = 5.16 \pm 0.06$ Gy

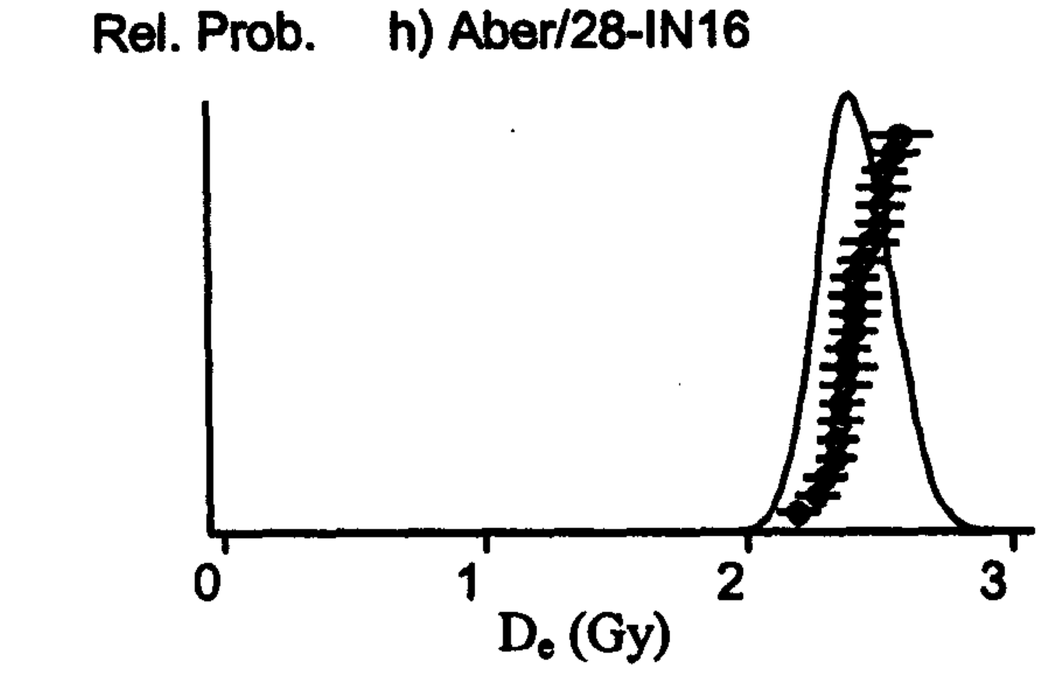

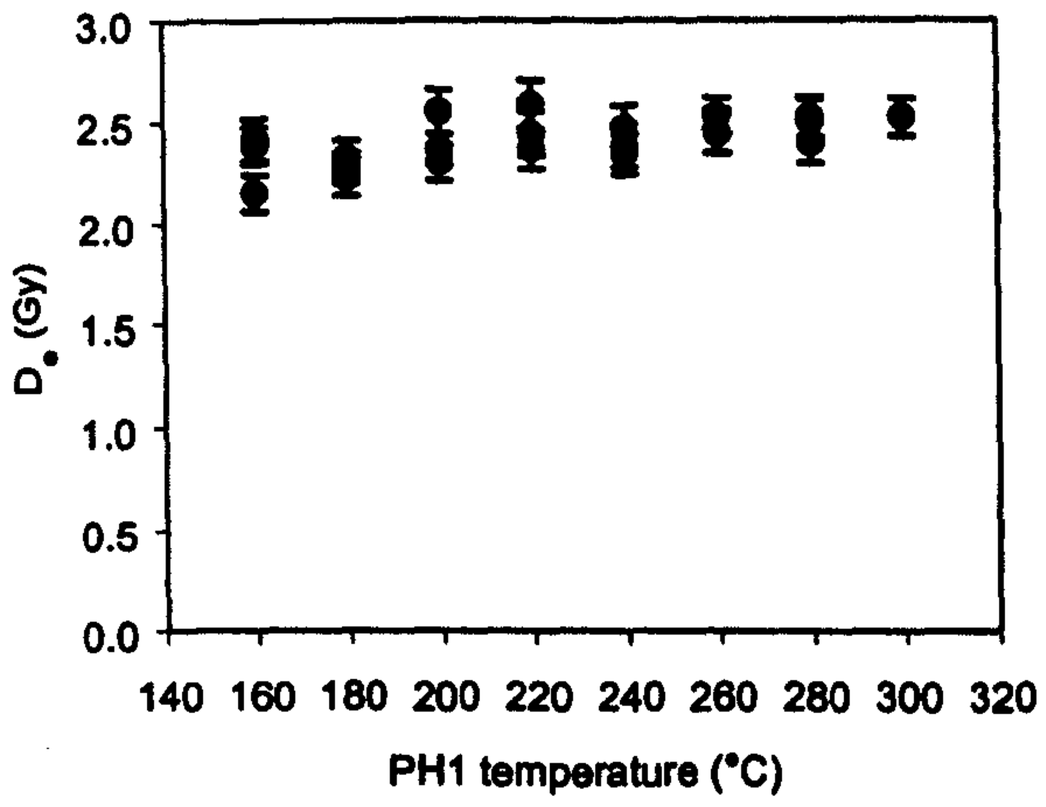

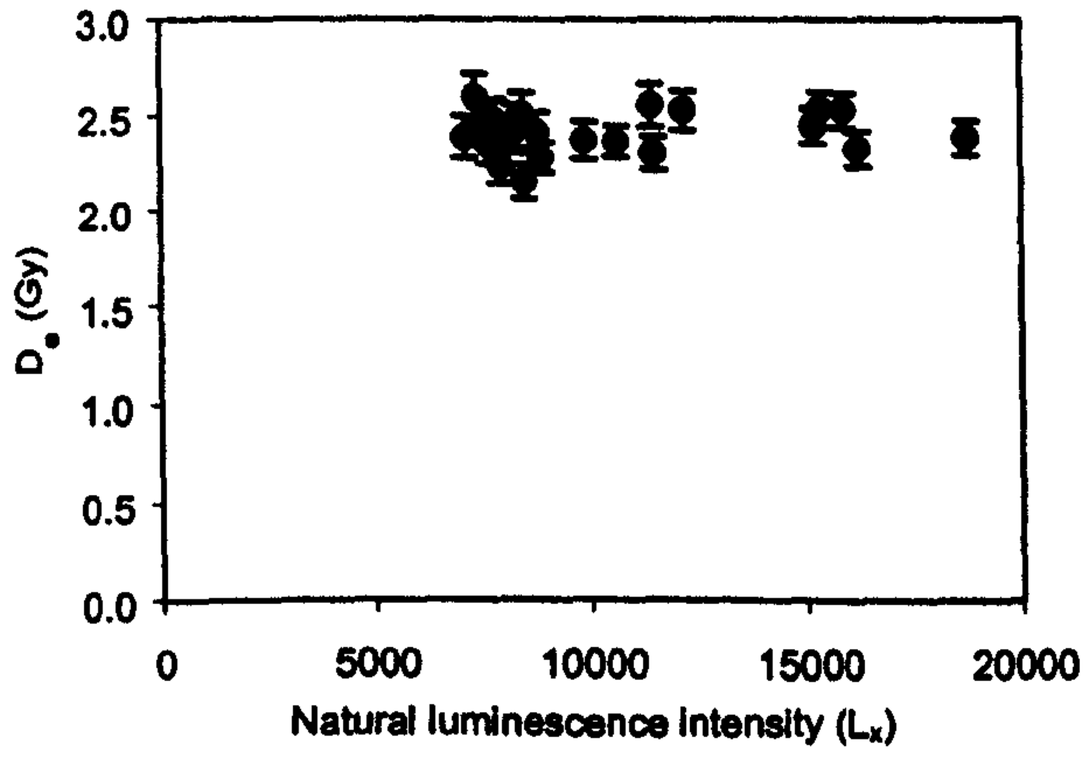

Aber/28-IN16

Exposure: pit (tube)

Average: mean

$D_e = 2.41 \pm 0.02$ Gy

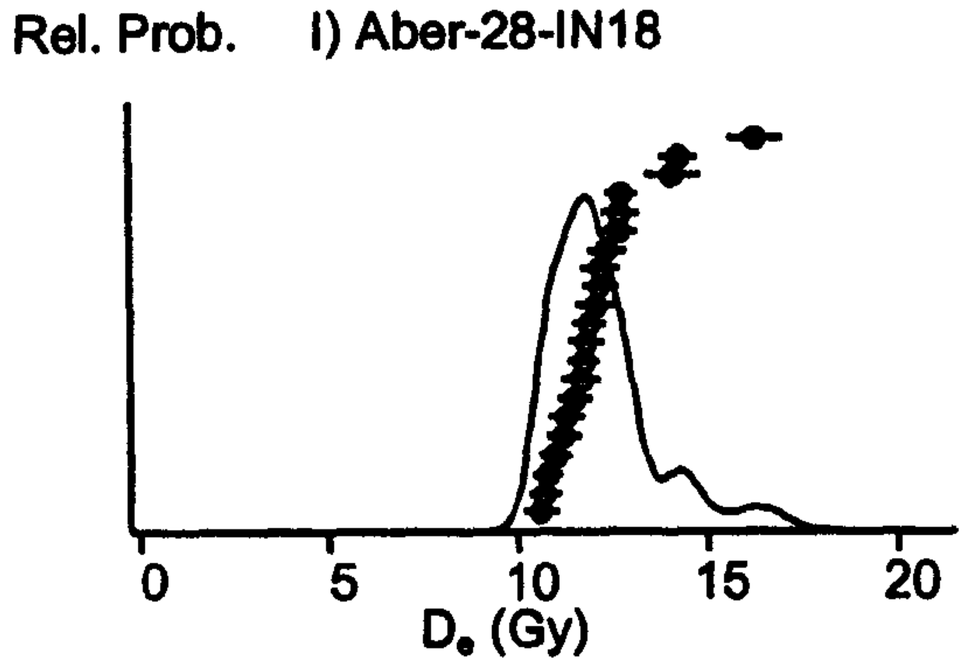

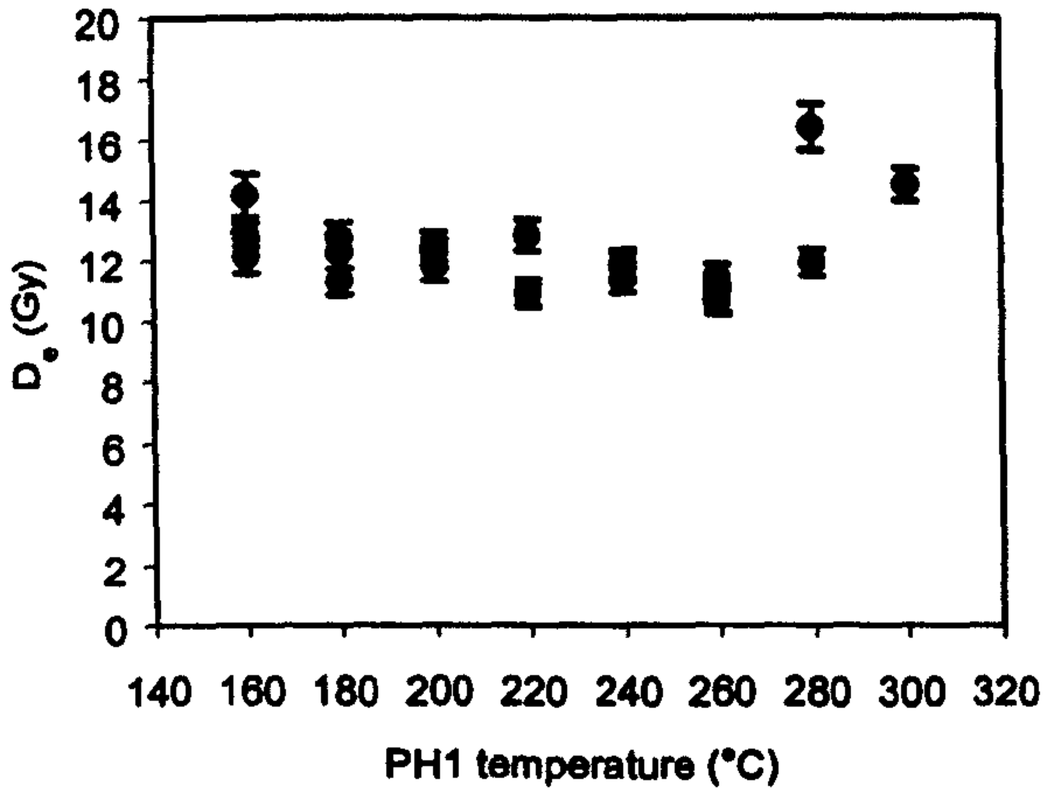

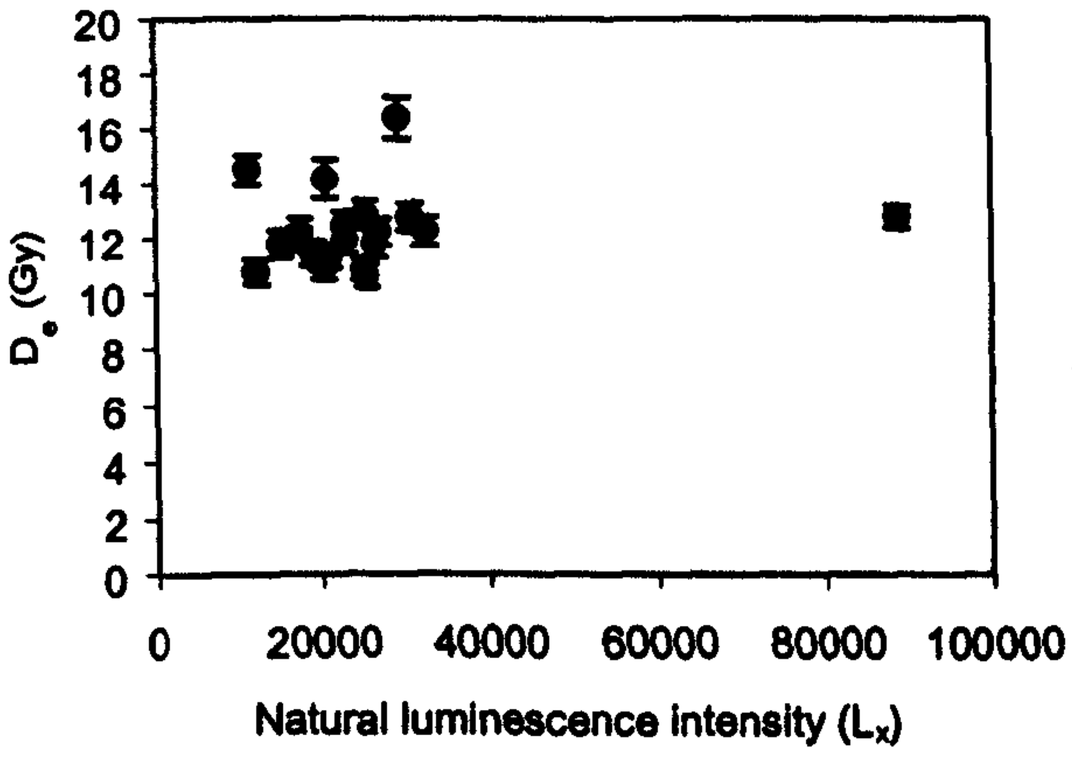

Aber/28-IN18

Exposure: pit (tube)

Average: mean

$D_e = 12.2 \pm 0.3$ Gy

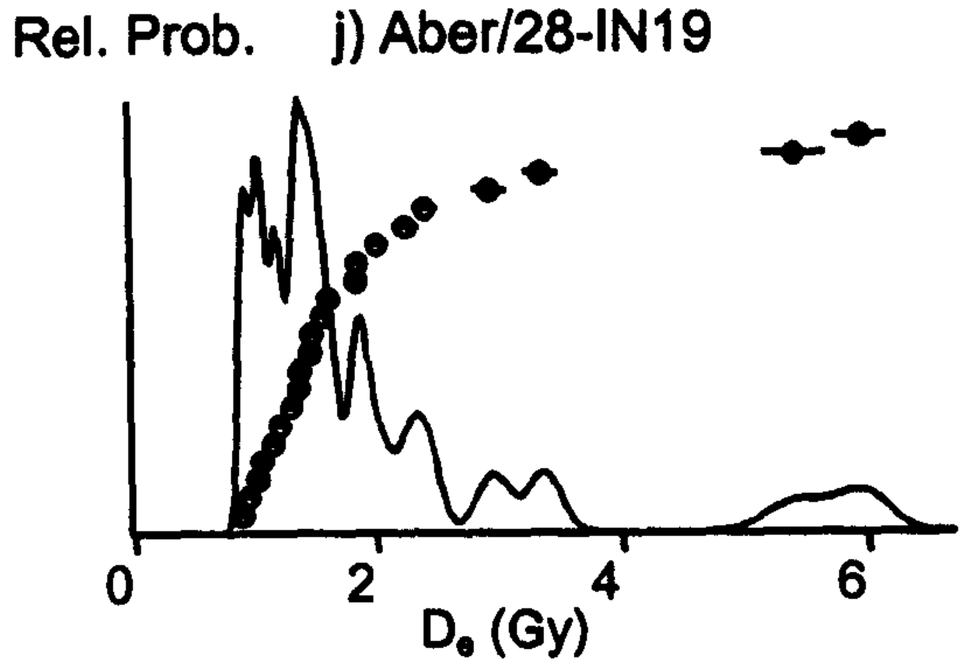

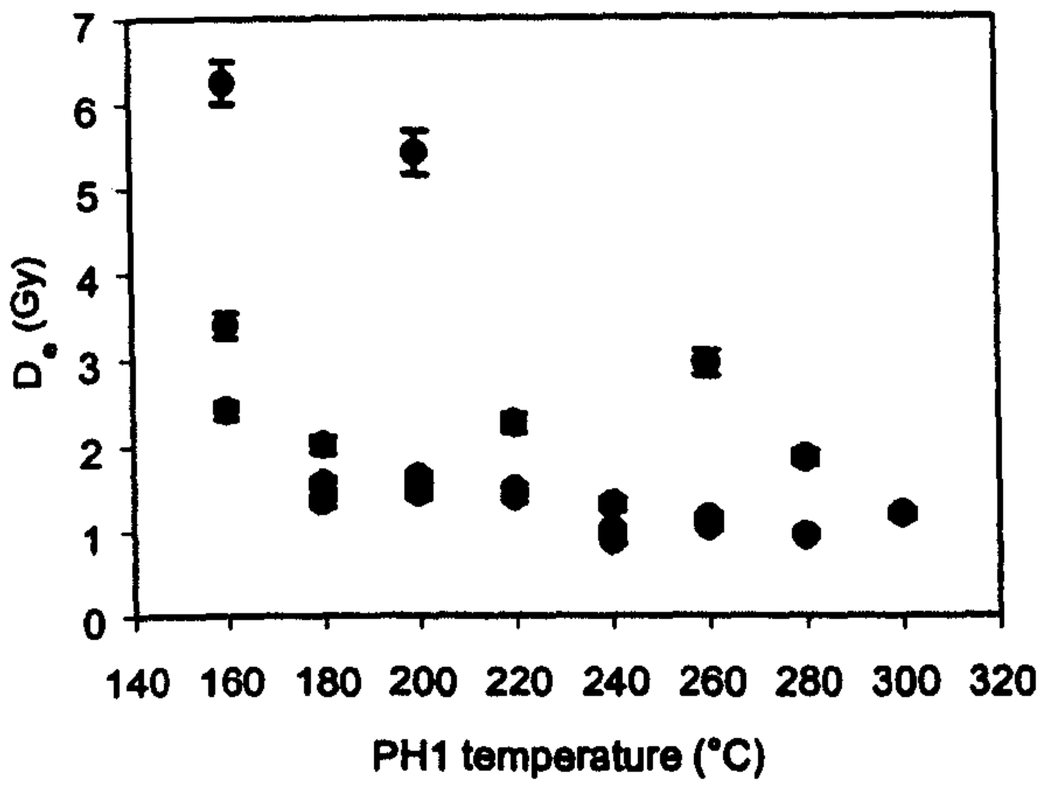

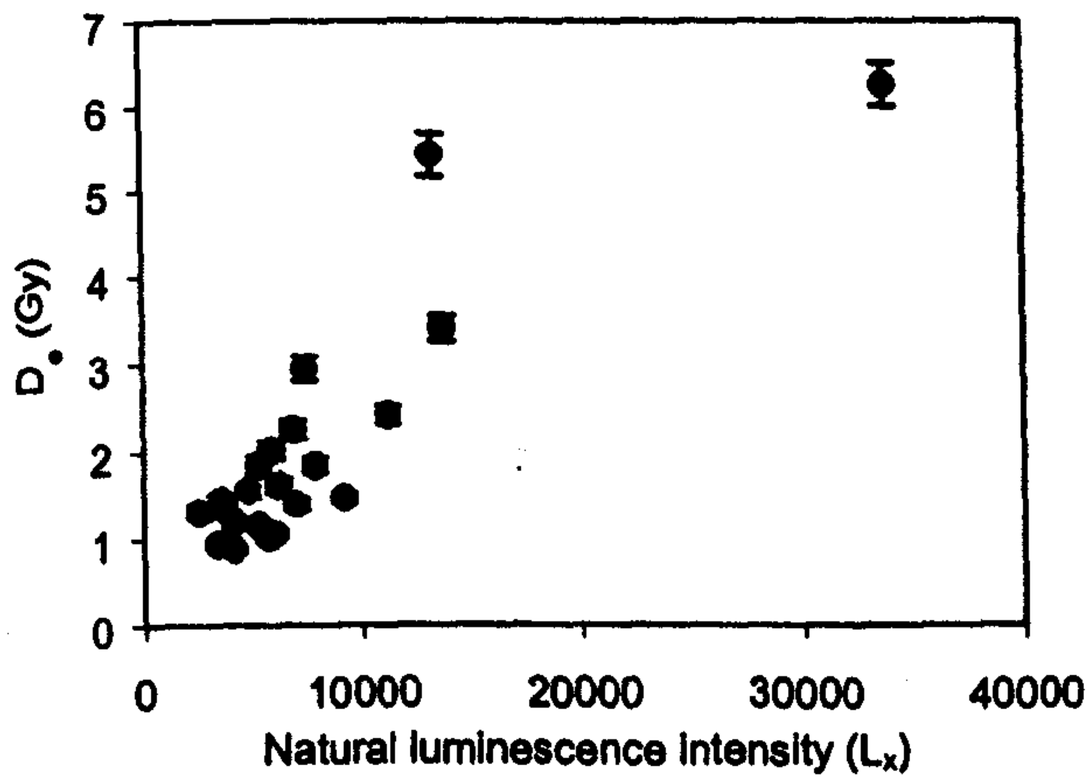

Aber/28-IN19

Exposure: pit (tube)

Average: mean

$D_e = 2.04 \pm 0.30$ Gy

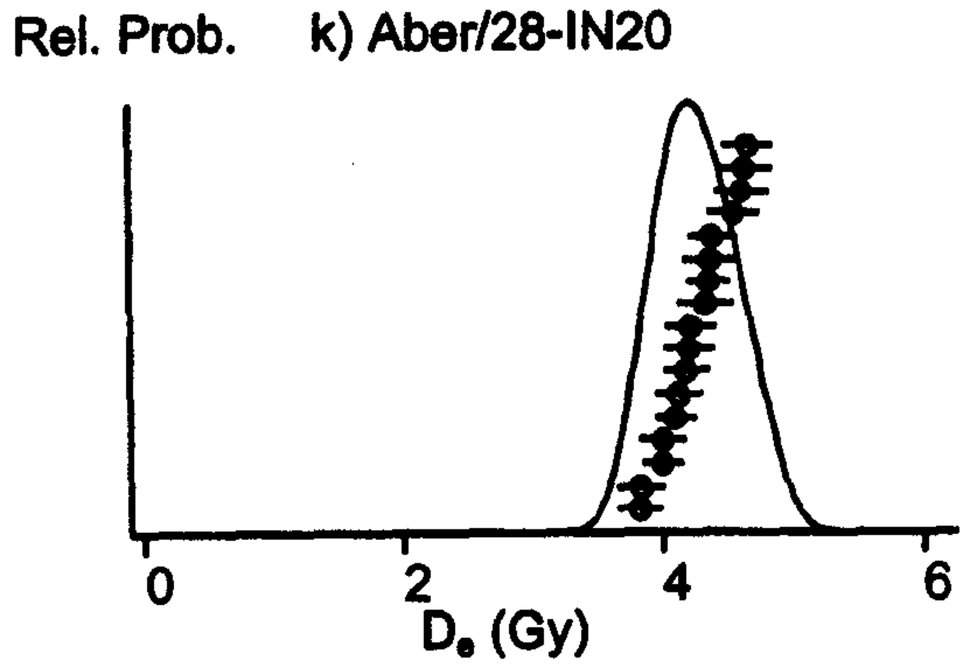

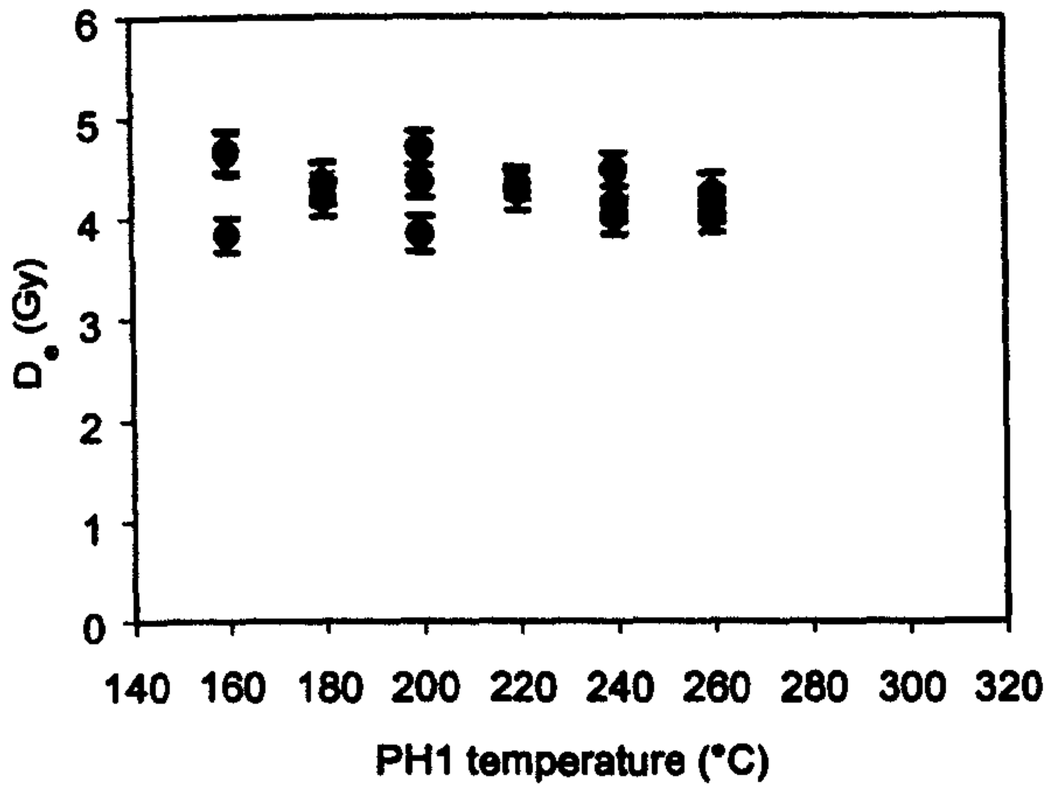

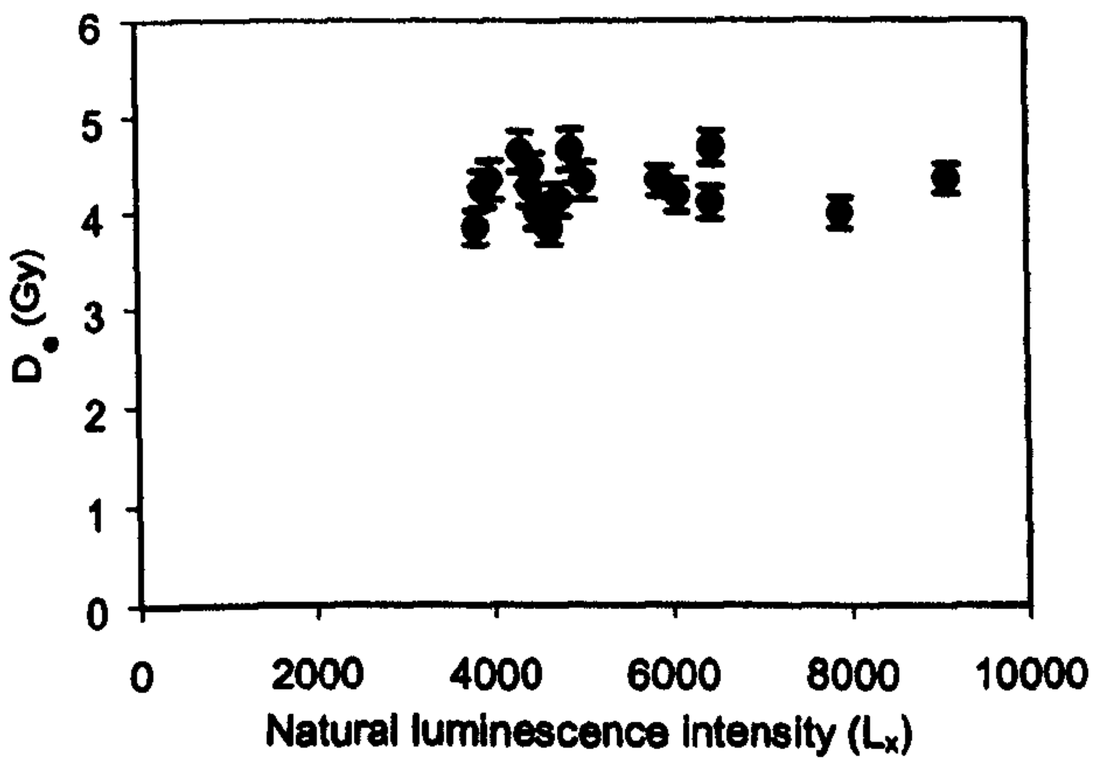

Aber/28-IN20

Exposure: pit (tube)

Average: mean

D_e = 4.28 ± 0.07 Gy

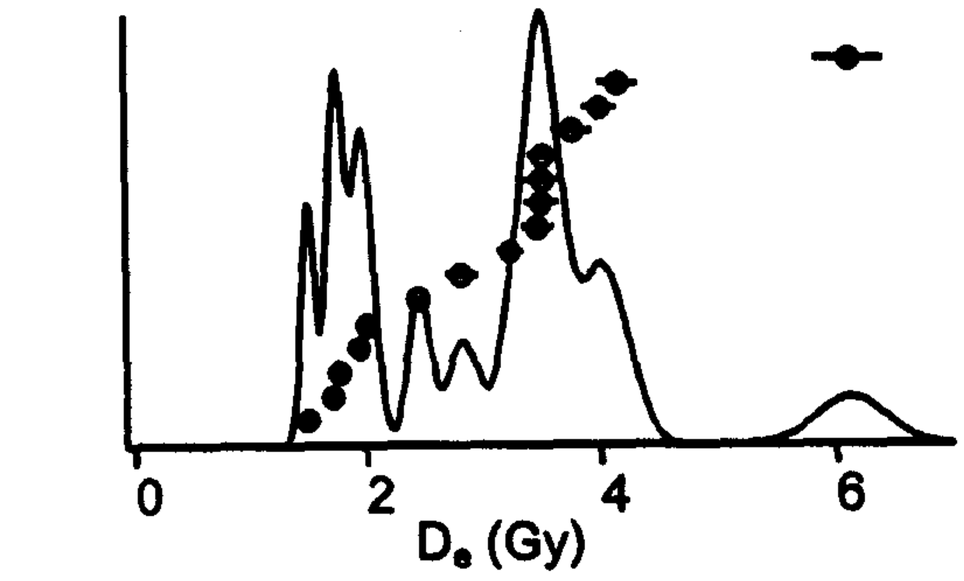

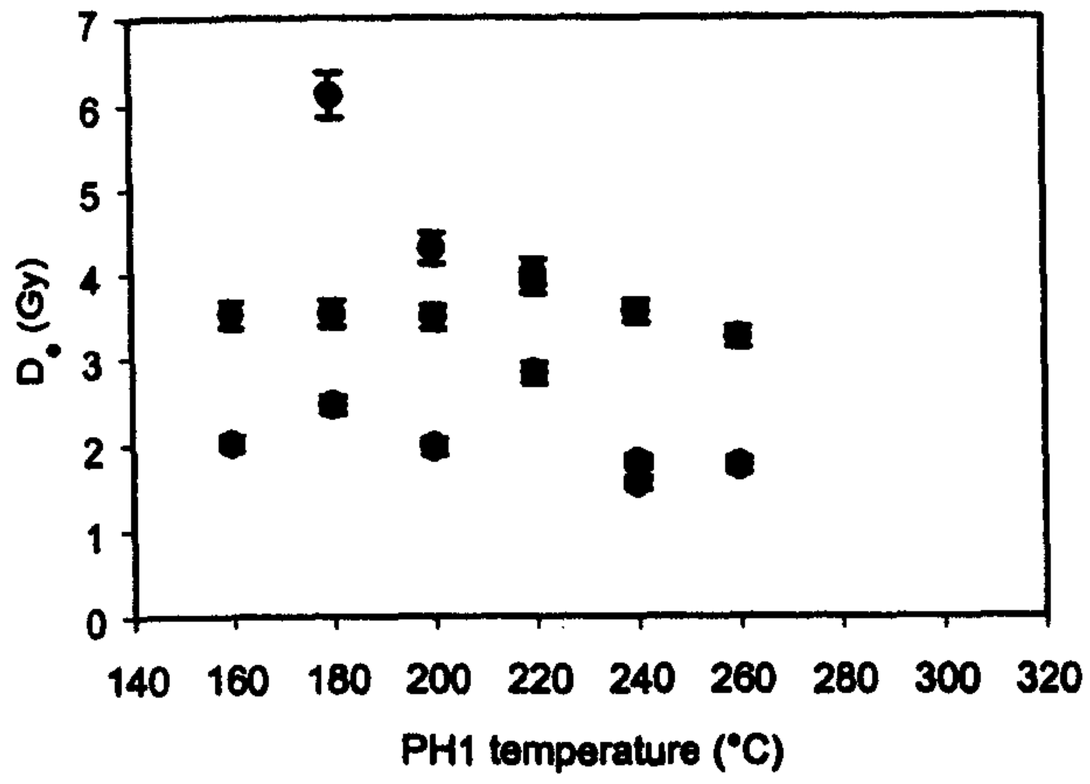

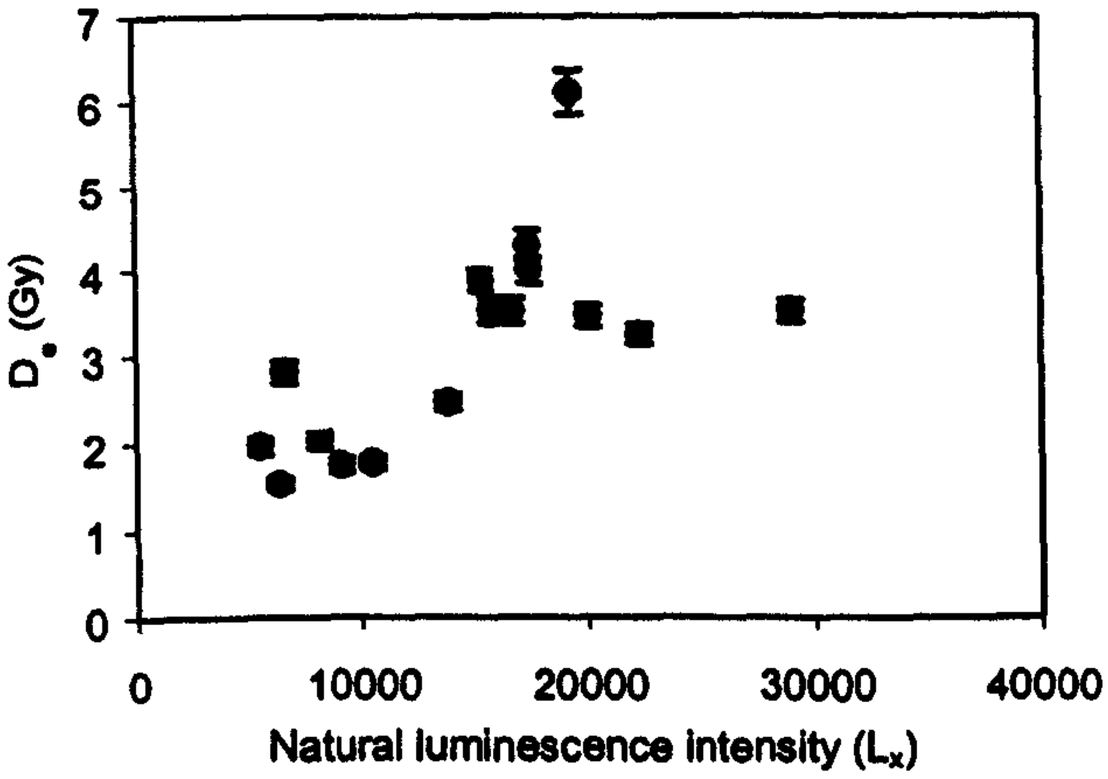

Aber/28-IN21

Exposure: pit (tube)

Average: mean

$D_e = 3.12 \pm 0.30$ Gy

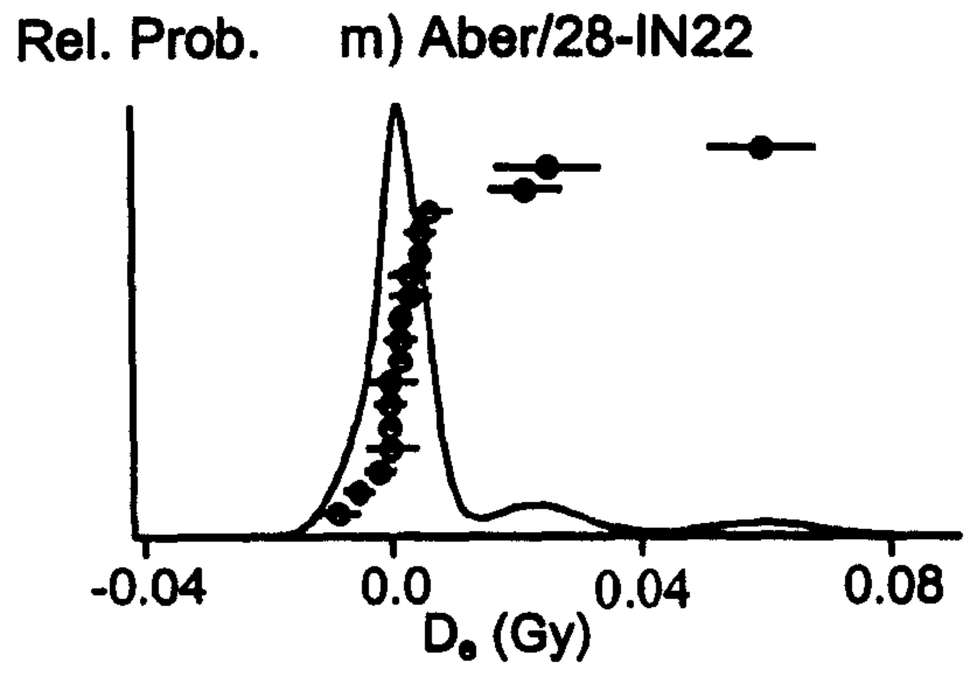

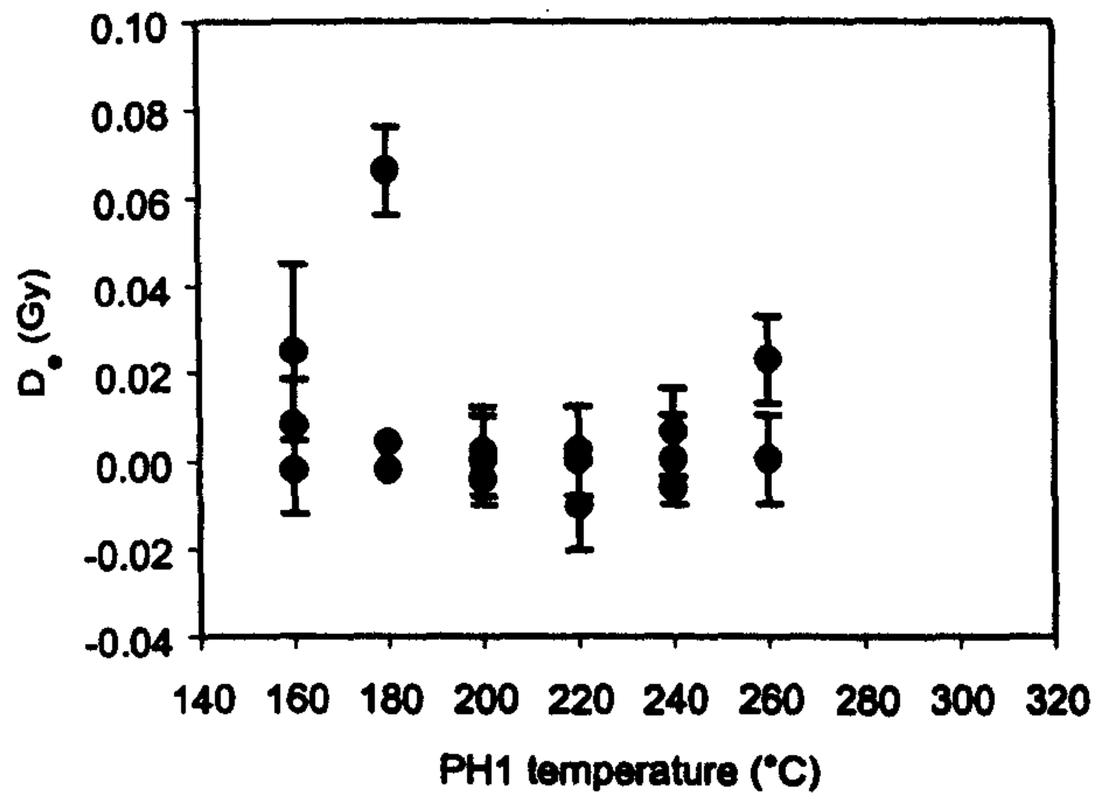

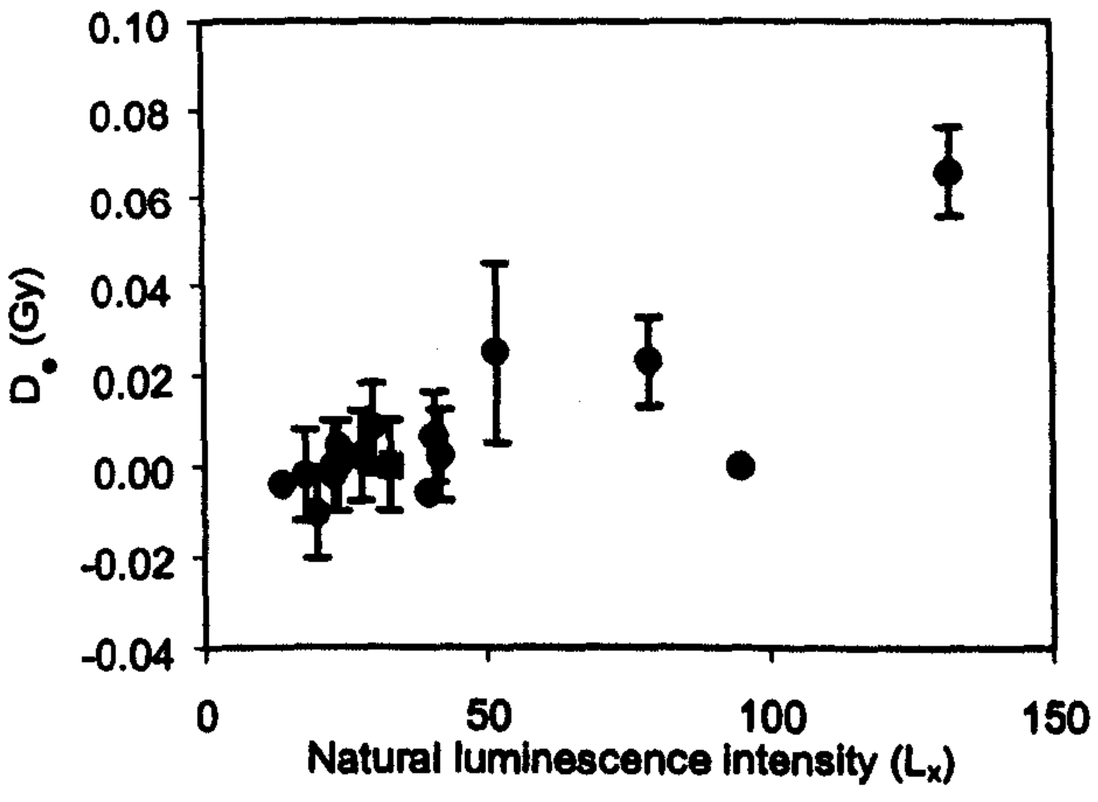

Aber/28-IN22

Exposure: surface (modern)

Average: mean

D_e = 0.006 ± 0.004 Gy

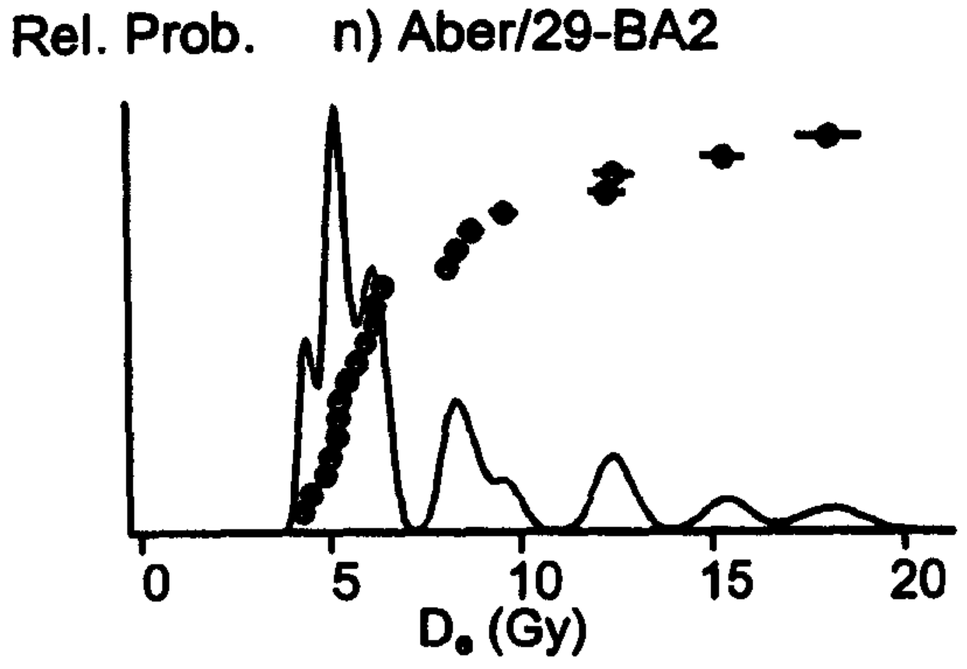

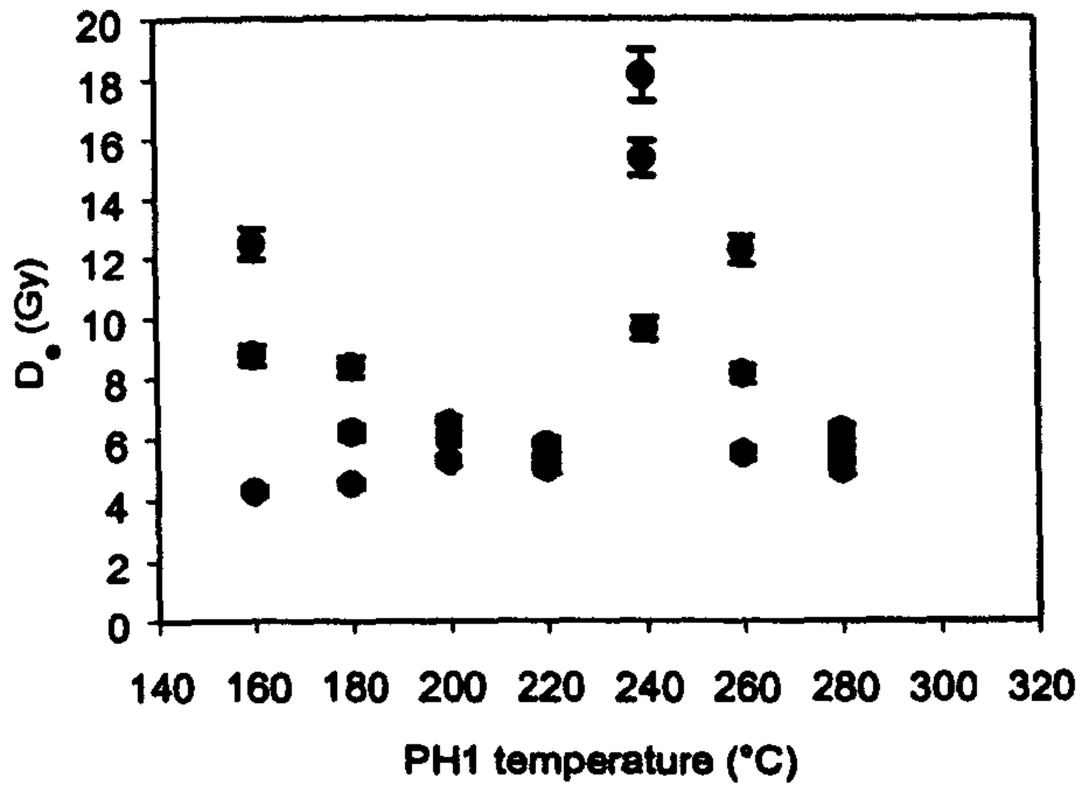

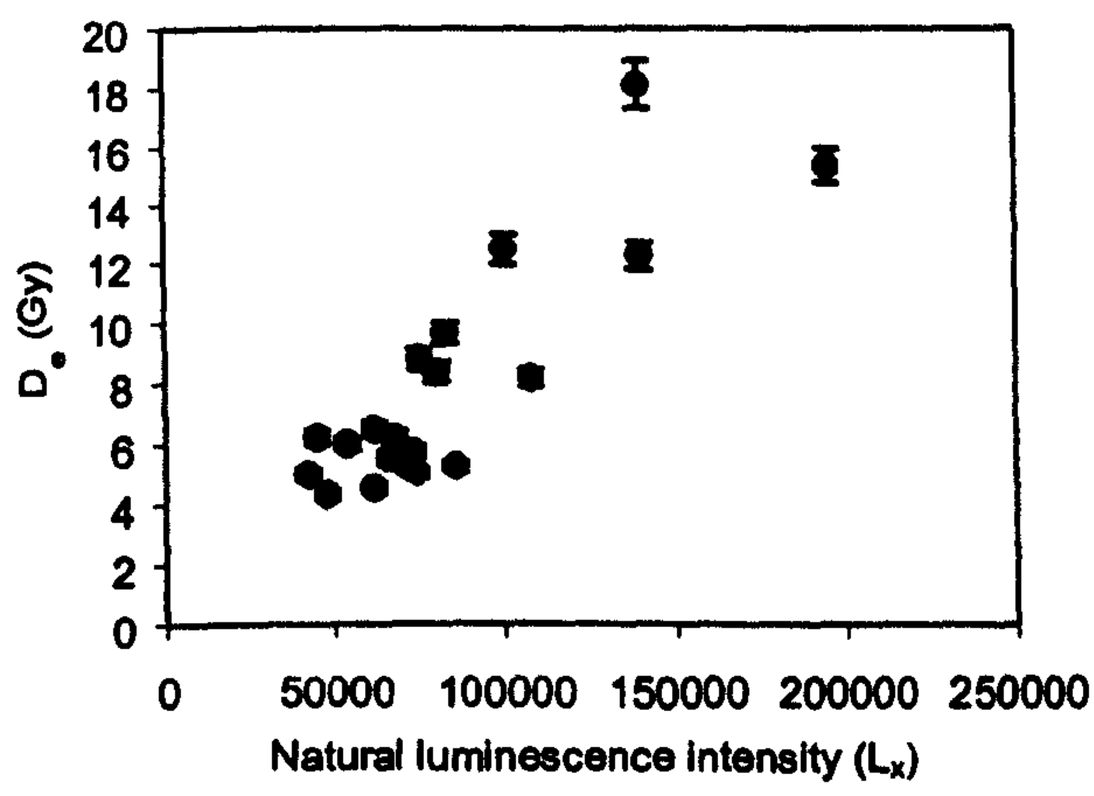

Aber/29-BA2

Exposure: Beachrock (block)

Average: mean

$D_e = 7.83 \pm 0.83$ Gy

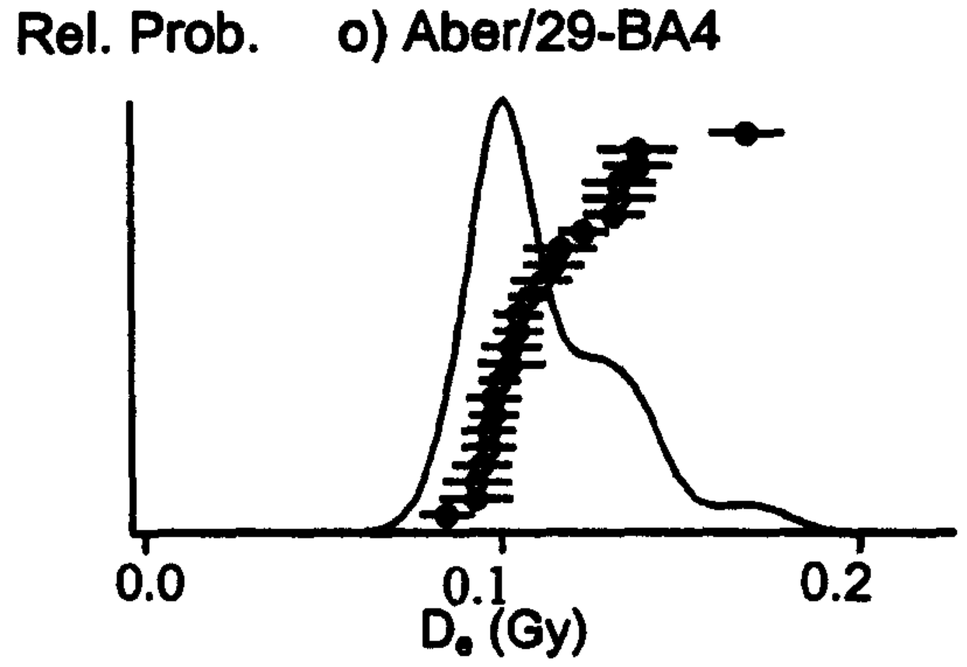

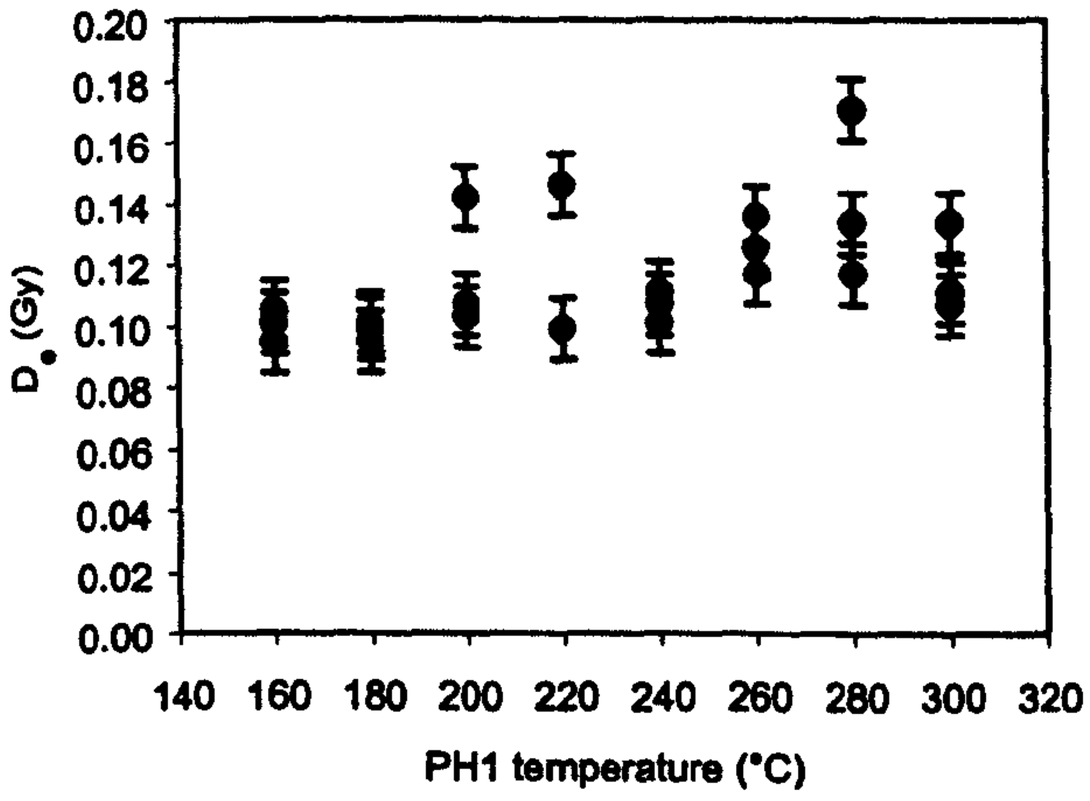

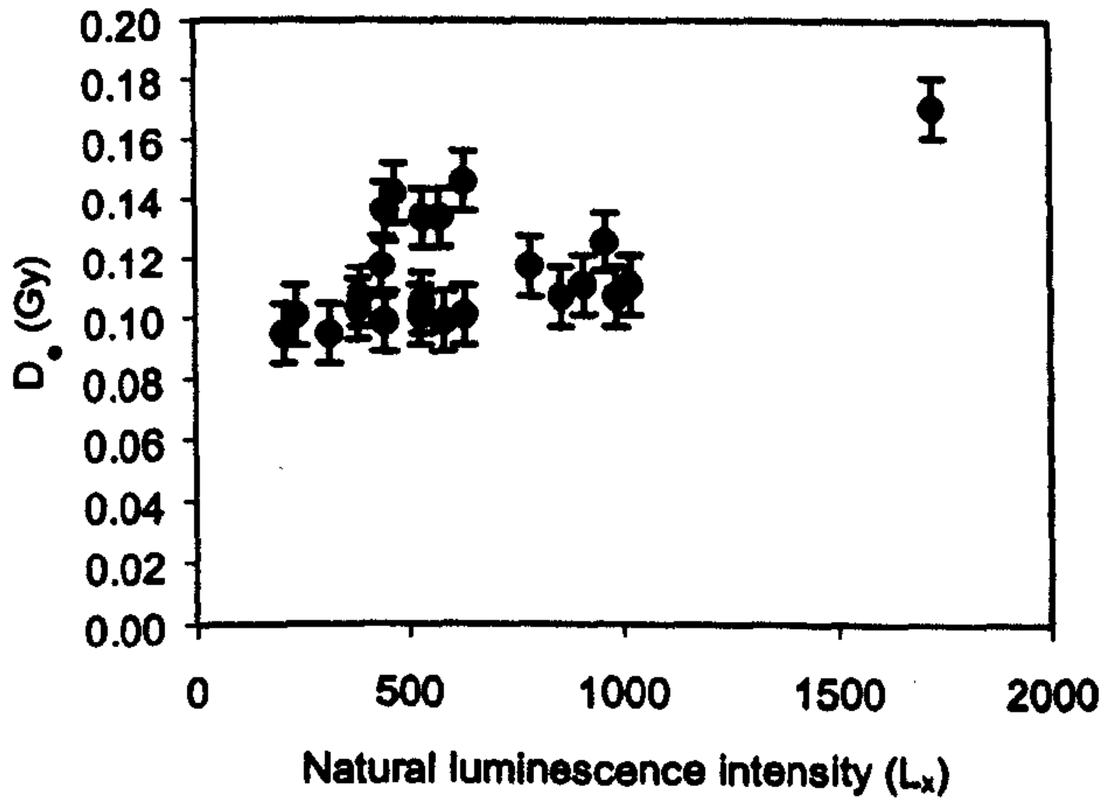

Aber/29-BA4

Exposure: pit (tube)

Average: mean

$D_e = 0.114 \pm 0.004$ Gy

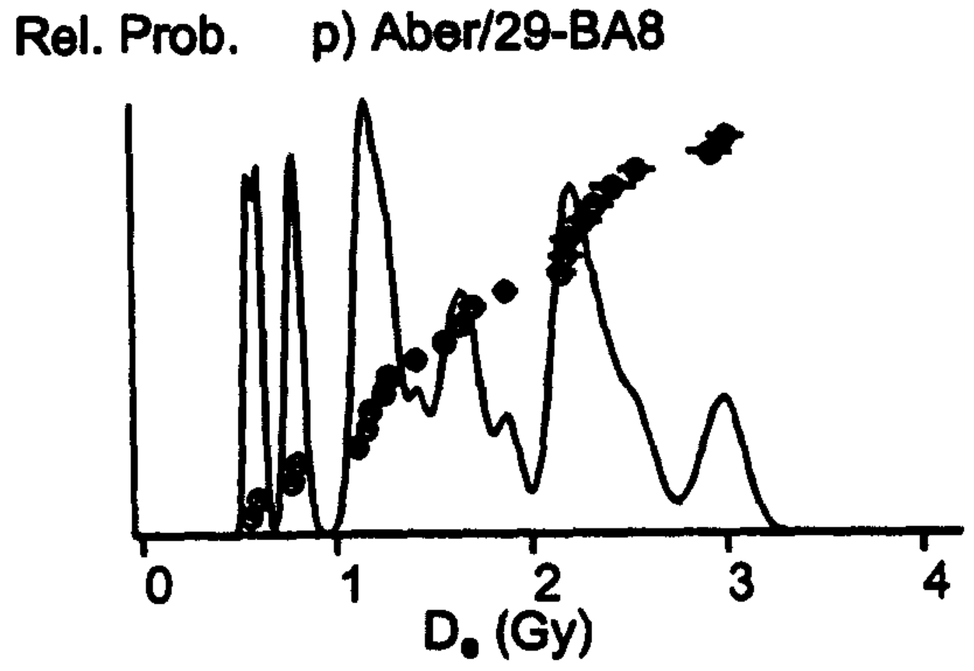

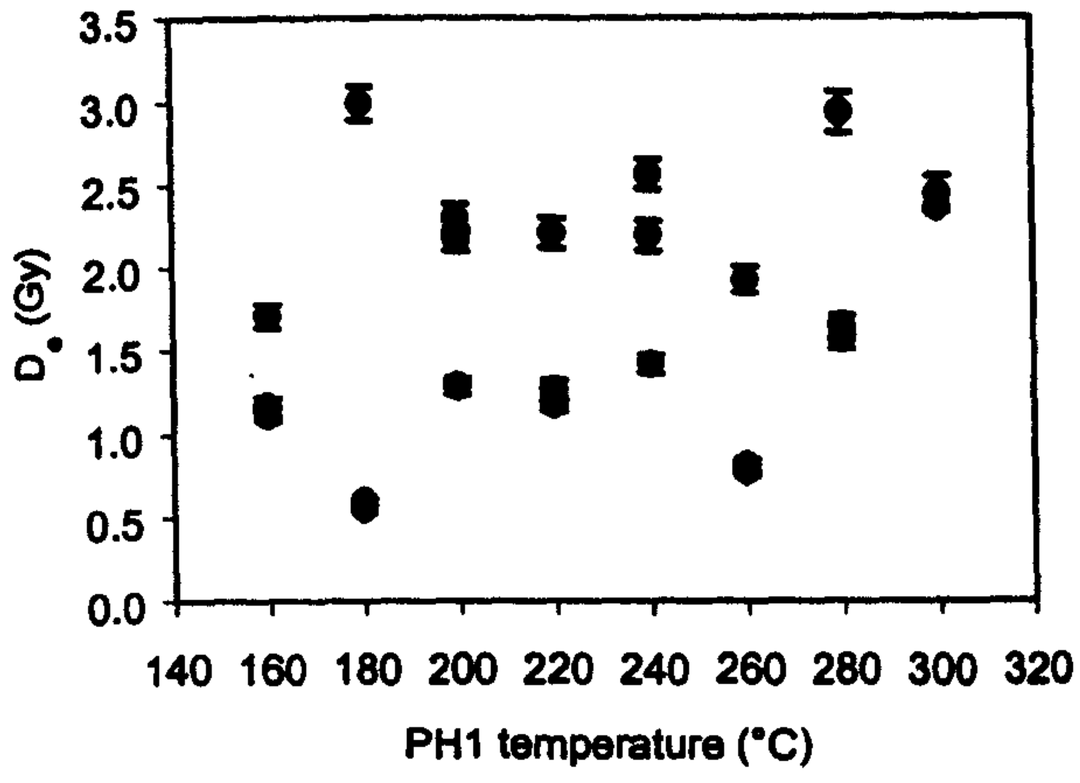

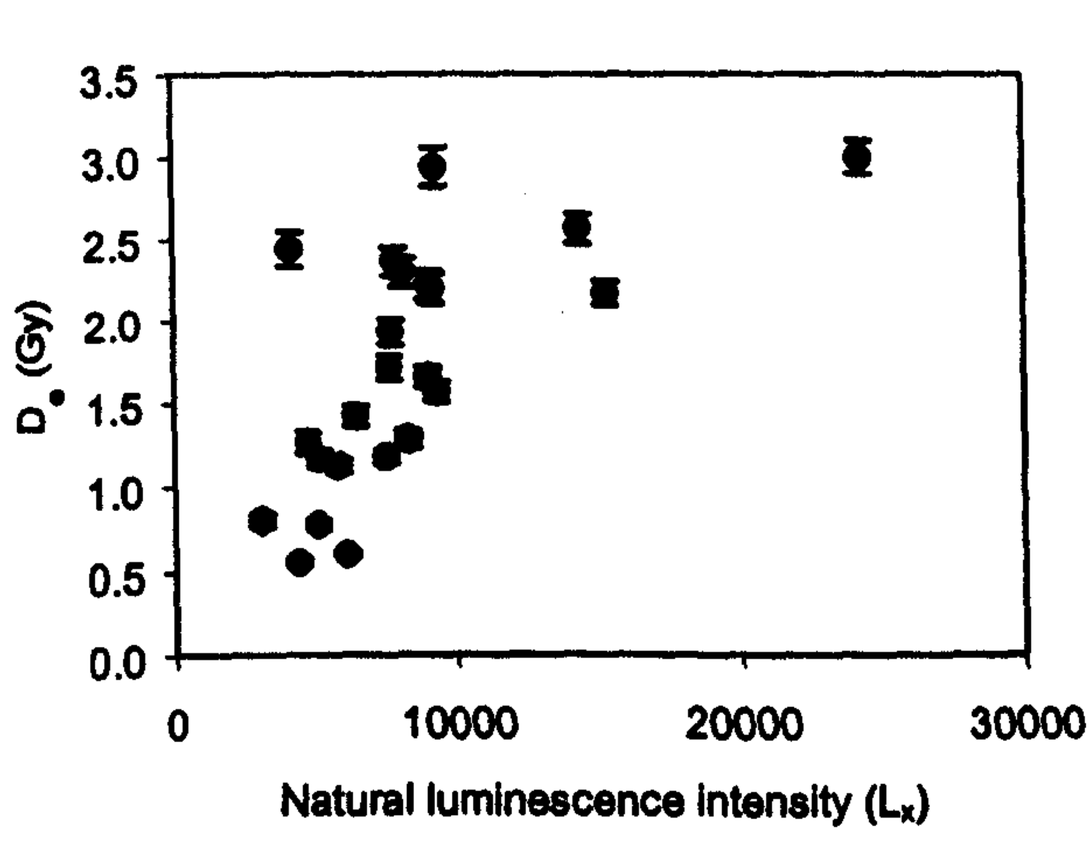

Aber/29-BA8

Exposure: beachrock (block)

Average: mean

$D_e = 1.70 \pm 0.15$ Gy

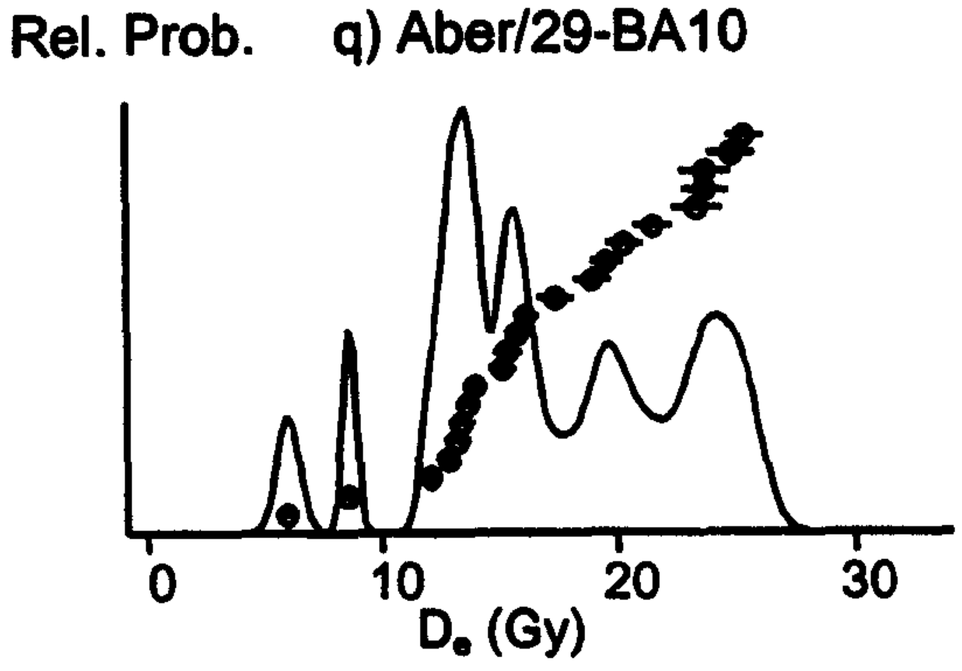

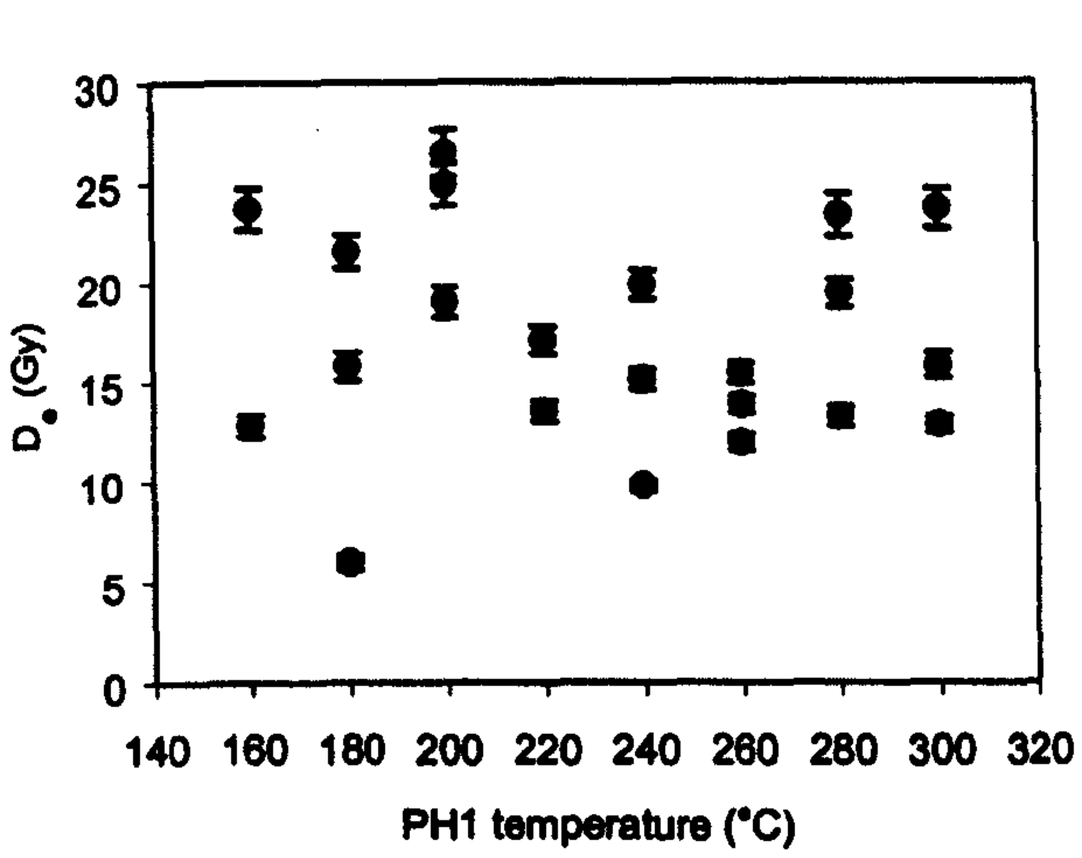

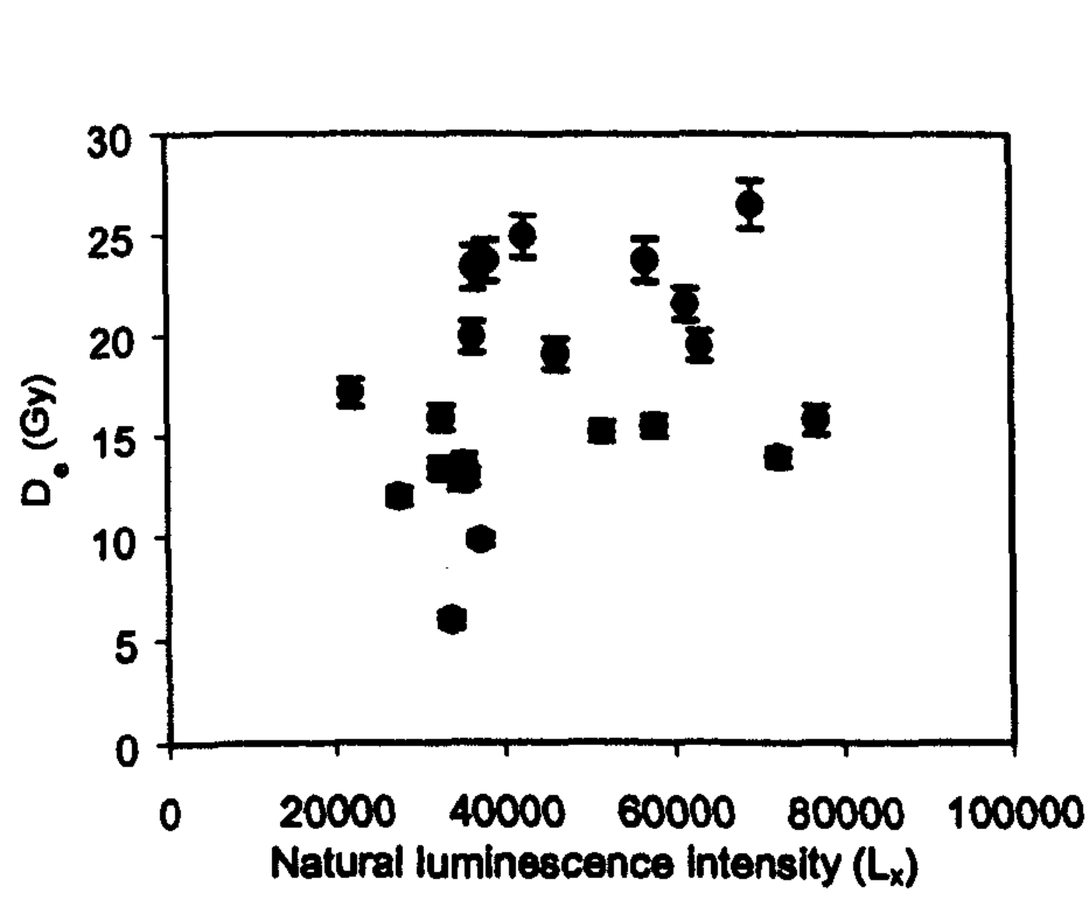

Aber/29-BA10

Exposure: pit (tube)

Average: mean

$D_e = 17.1 \pm 1.1$ Gy

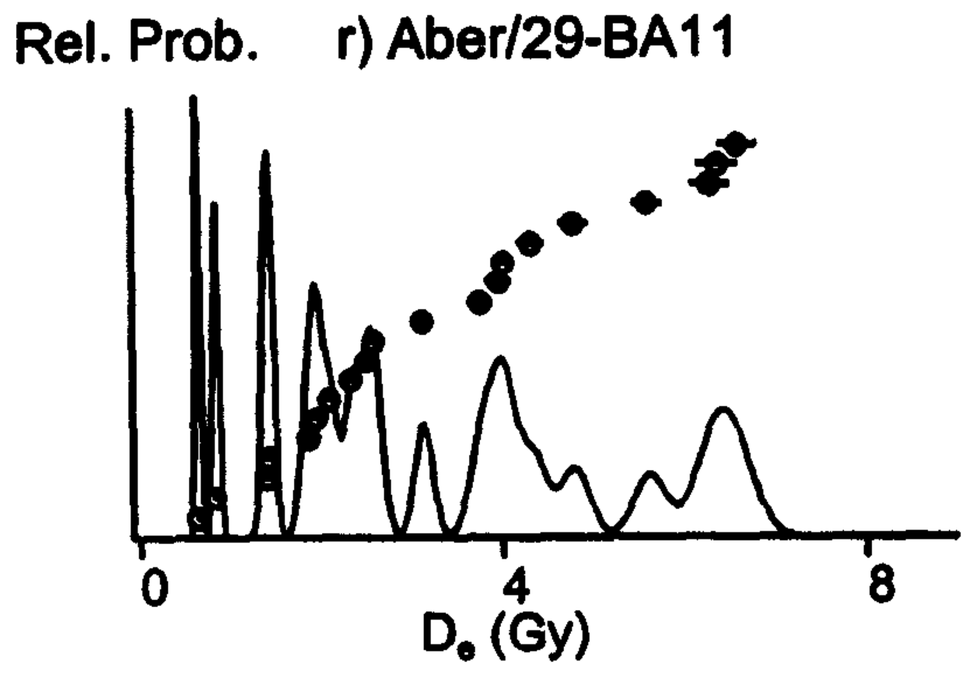

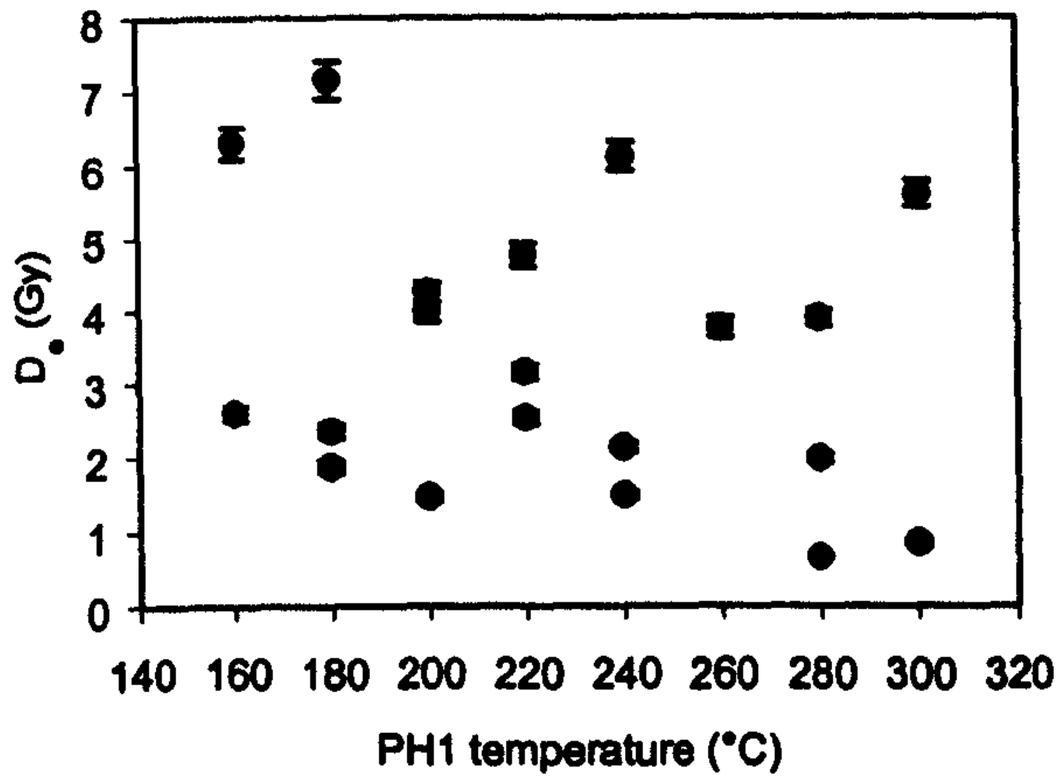

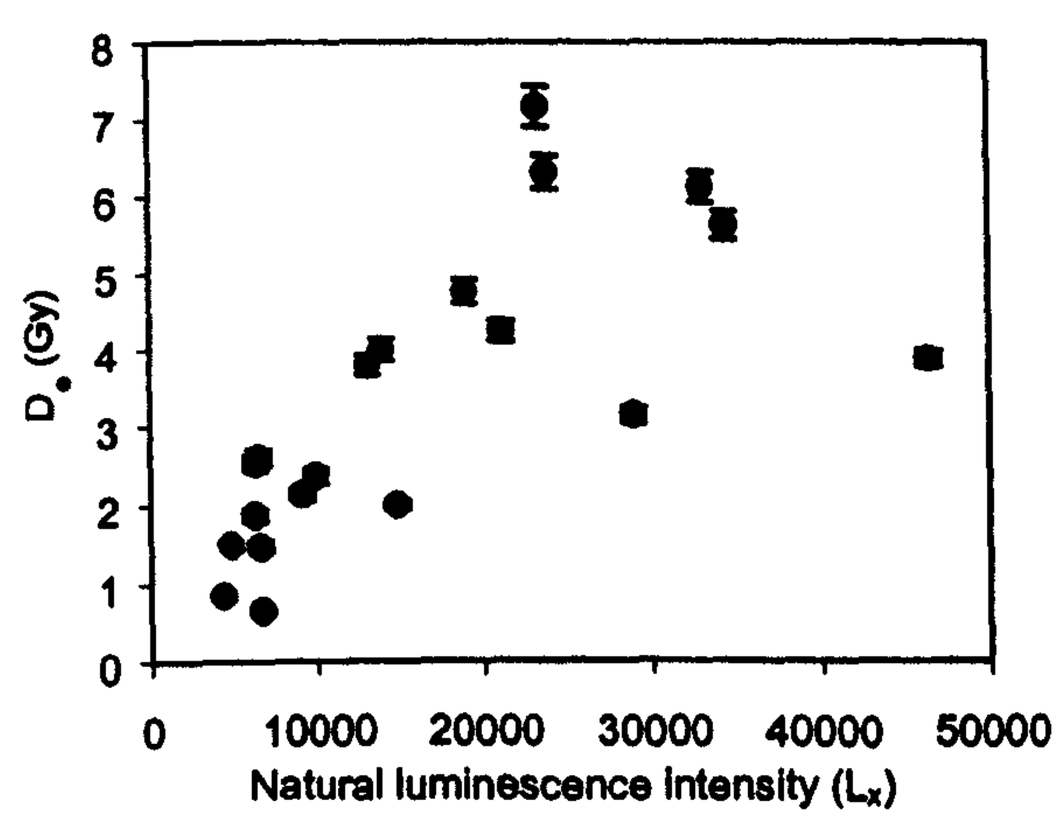

Aber/29-BA11

Exposure: cliff (tube)

Average: mean

$D_e = 3.37 \pm 0.43$ Gy

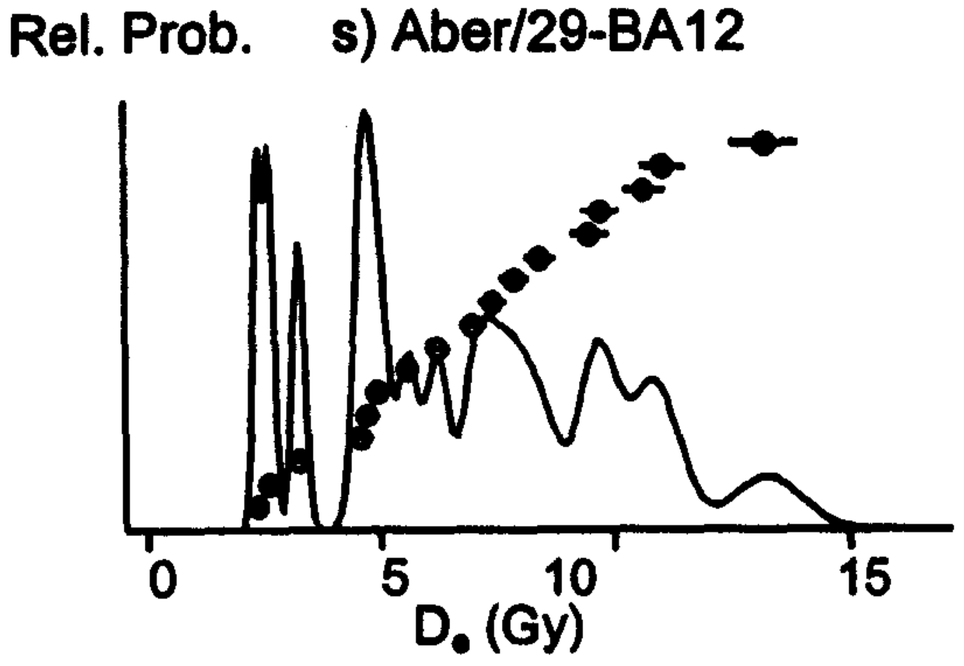

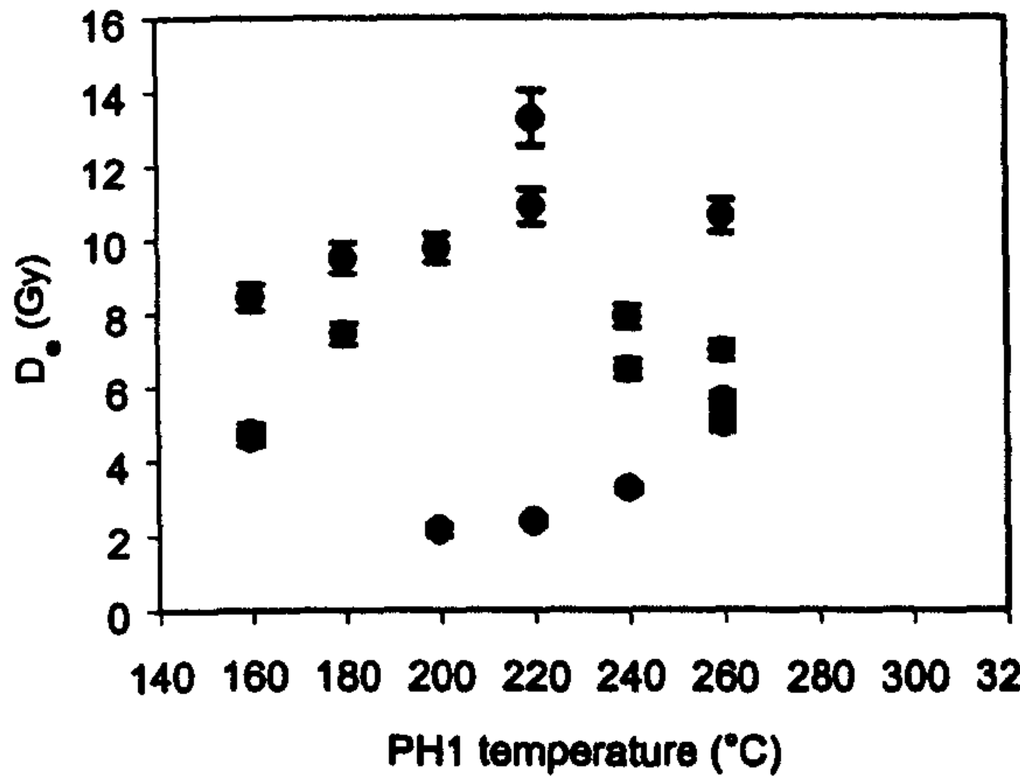

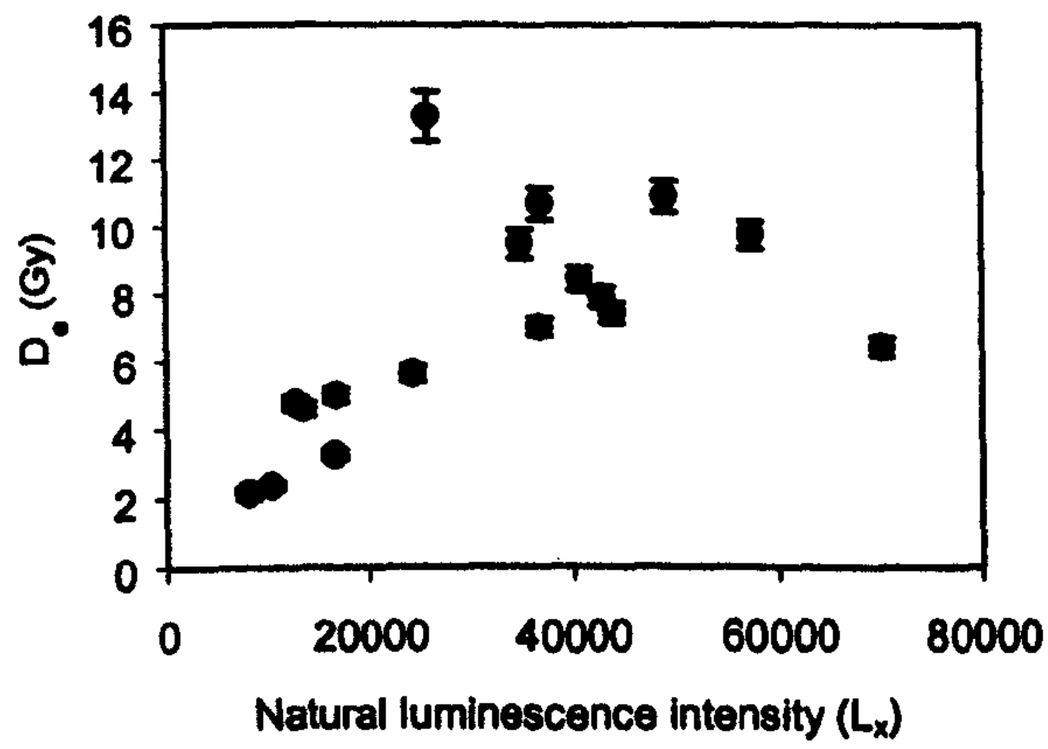

Aber/29-BA12

Exposure: cliff (tube)

Average (mean)

$D_e = 7.02 \pm 0.77$ Gy

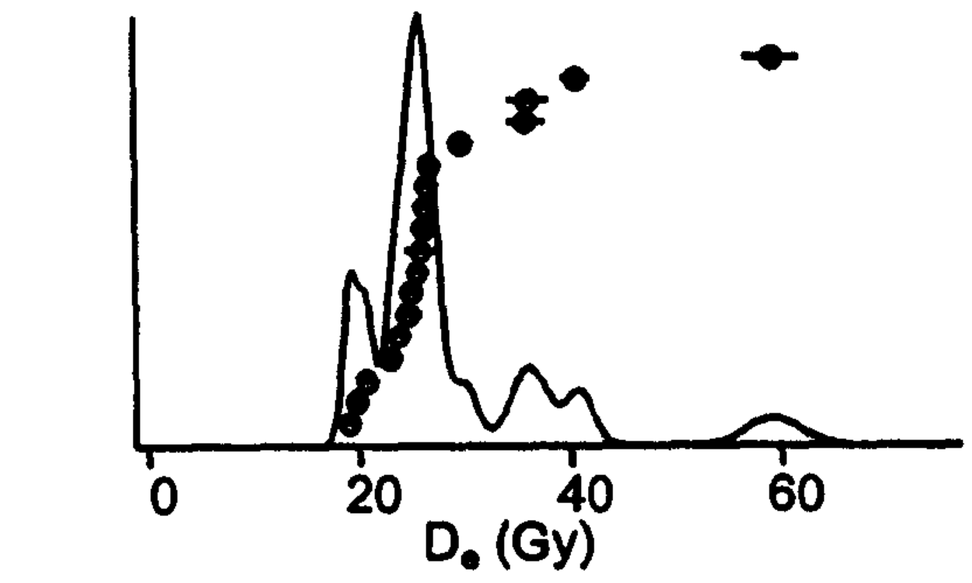

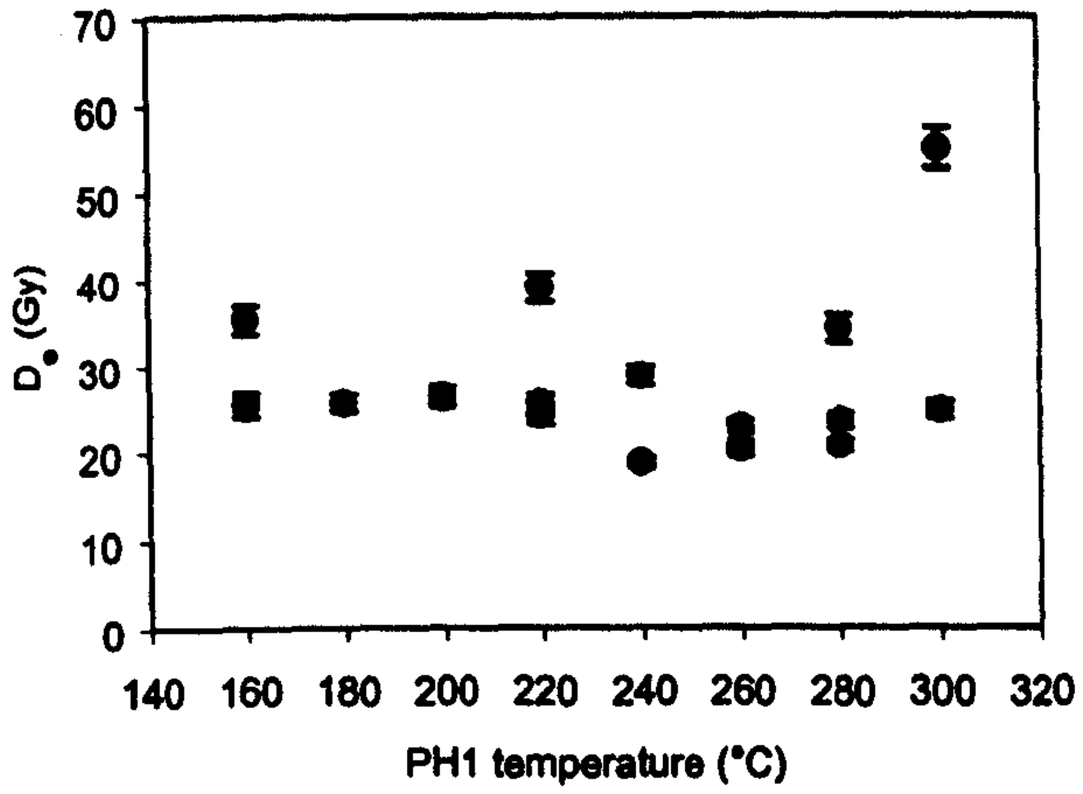

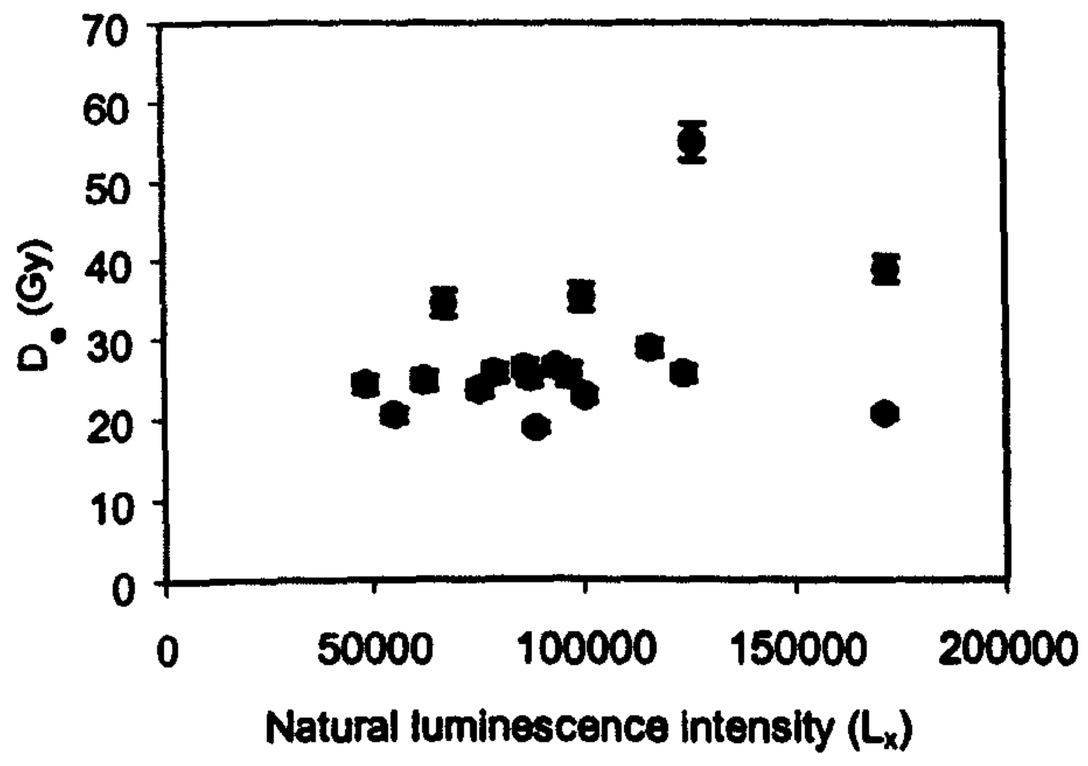

Aber/29-BA13

Exposure: cliff (tube)

Average: mean

$D_e = 29.7 \pm 2.4$ Gy

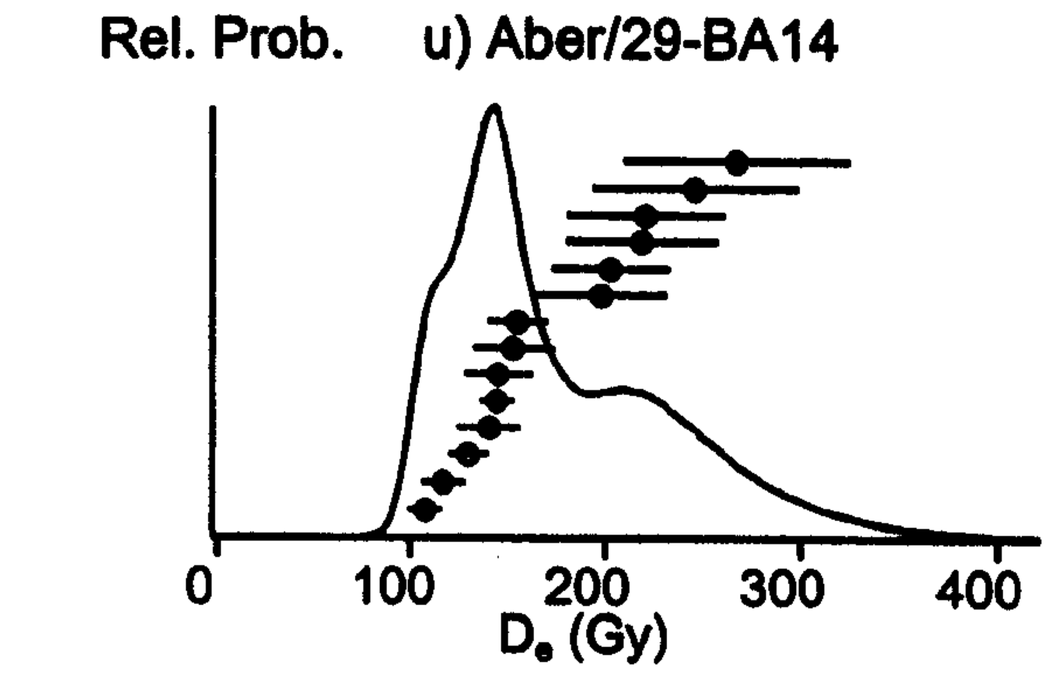

Aber/29-BA14

Exposure: cliff (tube)
Average: median
$D_e = 176 \pm 13$ Gy

Figure 6.3. D_e distributions for the majority of samples dated during this study. Top) Combined PDF and scatter plot, middle) D_e versus PH1 temperature and bottom) D_e versus natural luminescence intensity. The caption under each set of plots gives sample details. The sampling technique used is given in parentheses after the exposure type.

reported in Section 3.5 give some confidence that the SAR procedure does not cause electron trapping probability changes. However, the only check which could demonstrate that the natural luminescence intensity is being measured correctly using SAR is to date known age samples. Even in this case, other sources of error may possibly allow the correct age to be calculated, despite the occurrence of electron trapping probability changes during the first measurement cycle. No further experimental work has been carried out to assess the possible impact of electron trapping probability changes on the scatter observed in an SAR dataset. Scatter due to measurement reproducibility is investigated in Section 6.4.1. Scatter due to environmental conditions and measurement procedure errors are discussed in Sections 6.4.2 to 6.4.4.

6.4.1 Modelling the minimum achievable scatter

Prior to discussing other sources of scatter, it is important to assess the scatter imparted to a dataset by the 1.5% measurement reproducibility error measured in Section 5.3.2. This is the minimum scatter achievable, and has been modelled using the standardized growth curve (Section 6.2.2), and a synthetic, normally distributed, dataset.

For a normally distributed parent population with a constant percentage standard deviation, the scatter of measured D_e values, will increase with age due to the curvature of the growth curve. The variability in D_e values associated with the 1.5% measurement reproducibility error (Section 5.3.2), can be assessed by applying a normally distributed dataset to the standardized growth curve, and calculating the resulting scatter.

An approximately normally distributed dataset[d] was produced by generating 500 Gaussian deviates (members of a Gaussian distribution), for a population with a mean of zero and a standard deviation of unity. This was achieved by repeatedly generating N random numbers[e] (r) from a distribution from 0 to < 1, and calculating values for the variable r_G using Equation 6.2 (Bevington and Robinson, 1992, their equation 5.19)

---

[d] The Gaussian distribution is defined between $-\infty$ and $+\infty$, whereas datasets produced using Equation 6.2 have a possible range of the mean $\pm N/2$, in this case 0 ± 6 (Bevington and Robinson, 1992).
[e] Generated using a Microsoft Excel spreadsheet.

$$r_G = \sum_{i=1}^{N} r_i \; - \; N/2 \tag{6.2}$$

Since the standard deviation of the population from which r_G is drawn has a standard deviation of $\sigma = \sqrt{N/12}$, twelve values of r_i were used in each calculation to give a standard deviation of one. The resulting distribution[f] was then scaled to different means (μ) and standard deviations (σ) as required using Equation 6.3 (Bevington and Robinson, 1992)

$$x = \sigma \; r_G \; + \mu \tag{6.3}$$

The distribution of natural luminescence intensities, for a population with a single equivalent dose, caused by the 1.5% measurement reproducibility error, was calculated as follows. The standardized luminescence intensity pertaining to a range of equivalent doses between 1 and 200 Gy was calculated using Equation 6.1[g]. The synthetic dataset was then scaled using Equation 6.3, using the standardized luminescence intensity as the mean, with 1.5% standard deviation. D_e values were calculated from these synthetic natural luminescence intensities using Equation 6.1[g]. The standard deviation of the resulting D_e distributions are shown in Figure 6.4, and represent the minimum achievable scatter in an SAR dataset, measured using the Risø TL/OSL readers used in this study. The majority of samples measured in this study have equivalent doses below 30 Gy, or above 100 Gy. Figure 6.4 shows that the 1.5% measurement reproducibility error makes a limited contribution to the scatter observed for the samples with equivalent doses below 30 Gy, whereas it is potentially a significant source of scatter for the samples with equivalent doses above 100 Gy.

The scatter observed for samples from Inhaca and Bazaruto Islands is shown in Figure 6.5. In most cases, the observed scatter is considerably larger than that caused by the 1.5% measurement reproducibility error (represented by the solid line in Figure 6.5),

---

[f] The distribution generated is very close to that expected, having a mean of 0.008 and a standard deviation of 1.01.

[g] I_o was set at zero and A and B were as calculated by Roberts and Duller (submitted).

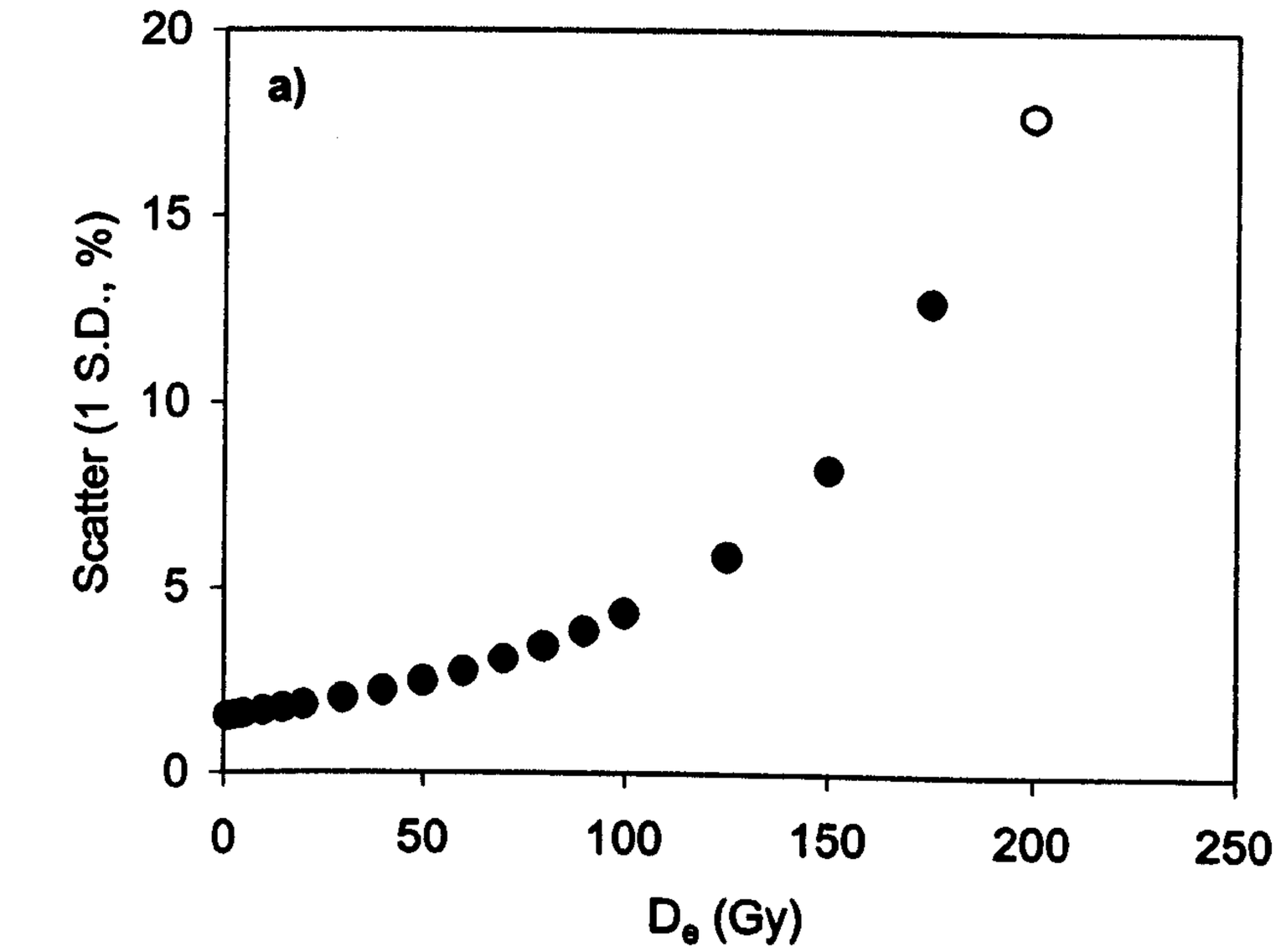

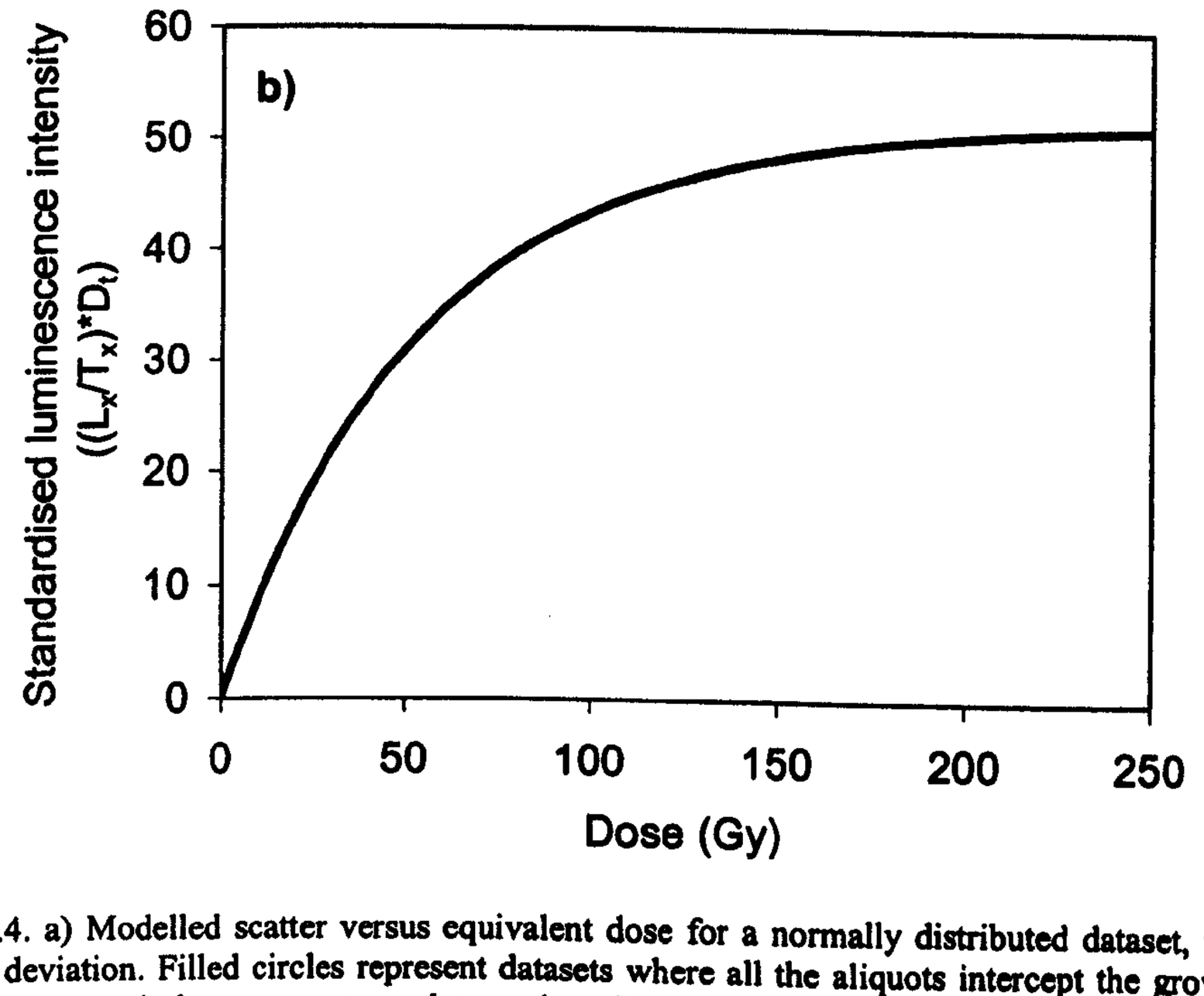

Figure 6.4. a) Modelled scatter versus equivalent dose for a normally distributed dataset, with 1.5% standard deviation. Filled circles represent datasets where all the aliquots intercept the growth curve, while the open circle represents a dataset in which several aliquots have natural luminescence intensities greater than the curve fitting parameter *A*. b) The standardised growth curve generated using Equation 6.1. This growth curve was used to generate the dataset shown in Figure 6.4a. Consequently, comparison of Figures 6.4.a and b shows the relationship between growth curve curvature and scatter.

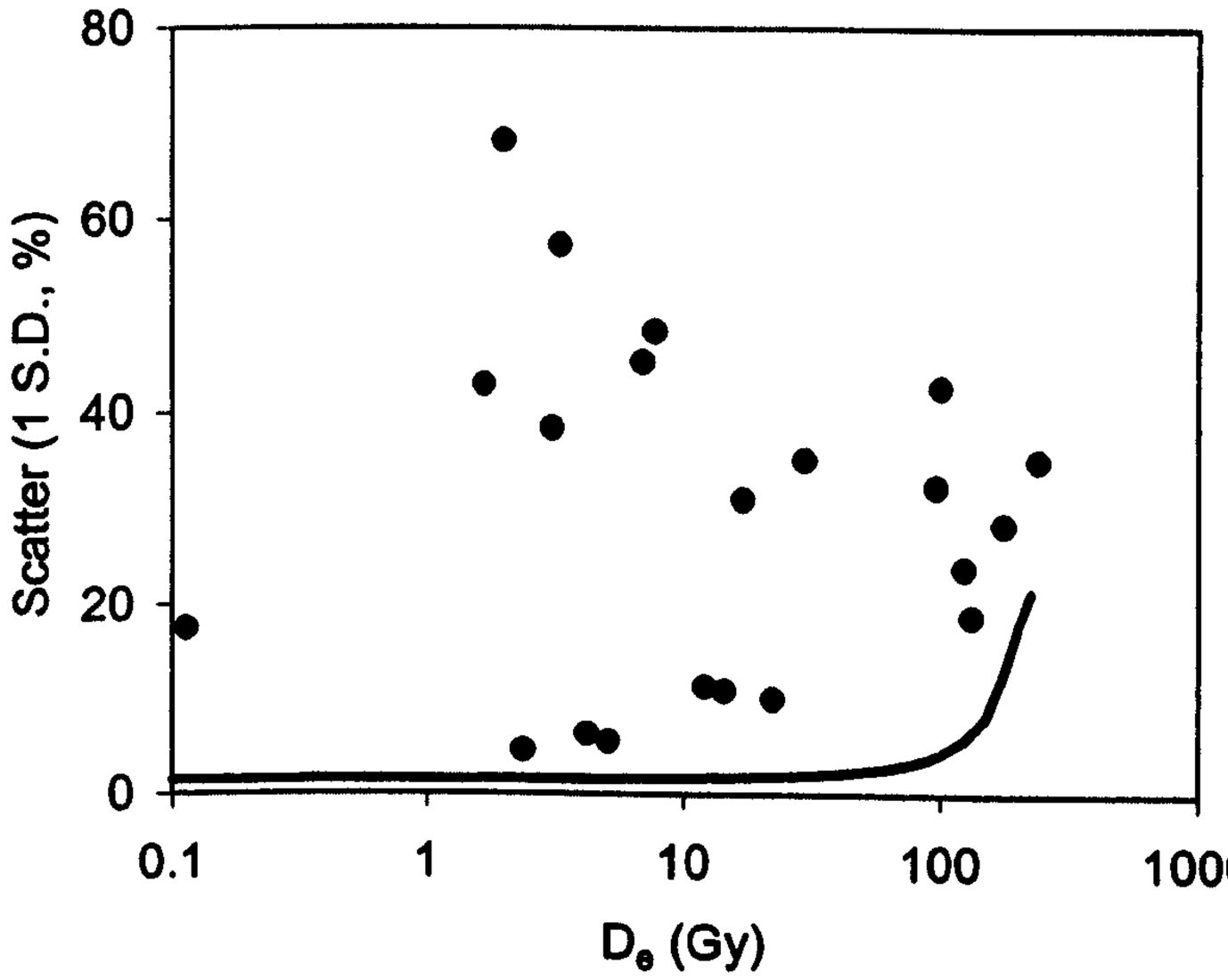

Figure 6.5. Scatter versus D_e for the samples measured during this study. The scatter is 1 standard deviation, expressed as a percentage of the mean D_e. The solid line represents scatter due to 1.5% measurement reproducibility error. Note the logarithmic dose axis.

indicating that other sources of scatter are also important. These sources of scatter are discussed in Section 6.4.2. However, the lower edge of the distribution (i.e. those samples displaying the least scatter) does rise as equivalent dose increases, mimicking the rise in scatter caused by measurement reproducibility error. This suggests that, for the older samples at least, measurement reproducibility error does contribute a significant proportion of the scatter measured from natural samples.

Extension of the dataset in Figure 6.4 beyond 200 Gy is hampered by the fact that above this dose, the tail of the simulated normal distribution produces natural OSL intensities which are greater than the fitting parameter *A* (i.e. the natural measurement "misses" the growth curve). This phenomenon is discussed in Section 6.4.4.

6.4.2 Sources of scatter in the datasets presented in this study

Potential sources of scatter (other than the 1.5% measurement reproducibility error) are described in Table 6.1, and discussed below.

Cause of scatter	D_e distribution caused	Solution
β-microdosimetry[h]	Skewed	Large aliquots, to assess mean D_e of bulk sample.
Partial bleaching	Situation dependent	Large number of small aliquots. D_e taken from lower edge of distribution.
Mixing	Bimodal / Polymodal	Large number of small aliquots, pick appropriate peak.
Bioturbational zeroing (near surface deposits)	Positive skew (unless very severe)	Large number of small aliquots. D_e taken from upper edge of distribution.
Measurement procedure (SAR) failure	Situation dependent	None. May be revealed by D_e versus PH1 plot.

Table 6.1. Principal causes of scatter and their remedies.

a) β-microdosimetry is likely to contribute to the scatter observed in all samples. A significant proportion of the radioisotopes present in a sample will be contained in

[h] The α contribution is removed by HF etching of the separated quartz grains (Section 2.3.2), while the range of gamma rays is sufficiently large to provide a homogenous γ-field.

feldspar (K) and heavy mineral grains such as zircon (U and Th), providing discrete β sources. The environmental dose rate (calculated from bulk, homogenized sub-samples, Section 7.2) is relatively low for most samples (c.1-1.5 Gy/ka). Consequently, these grains will cause significant local enhancement of the environmental dose rate. This effect will, to some extent, be averaged out by the relatively large mass aliquots used in the dating study (large and medium mask sizes, Table 2.2), with 95% of the OSL signal being emitted by 43 and 17 grains respectively[i].

b) Partial bleaching is unlikely to be a significant source of scatter for the samples measured in this study (Section 3.2), since the majority were deposited by aeolian processes. In addition, the unscattered equivalent dose distributions for the modern samples measured in this study (Figures 6.3d and m) indicate that partial bleaching is unlikely to be a significant source of scatter.

c) Mixing of two adjacent units, probably by bioturbation, may have occurred in the unconsolidated samples. This is especially true where the samples were taken from pits dug into the surface of dunes, and the presence/depth of underlying units was impossible to assess. The scatter observed in some of the samples collected in this way is small (e.g. Aber/28-IN15 and 16, Figures 6.3g and h). In these cases, mixing of adjacent units can be discounted. However, mixing of older and younger material is considered to be the most likely cause for the significant scatter observed in some of the younger samples (e.g. Aber/28-IN19 and 21, Figures 6.3j and l).

For the few exposed sections studied, individual units were large, allowing widely spaced sampling locations, thereby minimizing the possibility of mixing between units. However, significant scatter is observed for both Aber/29-BA11 and 12 (Figures 6.3r and s), which were sampled relatively close together (2m), indicating that the possibility of mixing cannot be discounted.

---

[i] Calculated assuming grain to grain intrinsic luminescence intensity distribution measured for 29/Aber-BA14 (Duller *et al.*, 2000) with 867 grains on a large mask aliquot and 333 grains on a medium mask aliquot (Section 2.3.3).

Mixing of consolidated material from two or more phases of deposition may have occurred in the beachrock samples from Bazaruto (Aber/29-BA2 and Aber/29-BA8, Figures 6.3n and p). Cooper (1991) has observed that many beachrocks on the Natal coast contain, within their matrix, clasts from earlier beachrock formations. Although this type of structure was not observed in the Bazaruto beachrock samples, it may explain the relatively high scatter observed for both samples. Mixing of unconsolidated material prior to cementation is considered to be an unlikely source of the scatter observed in these samples, since Aber28-IN9 (a modern tidal bar, and therefore an approximate depositional analogue) yielded an unscattered D_e distribution consistent with a zero-age (Figure 6.3d).

d) Bioturbational zeroing of near surface deposits is possible, since many of the samples were collected from pits dug into the surface of a dune. However, some of these samples show little variation in equivalent dose between aliquots. This indicates that for these samples, bioturbational zeroing of near surface deposits is unlikely. Consequently, bioturbational zeroing is considered an unlikely cause for the larger scatter observed in some of the D_e distributions for younger samples.

e) For the majority of samples, failure of the SAR is an unlikely source of scatter (Chapters 3 and 5). However, for three of the samples close to dose response saturation, aliquots yielding growth curves which never reach the natural luminescence intensity are observed. This phenomenon indicates that the SAR procedure may occasionally fail at large natural radiation doses, identifying it as a possible source of scatter for very old samples (see also Section 6.4.4).

For the above reasons, the majority of samples dated during the course of this study are expected to come from deposits with a normal distribution of equivalent doses, caused by the 1.5% measurement reproducibility of the Risø reader, and β-microdosimetry. In some cases, mixing of two units may have occurred, possibly by bioturbation.

6.4.3 Large dose distributions obtained from older samples

Some of the older samples (with equivalent doses >100Gy) yield a very large spread of equivalent doses. This range cannot sensibly be ascribed to the 1.5% measurement reproducibility error or β-microdosimetry. Aber/28-IN1 is a good example of such a sample, and has been used to investigate this phenomenon further. This sample is laminated, indicating limited bioturbation (Section 8.3.1). It is overlain by a rhizolith layer, which is itself overlain by another laminated aeolian unit from which Aber/28-IN3 was taken. This sample yields a D_e of 96 Gy. Combined with the laminations observed in Aber/28-IN1, and the intervening rhizolith layer, this indicates that the scatter in the Aber/28-IN1 dataset cannot be caused by bioturbational mixing with a younger overlying unit.

Figure 6.6 shows a selection of growth curves for aliquots of Aber/28-IN1. These aliquots yield the three lowest (Figure 6.6a-c), and highest (Figure 6.6f-h) equivalent doses measured for this sample. In addition, two aliquots yielding equivalent doses close to the mean (Figure 6.6d and e) are shown for comparison. The growth curves all appear "sensible", i.e. they are the shape that would be expected for quartz in this dose range, and have very small curve fitting errors. The shapes of the growth curves are similar and do not show a systematic change from low to high doses. This strongly suggests that feldspar contamination does not cause the very low equivalent doses observed for some aliquots of this sample. If this was the case, aliquots with a feldspar dominated signal (and hence low equivalent doses due to fading) would be expected to yield more linear growth curves. This is due to the fact that feldspar has a higher dose response saturation point than quartz. In addition, the relatively early dose response saturation shown by all the curves in Figure 6.6 indicates that the signal is dominated by quartz and not feldspar.

All the aliquots yield recycling ratios within 10% of unity, indicating that the SAR sensitivity correction procedure is appropriate for these aliquots. In addition, recycling ratios do not decrease as the measured equivalent dose increases, as would be expected if sensitivity correction failure did account for the wide range of D_e values measured (since the recycling ratio was calculated as R_x/R_1). This suggests that systematic failure of the sensitivity correction procedure is not responsible for the range of D_e values observed.

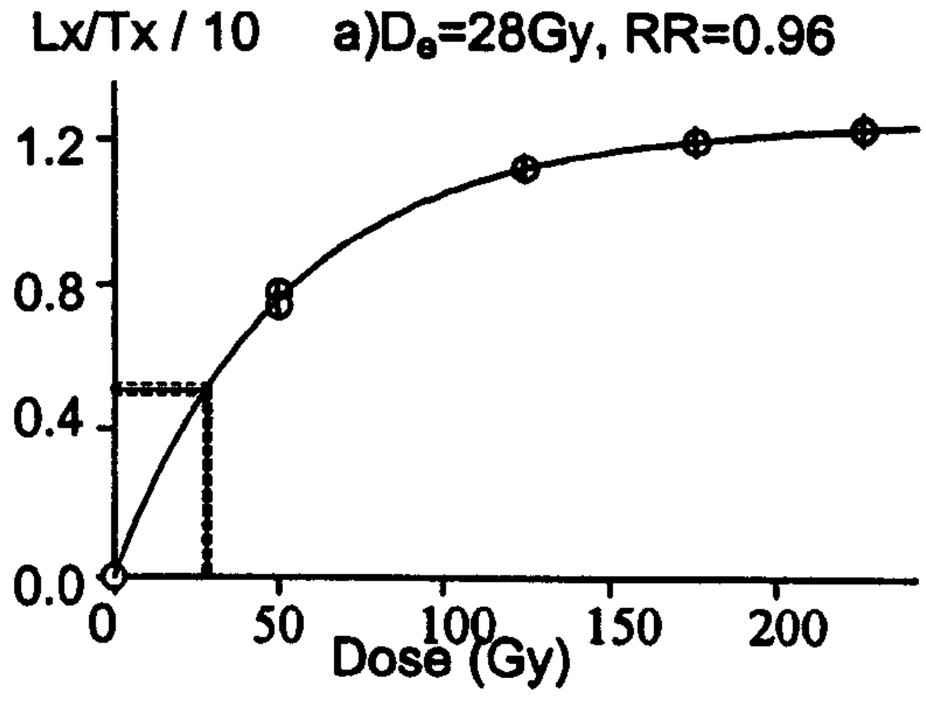
Lx/Tx / 10
a)De=28Gy, RR=0.96
1.2
0.8
0.4
0.0
0
50
100
150
200
Dose (Gy)

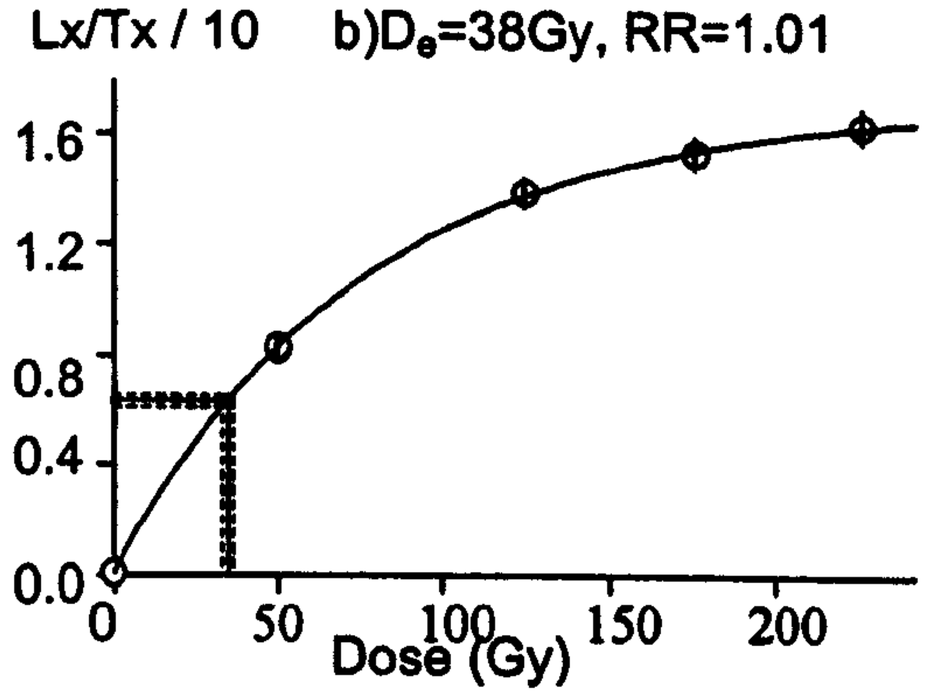
Lx/Tx / 10
b)De=38Gy, RR=1.01
1.6
1.2
0.8
0.4
0.0
0
50
100
150
200
Dose (Gy)

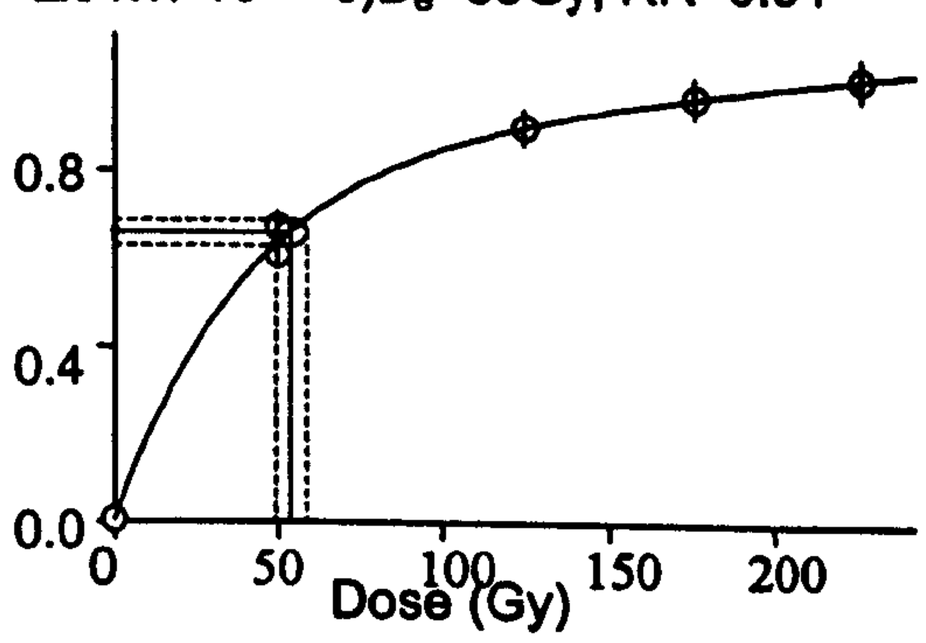
Lx/Tx / 10
c)De=53Gy, RR=0.91
0.8
0.4
0.0
0
50
100
150
200
Dose (Gy)

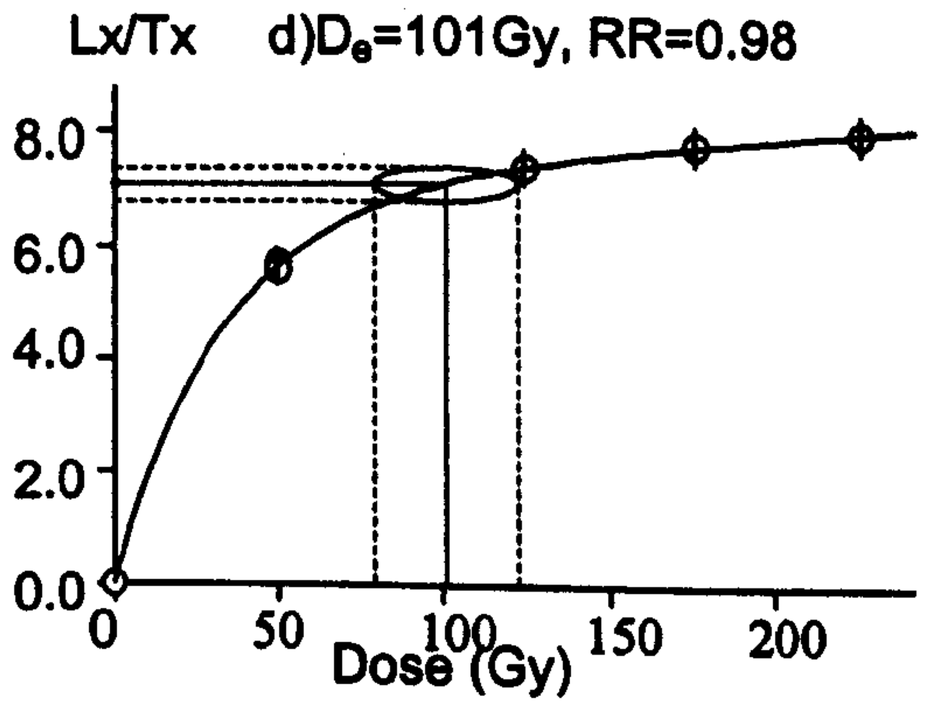
Lx/Tx
d)De=101Gy, RR=0.98
8.0
6.0
4.0
2.0
0.0
0
50
100
150
200
Dose (Gy)

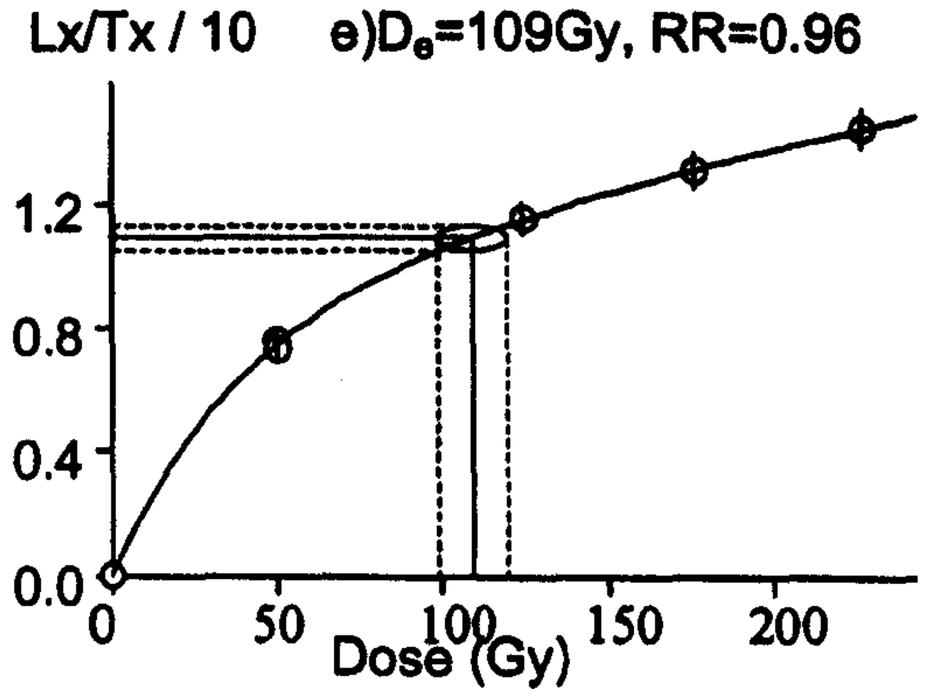

Figure 6.6. Growth curves for individual aliquots of Aber/28-IN1. The curves were fitted using a saturating exponential plus linear function. The solid line represents the natural luminescence intensity, with errors represented by the dashed lines. All aliquots were produced using a medium mask size (Section 2.3.3). The test dose was 5 Gy.

Consequently, the large spread in D_e values obtained for Aber/28-IN1 cannot be explained by the possible causes of scatter discussed in Sections 6.4.1 and 2. A further source of scatter remains to be found for this sample.

6.4.4 The natural luminescence intensity "misses" the growth curve

Several samples analysed during this study yield aliquots whose sensitivity corrected natural luminescence intensity (L_n/T_n) is greater than that for the largest regeneration dose measured (Figure 6.7a and Table 6.2). These data were fitted using a saturating exponential plus linear function (Section 2.2). The natural luminescence intensity will always intercept the growth curve if the linear component of the growth curve is positive (Figure 6.7b). These data were fitted using "Analyst" version 2.24, using the "exponential + linear fit" function. The linear component of the growth curve may be positive, zero or negative, with the latter two scenarios potentially allowing L_n/T_n to miss the growth curve. Aliquots where this occurs have only been included in Table 6.2 when the fit provided by Analyst appears to be appropriate. In all cases, negative linear components are very small, and are interpreted as representing aliquots which display no linear growth curve component. The occurrence of aliquots which yield natural luminescence intensities greater than the saturation intensity of their growth curve was first discussed by Armitage *et al.* (2000, Figure 5) and has since been observed for single-aliquots by Bailey (pers. comm.) and single-grains by Jacobs (pers. comm.). It is important to consider the possible causes of this phenomenon, since it may be indicative of a general failure of the SAR technique, which only becomes apparent as an aliquot nears dose-response saturation.

Four possible causes for this failure have been considered.

1) Restricted regeneration dose range (i.e. the largest regeneration dose is too small).
2) Measurement reproducibility.
3) Inappropriate sensitivity correction of the natural luminescence intensity.
4) Inappropriate sensitivity correction of the regenerated luminescence intensities.

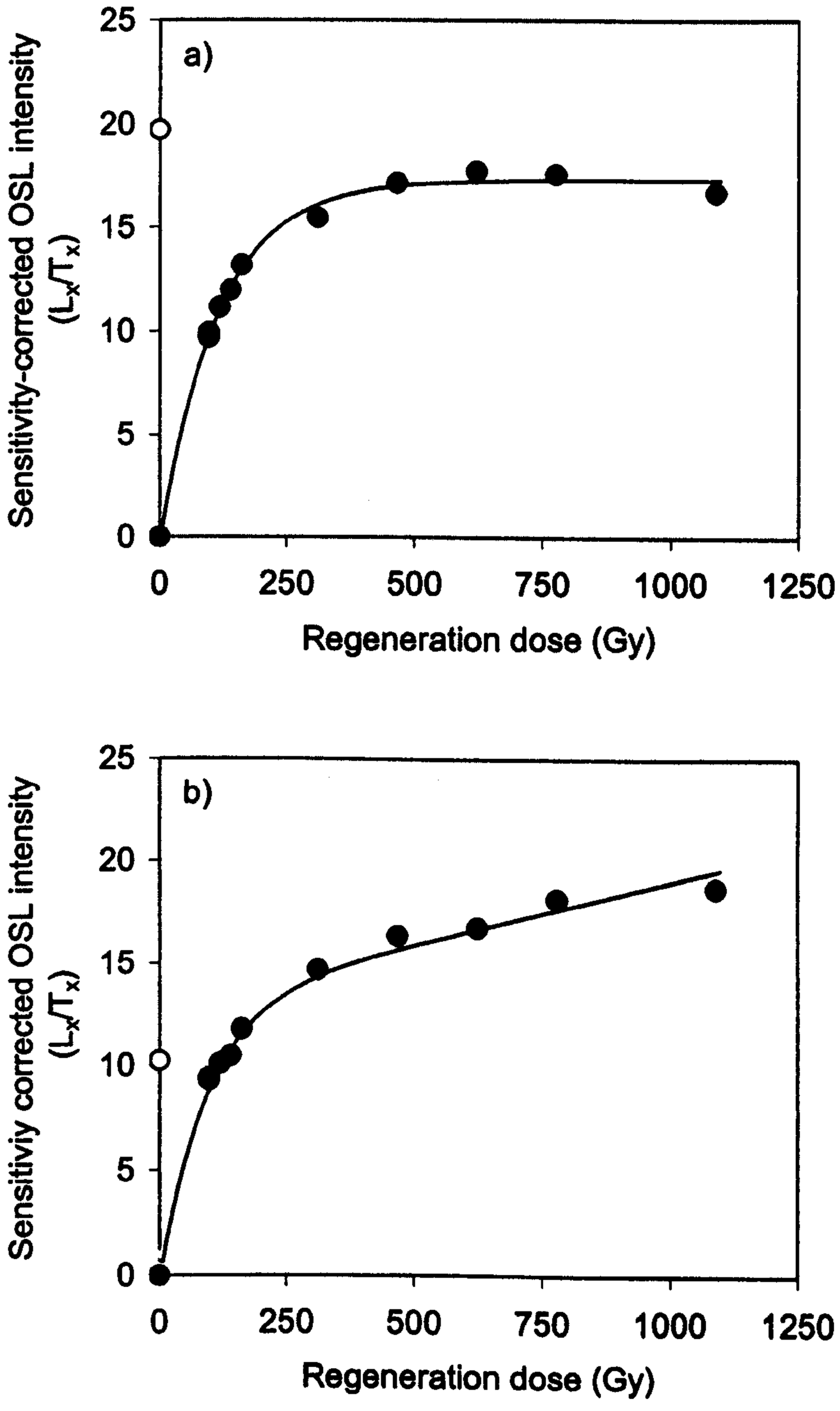

Figure 6.7. Growth curves for two aliquots of Aber/29-BA14. a) Growth curve shows no linear growth component at high regeneration doses. The natural luminescence intensity is shown as an open circle in the y-axis, and is larger than the intensity of the growth curve at saturation. Consequently, no equivalent dose can be calculated. b) Growth curve has a significant linear growth component at higher doses, and does not appear to have reached dose response saturation at the largest regeneration dose. The natural luminescence intensity is shown as an open circle in the y-axis.

Sample code (Aber/...)	Largest regeneration dose used (Gy)	D_e (Gy)	Aliquots where L_n/T_n does not intercept the growth curve
28-IN1	225.7	101 ± 10	0
28-IN3	225.7	96.2 ± 6.5	0
28-IN4	342.8	242 ± 18	8
28-IN11	225.7	133 ± 6	4
29-BA1	170.0	124 ± 7	0
29-BA14	1090	176 ± 13	4 (2)[j]

Table 6.2. Largest regeneration dose, mean calculated D_e and number of aliquots where the natural does not intercept the growth curve, for samples with age estimates greater than 100 ka. 24 aliquots of each samples were measured. Where the extrapolated growth curve may plausibly rise to the intensity of the natural signal, the aliquot has not been counted as missing the growth curve. D_e values are taken from Tables 6.3 and 6.4.

6.4.4.1 Restricted regeneration dose range

If the largest regeneration dose is smaller than the equivalent dose of the sample measured, the measured growth curve must be extrapolated to produce an equivalent dose. In this scenario, the extrapolated growth curve may never reach the natural luminescence intensity, if the measured dose points were insufficient to accurately model the dose response at higher regeneration doses. This is especially true of aliquots with growth curves displaying a significant linear growth at high regeneration doses, since this component is dwarfed by the saturating exponential component at low doses.

However, the three samples which yielded aliquots with natural luminescence intensities which do not intercept the growth curve, received regeneration doses considerably larger than the mean equivalent dose of the sample (Table 6.2). In the case of Aber/29-BA14, the largest regeneration dose was six times the mean equivalent dose, and the range of dose points allow the linear component of the growth curve to be defined. Despite this, the natural luminescence intensity of two aliquots of Aber/29-BA14 still failed to intercept the growth curve. Consequently, the use of an inappropriate range of regeneration doses does not appear to explain this phenomenon, for these samples.

[j] Two of these aliquots also display scattered growth curves, with some regenerated luminescence intensities being greater than L_n/T_n. However, the best fit growth curve saturates below the natural luminescence intensity. A PH1 temperature of 300°C was used for both aliquots. These aliquots have not been included in the subsequent investigation.

6.4.4.2 Measurement reproducibility

The 1.5% measurement reproducibility error measured in Section 5.3.2 may also cause the natural luminescence intensity to be greater than the dose-response saturation value of the growth curve. This possibility has been investigated by applying the synthetically generated normally distributed L_n/T_n data (1.5% standard deviation)[k] to the standardized growth curve, using the same method as that used in Section 6.4.1. The results, for a range of equivalent doses, are shown in Figure 6.8. Using the standardized growth curve and appropriate sample D_e, the number of growth curve misses expected from 24 aliquots of Aber/28-IN4, Aber/28-IN11 and Aber/29-BA14 is 6.3, 0 and 0 respectively. The values for the younger samples (Aber/28-IN11 and Aber/29-BA14) indicate that measurement reproducibility error cannot account for the failure of the natural dose point to intercept with the growth curve. However, measurement reproducibility error does give a good approximation of the number of aliquots expected to fail in the oldest sample (Aber/28-IN4). These data suggest that, the 1.5% measurement reproducibility error may cause a relatively small number of aliquots to yield natural luminescence intensities greater than the saturation intensity of their growth curve. However, since no aliquots of Aber/28-IN11 or Aber/29-BA14 would be expected to fail due to the effects of measurement reproducibility errors, it is unlikely to be the main cause of this phenomenon.

6.4.4.3 Inappropriate sensitivity correction of the natural luminescence intensity

Assuming the growth curve is internally consistent, the sensitivity corrected natural luminescence intensity must be erroneously large to cause it to miss the growth curve. It can be hypothesized that L_n may be measured at a higher activated L:R-centre ratio (sensitivity) than T_n, leading to an erroneously large value for L_n/T_n, relative to subsequent regeneration dose points. During burial, samples sensitize due to the thermal decay of holes trapped at R-centres. Over long burial periods, the number of holes trapped at R-centres becomes independent of time, since the R-centre hole trapping rate and thermal decay are in equilibrium. Conversely, the L-centre population is proportional

---

[k] The larger standard deviations observed for all natural samples appear to be caused by a combination of the 1.5% measurement reproducibility error and microdosimetry. The latter cannot be included in this calculation since it represents real variation in D_e, and consequently the natural intensity ought to follow the measured growth curve, other factors being equal.

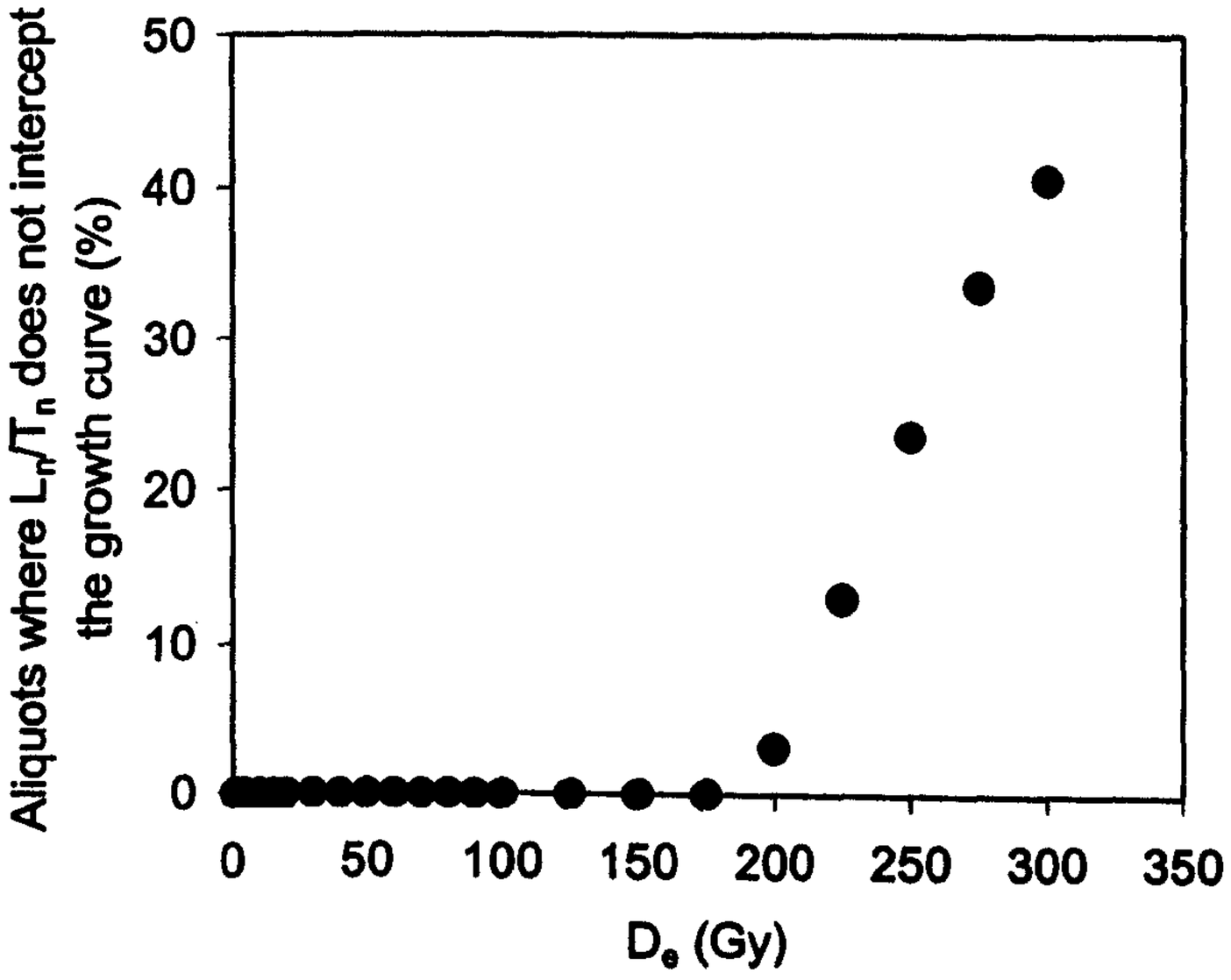

Figure 6.8. A plot showing the percentage of aliquots where L_n/T_n does not intercept the growth curve, versus the equivalent dose. The synthetic normally distributed dataset (n=500) generated using Equation 6.2 manipulated using Equation 6.3 to yield a dataset with a standard deviation of 1.5%. The mean for each dose point was calculated using the growth curve parameters defined for coarse grained quartz by Roberts and Duller (submitted). This synthetic distribution of natural luminescence intensities was then applied to the standardised (saturating exponential) growth curve defined by Roberts and Duller (submitted), and the percentage of aliquots yielding values of L_n/T_n which did not intercept the growth curve was calculated.

to the burial dose over dateable timespans (though saturation of the L-centre may occur), owing to its greater thermal stability. Consequently, old samples have a very high natural L:R-centre ratio (see also Section 5.4). L_n is measured with this high sensitivity, but (if this hypothesis is correct) T_n is not, since R-centres are activated during the test dose irradiation, reducing the activated L:R-centre ratio. However, since the regeneration doses used in a measurement sequence are usually larger than the test dose, significant dose quenching occurs during administration of the regeneration dose and the additional dose quenching which occurs during the test dose is negligible. Consequently, the activated L:R-centre ratio for L_x is similar to that for T_x. Hence, the growth curve is internally consistent since the sensitivity correction procedure is appropriate. However, T_n does not accurately reflect the sensitivity of the sample during measurement of L_n (i.e. T_n is too small), and L_n/T_n is erroneously large relative to the growth curve.

Circumstantial evidence for this process is provided by a single-aliquot dose recovery experiment performed using a range of test doses. A natural aliquot of Aber/28-IN21 was cut-heated to 500°C, to remove charge from most of the optically stimulable traps, and then given a regeneration dose of 5 Gy. A standard SAR measurement sequence was then performed using a 2.5 Gy test dose, regeneration doses of 2.5, 5, 7.5, 10, 0 and 2.5 Gy, and a 160°C PH1. Using the same aliquot, the entire measurement sequence was repeated using a 5 Gy test dose. Subsequently the sequence was repeated using test doses of 7.5, 15, 25, 37.5 and 50 Gy. The experiment was repeated using PH1 temperatures of 200 and 260°C, using a different aliquot for each preheat temperature. The results are presented in Figure 6.9. All three aliquots yield the correct D_e value using a 2.5 Gy test dose. However as the test dose is increased, the aliquot preheated at 160°C yields progressively larger overestimates of the equivalent dose. In contrast, the aliquot preheated at 260°C yields equivalent doses close to the known dose with all test doses used. The data for a 200°C PH1 are intermediate. In all cases recycling ratios were within 5% of unity, indicating that the SAR sensitivity correction was accurate (Section 3.3).

The data for the aliquot preheated at 160°C may be explained in terms of sensitivity change between the measurement of L_n and T_n, as described above. The 500°C cut-heat sensitizes the sample prior to administration of the 5 Gy "natural" dose, which causes

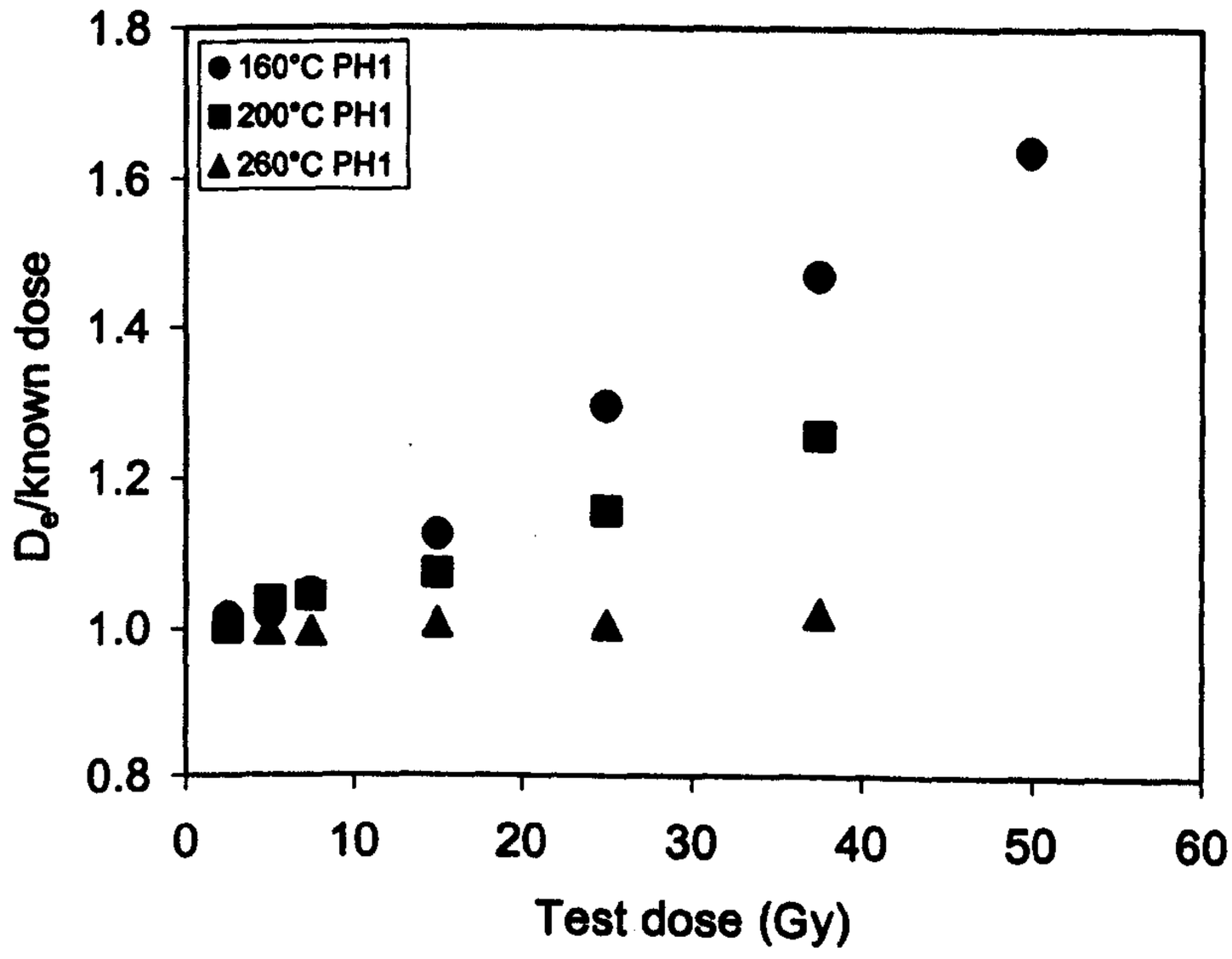

Figure 6.9. D_e/known (recovered) dose versus test dose for aliquots of Aber/28-IN21 using various PH1 temperatures. The aliquot was cut-heated to 500°C prior to administration of the known dose (5 Gy).

some dose quenching. The additional dose quenching caused when the subsequent test dose is administered is small, provided that the test dose is also small. However, as progressively larger test doses are used, dose quenching during administration of the test dose becomes much larger than that during administration of the "natural dose". Consequently, the change in sensitivity between measurement of L_n and T_n becomes larger, and the sensitivity corrected "natural" luminescence intensity rises. This effect does not occur during measurement of the regenerated luminescence intensities since significant dose quenching has already occurred in the first measurement cycle. Consequently, the growth curve is internally consistent, and the aliquot yields a recycling ratio close to unity, but the natural sensitivity corrected luminescence is erroneously high.

The same effect is not observed using a 260°C PH1, since this preheat significantly sensitizes (thermal activation) the aliquot prior to measurement of L_x. Consequently, significant dose quenching occurs between measurement of L_x and T_x when using higher test doses, but the scale of this effect is similar for both the "natural" and regenerated dose points. Hence, while T_x does not reflect the sensitivity during measurement of L_x, the ratio is constant for both natural and regenerated doses. Consequently, the measured D_e is not dependent on test dose size, as shown in Figure 6.9 for the 260°C PH1.

The above experiment was repeated, cut-heating the aliquot to 500°C between the measurement of T_x and administration of the next regeneration dose (see Section 4.7). The measured D_e was found to be consistent with the known "natural" dose irrespective of test dose and PH1 temperature[1]. The 500°C cut-heat fully sensitizes the aliquot prior to each regeneration dose irrespective of the PH1 temperature used. Consequently, the drop in sensitivity between measurement of L_x and T_x is similar for both the "natural" and regenerated dose points. L_n/T_n is therefore comparable with the growth curve, and yields the correct D_e.

While the experiment described above is not an exact analogue for the postulated L:R-centre ratio in old natural samples, it does provide some evidence that this effect may

[1] PH1 temperatures of 160 and 260°C were used.

cause the natural luminescence intensity to be greater than the saturation intensity of the growth curve. The absence of a natural sample for which all aliquots yield natural luminescence intensities greater than the saturation level of the growth curve precludes further experimental investigation of this phenomenon. However, the physical feasibility of this hypothesis could be tested using a kinetic model, such as that developed by Bailey (1998b, 2001).

6.4.4.4 Inappropriate sensitivity correction of the regenerated luminescence intensities

When an aliquot has a luminescence intensity close to that at saturation, small decreases in the regenerated luminescence intensity will depress the regenerated growth curve relative to the natural. In some cases this will cause L_n/T_n to be greater than the saturation intensity of the measured growth curve. In the present study, erroneous regenerated luminescence intensities are most likely to be caused by failure of the SAR sensitivity correction procedure. The quality of SAR sensitivity correction appears to be dependent on both PH1 temperature and regeneration dose (Section 5.3.1). In particular, when repeatedly administering the same regeneration dose, the sensitivity corrected luminescence intensity measured using a 160°C PH1 decreased with cycle. The maximum decrease measured was c.10%, large enough to cause L_n/T_n to miss the growth curve (for a sample close to saturation), but not large enough to fail the recycling ratio test (Section 3.3). In addition, the SAR sensitivity correction appears to function less well using larger regeneration doses (Section 5.3.1).

If sensitivity correction failure causes L_n/T_n to miss the growth curve, it is possible that this effect is PH1 dependent since the direction of sensitivity change is determined by the PH1 temperature used (Armitage *et al.*, 2000, and Section 5.2.1). This was assessed by plotting the number of aliquots where L_n/T_n does not intercept the growth curve against PH1 temperature (Figure 6.10). Figure 6.10 suggests that this phenomenon can occur across the full range of PH1 temperatures used in this study. In particular, the tendency for aliquots preheated at 160°C to show a decrease in sensitivity corrected luminescence intensity with increasing regeneration cycle (Section 5.3.1), does not lead to an increased occurrence of aliquots where L_n/T_n misses the growth curve at this temperature. In fact, more aliquots appear to yield natural luminescence intensities which do not intercept the

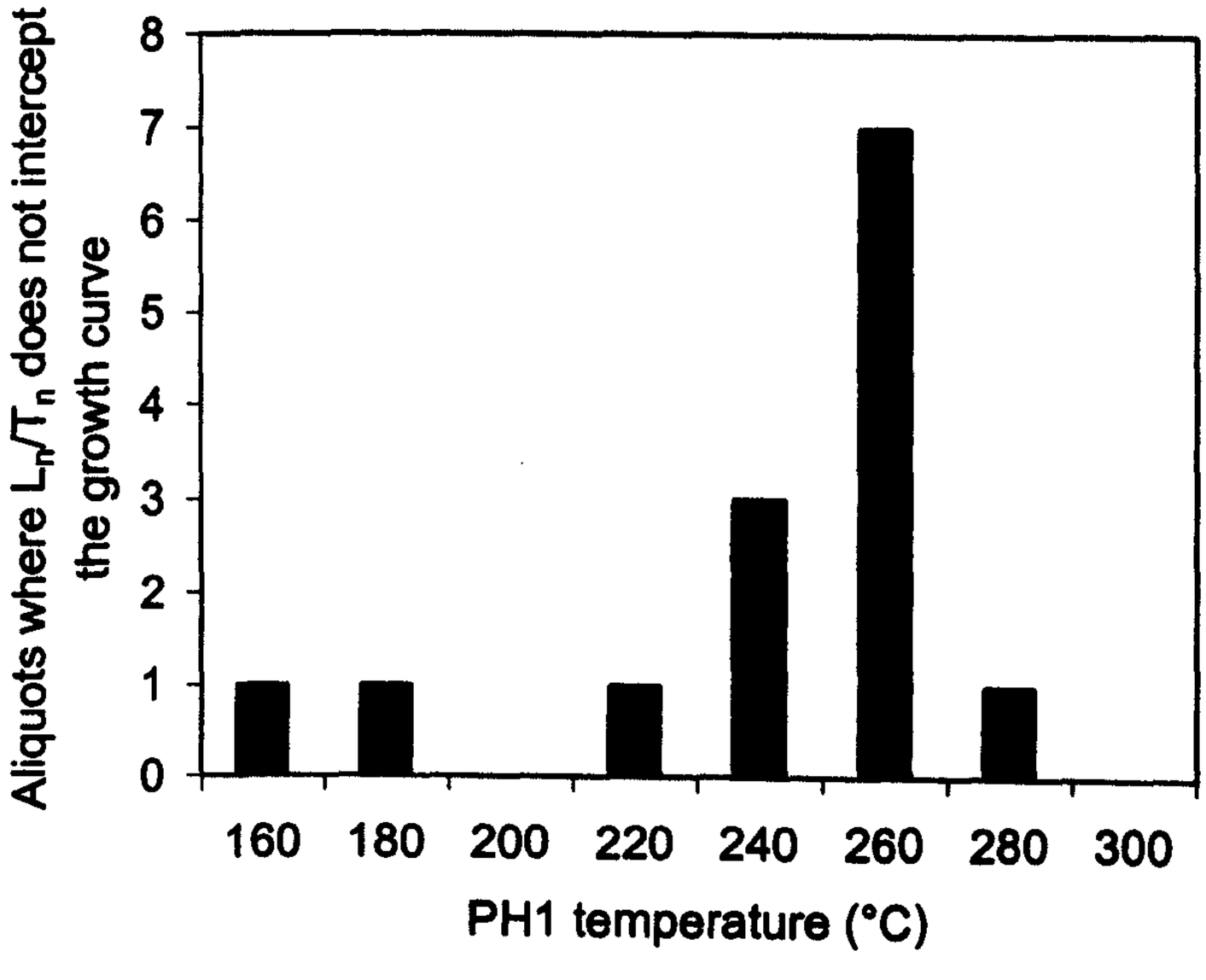

Figure 6.10. A histogram showing the number of aliquots where L_n/T_n does not intercept the growth curve versus PH1 temperature. A restricted range of PH1 temperatures (160-260°C) was used to measure Aber/28-IN4 and Aber/28-IN11 while the full range of temperatures (160-300°C) was used for Aber/29-BA14. Consequently, 11 aliquots were measured for each PH1 temperature in the range 160-260°C, while only three aliquots were measured using 280 and 300°C preheats.

growth curve at higher PH1 temperatures. This suggests that the explanation outlined in Section 6.4.4.3 is unlikely, since negligible D_e overestimates were measured for the aliquot preheated at 260°C.

The mean recycling ratio for the aliquots with natural luminescence intensities which do not intercept the growth curve is 0.979 ± 0.043. This figure, though indicating a slight decrease in sensitivity corrected luminescence intensity with measurement cycle, is consistent with unity (perfect sensitivity correction) suggesting that poor sensitivity correction is not the cause of this phenomenon.

6.4.4.5 Discussion

Having investigated four possible causes for single-aliquot datasets in which the natural luminescence intensity is greater than the saturation intensity of the growth curve, it is impossible to conclude which process is responsible. However, from the above data it is unlikely that the regeneration dose range (Section 6.4.4.1) is too restricted, leading to a poor characterization of the high dose response of an aliquot. Similarly, measurement reproducibility error (Section 6.4.4.2) does not adequately explain the phenomenon for two of the three samples. Poor sensitivity correction of the natural luminescence intensity (Section 6.4.4.3) and regeneration luminescence intensities (Section 6.4.4.4) are both plausible explanations of the phenomenon. If poor sensitivity correction of either the natural or regenerated luminescence intensities does explain the occurrence of aliquots where L_n/T_n does not intercept the growth curve, the effect is likely to exist, though go undetected, in other datasets (e.g. for younger samples). Consequently, this phenomenon requires further investigation.

6.5 Calculation of the sample D_e from an SAR dataset

In the absence of complicating factors, most researchers calculate the sample equivalent dose from an SAR dataset using the mean D_e with one standard error uncertainties[m]. Recently however, Bray *et al.* (in prep.) have suggested that in certain circumstances this

[m] Error calculations were carried out using "Analyst" and "LDBase" software (Appendix 6.1).

analysis does not yield the most appropriate equivalent dose. This suggestion is discussed in terms of its relevance to the present study.

6.5.1 Best estimate of the sample equivalent dose

For a normally distributed parent population (i.e. the group of corrected natural OSL measurements) with a constant percentage standard deviation, the measured D_e values may range from normally distributed at low doses, to positively skewed at higher doses, due to the saturating exponential shape of the growth curve. The correct D_e is given by the intersection of the mean of the OSL distribution onto the growth curve. However, as the measured D_e distribution becomes more positively skewed, the mean D_e rises relative to this value, and hence is an overestimate of the correct D_e. This effect led Bray *et al.* (in prep) to suggest that, for positively skewed measured D_e distributions, the median is a more appropriate measure of the average D_e than the mean (i.e. it provides a more accurate assessment of the intersection of the mean of the OSL distribution onto the growth curve). The scale of this effect has been calculated by applying the normally distributed dataset described in Section 6.4.1 to the standardized growth curve, using a range of different equivalent doses and 5% standard deviation[n]. The results are shown in Figure 6.11, and indicate that for equivalent doses up to 100 Gy, both the mean and median of the measured D_e distribution provide adequate estimates of the parent population mean D_e (<2% error). At larger doses, the mean rises, yielding measured values up to 6% higher than the median, which is similar to the true palaeodose. However, above c.125 Gy the highest natural luminescence intensities are larger than the saturation intensity of the growth curve (see Section 6.4.4) Consequently, the upper end of the equivalent dose distribution is lost, and both mean and median rapidly fall below the true palaeodose. For this reason, a minimum age has been quoted for Aber/28-IN4, since a third of the aliquots for this sample have natural luminescence intensities which are greater than then saturation intensity of the growth curve.

Many (though not all, see Figure 6.7) aliquots display a saturating exponential plus linear growth curve shape, and this function has been used to fit all growth curves. The natural

---

[n] This value is intended to approximate the scatter observed in a "well behaved" sample. More significant scatter causes the effects described below to occur at lower palaeodoses.

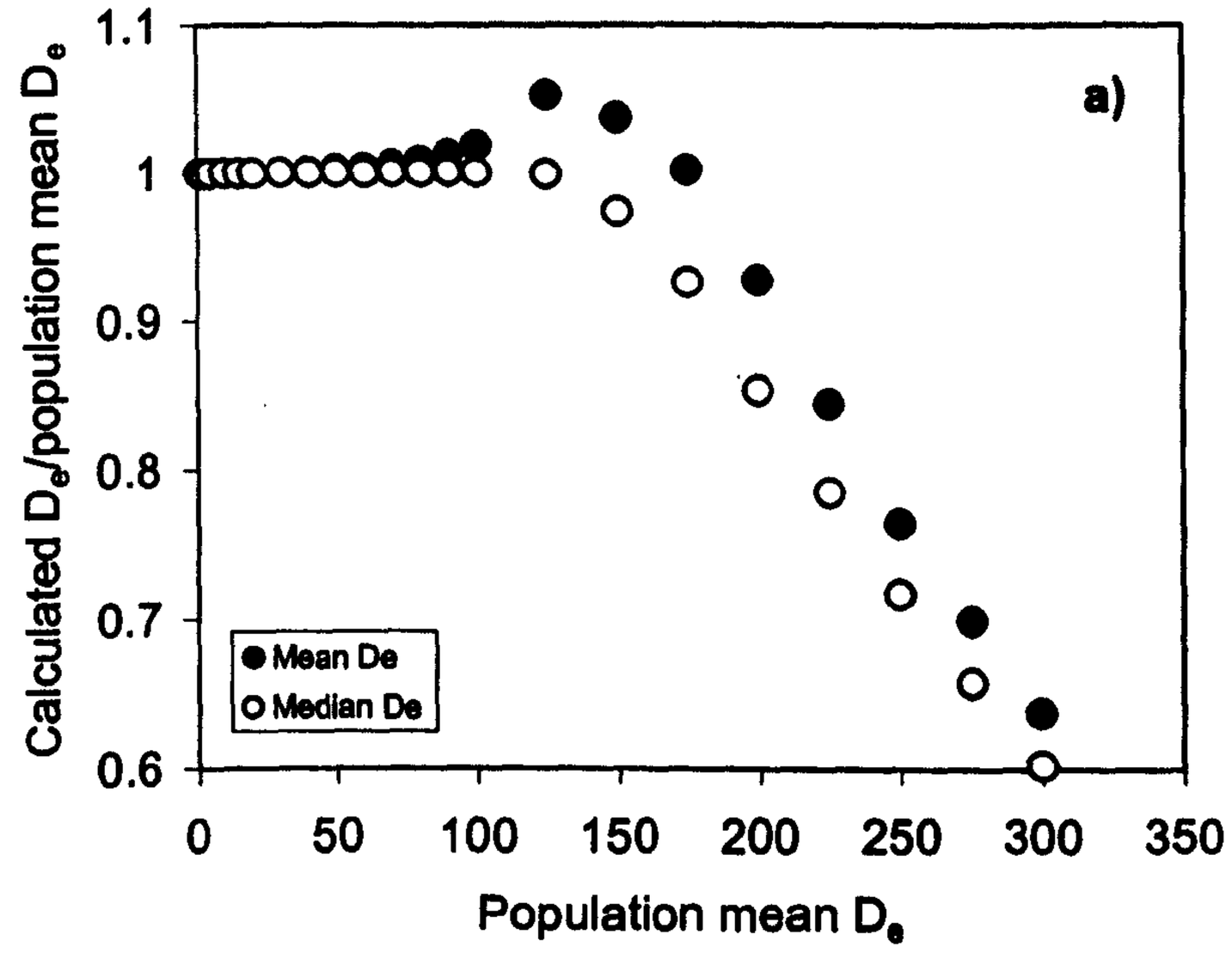

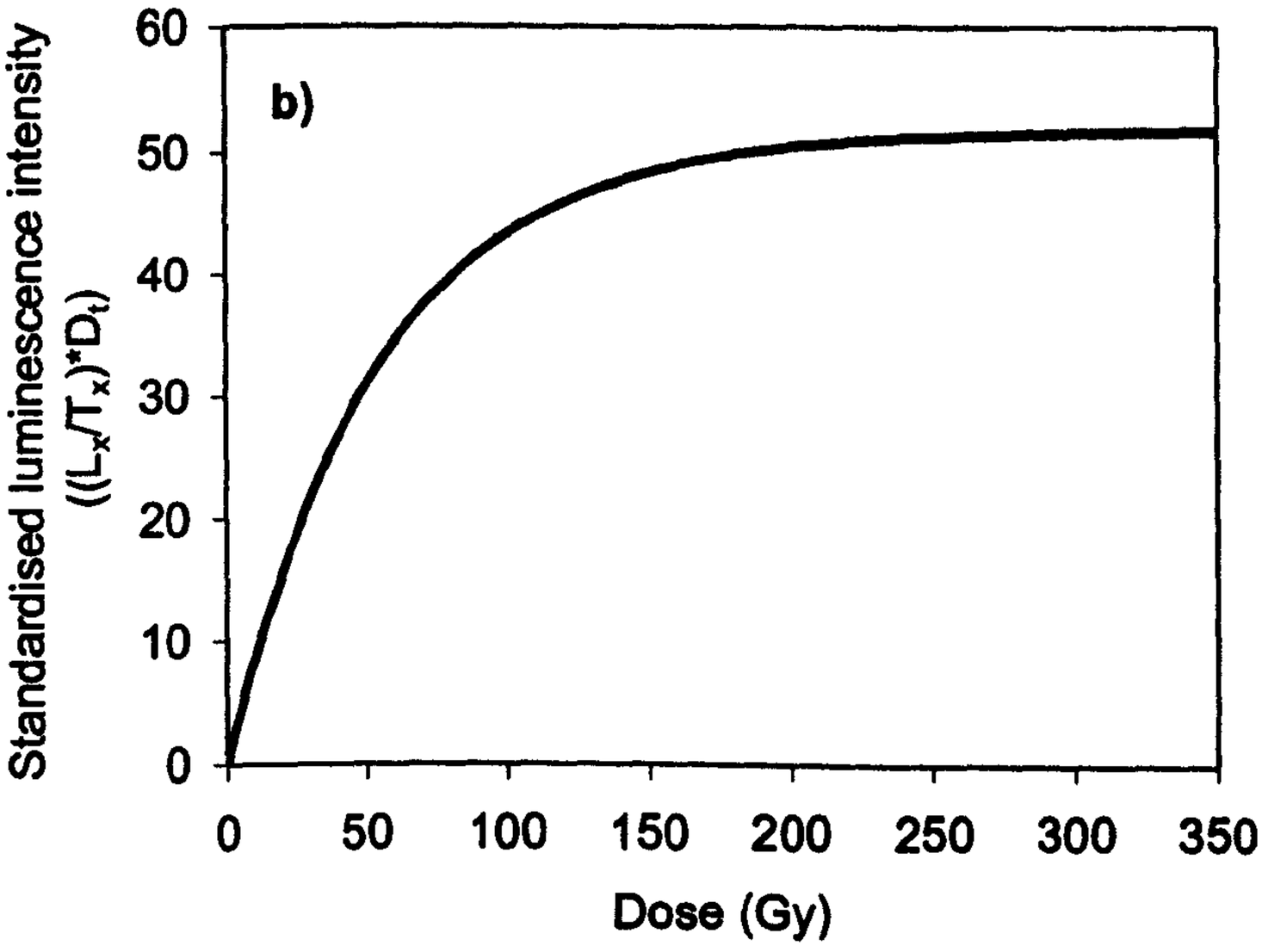

Figure 6.11. a) Calculated D_e / population mean D_e versus population mean D_e. These data were produced by applying a synthetic normally distributed population of natural luminescence intensities to the standardised growth curve shown in Figure 6.11b (single saturating exponential).

luminescence intensity for aliquots displaying a linear growth component will always intercept the growth curve. Consequently, the equivalent dose distribution at doses above 125 Gy may be more positively skewed than the modelled datasets calculated above. In these circumstances, the median provides a better approximation of the palaeodose than the mean, which will tend to yield an overestimate (Bray *et al.*, in prep.).

For doses up to 100 Gy, the modelled data indicate that the mean D_e is a good approximation of the palaeodose. Consequently, for samples yielding mean equivalent doses under 100 Gy, this value was used in the age calculation. The median equivalent dose has been used for samples with mean D_e values above 100 Gy. In practice, although the mean D_e is slightly larger than the median for these samples, the effect is relatively small (c.5%)°.

6.5.2 Calculated equivalent doses

Equivalent doses have been calculated for each of samples dated in this study (Tables 6.3 and 6.4). Each equivalent dose is the mean (or median as appropriate, see Section 6.5.1) with one standard error uncertainty. The equivalent doses are used to calculate the sample age in Chapter 7.

° One potential disadvantage of this approach is that the median is a poorly known statistic, whereas the mean is relatively well known. The choice between the median and mean of a dataset is therefore a trade-off between an imprecisely known median, with low systematic uncertainties, and a more precisely known mean, but with a risk of large systematic uncertainties.

Sample (Aber/…)	Aliquots used[P]	Aliquots rejected (%)	Average used	D_e (Gy)
28-IN1	18	25	median	101 ± 10
28-IN3	23	4	mean	96.2 ± 6.5
28-IN4	14	42	median	242 ± 18
28-IN9	24	0	mean	0.060 ± 0.005
28-IN11	19	21	median	133 ± 6
28-IN12	21	13	mean	22.4 ± 0.5
28-IN14	21	13	mean	14.5 ± 0.3
28-IN15	21	13	mean	5.16 ± 0.06
28-IN16	22	8	mean	2.41 ± 0.02
28-IN18	21	13	mean	12.2 ± 0.3
28-IN19	22	8	mean	2.04 ± 0.30
28-IN20	17	29	mean	4.28 ± 0.07
28-IN21	16	33	mean	3.12 ± 0.30
28-IN22	18	25	mean	0.006 ± 0.004

Table 6.3. Final D_e estimates for samples from Inhaca Island. Error terms are one standard error, irrespective of the average used.

Sample (Aber/…)	Aliquots used	Aliquots rejected (%)	Average used	D_e (Gy)
29-BA1	18	25	median	124 ± 7.0
29-BA2	21	13	mean	7.83 ± 0.83
29-BA4	24	0	mean	0.114 ± 0.004
29-BA5	18	25	mean	0.003 ± 0.010
29-BA8	23	4	mean	1.70 ± 0.15
29-BA10	22	8	mean	17.1 ± 1.1
29-BA11	20	17	mean	3.37 ± 0.43
29-BA12	17	29	mean	7.02 ± 0.77
29-BA13	18	25	mean	29.7 ± 2.4
29-BA14	14	42	median	176 ± 13
12-MAP3	25	0	mean	29.0 ± 0.6
12-RBM2	17	29	mean	93.5 ± 9.5

Table 6.4. Final D_e estimates for samples from Bazaruto Island and Maputaland (Aber/12-MAP3 and Aber/12-RBM2). Error terms are one standard error, irrespective of the average used.

[P] In most cases 24 aliquots were measured. Aliquots with poor recycling ratios, significant infra-red stimulable signals or which yield L_n/T_n values which miss the growth curve have been excluded from the final equivalent dose calculation.

6.6 Conclusions

1) All the datasets presented in this study contain scatter caused by β-microdosimetry and measurement reproducibility error. The latter becomes particularly significant at higher equivalent doses, due to the curvature of the growth curve. In addition, some scatter may be introduced by mixing of adjacent units, possibly by bioturbation. Some of the older samples (D_e>100 Gy) yield a very large range of equivalent doses. This cannot be explained in terms of β-microdosimetry, measurement reproducibility error or mixing (bioturbation). No cause for this additional scatter has been found.
2) The standardized growth curve (SGC) defined for coarse grained quartz by Roberts and Duller (submitted) appears to be applicable to the samples measured in this study.
3) Three samples yield aliquots whose sensitivity corrected natural luminescence intensity is larger than the saturation level of the growth curve. Although no single cause could be determined for this phenomenon, it appears to result from imperfect sensitivity correction of either the natural or regenerated dose points. This effect cannot be explained by measurement reproducibility errors, or the use of a restricted regeneration dose range.
4) At equivalent doses above 100 Gy, the median is a more appropriate estimate of the sample palaeodose than the mean. On the basis of modelled data, the mean may significantly overestimate the palaeodose. However, for the five samples with equivalent doses greater than 100 Gy measured in this study, the effect is small. Below 100 Gy either the mean or median may be used.

Chapter 7: Environmental dose rate evaluation

7.1 Introduction

Mineral grains in a sediment are exposed to an ionizing radiation field. This radiation is derived from three main areas, an internal dose from within the grains themselves, an external dose from the bulk sediment matrix and a contribution from cosmic radiation. The internal dose rate for quartz is has been assumed to be zero[a], and consequently only the external sources of radiation have been quantified for this project.

7.1.1 Radiation derived from the bulk sediment matrix

For most samples the environmental dose rate is provided primarily, and in roughly equal parts, by potassium, thorium and uranium contained within the sediment matrix (Aitken, 1985). Interestingly, for samples analysed in this study, the majority of the environmental dose rate is provided by potassium[b]. A small contribution is also made by an isotope of rubidium[c]. ^{40}K (0.0117% natural abundance) undergoes radioactive decay to form stable isotopes of calcium or argon by the emission of β or γ radiation respectively (Figure 7.1). The gamma emission is accompanied by electron capture. The natural parent isotopes of thorium (^{232}Th) and uranium (^{235}U and ^{238}U) decay to form stable isotopes of lead via several intermediate radioisotopes. The series of decays which each nucleus must undergo to form a stable lead isotope is termed a "decay chain". Decay chains for ^{232}Th, ^{235}U and ^{238}U are given in Figures 7.2-4, where A and Z are defined as the atomic mass number and atomic number respectively, and the times quoted are half lives. α, β and γ radiations are emitted by members of these chains.

Alpha, beta and gamma radiation are able to penetrate different thicknesses of sediment. Although the maximum penetration for each type of radiation is dependent upon the

---

[a] This is the standard assumption used by the Aberystwyth laboratory, however the Nordic Laboratory for Luminescence Dating use an internal quartz dose rate of 0.06 Gy/ka.

[b] For the Inhaca and Bazaruto samples, potassium accounts for 66 ± 5 % and 75 ± 7 % of the total dose rate.

[c] ^{87}Rb emits a low energy β particle. For a K:Rb ratio of 200:1, rubidium provides 2.4 % of the unattenuated β dose from potassium (Adamiec and Aitken, 1998).

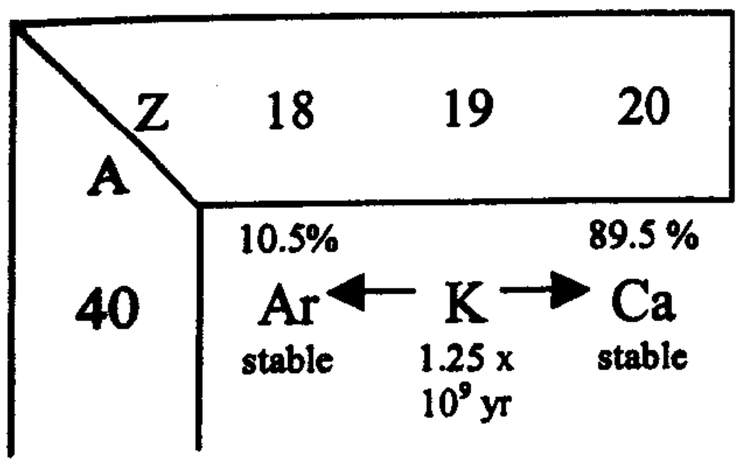

Figure 7.1. ^{40}K decay (data from Aitken, 1985).

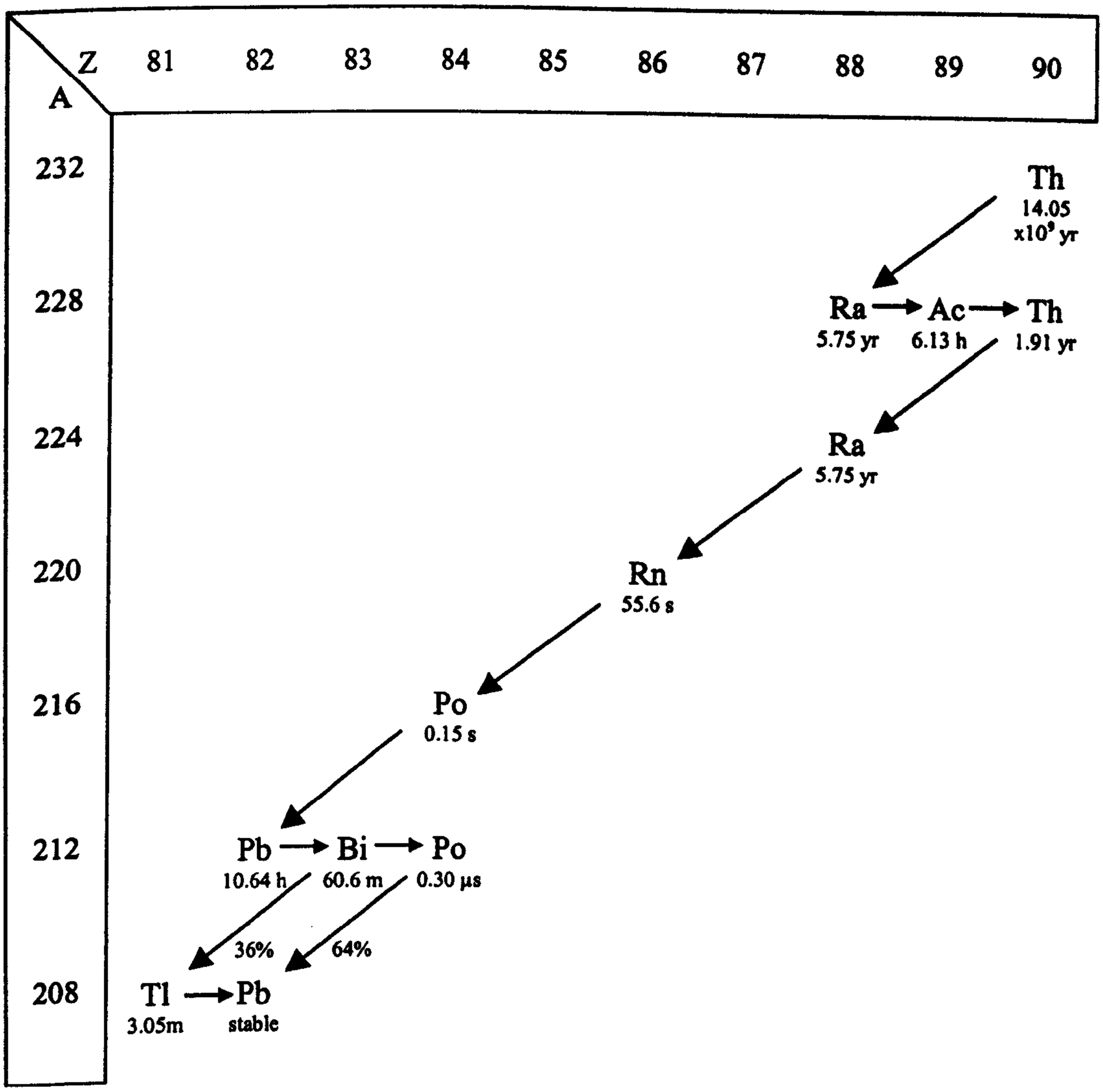

Figure 7.2. ^{232}Th decay series. Long arrows represent α and short arrows β particle emission. γ emissions are not shown.

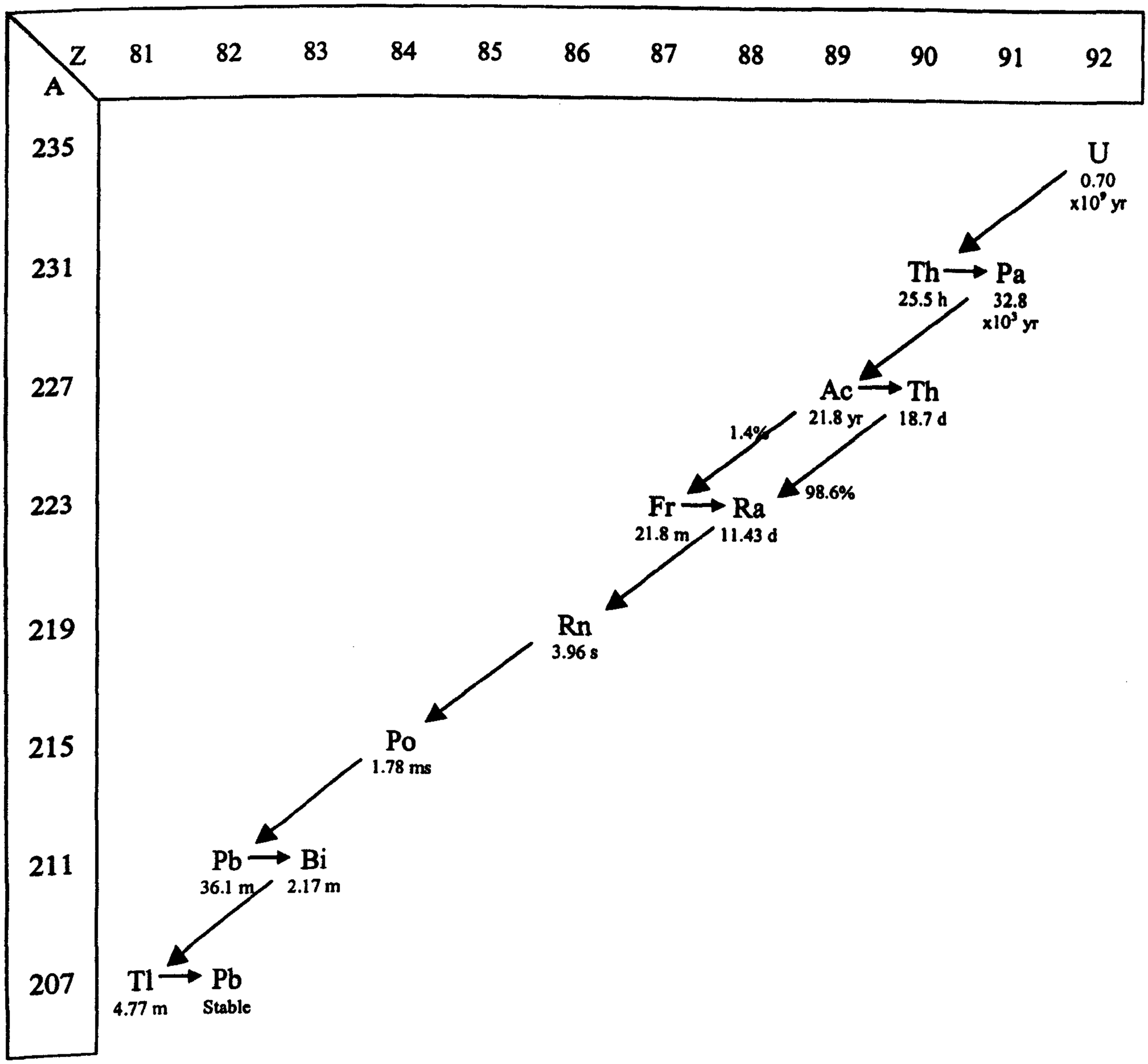

Figure 7.3. ^{235}U decay series. Naturally occurring uranium contains 0.72% ^{235}U, the remainder being ^{238}U. Long arrows represent α and short arrows β particle emission. γ emissions are not shown.

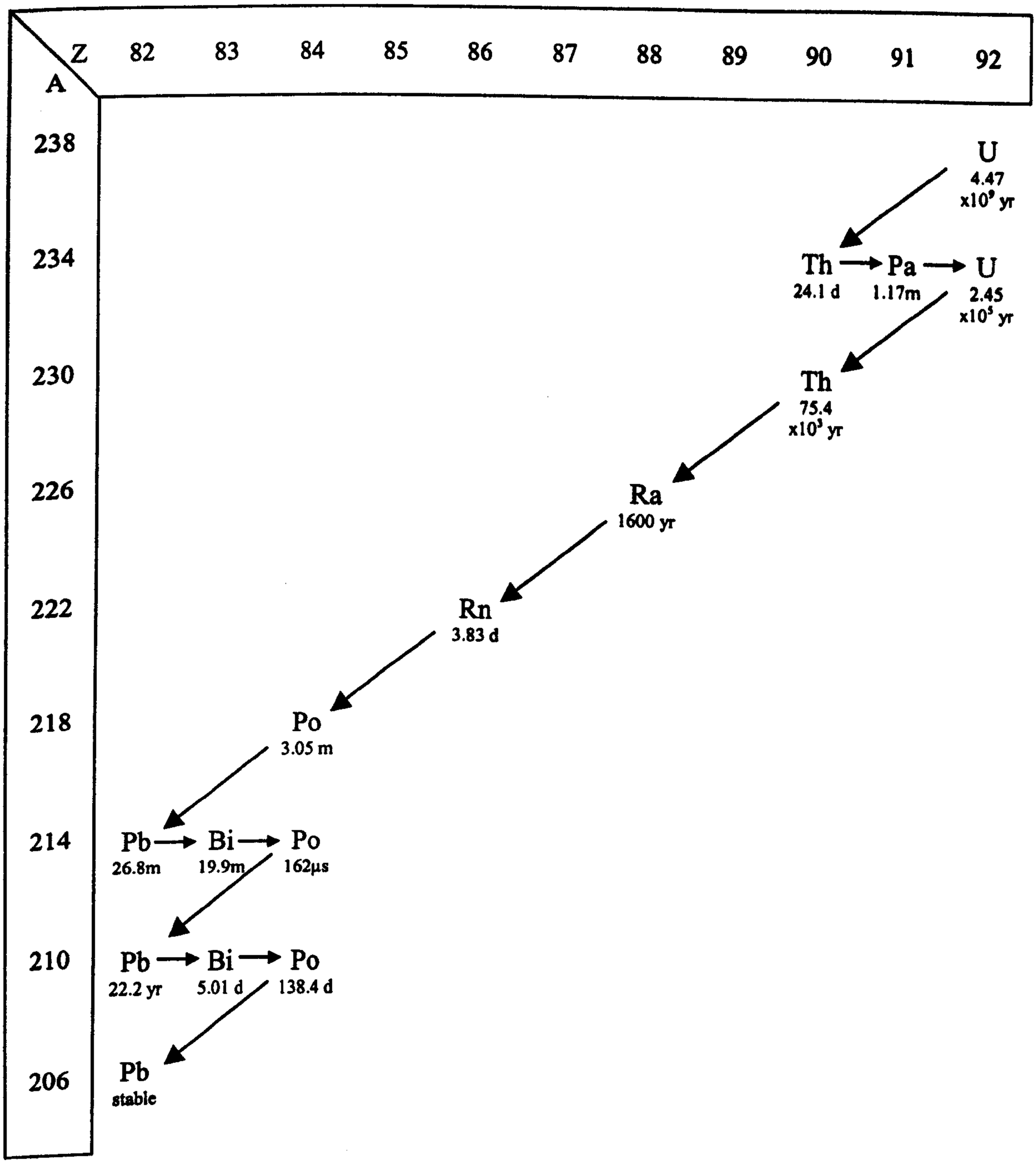

Figure 7.4. ^{238}U decay series. Long arrows represent α and short arrows β particle emission. γ emissions are not shown.

energy it carries, some generalizations can be made. Alpha particles are highly ionizing and lose their energy rapidly. Consequently they have very short ranges. Beta particles are less strongly ionizing and have longer ranges. Gamma rays are attenuated exponentially, and make a significant contribution to the environmental dose rate of sediment up to 30 cm from their source (Figure 7.5). Consequently, a sample will receive its gamma dose from a sphere of sediment with this radius. For the purposes of laboratory based dose rate evaluation methods, it is generally assumed that radioisotopes are evenly distributed within this sphere. In this work, samples were taken at least 30 cm from any lithostratigraphic boundary in an attempt to justify this assumption. Similarly, for the purposes of environmental dose rate estimation, it has been assumed that the sediment sampled was buried to a depth of at least 30 cm relatively rapidly (see also Section 7.5.1).

7.1.2 Cosmic radiation

Cosmic radiation consists of two particle types, electrons (the "soft" component) and muons (the "hard" component). The penetration of each type of particle is dependent upon the bulk density of the sample. For a given overburden density, the cosmic ray dose rate can be estimated from the depth of the sample. Geographic location and altitude may also affect the cosmic ray dose rate (see Section 7.2.5).

7.2 Methods for assessing radioisotope concentrations and cosmic ray dose rate

Three methods have been used to assess the dose rates for samples analysed in this study. Thick-source alpha counting (TSAC) and Geiger-Muller-beta counting (GM-beta) has been performed on all samples. Potassium content was measured for a selection of samples using atomic absorption spectrophotometry (AAS).

For routine dose rate evaluation, TSAC has been used to assess the uranium and thorium content of a sample. GM-beta counting provides an estimate of the infinite β dose rate. The potassium content can be estimated from the combination of these two analyses (see Appendix 7.1 for a worked example). The cosmic ray dose rate was estimated from sample depth for all samples.

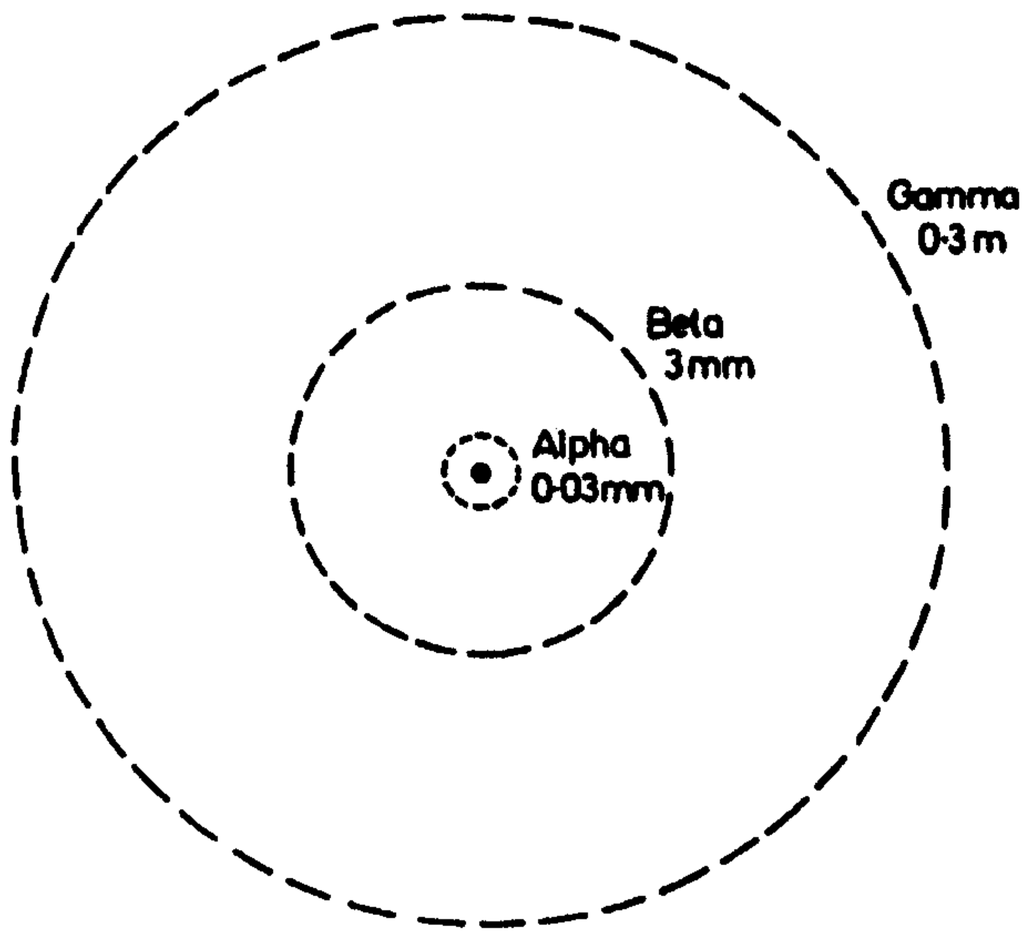

Figure 7.5. Maximum spheres of influence for relevant radiation types (not to scale). From Aitken (1998)

7.2.1 Thick-source alpha counting

TSAC measures the alpha emissions from a sample due to the decay of members of the uranium and thorium decay chains. A refinement of the basic TSAC method is to measure the number of coincident pairs of alpha emissions due to the rapid decay of ^{216}Po to ^{212}Pb following its formation from ^{220}Rn, an isotope in the ^{232}Th decay chain (Figure 7.2). Thorium and uranium concentrations can be calculated by comparing the "pairs" count rate with the total alpha count rate (see Appendix 7.1). Although good at measuring specific alpha activities, TSAC is relatively poor at determining uranium and thorium concentrations due to the relatively small number of pairs observed in a measurement period[d]. This technique assumes secular equilibrium in the thorium and uranium decay chains. A more detailed account of TSAC techniques can be found in Aitken (1985).

Alpha counting, using Daybreak model 582 or 583 systems, was carried out on subsamples which had previously been dried and homogenized in a ball mill. Immediately prior to use, ZnS scintillation screens were counted for 24 hours to assess their background count rate. This was generally an order of magnitude lower than the value of 0.1 cts/ks suggested by Aitken (1990) as a rejection threshold. The alpha count of the sample was continued until a minimum of 3000 counts had been registered. Full TSAC results are presented in Appendix 7.2. For both the background and sample counts, the first two hours of counting were subtracted, because ZnS scintillation screens acquire a temporarily elevated background on exposure to daylight (Daybreak model 583 Users Manual).

Midway through the thorium and each of the uranium decay chains is an isotope of the gas radon. This gas sometimes migrates through the interstices of the sample and causes disequilibrium in the decay chain[e]. Radon loss during alpha counting can be assessed by comparing count rates with the perspex counting cell unsealed and sealed. For samples

---

[d] Typically, 70-80 pairs had been observed by the time a total of 3000 counts had been registered. This gives an uncertainty in the pairs count rate of c.12%.

[e] The only important radon isotope in this respect is ^{222}Rn in the ^{238}U decay series (Figure 7.4), since the radon isotopes in the ^{235}U (Figure 7.3) and ^{232}Th (Figure 7.2) decay series have very short half-lives.

where radon emanation is significant, the sealed count rate will increase with time over a period of days, as the daughter isotopes of radon build up. This will lead to a sealed/unsealed ratio greater than unity. Due to low total alpha count rates (c.2 cts/ks), sealed counts were stopped once 1000 counts had been measured.

Sealed/unsealed TSAC ratios for 25 samples were measured, yielding a mean ratio of 1.014±0.045 (Figure 7.6), indicating that the two count rates are indistinguishable, and radon emanation is not significant.

7.2.2 GM-beta counting

GM-beta counting was performed using a Risø GM-25-5 five sample low-level beta GM multicounter system. A detailed description of this system is provided by Bøtter-Jensen and Mejdahl (1988). Three dried, ground 1g subsamples of each sample were measured for a period of not less than 24 hours. In addition, two standard samples, with known beta dose rates of 0 (MgO) and 6.25 Gy/ka (Shap granite), were measured in each run. Full GM-beta counting results are given in Appendix 7.3. From these data the infinite beta dose rate of the sample can be calculated. Where the uranium and thorium concentrations are known (fron TSAC), the potassium content of the sample can also be calculated[f] (see Appendix 7.1).

7.2.3 Atomic absorption spectrophotometry

A small number of samples were analysed using AAS. Approximately 0.5g of the dried, ground sample, previously used for TSAC and GM-beta counting, was digested in HF acid. AAS was used to directly measure the potassium content. This work was performed by Mrs. Lorraine Hill, IGES, Aberystwyth.

---

[f] Rubidium will also make a contribution to the β dose rate measured using a GM-beta counter. This will cause a slight overestimate of the potassium content calculated using the method outlined in Appendix 7.1. The error in the environmental dose rate caused by this overestimate will be small, due to the low abundance of rubidium, and the low energy of the beta particle emitted.

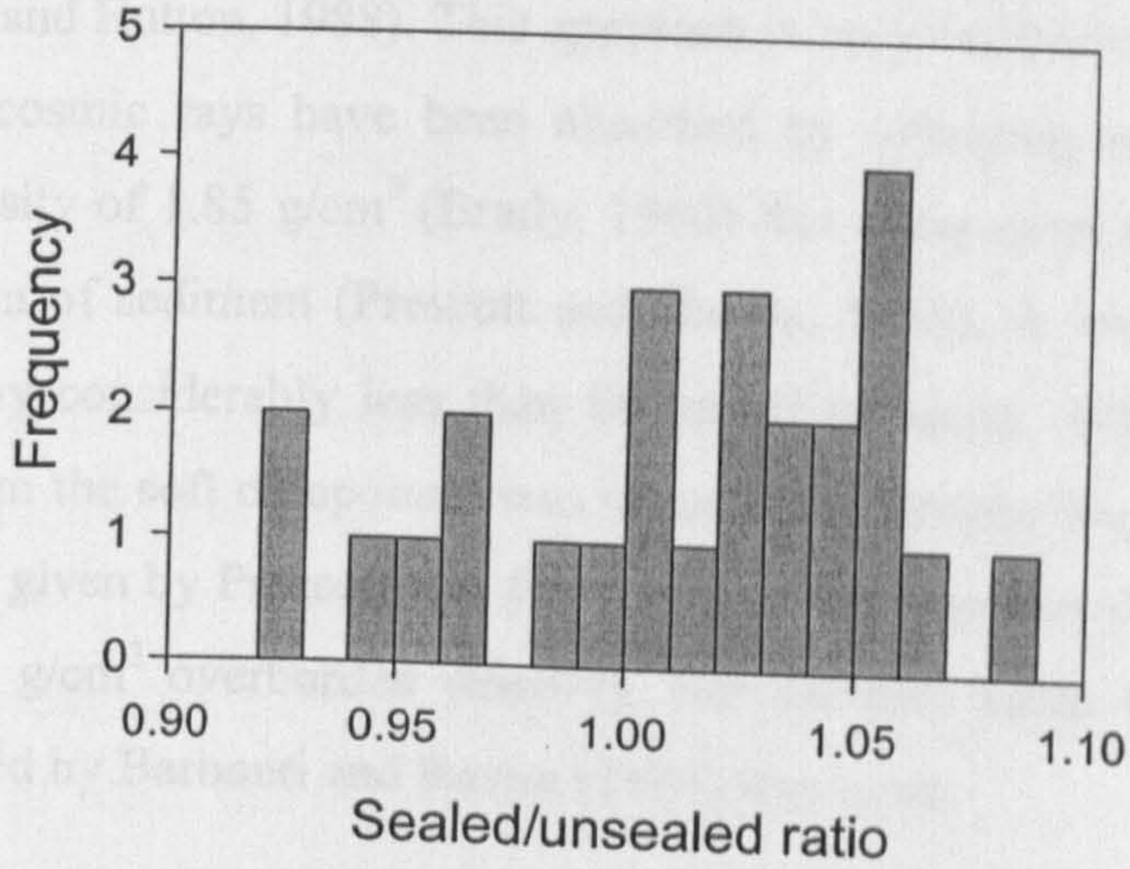

Figure 7.6. Sealed/unsealed TSAC ratios.

7.2.4 Calculation of dose rates

Environmental dose rates were calculated from radioisotope concentrations using the dose-rate conversion factors of Adamiec and Aitken (1998). These calculations were performed using the Aberystwyth Luminescence Database software (written by Dr. Geoff Duller), and a worked example can be found in Appendix 7.1. Adamiec and Aitken (1998) provide a useful comparison between their conversion factors and previously published values (notably Nambi and Aitken, 1986) as an appendix.

7.2.5 Cosmic ray dose rate

The cosmic ray dose rate can be calculated from the overburden density and sampling depth (Prescott and Hutton, 1988). This approach is only valid where the "soft" (electron) component of cosmic rays have been absorbed by overlying sediment. Assuming an overburden density of 1.85 g/cm^3 (Brady, 1990) this component reduced to a negligible level by c.80 cm of sediment (Prescott and Hutton, 1988). A small number of samples were overlain by considerably less than 80 cm of sediment. Where this occurred, the contribution from the soft component was taken from Prescott and Hutton (1988, Figure 1). The formula given by Prescott and Hutton (1988) is also inapplicable beyond a depth of c.27m (1.85 g/cm^3 overburden density). For samples taken below this depth, the equation provided by Barbouti and Rastin (1983) was used.

Prescott and Hutton (1994) identified long-term variations in the muon dose rate due to changes in the geomagnetic field. The largest correction required for a sample dated in this study (Aber/28-IN19) decreases the environmental dose rate by 0.4%. This correction is regarded as being insignificant, and has not been incorporated into the environmental dose rate calculation. All samples were taken within 50 m of sea-level and hence no correction for sample altitude was required.

7.3 Comparison of AAS and TSAC/GM-beta derived potassium contents

Table 7.1 shows AAS and TSAC/GM-beta derived potassium contents for a selection of samples. The AAS values are approximately 8 % lower than those produced using TSAC and GM-beta measurements. There is no obvious reason to prefer one dataset over the

other, and hence all environmental dose rates were calculated using TSAC/GM-beta counting derived potassium values, even where an AAS value had been measured.

Sample code (Aber/...)	%K (TSAC/GM-beta)	%K (AAS)	TSAC/GM-beta : AAS
12-RBM2	0.78 ± 0.04	0.66	1.18
12-RBM2a	0.70 ± 0.02	0.66	1.06
12-MAP3	0.33 ± 0.02	0.24	1.38
29-BA6	1.94 ± 0.03	1.70	1.14
29-BA9	1.58 ± 0.04	1.45	1.09
29-BA10	2.05 ± 0.03	1.91	1.07
29-BA11	1.18 ± 0.03	1.18	1.00
29-BA12	1.48 ± 0.04	1.44	1.03
29-BA13	1.03 ± 0.03	1.00	1.03
29-BA14	1.30 ± 0.02	1.24	1.05

Table 7.1. Potassium contents determined using TSAC/GM-beta counting and AAS.

7.4 Assessment of the water content during burial

Water absorbs some of the radiation that would otherwise reach the constituent mineral grains of a sample. This significantly reduces the α, β and γ dose rates experienced by mineral grains, relative to those evaluated using dry dosimetry samples. Attenuation of the environmental dose rate has been calculated using the absorption coefficients suggested by Aitken (1985, p75).

Estimation of the water content during burial can be the largest source of error in the assessment of environmental dose rates. Figure 7.7 shows the effect water content has on the environmental dose rate for two Mozambican samples. The main difference between the two samples is the size of the cosmic ray contribution to the dose rate. Although the trend is not linear, the dose rate decreases by about 1% per 1% increase in the water content from 0-10%. Modern, "as found", water contents were measured for a range of samples and are summarized in Table 7.2. The unconsolidated dune and cliff face samples have modern water contents of c.2%, though there is considerable scatter in these results. The sample taken below the current water table yielded a value considerably lower than the saturation water content for dune sands (37%) calculated by

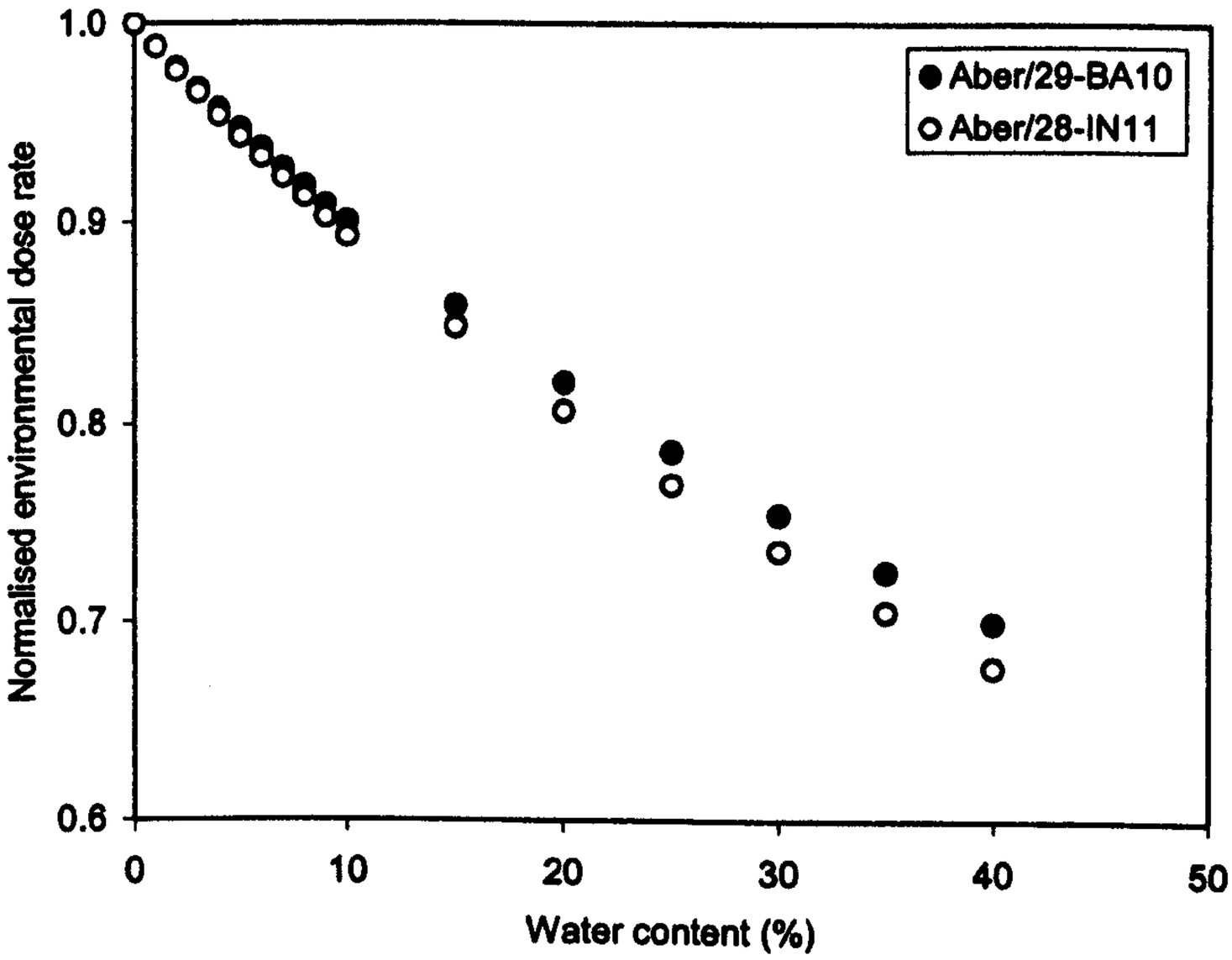

Figure 7.7. The effect of water content on environmental dose rate ($\beta + \gamma +$ cosmic). Both samples are 212-180 μm etched quartz, overburden density 1.85 g/cm^3.

Duller (1996). Adoption of the modern values has two main objections. Firstly, fieldwork in Mozambique was conducted in April, at the end of the Austral summer. Secondly, sample preparation occurred up to 18 months after collection. Both factors may lead to an underestimation of the mean burial water content.

Sample type	Mean (%)	Standard deviation (%)	No. of samples
Unconsolidated dune	2.01	1.24	9
Sand from cliff face	2.39	1.09	11
Beachrocks	No measurements	-	-
Below modern watertable	19.7	NA	1

Table 7.2. Modern percentage water content (mass of water/ mass of dry sediment).

The approach used for this study is to group samples according to their present situation and modify the modern water contents appropriately. For both the unconsolidated dune and cliff face samples, a mean burial water content of 5±2% has been assumed. The same value has been assumed for the beachrocks. These samples were taken from the present intertidal zone, and hence are probably saturated. However, the carbonate cement appears to fill almost all the pore spaces, and consequently a relatively low porosity has been assumed. A saturation water content of 5±2% equates to a porosity of 9.3±3.7%. For the samples taken below the modern water table (Aber/28-IN9 and Aber/28-IN20) the saturation water content of Duller (1996) has been adopted. These samples are from (palaeo)tidal flats of Holocene age. Consequently, given their position below the present water table, a saturation water content is appropriate.

7.5 Post depositional alteration of the environmental dose rate

For practical purposes the environmental dose rate is generally assumed to be constant over the burial period. In practice, due to the mobility of sediment and the radioisotopes contained within it, minor alterations of the environmental dose rate are probably quite common. Possible causes of dose rate change relevant for this study are discussed below.

7.5.1 Changes in overburden thickness

Changes in overburden thickness affect the γ and cosmic ray dose rates experienced by a mineral grain. The γ photon field is derived from a 30 cm radius sphere of sediment surrounding the sample (Section 7.1.1). It is generally valid to assume rapid burial of a sample to this depth, and consequently use the full gamma dose rate derived from radioisotope concentrations. Similarly, where samples were taken from sea-cliff faces, care was taken to excavate this depth into the cliff face prior to sample collection. Where this approach was not feasible, due to the strength of the rock, cliff retreat is likely to have exposed sediment which experienced the full γ dose rate during burial. For the beachrock and modern analogue samples, which were taken at the surface, a full 30 cm sphere of sediment surrounding the sample cannot be assumed. For surface samples the γ dose rate is half of that at infinite depth. It is likely that for most of the burial period the beachrocks (Aber/29-BA2 and Aber/29-BA8) were buried by a small thickness of beach sand. For a mean thickness of 10 cm[g], the γ dose rate the beachrocks will have experienced will be greater than 88% of that at infinite depth (Aitken, 1985, Figure 4.3). Given the size of the correction, and the inability to measure a mean burial depth, the γ contributions to the environmental dose rate for these samples have been calculated assuming infinite overburden thickness.

For most samples, the cosmic ray dose rate has been calculated using the sampling depth below the modern ground surface. The exceptions to this are the beachrock samples and two samples from the Zingalema Point section on Bazaruto (Aber/29-BA13 and Aber/29-BA14). For the latter samples, the cosmic ray dose rate was calculated in stages, allowing for the deposition of subsequent sedimentary units.

7.5.2 Carbonate cementation/leaching.

Cementation has the potential to either increase or decrease the environmental dose rate experienced by mineral grains. The carbonate cement may contain additional

---

[g] 50 cm overburden has been assumed for environmental dose rate calculation. The figure of 10 cm is illustrative.

radioisotopes which will increase the dose rate. Conversely, by filling the interstices of the sediment, the dose rate may be decreased. The magnitude of this effect can be calculated for sample Aber/12-RBM2, since a sample of the uncemented parent material has also been analysed (Aber/12-RBM2a). The dose rate for the cemented sample is c.50% higher than that for the uncemented material (Table 7.3).

Sample (Aber/12-...)	Th content (ppm)	U content (ppm)	K content (%)	Dose rate (Gy/ka)[b]
RBM2a	0.974 ± 0.126	0.353 ± 0.040	0.699 ± 0.024	0.896 ± 0.029
RBM2	2.854 ± 0.418	1.504 ± 0.128	0.783 ± 0.034	1.339 ± 0.043

Table 7.3. Dose rates to a sample before (Aber/12-RBM2a) and after (Aber/12-RBM2) carbonate cementation.

This increase is largely due to increased uranium and thorium concentrations, though a small rise in the potassium content is also noted. Similar considerations apply for the removal of carbonates by leaching, though the effect is less likely to be homogenous since carbonate leached from coastal dunes will have existed as discrete shell fragments. The majority of beachrocks in the study area were cemented immediately after deposition (Ramsay, 1995) and consequently the modern dose rate has been used. For other samples, the timing and effect of carbonate cementation/leaching is impossible to assess, and the modern dose rate has also been used. This constitutes a considerable potential error in the age calculation. This potential error may be avoided by using the "quartz-feldspar subtraction dating technique" (McKerrell and Mejdahl, 1981). This technique utilizes the radioisotope content of feldspars to provide an internal dose rate to the grain. By subtracting the D_e measured using quartz from that measured from feldspar, an equivalent dose derived solely from the internal radioactivity of the feldspar can be calculated. Consequently, the date produced is not affected by changes in the external dose rate. This technique has recently been applied to South African coastal dunes by Vogel *et al.* (1999). Although elegant, the subtraction dating technique relies on the routine production of precise and accurate feldspar dates. This is not currently possible, and consequently subtraction dating has not been used in this study.

[b] For etched 212-180 μm grains assuming 5±2 % water content, due to radioisotopes within the sediment only.

7.6 Environmental dose rates for dated samples

Data relevant to the calculation of environmental dose rates is listed in Tables 7.4-7.7. Uranium and thorium concentrations were calculated using TSAC data. The potassium content was calculated from TSAC and GM-beta counting. The β dose rates in Tables 7.5 and 7.7 have been corrected for grain size, sediment water content and the effects of an HF acid etch. γ dose rates have been corrected for water content only. In all cases, secular equilibrium in the uranium and thorium decay chains has been assumed.

The environmental dose rates themselves are relatively low, although not as extreme as those noted by Munyikwa (2000, Table 1). The mean dose rate for Inhaca is 0.99 ± 0.18 Gy/ka, while the equivalent value for Bazaruto is 1.48 ± 0.30 Gy/ka (Tables 7.5 and 7.7).

7.7 Conclusions

1) Little or no radon emanation was measured during TSAC measurements.
2) Potassium contents measured using AAS and TSAC/GM-beta are in reasonable agreement.
3) In the range 0-10%, a 1% increase in the water content of a sample leads to c.1% decrease in the environmental dose rate.
4) Carbonate cementation of a sand body has the potential to significantly alter the environmental dose rate. For the one sample examined, cementation increased the Th and U activities by factors of ~3 and ~4 respectively.
5) Environmental dose rates of both Inhaca and Bazaruto islands relatively low (<1.5 Gy/ka).

Sample code (Aber/28-...)	Depth (m)	Th content (ppm)	U content (ppm)	K content (%)	H_2O content (%)
IN1	3.0 ± 1.0	0.431 ± 0.023	0.310 ± 0.065	0.513 ± 0.021	5 ± 2
IN3	4.0 ± 2.0	1.461 ± 0.168	0.353 ± 0.052	0.808 ± 0.028	5 ± 2
IN4	30 ± 5.0	1.770 ± 0.203	0.428 ± 0.063	0.767 ± 0.028	5 ± 2
IN9	0.1 ± 0.1	2.308 ± 0.281	0.792 ± 0.085	0.799 ± 0.032	37 ± 5
IN11	40 ± 5.0	3.456 ± 0.390	0.765 ± 0.118	1.092 ± 0.033	5 ± 2
IN12	1.4 ± 0.2	1.500 ± 0.171	0.369 ± 0.052	0.778 ± 0.020	5 ± 2
IN14	1.4 ± 0.2	2.079 ± 0.228	0.433 ± 0.069	1.013 ± 0.032	5 ± 2
IN15	1.5 ± 0.2	1.107 ± 0.131	0.334 ± 0.040	0.643 ± 0.018	5 ± 2
IN16	1.2 ± 0.2	1.552 ± 0.174	0.380 ± 0.053	0.910 ± 0.022	5 ± 2
IN18	1.2 ± 0.2	0.805 ± 0.116	0.436 ± 0.036	0.627 ± 0.018	5 ± 2
IN19	1.2 ± 0.2	1.280 ± 0.145	0.339 ± 0.045	0.589 ± 0.018	5 ± 2
IN20	0.6 ± 0.2	1.372 ± 0.215	0.921 ± 0.067	1.240 ± 0.034	37 ± 5
IN21	1.2 ± 0.2	1.838 ± 0.225	0.560 ± 0.069	0.894 ± 0.024	5 ± 2

Table 7.4. Depth, radioisotope and water content values for samples from Inhaca Island. Errors on the radioisotope concentrations are counting statistics only.

Sample code (Aber/28-...)	D_e (Gy)	β dose rate (Gy/ka)	γ dose rate (Gy/ka)	Cosmic radiation (Gy/ka)	Total dose rate (Gy/ka)	Age (ka)
IN1	101 ± 10	0.358 ± 0.015	0.178 ± 0.007	0.144 ± 0.076	0.680 ± 0.078	149 ± 23
IN3	96.2 ± 6.5	0.549 ± 0.021	0.289 ± 0.013	0.128 ± 0.135	0.966 ± 0.137	99.6 ± 15.6
IN4	242 ± 18	0.539 ± 0.022	0.302 ± 0.015	0.018 ± 0.027	0.858 ± 0.038	>250
IN9	0.060 ± 0.005	0.443 ± 0.025	0.139 ± 0.017	0.262 ± 0.026	0.844 ± 0.040	0.071 ± 0.006
IN11	133 ± 6	0.805 ± 0.027	0.489 ± 0.025	0.011 ± 0.014	1.305 ± 0.040	102 ± 5
IN12	22.4 ± 0.5	0.534 ± 0.019	0.286 ± 0.012	0.175 ± 0.018	0.995 ± 0.029	22.5 ± 0.8
IN14	14.5 ± 0.3	0.692 ± 0.027	0.373 ± 0.017	0.175 ± 0.018	1.240 ± 0.037	11.7 ± 0.4
IN15	5.16 ± 0.06	0.441 ± 0.016	0.233 ± 0.010	0.173 ± 0.018	0.847 ± 0.026	6.09 ± 0.20
IN16	2.41 ± 0.02	0.615 ± 0.021	0.320 ± 0.013	0.180 ± 0.019	1.115 ± 0.031	2.16 ± 0.06
IN18	12.2 ± 0.3	0.437 ± 0.016	0.227 ± 0.009	0.180 ± 0.019	0.844 ± 0.026	14.5 ± 0.6
IN19	2.04 ± 0.30	0.414 ± 0.016	0.229 ± 0.010	0.180 ± 0.019	0.823 ± 0.027	2.48 ± 0.37
IN20	4.28 ± 0.07	0.629 ± 0.034	0.331 ± 0.017	0.204 ± 0.020	1.164 ± 0.043	3.68 ± 0.15
IN21	3.12 ± 0.30	0.631 ± 0.022	0.348 ± 0.016	0.180 ± 0.019	1.159 ± 0.033	2.69 ± 0.27
IN22	0.006 ± 0.004	-	-	-	-	-

Table 7.5. Equivalent dose, dose rates and ages for samples from Inhaca Island. Equivalent dose values are those from Table 6.3.

Sample code (Aber/29-…)	Depth (m)	Th content (ppm)	U content (ppm)	K content (%)	H_2O content (%)
BA1	6.0 ± 0.5	1.452 ± 0.168	0.373 ± 0.051	1.327 ± 0.024	5 ± 2
BA2	0.5 ± 0.2	1.047 ± 0.127	0.326 ± 0.040	0.882 ± 0.027	5 ± 2
BA4	1.2 ± 0.2	2.489 ± 0.302	0.736 ± 0.092	0.969 ± 0.028	5 ± 2
BA8	0.5 ± 0.2	0.487 ± 0.074	0.314 ± 0.024	1.680 ± 0.034	5 ± 2
BA10	1.2 ± 0.2	1.330 ± 0.157	0.395 ± 0.048	2.052 ± 0.028	5 ± 2
BA11	2.0 ± 0.5	2.165 ± 0.237	0.565 ± 0.072	1.177 ± 0.033	5 ± 2
BA12	4.0 ± 0.5	3.591 ± 0.391	0.755 ± 0.118	1.478 ± 0.041	5 ± 2
BA13	6.0 ± 0.5	2.090 ± 0.233	0.581 ± 0.071	1.032 ± 0.025	5 ± 2
BA14	20 ± 2	1.094 ± 0.147	0.496 ± 0.045	1.300 ± 0.023	5 ± 2

Table 7.6. Depth, radioisotope and water content values for samples from Bazaruto Island. Errors on the radioisotope concentrations are counting statistics only.

Sample code (Aber/29-…)	D_e (Gy)	β dose rate (Gy/ka)	γ dose rate (Gy/ka)	Cosmic radiation (Gy/ka)	Total dose rate (Gy/ka)	Age (ka)
BA1	124 ± 7	0.859 ± 0.028	0.410 ± 0.014	0.102 ± 0.026	1.372 ± 0.041	90.0 ± 5.8
BA2	7.83 ± 0.83	0.581 ± 0.014	0.285 ± 0.011	0.207 ± 0.020	1.073 ± 0.027	7.30 ± 0.79
BA4	0.114 ± 0.004	0.708 ± 0.024	0.414 ± 0.020	0.180 ± 0.019	1.302 ± 0.036	0.088 ± 0.004
BA8	1.70 ± 0.15	1.158 ± 0.037	0.442 ± 0.013	0.207 ± 0.020	1.806 ± 0.044	0.94 ± 0.09
BA10	17.1 ± 1.1	1.290 ± 0.041	0.574 ± 0.017	0.180 ± 0.019	2.044 ± 0.048	8.37 ± 0.54
BA11	3.37 ± 0.43	0.806 ± 0.030	0.429 ± 0.018	0.163 ± 0.043	1.397 ± 0.055	2.41 ± 0.32
BA12	7.02 ± 0.77	1.035 ± 0.036	0.583 ± 0.027	0.128 ± 0.034	1.745 ± 0.056	4.02 ± 0.46
BA13	29.7 ± 2.4	0.720 ± 0.024	0.394 ± 0.016	0.120 ± 0.024[1]	1.234 ± 0.038	24.1 ± 2.1
BA14	176 ± 13	0.850 ± 0.028	0.401 ± 0.013	0.116 ± 0.023	1.367 ± 0.039	128 ± 10

Table 7.7. Equivalent dose, dose rates and ages for samples from Bazaruto Island. Equivalent dose values are those from Table 6.4.

[1] Cosmic ray dose rates for Aber/29-BA13 and 14 were calculated in stages, to allow for accumulation of the overlying deposit (see Section 7.5.1). The cosmic ray dose rate quoted is the mean annual value, with a 20 % error term.

Chapter 8: Geological setting and evolution of Inhaca and Bazaruto Islands, Mozambique

8.1 Introduction

This chapter uses the OSL ages produced for samples from Inhaca (Table 7.5) and Bazaruto (Table 7.7) to describe and explain the geological evolution of the islands. To do this, the chapter has been split into three major sections. Section 8.2 discusses previous research into the geological evolution of the southeastern coast of Africa, based on the summary provided by Maud and Botha (2000), and provides a regional framework within which to discuss Inhaca and Bazaruto. Sections 8.3 and 8.4 discuss the geological evolution of Inhaca and Bazaruto respectively.

8.2 Geological setting and evolution of the southeast coast of Africa

The majority of previous work was carried out on the South African section of the Maputaland coastal plain, which extends northwards into Mozambique (Figure 8.1). Inhaca Island lies at the northernmost seaward tip of this region. Consequently, research concerning the geological evolution of the Maputaland coastal plain is directly relevant to that of Inhaca. Bazaruto is located, lying c.500 km north of Inhaca. However, Ramsay (1994, p225) has noted that the morphological and sedimentological features observed in Maputaland, are representative of the southeast coast of Africa. Similarly, Maud and Botha (2000, their Figure 2-1) include much of Mozambique up to 20°S in the Maputaland lithostratigraphic group (Bazaruto lies between 22 and 21°S). In addition, Bazaruto Island has been used as an analogy for the Last Interglacial barrier archipelagos thought to have existed along the Maputaland coast (Wright, 1997 and Wright *et al.*, 2000). Consequently, cautious use of Maputaland as an analogue for the geological setting of Bazaruto Island is justified.

8.2.1 The Maputaland coastal plain

The Maputaland coastal plain is located between the Lebombo Mountains in the west, and the Indian Ocean in the east. It is bounded to the north and south by Maputo Bay and the St Lucia estuary respectively (Figure 8.1). The coastline itself is SSW-NNE in orientation, and is characterised by a high coastal barrier dune (often >100 m high) and a sandy beach frequently underlain by c.2 m thickness of beachrock (Cooper, 1991). The plain has a low gradient, and for most of its length is about 60 km wide

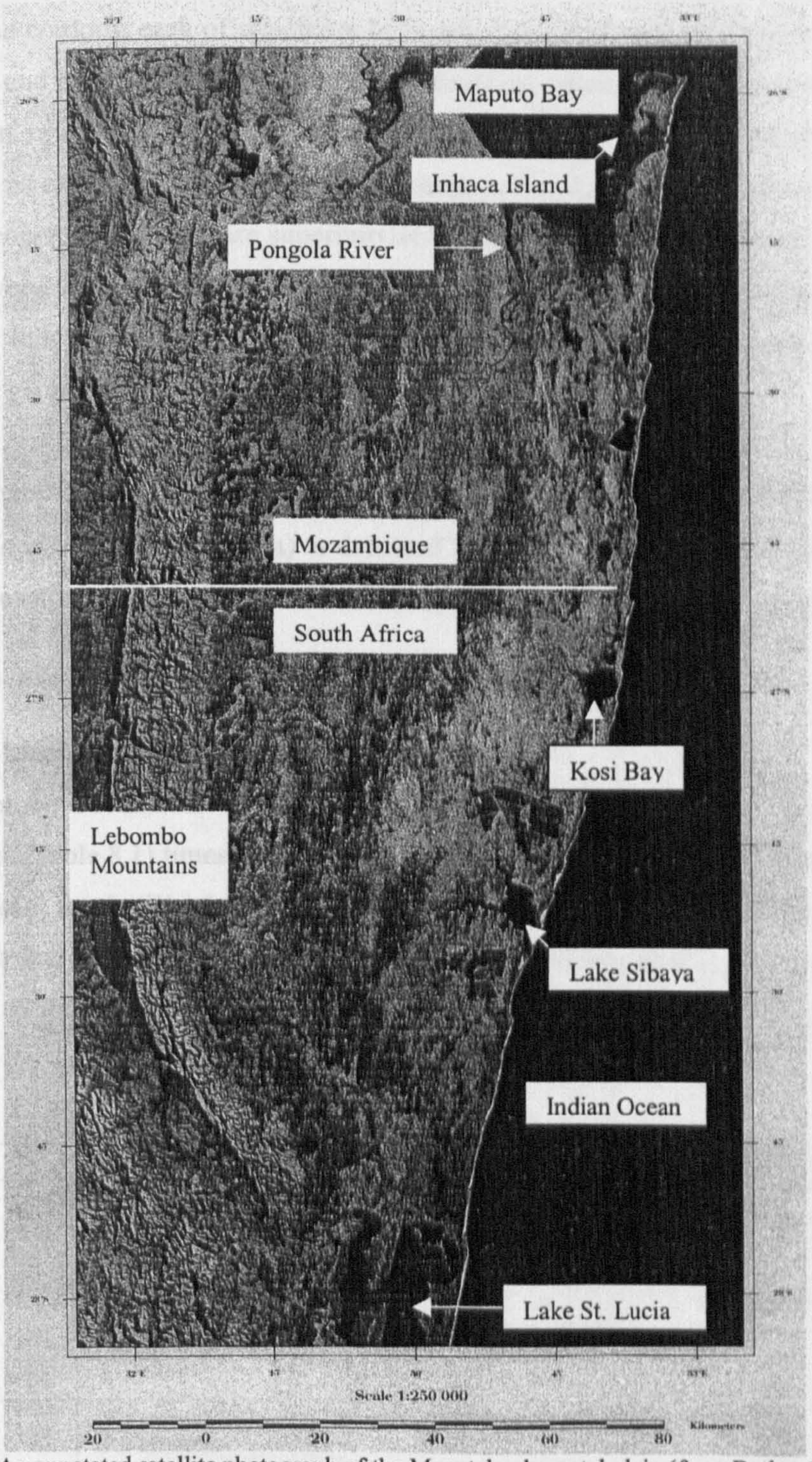

Figure 8.1. An annotated satellite photograph of the Maputaland coastal plain (from Botha, 1997)

(Maud and Botha, 2000). The undulating topography is dominated by coast-parallel fossil dune cordons, each of which are believed to have formed adjacent to a former coastline, and become younger in a seaward direction. These fossil dune cordons have often been extensively reworked after deposition. The reworked sediment has been deposited as extended parabolic dunes and hummocky dune systems. In many areas, several generations of dune are superimposed upon each other (Botha *et al.*, in press). Because very few natural or man-made sections through these composite features are available, this superimposition of several generations of dune upon each other has hampered geological study of the area.

Several rivers cross the coastal plain and are either diverted in a N/S direction by the dune cordons (e.g. River Pongola) or dammed by the active coastal barrier dune at the modern coastline, forming coastal lakes (e.g. Kosi Bay, Lake Sibaya and Lake St. Lucia).

8.2.2 The Maputaland lithostratigraphic group

The Lebombo Mountains are formed from extruded volcanic lava, and by late Cretaceous (Table 8.1) times marked the palaeoshoreline, with the beach raised 130 m above present levels (Wright, 1997), and the current coastal plain submerged. During the mid to late Cretaceous, a succession of marine and terrigenous sediments were deposited. A long period of deep weathering and erosion followed, persisting until the Miocene.

Era	Period		Epoch	Base (Ma)
Cenozoic	Quaternary		Holocene	0.01
			Pleistocene	1.64
	Tertiary	Neogene	Pliocene	5.2
			Miocene	23.3
		Palaeogene		65.0
Mesozoic	Cretaceous			145.6

Table 8.1 A geologic timescale for the period covered by Chapter 8, based on information from Harland *et al.* (1989).

The Maputaland lithostratigraphic group has been developed by Botha (1997) and Maud and Botha (2000) to describe the onshore deposits laid down along the

Maputaland coastal plain during and since the Miocene. It consists of seven formations, and is summarised in Figure 8.2[a].

1) Uloa Formation

A sequence of littoral and shallow marine coquina, conglomerate and sandstone, deposited along the Lebombo foothills, and resting on earlier Cretaceous sediments. It is thought to have been deposited by a series of sea-level stillstands and regressions, producing a polyphase wave-cut surface. Although the age of this formation has been the subject of considerable dispute, it is now widely accepted to be middle-Miocene to early Pliocene (Maud and Botha, 2000). However, on the basis of foraminiferal evidence, McMillan (1993) regards the formation as being of Pleistocene age.

2) Umkwelane Formation

The Umkwelane Formation rests on either the Uloa Formation, or the underlying Cretaceous sediments. It comprises a lower littoral marine calcarenite, with a maximum thickness of 5-8 m, and an upper cross-bedded aeolianite with a maximum thickness of 25 m. This unit is thought to be early Pliocene in age, and the upper surfaces of both units are heavily weathered to form Berea-type rubified sand.

3) Port Durnford Formation

The Port Durnford Formation underlies the seaward portion of the southern Maputaland coastal plain, and unconformably overlies either Cretaceous deposits, or the Uloa and Umkwelane Formations. It consists of a basal aeolianite, unconformably overlain by a succession of flat-lying mudstones and sands, and attains a thickness of 20-25 m. The aeolianite may belong to the Umkwelane Formation. The mudstone is grey or black in colour with sandy laminae, and is interpreted as estuarine in origin. It contains numerous fossil remains, which have recently been interpreted as Last Interglacial (Oschadleus *et al.*, 1996), on the basis of a $^{230}Th/^{234}U$ disequilibrium date of 70 ± 6 ka on the overlying lignite (peat, see below).

---

[a] Although this lithostratigraphy is not used extensively in the subsequent analysis of the dates produced for Inhaca and Bazaruto, it has been described here to illustrate the geological history of the Maputaland coastal plain.

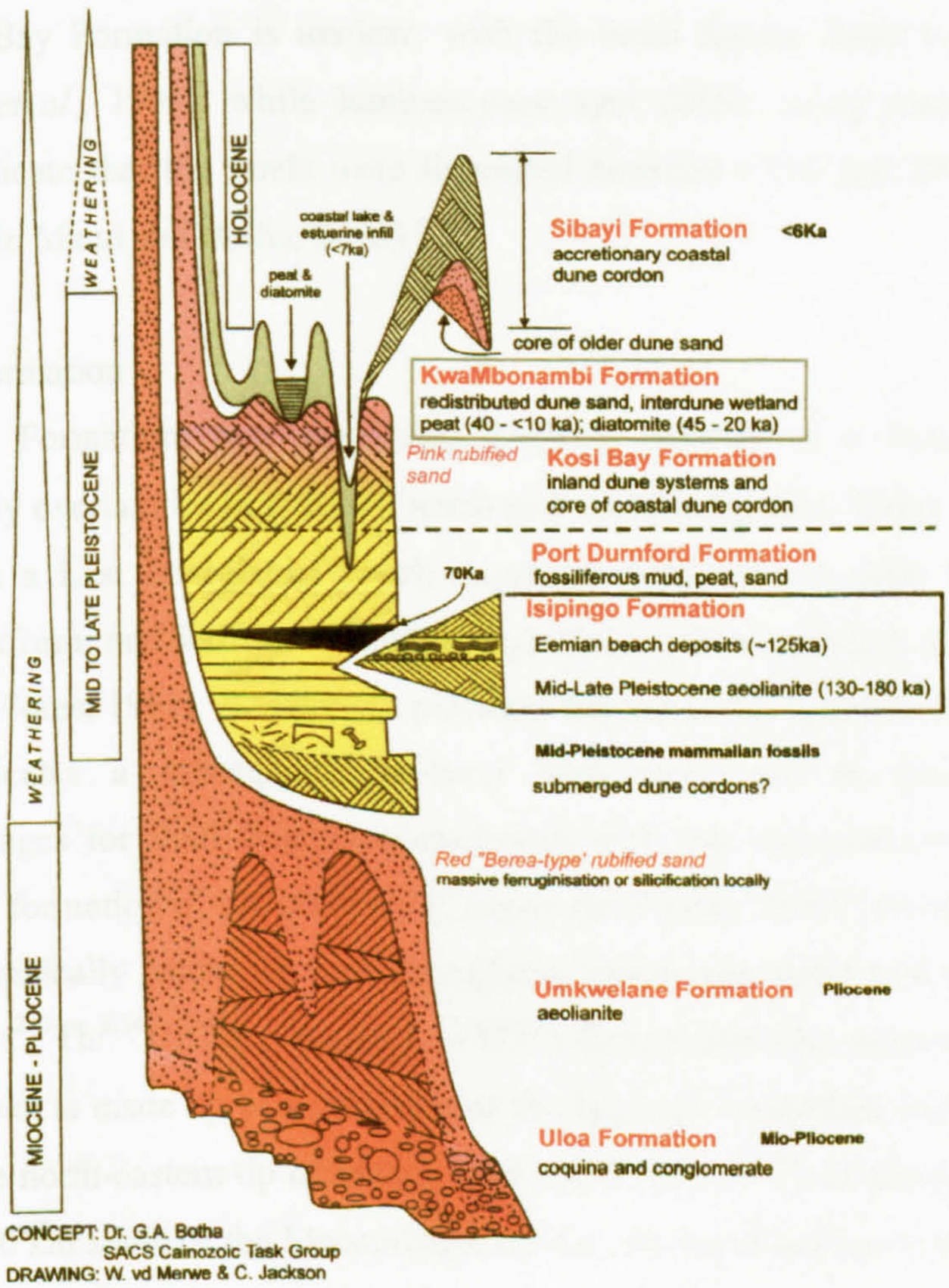

Figure 8.2. The Maputaland Stratigraphic group, describing the onshore deposits laid down along the Maputaland coastal plain during and since the Miocene. Provided to the author by Dr. Greg Botha, Council for Geoscience, South Africa. This diagram is an updated version of that which appears in Botha (1997).

4) Kosi Bay Formation

At the base of the Kosi Bay Formation is a basal lignite bed, and this overlies the Port Durnford Formation. Aeolian and lacustrine deposits rest unconformably on the Uloa, Umkwelane and Port Durnford Formations, and are thought to result from mid- to late Pleistocene aeolian deposition, with associated interdune wetlands. The aeolian member of the Kosi Bay Formation forms the core of the coastal dune cordon, where it is sometimes cemented, as well as lower parts of the inland dune cordons. The age of the Kosi Bay Formation is unclear, with the basal lignite dated to 70 ± 6 ka (Oschadleus *et al.*, 1996), while luminescence ages (IRSL using coarse grain K-fledspars) indicate that the sands were deposited between c.350 and 250 ka (Porat, pers. comm., in Maud and Botha, 2000).

5) Isipingo Formation

The Isipingo Formation, best seen near Durban, consists of a basal aeolianite unconformably overlain by nearshore, beach and aeolian deposits. These deposits are interpreted as a Last Interglacial beach sequence overlying an older wave-planed aeolianite platform, and indicate a Last Interglacial sea-level 4.5-5 m above present (Cooper and Flores, 1991). A wave-cut platform formed in the Last Interglacial beach deposits indicates a subsequent sea-level high stand 5-6 m above present. Radiocarbon ages for shell fragments associated with this sea-level event, indicate pre-Holocene formation of the platform (Cooper and Flores, 1991). An elephant tusk from stratigraphically below the Last Interglacial beach was dated to a minimum of 112 ± 23 ka ($^{230}Th/^{234}U$, Ramsay *et al.*, 1993[b]). Every shoreline promontory to the north of Durban is made up of an outcrop of the Isipingo Formation, including Cabo Inhaca[c], at the north-eastern tip of Inhaca Island (Hobday, 1977). In places, such as at Black Rock 20 km south of the Mozambique border, the basal aeolianite extends to 20 m above present sea-level (Coetzee, 1975). The basal calcareous member of the Isipingo Formation is pre-dated by the Port Durnford Formation (Maud and Botha, 2000).

---

[b] The older part of this age range was preferred by Ramsay *et al.* (1993) on the basis of stratigraphy.
[c] Mozambican names have been used for locations on Inhaca and Bazaruto.

6) KwaMbonambi Formation

The Kosi Bay Formation dunes were extensively remobilised between the Last Interglacial and Holocene, forming extended parabolic dunes and low hummocky dune complexes. These dunes are composed of yellowish red, grey and white sand, and together with interdune wetland peats and diatomites, comprise the KwaMbonambi Formation (Maud and Botha, 2000). The regional scale remobilisation of the Kosi Bay Formation is likely to have been a response to falling eustatic sea-level between the Last Interglacial and Last Glacial Maximum. Drainage networks incised rapidly through unconsolidated sands in response to the lowered base-level, causing a long term draw-down of the water table. This lowering of the water table resulted in loss/change of vegetation, which had previously stabilised the Kosi Bay formation dunes (Botha *et al.*, in press). Some blow-outs in KwaMbonambi Formation dunes are presently active. The KwaMbonambi Formation varies in thickness from 5 to 15 m.

7) Sibayi Formation

The Sibayi Formation is of Holocene age, and is composed of the youngest phase of sand accreted onto the coastal dune cordon, in response to the Holocene transgression which followed the Last Glacial Maximum sea-level low stand c.120 m below present (Section 8.2.6). The unit may contain stacked sand units separated by palaeosols, such as at Durban Bluff (Maud and Botha, 2000), and overlies the Isipingo, Port Durnford and Kosi Bay Formations. Ramped parabolic dunes overriding older dunes are common, occasionally blocking estuaries and forming coastal lakes such as Lake Sibaya, which had previously been a lagoon (Wright *et al.*, 2000). Sands of the Sibayi Formation are generally calcareous and grey, though they may also be rubified and/or decalcified to a significant depth. The Sibayi formation reaches a maximum thickness of 150 m, though in many places it overlies older dune cores.

8.2.3 Present climate

The Maputaland climate is humid subtropical. The average annual wind rose for Maputaland is shown in Figure 8.3. The dominant winds are approximately coast-parallel. North and north-easterly winds dominate in the summer, while in the winter there is a rough balance between north and south winds (Ramsay, 1994). The southerly winds are generally stronger. Northerly dipping foresets in the basal

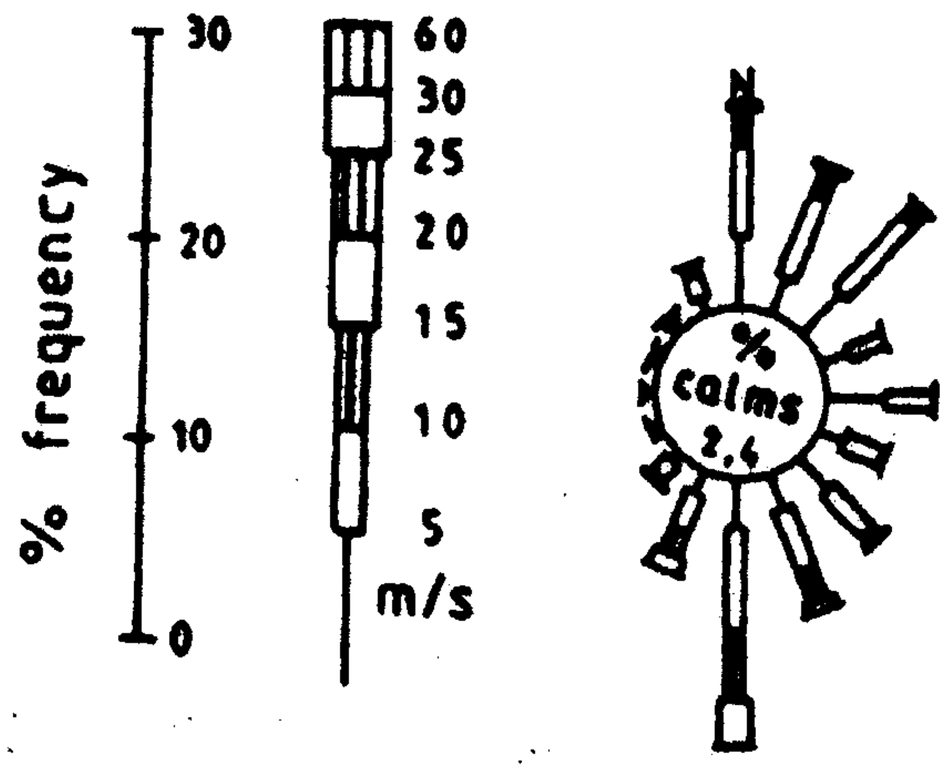

Figure 8.3. All year wind rose for Maputaland (From Ramsay, 1994)

aeolianite of the Isipingo Formation, led Cooper and Flores (1991) to suggest that southerly winds were dominant during its formation. The north-north-west trending blowouts on Inhaca Island indicate a similar palaeo-wind direction (Hobday, 1977).

Annual rainfall ranges from >1000 mm at the coast to 700 mm in the centre of the coastal plain, and falls mainly during the summer. Intense rainfall occasionally occurs due to the influence of Indian Ocean cyclones during the summer months. Average annual temperatures are around 22°C (Botha *et al.*, in press).

8.2.4 Marine geology

A brief description of the marine geology of the Maputaland shelf is provided here, since for most of the Quaternary, the shelf has been subaerially exposed. The average spring tidal range in this area is 2 m, making this coastline high microtidal or low mesotidal depending on definition (Ramsay, 1994, Ramsay *et al.*, 1996). The continental shelf is extremely narrow, with the shelf-break occurring ~3 km offshore (Ramsay *et al.*, 1996). The shelf-break occurs at –65 m, with a steep continental slope occasionally exceeding 12° (Flemming, 1981). Consequently, the Last Glacial Maximum low sea-level (-120 m in South Africa, Ramsay and Cooper, 2002) would only have caused the shoreline to migrate a few kilometres east (c.5 km, Ramsay, 1994, Figure 3). The sea-level curve for the southeast coast of Africa is discussed in Section 8.2.6.

The dominant consolidated geology on the Maputaland shelf is made up of four semi-continuous, coast-parallel beachrock and aeolianite outcrops. They are believed to delineate four late Pleistocene palaeocoastlines (Ramsay, 1994), two of which have been dated (uranium-series on beachrock cements) to 84 ± 3 ka (-17 m, Ramsay, 1994) and 117 ± 7 ka (-44 m, Ramsay and Cooper, 2002). The unconsolidated sediment on the shelf is composed of terrigenous quartz with a low (<20 %) carbonate content (Ramsay, 1994). Limited bioclastic sediment is provided by erosion of a thin coral reef which veneers the shallower (<25 m) consolidated ridges, and marine molluscs (Ramsay *et al.*, 1996). Unconsolidated subaqueous dunes occur along the Maputaland shelf as two distinct fields at depths of 35 and 70 metres below sea-level (Ramsay *et al.*, 1996). These dunefields are bounded by the beachrock and aeolianite ridges, causing them to migrate along a "track". Numerous submarine canyons are

incised into the shelf, with canyon heads occurring in water as shallow as –38 m (Ramsay, 1994). These canyons extend seaward onto the continental slope, and provide pathways for sediment transport off the shelf. Although not related to the position of modern river mouths, these canyons probably formed as palaeochannels during marine regressions, e.g. Leven Canyon is situated seaward of the Lake St. Lucia palaeo-outlet (Wright *et al.*, 2000).

8.2.5 Past and present sediment status of the Maputaland coast

Although the Maputaland coast is presently relatively sediment poor, large thicknesses of Holocene dune exist, indicating that this has not always been the case. The present scarcity of sediment is demonstrated by the ongoing formation of zeta bays. These bays are formed where sediment transported by longshore drift is trapped behind cemented outcrops of the Isipingo Formation, which due to their resistance to marine erosion, form promontories along the coast. On the down drift side of these promontories, erosion of unconsolidated sediment occurs, causing the shoreline to migrate inland and form an embayment (Ramsay, 1994, Figure 2). This process gives the Maputaland coast its characteristic log-spiral shape. However, during the Holocene vast quantities of sediment have been supplied to the coastal dune cordon, forming the Sibayi Formation, which in places reaches thicknesses of 150 m (Botha and Maud, 2000).

8.2.5.1 Sediment supply

Most sediment supplied to the Maputaland coast is fluvially derived, though biogenic carbonate makes up a small proportion (<20%) of the unconsolidated shelf sediment (Ramsay, 1994). However, the absence of significant mud deposits on the east coast shelf indicates that the suspended sediment load is rapidly expelled from the shelf (Flemming, 1981), and therefore not available to the coastal plain. The remaining coarse bedload is deposited on the continental shelf as a coastal sediment wedge. During periods of rising or falling sea-level, this sediment may be supplied to the coastal plain by one of the following mechanisms.

1) Falling sea-level exposes parts of the continental shelf, on which terrigenous sediment has been deposited. This sediment is then available to the coastal plain.

2) Rising sea-levels submerge and erode pre-existing terrestrial dunes, making sediment available to the coastal plain.

8.2.5.2 Sediment transport

During the Holocene, two main transport pathways have existed for sediment on the continental shelf. Sediment transport in the nearshore zone is wave dominated (i.e. longshore drift), whereas towards the shelf break the Mozambique and Agulhas Currents become dominant (Figure 8.4).

The Maputaland coast has a predominantly southeasterly swell regime (Ramsay, 1994 and Figure 8.5). Consequently, the modern direction of longshore drift is northward. Conversely, the Mozambique/Agulhas Currents flow southwards, with a peak surface current velocity of >9 kilometres per hour, just beyond the shelf break. This current intrudes onto the shelf, transporting sediment southwards. Inherent instability in the current causes it to migrate across the middle and outer shelf, allowing material from the nearshore sediment wedge to be entrained (Flemming, 1981). However, in several places the southerly flow of the Agulhas/Mozambique current is reversed in an eddy system, the largest of these eddies being located in Maputo Bay (Figure 8.6). This eddy forms in the lee of a structural offset in the Mozambique shoreline, causing the main Mozambique Current to move offshore. Consequently, sediment movement along much of the Maputaland shelf is northwards.

8.2.5.3 Sediment sinks

The importance of the Agulhas/Mozambique Current driven nearshore sediment flow is that it facilitates significant loss of sediment from the Maputaland shelf by two mechanisms. Firstly, due to the narrowness of the shelf in the area, submarine canyon heads are found very close to the shore. Sediment streams transported by the Agulhas/Mozambique Currents spill into canyons, and this material is lost from the shelf. Secondly, where the Agulhas/Mozambique Current breaks away from the coastline at structural offsets, the entrained sediment flows over the shelf break which follows the shore, and is lost from the shelf. For example, Maputo Bay eddy system removes sediment from the shelf seaward of the mouth of the Limpopo (Figure 8.6).

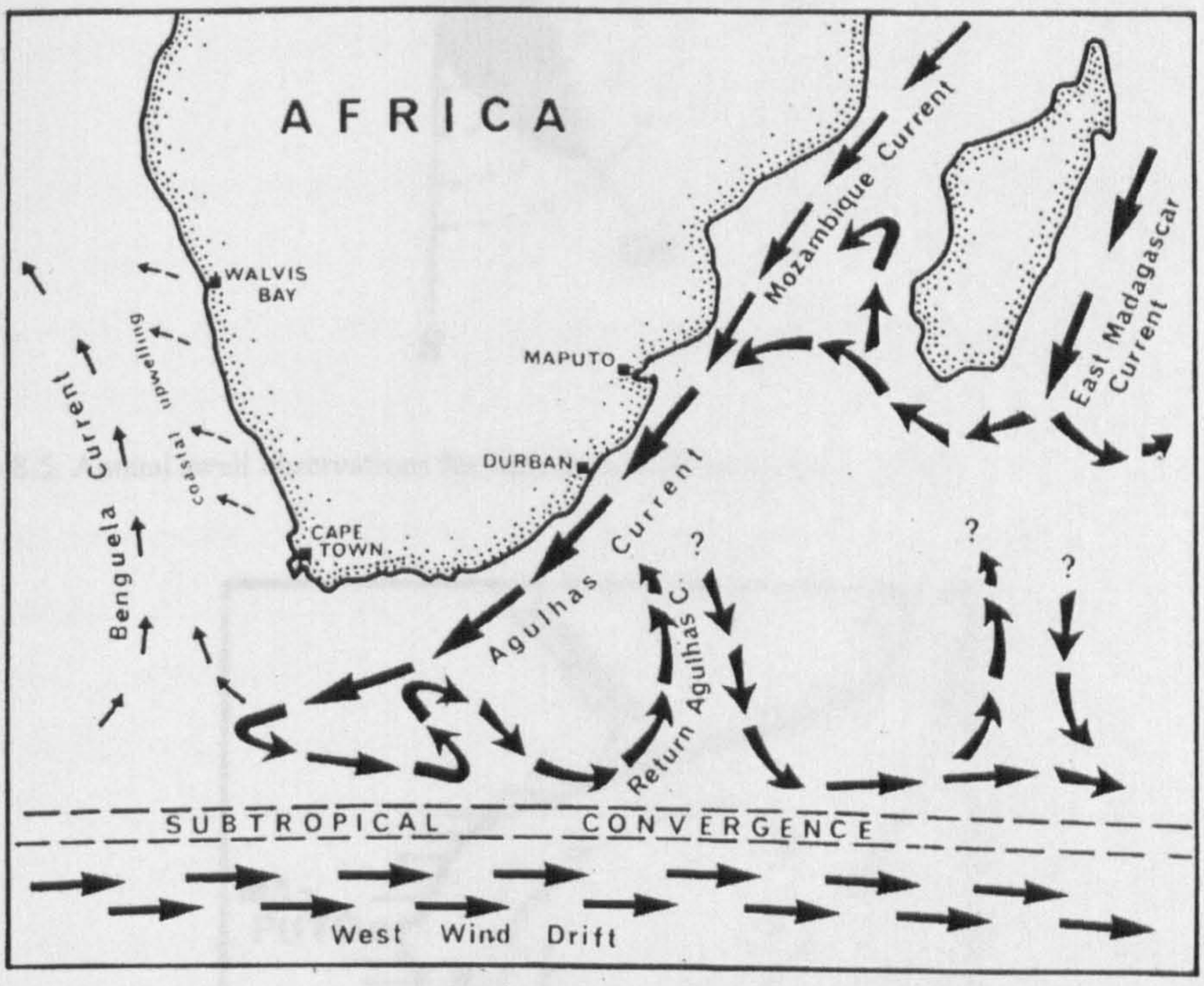

Figure 8.4. The main ocean currents around southern Africa (from Flemming, 1981). The Agulhas and Mozambique currents flow southwards along the southeast African coast. Maputaland is located between Maputo and Durban.

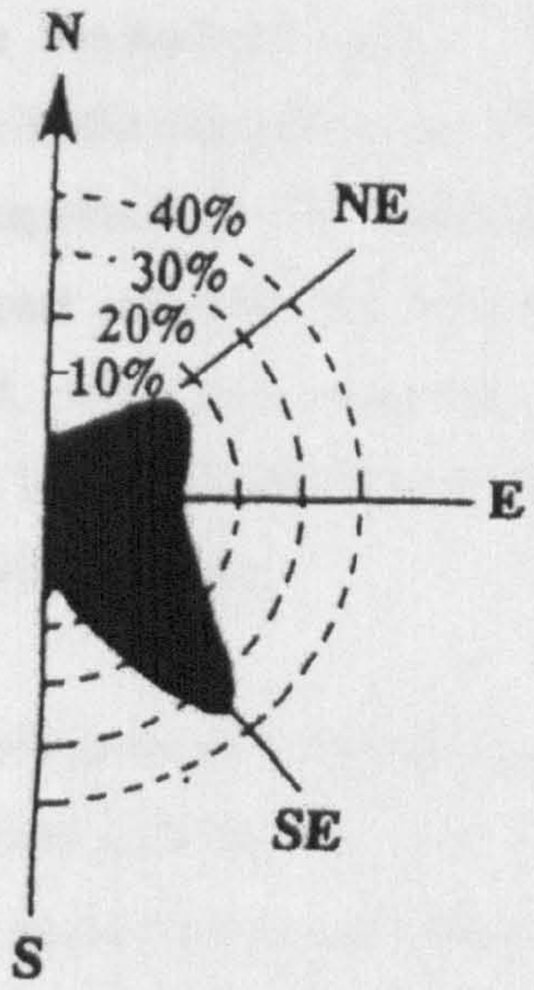

Figure 8.5. Annual swell observations for Maputaland (from Ramsay, 1994).

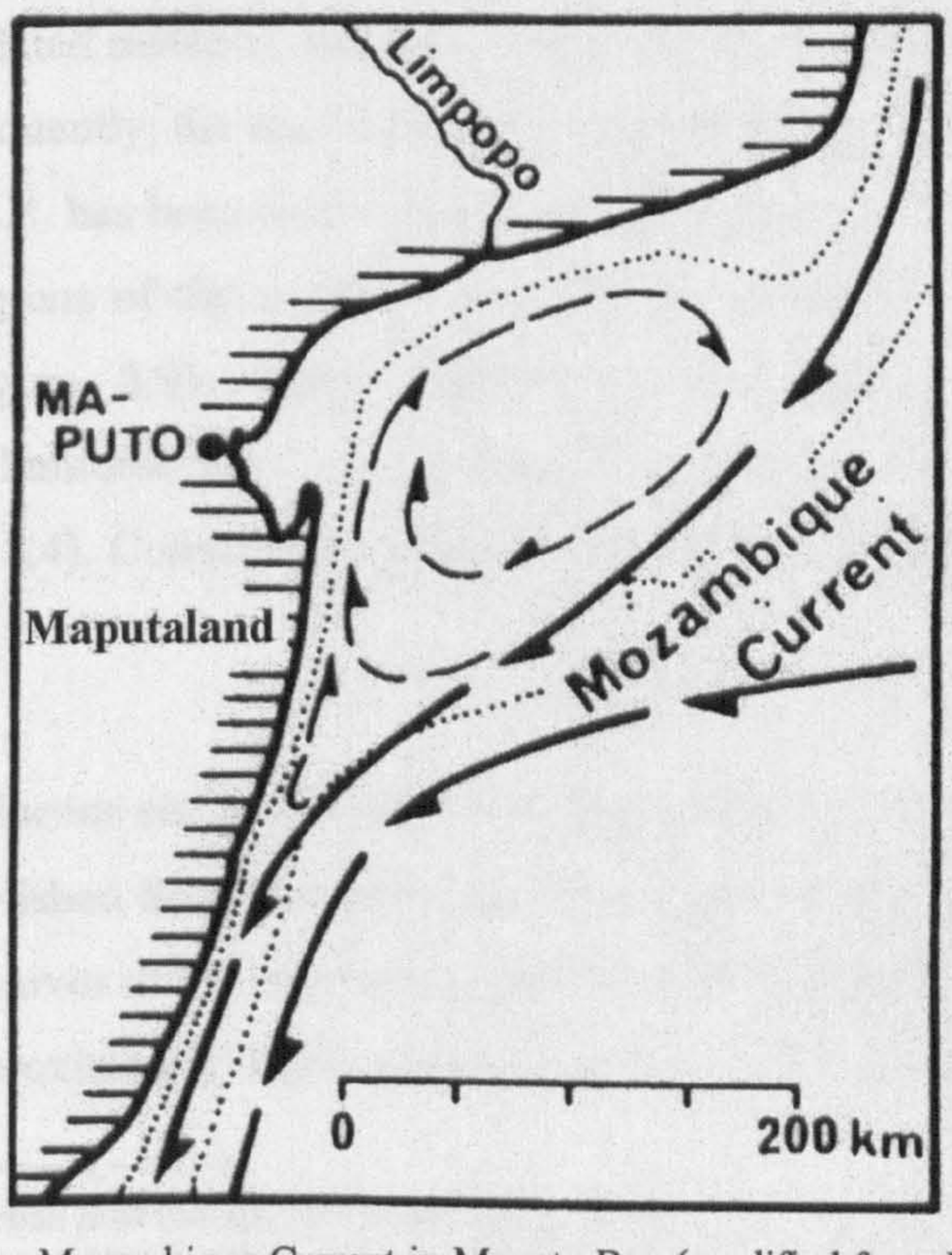

Figure 8.6. Eddy of the Mozambique Current in Maputo Bay (modified from Flemming, 1981). Due to this eddy, the nearshore movement of sediment is southwards for much of Maputaland. As the eddy current moves offshore to the east of the Limpopo, it flows over the shelf break, transporting sediment off the continental shelf.

Beachrock formation also significantly reduces the coastal sediment supply, since formation is generally much faster than erosion. Cooper (1991) estimates that the beachrock volume along the Maputaland coast is 120,000 m^3/km. This value is significant, when compared with the annual loss of 3,000 m^3/km of coastal sediments due to landward aeolian transportation[d]. The beachrocks found along the coastline also give an indication of past sediment supplies. Often, several generations of beachrock are superimposed, with early generations being sandy, while later generations consist of eroded beachrock pebbles, indicating a reduction in sediment supply over time (Cooper, 1991, Figure 5).

8.2.6 Late Quaternary sea-level history of the southeast African coast

A large body of literature exists detailing the Late Quaternary sea-level curve for Southern Africa, and has been summarised by Ramsay and Cooper (2002). These data cover a large geographical range, from the mouth of the Orange River on the western coast of South Africa to Kosi Bay in Maputaland (Figure 8.7), and consequently form a subcontinental scale dataset. For most of the Quaternary, this approach is valid, due to the paucity of dated material, and the eustatic nature of the sea-level changes they document[e]. Consequently, the sea-level curve provided by Ramsay and Cooper (2002) shown in Figure 8.8, has been used in this study. However, sea-level curves produced from different regions of the southern African coast differ in detail during the last 9,000 years (Figure 8.9). These differences are potentially important when interpreting the luminescence ages produced for Inhaca and Bazaruto Islands (Sections 8.3 and 8.4). Consequently, the most appropriate Holocene[f] sea-level curve must be selected.

8.2.6.1 Which Holocene sea-level curve is most appropriate for this study?

Two recently published Southern African sea-level curves are shown in Figure 8.9. The detail of the curves differ in several respects. Notably, Holocene sea-level reaches its maximum approximately 1500 years earlier in Compton's (2001, Figure 8.9.a)

---

[d] Measured in the Durban area (Swart, 1987 in Cooper, 1991).

[e] The sea-level curve provided by Ramsay and Cooper (2002) is similar to those produced in other locations, e.g. Barbados (Bard *et al.*, 1990, their Figure 1), indicating the dominance of eustatic processes in these records.

[f] The term "Holocene sea-level curve" has been used here to describe the records produced by Ramsay (1995) and Compton (2001). In practice, since both of these curves cover the last 9,000 years, neither spans the entire Holocene.

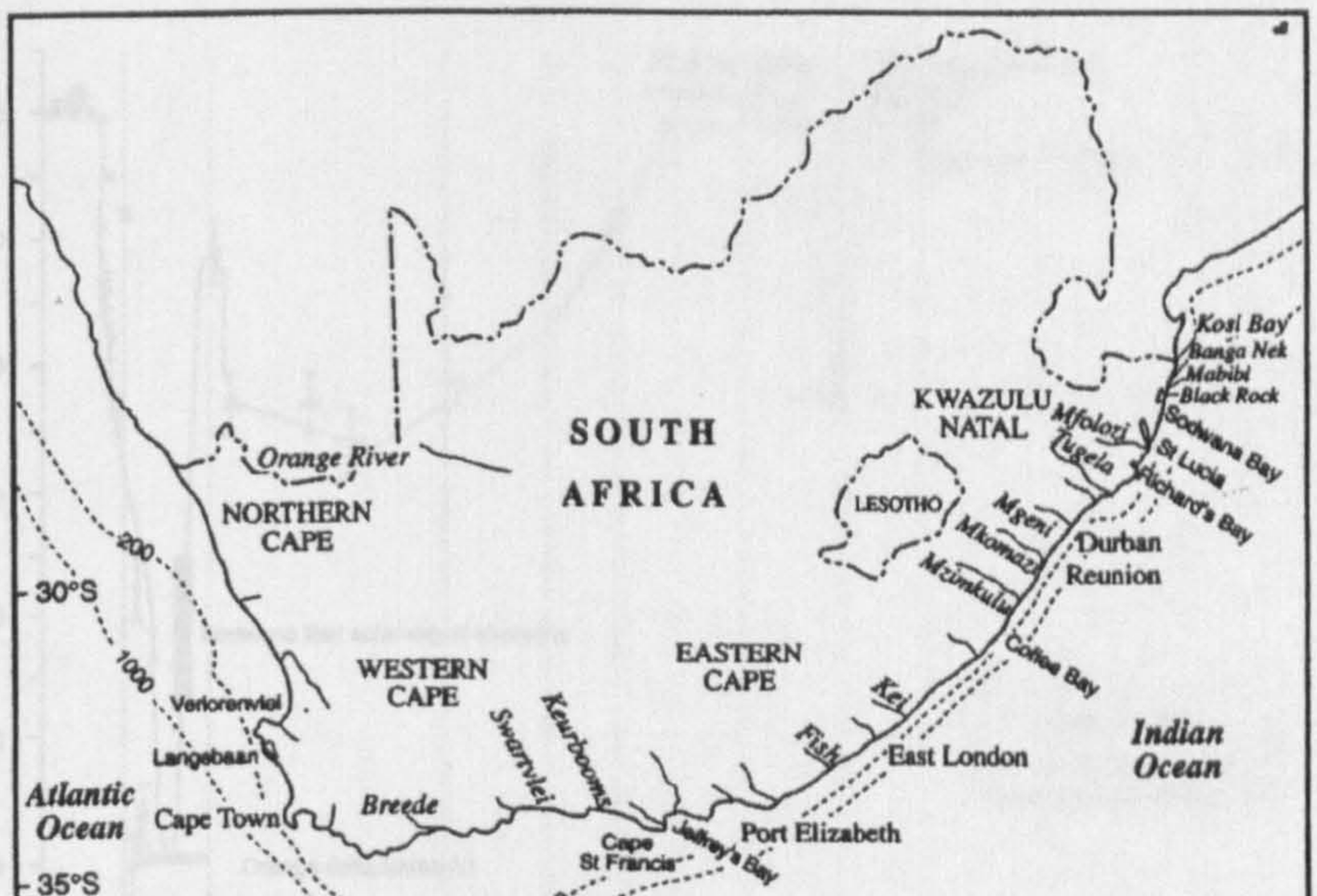

Figure 8.7. A map showing the location of sites used by Ramsay and Cooper (2002) to produce their Southern African Late Quaternary sea-level curve (from Ramsay and Cooper, 2002).

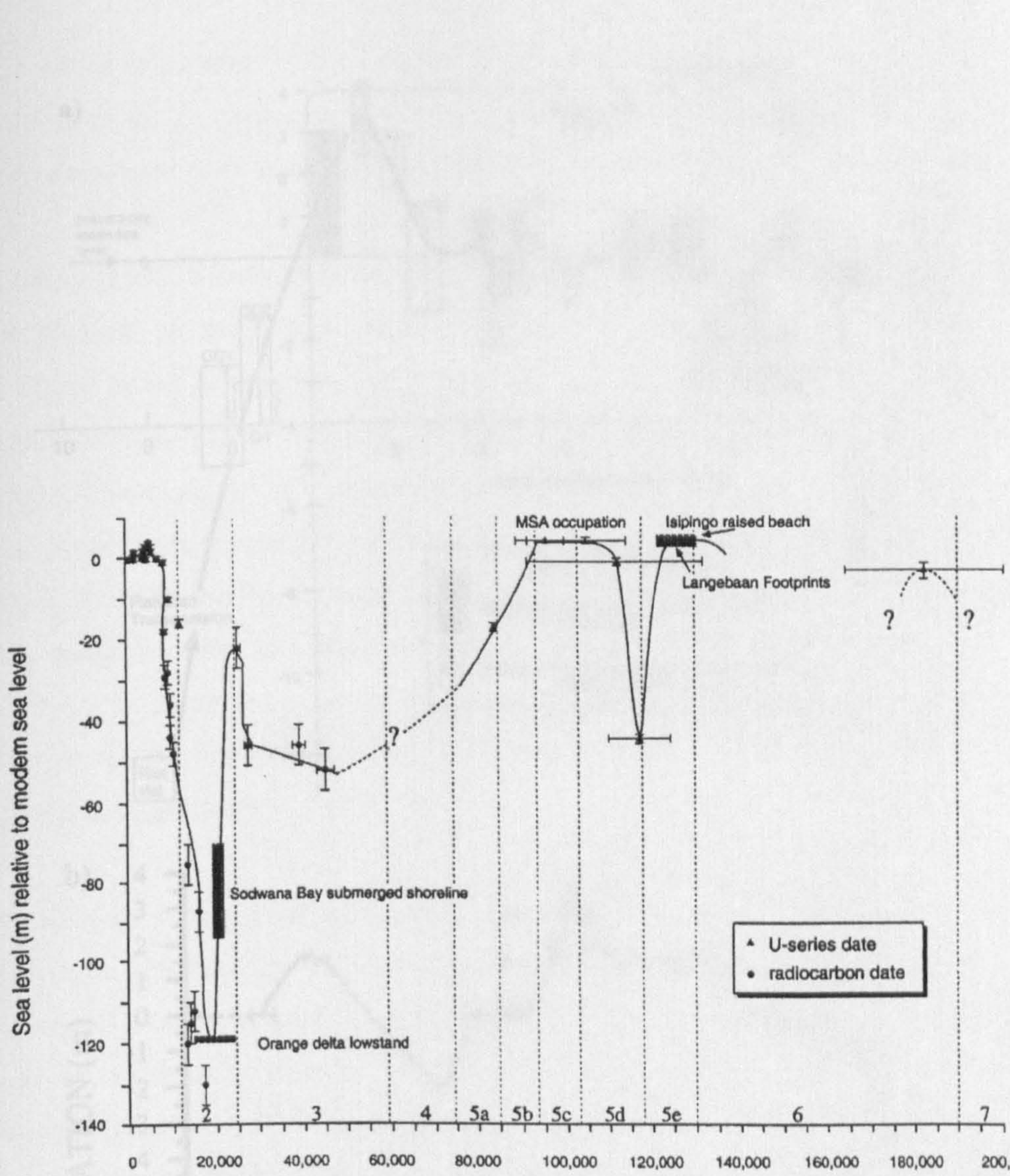

Figure 8.8. The Late Quaternary sea-level curve for Southern Africa (from Ramsay and Cooper, 2002). The radiocarbon dates are uncalibrated but corrected for apparent age of seawater where appropriate. Numbers on the age axis are oxygen isotope stages.

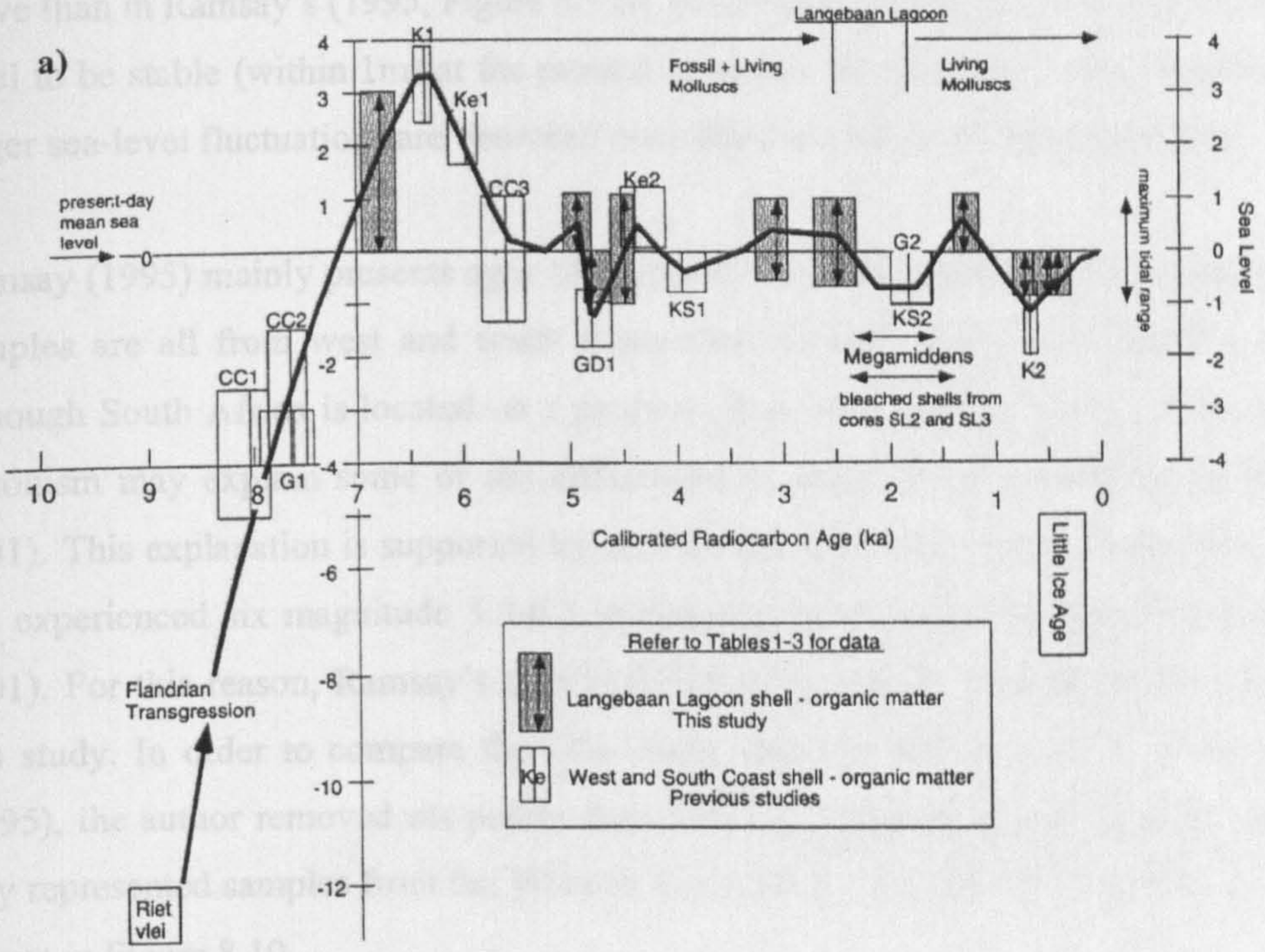

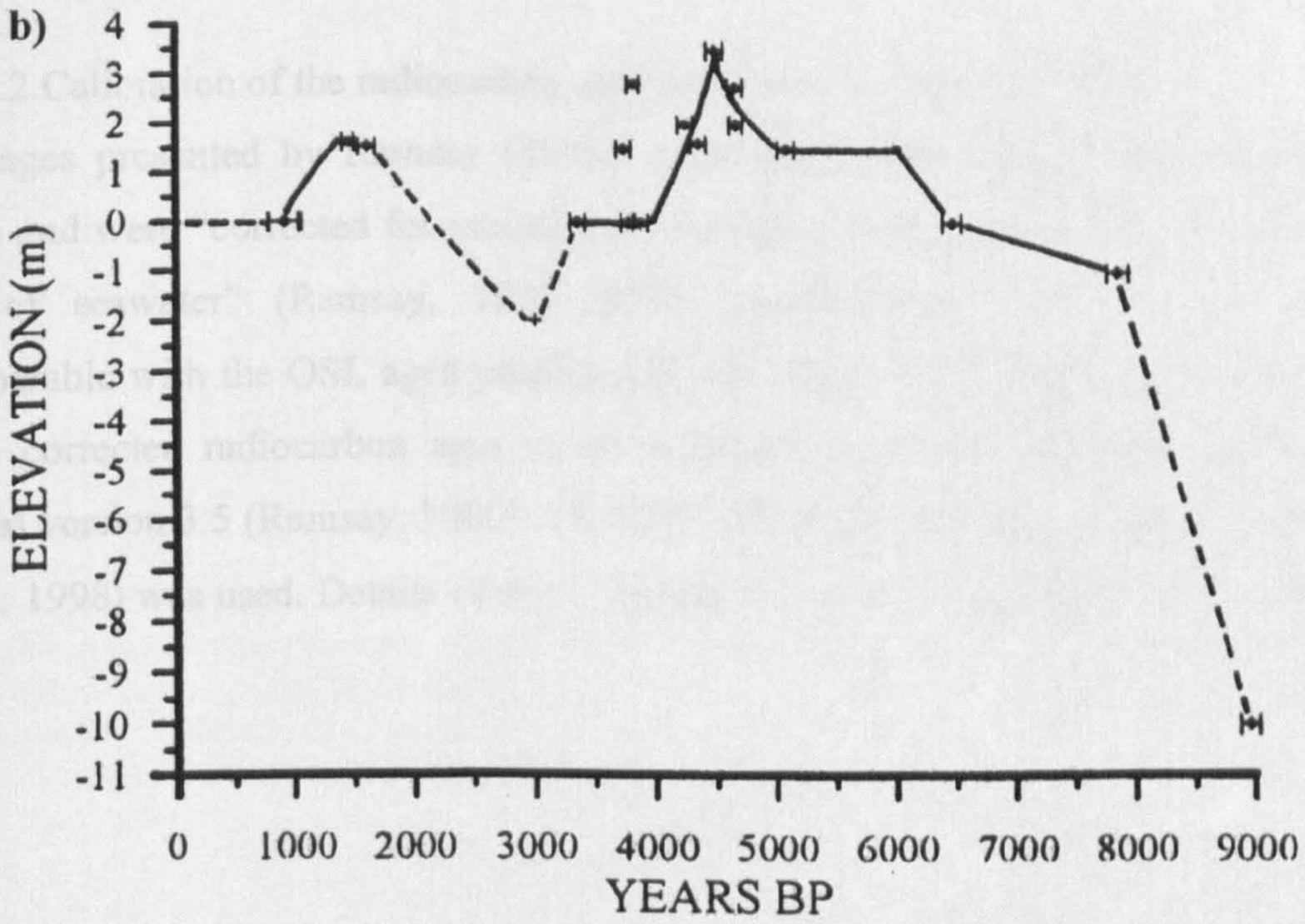

Figure 8.9. Alternative Holocene sea-level curves for southern Africa a) Compton (2001) and b) Ramsay (1995). The ages in Figure 8.9.a are calibrated, while those in Figure 8.9.b are uncalibrated (see also Section 8.2.6.2). Note that the timescales on Figures 8.9.a and b run in opposite directions.

curve than in Ramsay's (1995, Figure 8.9.b). In addition, Compton's curve shows sea-level to be stable (within 1m) at the present level for the last 5500 years. In contrast, larger sea-level fluctuations are observed over this time range in Ramsay's curve.

Ramsay (1995) mainly presents ages for samples from Maputaland, while Compton's samples are all from west and south coast sites. Consequently, it is possible that, although South Africa is located on a passive continental margin, local variations in tectonism may explain some of the differences between the two curves (Compton, 2001). This explanation is supported by the fact that the southwestern Cape Province has experienced six magnitude 5.5-6.3 earthquakes in the last 350 years (Compton, 2001). For this reason, Ramsay's (1995) Holocene sea-level curve has been used in this study. In order to compare the OSL dates with the sea-level curve of Ramsay (1995), the author removed six points from Ramsay's original sea-level curve, since they represented samples from the Western Cape coast. The revised sea-level curve is shown in Figure 8.10.

8.2.6.2 Calibration of the radiocarbon ages presented by Ramsay (1995)

The ages presented by Ramsay (1995) were reported in conventional radiocarbon years and were "corrected for variations in isotope fractionation and for the apparent age of seawater" (Ramsay, 1995, p73). Consequently, they are not directly comparable with the OSL ages produced in this study. To facilitate this comparison, these corrected radiocarbon ages were calibrated using the calibration programme OxCal version 3.5 (Ramsay, 2000). The INTCAL98 marine calibration curve (Stuiver *et al.,* 1998) was used. Details of this calibration procedure are presented in Appendix 8.1.

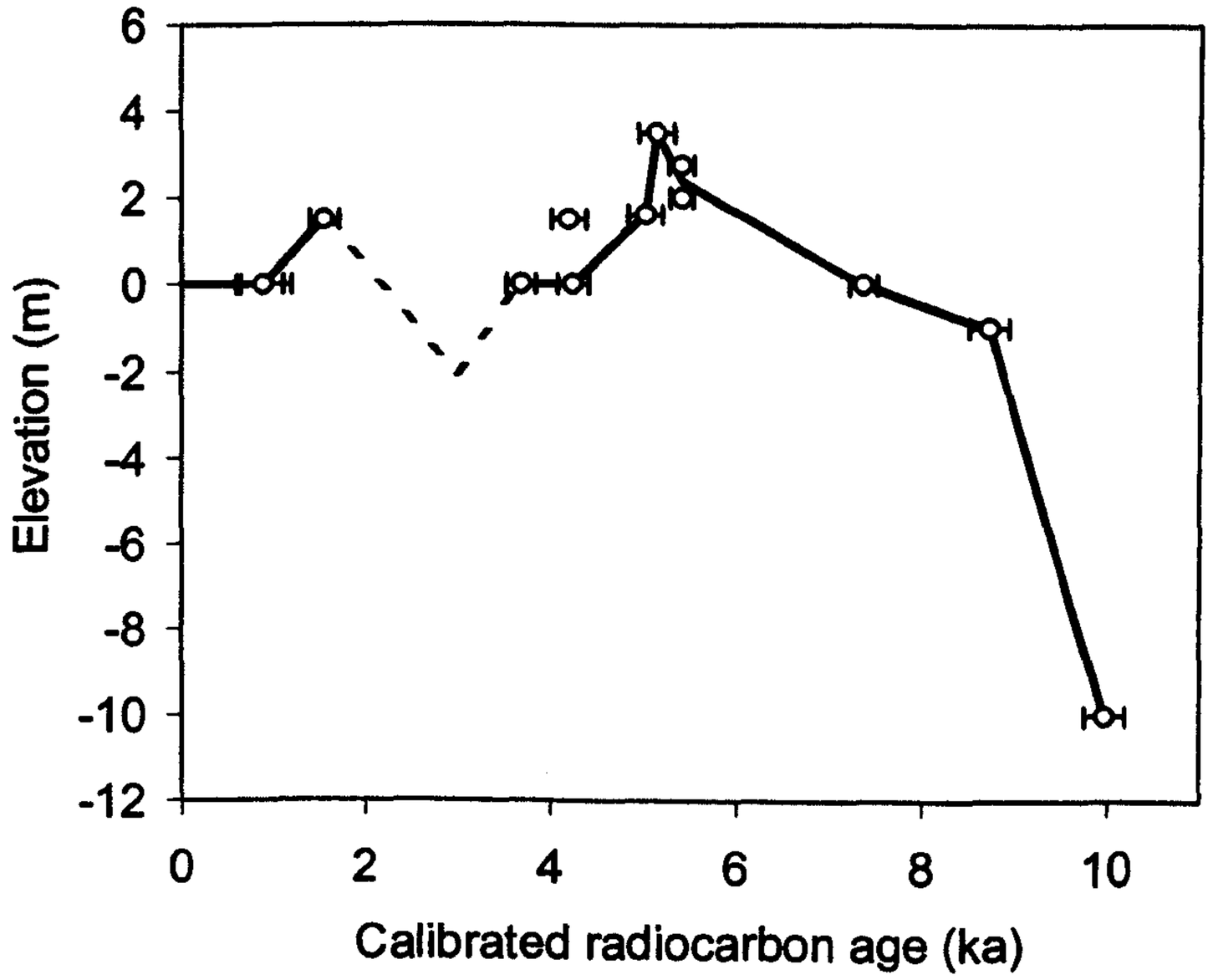

Figure 8.10. A modified version of Ramsay's (1995) sea-level curve for the southern African coast. Six points from the original (Ramsay, 1995) curve have been removed, since they were for samples from the Western Cape region of South Africa. Each open circle represents a single sample. The radiocarbon ages have been calibrated (see Section 8.2.6.2 and Appendix 8.1). The –2 m point at 3 ka represents the elevation and inferred age of a buried beachrock at Sodwana Bay (Ramsay, 1995).

8.3 Inhaca Island

Inhaca Island is located at the northern end of the Maputaland coastal plain, on the eastern side of Maputo Bay. The island itself consists of two high north-south trending ridges, forming its eastern and western margins (Figure 8.11). These main ridges are continuations of the two most seaward coast parallel dunes of the Maputaland coastal plain, which were presumably breached during a sea-level highstand, forming the present island. It is separated from mainland Mozambique (Cabo de Santa Maria, north of Ponta Torres) by an inlet 800 m wide and up to 15 m deep (Hobday, 1977). Between the two main ridges is a lower lying undulating plain. This undulating morphology is produced by a series of north-north-west trending parabolic dunes. In places individual dunes are discernable, though in others several dunes merge. At the northern end of the island, the undulating topography is replaced by a palaeo-tidal flat, with an elevation of c.3.5 m. Some of the parabolic dunes forming the undulating plain are truncated at their northern end by the palaeo-tidal flat, while others override it.

8.3.1 Description of the main dune ridges and sample sites

The main dune ridges form the eastern and western margins of Inhaca, and are the largest geomorphic features on the island. The eastern ridge reaches a maximum height 115 m above sea-level, with a mean height of around 60 m. It is densely vegetated, though locally smaller parabolic dunes migrate over this vegetation, reaching the interior of the island. Aerial photography indicates that the surface morphology of the eastern ridge is dominated by the trailing limbs of these parabolic dunes (Botha, pers. comm.). The ridge itself is fairly straight, with a small zeta-bay occurring half-way along its length. A large outcrop of Isipingo Formation aeolianite occurs at the northern end of the ridge, at Cabo Inhaca. This outcrop is notched at 5-6 m, which Hobday (1977) suggests was formed during a Last Interglacial high sea-level event, though Ramsay (pers.comm.) regards it as mid-Holocene in age. The Cabo Inhaca aeolianite consists of three main units (Photograph 8.1). The lower unit, into which the 5-6 m notch is incised, is a laminated aeolianite. The overlying unit contains abundant rhizoliths, while the upper unit is a second laminated aeolianite. Laminations in the lower and upper units are intact and show no signs of bioturbation. One sample has been dated from each of the laminated aeolianites at Cabo Inhaca (Aber/28-IN1 and 3, Table 8.2).

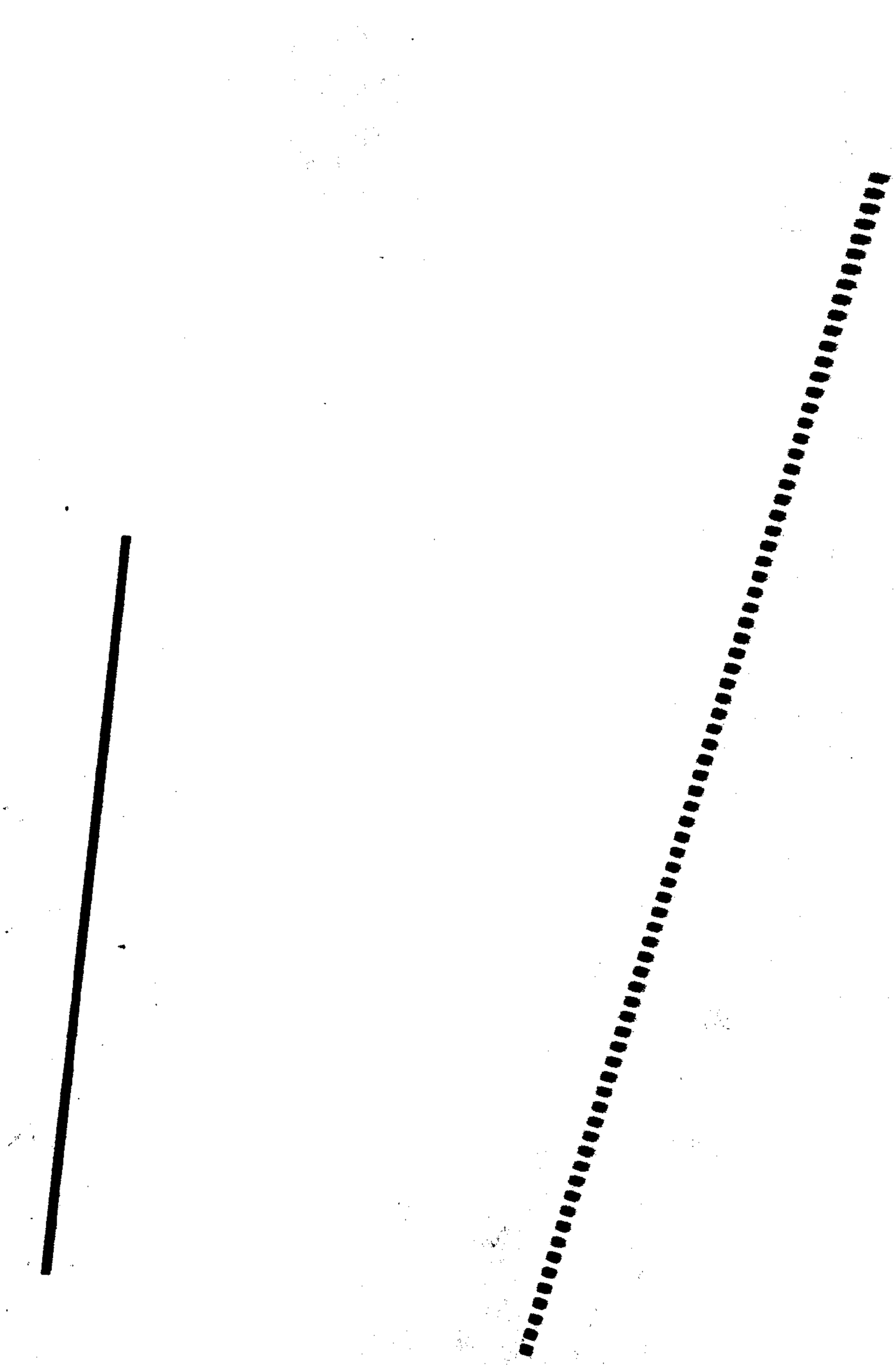

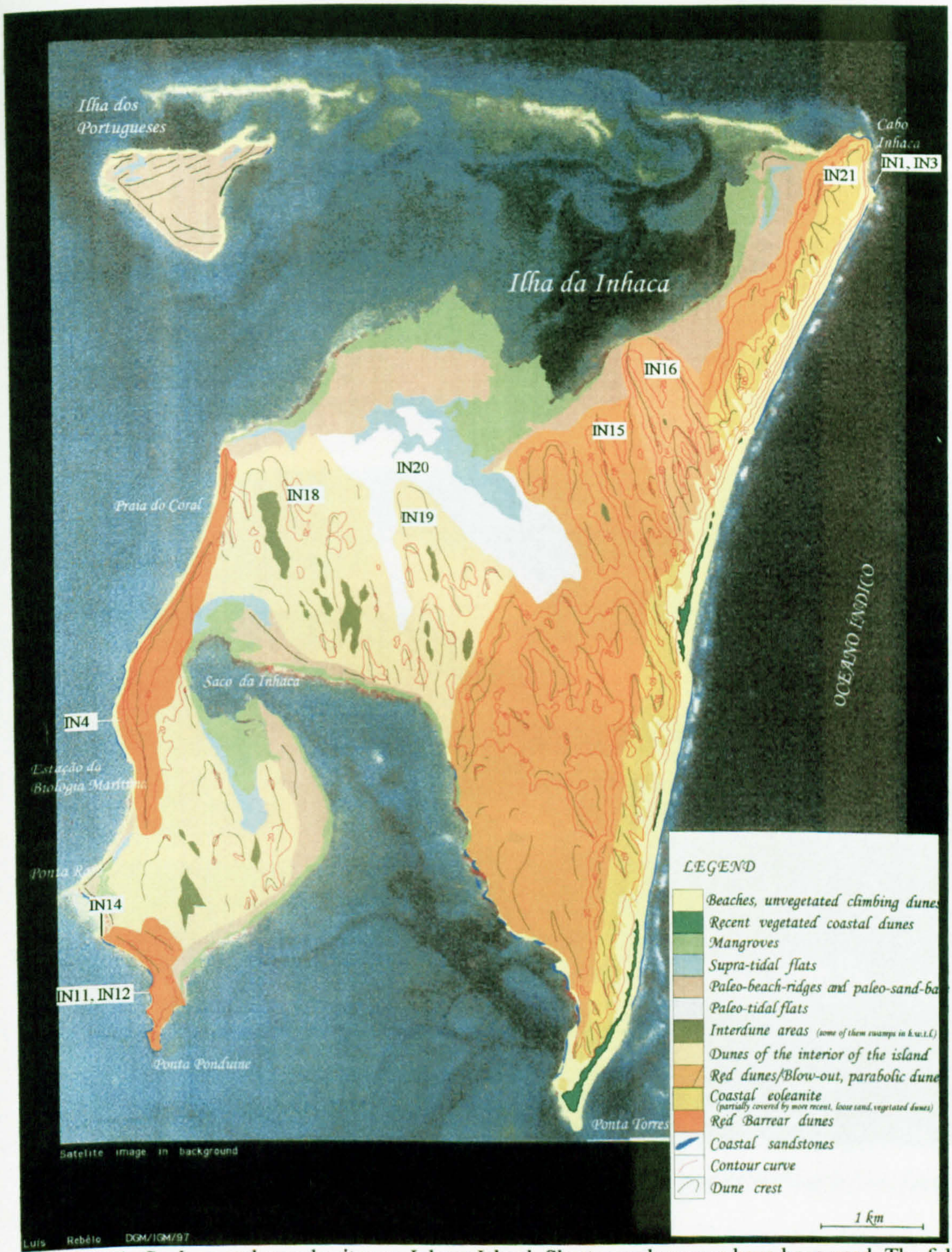

Figure 8.11. Geology and sample sites on Inhaca Island. Short sample names have been used. The full sample identification code is obtained by adding Aber/28-IN to the name given in this figure. The map was provided to the author by Luís Rebêlo, Instituto Geológico e Mineiro, Portugal. The dashed line on the acetate overlay indicates the position of the eastern dune cordon while the solid line indicates the position of the western dune cordon

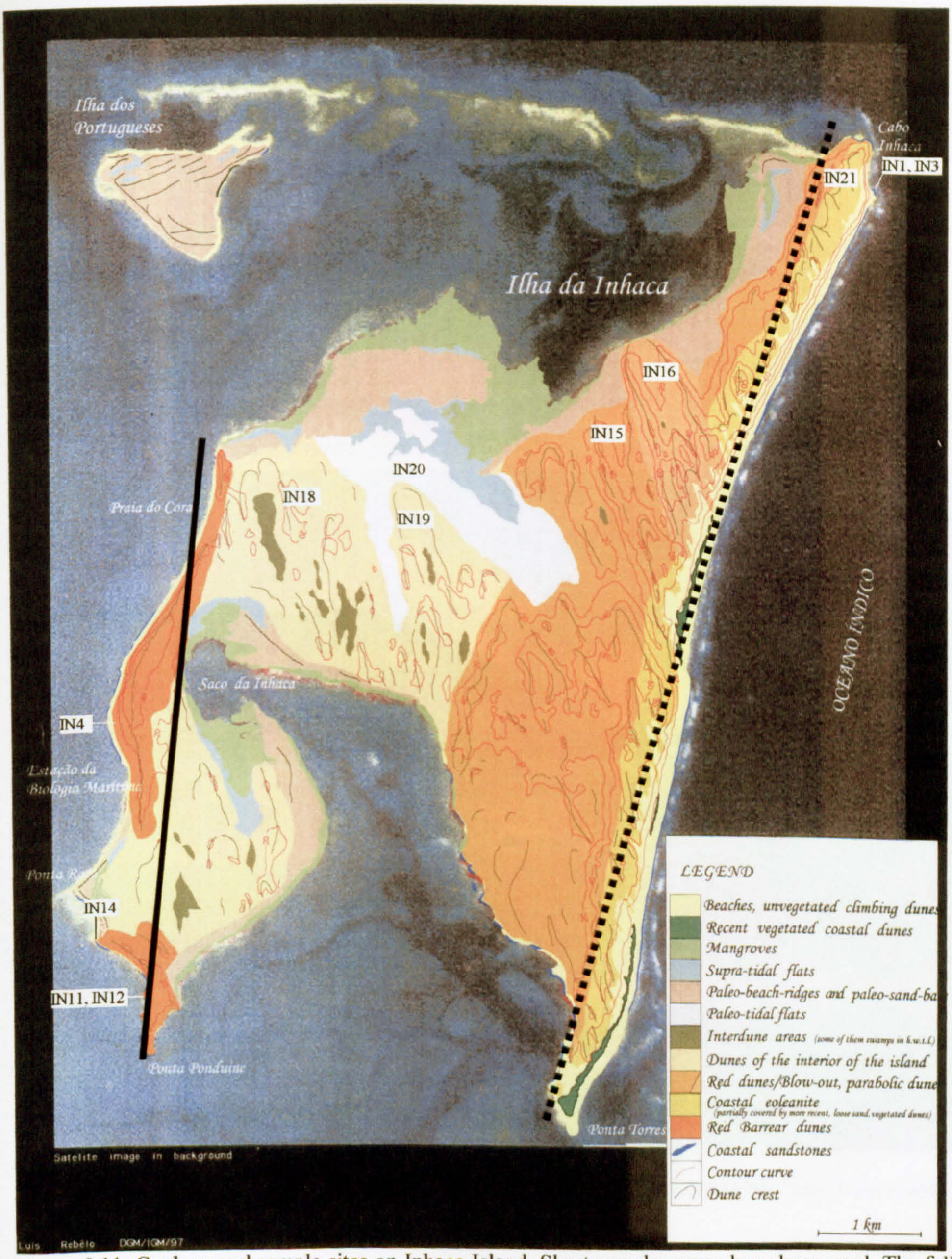

Figure 8.11. Geology and sample sites on Inhaca Island. Short sample names have been used. The full sample identification code is obtained by adding Aber/28-IN to the name given in this figure. The map was provided to the author by Luís Rebêlo, Instituto Geológico e Mineiro, Portugal. The dashed line on the acetate overlay indicates the position of the eastern dune cordon while the solid line indicates the position of the western dune cordon

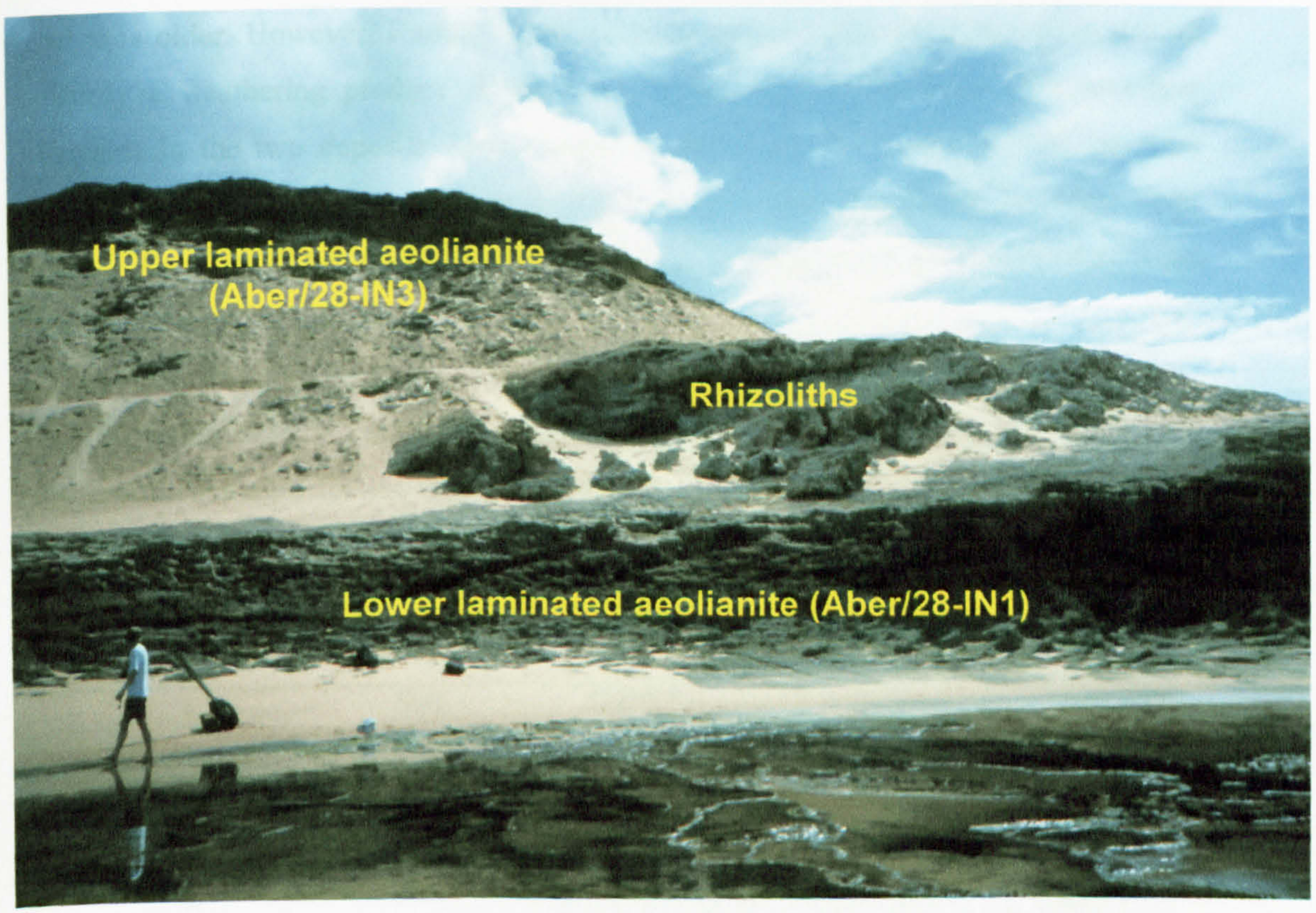

Photograph 8.1. Cabo Inhaca, showing the units from which samples Aber/28-IN1 and 3 were taken, and the intervening aeolianite containing abundant rhizoliths.

The western ridge reaches a maximum height of 66 m above sea-level, with a mean value of c.20-40 m. It has been breached at Ponta Rasa, dividing the ridge into two sections, of which the northern portion is longer. Hobday (1977) describes two main units forming this ridge. The lower unit is a fine to medium-grained cross-bedded calcareous sandstone, which he ascribes to aeolian activity during the marine regression associated with the penultimate glaciation. This aeolianite unit is overlain at an elevation of 5 to 12 m by an upper, deeply reddened, weakly cemented sand. The uppermost 3 m of this unit is uncemented, and not as deeply reddened as that below. Shell fragments in the sand unit show advanced diagenesis and neomorphism, unlike those in the eastern ridge, leading Hobday (1977) to conclude that the western ridge is older. However, Ramsay (pers comm.) suggests that the upper sand unit is simply a weathering product of the lower aeolianite, on the basis of concordant foresets in the two deposits. One sample of the aeolianite (Aber/28-IN4) and two samples of the overlying sand unit (Aber/28-IN11 and Aber/28-IN12) have been dated. Aber/28-IN11 is from the main sandy unit, while Aber/28-IN12 was taken from the uncemented upper area.

8.3.1.1 Luminescence ages and discussion

Luminescence ages for the four samples from the main dune ridges are presented in Table 8.2.

Sample (Aber/28-IN...)	Ridge	Brief description	Age (ka)
1	East	Cabo Inhaca: Lower aeolianite	149 ± 23
3	East	Cabo Inhaca: Upper aeolianite	99.6 ± 15.6
4	West	Western ridge: Lower aeolianite	> 250
11	West	Sand unit overlying Aber/28-IN4	102 ± 5
12	West	Uncemented sand overlying Aber/28-IN11	22.5 ± 0.8

Table 8.2. Descriptions and ages for the samples taken from main dune ridges on Inhaca Island. Ages are taken from Table 75.

The ages for the main dune cordon units (Aber/28-IN1, 3, 4 and 11) do not allow conclusive inferences about the relationship between sea-level and the formation of these units to be made. However, two of the four samples yield Last Interglacial ages, while that for Aber/28-IN1 has a large error term which includes the beginning of the

Last Interglacial. These data tend to suggest that the main dune cordons were emplaced during periods of high/rising sea-level. Intuitively, this conclusion is supported by the fact that the main dune cordons are coast-parallel, suggesting that they were formed immediately adjacent to the palaeo-coastline. In addition, the area of continental shelf exposed during glacial low sea-level events is relatively small. Consequently, the potential sediment yield from this area is also small.

Aber/28-IN12, the uppermost unit in the western dune cordon, was deposited during the Last Glacial Maximum (LGM), when sea-level was much lower than at present (Figure 8.8). While this may reflect input of sediment from the exposed continental shelf, it is also possible that the unit represented by Aber/28-IN12 was produced by very localised aeolian reworking of the underlying, weakly cemented sand unit, during the LGM. It is reasonable to expect some reworking of aeolian deposits at this time, since the low sea-level probably led to a drawdown of the regional water table. This would reduce the vegetation cover on the dune, thereby allowing localised reworking of the surface (Section 8.2.2, KwaMbonambi Formation). The reddened colour of the upper sand unit is similar, though lighter, than that for the underlying weakly cemented sand. This provides circumstantial evidence that Aber/28-IN12 was produced by localised reworking of the underlying unit, since fresh sediment from the continental shelf does not weather sufficiently rapidly to develop this colour during the burial period.

In summary, it appears likely that the main dune cordons were formed in response to rising or high sea-levels. Localised reworking of this sediment may have occurred during the LGM in response to a regional drawdown of the water table.

8.3.1.2 Do the main dune ridges represent one or more depositional event?

The ages presented in Table 8.2 also indicate that both ridges are composite features, relating to more than one depositional event. The basal unit of the western ridge (Aber/28-IN4) yielded only a minimum age (Section 6.5.1), but was clearly deposited much earlier than the overlying sand unit (Aber/28-IN11), which is Last Interglacial in age. These ages disprove Ramsay's (pers. comm.) suggestion that the upper unit is simply a weathering product of the overlying aeolianite. The eastern limb of the island is also composite, containing Last Interglacial aeolianite units, with overlying

Holocene material, the deposition of which still occurs at present. Due to the large scatter observed in the D_e distributions for Aber/28-IN1 and 3 (Sections 6.3 and 6.4.3), the OSL ages alone are not enough to conclude that they represent to separate episodes of deposition. However, the presence of abundant rhizoliths in the aeolianite which separates Aber/28-IN1 and 3, indicates that the dune from which Aber/28-IN1 was taken was well vegetated prior to the deposition of a second sand unit (Aber/28-IN3), indicating an hiatus in deposition. These distinct phases of aeolian deposition are probably related to the two Last Interglacial high sea-level events reported by Ramsay and Cooper (2002), based on uranium-series dates .

The age of the 5-6 m notch in the lower aeolianite unit at Cabo Inhaca, cannot be deduced from these ages. However, if it is Last Interglacial in origin (Hobday, 1977), this suggests that the lower aeolianite was fully cemented prior to the second high-sea level event.

8.3.2 Description of the interior of Inhaca Island and sample sites

Between the main dune ridges is a lower-lying undulating plain, composed of north-north-westerly trending parabolic dunes. In places, individual dunes are discernable, while in others dunes merge. In the east of the island, the trailing limbs of individual parabolic dunes can often be traced over the main dune ridge. At the northern end of Inhaca is a large palaeo-tidal flat, with an elevation of c.3.5 m. This palaeo-tidal flat truncates some of the parabolic dunes at their northern extremity, while other dunes override it (Photograph 8.2). Ages have been calculated for five samples from the parabolic dunes (Aber/28-IN15, 16, 18, 19 and 21), and one from the palaeo-tidal flat (Aber/28-IN20).

8.3.2.1 Luminescence ages and discussion

Luminescence ages for the palaeo-tidal flat and parabolic dunes are presented in Table 8.3, and are plotted on the revised version of Ramsay's (1995) Holocene sea-level curve (Figure 8.12).

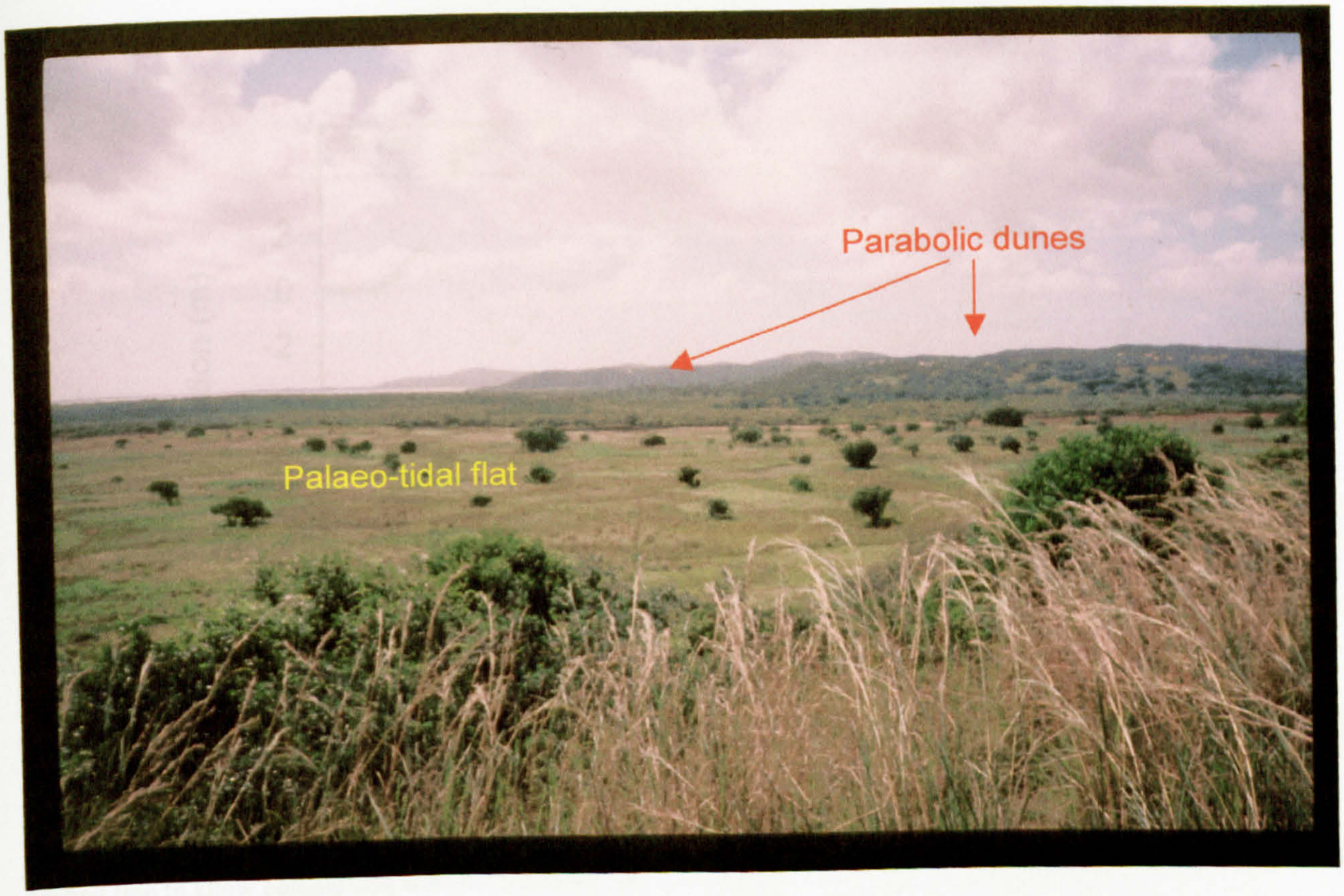

Photograph 8.2. The palaeo-tidal flat at the northern end of Inhaca.

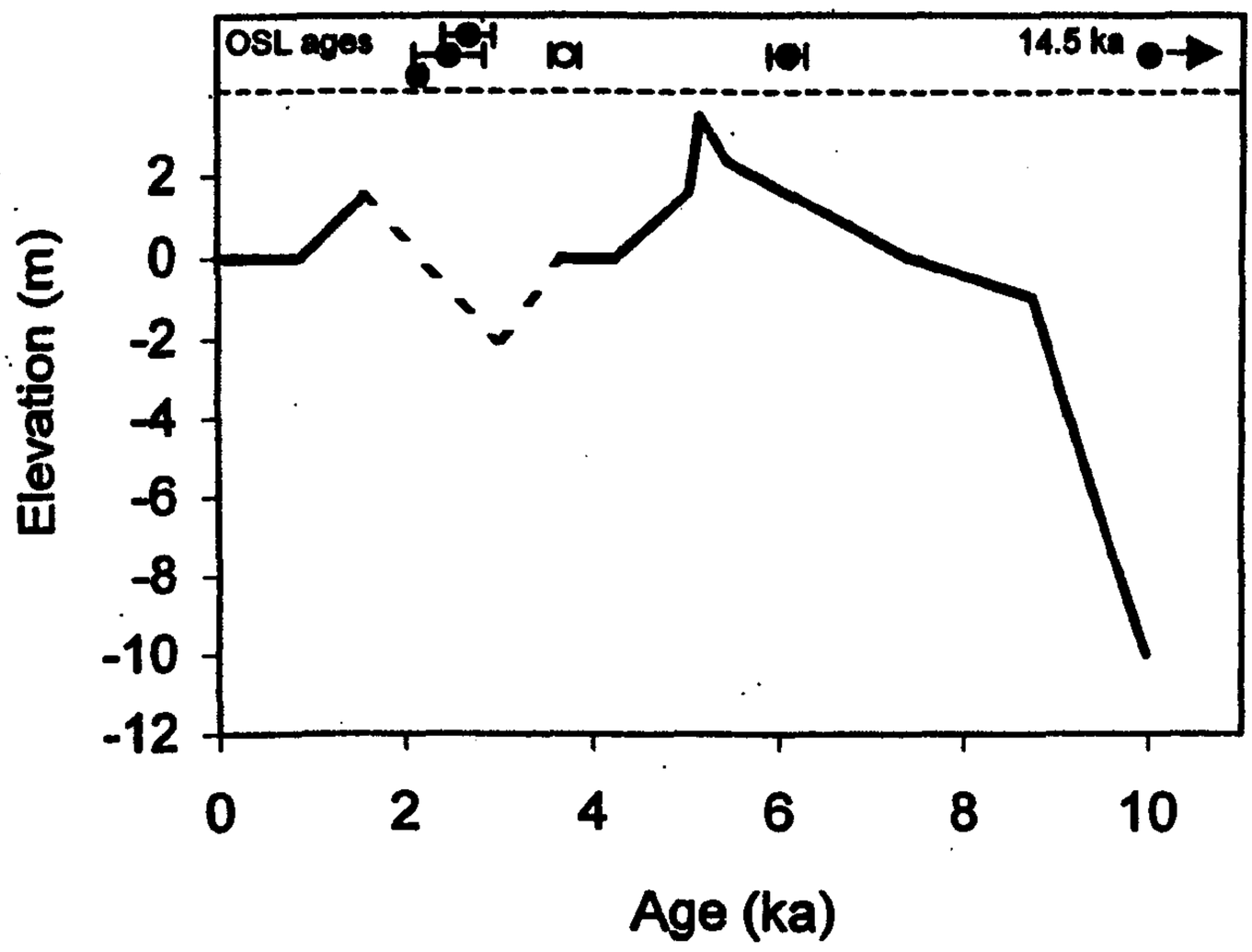

Figure 8.12. OSL ages for parabolic dunes (closed circles) and the palaeo-tidal flat (open circle) on Inhaca Island, shown on the revised sea-level curve of Ramsay (1995). Ages are displayed above the dashed line to allow comparison with the sea-level curve.

Sample (Aber/28-IN...)	Brief description of site	Age (ka)
15	Northern end of a truncated parabolic dune	6.09 ± 0.20
16	Northern end of a parabolic overriding the palaeo-tidal flat	2.16 ± 0.06
18	Area of merged parabolic dunes	14.5 ± 0.6
19	Northern end of a truncated parabolic dune	2.48 ± 0.37
20	Palaeo-tidal flat	3.68 ± 0.15
21	Parabolic dune overriding the eastern dune cordon	2.69 ± 0.27

Table 8.3. Descriptions and OSL ages for samples taken from the parabolic dunes and palaeo-tidal flat. Ages are taken from Table 7.5.

The palaeo-tidal flat (Aber/28-IN20) yields an age approximately 1400 years younger than the mid-Holocene high sea-level observed in Figure 8.12. However, a luminescence age for this type of deposit relates to its abandonment as sea-level falls, since this is the point at which vegetation colonises the flat, and the sediment is stabilised. Consequently, the age measured for the palaeo-tidal flat should be younger than that for the high sea-level event itself, though this does not completely explain the discrepancy between the two ages. The ages for the parabolic dunes are consistent with formation of the palaeo-tidal flat during the mid-Holocene high sea-level event. Two dunes yielding ages older than the high sea-level event (Aber/28-IN15 and 18) are truncated by the palaeo-tidal flat, while two younger dunes override it (Aber/28-IN16 and 19). Consequently, although the age for Aber/28-IN20 is a little young, the palaeo-tidal flat can reasonably be attributed to the mid-Holocene high sea-level event identified by Ramsay (1995).

The parabolic dunes dated in this study were all deposited during the Holocene, or in the transgression following the LGM low sea-level event. The oldest date for a parabolic dune (Aber/28-IN18) was found at the north-western tip of the island, while the dunes in the centre and north-east are younger. It is possible to explain this pattern in terms of sediment transport pathway availability. The younger dunes (Aber/28-IN15,16,19 and 21) are all found down drift (relative to the north-north-west transport direction indicated by their orientation) of the eastern dune ridge, with no intervening sea or tidal flat. Consequently, sediment supplied to the beach had an uninterrupted transport pathway to the centre of the island, even when sea-level is high during the Holocene. In contrast, the older parabolic dune on the north-western tip of the island is down drift of the present tidal-flat which extends from Saco da Inhaca to the south. When the sea-level reached approximately present day levels (c.9 ka), the tidal-flats

were flooded. This cut off the north-west of the island from its sediment supply, and hence no more recent aeolian deposition occurred. The sample collection strategy used in this study only allowed the uppermost portion of each dune to be sampled. Consequently, the ages produced only represent the most recent period of deposition if the parabolic dunes are composite features[g]. Hence it is probable that the entire centre of the island experienced aeolian activity during the LGM-Holocene transgression. The only sample of this age was taken from the north-western tip of the island, since this part of Inhaca was cut off from its sediment supply at the beginning of the Holocene. In contrast, the central and north-eastern parts of Inhaca have never been isolated from their sediment supply, and hence more recent aeolian deposits lie at the surface. Hence, younger ages are obtained for the central and eastern dunes than for the western dune.

8.3.2.2 Sediment supply to the centre of Inhaca

The ages presented in Table 8.3 allow tentative conclusions to be drawn about the mechanisms which have supplied sediment to the centre of Inhaca. During the transgression associated with the end of the last glaciation, it is probable that aeolian activity occurred over much of the island. The likely sediment source during this period is the continental shelf, which was at the time being submerged. This destroyed the vegetation, which had previously stabilised sediment on the continental shelf, making it available for aeolian transportation. During the Holocene however, sea-level fluctuations are not large enough to expose/submerge significant areas of the continental shelf. During this period, sediment must be supplied either by longshore drift/Mozambique Current, or erosion of the main eastern dune cordon itself. Both the cluster of ages at c.2.5 ka and the single age at 6 ka occur during periods of rising sea-level (Figure 8.12) suggesting that the latter explanation is more likely. However, since relatively few ages have been obtained from the parabolic dunes, it is not possible to unequivocally correlate parabolic dune formation to rising sea-level, and therefore reject longshore drift/the Mozambique current as a source of sediment.

---

[g] After the initial deposition of a parabolic dune, subsequent sediment pulses may migrate along the "track" provided by the trailing limbs of the original feature, depositing a veneer of modern sediment on top of the older dune. This process is currently active on many of the parabolic dunes near Maputo, and was also observed on Bazaruto Island (Section 8.4.1.3).

The absence of dates for parabolic dunes prior to 14.5 ka may be explained in two ways.

1) When sea-level is low or falling, vegetation colonises the exposed continental shelf, stabilising sediments stored on it, thereby reducing the quantity of sediment available for aeolian transportation.
2) More recent aeolian activity has buried older dunes, which were consequently not sampled.

The relatively small number of parabolic dunes sampled, and the sampling technique used, do not allow these possibilities to be explored.

8.3.3 A model for the evolution of Inhaca Island

From the above data, a tentative model for the evolution of Inhaca Island is proposed

1) The earliest part of Inhaca to be deposited was the western dune cordon, prior to 250 ka.
2) During the Last Interglacial, further sediment was deposited on the western dune cordon, and the eastern dune cordon was formed. The latter formed in two phases. The first, caused by the transgression at the beginning of the Last Interglacial, was followed by a period of stability, during which the dune was vegetated. A second phase of deposition occurred on the eastern dune cordon in response to a second high-sea level event.
3) During the LGM, limited aeolian reworking of the surface of the western dune cordon occurred, in response to lowered regional water tables and a consequent loss of vegetation.
4) Parabolic dunes were deposited during the transgression following the LGM, and during the Holocene.
5) In the mid Holocene, sea-level rose to c.3.5 m above present levels. This event deposited an elevated tidal-flat at the northern end of Inhaca, which truncated the pre existing parabolic dunes.
6) Limited aeolian activity occurs at present, though small parabolic dunes can be seen migrating from blowouts on the seaward side of the eastern dune cordon.

8.4 Bazaruto Island

Bazaruto Island is the largest island in the Bazaruto Archipelago, and forms part of an offshore barrier complex. It is long (c.30 km N-S) and thin (c.5 km), and lies approximately 20 km off the coast of central Mozambique. The intervening sea is relatively shallow (10-20 m depth) and contains extensive tidal-flats, which are protected from high-energy Indian Ocean waves by the archipelago. To the east of Bazaruto, the continental shelf is steep, reaching a depth of 200 m below present sea-level 5-10 km offshore.

The island appears to have formed as a single, coast-parallel dune cordon, which has subsequently been isolated from the mainland by rising sea-levels. Much of the eastern side of Bazaruto, which faces the Indian Ocean, is covered by active dunes. These dunes migrate in a north-westerly direction, and in places are partially stabilised by vegetation. The interior and western side of Bazaruto is covered by older dunes, which are stabilised by grass, shrubs and occasionally trees. The morphology of this area is generally subdued, though small lakes frequently occupy the depressions between dune crests. Like the presently active dunes, these dune crests are oriented NW-SE.

The formation and evolution of Bazaruto have not been extensively studied. However, Cooper (1991) suggests that the eastern shoreline of Bazaruto has migrated westwards by up to 5 km during the Holocene. According to Cooper (1991) the early Holocene shoreline of Bazaruto was located on the break of slope in the continental shelf, between the flat western portion and the steeply sloping eastern margin. When sea-level reached approximately its present level in the early Holocene (c.9 ka), a line of beachrock formed along the eastern beaches of Bazaruto. The position of this initial shoreline is indicated by the dashed line on Figure 8.13. Subsequent shoreline retreat occurred due to continuing wave attack (Cooper, 1991), leaving the beachrocks as an intertidally exposed reef. When the shoreline subsequently stabilised, a second phase of beachrock formation occurred along the modern coast. No beachrocks are found between the early-Holocene, and present shorelines. This led Cooper (1991) to conclude that shoreline displacement following detachment from the initial beachrock

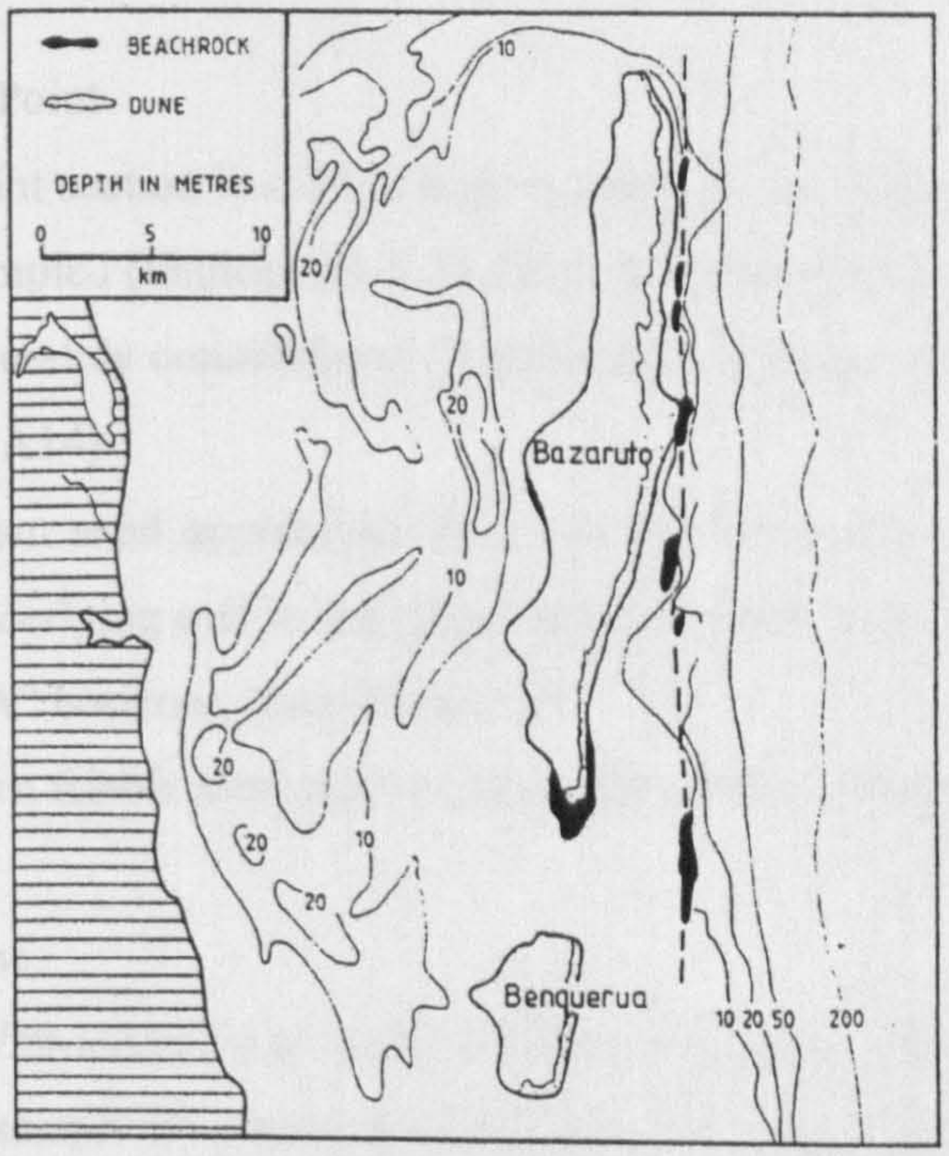

Figure 8.13. The two Holocene shorelines described by Cooper (1991). The position of the initial shoreline is indicated by the dashed line. This line joins areas of early Holocene beachrock. The shoreline retreated to its present position due to wave action during the Holocene. Isobaths are in metres. From Cooper (1991).

line was rapid, possibly due to reduced sediment supply caused by the early beachrock formation[h].

8.4.1 Description of the sample sites on Bazaruto

Five sites on Bazaruto were chosen for sampling (Figure 8.14). Only one exposure, the sea cliff at Zingalema Point, gave access to more than one depositional unit. However, samples representative of the range of features occurring on Bazaruto were collected and dated. Details of these samples are given below and in Table 8.4.

8.4.1.1 Zingalema Point

The Zingalema Point section is a 30 m high sea cliff on the western side of Bazaruto. Four units were sampled (Photograph 8.3). From the base upwards these were

1) A red, moderately consolidated, heavily rilled sand, approximately 14 m thick (Aber/29-BA14)
2) A fine brown sand approximately 11 m thick (Aber/29-BA13). The contact with the underlying unit is indistinct, and the colour grades to red at the base.
3) A buried "A" horizon (Aber/29-BA12).
4) A fine brown friable sand, approximately 3 m thick (Aber/29-BA11).

8.4.1.2 Interior dune

One sample (Aber/29-BA10) was taken from the subdued morphology of the interior of the island. The sample was taken from the side of a sample pit, dug into a flat area of grassland.

8.4.1.3 Parabolic dune limb

One sample (Aber/29-BA4) was taken from a pit dug into the trailing limb of a parabolic dune in the north of Bazaruto. A modern dune was migrating up the "track" defined by the two trailing limbs of this parabolic dune, depositing fresh sediment. A modern sample (Aber/29-BA5) was taken from the slip face of this second dune.

---

[h] No major sediment-carrying rivers discharge into the area (Cooper, 1991).

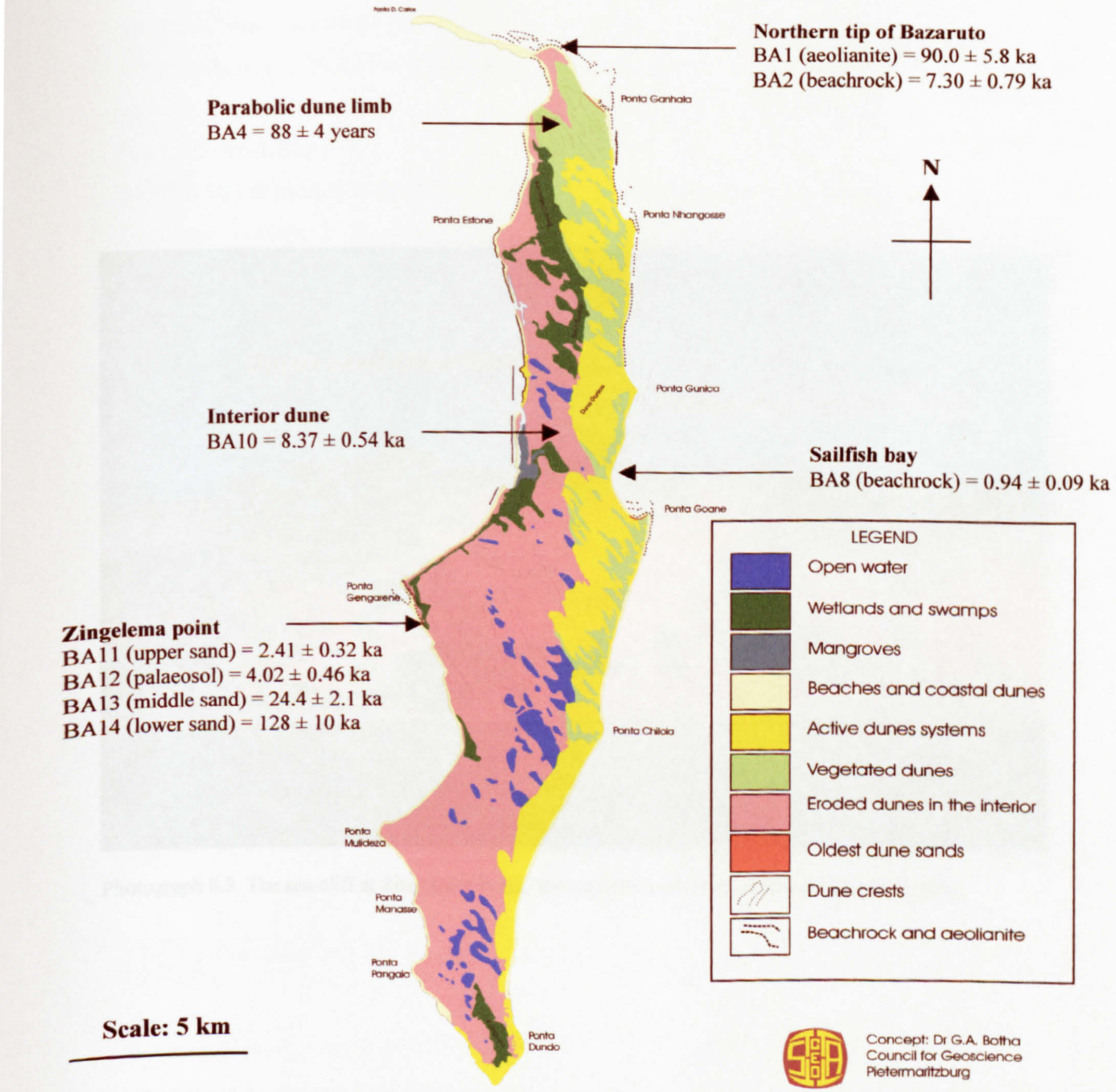

Figure 8.14. A map of Bazaruto Island showing the main landform/vegetation types present. Sampling locations and luminescence ages are also shown. Short sample names are used. The full sample identification code is obtained by adding Aber/29- to the names given on this figure. The map was provided by Dr. Greg Botha, Council for Geoscience, South Africa.

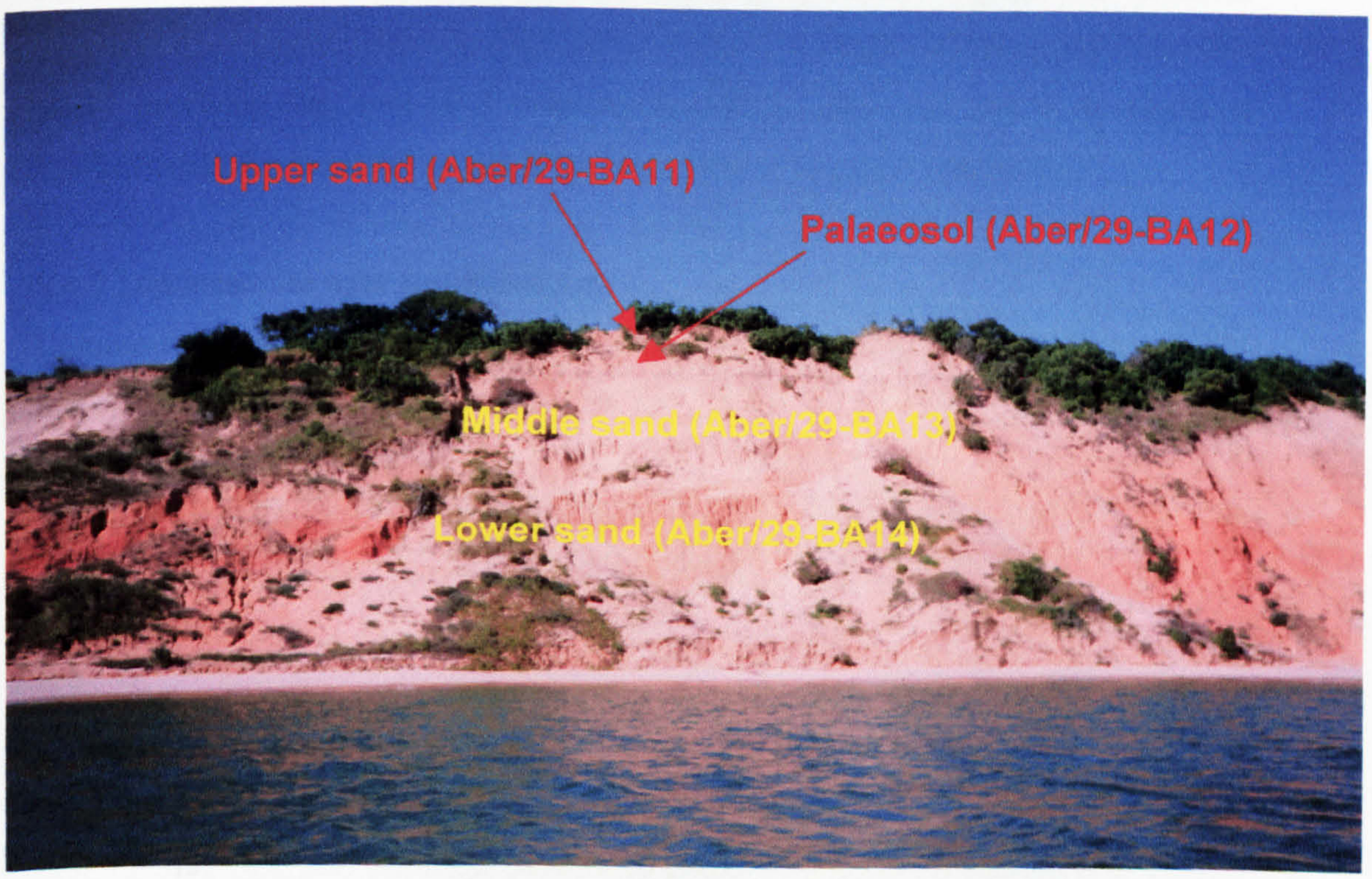

Photograph 8.3. The sea-cliff at Zingalema Point, showing the units from which samples were taken.

8.4.1.4 Northern tip of Bazaruto

A sample of light brown, moderately well consolidated aeolianite (Aber/29-BA1) was taken from a 7 m high sea cliff at the northern tip of Bazaruto. An inter-tidal platform seaward of the cliff, appears to be formed in the same aeolianite. Overlying this platform, and therefore post-dating its formation, is a discontinuous layer of beachrock, from which a sample (Aber/29-BA2) was taken.

8.4.1.5 Sailfish Bay

Sailfish Bay is located to the north of Ponta Goane, a headland anchored to the early-Holocene beachrock. However, the bay itself was formed during the landward shoreline displacement described by Cooper (1991). A sample of beachrock (Aber/29-BA8) overlying the inter-tidal platform at Sailfish Bay was taken, to obtain a minimum age for the stabilisation of this shoreline at its present position.

8.4.2 Luminescence ages and discussion

Luminescence ages for the geological samples from Bazaruto are presented in Table 8.4.

Sample (Aber/29-BA…)	Brief description of site	Age (ka)
1	Aeolianite from sea cliff	90.0 ± 5.8
2	Beachrock	7.30 ± 0.79
4	Limb of parabolic dune	0.088 ± 0.004
8	Beachrock	0.94 ± 0.09
10	Interior dune	8.37 ± 0.54
11	Upper sand unit at Zingalema	2.41 ± 0.32
12	"A" horizon of palaeosol	4.02 ± 0.46
13	Middle sand unit at Zingalema	24.1 ± 2.1
14	Lower, sand unit at Zingalema	128 ± 10

Table 8.4. Descriptions and OSL ages for samples taken from Bazaruto Island. Ages are taken from Table 7.7.

The two oldest samples from Bazaruto (Aber/29-BA1 and 14) indicate that the core of the island was deposited during the Last Interglacial. It is possible that this material was deposited in two stages, corresponding to the two high sea-level events recorded by Ramsay and Cooper (2002), although there is no clear evidence of an hiatus in deposition (cf. Aber/28-IN1 and 3 on Inhaca Island, Section 8.3.1.2).

Aber/29-BA13 (24.1 ± 2.1 ka) was deposited during the low sea-level event associated with the LGM. As in Maputaland (Botha *et al.*, in press) this mobilisation of sediment is probably associated with a drawdown of the regional water during periods of low sea-level, leading to reduced vegetation cover. The thickness of the unit from which Aber/29-BA13 was taken, suggests that large amounts of sediment were mobilised at this period.

Significant aeolian activity also appears to have occurred during the Holocene. The age for Aber/29-BA10 (8.37 ± 0.54 ka) suggests that the interior dunes were deposited during the early Holocene, at approximately the time that sea-level reached its present position (Figure 8.10). More recent aeolian activity is indicated by the ages from Aber/29-BA4, 11 and possibly 12 (see below). However, there are insufficient ages to indicate whether aeolian activity is continuous, or phased.

The beachrock samples (Aber/29-BA2 and 8) yield a useful insight into the migration of the eastern coast of Bazaruto during the Holocene. Aber/29-BA2, from the northern tip of Bazaruto, was formed during the early Holocene (7.30 ± 0.79 ka), when sea-level reached its present level. This indicates that the coastline of northern Bazaruto reached its present position early in the Holocene, and has been stable since. It is likely that the age for this sample corresponds to that for the first phase of beachrock formation along the early Holocene shoreline of Bazaruto, as described by Cooper (1991). In contrast, the beachrock from Sailfish Bay (Aber/29-BA8) formed quite recently (0.94 ± 0.09 ka) when sea-level stabilised at its present level. This indicates that the stabilisation of the eastern shoreline of Bazaruto is relatively recent. The ages for Aber/29-BA2 and 8 indicate that Cooper (1991) was correct to suggest that the eastern shoreline of Bazaruto migrated a significant distance westwards during the Holocene. Since the lowest unit in the Zingalema Point section (Aber/29-BA14, Figure 8.14 and Table 8.4) on the west coast is Last Interglacial in age, it appears that redeposition of eroded material on the shallow landward side of Bazaruto did not occur. Consequently, the westward migration of the eastern shoreline of Bazaruto must have resulted in a significant reduction in the width, and therefore area, of the island. This suggests that Bazaruto may be relatively unstable during periods of high sea-level.

8.4.3 A model for the evolution of Bazaruto Island

From the above data, a tentative model for the evolution of Bazaruto Island is proposed

1) The core of the island was deposited as a coast-parallel dune during the Last Interglacial. This may have occurred in two phases, in response to at least two high sea-level events recorded for the Maputaland area during the Last Interglacial (Ramsay and Cooper, 2002).
2) Considerable remobilisation of sediment occurred around 25 ka, possibly in response to a drawdown of the regional water table due to very low sea-levels.
3) In the early Holocene, extensive beachrock formation occurred along the eastern coast of Bazaruto. Subsequently, the eastern shoreline migrated westwards, due to erosion, leaving the early Holocene beachrock as an offshore reef. The shoreline appears to have stabilised at its present position around a thousand years ago.
4) Significant aeolian activity occurred during the Holocene, possibly involving redeposition of material eroded from the eastern shore. There are insufficient ages from this period to identify patterns in this activity.

8.5 Conclusions

1) Prior to this study, understanding of the evolution of Inhaca and Bazaruto Islands was based on stratigraphic interpretation alone. During this study, the major aeolian units of these islands have been dated using OSL, allowing models for the evolution of each island to be proposed.
2) The coast-parallel dunes which form the core of both islands, appear to have been deposited during interglacials, indicating that significant quantities of sediment were available at this time. This suggests that the sediment was derived from dunes on the continental shelf, which were drowned and eroded as sea-level rose at the beginning of the interglacial.
3) On Inhaca Island, at least, the main dune cordons are composite features, representing more than one interglacial.
4) Sediment remobilisation during the LGM low sea-level event occurred on both islands, possibly in response to vegetation loss due to a drawdown of the regional water table as sea-level fell.
5) Significant Holocene aeolian activity is recorded on both islands.
6) Significant erosion of the eastern shore of Bazaruto has occurred during the Holocene. This erosion was not matched by redeposition of material on the western shore, resulting in a significant decrease in area. This suggests that Bazaruto may be relatively unstable during periods of high sea-level.

Chapter 9: General conclusions and recommendations for further study

9.1 Introduction

This thesis aimed to test the single-aliquot regenerative-dose (SAR) technique (Murray and Wintle, 2000) using a suite of samples from the southeast African coast. In general the SAR technique was found to be robust. Dates for the main sedimentary units of two Mozambican islands, produced using the SAR technique, allowed models for the evolution of each island to be proposed. Specific conclusions are presented at the end of each chapter. This chapter presents more general conclusions, drawn from the thesis as a whole, and goes on to suggest topics that require further research.

9.2 General conclusions

1) Several components have previously been identified within the quartz OSL signal. A new slow-bleaching, thermally-unstable OSL component was found. This component causes significant age underestimates as a larger proportion of the total signal is integrated. The effect is largest when low preheat temperatures (c.160°C) are used, though it was observed at preheat temperatures as high as 300°C. The effects of this slow-bleaching, thermally-unstable component can be avoided by using the initial part of the OSL signal when calculating the equivalent dose.

2) The SAR sensitivity correction, using the OSL response to a small test dose as a proxy for the sensitivity of the preceding natural/regenerated OSL intensity, is appropriate irrespective of the direction and size of the sensitivity change. In contrast, use of the 110°C TL signal as a proxy for OSL sensitivity is only appropriate where sensitivity is constant or rising. The direction of sensitivity change during a measurement sequence is, in part, dependent on PH1 temperature. Consequently, the independence of D_e upon preheat temperature indicates that the SAR sensitivity correction procedure is appropriate for that sample. To make this test robust, the author advocates the routine use of a wide range of PH1 temperatures. However, using high PH1 temperatures (280 and 300°C), a large proportion of aliquots fail the recycling ratio test, indicating poor sensitivity correction. Prudence dictates that these preheat temperatures are avoided.

3) The patterns of sensitivity change observed during an SAR measurement sequence are dependent on sample age, PH1 temperature and the size of the regeneration dose. Young samples generally show increases in sensitivity while older samples show decreases. However, this behaviour is modified by PH1 temperature. Lower temperature preheats cause decreases in sensitivity, while the opposite is true of higher temperature preheats. The rate at which these sensitivity changes occur is higher using larger regeneration doses. These observations may be explained in terms of dose quenching and thermal activation, leading to variations in the ratio of activated R and L-centres, and hence radiative recombination probability. A minimum of three recombination centres, of which only one was radiative, were required to explain the patterns of OSL sensitivity change observed during this study.

4) Several different patterns of equivalent dose distributions were found for the samples dated. For all samples, β-microdosimetry and the effect of 1.5% measurement reproducibility errors contribute to the range of equivalent doses measured for a given sample. The latter may be significant for samples with large equivalent doses (>100 Gy). However, for some samples with doses ranging from 2 to 100 Gy, the scatter observed is larger than can be accounted for by these two mechanisms. It is possible that mixing, possibly by bioturbation, of adjacent units also contributes to the scatter for these samples. A further source of scatter is required to account for the range of equivalent doses measured for some of the older samples. However, the cause of this scatter has not yet been identified.

5) At low regeneration doses, there is remarkably little inter-aliquot or inter-sample variation in the shape of the growth curve (normalised for the *size* of the test dose) produced using the SAR method. However, using regeneration doses greater than 100 Gy, considerable variability in growth curve shape is observed. Some growth curves are best fitted using a saturating exponential plus linear function, while others require only a saturating exponential. In the latter case, the natural luminescence intensity is occasionally greater than the maximum luminescence intensity reached by the growth curve. When this occurs, no equivalent dose may be calculated for that aliquot. No single cause for this phenomenon has been found.

6) A suite of samples from the Mozambican islands of Inhaca and Bazaruto were dated using the SAR technique. These islands are composed of large dunes, and the ages obtained were used to understand the evolution of each island, in relationship to previously published records of sea-level change. On both islands, the main sedimentary units were deposited during previous interglacials (high sea-level). However, some localised remobilisation of these dunes occurred during the Last Glacial Maximum, possibly in response to lowered regional water tables, due to low sea-levels. Significant aeolian activity is also recorded during the Holocene.

9.3 Suggested topics for further research

The research undertaken for this thesis demonstrates that the SAR technique is appropriate for most of the samples studied. However, further research into the following topics is required:

1) Identification of the trap responsible for the slow-bleaching, thermally-unstable OSL signal observed when using long signal integration periods. Identification of this trap would allow its effect on the calculated D_e to be minimised, either by appropriate preheating, or the production of component-resolved growth curves. This would mean that measurement procedures that require integration of larger parts of the OSL decay curve (e.g. single grain measurements) could be used without risking underestimation of the palaeodose.

2) Sources of scatter. The range of equivalent doses observed for sample Aber/28-IN1 cannot be explained solely in terms of measurement reproducibility, β-microdosimetry, mixing, bioturbational zeroing or measurement procedure errors. It is important to identify the cause of the additional scatter, because the most appropriate method of calculating an equivalent dose from a scattered dataset depends on its source.

3) Growth curves which saturate before the natural luminescence intensity (L_n/T_n) is reached. This phenomenon can only be observed for signals for which the palaeodose is close to the saturation dose of the growth curve. However, younger samples may also yield natural luminescence intensities that are greater than the corresponding

regenerated luminescence intensity measured for the growth curve. Consequently, L_n/T_n still intercepts the growth curve, but the error is not detected, and thus the ages calculated using equivalent doses from these aliquots will be erroneously high.

4) The development of other luminescence methods for dating old sediments. The relatively rapid saturation of the quartz OSL signal, measured using the experimental conditions of this study, hampers the production of reliable equivalent doses for old (D_e >100 Gy) samples. Use of a luminescence signal which reaches dose response saturation at higher doses, would reduce the scatter imparted on a dataset by the projection of the natural luminescence intensity onto a saturating growth curve. In addition, use of such a signal may circumvent problems caused by the natural luminescence intensity being greater than the saturation intensity of the growth curve.

References

Adamiec, G., (2000) Variations in luminescence properties of single quartz grains and their consequences for equivalent dose estimation. *Radiation Measurements*, **32**, 427-432.

Adamiec, G., and Aitken, M.J., (1998) Dose-rate conversion factors: update. *Ancient TL*, **16**, 37-50.

Aitken, M.J., (1985) *Thermoluminescence Dating*. Academic Press, London.

Aitken, M.J., (1998) *An Introduction to Optical Dating*. Oxford University Press, Oxford.

Aitken, M.J., (1990) Pairs precision required in alpha counting. *Ancient TL*, **8**, 12-14.

Aitken, M.J. and Smith, B.W., (1988) Optical dating: Recuperation after bleaching. *Quaternary Science Reviews*, **7**, 387-393.

Armitage, S.J., Duller, G.A.T., and Wintle, A.G., (2000) Quartz from southern Africa: sensitivity changes as a result of thermal pretreatment. *Radiation Measurements*, **32**, 571-577.

Bailey, R.M., (1997) Optical detrapping of charge from the 110°C quartz TL region. *Ancient TL*, **15**, 7-10.

Bailey, R.M., (1998a) Depletion of the quartz OSL signal using low photon energy stimulation. *Ancient TL*, **16**, 33-36.

Bailey, R.M., (1998b) *The Form of the Optically Stimulated Luminescence Signal of Quartz: Implications for Dating*. Unpublished Ph.D. Thesis, Royal Holloway, University of London.

Bailey, R.M., (2000a) The slow component of quartz optically stimulated luminescence. *Radiation Measurements*, **32**, 233-246.

Bailey, R.M., (2000b) Circumventing possible inaccuracies of the single aliquot regeneration method for the optical dating of quartz. *Radiation Measurements*, **32**, 833-840.

Bailey, R.M., (2000c) The interpretation of quartz optically stimulated luminescence equivalent dose versus time plots. *Radiation Measurements*, **32**, 129-140.

Bailey, R.M., (2001) Towards a general kinetic model for optically and thermally stimulated luminescence of quartz. *Radiation Measurements*, **33**, 17-45.

Bailey, R.M., (submitted) Investigation of a possible SAR $D_e(t)$ method for the identification of partially bleached sediments. *Radiation Measurements*.

Bailey, R.M., Smith, B.W., and Rhodes, E.J., (1997) Partial bleaching and the decay form characteristics of quartz OSL. *Radiation Measurements*, **27**, 123-136.

Bailey, S.D., Wintle, A.G., Duller, G.A.T., and Bristow, C.S., (2001) Sand deposition during the last millennium at Aberffraw, Anglesey, North Wales as determined by OSL dating of quartz. *Quaternary Science Reviews*, **20**, 701-704.

Banerjee, D., (2000) Thermal transfer and recuperation in quartz OSL and their consequences regarding luminescence dating procedures. *ISLA 2000 Conference Proceedings*

Banerjee, D., Bøtter-Jensen, L., and Murray, A.S., (2000) Retrospective dosimetry: estimation of the dose to quartz using the single-aliquot regenerative-dose protocol. *Applied Radiation and Isotopes*, **52**, 831-844.

Barbouti, A.I. and Rastin, B.C., (1983) A study of the absolute intensity of muons at sea level and under various thicknesses of absorber. *Journal of Physics G: Nuclear Physics*, **9**, 1577-1595.

Bard, E., Hamelin, B., and Fairbanks, R.G., (1990) U-Th ages obtained by mass spectrometry in corals from Barbados: sea level during the past 130,000 years. *Nature*, **346**, 456-458.

Bevington, P.R., and Robinson, D.K., (1992) *Data Reduction and Error Analysis for the Physical Sciences*. 2nd Ed. McGraw-Hill, Boston, Massachusetts.

Botha, G.A., (1997) The Maputaland Group: A provisional lithostratigraphy for coastal KwaZulu-Natal. In Botha, G.A., (ed). *Maputaland: Focus on the Quaternary evolution of the south-east African coastal plain, field guide and abstracts*. INQUA Commission on Quaternary Shorelines, Africa subcommission, pp. 21-27.

Botha, G.A., Bristow, C.S., Duller, G.A.T., Porat, N., Armitage, S.J., Roberts, H.M., Clarke, B.M., Kota, M.W. and Schoeman, P. (in press) Dune development and remobilization on the Maputaland coastal plain, South Africa: a ground penetrating radar (GPR) perspective. *Geol. Soc. Special Publication.*

Bøtter-Jensen, L. and Duller, G.A.T., (1992) A new system for measuring optically stimulated luminescence from quartz samples. *Nuclear Tracks and Radiation Measurements*, **20**, 549-553.

Bøtter-Jensen, L., and Mejdahl, V., (1988) Assessment of beta dose-rate using a GM multicounter system. *Nuclear Tracks and Radiation Measurements*, **14**, 187-191.

Bøtter-Jensen, L., Mejdahl, V., and Murray, A.S., (1999a) New light on OSL. *Quaternary Science Reviews*, **18**, 303-309.

Bøtter-Jensen, L., Duller, G.A.T., Murray, A.S., and Banerjee, D., (1999b) Blue light emitting diodes for optical stimulation of quartz in retrospective dosimetry and dating. *Radiation Protection Dosimetry*, **84**, 335-340.

Bøtter-Jensen, L., Bulur, E., Duller, G.A.T., and Murray, A.S., (2000) Advances in luminescence instrument systems. *Radiation Measurements*, **32**, 523-528.

Brady, N.C., (1990) *Nature and Properties of Soils*, 10th edition. Macmillan, New York.

Bray, H.E., Bailey, R.M., and Stokes, S., (2002) Quantification of cross-talk and cross-illumination using a Risø TL/OSL DA-15 reader. *Radiation Measurements*, **35**, 275-280.

Bray, H., Duller, G.A.T., Bailey, R.M., and Stokes, S., (in prep.) Data Visualisation and Error Analysis in Luminescence Dating Measurements. In *A Handbook of Luminescence Dating*. Springer-Verlag.

Chen, G. and Li, S.-H., (2000) Studies of quartz 110°C thermoluminescence peak sensitivity change and its relevance to optically stimulated luminescence dating. *Journal of Physics D: Applied Physics*, **33**, 437-443.

Chen, G., Li, S.-H., and Murray, A.S., (2000) Study of the 110°C TL peak sensitivity in optical dating of quartz. *Radiation Measurements*, **32**, 641-645.

Chen, R. and Kristianpoller, N., (1986) Investigation of phosphorescence decay using TL-like presentation. *Radiation Protection Dosimetry*, **17**, 443-446.

Chen, R. and McKeever, S.W.S., (1997) *Theory of Thermoluminescence and Related Phenomena*. World Scientific, Singapore.

Chu S.Y.F., Ekstrom L.P. and Firestone R.B. (1999) WWW Table of Radioactive Isotopes, database version 1999-02-28 from URL http://nucleardata.nuclear.lu.se/nucleardata/toi/

Coetzee, F., (1975) Coastal aeolianites at Black Rock, northern Zululand. *Transactions of the Geological Society of South Africa*, **78**, 313-322.

Compton, J.S., (2001) Holocene sea-level fluctuations inferred from the evolution of depositional environments of the southern Langebaan Lagoon salt marsh, South Africa. *The Holocene*, **11**, 395-405.

Cooper, J.A.G., (1991) Beachrock formation in low latitudes: implications for coastal evolutionary models. *Marine Geology*, **98**, 145-154.

Cooper, J.A.G., and Flores, R.M., (1991) Shoreline deposits and diagenesis resulting from two Late Pleistocene highstands near +5 and +6 metres, Durban, South Africa. *Marine Geology*, **97**, 325-343.

Duller, G.A.T., (1996) The age of the Koputaroa dunes, southwest North Island, New Zealand. *Palaeogeography, Palaeoclimatology, Palaeoecology*, **121**, 105-114.

Duller, G.A.T. and Bøtter-Jensen, L., (1996) Comparison of optically stimulated luminescence signals from quartz using different stimulation wavelengths. *Radiation Measurements*, **26**, 603-609.

Duller, G.A.T., Bøtter-Jensen, L., and Murray, A.S., (2000) Optical dating of single sand-sized grains of quartz: sources of variability. *Radiation Measurements*, **32**, 453-457.

Duller, G.A.T., Bøtter-Jensen, L., Murray, A.S., and Truscott, A.J., (1999) Single grain laser luminescence (SGLL) measurements using a novel automated reader. *Nuclear Instruments and Methods in Physics Research B*, **155**, 506-514.

Flemming, B.W., (1981) Factors controlling shelf sediment dispersal along the southeast African continental margin. *Marine Geology*, **42**, 259-277.

Franklin, A.D. and Hornyak, W.F., (1990) Isolation of the rapidly bleaching peak in quartz TL curves. *Ancient TL*, **8**, 29-31.

Franklin, A.D., Prescott, J.R., and Scholefield, R.B., (1995) The mechanism of thermoluminescence in an Australian sedimentary quartz. *Journal of Luminescence*, **63**, 317-326.

Galloway, R.B., (1993) Stimulation of luminescence using green light emitting diodes. *Radiation Protection Dosimetry*, **47**, 679-682.

Godfrey-Smith, D.I., (1994) Thermal effects in the optically stimulated luminescence of quartz and mixed feldspars from sediments. *Journal of Physics D: Applied Physics*, **27**, 1737-1746.

Goudie, A.S., Colls, A.E.L., Stokes, S., Parker, A.G., White, K., and Al-Farraj, A., (2000) Latest Pleistocene and Holocene dune construction at the north-eastern edge of the Rub Al Khali, United Arab Emirates. *Sedimentology*, **47**, 1011-1021.

Harland, W.B., Armstrong, A.V., Cox, L.E., Craig, A.G., and Smith, D.G., (1989) *A Geologic Timescale 1989*, Cambridge University Press, Cambridge.

Hobday, D.K., (1977) Late Quaternary sedimentary history of Inhaca Island, Mozambique. *Transactions of the Geological Society of South Africa*, **80**, 183-191.

Hong, D.G., (1998) *Luminescence stimulated from quartz by green light : developments relevant to dating*. Unpublished Ph.D. Thesis, University of Edinburgh.

Huntley, D.J., and Wintle, A.G., (1981) The use of alpha scintillation counting for measuring Th-230 and Pa-231 contents of ocean sediments. *Canadian Journal of Earth Sciences*, **18**, 419-432.

Huntley, D.J., Godfrey-Smith, D.I., and Thewalt, M.L.W., (1985) Optical dating of sediments. *Nature*, **313**, 105-107.

Huntley, D.J., Godfrey-Smith, D.I., and Haskell, E.H., (1991) Light-induced emission-spectra from some quartz and feldspars. *Nuclear Tracks and Radiation Measurements*, **18**, 127-131.

Huntley, D.J., Short, M.A., and Dunphy, K., (1996) Deep traps in quartz and their use for optical dating. *Canadian Journal of Physics*, **74**, 81-91.

Jain, M., Murray, A.S., Bøtter-Jensen, L., and Thomsen, K., (2001) Luminescence characteristics of a thermally unstable fast component in quartz. *Luminescence and ESR Dating Meeting, Book of Abstracts*, University of Glasgow.

Jungner, H. and Bøtter-Jensen, L., (1994) Study of sensitivity change of OSL signals from quartz and feldspars as a function of preheat temperature. *Radiation Measurements*, **23**, 621-624.

Krane, K.S., (1987) *Introductory Nuclear Physics*. John Wiley and Sons.

Li, S.-H. and Chen, G., (2001) Studies of thermal stability of trapped charges associated with OSL from quartz. *Journal of Physics D: Applied Physics*, **34**, 493-498.

Markey, B.G., Bøtter-Jensen, L., and Duller, G.A.T., (1997) A new flexible system for measuring thermally and optically stiumlated luminescence. *Radiation Measurements*, **27**, 83-89.

Maud, R.R., and Botha, G.A., (2000) Deposits of the South Eastern and Southern Coasts. In Partridge, T.C., and Maud, R.R., (eds). *The Cenozoic of Southern Africa.* Oxford University Press, Oxford, pages 19-32.

McKerrell, H., and Mejdahl, V., (1981) Progress and problems with automated TL dating. Proceedings of the 16th International Symposium on Archaeometry, National Museum of Antiquities of Scotland, Edinburgh and Risø Report M-2265, 36pp.

McMillan, I.K., (1993) Foraminiferal biostratigraphy, sequence stratigraphy and interpreted chronostratigraphy of marine Quaternary sedimentation on the South African continental shelf. *South African Journal of Science*, **89**, 83-89.

Munyikwa, K., (2000) Cosmic ray contribution to environmental dose rates with varying overburden thickness. *Ancient TL*, **18**, 27-34.

Murray, A.S. and Roberts, R.G., (1997) Determining the burial time of single-grains of quartz using optically stimulated luminescence. *Earth and Planetary Science Letters*, **152**, 163-180.

Murray, A.S. and Wintle, A.G., (1998) Factors controlling the shape of the OSL decay curve in quartz. *Radiation Measurements*, **29**, 65-79.

Murray, A.S. and Roberts, R.G., (1998) Measurement of the equivalent dose in quartz using a regenerative-dose single-aliquot protocol. *Radiation Measurements*, **29**, 503-515.

Murray, A.S. and Mejdahl, V., (1999) Comparison of regenerative-dose single-aliquot and multiple- aliquot (SARA) protocols using heated quartz from archaeological sites. *Quaternary Science Reviews*, **18**, 223-229.

Murray, A.S. and Wintle, A.G., (1999a) Isothermal decay of optically stimulated luminescence in quartz. *Radiation Measurements*, **30**, 119-125.

Murray, A.S. and Wintle, A.G., (1999b) Sensitisation and stability of quartz OSL: Implications for interpretation of dose-response curves. *Radiation Protection Dosimetry*, **84**, 427-432.

Murray, A.S. and Wintle, A.G., (2000) Luminescence dating of quartz using an improved single-aliquot regenerative-dose protocol. *Radiation Measurements*, **32**, 57-73.

Murray, A.S. and Wintle, A.G., (2002) Retrospective dose assessment: the measurement of the dose in quartz in dating and accident dosimetry. *Radiation Protection Dosimetry*, **101**, 301-308.

Murray, A.S., Roberts, R.G., and Wintle, A.G., (1997) Equivalent dose measurement using a single aliquot of quartz. *Radiation Measurements*, **27**, 171-184.

Murray, A.S., Wintle, A.G., and Wallinga, J., (in prep) The estimation of the dose in quartz close to saturation.

Nambi, K.S.V. and Aitken, M.J., (1986) Annual dose conversion factors for TL and ESR dating. *Archaeometry*, **28**, 202-205.

Ollerhead, J., (2001) Light transmittance through dry, sieved sand: some test results. *Ancient TL*, **19**, 13-17.

Oschadleus, H.D., Vogel, J.C., and Scott, L., (1996) Radiometric date for the Port Durnford peat and development of yellow-wood forest along the South African east coast. *South African Journal of Science*, **92**, 43-45.

Perkins, N.K. and Rhodes, E.J., (1994) Optical dating of fluvial sediments from **Tattershall**, U.K. *Quaternary Science Reviews*, **13**, 517-520.

Petrov, S.A. and Bailiff, I.K., (1995) The "110°C" TL peak in synthetic quartz. *Radiation Measurements*, **24**, 519-523.

Prescott, J.R. and Hutton, J.T., (1988) Cosmic-ray and gamma-ray dosimetry for TL and **electron**-spin resonance. *Nuclear Tracks and Radiation Measurements*, **14**, 223-227.

Prescott, J.R. and Hutton, J.T., (1994) Cosmic ray contributions to dose rates for **luminescence** and ESR dating: large depths and long-term time variations. *Radiation Measurements*, **23**, 497-500.

Ramsay, C. B., (2000) OxCal Program v3.5, Users Manual. From URL http://www.rlaha.ox.ac.uk/orau/index.htm

Ramsay, P.J., (1994) Marine geology of the Sodwana Bay shelf, southeast Africa. *Marine Geology*, **120**, 225-247.

Ramsay, P.J., (1995) 9000 years of sea-level change along the southern African coastline. *Quaternary International*, **31**, 71-75.

Ramsay, P.J., and Cooper, J.A.G., (2002) Late Quaternary sea-level change in South Africa. *Quaternary Research*, **57**, 82-90.

Ramsay, P.J., Smith, A.M., Lee-Thorp, J.C., Vogel, J.C., Tyldsley, M., and Kidwell, W., (1993) 130,000-year-old fossil elephant found near Durban, South Africa: preliminary report. *South African Journal of Science*, **89**, 165.

Ramsay, P.J., Smith, A.M., and Mason, T.R., (1996) Geostrophic sand ridge, dune fields and associated bedforms from the Northern KwaZulu-Natal shelf, south-east Africa. *Sedimentology*, **43**, 407-419.

Rhodes, E.J., (1988) Methodological considerations in the optical dating of quartz. *Quaternary Science Reviews*, **7**, 395-400.

Rhodes, E.J., (1990) *Optical dating of quartz from sediments*. Unpublished D.Phil. Thesis, University of Oxford.

Rhodes, E.J., (2000) Observations of thermal transfer OSL signals in glacigenic quartz. *Radiation Measurements*, **32**, 595-602.

Richards, M.P., (1994) *Luminescence dating of quartzite from the Diring Yuriakh site*. Unpublished Masters Thesis, Simon Fraser University, British Colombia.

Roberts, H.M. and Wintle, A.G., (2001) Equivalent dose determinations for polymineralic fine-grains using the SAR protocol: application to a Holocene sequence of the Chinese Loess Plateau. *Quaternary Science Reviews*, **20**, 859-863.

Roberts, H.M., and Duller, G.A.T., (submitted) Universal growth curves for optically stimulated luminescence dating of sediments. *Radiation Measurements.*

Roberts, R.G., Spooner, N.A., and Questiaux, D.G., (1994) Paleodose underestimates caused by extended-duration preheats in the optical dating of quartz. *Radiation Measurements*, **23**, 647-653.

Scholefield, R.B., Prescott, J.R., Franklin, A.D., and Fox, P.J., (1994) Observations on some thermoluminescence emission centres in geological quartz. *Radiation Measurements*, **23**, 409-412.

Singarayer, J.S. and Bøtter-Jensen, L., (in prep) Linear modulation of optically-stimulated luminescence (LM-OSL). *A Handbook of Luminescence.*

Singarayer, J.S. and Bailey, R.M., (in press) Component-resolved bleaching spectra of quartz optically stimulated luminescence: preliminary results and implications for dating. *Radiation Measurements.*

Singarayer, J.S., Bailey, R.M., and Rhodes, E.J., (2000) Potential of the slow component of quartz OSL for age determination of sedimentary samples. *Radiation Measurements*, **32**, 873-880.

Smith, B.W. and Rhodes, E.J., (1994) Charge movements in quartz and their relevance to optical dating. *Radiation Measurements*, **23**, 329-333.

Smith, B.W., Rhodes, E.J., Stokes, S., and Spooner, N.A., (1990) The optical dating of sediments using quartz. *Radiation Protection Dosimetry*, **34**, 75-78.

Smith, B.W., Aitken, M.J., Rhodes, E.J., Robinson, P.D., and Geldard, D.M., (1986) Optical dating: Methodological aspects. *Radiation Protection Dosimetry*, **17**, 229-233.

Smith, B.W., Rhodes, E.J., Stokes, S., Spooner, N.A., and Aitken, M.J., (1990) Optical dating of sediments: Initial quartz results from Oxford. *Archaeometry*, **32**, 19-31.

Spooner, N.A., (1994) On the optical dating signal from quartz. *Radiation Measurements*, **23**, 593-600.

Spooner, N.A. and Questiaux, D.G., (2000) Kinetics of red, blue and UV thermoluminescence and optically-stimulated luminescence from quartz. *Radiation Measurements*, **32**, 659-666.

Spooner, N.A., Prescott, J.R., and Hutton, J.T., (1988) The effect of illumination wavelength on the bleaching of the thermoluminescence (TL) of quartz. *Quaternary Science Reviews*, **7**, 325-329.

Stokes, S., (1992) Optical dating of young (modern) sediments using quartz: results from a selection of depositional environments. *Quaternary Science Reviews*, **11**, 153-159.

Stokes, S., (1994a) The timing of OSL sensitivity changes in a natural quartz. *Radiation Measurements*, **23**, 601-605.

Stokes, S., (1994b) Optical dating of selected Late Quaternary aeolian sediments from the Southwestern United States. Unpublished D.Phil thesis, University of Oxford.

Stokes, S., (1996) Further comparisons of quartz OSL additive dose palaeodoses generated using long and short duration preheats. *Ancient TL*, **14**, 1-3.

Stokes, S., (1999) Luminescence dating applications in geomorphological research. *Geomorphology*, **29**, 153-171.

Stokes, S., Colls, A.E.L., Fattahi, M., and Rich, J., (2000) Investigating the performance of quartz single aliquot D_E determination procedures. *Radiation Measurements*, **32**, 585-594.

Stoneham, D. and Stokes, S., (1991) An investigation of the relationship between the 110°C TL peak and optically stimulated luminescence in sedimentary quartz. *Nuclear Tracks and Radiation Measurements*, **18**, 119-123.

Stuiver, M., Reimer, P.J., Bard, E., Beck, J.W., Burr, G.S., Hughen, K.A., Kromer, B., McCormac, G., Van der Plicht, J., and Spurk, M., (1998) INTCAL98 radiocarbon age calibration 24,000-0 cal BP. *Radiocarbon*, **40**, 1041-1083.

Taylor, R.E. and Aitken, M.J., (1997) *Chronometric Dating in Archaeology*. Kluwer Academic/Plenum.

Truscott, A.J., Duller, G.A.T., Bøtter-Jensen, L., Murray, A.S., and Wintle, A.G., (2000) Reproducibility of optically stimulated luminescence measurements from single grains of Al_2O_3:C and annealed quartz. *Radiation Measurements*, **32**, 447-451.

Vogel, J.C., Wintle, A.G., and Woodborne, S.M., (1999) Luminescence dating of coastel sands: Overcoming changes in environmental dose rate. *Journal of Archaeological Science*, **26**, 729-733.

Wallinga, J., Murray, A.S., and Duller, G.A.T., (2000) Underestimation of equivalent dose in single-aliquot optical dating of feldspars caused by preheating. *Radiation Measurements*, **32**, 691-695.

Wallinga, J., Murray, A.S., and Bøtter-Jensen, L., (in press) Measurement of the dose in quartz in the presence of feldspar contamination. *Radiation Protection Dosimetry*.

Wintle, A.G., (1975) Thermal quenching of thermoluminescence in quartz. *Geophysical Journal of the Royal Astronomical Society*, **41**, 107-113.

Wintle, A.G., (1977) Thermoluminescence dating of minerals - Traps for the unwary. *Journal of Electrostatics*, **3**, 281-288.

Wintle, A.G., (1996) Archaeologically-relevant dating techniques for the next century. *Journal of Archaeological Science*, **23**, 123-138.

Wintle, A.G. and Murray, A.S., (1997) The relationship between quartz thermoluminescence, photo-transferred thermoluminescence, and optically stimulated luminescence. *Radiation Measurements*, **27**, 611-624.

Wintle, A.G. and Murray, A.S., (1998) Towards the development of a preheat procedure for OSL dating of quartz. *Radiation Measurements*, **29**, 81-94.

Wintle, A.G. and Murray, A.S., (1999) Luminescence sensitivity changes in quartz. *Radiation Measurements*, **30**, 107-118.

Wintle, A.G. and Murray, A.S., (2000) Quartz OSL: Effects of thermal treatment and their relevance to laboratory dating procedures. *Radiation Measurements*, **32**, 387-400.

Wright, C.I., (1997) A broad overview of the Cenozoic evolution of the northern KwaZulu-Natal palaeodune cordons. In Botha, G.A., (ed). *Maputaland: Focus on the Quaternary evolution of the south-east African coastal plain, field guide and abstracts*. INQUA Commission on Quaternary Shorelines, Africa subcommission, pp. 27-33.

Wright, C.I., Miller, W.R., and Cooper, J.A.G., (2000) The late Cenozoic evolution of coastal water bodies in Northern KwaZulu-Natal, South Africa. *Marine Geology*, **167**, 207-229.

Zimmerman, J., (1971) The radiation-induced increase of the 110°C thermoluminescence sensitivity of fired quartz. *Journal of Physics C: Solid State Physics*, **4**, 3265-3276.

Acknowledgements

I am enormously grateful to the huge number of people who have helped me through the PhD process. I will always remember my time in Aberystwyth with much fondness.

Financial support was provided by the University of Wales Aberystwyth, for which I feel extremely privileged.

My supervisors, Geoff Duller and Ann Wintle provided invaluable advice and encouragement throughout my time in Aberystwyth. In addition I am hugely indebted to Greg Botha, Luís Rebêlo, Naomi Porat, Fatima Momade and Charlie Bristow for organising two fieldtrips in southern Africa.

I thank all the members of the Quaternary Environmental Change Research Group in Aberystwyth, especially Helen Roberts, my fellow students Jacob Wallinga, Chris Burbidge, Zenobia Jacobs, Simon Bailey and Susan Packman, and various visitors including Michel Lamothe.

I thank the staff and postgrads of the Institute of Geography and Earth Sciences, especially Lorraine Hill, Lorraine Morrison, Dave Kelly and Valerie Grant.

I thank my (many) housemates at Lugaga, including Andy Mitchell, Dave Graham, Keren Smith and Becky Goodsell, for their support and humour.

Most of all I thank my parents, sister and Natalie for their love and support.

Appendix 2.1 Glossary of shorthand terms used to describe actions and measurements performed during standard SAR sequences

PH1	The preheat preceding measurement of L_x.
L_x	Natural (L_n) or regenerated (L_x) OSL intensity (x = 1,…), with the background signal subtracted (Section 2.2.2).
PH2	The cut-heat prior to measurement of T_x.
T_x	Test dose OSL intensity. Natural test dose (T_n) or regeneration dose test dose (T_x) (x = 1,…), with the background signal subtracted (Section 2.2.2).
β_x	β regeneration dose, (x = 1,…).
N	Sensitivity-corrected natural OSL intensity (L_n/T_n).
R_x	Sensitivity-corrected regenerated OSL intensity i.e. L_x/T_x, (x = 1,…).

Appendix 6.1 Equivalent dose error analysis using Analyst and LD Base

The errors quoted on D_e measurements were calculated in Analyst or LD Base software, written by Dr. Geoff Duller, and are explained below.

Errors in individual aliquot D_e values

Errors on individual D_e estimates were calculated using Analyst, and subsequently used in some of the graphic representations of equivalent dose variability produced by LD Base (e.g. probability density functions). Three components are used.

1) Curve fitting error. The mean distance of each regenerated dose point from the growth curve is calculated, and applied to the natural luminescence intensity.

2) Photon counting statistics. The random uncertainty arising from counting statistics is calculated using the expression

$$\sigma = \frac{\sqrt{\sum_i S_i + 2\overline{B}n}}{\sum_i S_i - \overline{B}n} \qquad \text{(A5.1.1)}$$

where S_i is the signal from the ith channel (i=1, 2,...n) and $\overline{B}$ is the average background count per channel (from Banerjee *et al.*, 2000).

3) Systematic error. A percentage systematic error designed to reflect measurement reproducibility. A value of 1.5% systematic error was used throughout this study (see Section 5.3.2)

To estimate the error on the natural luminescence intensity (L_n/T_n), the curve fitting and photon counting errors are added, and multiplied by the systematic error. The upper and lower limits of this distribution are then superimposed on the growth curve to yield the error on the equivalent dose. This error is symmetrical irrespective of the slope of the growth curve, and represents the mean of the positive and negative errors. The error calculations performed by Analyst yield a conservative estimate of the

uncertainties on the equivalent dose. This is because the systematic (measurement) error will increase the curve fitting error.

Errors in mean sample equivalent dose values

LD Base allows two different error terms to be calculated for a single aliquot dataset, the standard deviation and the standard error. In all cases one standard error uncertainty has been quoted on equivalent dose estimates used to calculate ages (Tables 6.3 and 6.4). It should be noted that this error does not take into account uncertainties on the $^{90}Sr/^{90}Y$ β-source calibration.

Appendix 7.1 Dose rate calculation: A worked example

Routine dose rate calculations were performed using the Aberystwyth Luminescence Database software written by Dr. Geoff Duller. To ensure that this software is functioning correctly the environmental dose rate for Aber/28-IN15 was calculated by hand. K, Th and U concentrations were calculated using TSAC and GM-beta counting data, since these techniques were applied to all samples for which absolute ages have been produced.

Thorium and Uranium concentrations from TSAC

Background count rate (cts/ks) = 0.0116[a] cts/ks
True sample count rate (cts/ks) = 1.1995 cts/ks

The true pairs rate, p, is calculated by subtracting the random coincidence rate, r, from the observed pairs rate, d. For a coincidence time of 0.38 s (the coincidence window in Daybreak 582/583 alpha counters is open from 0.02 to 0.4 seconds after each α event), r is given by

$$r = \alpha^2/2631$$

(Aitken, 1990) where α is the alpha count rate in counts/ks. For this sample the values for d and r are

$d = 74/2579.52 = 0.0287$ pairs/ks
$r = 1.1995^2/2631 = 5.468 \times 10^{-4}$ pairs/ks

From these values p = 0.0281 pairs/ks

---

[a] Values have been given to an appropriate number of decimal places in the worked example below. However, for the purposes of this calculation the eight digit memory of a pocket calculator has been used.

The thorium concentration (ppm) is related to the count rate of true pairs according to

$Th = p/0.0022a$

Where a is the proportion of pairs that are measured using the 0.02-0.40s coincidence window (Huntley and Wintle, 1981) and p is in $cts.cm^{-2}.ks^{-1}$ [b]. Taking r to be 0.76 (Daybreak model 583 Users Manual) this yields a **thorium concentration of 1.107 ppm**. The count rate due to thorium, α_h is given by

$\alpha_h = 1.107*0.0349 = 0.0386$ $cts.cm^{-2}.ks^{-1}$

Adamiec and Aitken (1998). By subtracting this figure from the total count rate, and dividing by 0.1206 (the count rate due to 1 ppm uranium, Adamiec and Aitken, 1998) the uranium content can be calculated. This yields an **uranium content of 0.334 ppm**.

These values are identical to those produced by the Aberystwyth Luminescence Database.

The environmental dose rate

The dose rates due to calculated U, Th and K elemental concentrations within the sediment are obtained from Adamiec and Aitken (1998). These figures assume secular equilibrium, and natural uranium containing 0.71% ^{235}U. Attenuation values are calculated in the database, based on a mean grain diameter of 196 μm. All dose rates are for dry sediment.

α contribution:

The α dose rate is assumed to be negligible since the outer 10 μm of each grain has been removed due to the HF etch.

---

[b] The alpha counting area is 15.20 cm^2.

β contribution:

The infinite beta dose rate is calculated from GM-beta counting data. The instrument is calibrated during each run using two standards, MgO (0 Gy/ka) and Shap granite (6.25 Gy/ka). The sediment dose rate was then calculated from the mean count for three subsamples. For this sample the calculation is as follows.

True Shap count = Shap – MgO = 34588 – 492 = 34096 counts

True Shap count rate = (34096 / 6.25)/48[c] = 113.65 cts/hr per Gy/ka

True IN15 count rate = (IN15 – MgO)/48 = (3664 – 492)/48 = 66.08 cts/hr

Infinite β dose rate for IN15 = 66.08/113.65 = 0.581 Gy/ka

This value is identical to that produced by the database.

The β dose rate due to potassium content was calculated by subtracting the unattenuated dose rate due to Th and U, from the infinite beta dose rate measured using GM-beta counting. This was then converted to percentage potassium content by dividing by the dose rate from 1% potassium (0.782 Gy/ka).

U	0.334 ppm	@0.1460 Gy/ka per ppm	0.0488 Gy/ka
Th	1.107 ppm	@0.0273 Gy/ka per ppm	0.0302 Gy/ka

β dose rate due to K = 0.581 – (0.0488 + 0.0302) = 0.5025 Gy/ka.

%K = 0.5025 / 0.782 = 0.643 %

The β dose rates must then be corrected for attenuation due to grain size

U	0.0488*0.854	0.0416 Gy/ka
Th	0.0302*0.794	0.0240 Gy/ka
K	0.5025*0.931	0.4678 Gy/ka

[c] This sample was measured for 48 hours.

This yields a "dry" attenuated β dose rate of 0.533 Gy/ka. The corresponding dose rate from the Aberystwyth Database (0.521 Gy/ka) is marginally lower than this value because a mean β attenuation factor was used[d]. Given the imprecision with which the Th/U ratio (and hence the potassium content) is known, this discrepancy (2.3 %) is satisfactory.

γ contribution:

U	0.334 ppm	@0.1130 Gy/ka per ppm	0.0377 Gy/ka
Th	1.107 ppm	@0.0477 Gy/ka per ppm	0.0528 Gy/ka
K	0.643 %	@0.2430 Gy/ka per %	0.1562 Gy/ka

No significant attenuation of γ occurs due to grain size.

This yields a "dry" γ dose rate of 0.247 Gy/ka, identical to that produced by the database.

Cosmic dose rate

The cosmic dose rate (Gy/ka) is calculated using the formula of Barbouti and Rastin (1983):

$$D = \frac{C}{((x + d)^{\alpha} + a)(x + H)} \exp(-Bx)$$

where x is in hg cm^{-2}, C = 6072, B = 5.50 x 10^{-4}, d = 11.6, α = 1.68, a = 75 and H = 212.

---

[d] A weighted mean attenuation factor assuming a β dose rate ratio of 7:2:1 (K:Th:U).

For this sample, with a depth of 1.5 m and an assumed overburden density of 1.85 g/cm^3

x = density of overburden (g/cm^3) * thickness of overburden (m) = 2.775 hg cm^{-2}

This yields a cosmic dose rate of 0.173 Gy/ka. The Aberystwyth Database gives an identical value.

Correction for moisture content

Correction of the dry dose rates for moisture content were made using the following equations,

$$D_\beta = D_{\beta(dry)}/1 + 1.25W$$
$$D_\gamma = D_{\gamma(dry)}/1 + 1.14W$$

where D_β and D_γ are the corrected β and γ dose rates and W is the water content (mass of water / mass of dry sediment)[e]. For dry beta[f] and gamma dose rates of 0.533 Gy/ka and 0.247 Gy/ka, and a water content of 5% (W=0.05), this yields

$D_\beta = 0.502$ Gy/ka

$D_\gamma = 0.233$ Gy/ka

The β dose rate must now be multiplied by 0.9 to compensate for the loss of β irradiated material during the HF etch (Aitken, 1985, p259). This yields a final dose rate of 0.858 Gy/ka. The equivalent figure from the Aberystwyth Luminescence Database is 0.847 Gy/ka, the discrepancy (1.3 %) being due to the use of a weighted mean β attenuation factor.

---

[e] W has been used instead of WF and W_1F in Aitken (1985, p75). For homogenous sediments WF and W_1F are identical.
[f] Attenuated for grain size.

Appendix 7.2 Alpha counting data

Sample code (Aber/…)	Count time (ks)	Total counts[a]	Pairs[b]	Count rate[c] (cts.cm^{-2}.ks^{-1})
28-IN1	3023.58	2887.72	23.95	0.063 ± 0.002
28-IN3	2081.82	2962.41	77.40	0.094 ± 0.002
28-IN4	1732.56	2985.34	78.06	0.113 ± 0.003
28-IN9	1205.40	3225.76	70.72	0.176 ± 0.003
28-IN11	936.00	3029.02	82.27	0.213 ± 0.004
28-IN12	2076.96	3056.40	79.29	0.097 ± 0.002
28-IN14	1622.04	3076.88	85.78	0.125 ± 0.003
28-IN15	2579.52	3094.08	72.59	0.079 ± 0.002
28-IN16	2058.42	3128.13	81.19	0.100 ± 0.002
28-IN18	2421.42	2971.37	49.61	0.081 ± 0.002
28-IN19	2439.42	3172.01	79.43	0.086 ± 0.002
28-IN20	1239.36	2995.10	43.25	0.159 ± 0.003
28-IN21	1470.48	2942.66	68.76	0.132 ± 0.003
29-BA1	2068.68	3005.56	76.34	0.096 ± 0.002
29-BA2	2615.04	3017.29	69.68	0.076 ± 0.002
29-BA4	1121.28	2993.30	70.96	0.176 ± 0.003
29-BA8	3551.28	2961.99	44.06	0.055 ± 0.001
29-BA10	2167.80	3099.00	73.32	0.094 ± 0.002
29-BA11	1565.70	3419.00	86.16	0.144 ± 0.003
29-BA12	964.26	3172.22	88.03	0.216 ± 0.004
29-BA13	1565.76	3403.00	83.19	0.143 ± 0.003
29-BA14	2058.00	3066.72	57.29	0.098 ± 0.002
40-SA1	3112.14	3120.47	61.81	0.066 ± 0.001
40-SA2	960.12	3233.72	73.86	0.222 ± 0.004
40-SA3	1475.94	2953.56	55.75	0.132 ± 0.003
40-SA4	2677.86	3006.95	60.72	0.074 ± 0.002
40-SA5	795.90	3015.21	46.66	0.249 ± 0.005
40-SA6	1449.78	3266.51	65.20	0.148 ± 0.003
40-SA13	50.46	3227.15	89.55	4.21 ± 0.070
40-SA14	1099.44	9640.79	218.87	0.577 ± 0.006
40-SA15	488.04	4215.82	100.16	0.568 ± 0.009
12-RBM2	703.98	3006.31	51.12	0.281 ± 0.005
12-RBM2a	2488.26	2895.00	61.72	0.077 ± 0.002
12-MAP3	1712.64	3425.50	75.40	0.132 ± 0.002

[a] Background counts have been subtracted.
[b] Random doubles have been subtracted. A worked example of this procedure is found in Appendix 7.1.
[c] Assuming an alpha counting area of 15.2 cm^2.

Appendix 7.3 Beta counting data

Sample code (Aber/...)	Count rates (cts/min)		
	MgO	Shap	Sample
28-IN1	0.18 ± 0.01	12.07 ± 0.09	1.08 ± 0.03
28-IN3	0.25 ± 0.01	12.10 ± 0.09	1.63 ± 0.03
28-IN4	0.24 ± 0.01	12.21 ± 0.09	1.60± 0.03
28-IN9	0.18 ± 0.01	12.07 ± 0.09	1.71 ± 0.03
28-IN11	0.17 ± 0.01	11.73 ± 0.06	2.13 ± 0.03
28-IN12	0.16 ± 0.01	12.07 ± 0.06	1.50 ± 0.02
28-IN14	0.18 ± 0.01	11.47 ± 0.09	1.83 ± 0.04
28-IN15	0.17 ± 0.01	12.01 ± 0.06	1.27 ± 0.02
28-IN16	0.17 ± 0.01	11.89 ± 0.06	1.69 ± 0.02
28-IN18	0.17 ± 0.01	11.78 ± 0.06	1.24 ± 0.02
28-IN19	0.17 ± 0.01	11.60 ± 0.06	1.17 ± 0.02
28-IN20	0.18 ± 0.01	11.56 ± 0.09	2.26 ± 0.04
28-IN21	0.17 ± 0.01	12.33 ± 0.07	1.74 ± 0.02
29-BA1	0.18 ± 0.01	12.33 ± 0.07	2.38 ± 0.03
29-BA2	0.19 ± 0.01	12.03 ± 0.09	1.64 ± 0.03
29-BA4	0.16 ± 0.01	12.36 ± 0.07	1.98 ± 0.03
29-BA8	0.17 ± 0.01	11.98 ± 0.09	2.77 ± 0.04
29-BA10	0.17 ± 0.01	12.17 ± 0.07	3.43 ± 0.03
29-BA11	0.17 ± 0.01	12.43 ± 0.09	2.25 ± 0.04
29-BA12	0.16 ± 0.01	12.59 ± 0.09	2.87 ± 0.04
29-BA13	0.15 ± 0.01	12.36 ± 0.07	2.00 ± 0.03
29-BA14	0.15 ± 0.01	12.38 ± 0.07	2.34 ± 0.03
40-SA1	0.16 ± 0.01	11.36 ± 0.06	0.70 ± 0.02
40-SA2	0.15 ± 0.01	11.33 ± 0.06	1.84 ± 0.03
40-SA3	0.18 ± 0.01	10.99 ± 0.05	1.10 ± 0.02
40-SA4	0.16 ± 0.01	11.01 ± 0.05	0.41 ± 0.01
40-SA5	0.16 ± 0.01	11.45 ± 0.06	1.04 ± 0.02
40-SA6	0.16 ± 0.01	11.43 ± 0.06	0.62 ± 0.01
40-SA13	0.32 ± 0.01	12.44 ± 0.09	8.70 ± 0.08
40-SA14	0.18 ± 0.01	11.85 ± 0.09	2.45 ± 0.04
40-SA15	0.16 ± 0.01	11.99 ± 0.09	2.34 ± 0.04
12-RBM2	0.17 ± 0.01	11.63 ± 0.09	1.84 ± 0.04
12-RBM2a	0.17 ± 0.01	12.28 ± 0.09	1.38 ± 0.03
12-MAP3	0.16 ± 0.01	11.91 ± 0.09	0.89 ± 0.02

During each counting run, three aliquots of sample and one aliquot each of MgO and the Shap standard were counted. The samples were run over a period of two years, and demonstrate the stability of the system. The MgO count rate for Aber/40-SA13 is significantly larger than that for other samples. Replacing the measured MgO count rate with a more normal value of 0.17 ± 0.01 cts/min results in a small increase in calculated environmental dose rate (0.007 Gy/ka) attributable to a small increase in the calculated potassium content (0.029%).

Appendix 8.1 Radiocarbon calibration

The radiocarbon ages presented by Ramsay (1995) have been corrected for the apparent age of seawater. Although the exact nature of this correction is not stated, it is likely to be a correction for the apparent age of local seawater. This correction consists of two components, the apparent age of world seawater (R_t, c.400 years) and an additional regional correction factor (ΔR). It is not appropriate to calibrate the corrected radiocarbon ages presented by Ramsay (1995), since the INTCAL98 calibration curve contains a correction for the apparent age of world seawater, R_t (Stuiver *et al.*, 1998). Consequently, calibrating these ages would subtract R_t twice. But, ΔR must be subtracted from the uncorrected conventional radiocarbon age prior to calibration. Therefore, R_t must be added to the ages presented by Ramsay (1995), prior to calibration. Unfortunately this value is time dependent, varying by about ±100 radiocarbon years, due to lags in the oceanic response to changing atmospheric radiocarbon production. However, a constant value of 400 radiocarbon years has been used for R_t, since it is likely that the correction for the apparent age of local seawater performed by Ramsay (1995) is also constant. Consequently, the calibrated radiocarbon ages produced in this study must be regarded as approximate. It is worth noting however, that the maximum error in R_t, is smaller than the change in age caused by calibration. This suggests that the calibrated dataset, while imperfect, is likely to be more appropriate for comparison with the OSL ages than the uncalibrated one. Uncalibrated and calibrated ages are given in Table A8.1.1 overleaf.

A worked example

A worked example of the calibration process, using sample Pta-6429, is presented below.

Uncalibrated age (from Ramsay, 1995)	3360 ± 60
Uncalibrated age (correction for apparent age of seawater subtracted)	3760 ± 60
Calibrated age range (2 σ)	3530-3850

The chart used to produce this calibrated age is shown in Figure A8.1.1.

Sample number	Age (^{14}C yr B.P.)	Calibrated age (2 σ range, yr B.P.)
?	910 ± 120	640 - 1110
?	920 ± 140	600 - 1200
Pta-4972	1610 ± 70	1390 - 1740
Pta-6429	3360 ± 60	3530 - 3850
Pta-6300	3740 ± 60	4020 - 4390
Pta-5052	3780 ± 60	4080 - 4410
Pta-6297	4350 ± 60	4840 - 5210
Pta-6252	4480 ± 70	4950 - 5340
Pta-6191	4650 ± 60	5280 - 5550
Pta-4998	4660 ± 50	5300 - 5540
Pta-6428	6460 ± 80	7220 - 7510
Pta-6431	7840 ± 90	8510 - 8940
Pta-4469	8950 ± 80	9600 - 10350

Table A8.1.1. Uncalibrated (from Ramsay, 1995) and calibrated radiocarbon ages used to produce Figure 8.10.

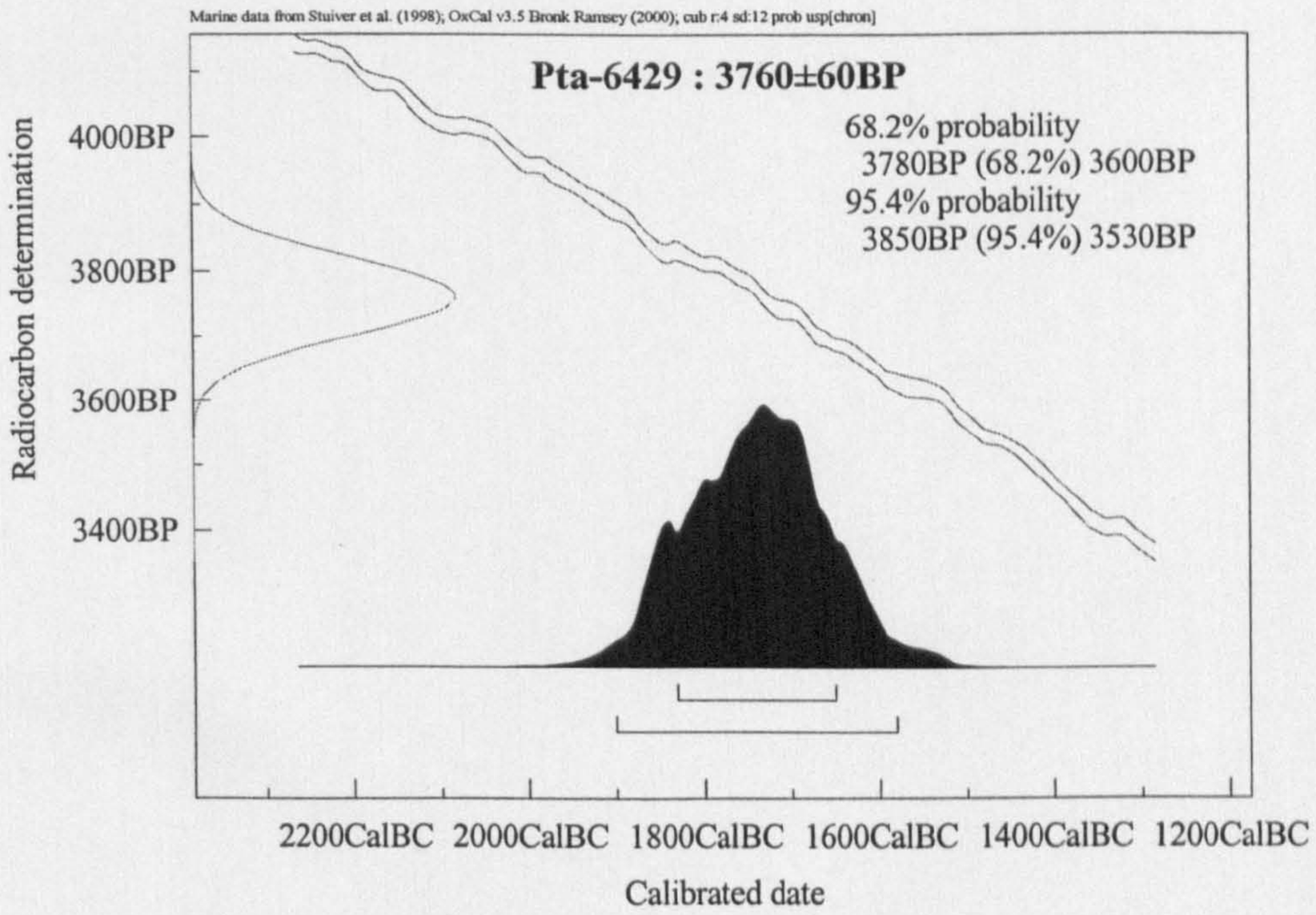

Figure A8.1.1. A plot, produced by OxCal v3.5, showing the calibration of the age for sample Pta-6429. The Gaussian distribution on the y-axis represents the uncalibrated radiocarbon age, minus the correction for the apparent age of seawater. This distribution is projected onto the INTCAL98 marine calibration curve (the pair of lines across the middle of the plot), to produce a probability density function (on the x-axis) of the calibrated ages. The 2σ (95.4% probability) range of these values were been used to produce the calibrated radiocarbon age in Figure 8.10.